

THE USE OF UPCONVERTING NANOPARTICLES TO DRIVE ORGANIC PHOTOREACTIONS

by

Carl-Johan Carling
M. Sc., Lund University/Queen's University, 2007

THESIS SUBMITTED IN PARTIAL FULFILLMENT OF
THE REQUIREMENTS FOR THE DEGREE OF

DOCTOR OF PHILOSOPHY

In the
Department of Chemistry
Faculty of Science

© Carl-Johan Carling 2012
SIMON FRASER UNIVERSITY
Summer 2012

All rights reserved. However, in accordance with the *Copyright Act of Canada*, this work may be reproduced, without authorization, under the conditions for *Fair Dealing*. Therefore, limited reproduction of this work for the purposes of private study, research, criticism, review and news reporting is likely to be in accordance with the law, particularly if cited appropriately.

APPROVAL

Name: Carl-Johan Carling
Degree: Doctor of Philosophy
Title of Thesis: *The Use of Upconverting Nanoparticles to Drive Organic Photoreactions*

Examining Committee:

Chair: **Dr. Krzysztof Starosta**
Associate Professor

Dr. Neil Branda
Senior Supervisor
Professor

Dr. Gary Leach
Supervisor
Associate Professor

Dr. Robert Britton
Supervisor
Associate Professor

Dr. Tim Storr
Internal Examiner, Department of Chemistry
Assistant Professor

Dr. Peter Chun-Fu Wan
External Examiner
Professor, Department of Chemistry
University of Victoria

Date Defended: August 27, 2012

Partial Copyright Licence



The author, whose copyright is declared on the title page of this work, has granted to Simon Fraser University the right to lend this thesis, project or extended essay to users of the Simon Fraser University Library, and to make partial or single copies only for such users or in response to a request from the library of any other university, or other educational institution, on its own behalf or for one of its users.

The author has further granted permission to Simon Fraser University to keep or make a digital copy for use in its circulating collection (currently available to the public at the "Institutional Repository" link of the SFU Library website (www.lib.sfu.ca) at <http://summit/sfu.ca> and, without changing the content, to translate the thesis/project or extended essays, if technically possible, to any medium or format for the purpose of preservation of the digital work.

The author has further agreed that permission for multiple copying of this work for scholarly purposes may be granted by either the author or the Dean of Graduate Studies.

It is understood that copying or publication of this work for financial gain shall not be allowed without the author's written permission.

Permission for public performance, or limited permission for private scholarly use, of any multimedia materials forming part of this work, may have been granted by the author. This information may be found on the separately catalogued multimedia material and in the signed Partial Copyright Licence.

While licensing SFU to permit the above uses, the author retains copyright in the thesis, project or extended essays, including the right to change the work for subsequent purposes, including editing and publishing the work in whole or in part, and licensing other parties, as the author may desire.

The original Partial Copyright Licence attesting to these terms, and signed by this author, may be found in the original bound copy of this work, retained in the Simon Fraser University Archive.

Simon Fraser University Library
Burnaby, British Columbia, Canada

ABSTRACT

One of the primary disadvantages of organic photochemistry is the need for high-energy UV light, light that has many detrimental qualities. A viable solution to this problem is the use of upconverting nanoparticles (UCNP) that can locally convert near infrared (NIR) laser light into UV light or visible light of sufficient energy to drive organic photoreactions.

In an initial study (*Chapter 3*), the use of UCNPs to drive both UV and visible light dependent photoreactions with NIR light was demonstrated using 1,2-dithienylethene (DTE) molecular switches functioning as probes. In this study the concept of NIR-to-visible 'remote-control' photorelease was also introduced.

In a second study (*Chapter 4*), two multicolour UCNPs were developed. It was demonstrated that by only altering the power-density of the one wavelength NIR excitation source, the photochemistry of two DTE molecular switches could be selectively and bi-directionally driven along its two reaction pathways.

In a third study (*Chapter 5*), fluorescence modulation bioimaging was demonstrated *in vivo* in *C. elegans* nematodes. The fluorescence modulation in aqueous medium was achieved by decorating the surface of an UCNP with polyethylene glycol functionalized DTE molecular switches by 'click' chemistry.

In a fourth study (*Chapter 6*), multimodal fluorescence modulation of a multicolour UCNP by two DTE molecular switches decorated on the surface of

the UCNP was demonstrated. Apart from a greater degree of control in this more advanced system, it is also capable of NIR-to-UV 'remote-control' photoswitching.

In a fifth study (*Chapter 8*), the surface of an UCNP was decorated with 3',5'-dialkoxybenzoin photocages and the concept of NIR-to-UV 'remote-control' photorelease for potential use in drug-delivery was demonstrated.

In a sixth study (*Chapter 9*), a fully water dispersible drug-delivery system was synthesized. Unfortunately the system proved impractical due to the choice of both photorelease system and therapeutic payload.

In a seventh study (*Chapter 10*), a donor-acceptor 4-dimethylamino-3',5'-dimethoxybenzoin photocage with both red-shifted absorbance and a significantly enhanced molar absorbance coefficient was synthesized and its initial and unique photochemistry was studied.

Keywords: UCNP; upconversion; 'remote-control'; NIR-to-UV; NIR-to-visible; DTE; photochromism; photochromism-gated reactivity; 3',5'-dimethoxybenzoin; photorelease; PEG; fluorescence modulation

DEDICATION

To the earth, my extended family and friends.

ACKNOWLEDGEMENTS

I would firstly like to thank my senior supervisor Prof. Neil Branda for all your support throughout my degree.

I would also like to thank my colleague Dr. Chris Boyer for an amazing collaboration.

I further want to acknowledge the members of my supervisory committee Prof. Rob Britton and Prof. Gary Leach for all the support you have provided throughout my degree.

I am also very grateful to all my collaborators and co-authors for with whom I would not have been able to accomplish what we did and almost did. Dr. Chris Boyer, Prof. Farahnaz Nourmohammadian, Danielle Wilson, Chad Warford, Shu Yi Chua, Dr. Seon-Jeong Lim, Dr. Matt Roberts, Dennis Hsaio, Amir Asadirad, Tony Wu, Madeleine Barker, Prof. Byron Gates, Prof. Michael Wolf and Prof. David Baillie.

I would also like to thank all the technicians at SFU that have helped me throughout the years. Dr. Andrew Lewis, Dr. Colin Zhang, Dr. Hongwen Chen, Bruce Harwood and Dr. Saeid Kamal.

I further want to thank all the staff at SFU chemistry department especially Lynn Wood, Yolanda Broderick, Evon Khor, Prof. Nabyl Merbouh, Prof. Lee Hanlan, Prof. Tim Storr, Prof. Peter Wilson, Prof. David Voadlo and Prof. Charles Walsby.

I would also like to thank all my friends and colleagues at SFU and 4D-Labs that have contributed positively to my time at SFU.

I further want to thank all the members of the Branda lab, both present and past.

I would like to thank Steve Hutchinson and Chad Warford for proof reading my thesis.

I also would like to thank my past supervisors Prof. Kenneth Wärnmark and Prof. Bob Lemieux for all the things you have done for me.

I would also like to thank Sixten Gémzeus Stiftelse for financial support.

I further want to thank my extended family for all the support and love.

Lastly I would like to thank all my friends and loved ones. Thanks for all the great times I love you all.

TABLE OF CONTENTS

Approval.....	ii
Abstract.....	iii
Dedication.....	v
Acknowledgements.....	vi
Table of Contents.....	viii
List of Figures.....	xii
List of Schemes.....	xxix
List of Tables.....	xlvi
Glossary.....	xlviii
1: Introduction to the Thesis.....	1
1.1 'Remote-control' photochemistry.....	1
1.2 Photon upconverting nanoparticles.....	3
1.2.1 Upconversion.....	3
1.2.2 Applications of upconverting nanoparticles.....	6
1.3 Upconverting nanoparticles and organic photochemistry.....	8
1.3.1 Structure of the thesis.....	9
2: Photochromism.....	11
2.1 Thermal (T-type) photochromism.....	12
2.2 Photochemical (P-type) photochromism.....	14
2.3 The dithienylethene P-type photochromic molecular switch.....	16
2.3.1 Design of the DTE chromophore.....	17
2.3.2 The ring-closing reaction and the ring-closed isomer.....	18
2.3.3 The ring-opening reaction.....	21
2.3.4 Multiphoton photoswitching.....	22
2.3.5 Applications of the DTE class.....	23
2.3.6 Outlook.....	28
3: Remote-Control Photoswitching Using NIR Light.....	29
3.1 Contributions.....	29
3.2 Abstract.....	29
3.3 Introduction.....	30
3.4 Results and Discussion.....	32
3.5 Conclusion.....	36
3.6 Acknowledgement.....	36
3.7 Experimental.....	37
3.7.1 General methods.....	37
3.7.2 Synthetic procedures.....	38
3.7.3 Preparation of solid-state films.....	41

3.7.4	Transmission Electron Microscopy (TEM)	44
3.7.5	Powder X-ray Diffraction (XRD)	44
3.7.6	Visible Room Temperature Upconversion Emission Spectroscopy($\lambda_{\text{exc}} = 980 \text{ nm}$)	45
3.7.7	Photoswitching and Photochemistry	46
4: Two-Way Photoswitching Using One Type of NIR Light, Upconverting Nanoparticles and Changing Only the Light Intensity		50
4.1	Contributions	50
4.2	Abstract	50
4.3	Introduction	51
4.4	Results and discussion	59
4.4.1	Choice and Synthesis of DTEs and Nanoparticles	59
4.4.2	Optical Properties of UCNPs	64
4.4.3	'Remote-Control' Photoswitching of DTE derivatives	68
4.5	Conclusion	73
4.6	Acknowledgement	74
4.7	Experimental	74
4.7.1	General methods	74
4.7.2	Synthetic procedures	76
4.7.3	Powder X-ray Diffraction	84
4.7.4	Transmission Electron Microscopy	84
4.7.5	Spectroscopic measurements	90
5: Photomodulation of Fluorescent Upconverting Nanoparticle Markers in Live Organisms by Using Molecular Switches		92
5.1	Contributions	92
5.2	Abstract	93
5.3	Introduction	93
5.4	Results and discussion	96
5.5	Conclusion	105
5.6	Acknowledgments	105
5.7	Experimental	107
5.7.1	General methods	107
5.7.2	Synthesis	111
5.7.3	Biological Experiments	123
6: Multimodal Fluorescence Modulation Using Molecular Photoswitches and Upconverting Nanoparticles		126
6.1	Contributions	126
6.2	Abstract	126
6.3	Introduction	127
6.4	Results and discussion	131
6.4.1	Synthesis of dithienylethene ligands and decorated nanoparticles	131
6.4.2	Absorption spectroscopy and selective quenching of emission	132
6.4.3	Selective photochromism and quenching in the mixed system	140
6.4.4	'Remote-control' ring-closing	147
6.5	Conclusions	148

6.6	Acknowledgements.....	149
6.7	Experimental.....	150
6.7.1	General methods	150
6.7.2	Synthesis	153
6.7.3	Calculation of loading.....	160
6.7.4	Spectroscopy and photographs	163
7:	Light-Triggered Release.....	182
7.1	Common UV light triggered photocages.....	184
7.1.1	The 2-nitrobenzyl photocage	184
7.1.2	The coumarin photocage	185
7.1.3	The 3',5'-dialkoxybenzoin photocage.....	186
7.1.4	The p-hydroxyphenacyl photocage.....	187
7.1.5	The hydroxy-cinnamoyl photocage	188
7.1.6	Other UV light triggered photocages.....	189
7.2	Visible light triggered photocages.....	191
7.3	The 3',5'-dialkoxybenzoin photocage	194
7.3.1	Photolysis mechanism of 3',5'-dialkoxybenzoin in organic solvent.....	195
7.3.2	Photosolvolytic mechanism of 3',5'-dialkoxybenzoin in water.....	196
8:	'Remote-Control' Photo-Release of 'Caged' Compounds Using Near Infrared Light and Upconverting Nanoparticles	199
8.1	Contributions.....	199
8.2	Abstract.....	200
8.3	Introduction	200
8.4	Results and discussion	204
8.5	Conclusion	208
8.6	Acknowledgement	209
8.7	Experimental.....	209
8.7.1	General methods	209
8.7.2	Synthetic procedures	211
8.7.3	Powder X-ray Diffraction	213
8.7.4	Transmission Electron Microscopy (TEM)	214
8.7.5	Estimating the loading of 'cage' 1a onto NaYF ₄ :TmYb nanoparticles.....	215
8.7.6	Photolysis experiments	217
9:	Development of a Multifunctional Theranostic Drug-Delivery System	220
9.1	Contributions.....	220
9.2	Introduction	220
9.3	Development of ligand attachment systems and water-dispersible upconverting nanoparticles – a historical perspective about the development process	222
9.3.1	Introduction	222
9.3.2	PEGylated bis-carboxylate anchor.....	223
9.3.3	Phosphate/phosphonate anchor	224
9.3.4	Surface functionalization through 'click' chemistry.....	225
9.4	Development of a functional drug-release system part 1	226
9.4.1	Choice of anti-cancer drug	226
9.4.2	First-generation drug-delivery system.....	227

9.4.3	Tuning of the absorption-emission overlap	228
9.5	Development of a functional drug-release system part 2	230
9.5.1	Introduction	230
9.5.2	Results and discussion	231
9.5.3	Synthesis of the second generation drug delivery system 5-NP.....	231
9.5.4	Characterization of organic-nanoparticle hybrid system	237
9.5.5	Stability of the hybrid organic-nanoparticles (5-NP) in physiological medium	238
9.5.6	Emission of the PEGylated nanoparticles in water and acetonitrile.....	240
9.5.7	One photon photoreactivity of 5 and 5-NP.....	241
9.5.8	Multiphoton NIR-to-UV 'remote-control' photoreactivity of 5-NP.....	242
9.5.9	Phototriggered release from 5-NP, detection of Chlorambucil.....	248
9.6	Conclusion	255
9.7	Future directions	257
9.7.1	Release system	257
9.7.2	Therapeutic drug.....	260
9.7.3	Ligands for selective targeting and remote detection	261
9.8	Experimental.....	262
9.8.1	General methods	262
9.8.2	Synthesis of organic molecules and organic-nanoparticle hybrid systems.....	266
9.8.3	Photochemistry of 5, 5-NP and 22-NP.....	284
10: The Preliminary Photochemistry of a Novel Donor-Acceptor 4- Dimethylamino-3',5'-Dimethoxybenzoin Photocage		286
10.1	Contributions.....	286
10.2	Introduction	286
10.3	Results and Discussion	287
10.3.1	Synthesis	288
10.3.2	Comparison of photocages 1, 2 and 3.....	289
10.3.3	NIR-to-UV 'remote-control' photolysis of photocage 1.....	294
10.4	Conclusion	295
10.5	Experimental.....	296
10.5.1	General methods	296
10.5.2	Synthesis	298
11: Conclusions and outlook.....		308
12: Appendices		313
12.1	NMR spectra of new compounds from <i>Chapter 3</i>	313
12.2	NMR spectra of new compounds from <i>Chapter 5</i>	315
12.3	NMR spectra of new compounds from <i>Chapter 9</i>	320
12.4	NMR spectra of new compounds from <i>Chapter 10</i>	328
12.5	Curriculum vitae.....	333
References and notes.....		338

LIST OF FIGURES

Figure 1.1	(a) Schematic 3D representation of an energy transfer upconversion UCNP co-doped with both absorber ions and emitter ions. (b) Non-comprehensive Dieke diagram representation of energy transfer upconversion.	6
Figure 2.1	Common design of a DTE molecular switch.....	17
Figure 2.2	Transition state orbital symmetry in the S_1 -excited state according to the Woodward-Hoffman rules and photochemical reaction schemes for the (a) ring-closing and (b) ring-opening reactions and a schematic representation of the potential energy surfaces along the reaction coordinates of the photochromic reactions of the DTE molecular switch. ^[46]	20
Figure 2.3	Thermal stability of the ring-closed isomer of various diarylethene derivatives.....	21
Figure 3.1	Emission spectra of colloidal CHCl_3 solutions of (a) $\text{NaYF}_4:\text{TmYb}$ and (b) $\text{NaYF}_4:\text{ErYb}$ UCNPs when excited with a 980 nm laser diode. ^[69] The light used to trigger photoswitch 1 is highlighted. TEM images are shown as insets. Changes in the UV-vis absorption spectra (left) and photographs (right) of acrylate films ($12 \times 8 \times 1$ mm) containing (c) 1a + $\text{NaYF}_4:\text{TmYb}$, and (d) 1b + $\text{NaYF}_4:\text{ErYb}$ as they are irradiated with 980 nm light. The stripes observed in the right panel of (c) and (d) correspond to the direction of the beam of the 980 nm laser. ^[69] The irradiation in (c) was carried out two times with perpendicular orientations. The small squares in all images are the cut-out holes in the sample holder through where the absorption was measured.	33
Figure 3.2	(a) Scheme illustrating the ring-opening and release reactions of bicyclic compound 2b as it is irradiated with visible or NIR light. (b) Changes in the UV-vis absorption spectra (left) and photographs (right) of an acrylate film ($8 \times 7 \times 1$ mm) containing 2b + $\text{NaYF}_4:\text{ErYb}$ as it is irradiated with 980-nm light. The stripe observed in the right panel corresponds to the direction of the beam of the 980-nm laser.	36
Figure 3.3	Transmission Electron Microscopy (TEM) micrographs of (a) $\text{NaYF}_4:\text{TmYb}$ and (b) $\text{NaYF}_4:\text{ErYb}$ nanoparticle samples.....	44
Figure 3.4	Powder X-ray diffraction (XRD) patterns for (a) $\text{NaYF}_4:\text{TmYb}$ and (b) $\text{NaYF}_4:\text{ErYb}$ nanoparticle samples and (c) $\beta\text{-NaYF}_4$ JCPDS standard card #28-1192.....	45

Figure 3.5	Luminescence upconversion emission spectra of 1 wt-% colloidal solutions of (a) NaYF ₄ :TmYb and (b) NaYF ₄ :ErYb nanoparticle samples in CHCl ₃ excited with a 980 nm laser diode (Power Density = 150 W/cm ²). The inset in (b) shows the total upconversion luminescence of a dispersion of NaYF ₄ :ErYb when stimulated with a 980 nm diode laser.	46
Figure 3.6	Changes in the UV-vis absorption spectra of a CH ₃ CN solution (2.1 × 10 ⁻⁵ M) of 1a as it is irradiated with 365 nm light until the photostationary state is reached. The images on the right illustrate how the photoswitch retains its activity when cast in a polyacrylate film.	47
Figure 3.7	Sample of compound 1a and NaYF ₄ :TmYb cast in an acrylate film (a) before, (b) during and (c) after exposure to 980 nm light. Sample of compound 1b and NaYF ₄ :ErYb cast in an acrylate film (d) before, (e) during and (f) after exposure to 980 nm light. (g) Changes in the UV-vis absorption spectra and images of an acrylate film containing only 1b before (left) and after (right) being irradiated with 980 nm light.	48
Figure 3.8	(a) Sample of compound 1 and NaYF ₄ :TmYb cast in a PMMA gel showing coloured lines due to ring-closing induced by 980 nm light. The lines represent the direction of the laser beam. The bulk composites gels were prepared using the colloidal stock nanoparticle dispersion in CHCl ₃ . The appropriate amount of the stock dispersion was added to a 4 dram screw top vial. Poly(ethylene glycol)-monooleate (typical M _n = 860) (0.15 g) was added to vial and the CHCl ₃ was removed under vacuum using a rotary evaporator. Methyl methacrylate (3.85 g) and 1a (2 mg) were then added to the vial and the resulting dispersion was sonicated for 2 min to obtain a clear dispersion. Azobisisobutyronitrile (AIBN) radical initiator (<1% (w/w)) was subsequently added to the dispersion and sonicated for 30 s. The monomer solution was then transferred to a 1 dram screw top vial with the dimensions 60 mm × 15 mm (length × diameter), which was then sealed. The vial was placed in a 70 °C oil bath for 30 min to initiate the polymerization process and subsequently transferred to a 45–50 °C oven until the polymerization was complete. A transparent NP-1a-PMMA composite rod was obtained by breaking the glass vial. (b) A drop-cast sample of 1 in PMMA before (top) and after (bottom) irradiation with 980 nm light. The sample was prepared by dissolving 1 (1.6 mg) and NaYF ₄ :ErYb (303 mg of a 1.7 wt-% solution in chloroform) in 88 mg of a solution made from PMMA (17.5 mg) and acetone (894 mg). One drop of the solution was spin-cast onto a glass slide (15 × 25 mm; 10 s gradient to 200 rpm, 200 rpm 1 min) using Laurell WS-400A6NPP/LITE spincoater. (c) Experimental set-up showing how the glass plate was exposed to 980 nm light.	49

Figure 4.1	<p>The ‘<i>direct</i>’ photoreactions of the DTE derivatives used in this study are triggered by UV light (for ring-closing) and visible light (for ring-opening). These reactions can also be triggered in a ‘<i>remote-control</i>’ process using the UV light generated under high excitation power densities and the visible light generated under low excitation power densities when the <i>core-shell-shell</i> UCNPs (ErTm and TmEr) absorb near-infrared light (980 nm). The sizes of the coloured arrows represent the relative amount of each type of light excited or emitted during the multi-photon process.</p>	58
Figure 4.2	<p>TEM images of the <i>core</i>, <i>core-shell</i>, and <i>core-shell-shell</i> nanoparticles for NaYF₄:ErYb–NaYF₄ (Er), NaYF₄:TmYb–NaYF₄ (Tm), NaYF₄:ErYb–NaYF₄:TmYb–NaYF₄ (ErTm) and NaYF₄:TmYb–NaYF₄:ErYb–NaYF₄ (TmEr) UCNPs illustrating their uniform size and shape.</p>	64
Figure 4.3	<p>UV-vis absorption spectra of THF solutions (1.5×10^{-5} M) of (a) 1o and (b) 2o before (solid line) and after irradiation with 365 nm light (dashed line) for 2 min. Emission spectra of THF solutions (1.5 wt-%, $\lambda_{\text{ex}} = 980$ nm) of (c) NaYF₄:ErYb (Er) and (d) NaYF₄:TmYb (Tm) <i>core-shell</i> UCNPs, and of (e) ErTm and (f) TmEr <i>core-shell-shell</i> UCNPs at high power (500 W/cm², top graph) and low power (15 W/cm², bottom graph). The shaded, colored regions in all cases represent each emission region and show the suitable spectral overlap with the appropriate absorption bands for the ring-open and ring-closed isomers of DTEs 1 and 2.</p>	66
Figure 4.4	<p>Changes in the absorbances ($\lambda_{\text{max}} = 632$ and 601 nm for 1c and 2c, respectively) when THF solutions of (a) DTEs 1o and 2o containing NaYF₄:TmYb nanoparticles (Tm) are irradiated with 980 nm light at high excitation power densities (500 W/cm²), and (b) DTEs 1c and 2c containing NaYF₄:ErYb (Er) nanoparticles are irradiated with 980 nm light at low excitation power densities (15 W/cm²). The horizontal lines show the absorbance values when similar solutions are irradiated with UV light (313 nm) for graph ‘a’ or visible light (> 450 nm) for graph ‘b’ until the photostationary states are obtained. (c) The degree to which the ring-closing and ring-opening reactions are induced with 980 nm light (high power for the former and low power for the latter) using the different types of nanoparticles.</p>	70
Figure 4.5	<p>Bidirectional photoswitching of a THF solution of DTE 2 dispersed with TmEr <i>core-shell-shell</i> nanoparticles by varying only the intensity of the NIR light. The plot shows the absorption intensities corresponding to the ring-closed isomers (632 nm for 1c and 601 nm for 2c) as solutions of the photoswitches and the <i>core-shell-shell</i> nanoparticles are exposed to alternating intensities of 980 light. The colors correspond to the light emitted by the nanoparticles (green at low power and blue at high power).</p>	72

Figure 4.6	Powder X-ray diffraction (XRD) patterns for (a) NaYF ₄ :ErYb-NaYF ₄ <i>core-shell</i> nanoparticles, (b) NaYF ₄ :TmYb-NaYF ₄ <i>core-shell</i> nanoparticles, (c) NaYF ₄ :ErYb-NaYF ₄ :TmYb-NaYF ₄ <i>core-shell-shell</i> nanoparticles, (d) NaYF ₄ :TmYb-NaYF ₄ :ErYb-NaYF ₄ <i>core-shell-shell</i> nanoparticles and (f) β-NaYF ₄ JCPDS standard card #28-1192.	84
Figure 4.7	Transmission Electron Microscopy (TEM) micrographs of (top) NaYF ₄ :ErYb nanoparticles and (bottom) NaYF ₄ :ErYb-NaYF ₄ <i>core-shell</i> nanoparticles.....	86
Figure 4.8	Transmission Electron Microscopy (TEM) micrographs of (top) NaYF ₄ :TmYb nanoparticles and (bottom) NaYF ₄ :TmYb-NaYF ₄ <i>core-shell</i> nanoparticles.....	87
Figure 4.9	Transmission Electron Microscopy (TEM) micrographs of (top) NaYF ₄ :ErYb nanoparticles, (middle) NaYF ₄ :ErYb-NaYF ₄ :TmYb <i>core-shell</i> and (bottom) NaYF ₄ :ErYb-NaYF ₄ :TmYb-NaYF ₄ <i>core-shell-shell</i> nanoparticles.	88
Figure 4.10	Transmission Electron Microscopy (TEM) micrographs of (top) NaYF ₄ :TmYb nanoparticles, (middle) NaYF ₄ :TmYb-NaYF ₄ :ErYb <i>core-shell</i> and (bottom) NaYF ₄ :TmYb-NaYF ₄ :ErYb-NaYF ₄ <i>core-shell-shell</i> nanoparticles.	89
Figure 4.11	UV-vis absorption spectra of THF solutions (1.5 × 10 ⁻⁵ M) of (left) 1o and (right) 2o containing 1.5 wt% NaYF ₄ :TmYb nanoparticles (Tm) before (black line) and after irradiation with either 365 nm light (blue line) or 980 nm light at high excitation power densities (500 W/cm ²).	91
Figure 4.12	Emission spectra of THF solutions of the TmEr (left) and ErTm <i>core-shell-shell</i> nanoparticles as they are exposed to the higher-power NIR laser light (980 nm, 500 W/cm ²) used in the experiments. The lack of any spectral changes (all three spectra overlap) after 1 h highlights the stability of the nanoparticles.	91
Figure 5.1	Synthesis of the photoresponsive hybrid system (1o[NaF ₄ :ErYb]) and a conceptual description of selective quenching of the emission from the nanoparticles by ring-closing the photoswitch. The images are TEM micrographs showing (a) the oleate coated nanoparticle starting material, (b) the azide coated nanoparticles and (c) the nanoparticles decorated with the ring-open form of the photoswitch (1o[NaF ₄ :ErYb]) illustrating their uniform size and shape.....	95
Figure 5.2	(a) UV-vis absorption and emission spectra (λ _{ex} = 980 nm, 150 W/cm ²) of an aqueous solution (9.0 × 10 ⁻⁶ M) of 1o[NaF ₄ :ErYb] before (solid line/dark shading) and after irradiation with 365 nm light (dashed line/light shading) for 2.5 min (1.3 mW/cm ²). (b) Changes in the absorbance at 530 nm (black circles), and emission intensities at 538 nm (green diamonds) and 652 nm (red diamonds) of a similar solution of 1o[NaYF ₄ :ErYb] when it is alternately irradiated with UV and visible light. (c) Changes	

	in the absorbance at 530 nm of a similar solution of 1c[NaYF ₄ :ErYb] when it is continuously irradiated with 980 nm light.....	101
Figure 5.3	Optical (left) and two-photon upconversion fluorescence (middle and right) microscopy images of wild-type N2 <i>C. elegans</i> incubated with 1o[NaYF ₄ :ErYb] (0.25 mg of a 0.5 mg/mL solution in M9 buffer) showing the changes in fluorescence due to the photoswitching of the DTE component within the bodies of the worms. The middle panel shows the strong initial fluorescence prior to exposure to UV light. The right panel shows the reduced emission that is a result of ring-closing the photoswitch with 365 nm light for 2.5 minutes.....	104
Figure 5.4	(a) Transmission Electron Microscopy (TEM) micrograph of oleate-coated NaYF ₄ :ErYb nanoparticles. (b) High-angle annular dark-field (HAADF) image of NaYF ₄ :ErYb nanoparticles (c) Powder X-ray diffraction (XRD) patterns for (top) NaYF ₄ :ErYb nanoparticles and (bottom) β-NaYF ₄ JCPDS standard card #28-1192. (d) Selected area electron diffraction (SAED) pattern of the NaYF ₄ :ErYb nanoparticles.	118
Figure 5.5	Transmission Electron Microscopy (TEM) micrographs of (a) oleate-coated NaYF ₄ :ErYb nanoparticles, (b) azide-coated NaYF ₄ :ErYb nanoparticles and (c) “clicked” NaYF ₄ :ErYb nanoparticles.	120
Figure 5.6	Size histograms (diameter) from TEM micrographs for (a) oleate-coated NaYF ₄ :ErYb nanoparticles, (b) azide-coated NaYF ₄ :ErYb nanoparticles and (c) “clicked” NaYF ₄ :ErYb nanoparticles.	120
Figure 5.7	Size histograms (diameter) from DLS results for (a) oleate-coated NaYF ₄ :ErYb nanoparticles, (b) azide-coated NaYF ₄ :ErYb nanoparticles and (c) “clicked” NaYF ₄ :ErYb nanoparticles.	121
Figure 5.8	Selected region of the FTIR spectra for (a) oleate-coated NaYF ₄ :ErYb nanoparticles, (b) azide-coated NaYF ₄ :ErYb nanoparticles and (c) “clicked” NaYF ₄ :ErYb nanoparticles.....	121
Figure 5.9	UV-vis absorption spectra for aqueous solutions of (a) ligand 1 and (b) the decorated nanoparticles (1[NaYF ₄ :ErYb]) in their original ring-open (black lines) and photostationary (red lines). The photostationary states were generated by irradiating the solutions with 365 nm light until no more changes were observed. The changes in the spectra when the complexes are exposed to (c) UV (365 nm) and (d) visible light. (e) Summary of the changes in absorbance over time.	122
Figure 5.10	(a) UV-vis absorption cycling data for aqueous solutions of the decorated nanoparticles (1[NaYF ₄ :ErYb]). (b) Emission spectra (λ _{ex} = 980 nm, 150 W/cm ²) for cycling experiments of an aqueous solution of 1[NaF ₄ :ErYb]. (c) UV-vis absorption spectra for an aqueous solution of the decorated nanoparticles	

	(1[NaYF ₄ :ErYb]) before and after 90 minutes of continuously irradiated with 980 nm light (150 W/cm ²). (d) Percent quenching versus wavelength for an aqueous solutions of the decorated 1c[NaYF ₄ :ErYb] nanoparticles (black diamonds) superimposed on the green and red emissions.....	123
Figure 5.11	Optical (left) and two-photon upconversion fluorescence (middle and right) microscopy images of wild-type N2 <i>C. elegans</i> incubated with 1o[NaYF ₄ :ErYb] showing the changes in fluorescence due to the photoswitching of the DTE component within the bodies of the worms. The middle panels show the strong initial fluorescence prior to exposure to UV light. The right panels show the reduced emission that is a result of ring-closing the photoswitch with 365 nm light for 2.5 minutes. The difference between the two samples is the omission (top) or inclusion (bottom) of a washing/centrifugation step in the preparation and accounts for the small changes in background fluorescence.	125
Figure 5.12	The upconverting fluorescence ($\lambda_{\text{ex}} = 980 \text{ nm}$) from the hybrid 1o[NaYF ₄ :ErYb] and 1c[NaYF ₄ :ErYb] from inside the digestive tract of the nematodes obtained with the 2-photon microscope.	125
Figure 6.1	UV-vis absorption spectra of solutions (10 ⁻⁵ M) of two-component systems (a) 1a-NP (THF) and (b) 1b-NP (CH ₂ Cl ₂) before (solid lines) and after irradiation with 365 nm (16 mW/cm ²) light (shaded areas) for 120 s. The spectra for the ligands (3a and 3b) are shown for comparison (dashed lines). The molar concentration refers to the estimated amount of photoswitch in each sample, [□] while the amount of decorated nanoparticle in each solution is 0.05 wt-% for 1a-NP and 0.03 wt-% for 1b-NP. Emission spectra of the same solutions ($\lambda_{\text{ex}} = 980 \text{ nm}$) of (c) 1a-NP and (d) 1b-NP at high 980 nm excitation power (38 W/cm ² , top graphs) and low 980 nm excitation power (2 W/cm ² , bottom graphs) showing how the intensity of specific bands in the original emission spectrum (white areas) are reduced when the photoswitches are converted into their ring-closed forms (shaded areas) based on the overlap with the absorption bands of 1a ^c -NP and 1b ^c -NP.	134
Figure 6.2	Changes in the absorbances at (a) 570 nm when the same solution of 1a-NP used in Figure 6.1(a,c) and (b) 520 nm when the same solution of 1b-NP used in Figure 6.1(b,d) are irradiated alternately with 365 nm light (16 mW/cm ²) for 120 s for 1a-NP and 130 s for 1b-NP (white areas), and > 434 nm (377 mW/cm ²) light for 60 s for 1a-NP and 120 s for 1b-NP (shaded areas). (c–f) Changes in the emission intensities at 471 nm (◆), 537 nm (■) and 651 nm (○) when the same solutions are irradiated under identical conditions at (c,d) high 980 nm excitation power and (e,f) low 980 nm excitation power. [□]	141

Figure 6.3	<p>(a) The UV-vis absorption spectrum of a THF solution of the two-component hybrid system 1ab-NP before (white) and after (dark shaded) irradiation with 365 nm light (16 mW/cm²). The total concentration of chromophore is 10⁻⁵ M (in a 5:4 1a:1b ratio), while the amount of decorated nanoparticle is 0.03 wt-%. The inset shows the time-dependent growth of the absorptions at 570 nm (○) and 520 nm (◆) corresponding to the two ring-closed isomers in 1a^cb^c-NP. (b) The UV-vis absorption spectrum of the same photostationary state before (dark shaded), after irradiation with > 630 nm light (120 mW/cm²) (light shaded) and after irradiation with > 434 nm light (377 mW/cm²) (white). The inset shows the time-dependent changes of the absorptions at 570 nm (○) and 520 nm (◆) during the > 630 nm irradiation, and at 520 nm (□) for a CH₃CN solution of ligand 3b (1.0 × 10⁻⁵ M) when it is irradiated with > 630 nm light.</p>	142
Figure 6.4	<p>Changes in the emission intensities at 471 nm (◆), 537 nm (■) and 651 nm (○) when the same solution of 1ab-NP used in Figure 6.3 is exposed to 365 nm, > 630 nm and > 434 nm light at (a) high 980 nm excitation power and (b) low 980 nm excitation power. (c) Relative areas under the peaks in the emission spectra of the same solution before, (white) and after irradiation with 365 nm light (black) and > 630 nm light (grey). High 980 nm excitation power was used in (c). In each case, the emitting ion is labelled.</p>	146
Figure 6.5	<p>Changes in the UV-vis absorption spectra when (a) a THF solution of 1a-NP (10⁻⁵ M, 0.05 wt-%) and (b) a CH₂Cl₂ solution of 1b-NP (10⁻⁵ M, 0.03 wt-%) are irradiated with 980 nm light (143 W/cm²). The insets show the growth of the absorbances at 570 nm for 1a-NP → 1a^c-NP and 520 nm for 1b-NP → 1b^c-NP corresponding to the ring-closed isomers. The arrows in each inset plot indicate when the excitation light was changed from 980 nm to 365 nm.</p>	148
Figure 6.6	<p>Selected region of the FTIR spectra for (a) azide-coated <i>core-shell-shell</i> NaYF₄:TmYb:ErYb nanoparticles (a-NP), (b) the 2-component nanoparticles 1a-NP, (c) the 2-component nanoparticles 1b-NP, and (d) the mixed 3-component nanoparticles 1ab-NP.</p>	163
Figure 6.7	<p>Changes in the UV-vis absorption spectra when CH₃CN solutions (1 × 10⁻⁵ M) of (a) 3a and (b) 3b are irradiated with 365 nm light (16 mW/cm²). The insets show the growth of the bands at 590 nm for 3a → 3a^c and 520 nm for 3b → 3b^c corresponding to the ring-closed isomers, which are present in 72% for 3a and 56% for 3b in the photostationary states according to ¹H NMR spectroscopy (in CD₂Cl₂). Changes in the UV-vis absorption spectra when the same solutions of the photostationary states of (c) 3a^c and (d) 3b^c are irradiated with > 434 nm light (377 mW/cm²). The insets show the reduction of the bands at 590 nm for 3a^c → 3a and 520 nm for 3b^c → 3b.</p>	

	Changes in the UV-vis absorption spectra when the same solutions of the photostationary states of (e) 3a ^c and (f) 3b ^c are irradiated with > 630 nm light (120 mW/cm ²). The insets show the reduction of the bands at 590 nm for 3a ^c → 3a and 520 nm for 3b ^c → 3b.....	164
Figure 6.8	UV-vis absorption spectra of solutions (10 ⁻⁵ M) of the ligands (a) 3a in CH ₃ CN (black) and THF (blue) and (b) 3b in CH ₃ CN (black) and CH ₂ Cl ₂ (red) before (solid lines) and after irradiation with 365 nm (16 mW/cm ²) light (dashed lines). The spectra were normalized for any small errors in concentration.	165
Figure 6.9	Changes in the UV-vis absorption spectra when (a) a THF solution (1 × 10 ⁻⁵ M, 0.05 wt-%) of 1a-NP and (b) a CH ₂ Cl ₂ solution (1 × 10 ⁻⁵ M, 0.03 wt-%) of 1b-NP are irradiated with 365 nm light (16 mW/cm ²). The molar concentration refers to the amount of photoswitch in each sample, while the wt-% refers to the amount of decorated nanoparticle in each solution. The insets show the growth of the bands at 570 nm for 1a-NP → 1a ^c -NP and 520 nm for 1b-NP → 1b ^c -NP corresponding to the ring-closed isomers. Changes in the UV-vis absorption spectra when the same solutions of the photostationary states of (c) 1a ^c -NP and (d) 1b ^c -NP are irradiated with > 434 nm light (377 mW/cm ²). The insets show the reduction of the bands at 570 nm for 1a ^c -NP → 1a-NP and 520 nm for 1b ^c -NP → 1b-NP. The spectra for 1a-NP and 1b-NP (black lines) are compared to the ligands 3a and 3b (red lines) in (e) and (f), respectively in the same solvents (THF for 1a-NP and 3a and CH ₂ Cl ₂ for 1b-NP and 3b).....	166
Figure 6.10	Observed (black dashed line), individual calculated bands (green lines), sum of the fit (red line) and the residual (blue line) for the UV-vis absorption spectra of (a) ligand 3a, (b) hybrid system 1a-NP, (c) ligand 3b and (d) hybrid system 1b-NP. The calculated bands in the UV region of the spectrum were removed from the figures for clarity. The peak fitting was performed using MagicPlot software from MagicPlot Systems.	167
Figure 6.11	(a) The observed UV-vis absorption spectra of a THF solution of the two-component hybrid system 1ab-NP (black trace) and the calculated spectrum obtained by combining the spectra of the one-component systems 1a-NP and 1b-NP in a 5:4 ratio (red trace). The concentration of chromophore is approximately 5.9 × 10 ⁻⁶ M for 1a and 4.7 × 10 ⁻⁶ M for 1b, while the amount of decorated nanoparticle is 0.03 wt-%. (b) The observed UV-vis absorption spectra of the same THF solutions of the photostationary state for 1a ^c b ^c -NP (black trace) and the calculated spectrum obtained by combining the spectra of the one-component systems 1a-NP and 1b-NP in a 5:4 ratio (red trace). (c) The UV-vis absorption spectra of 1a-NP and 1b-NP in a 5:4 ratio. (d) The UV-vis absorption spectra	

	of 1a ^c -NP and 1b ^c -NP at their photostationary states in a 5:4 ratio.....	168
Figure 6.12	Images of (a) the colour of a THF solution (1×10^{-5} M, 0.05 wt-%) of 1a-NP, (b) the emission when this solution is irradiated with high 980 nm excitation power (38 W/cm^2), (c) the emission when this solution is irradiated with low 980 nm excitation power (2 W/cm^2), (d) the colour after irradiating the solution with 365 nm light (16 mW/cm^2) until the photostationary state is reached, (e) the emission when this solution is irradiated with high 980 nm excitation power (38 W/cm^2), and (f) the emission when this solution is irradiated with low 980 nm excitation power (2 W/cm^2).....	169
Figure 6.13	Images of (a) the colour of a CH ₂ Cl ₂ solution (1×10^{-5} M, 0.03 wt-%) of 1b-NP, (b) the emission when this solution is irradiated with high 980 nm excitation power (38 W/cm^2), (c) the emission when this solution is irradiated with low 980 nm excitation power (2 W/cm^2), (d) the colour after irradiating the solution with 365 nm light (16 mW/cm^2) until the photostationary state is reached, (e) the emission when this solution is irradiated with high 980 nm excitation power (38 W/cm^2), and (f) the emission when this solution is irradiated with low 980 nm excitation power (2 W/cm^2).....	170
Figure 6.14	Changes in the UV-vis absorption spectra when (a) the same solution of 1a-NP used in Figure 6.7(a) and (b) the same solution of 1b-NP used in Figure 6.7(b) are irradiated alternately with 365 nm light (16 mW/cm^2) for 120 s for 1a-NP and 130 s for 1b-NP, and $> 434 \text{ nm}$ (377 mW/cm^2) light for 60 s for 1a-NP and 120 s for 1b-NP. Changes in the absorbances (c) at 570 nm and (d) at 520 nm when the same solutions are irradiated alternately with 365 nm (blue shaded areas) and $> 434 \text{ nm}$ light (yellow shaded areas).....	171
Figure 6.15	Changes in the emission spectra when the same solution of 1a-NP used in Figure 6.7(a) is irradiated alternately with 365 nm light (16 mW/cm^2) for 120 s and $> 434 \text{ nm}$ (377 mW/cm^2) light for 60 s (a) at high 980 nm excitation power (38 W/cm^2) and (b) at low 980 nm excitation power (2 W/cm^2). Changes in the emission intensities at 471 nm (◆), 537 nm (◆) and 651 nm (◆) when the same solution is irradiated alternately with 365 nm (blue shaded areas) and $> 434 \text{ nm}$ light (yellow shaded areas) at (c) high 980 nm excitation power and (d) low 980 nm excitation power.....	172
Figure 6.16	Changes in the emission spectra when the same solution of 1b-NP used in Figure 6.7(b) is irradiated alternately with 365 nm light (16 mW/cm^2) for 130 s and $> 434 \text{ nm}$ (377 mW/cm^2) light for 120 s (a) at high 980 nm excitation power (38 W/cm^2) and (b) at low 980 nm excitation power (2 W/cm^2). Changes in the emission intensities at 471 nm (◆), 537 nm (◆) and 651 nm (◆) when the same solution is irradiated alternately with	

	365 nm (blue shaded areas) and > 434 nm light (yellow shaded areas) at (c) high 980 nm excitation power and (d) low 980 nm excitation power.....	173
Figure 6.17	(a) Changes in the UV-vis absorption spectrum of a THF solution of the two-component hybrid system 1ab-NP as it is irradiated with 365 nm light (16 mW/cm ²). The concentration of chromophore is approximately 5.9 × 10 ⁻⁶ M for 1a and 4.7 × 10 ⁻⁶ M for 1b, while the amount of decorated nanoparticle is 0.03 wt-%. The inset shows the growth of the absorptions at 570 nm (○) and 520 nm (◆) corresponding to the two ring-closed isomers in 1a ^c b ^c -NP. (b) Changes in the spectrum of the same photostationary state as it is irradiated with > 630 nm light (120 mW/cm ²). The inset shows the changes in the absorptions at 570 nm (○) and 520 nm (◆) corresponding to the two ring-closed isomers in 1a ^c b ^c -NP. (c) Changes in the spectrum of the photostationary state in Figure 6.10(b) as it is irradiated with > 434 nm light (377 mW/cm ²).....	174
Figure 6.18	The emission spectra a THF solution of the two-component hybrid system 1ab-NP before (grey) and after irradiation with 365 nm light (16 mW/cm ²) (violet) and > 630 nm light (120 mW/cm ²) (red). The concentration of chromophore is approximately 5.9 × 10 ⁻⁶ M for 1a and 4.7 × 10 ⁻⁶ M for 1b, while the amount of decorated nanoparticle is 0.03 wt-% at (a) high 980 nm excitation power (38 W/cm ²) and (b) low 980 nm excitation power (2 W/cm ²).....	175
Figure 6.19	Images of (a) the colour of a THF solution of 1ab-NP, (b) the emission when this solution is irradiated with high 980 nm excitation power (38 W/cm ²), (c) the emission when this solution is irradiated with low 980 nm excitation power (2 W/cm ²), (d) the colour after irradiating the solution with 365 nm light (16 mW/cm ²) until the photostationary state is reached, (e) the emission when this solution is irradiated with high 980 nm excitation power (38 W/cm ²), (f) the emission when this solution is irradiated with low 980 nm excitation power (2 W/cm ²), (g) the colour after irradiating the solution with > 630 nm light (120 mW/cm ²) until no changes were observed in the spectrum, (h) the emission when this solution is irradiated with high 980 nm excitation power (38 W/cm ²), and (i) the emission when this solution is irradiated with low 980 nm excitation power (2 W/cm ²).....	176
Figure 6.20	Images of a THF solution of 1a-NP, a CH ₂ Cl ₂ solution of 1b-NP, and a THF solution of 1ab-NP as they are irradiated with very high 980 nm excitation power (143 W/cm ²), showing the 'remote-control' photoswitching.....	177
Figure 6.21	¹ H NMR spectrum for a CD ₂ Cl ₂ solution of ligand 3b. The residual solvent peaks are highlighted.	178
Figure 6.22	¹³ C NMR spectrum for a CD ₂ Cl ₂ solution of ligand 3b.	179

Figure 6.23	¹ H NMR spectrum for a CD ₂ Cl ₂ solution of 4-(4-(2-(5-(4-methoxyphenyl)-2-methylthiophen-3-yl)cyclopent-1-en-1-yl)-5-methylthiophen-2-yl)phenol. The compound decomposes rapidly at ambient temperature.	180
Figure 6.24	¹³ C NMR spectrum for a CD ₂ Cl ₂ solution of 4-(4-(2-(5-(4-methoxyphenyl)-2-methylthiophen-3-yl)cyclopent-1-en-1-yl)-5-methylthiophen-2-yl)phenol.	181
Figure 8.1	(a) UV-vis absorption spectra of a CH ₃ CN solution (8.54 × 10 ⁻⁶ M) of 3',5'-di(carboxymethoxy)benzoic acid 1a before (solid line) and after irradiation with 365 nm light (dashed line) for 35 min, and the emission spectrum of a THF solution (1 wt-%, λ _{ex} = 980 nm) of the NaYF ₄ :TmYb core-shell UCNPs (shaded). The inset shows the TEM photograph of 1a[NaYF ₄ :TmYb] illustrating their uniform size and hexagonal prism shape. (b) Changes in the UV-vis absorption spectra of a CH ₃ CN solution of 1a[NaYF ₄ :TmYb] when it is irradiated with 980 nm light (power = 4.4 W, power density = 550 W/cm ²). ^[236] The inset shows the changes in the absorbance at 300 nm when samples of the same solution are irradiated with 290 nm (circles) and 980 nm light (diamonds).	206
Figure 8.2	Powder X-ray diffraction (XRD) patterns for NaYF ₄ :TmYb nanoparticles (top) and β-NaYF ₄ standard pattern (bottom). The intensities (<i>I</i>) were normalized in both cases.	214
Figure 8.3	Transmission Electron Microscopy (TEM) micrographs of (a,b) NaYF ₄ :TmYb nanoparticles and (c,d) decorated 1a[NaYF ₄ :ErYb] nanoparticles, and (e,f) size histograms for NaYF ₄ :TmYb showing the number of nanoparticles (<i>n</i>) for diameter (<i>d</i>) and height (<i>h</i>).	215
Figure 8.4	¹ H NMR spectra of a CD ₃ CN solution of 1a before (top) and after (bottom) it was exposed to 313 nm light for 100 min.	218
Figure 8.5	(a) Luminescence upconversion emission spectra of a 1 wt-% colloidal solution of NaYF ₄ :TmYb core-shell nanoparticles in THF excited with a 980 nm laser diode (Power Density = 150 W/cm ²). Changes in the UV-vis absorption spectra of CH ₃ CN solutions of (b) 1a as it is irradiated with 312-nm light, (c) 1a[NaYF ₄ :TmYb] as it is irradiated with 290-nm light, and (d) 1a[NaYF ₄ :TmYb] as it is irradiated with 980-nm light until no further spectral changes are observed. The data in (c) and (d) were used to generate Figure 8.1c. The insets in (b), (c) and (d) show the initial (blue) and final (red) traces corresponding to 1a and 1a[NaYF ₄ :TmYb], and 2a and 2a[NaYF ₄ :TmYb], respectively.	219
Figure 9.1	Schematic representation of NIR-to-UV 'remote-control' photorelease from a fluorescent UCNP coated with PEG.	221
Figure 9.2	The bis-carboxylate PEGylated ligand attached to the UCNP 1-NP is displaced by inorganic phosphate in 0.01 M PBS	

	buffer, which rapidly led to aggregation and precipitation of the nanoparticles.	224
Figure 9.3	Synthesized phosphate (2) and phosphonate (3) functionalized photochromic molecules. The highly polar molecules were extremely hard to purify and neither molecule were isolated devoid of impurities.....	225
Figure 9.4	General functionalization strategy using CuAAC ‘click’ chemistry.	226
Figure 9.5	Common anticancer drugs	227
Figure 9.6	Structures of the synthesized organic ligand 5 and organic-nanoparticle hybrid system 5-NP.....	230
Figure 9.7	Absorbance and emission spectra of 5-NP in water. <i>Left y-axis:</i> Absorbance spectrum of 5-NP in water (0.05 ml stock-solution in 2 ml H ₂ O). <i>Right y-axis:</i> Emission spectra of the same sample upon 980 nm excitation (1.45 W/cm ² , 0.41 W).....	230
Figure 9.8	Absorbance spectra of the ligand 5 (black trace, left y-axis) and 5-NP (red trace, right y-axis) in water.....	237
Figure 9.9	(a) DLS spectra of 5-NP in water before (solid line) and after irradiation with 365 nm light (dashed line). (b) TEM images of 5-NP, the scale bar is 50 nm.	238
Figure 9.10	<i>Left y-axis:</i> Absorbance of 5-NP in H ₂ O (blue trace) and CH ₃ CN (black trace) indicating similar concentration (0.05 ml 5-NP in 2 ml solvent). <i>Right y-axis:</i> Emission from the same samples in H ₂ O (blue shaded) and CH ₃ CN (grey shaded) upon 980 nm excitation (1.45 W /cm ² , 0.41 W). The emission quenching values are calculated based on the areas under the curves. The emission bands from 671–750 nm were not included in the analysis because these emissions are due to the second order diffraction of the upconverted UV light off the grating of the emission monochromator	241
Figure 9.11	Changes in absorbance of 5 (2x10 ⁻⁵ M) during irradiation with 365 nm light (1.4 mW/cm ² , 3.9 mW) in (a) CH ₃ CN and (b) water. (c) Absorbance of 5-NP in CH ₃ CN (0.05 ml stock dispersion in 0.2 ml CH ₃ CN) before and after irradiation with 980 nm along the horizontal axis (1 hour 1.45 W/cm ² and 1 hour 4.27 W/cm ²) and 312 nm light (40 minutes, 2.1 mW/cm ²). (d) Changes in absorbance of 5-NP in water (0.1 ml stock dispersion in 2 ml H ₂ O) during irradiation with 365 nm light (1.4 mWcm ⁻² , 3.9 mW).....	242
Figure 9.12	UV-vis absorbance changes of 5-NP (0.05 ml 5-NP in 0.4 ml water) during NIR-to-UV ‘remote-control’ photosolvolysis in a micro cuvette. (a) Changes in absorbance during irradiation with 980 nm light (1.45 W/cm ² , 0.41 W) along the vertical axis. (b) Changes in absorbance of the same sample during time plotted at 257 nm. (c) Changes in absorbance of a second sample cooled in a water bath during irradiation with 980 nm	

	light (4.27 W/cm ² , 1.21 W) along the vertical axis. (d) Changes in absorbance of the same sample during time plotted at 257 nm.....	245
Figure 9.13	UV-vis absorbance changes of 5-NP (0.05 ml 5-NP in 0.2 ml CH ₃ CN) during NIR-to-UV 'remote-control' photosolvolysis in a micro cuvette. (a) Changes in absorbance during irradiation with 980 nm light (1.45 W/cm ² , 0.41 W) along the horizontal axis. (b) Changes in absorbance of the same sample during time plotted at 257 nm. (c) Changes in absorbance of the same sample during irradiation with 980 nm light (4.27 W/cm ² , 1.21 W) along the vertical axis. (d) Changes in absorbance of the same sample during time plotted at 257 nm.....	246
Figure 9.14	(a) Schematic representation of the synthesized DTE functionalized nanoparticle 22-NP before and after photoswitching. (b) <i>Left y-axis</i> : Changes in the UV-vis absorbance spectra during the 'remote-control' photochemical reaction 22-NP→22c-NP upon 'biologically benign' power levels of 980 nm irradiation (0-60 min, 1.45 W/cm ² , 0.41 W) in THF (0.025 ml stock dispersion of 22-NP in 0.2 ml THF). The blue trace is the absorbance of 22c-NP at the photostationary state after irradiation with 365 nm light (60 s, 1.4 mW/cm ² , 3.9 mW). <i>Right y-axis</i> : Emission spectra of 5-NP in CH ₃ CN upon 980 nm excitation (1.45 W/cm ² , 0.41 W), emissions past 670 nm are not included in the spectra. (c) Normalized changes in absorbance during time, plotted at 608 nm. The arrow indicates the time the excitation source was changed from 980 nm to broadband 365 nm light (1.4 mW/cm ² , 3.9 mW).	247
Figure 9.15	The figure describes a photorelease experiment examined by UV-vis spectroscopy. An aliquot of acetonitrile stock dispersion of 5-NP (0.05 ml) was diluted with water (0.4 ml) in a 10 kDa spin-filter and washed with water (3 x 0.4 ml) by three centrifugation/re-dispersion cycles. The green trace is the filtrate from the third wash. The black trace is the sample in the filter after three washes, re-diluted with water (0.4 ml). The blue trace is after irradiation with broadband 365 nm light (1.4 mW/cm ² , 3.9 mW) for 10 minutes. The red trace is the spin-filtrate after irradiation.....	249
Figure 9.16	UV-vis absorption spectra of Chlorambucil (1x10 ⁻⁵ M in water, black trace, <i>left y-axis</i>) and the spin-filtrate of 5-NP from figure 9.15 after 10 min broadband 365 nm light irradiation (red trace, <i>right y-axis</i>) (1.4 mW/cm ² , 3.9 mW).....	250
Figure 9.17	Changes in absorption of Chlorambucil (1x10 ⁻⁵ M in H ₂ O) upon broadband 365 nm light irradiation (1.4 mW/cm ² , 3.9 mW). The inset display the changes in absorption plotted at 257 nm.....	251
Figure 9.18	UV-vis absorbance spectra of Chlorambucil after 10 minutes of 365 nm light irradiation (1.4 mW/cm ² , 3.9 mW) (black trace, <i>left y-axis</i>) and the spin-filtrate of 5-NP after 10 minutes of 365 nm	

	light irradiation (1.4 mW/cm ² , 3.9 mW) from Figure 9.15 (red trace, <i>right y-axis</i>).....	252
Figure 9.19	LRMS raw data of the spin-filtrate from figure 9.15 after 10 min broadband 365 nm light irradiation (1.4 mW/cm ² , 3.9 mW). Chlorambucil exact mass: 303.0793 g/mol. Proposed de-alkylated photoproduct ^[267] exact mass: 241.0870 g/mol.	253
Figure 9.20	(a) The figure describes a photorelease experiment examined by UV-vis spectroscopy. An aliquot of acetonitrile stock dispersion of 5-NP (0.05 ml) was diluted with water (0.4 ml) in a 10 kDa spin-filter and washed with water (3 x 0.4 ml) by three centrifugation/re-dispersion cycles. The green trace is the spin-filtrate from the third wash. The black trace is the sample in the filter after three washes, re-diluted with water (0.4 ml). The blue trace is after irradiation with 980 nm light (4.27 W/cm ² , 1.21 W) for 120 minutes. The red trace is the spin-filtrate after irradiation. (b) Magnification of the UV-vis absorbances of the spin-filter wash (green trace) and the spin-filtrate after 980 nm irradiation (red trace).	254
Figure 9.21	LRMS raw data of the spin-filtrate from Figure 9.21 after 2 hours irradiation with 980 nm light irradiation. Chlorambucil exact mass: 303.0793 g/mol. Proposed de-alkylated photoproduct ^[267] exact mass: 241.0870 g/mol.	255
Figure 9.22	Schematic illustration of a multifunctional UCNP for advanced theranostic drug delivery using CuAAC chemistry as a means to decorate the nanoparticle with multiple ligands.....	262
Figure 9.23	LRMS spectra of 5, due to the polydispersity of the sample no precise peak could be picked out.	281
Figure 10.1	Normalized kinetic data of 1, 2 and 3 in CH ₂ Cl ₂ (1x10 ⁻⁵ M) under 365 nm light (2.9 mW/cm ² , 8.1 mW) irradiation. Photocage 1 was irradiated in oxygen free CH ₂ Cl ₂ . The data is plotted from the data presented in Figure 10.2.....	290
Figure 10.2	UV-vis absorption spectra of 1x10 ⁻⁵ M CH ₂ Cl ₂ solutions of photocage 1, 2 and 3 during photolysis with broadband 365 nm light (2.9 mW/cm ² , 8.1 mW). (a) 1 in oxygen-free CH ₂ Cl ₂ , (b) 2 in CH ₂ Cl ₂ and (c) 3 in CH ₂ Cl ₂ . (d) Molar absorption coefficient (ε) plot comparison of photocages 1, 2 and 3.	291
Figure 10.3	Changes in ¹ H NMR spectra of photocage 1 (1 mg in 0.55 ml CD ₂ Cl ₂ , 5.1x10 ⁻³ M) during irradiation with 365 nm light (1.4 mW/cm ² , 3.9 mW).....	293
Figure 10.4	¹ H NMR spectrum of photocage 1 (1 mg in 0.55 ml CD ₂ Cl ₂) before (black trace) and after 20 min of 365 nm light irradiation (1.4 mW/cm ² , 3.9 mW) (red trace).....	294
Figure 10.5	Changes in absorption spectra of photocage 1 (1x10 ⁻⁵ M in CH ₂ Cl ₂) mixed with o-NP in (a) 0.07 wt-% and (b) 0.46 wt-% during irradiation with 980 nm light (1.45 W/cm ² , 0.41 W).	295

Figure 10.6	Absorption overlap of photocage 1 in CH ₂ Cl ₂ with the emission of 5-NP (Chapter 9) in water.....	295
Figure 12.1	¹ H NMR (600 MHz) spectrum of 3,3'-(4-(tricosan-12-ylidene)cyclopenta-2,5-diene-1,2-diyl)bis(2-methyl-5-phenylthiophene) in CD ₂ Cl ₂	313
Figure 12.2	¹³ C NMR (151 MHz) spectrum of 3,3'-(4-(tricosan-12-ylidene)cyclopenta-2,5-diene-1,2-diyl)bis(2-methyl-5-phenylthiophene) in CD ₂ Cl ₂	313
Figure 12.3	¹ H NMR (600 MHz) spectrum of (4 stereoisomers)-diethyl 5,6-dicyano-10a,10b-dimethyl-2,9-diphenyl-11-(tricosan-12-ylidene)-4,5,6,7,10a,10b-hexahydro-4,7-methanonaphtho[2,1- <i>b</i> :3,4- <i>b'</i>]dithiophene-5,6-dicarboxylate in CD ₂ Cl ₂	314
Figure 12.4	¹³ C NMR (151 MHz) spectrum of (4 stereoisomers)-diethyl 5,6-dicyano-10a,10b-dimethyl-2,9-diphenyl-11-(tricosan-12-ylidene)-4,5,6,7,10a,10b-hexahydro-4,7-methanonaphtho[2,1- <i>b</i> :3,4- <i>b'</i>]dithiophene-5,6-dicarboxylate in CD ₂ Cl ₂	314
Figure 12.5	¹ H NMR (400 MHz) spectrum of 1,2-bis(5-bromo-2-methylthiophen-3-yl)cyclopent-1-ene in CD ₂ Cl ₂	315
Figure 12.6	¹³ C NMR (100 MHz) spectrum of 1,2-bis(5-bromo-2-methylthiophen-3-yl)cyclopent-1-ene in CD ₂ Cl ₂	315
Figure 12.7	¹ H NMR (400 MHz) spectrum of (4,4'-(4,4'-(cyclopentene-1,2-diyl)bis(5-methylthiophene-4,2-diyl)-bis(4,1-phenylene))dimethanol in CD ₂ Cl ₂	316
Figure 12.8	¹³ C NMR (100 MHz) spectrum of (4,4'-(4,4'-(cyclopentene-1,2-diyl)bis(5-methylthiophene-4,2-diyl)-bis(4,1-phenylene))dimethanol in CD ₂ Cl ₂	316
Figure 12.9	¹ H NMR (400 MHz) spectrum of (4-(5-methyl-4-(2-(2-methyl-5-(4-((prop-2-ynoxy)methyl) phenyl)-thiophen-3-yl)cyclopent-1-enyl)thiophen-2-yl)phenyl)methanol in CD ₂ Cl ₂	317
Figure 12.10	¹³ C NMR (100 MHz) spectrum of (4-(5-methyl-4-(2-(2-methyl-5-(4-((prop-2-ynoxy)methyl) phenyl)-thiophen-3-yl)cyclopent-1-enyl)thiophen-2-yl)phenyl)methanol in CD ₂ Cl ₂	317
Figure 12.11	¹ H NMR (400 MHz) spectrum of 2-mPEG 4-(5-methyl-4-(2-(2-methyl-5-(4-((prop-2-ynoxy)-methyl)phenyl)thiophen-3-yl)cyclopent-1-enyl)thiophen-2-yl)benzyl glutarate in CD ₂ Cl ₂	318
Figure 12.12	¹³ C NMR (100 MHz) spectrum of 2-mPEG 4-(5-methyl-4-(2-(2-methyl-5-(4-((prop-2-ynoxy)-methyl)phenyl)thiophen-3-yl)cyclopent-1-enyl)thiophen-2-yl)benzyl glutarate in CD ₂ Cl ₂	319
Figure 12.13	¹ H NMR (400 MHz) spectrum of 3,5-bis(3-((<i>tert</i> -butyldimethylsilyl)oxy)propoxy) benzaldehyde in CD ₂ Cl ₂	320
Figure 12.14	¹³ C NMR (100 MHz) spectrum of 3,5-bis(3-((<i>tert</i> -butyldimethylsilyl)oxy)propoxy) benzaldehyde in CD ₂ Cl ₂	320

Figure 12.15	¹ H NMR (400 MHz) spectrum of (3,5-bis(3-((<i>tert</i> -butyldimethylsilyl)oxy)propoxy) phenyl)(2-(naphthalen-2-yl)-1,3-dithian-2-yl)methanol in CD ₂ Cl ₂	321
Figure 12.16	¹³ C NMR (100 MHz) spectrum of (3,5-bis(3-((<i>tert</i> -butyldimethylsilyl)oxy)propoxy) phenyl)(2-(naphthalen-2-yl)-1,3-dithian-2-yl)methanol in CD ₂ Cl ₂	321
Figure 12.17	¹ H NMR (400 MHz) spectrum of (3,5-bis(3-((<i>tert</i> -butyldimethylsilyl)oxy)propoxy) phenyl)(2-(naphthalen-2-yl)-1,3-dithian-2-yl)methyl 4-(4-(bis(2-chloroethyl)amino) phenyl)butanoate in CD ₂ Cl ₂	322
Figure 12.18	¹³ C NMR (100 MHz) spectrum of (3,5-bis(3-((<i>tert</i> -butyldimethylsilyl)oxy)propoxy) phenyl)(2-(naphthalen-2-yl)-1,3-dithian-2-yl)methyl 4-(4-(bis(2-chloroethyl)amino) phenyl)butanoate in CD ₂ Cl ₂	322
Figure 12.19	¹ H NMR (500 MHz) spectrum of (3,5-bis(3-hydroxypropoxy)phenyl)(2-(naphthalen-2-yl)-1,3-dithian-2-yl)methyl 4-(4-(bis(2-chloroethyl)amino)phenyl)butanoate in CD ₂ Cl ₂	323
Figure 12.20	¹³ C NMR (126 MHz) spectrum of (3,5-bis(3-((<i>tert</i> -butyldimethylsilyl)oxy)propoxy) phenyl)(2-(naphthalen-2-yl)-1,3-dithian-2-yl)methyl 4-(4-(bis(2-chloroethyl)amino) phenyl)butanoate in CD ₂ Cl ₂	323
Figure 12.21	¹ H NMR (500 MHz) spectrum of 1-(3,5-bis(3-hydroxypropoxy)phenyl)-2-(naphthalen-2-yl)-2-oxoethyl-4-(4-(bis(2-chloroethyl)amino)phenyl)butanoate in CD ₂ Cl ₂	324
Figure 12.22	¹³ C NMR (126 MHz) spectrum of 1-(3,5-bis(3-hydroxypropoxy)phenyl)-2-(naphthalen-2-yl)-2-oxoethyl-4-(4-(bis(2-chloroethyl)amino)phenyl)butanoate in CD ₂ Cl ₂	324
Figure 12.23	¹ H NMR (500 MHz) spectrum of 3-(3-(1-((4-(4-(bis(2-chloroethyl)amino)phenyl) butanoyl)oxy)-2-(naphthalen-2-yl)-2-oxoethyl)-5-(3-hydroxypropoxy) phenoxy)propyl pent-4-ynoate in CD ₂ Cl ₂	325
Figure 12.24	¹³ C NMR (126 MHz) spectrum of 3-(3-(1-((4-(4-(bis(2-chloroethyl)amino)phenyl) butanoyl)oxy)-2-(naphthalen-2-yl)-2-oxoethyl)-5-(3-hydroxypropoxy) phenoxy)propyl pent-4-ynoate in CD ₂ Cl ₂	325
Figure 12.25	¹ H NMR (500 MHz) spectrum of 3-(3-(1-((4-(4-(bis(2-chloroethyl)amino)phenyl) butanoyl)oxy)-2-(naphthalen-2-yl)-2-oxoethyl)-5-(3-(pent-4-ynoxy)propoxy) phenoxy) propyl-136-oxo-2,5,8,11,14,17,20,23,26,29,33,36,39,42,45,48,51,54,57,60,63,66,69,72,75,78,81,84,87,90,93,96,99,102,105,108,111,114,117,120,123,126,129,132-tetratetracontaoxa-135-azanonatriacontahectan-139-oate in CD ₂ Cl ₂	326
Figure 12.26	¹³ C NMR (126 MHz) spectrum of 3-(3-(1-((4-(4-(bis(2-chloroethyl)amino)phenyl) butanoyl)oxy)-2-(naphthalen-2-yl)-	

	2-oxoethyl)-5-(3-(pent-4-ynoiloxy)propoxy) phenoxy) propyl-136-oxo-2,5,8,11,14,17,20,23,26,29,33,36,39,42,45,48,51,54,57,60,63,66,69,72,75,78,81,84,87,90,93,96,99,102,105,108,111,114,117,120,123,126,129,132-tetratetracontaoxa-135-azanonatriacontahectan-139-oate in CD ₂ Cl ₂	327
Figure 12.27	¹ H NMR (400 MHz) spectrum of (3,5-dimethoxyphenyl)(2-(4-(dimethylamino) phenyl)-1,3-dithian-2-yl)methyl acetate in CD ₂ Cl ₂	328
Figure 12.28	¹³ C NMR (100 MHz) spectrum of (3,5-dimethoxyphenyl)(2-(4-(dimethylamino) phenyl)-1,3-dithian-2-yl)methyl acetate in CD ₂ Cl ₂	328
Figure 12.29	¹ H NMR (400 MHz) spectrum of 1-(3,5-dimethoxyphenyl)-2-(4-(dimethylamino) phenyl)-2-oxoethyl acetate in CD ₂ Cl ₂	329
Figure 12.30	¹³ C NMR (100 MHz) spectrum of 1-(3,5-dimethoxyphenyl)-2-(4-(dimethylamino) phenyl)-2-oxoethyl acetate in CD ₂ Cl ₂	329
Figure 12.31	¹ H NMR (400 MHz) spectrum of (3,5-dimethoxyphenyl)(2-phenyl-1,3-dithian-2-yl) methyl acetate in CD ₂ Cl ₂	330
Figure 12.32	¹³ C NMR (100 MHz) spectrum of (3,5-dimethoxyphenyl)(2-phenyl-1,3-dithian-2-yl) methyl acetate in CD ₂ Cl ₂	330
Figure 12.33	¹ H NMR (400 MHz) spectrum of (3,5-dimethoxyphenyl)(2-(naphthalen-2-yl)-1,3-dithian-2-yl)methyl acetate in CD ₂ Cl ₂	331
Figure 12.34	¹³ C NMR (100 MHz) spectrum of (3,5-dimethoxyphenyl)(2-(naphthalen-2-yl)-1,3-dithian-2-yl)methyl acetate in CD ₂ Cl ₂	332
Figure 12.35	¹ H NMR (400 MHz) spectrum of 1-(3,5-dimethoxyphenyl)-2-(naphthalen-2-yl)-2-oxoethyl acetate in CD ₂ Cl ₂	332
Figure 12.36	¹³ C NMR (100 MHz) spectrum of 1-(3,5-dimethoxyphenyl)-2-(naphthalen-2-yl)-2-oxoethyl acetate in CD ₂ Cl ₂	332

LIST OF SCHEMES

Figure 1.1	(a) Schematic 3D representation of an energy transfer upconversion UCNP co-doped with both absorber ions and emitter ions. (b) Non-comprehensive Dieke diagram representation of energy transfer upconversion.	6
Figure 2.1	Common design of a DTE molecular switch.....	17
Figure 2.2	Transition state orbital symmetry in the S_1 -excited state according to the Woodward-Hoffman rules and photochemical reaction schemes for the (a) ring-closing and (b) ring-opening reactions and a schematic representation of the potential energy surfaces along the reaction coordinates of the photochromic reactions of the DTE molecular switch. ^[46]	20
Figure 2.3	Thermal stability of the ring-closed isomer of various diarylethene derivatives.....	21
Figure 3.1	Emission spectra of colloidal CHCl_3 solutions of (a) $\text{NaYF}_4:\text{TmYb}$ and (b) $\text{NaYF}_4:\text{ErYb}$ UCNPs when excited with a 980 nm laser diode. ^[69] The light used to trigger photoswitch 1 is highlighted. TEM images are shown as insets. Changes in the UV-vis absorption spectra (left) and photographs (right) of acrylate films ($12 \times 8 \times 1$ mm) containing (c) 1a + $\text{NaYF}_4:\text{TmYb}$, and (d) 1b + $\text{NaYF}_4:\text{ErYb}$ as they are irradiated with 980 nm light. The stripes observed in the right panel of (c) and (d) correspond to the direction of the beam of the 980 nm laser. ^[69] The irradiation in (c) was carried out two times with perpendicular orientations. The small squares in all images are the cut-out holes in the sample holder through where the absorption was measured.	33
Figure 3.2	(a) Scheme illustrating the ring-opening and release reactions of bicyclic compound 2b as it is irradiated with visible or NIR light. (b) Changes in the UV-vis absorption spectra (left) and photographs (right) of an acrylate film ($8 \times 7 \times 1$ mm) containing 2b + $\text{NaYF}_4:\text{ErYb}$ as it is irradiated with 980-nm light. The stripe observed in the right panel corresponds to the direction of the beam of the 980-nm laser.	36
Figure 3.3	Transmission Electron Microscopy (TEM) micrographs of (a) $\text{NaYF}_4:\text{TmYb}$ and (b) $\text{NaYF}_4:\text{ErYb}$ nanoparticle samples.....	44
Figure 3.4	Powder X-ray diffraction (XRD) patterns for (a) $\text{NaYF}_4:\text{TmYb}$ and (b) $\text{NaYF}_4:\text{ErYb}$ nanoparticle samples and (c) $\beta\text{-NaYF}_4$ JCPDS standard card #28-1192.....	45

Figure 3.5	Luminescence upconversion emission spectra of 1 wt-% colloidal solutions of (a) NaYF ₄ :TmYb and (b) NaYF ₄ :ErYb nanoparticle samples in CHCl ₃ excited with a 980 nm laser diode (Power Density = 150 W/cm ²). The inset in (b) shows the total upconversion luminescence of a dispersion of NaYF ₄ :ErYb when stimulated with a 980 nm diode laser. 46
Figure 3.6	Changes in the UV-vis absorption spectra of a CH ₃ CN solution (2.1 × 10 ⁻⁵ M) of 1a as it is irradiated with 365 nm light until the photostationary state is reached. The images on the right illustrate how the photoswitch retains its activity when cast in a polyacrylate film. 47
Figure 3.7	Sample of compound 1a and NaYF ₄ :TmYb cast in an acrylate film (a) before, (b) during and (c) after exposure to 980 nm light. Sample of compound 1b and NaYF ₄ :ErYb cast in an acrylate film (d) before, (e) during and (f) after exposure to 980 nm light. (g) Changes in the UV-vis absorption spectra and images of an acrylate film containing only 1b before (left) and after (right) being irradiated with 980 nm light. 48
Figure 3.8	(a) Sample of compound 1 and NaYF ₄ :TmYb cast in a PMMA gel showing coloured lines due to ring-closing induced by 980 nm light. The lines represent the direction of the laser beam. The bulk composites gels were prepared using the colloidal stock nanoparticle dispersion in CHCl ₃ . The appropriate amount of the stock dispersion was added to a 4 dram screw top vial. Poly(ethylene glycol)-monooleate (typical M _n = 860) (0.15 g) was added to vial and the CHCl ₃ was removed under vacuum using a rotary evaporator. Methyl methacrylate (3.85 g) and 1a (2 mg) were then added to the vial and the resulting dispersion was sonicated for 2 min to obtain a clear dispersion. Azobisisobutyronitrile (AIBN) radical initiator (<1% (w/w)) was subsequently added to the dispersion and sonicated for 30 s. The monomer solution was then transferred to a 1 dram screw top vial with the dimensions 60 mm × 15 mm (length × diameter), which was then sealed. The vial was placed in a 70 °C oil bath for 30 min to initiate the polymerization process and subsequently transferred to a 45–50 °C oven until the polymerization was complete. A transparent NP-1a-PMMA composite rod was obtained by breaking the glass vial. (b) A drop-cast sample of 1 in PMMA before (top) and after (bottom) irradiation with 980 nm light. The sample was prepared by dissolving 1 (1.6 mg) and NaYF ₄ :ErYb (303 mg of a 1.7 wt-% solution in chloroform) in 88 mg of a solution made from PMMA (17.5 mg) and acetone (894 mg). One drop of the solution was spin-cast onto a glass slide (15 × 25 mm; 10 s gradient to 200 rpm, 200 rpm 1 min) using Laurell WS-400A6NPP/LITE spincoater. (c) Experimental set-up showing how the glass plate was exposed to 980 nm light. 49

Figure 4.1	<p>The ‘<i>direct</i>’ photoreactions of the DTE derivatives used in this study are triggered by UV light (for ring-closing) and visible light (for ring-opening). These reactions can also be triggered in a ‘<i>remote-control</i>’ process using the UV light generated under high excitation power densities and the visible light generated under low excitation power densities when the <i>core-shell-shell</i> UCNPs (ErTm and TmEr) absorb near-infrared light (980 nm). The sizes of the coloured arrows represent the relative amount of each type of light excited or emitted during the multi-photon process.</p>	58
Figure 4.2	<p>TEM images of the <i>core</i>, <i>core-shell</i>, and <i>core-shell-shell</i> nanoparticles for NaYF₄:ErYb–NaYF₄ (Er), NaYF₄:TmYb–NaYF₄ (Tm), NaYF₄:ErYb–NaYF₄:TmYb–NaYF₄ (ErTm) and NaYF₄:TmYb–NaYF₄:ErYb–NaYF₄ (TmEr) UCNPs illustrating their uniform size and shape.</p>	64
Figure 4.3	<p>UV-vis absorption spectra of THF solutions (1.5×10^{-5} M) of (a) 1o and (b) 2o before (solid line) and after irradiation with 365 nm light (dashed line) for 2 min. Emission spectra of THF solutions (1.5 wt-%, $\lambda_{\text{ex}} = 980$ nm) of (c) NaYF₄:ErYb (Er) and (d) NaYF₄:TmYb (Tm) <i>core-shell</i> UCNPs, and of (e) ErTm and (f) TmEr <i>core-shell-shell</i> UCNPs at high power (500 W/cm², top graph) and low power (15 W/cm², bottom graph). The shaded, colored regions in all cases represent each emission region and show the suitable spectral overlap with the appropriate absorption bands for the ring-open and ring-closed isomers of DTEs 1 and 2.</p>	66
Figure 4.4	<p>Changes in the absorbances ($\lambda_{\text{max}} = 632$ and 601 nm for 1c and 2c, respectively) when THF solutions of (a) DTEs 1o and 2o containing NaYF₄:TmYb nanoparticles (Tm) are irradiated with 980 nm light at high excitation power densities (500 W/cm²), and (b) DTEs 1c and 2c containing NaYF₄:ErYb (Er) nanoparticles are irradiated with 980 nm light at low excitation power densities (15 W/cm²). The horizontal lines show the absorbance values when similar solutions are irradiated with UV light (313 nm) for graph ‘a’ or visible light (> 450 nm) for graph ‘b’ until the photostationary states are obtained. (c) The degree to which the ring-closing and ring-opening reactions are induced with 980 nm light (high power for the former and low power for the latter) using the different types of nanoparticles.</p>	70
Figure 4.5	<p>Bidirectional photoswitching of a THF solution of DTE 2 dispersed with TmEr <i>core-shell-shell</i> nanoparticles by varying only the intensity of the NIR light. The plot shows the absorption intensities corresponding to the ring-closed isomers (632 nm for 1c and 601 nm for 2c) as solutions of the photoswitches and the <i>core-shell-shell</i> nanoparticles are exposed to alternating intensities of 980 light. The colors correspond to the light emitted by the nanoparticles (green at low power and blue at high power).</p>	72

Figure 4.6	Powder X-ray diffraction (XRD) patterns for (a) NaYF ₄ :ErYb-NaYF ₄ <i>core-shell</i> nanoparticles, (b) NaYF ₄ :TmYb-NaYF ₄ <i>core-shell</i> nanoparticles, (c) NaYF ₄ :ErYb-NaYF ₄ :TmYb-NaYF ₄ <i>core-shell-shell</i> nanoparticles, (d) NaYF ₄ :TmYb-NaYF ₄ :ErYb-NaYF ₄ <i>core-shell-shell</i> nanoparticles and (f) β-NaYF ₄ JCPDS standard card #28-1192.	84
Figure 4.7	Transmission Electron Microscopy (TEM) micrographs of (top) NaYF ₄ :ErYb nanoparticles and (bottom) NaYF ₄ :ErYb-NaYF ₄ <i>core-shell</i> nanoparticles.....	86
Figure 4.8	Transmission Electron Microscopy (TEM) micrographs of (top) NaYF ₄ :TmYb nanoparticles and (bottom) NaYF ₄ :TmYb-NaYF ₄ <i>core-shell</i> nanoparticles.....	87
Figure 4.9	Transmission Electron Microscopy (TEM) micrographs of (top) NaYF ₄ :ErYb nanoparticles, (middle) NaYF ₄ :ErYb-NaYF ₄ :TmYb <i>core-shell</i> and (bottom) NaYF ₄ :ErYb-NaYF ₄ :TmYb-NaYF ₄ <i>core-shell-shell</i> nanoparticles.	88
Figure 4.10	Transmission Electron Microscopy (TEM) micrographs of (top) NaYF ₄ :TmYb nanoparticles, (middle) NaYF ₄ :TmYb-NaYF ₄ :ErYb <i>core-shell</i> and (bottom) NaYF ₄ :TmYb-NaYF ₄ :ErYb-NaYF ₄ <i>core-shell-shell</i> nanoparticles.....	89
Figure 4.11	UV-vis absorption spectra of THF solutions (1.5×10^{-5} M) of (left) 1o and (right) 2o containing 1.5 wt% NaYF ₄ :TmYb nanoparticles (Tm) before (black line) and after irradiation with either 365 nm light (blue line) or 980 nm light at high excitation power densities (500 W/cm^2).	91
Figure 4.12	Emission spectra of THF solutions of the TmEr (left) and ErTm <i>core-shell-shell</i> nanoparticles as they are exposed to the higher-power NIR laser light (980 nm , 500 W/cm^2) used in the experiments. The lack of any spectral changes (all three spectra overlap) after 1 h highlights the stability of the nanoparticles.	91
Figure 5.1	Synthesis of the photoresponsive hybrid system (1o[NaF ₄ :ErYb]) and a conceptual description of selective quenching of the emission from the nanoparticles by ring-closing the photoswitch. The images are TEM micrographs showing (a) the oleate coated nanoparticle starting material, (b) the azide coated nanoparticles and (c) the nanoparticles decorated with the ring-open form of the photoswitch (1o[NaF ₄ :ErYb]) illustrating their uniform size and shape.....	95
Figure 5.2	(a) UV-vis absorption and emission spectra ($\lambda_{\text{ex}} = 980 \text{ nm}$, 150 W/cm^2) of an aqueous solution (9.0×10^{-6} M) of 1o[NaF ₄ :ErYb] before (solid line/dark shading) and after irradiation with 365 nm light (dashed line/light shading) for 2.5 min (1.3 mW/cm^2). (b) Changes in the absorbance at 530 nm (black circles), and emission intensities at 538 nm (green diamonds) and 652 nm (red diamonds) of a similar solution of 1o[NaYF ₄ :ErYb] when it is alternately irradiated with UV and visible light. (c) Changes	

	in the absorbance at 530 nm of a similar solution of 1c[NaYF ₄ :ErYb] when it is continuously irradiated with 980 nm light.....	101
Figure 5.3	Optical (left) and two-photon upconversion fluorescence (middle and right) microscopy images of wild-type N2 <i>C. elegans</i> incubated with 1o[NaYF ₄ :ErYb] (0.25 mg of a 0.5 mg/mL solution in M9 buffer) showing the changes in fluorescence due to the photoswitching of the DTE component within the bodies of the worms. The middle panel shows the strong initial fluorescence prior to exposure to UV light. The right panel shows the reduced emission that is a result of ring-closing the photoswitch with 365 nm light for 2.5 minutes.....	104
Figure 5.4	(a) Transmission Electron Microscopy (TEM) micrograph of oleate-coated NaYF ₄ :ErYb nanoparticles. (b) High-angle annular dark-field (HAADF) image of NaYF ₄ :ErYb nanoparticles (c) Powder X-ray diffraction (XRD) patterns for (top) NaYF ₄ :ErYb nanoparticles and (bottom) β-NaYF ₄ JCPDS standard card #28-1192. (d) Selected area electron diffraction (SAED) pattern of the NaYF ₄ :ErYb nanoparticles.	118
Figure 5.5	Transmission Electron Microscopy (TEM) micrographs of (a) oleate-coated NaYF ₄ :ErYb nanoparticles, (b) azide-coated NaYF ₄ :ErYb nanoparticles and (c) “clicked” NaYF ₄ :ErYb nanoparticles.	120
Figure 5.6	Size histograms (diameter) from TEM micrographs for (a) oleate-coated NaYF ₄ :ErYb nanoparticles, (b) azide-coated NaYF ₄ :ErYb nanoparticles and (c) “clicked” NaYF ₄ :ErYb nanoparticles.	120
Figure 5.7	Size histograms (diameter) from DLS results for (a) oleate-coated NaYF ₄ :ErYb nanoparticles, (b) azide-coated NaYF ₄ :ErYb nanoparticles and (c) “clicked” NaYF ₄ :ErYb nanoparticles.	121
Figure 5.8	Selected region of the FTIR spectra for (a) oleate-coated NaYF ₄ :ErYb nanoparticles, (b) azide-coated NaYF ₄ :ErYb nanoparticles and (c) “clicked” NaYF ₄ :ErYb nanoparticles.....	121
Figure 5.9	UV-vis absorption spectra for aqueous solutions of (a) ligand 1 and (b) the decorated nanoparticles (1[NaYF ₄ :ErYb]) in their original ring-open (black lines) and photostationary (red lines). The photostationary states were generated by irradiating the solutions with 365 nm light until no more changes were observed. The changes in the spectra when the complexes are exposed to (c) UV (365 nm) and (d) visible light. (e) Summary of the changes in absorbance over time.	122
Figure 5.10	(a) UV-vis absorption cycling data for aqueous solutions of the decorated nanoparticles (1[NaYF ₄ :ErYb]). (b) Emission spectra (λ _{ex} = 980 nm, 150 W/cm ²) for cycling experiments of an aqueous solution of 1[NaF ₄ :ErYb]. (c) UV-vis absorption spectra for an aqueous solution of the decorated nanoparticles	

	(1[NaYF ₄ :ErYb]) before and after 90 minutes of continuously irradiated with 980 nm light (150 W/cm ²). (d) Percent quenching versus wavelength for an aqueous solutions of the decorated 1c[NaYF ₄ :ErYb] nanoparticles (black diamonds) superimposed on the green and red emissions.....	123
Figure 5.11	Optical (left) and two-photon upconversion fluorescence (middle and right) microscopy images of wild-type N2 <i>C. elegans</i> incubated with 1o[NaYF ₄ :ErYb] showing the changes in fluorescence due to the photoswitching of the DTE component within the bodies of the worms. The middle panels show the strong initial fluorescence prior to exposure to UV light. The right panels show the reduced emission that is a result of ring-closing the photoswitch with 365 nm light for 2.5 minutes. The difference between the two samples is the omission (top) or inclusion (bottom) of a washing/centrifugation step in the preparation and accounts for the small changes in background fluorescence.	125
Figure 5.12	The upconverting fluorescence ($\lambda_{\text{ex}} = 980 \text{ nm}$) from the hybrid 1o[NaYF ₄ :ErYb] and 1c[NaYF ₄ :ErYb] from inside the digestive tract of the nematodes obtained with the 2-photon microscope.	125
Figure 6.1	UV-vis absorption spectra of solutions (10 ⁻⁵ M) of two-component systems (a) 1a-NP (THF) and (b) 1b-NP (CH ₂ Cl ₂) before (solid lines) and after irradiation with 365 nm (16 mW/cm ²) light (shaded areas) for 120 s. The spectra for the ligands (3a and 3b) are shown for comparison (dashed lines). The molar concentration refers to the estimated amount of photoswitch in each sample, [□] while the amount of decorated nanoparticle in each solution is 0.05 wt-% for 1a-NP and 0.03 wt-% for 1b-NP. Emission spectra of the same solutions ($\lambda_{\text{ex}} = 980 \text{ nm}$) of (c) 1a-NP and (d) 1b-NP at high 980 nm excitation power (38 W/cm ² , top graphs) and low 980 nm excitation power (2 W/cm ² , bottom graphs) showing how the intensity of specific bands in the original emission spectrum (white areas) are reduced when the photoswitches are converted into their ring-closed forms (shaded areas) based on the overlap with the absorption bands of 1a ^c -NP and 1b ^c -NP.	134
Figure 6.2	Changes in the absorbances at (a) 570 nm when the same solution of 1a-NP used in Figure 6.1(a,c) and (b) 520 nm when the same solution of 1b-NP used in Figure 6.1(b,d) are irradiated alternately with 365 nm light (16 mW/cm ²) for 120 s for 1a-NP and 130 s for 1b-NP (white areas), and > 434 nm (377 mW/cm ²) light for 60 s for 1a-NP and 120 s for 1b-NP (shaded areas). (c–f) Changes in the emission intensities at 471 nm (◆), 537 nm (■) and 651 nm (○) when the same solutions are irradiated under identical conditions at (c,d) high 980 nm excitation power and (e,f) low 980 nm excitation power. [□]	141

Figure 6.3	<p>(a) The UV-vis absorption spectrum of a THF solution of the two-component hybrid system 1ab-NP before (white) and after (dark shaded) irradiation with 365 nm light (16 mW/cm^2). The total concentration of chromophore is 10^{-5} M (in a 5:4 1a:1b ratio), while the amount of decorated nanoparticle is 0.03 wt-%. The inset shows the time-dependent growth of the absorptions at 570 nm (○) and 520 nm (◆) corresponding to the two ring-closed isomers in $1a^c b^c$-NP. (b) The UV-vis absorption spectrum of the same photostationary state before (dark shaded), after irradiation with $> 630 \text{ nm}$ light (120 mW/cm^2) (light shaded) and after irradiation with $> 434 \text{ nm}$ light (377 mW/cm^2) (white). The inset shows the time-dependent changes of the absorptions at 570 nm (○) and 520 nm (◆) during the $> 630 \text{ nm}$ irradiation, and at 520 nm (□) for a CH_3CN solution of ligand 3b ($1.0 \times 10^{-5} \text{ M}$) when it is irradiated with $> 630 \text{ nm}$ light.</p>	142
Figure 6.4	<p>Changes in the emission intensities at 471 nm (◆), 537 nm (■) and 651 nm (○) when the same solution of 1ab-NP used in Figure 6.3 is exposed to 365 nm, $> 630 \text{ nm}$ and $> 434 \text{ nm}$ light at (a) high 980 nm excitation power and (b) low 980 nm excitation power. (c) Relative areas under the peaks in the emission spectra of the same solution before, (white) and after irradiation with 365 nm light (black) and $> 630 \text{ nm}$ light (grey). High 980 nm excitation power was used in (c). In each case, the emitting ion is labelled.</p>	146
Figure 6.5	<p>Changes in the UV-vis absorption spectra when (a) a THF solution of 1a-NP (10^{-5} M, 0.05 wt-%) and (b) a CH_2Cl_2 solution of 1b-NP (10^{-5} M, 0.03 wt-%) are irradiated with 980 nm light (143 W/cm^2). The insets show the growth of the absorbances at 570 nm for 1a-NP \rightarrow $1a^c$-NP and 520 nm for 1b-NP \rightarrow $1b^c$-NP corresponding to the ring-closed isomers. The arrows in each inset plot indicate when the excitation light was changed from 980 nm to 365 nm.</p>	148
Figure 6.6	<p>Selected region of the FTIR spectra for (a) azide-coated <i>core-shell-shell</i> $\text{NaYF}_4:\text{TmYb}:\text{ErYb}$ nanoparticles (a-NP), (b) the 2-component nanoparticles 1a-NP, (c) the 2-component nanoparticles 1b-NP, and (d) the mixed 3-component nanoparticles 1ab-NP.</p>	163
Figure 6.7	<p>Changes in the UV-vis absorption spectra when CH_3CN solutions ($1 \times 10^{-5} \text{ M}$) of (a) 3a and (b) 3b are irradiated with 365 nm light (16 mW/cm^2). The insets show the growth of the bands at 590 nm for 3a \rightarrow $3a^c$ and 520 nm for 3b \rightarrow $3b^c$ corresponding to the ring-closed isomers, which are present in 72% for 3a and 56% for 3b in the photostationary states according to ^1H NMR spectroscopy (in CD_2Cl_2). Changes in the UV-vis absorption spectra when the same solutions of the photostationary states of (c) $3a^c$ and (d) $3b^c$ are irradiated with $> 434 \text{ nm}$ light (377 mW/cm^2). The insets show the reduction of the bands at 590 nm for $3a^c \rightarrow 3a$ and 520 nm for $3b^c \rightarrow 3b$.</p>	

	Changes in the UV-vis absorption spectra when the same solutions of the photostationary states of (e) 3a ^c and (f) 3b ^c are irradiated with > 630 nm light (120 mW/cm ²). The insets show the reduction of the bands at 590 nm for 3a ^c → 3a and 520 nm for 3b ^c → 3b.....	164
Figure 6.8	UV-vis absorption spectra of solutions (10 ⁻⁵ M) of the ligands (a) 3a in CH ₃ CN (black) and THF (blue) and (b) 3b in CH ₃ CN (black) and CH ₂ Cl ₂ (red) before (solid lines) and after irradiation with 365 nm (16 mW/cm ²) light (dashed lines). The spectra were normalized for any small errors in concentration.	165
Figure 6.9	Changes in the UV-vis absorption spectra when (a) a THF solution (1 × 10 ⁻⁵ M, 0.05 wt-%) of 1a-NP and (b) a CH ₂ Cl ₂ solution (1 × 10 ⁻⁵ M, 0.03 wt-%) of 1b-NP are irradiated with 365 nm light (16 mW/cm ²). The molar concentration refers to the amount of photoswitch in each sample, while the wt-% refers to the amount of decorated nanoparticle in each solution. The insets show the growth of the bands at 570 nm for 1a-NP → 1a ^c -NP and 520 nm for 1b-NP → 1b ^c -NP corresponding to the ring-closed isomers. Changes in the UV-vis absorption spectra when the same solutions of the photostationary states of (c) 1a ^c -NP and (d) 1b ^c -NP are irradiated with > 434 nm light (377 mW/cm ²). The insets show the reduction of the bands at 570 nm for 1a ^c -NP → 1a-NP and 520 nm for 1b ^c -NP → 1b-NP. The spectra for 1a-NP and 1b-NP (black lines) are compared to the ligands 3a and 3b (red lines) in (e) and (f), respectively in the same solvents (THF for 1a-NP and 3a and CH ₂ Cl ₂ for 1b-NP and 3b).....	166
Figure 6.10	Observed (black dashed line), individual calculated bands (green lines), sum of the fit (red line) and the residual (blue line) for the UV-vis absorption spectra of (a) ligand 3a, (b) hybrid system 1a-NP, (c) ligand 3b and (d) hybrid system 1b-NP. The calculated bands in the UV region of the spectrum were removed from the figures for clarity. The peak fitting was performed using MagicPlot software from MagicPlot Systems.	167
Figure 6.11	(a) The observed UV-vis absorption spectra of a THF solution of the two-component hybrid system 1ab-NP (black trace) and the calculated spectrum obtained by combining the spectra of the one-component systems 1a-NP and 1b-NP in a 5:4 ratio (red trace). The concentration of chromophore is approximately 5.9 × 10 ⁻⁶ M for 1a and 4.7 × 10 ⁻⁶ M for 1b, while the amount of decorated nanoparticle is 0.03 wt-%. (b) The observed UV-vis absorption spectra of the same THF solutions of the photostationary state for 1a ^c b ^c -NP (black trace) and the calculated spectrum obtained by combining the spectra of the one-component systems 1a-NP and 1b-NP in a 5:4 ratio (red trace). (c) The UV-vis absorption spectra of 1a-NP and 1b-NP in a 5:4 ratio. (d) The UV-vis absorption spectra	

	of 1a ^c -NP and 1b ^c -NP at their photostationary states in a 5:4 ratio.....	168
Figure 6.12	Images of (a) the colour of a THF solution (1 × 10 ⁻⁵ M, 0.05 wt-%) of 1a-NP, (b) the emission when this solution is irradiated with high 980 nm excitation power (38 W/cm ²), (c) the emission when this solution is irradiated with low 980 nm excitation power (2 W/cm ²), (d) the colour after irradiating the solution with 365 nm light (16 mW/cm ²) until the photostationary state is reached, (e) the emission when this solution is irradiated with high 980 nm excitation power (38 W/cm ²), and (f) the emission when this solution is irradiated with low 980 nm excitation power (2 W/cm ²).....	169
Figure 6.13	Images of (a) the colour of a CH ₂ Cl ₂ solution (1 × 10 ⁻⁵ M, 0.03 wt-%) of 1b-NP, (b) the emission when this solution is irradiated with high 980 nm excitation power (38 W/cm ²), (c) the emission when this solution is irradiated with low 980 nm excitation power (2 W/cm ²), (d) the colour after irradiating the solution with 365 nm light (16 mW/cm ²) until the photostationary state is reached, (e) the emission when this solution is irradiated with high 980 nm excitation power (38 W/cm ²), and (f) the emission when this solution is irradiated with low 980 nm excitation power (2 W/cm ²).....	170
Figure 6.14	Changes in the UV-vis absorption spectra when (a) the same solution of 1a-NP used in Figure 6.7(a) and (b) the same solution of 1b-NP used in Figure 6.7(b) are irradiated alternately with 365 nm light (16 mW/cm ²) for 120 s for 1a-NP and 130 s for 1b-NP, and > 434 nm (377 mW/cm ²) light for 60 s for 1a-NP and 120 s for 1b-NP. Changes in the absorbances (c) at 570 nm and (d) at 520 nm when the same solutions are irradiated alternately with 365 nm (blue shaded areas) and > 434 nm light (yellow shaded areas).....	171
Figure 6.15	Changes in the emission spectra when the same solution of 1a-NP used in Figure 6.7(a) is irradiated alternately with 365 nm light (16 mW/cm ²) for 120 s and > 434 nm (377 mW/cm ²) light for 60 s (a) at high 980 nm excitation power (38 W/cm ²) and (b) at low 980 nm excitation power (2 W/cm ²). Changes in the emission intensities at 471 nm (◆), 537 nm (◆) and 651 nm (◆) when the same solution is irradiated alternately with 365 nm (blue shaded areas) and > 434 nm light (yellow shaded areas) at (c) high 980 nm excitation power and (d) low 980 nm excitation power.....	172
Figure 6.16	Changes in the emission spectra when the same solution of 1b-NP used in Figure 6.7(b) is irradiated alternately with 365 nm light (16 mW/cm ²) for 130 s and > 434 nm (377 mW/cm ²) light for 120 s (a) at high 980 nm excitation power (38 W/cm ²) and (b) at low 980 nm excitation power (2 W/cm ²). Changes in the emission intensities at 471 nm (◆), 537 nm (◆) and 651 nm (◆) when the same solution is irradiated alternately with	

	365 nm (blue shaded areas) and > 434 nm light (yellow shaded areas) at (c) high 980 nm excitation power and (d) low 980 nm excitation power.....	173
Figure 6.17	(a) Changes in the UV-vis absorption spectrum of a THF solution of the two-component hybrid system 1ab-NP as it is irradiated with 365 nm light (16 mW/cm ²). The concentration of chromophore is approximately 5.9 × 10 ⁻⁶ M for 1a and 4.7 × 10 ⁻⁶ M for 1b, while the amount of decorated nanoparticle is 0.03 wt-%. The inset shows the growth of the absorptions at 570 nm (○) and 520 nm (◆) corresponding to the two ring-closed isomers in 1a ^c b ^c -NP. (b) Changes in the spectrum of the same photostationary state as it is irradiated with > 630 nm light (120 mW/cm ²). The inset shows the changes in the absorptions at 570 nm (○) and 520 nm (◆) corresponding to the two ring-closed isomers in 1a ^c b ^c -NP. (c) Changes in the spectrum of the photostationary state in Figure 6.10(b) as it is irradiated with > 434 nm light (377 mW/cm ²).....	174
Figure 6.18	The emission spectra a THF solution of the two-component hybrid system 1ab-NP before (grey) and after irradiation with 365 nm light (16 mW/cm ²) (violet) and > 630 nm light (120 mW/cm ²) (red). The concentration of chromophore is approximately 5.9 × 10 ⁻⁶ M for 1a and 4.7 × 10 ⁻⁶ M for 1b, while the amount of decorated nanoparticle is 0.03 wt-% at (a) high 980 nm excitation power (38 W/cm ²) and (b) low 980 nm excitation power (2 W/cm ²).....	175
Figure 6.19	Images of (a) the colour of a THF solution of 1ab-NP, (b) the emission when this solution is irradiated with high 980 nm excitation power (38 W/cm ²), (c) the emission when this solution is irradiated with low 980 nm excitation power (2 W/cm ²), (d) the colour after irradiating the solution with 365 nm light (16 mW/cm ²) until the photostationary state is reached, (e) the emission when this solution is irradiated with high 980 nm excitation power (38 W/cm ²), (f) the emission when this solution is irradiated with low 980 nm excitation power (2 W/cm ²), (g) the colour after irradiating the solution with > 630 nm light (120 mW/cm ²) until no changes were observed in the spectrum, (h) the emission when this solution is irradiated with high 980 nm excitation power (38 W/cm ²), and (i) the emission when this solution is irradiated with low 980 nm excitation power (2 W/cm ²).....	176
Figure 6.20	Images of a THF solution of 1a-NP, a CH ₂ Cl ₂ solution of 1b-NP, and a THF solution of 1ab-NP as they are irradiated with very high 980 nm excitation power (143 W/cm ²), showing the 'remote-control' photoswitching.....	177
Figure 6.21	¹ H NMR spectrum for a CD ₂ Cl ₂ solution of ligand 3b. The residual solvent peaks are highlighted.	178
Figure 6.22	¹³ C NMR spectrum for a CD ₂ Cl ₂ solution of ligand 3b.	179

Figure 6.23	¹ H NMR spectrum for a CD ₂ Cl ₂ solution of 4-(4-(2-(5-(4-methoxyphenyl)-2-methylthiophen-3-yl)cyclopent-1-en-1-yl)-5-methylthiophen-2-yl)phenol. The compound decomposes rapidly at ambient temperature.	180
Figure 6.24	¹³ C NMR spectrum for a CD ₂ Cl ₂ solution of 4-(4-(2-(5-(4-methoxyphenyl)-2-methylthiophen-3-yl)cyclopent-1-en-1-yl)-5-methylthiophen-2-yl)phenol.	181
Figure 8.1	(a) UV-vis absorption spectra of a CH ₃ CN solution (8.54 × 10 ⁻⁶ M) of 3',5'-di(carboxymethoxy)benzoic acid 1a before (solid line) and after irradiation with 365 nm light (dashed line) for 35 min, and the emission spectrum of a THF solution (1 wt-%, λ _{ex} = 980 nm) of the NaYF ₄ :TmYb core-shell UCNPs (shaded). The inset shows the TEM photograph of 1a[NaYF ₄ :TmYb] illustrating their uniform size and hexagonal prism shape. (b) Changes in the UV-vis absorption spectra of a CH ₃ CN solution of 1a[NaYF ₄ :TmYb] when it is irradiated with 980 nm light (power = 4.4 W, power density = 550 W/cm ²). ^[236] The inset shows the changes in the absorbance at 300 nm when samples of the same solution are irradiated with 290 nm (circles) and 980 nm light (diamonds).	206
Figure 8.2	Powder X-ray diffraction (XRD) patterns for NaYF ₄ :TmYb nanoparticles (top) and β-NaYF ₄ standard pattern (bottom). The intensities (<i>I</i>) were normalized in both cases.	214
Figure 8.3	Transmission Electron Microscopy (TEM) micrographs of (a,b) NaYF ₄ :TmYb nanoparticles and (c,d) decorated 1a[NaYF ₄ :ErYb] nanoparticles, and (e,f) size histograms for NaYF ₄ :TmYb showing the number of nanoparticles (<i>n</i>) for diameter (<i>d</i>) and height (<i>h</i>).	215
Figure 8.4	¹ H NMR spectra of a CD ₃ CN solution of 1a before (top) and after (bottom) it was exposed to 313 nm light for 100 min.	218
Figure 8.5	(a) Luminescence upconversion emission spectra of a 1 wt-% colloidal solution of NaYF ₄ :TmYb core-shell nanoparticles in THF excited with a 980 nm laser diode (Power Density = 150 W/cm ²). Changes in the UV-vis absorption spectra of CH ₃ CN solutions of (b) 1a as it is irradiated with 312-nm light, (c) 1a[NaYF ₄ :TmYb] as it is irradiated with 290-nm light, and (d) 1a[NaYF ₄ :TmYb] as it is irradiated with 980-nm light until no further spectral changes are observed. The data in (c) and (d) were used to generate Figure 8.1c. The insets in (b), (c) and (d) show the initial (blue) and final (red) traces corresponding to 1a and 1a[NaYF ₄ :TmYb], and 2a and 2a[NaYF ₄ :TmYb], respectively.	219
Figure 9.1	Schematic representation of NIR-to-UV 'remote-control' photorelease from a fluorescent UCNP coated with PEG.	221
Figure 9.2	The bis-carboxylate PEGylated ligand attached to the UCNP 1-NP is displaced by inorganic phosphate in 0.01 M PBS	

	buffer, which rapidly led to aggregation and precipitation of the nanoparticles.	224
Figure 9.3	Synthesized phosphate (2) and phosphonate (3) functionalized photochromic molecules. The highly polar molecules were extremely hard to purify and neither molecule were isolated devoid of impurities.....	225
Figure 9.4	General functionalization strategy using CuAAC ‘click’ chemistry.	226
Figure 9.5	Common anticancer drugs	227
Figure 9.6	Structures of the synthesized organic ligand 5 and organic-nanoparticle hybrid system 5-NP.....	230
Figure 9.7	Absorbance and emission spectra of 5-NP in water. <i>Left y-axis:</i> Absorbance spectrum of 5-NP in water (0.05 ml stock-solution in 2 ml H ₂ O). <i>Right y-axis:</i> Emission spectra of the same sample upon 980 nm excitation (1.45 W/cm ² , 0.41 W).....	230
Figure 9.8	Absorbance spectra of the ligand 5 (black trace, left y-axis) and 5-NP (red trace, right y-axis) in water.....	237
Figure 9.9	(a) DLS spectra of 5-NP in water before (solid line) and after irradiation with 365 nm light (dashed line). (b) TEM images of 5-NP, the scale bar is 50 nm.	238
Figure 9.10	<i>Left y-axis:</i> Absorbance of 5-NP in H ₂ O (blue trace) and CH ₃ CN (black trace) indicating similar concentration (0.05 ml 5-NP in 2 ml solvent). <i>Right y-axis:</i> Emission from the same samples in H ₂ O (blue shaded) and CH ₃ CN (grey shaded) upon 980 nm excitation (1.45 W /cm ² , 0.41 W). The emission quenching values are calculated based on the areas under the curves. The emission bands from 671–750 nm were not included in the analysis because these emissions are due to the second order diffraction of the upconverted UV light off the grating of the emission monochromator	241
Figure 9.11	Changes in absorbance of 5 (2x10 ⁻⁵ M) during irradiation with 365 nm light (1.4 mW/cm ² , 3.9 mW) in (a) CH ₃ CN and (b) water. (c) Absorbance of 5-NP in CH ₃ CN (0.05 ml stock dispersion in 0.2 ml CH ₃ CN) before and after irradiation with 980 nm along the horizontal axis (1 hour 1.45 W/cm ² and 1 hour 4.27 W/cm ²) and 312 nm light (40 minutes, 2.1 mW/cm ²). (d) Changes in absorbance of 5-NP in water (0.1 ml stock dispersion in 2 ml H ₂ O) during irradiation with 365 nm light (1.4 mWcm ⁻² , 3.9 mW).....	242
Figure 9.12	UV-vis absorbance changes of 5-NP (0.05 ml 5-NP in 0.4 ml water) during NIR-to-UV ‘remote-control’ photosolvolyis in a micro cuvette. (a) Changes in absorbance during irradiation with 980 nm light (1.45 W/cm ² , 0.41 W) along the vertical axis. (b) Changes in absorbance of the same sample during time plotted at 257 nm. (c) Changes in absorbance of a second sample cooled in a water bath during irradiation with 980 nm	

	light (4.27 W/cm ² , 1.21 W) along the vertical axis. (d) Changes in absorbance of the same sample during time plotted at 257 nm.....	245
Figure 9.13	UV-vis absorbance changes of 5-NP (0.05 ml 5-NP in 0.2 ml CH ₃ CN) during NIR-to-UV 'remote-control' photosolvolytic in a micro cuvette. (a) Changes in absorbance during irradiation with 980 nm light (1.45 W/cm ² , 0.41 W) along the horizontal axis. (b) Changes in absorbance of the same sample during time plotted at 257 nm. (c) Changes in absorbance of the same sample during irradiation with 980 nm light (4.27 W/cm ² , 1.21 W) along the vertical axis. (d) Changes in absorbance of the same sample during time plotted at 257 nm.....	246
Figure 9.14	(a) Schematic representation of the synthesized DTE functionalized nanoparticle 22-NP before and after photoswitching. (b) <i>Left y-axis</i> : Changes in the UV-vis absorbance spectra during the 'remote-control' photochemical reaction 22-NP→22c-NP upon 'biologically benign' power levels of 980 nm irradiation (0-60 min, 1.45 W/cm ² , 0.41 W) in THF (0.025 ml stock dispersion of 22-NP in 0.2 ml THF). The blue trace is the absorbance of 22c-NP at the photostationary state after irradiation with 365 nm light (60 s, 1.4 mW/cm ² , 3.9 mW). <i>Right y-axis</i> : Emission spectra of 5-NP in CH ₃ CN upon 980 nm excitation (1.45 W/cm ² , 0.41 W), emissions past 670 nm are not included in the spectra. (c) Normalized changes in absorbance during time, plotted at 608 nm. The arrow indicates the time the excitation source was changed from 980 nm to broadband 365 nm light (1.4 mW/cm ² , 3.9 mW).	247
Figure 9.15	The figure describes a photorelease experiment examined by UV-vis spectroscopy. An aliquot of acetonitrile stock dispersion of 5-NP (0.05 ml) was diluted with water (0.4 ml) in a 10 kDa spin-filter and washed with water (3 x 0.4 ml) by three centrifugation/re-dispersion cycles. The green trace is the filtrate from the third wash. The black trace is the sample in the filter after three washes, re-diluted with water (0.4 ml). The blue trace is after irradiation with broadband 365 nm light (1.4 mW/cm ² , 3.9 mW) for 10 minutes. The red trace is the spin-filtrate after irradiation.....	249
Figure 9.16	UV-vis absorption spectra of Chlorambucil (1x10 ⁻⁵ M in water, black trace, <i>left y-axis</i>) and the spin-filtrate of 5-NP from figure 9.15 after 10 min broadband 365 nm light irradiation (red trace, <i>right y-axis</i>) (1.4 mW/cm ² , 3.9 mW).....	250
Figure 9.17	Changes in absorption of Chlorambucil (1x10 ⁻⁵ M in H ₂ O) upon broadband 365 nm light irradiation (1.4 mW/cm ² , 3.9 mW). The inset display the changes in absorption plotted at 257 nm.....	251
Figure 9.18	UV-vis absorbance spectra of Chlorambucil after 10 minutes of 365 nm light irradiation (1.4 mW/cm ² , 3.9 mW) (black trace, <i>left y-axis</i>) and the spin-filtrate of 5-NP after 10 minutes of 365 nm	

	light irradiation (1.4 mW/cm ² , 3.9 mW) from Figure 9.15 (red trace, <i>right y-axis</i>).....	252
Figure 9.19	LRMS raw data of the spin-filtrate from figure 9.15 after 10 min broadband 365 nm light irradiation (1.4 mW/cm ² , 3.9 mW). Chlorambucil exact mass: 303.0793 g/mol. Proposed de-alkylated photoproduct ^[267] exact mass: 241.0870 g/mol.	253
Figure 9.20	(a) The figure describes a photorelease experiment examined by UV-vis spectroscopy. An aliquot of acetonitrile stock dispersion of 5-NP (0.05 ml) was diluted with water (0.4 ml) in a 10 kDa spin-filter and washed with water (3 x 0.4 ml) by three centrifugation/re-dispersion cycles. The green trace is the spin-filtrate from the third wash. The black trace is the sample in the filter after three washes, re-diluted with water (0.4 ml). The blue trace is after irradiation with 980 nm light (4.27 W/cm ² , 1.21 W) for 120 minutes. The red trace is the spin-filtrate after irradiation. (b) Magnification of the UV-vis absorbances of the spin-filter wash (green trace) and the spin-filtrate after 980 nm irradiation (red trace).	254
Figure 9.21	LRMS raw data of the spin-filtrate from Figure 9.21 after 2 hours irradiation with 980 nm light irradiation. Chlorambucil exact mass: 303.0793 g/mol. Proposed de-alkylated photoproduct ^[267] exact mass: 241.0870 g/mol.	255
Figure 9.22	Schematic illustration of a multifunctional UCNP for advanced theranostic drug delivery using CuAAC chemistry as a means to decorate the nanoparticle with multiple ligands.....	262
Figure 9.23	LRMS spectra of 5, due to the polydispersity of the sample no precise peak could be picked out.	281
Figure 10.1	Normalized kinetic data of 1, 2 and 3 in CH ₂ Cl ₂ (1x10 ⁻⁵ M) under 365 nm light (2.9 mW/cm ² , 8.1 mW) irradiation. Photocage 1 was irradiated in oxygen free CH ₂ Cl ₂ . The data is plotted from the data presented in Figure 10.2.....	290
Figure 10.2	UV-vis absorption spectra of 1x10 ⁻⁵ M CH ₂ Cl ₂ solutions of photocage 1, 2 and 3 during photolysis with broadband 365 nm light (2.9 mW/cm ² , 8.1 mW). (a) 1 in oxygen-free CH ₂ Cl ₂ , (b) 2 in CH ₂ Cl ₂ and (c) 3 in CH ₂ Cl ₂ . (d) Molar absorption coefficient (ε) plot comparison of photocages 1, 2 and 3.	291
Figure 10.3	Changes in ¹ H NMR spectra of photocage 1 (1 mg in 0.55 ml CD ₂ Cl ₂ , 5.1x10 ⁻³ M) during irradiation with 365 nm light (1.4 mW/cm ² , 3.9 mW).....	293
Figure 10.4	¹ H NMR spectrum of photocage 1 (1 mg in 0.55 ml CD ₂ Cl ₂) before (black trace) and after 20 min of 365 nm light irradiation (1.4 mW/cm ² , 3.9 mW) (red trace).....	294
Figure 10.5	Changes in absorption spectra of photocage 1 (1x10 ⁻⁵ M in CH ₂ Cl ₂) mixed with o-NP in (a) 0.07 wt-% and (b) 0.46 wt-% during irradiation with 980 nm light (1.45 W/cm ² , 0.41 W).	295

Figure 10.6	Absorption overlap of photocage 1 in CH ₂ Cl ₂ with the emission of 5-NP (Chapter 9) in water.....	295
Figure 12.1	¹ H NMR (600 MHz) spectrum of 3,3'-(4-(tricosan-12-ylidene)cyclopenta-2,5-diene-1,2-diyl)bis(2-methyl-5-phenylthiophene) in CD ₂ Cl ₂	313
Figure 12.2	¹³ C NMR (151 MHz) spectrum of 3,3'-(4-(tricosan-12-ylidene)cyclopenta-2,5-diene-1,2-diyl)bis(2-methyl-5-phenylthiophene) in CD ₂ Cl ₂	313
Figure 12.3	¹ H NMR (600 MHz) spectrum of (4 stereoisomers)-diethyl 5,6-dicyano-10a,10b-dimethyl-2,9-diphenyl-11-(tricosan-12-ylidene)-4,5,6,7,10a,10b-hexahydro-4,7-methanonaphtho[2,1- <i>b</i> :3,4- <i>b'</i>]dithiophene-5,6-dicarboxylate in CD ₂ Cl ₂	314
Figure 12.4	¹³ C NMR (151 MHz) spectrum of (4 stereoisomers)-diethyl 5,6-dicyano-10a,10b-dimethyl-2,9-diphenyl-11-(tricosan-12-ylidene)-4,5,6,7,10a,10b-hexahydro-4,7-methanonaphtho[2,1- <i>b</i> :3,4- <i>b'</i>]dithiophene-5,6-dicarboxylate in CD ₂ Cl ₂	314
Figure 12.5	¹ H NMR (400 MHz) spectrum of 1,2-bis(5-bromo-2-methylthiophen-3-yl)cyclopent-1-ene in CD ₂ Cl ₂	315
Figure 12.6	¹³ C NMR (100 MHz) spectrum of 1,2-bis(5-bromo-2-methylthiophen-3-yl)cyclopent-1-ene in CD ₂ Cl ₂	315
Figure 12.7	¹ H NMR (400 MHz) spectrum of (4,4'-(4,4'-(cyclopentene-1,2-diyl)bis(5-methylthiophene-4,2-diyl)-bis(4,1-phenylene))dimethanol in CD ₂ Cl ₂	316
Figure 12.8	¹³ C NMR (100 MHz) spectrum of (4,4'-(4,4'-(cyclopentene-1,2-diyl)bis(5-methylthiophene-4,2-diyl)-bis(4,1-phenylene))dimethanol in CD ₂ Cl ₂	316
Figure 12.9	¹ H NMR (400 MHz) spectrum of (4-(5-methyl-4-(2-(2-methyl-5-(4-((prop-2-ynyloxy)methyl) phenyl)-thiophen-3-yl)cyclopent-1-enyl)thiophen-2-yl)phenyl)methanol in CD ₂ Cl ₂	317
Figure 12.10	¹³ C NMR (100 MHz) spectrum of (4-(5-methyl-4-(2-(2-methyl-5-(4-((prop-2-ynyloxy)methyl) phenyl)-thiophen-3-yl)cyclopent-1-enyl)thiophen-2-yl)phenyl)methanol in CD ₂ Cl ₂	317
Figure 12.11	¹ H NMR (400 MHz) spectrum of 2-mPEG 4-(5-methyl-4-(2-(2-methyl-5-(4-((prop-2-ynyloxy)-methyl)phenyl)thiophen-3-yl)cyclopent-1-enyl)thiophen-2-yl)benzyl glutarate in CD ₂ Cl ₂	318
Figure 12.12	¹³ C NMR (100 MHz) spectrum of 2-mPEG 4-(5-methyl-4-(2-(2-methyl-5-(4-((prop-2-ynyloxy)-methyl)phenyl)thiophen-3-yl)cyclopent-1-enyl)thiophen-2-yl)benzyl glutarate in CD ₂ Cl ₂	319
Figure 12.13	¹ H NMR (400 MHz) spectrum of 3,5-bis(3-((<i>tert</i> -butyldimethylsilyl)oxy)propoxy) benzaldehyde in CD ₂ Cl ₂	320
Figure 12.14	¹³ C NMR (100 MHz) spectrum of 3,5-bis(3-((<i>tert</i> -butyldimethylsilyl)oxy)propoxy) benzaldehyde in CD ₂ Cl ₂	320

Figure 12.15	¹ H NMR (400 MHz) spectrum of (3,5-bis(3-((<i>tert</i> -butyldimethylsilyl)oxy)propoxy) phenyl)(2-(naphthalen-2-yl)-1,3-dithian-2-yl)methanol in CD ₂ Cl ₂	321
Figure 12.16	¹³ C NMR (100 MHz) spectrum of (3,5-bis(3-((<i>tert</i> -butyldimethylsilyl)oxy)propoxy) phenyl)(2-(naphthalen-2-yl)-1,3-dithian-2-yl)methanol in CD ₂ Cl ₂	321
Figure 12.17	¹ H NMR (400 MHz) spectrum of (3,5-bis(3-((<i>tert</i> -butyldimethylsilyl)oxy)propoxy) phenyl)(2-(naphthalen-2-yl)-1,3-dithian-2-yl)methyl 4-(4-(bis(2-chloroethyl)amino) phenyl)butanoate in CD ₂ Cl ₂	322
Figure 12.18	¹³ C NMR (100 MHz) spectrum of (3,5-bis(3-((<i>tert</i> -butyldimethylsilyl)oxy)propoxy) phenyl)(2-(naphthalen-2-yl)-1,3-dithian-2-yl)methyl 4-(4-(bis(2-chloroethyl)amino) phenyl)butanoate in CD ₂ Cl ₂	322
Figure 12.19	¹ H NMR (500 MHz) spectrum of (3,5-bis(3-hydroxypropoxy)phenyl)(2-(naphthalen-2-yl)-1,3-dithian-2-yl)methyl 4-(4-(bis(2-chloroethyl)amino)phenyl)butanoate in CD ₂ Cl ₂	323
Figure 12.20	¹³ C NMR (126 MHz) spectrum of (3,5-bis(3-((<i>tert</i> -butyldimethylsilyl)oxy)propoxy) phenyl)(2-(naphthalen-2-yl)-1,3-dithian-2-yl)methyl 4-(4-(bis(2-chloroethyl)amino) phenyl)butanoate in CD ₂ Cl ₂	323
Figure 12.21	¹ H NMR (500 MHz) spectrum of 1-(3,5-bis(3-hydroxypropoxy)phenyl)-2-(naphthalen-2-yl)-2-oxoethyl-4-(4-(bis(2-chloroethyl)amino)phenyl)butanoate in CD ₂ Cl ₂	324
Figure 12.22	¹³ C NMR (126 MHz) spectrum of 1-(3,5-bis(3-hydroxypropoxy)phenyl)-2-(naphthalen-2-yl)-2-oxoethyl-4-(4-(bis(2-chloroethyl)amino)phenyl)butanoate in CD ₂ Cl ₂	324
Figure 12.23	¹ H NMR (500 MHz) spectrum of 3-(3-(1-((4-(4-(bis(2-chloroethyl)amino)phenyl) butanoyl)oxy)-2-(naphthalen-2-yl)-2-oxoethyl)-5-(3-hydroxypropoxy) phenoxy)propyl pent-4-ynoate in CD ₂ Cl ₂	325
Figure 12.24	¹³ C NMR (126 MHz) spectrum of 3-(3-(1-((4-(4-(bis(2-chloroethyl)amino)phenyl) butanoyl)oxy)-2-(naphthalen-2-yl)-2-oxoethyl)-5-(3-hydroxypropoxy) phenoxy)propyl pent-4-ynoate in CD ₂ Cl ₂	325
Figure 12.25	¹ H NMR (500 MHz) spectrum of 3-(3-(1-((4-(4-(bis(2-chloroethyl)amino)phenyl) butanoyl)oxy)-2-(naphthalen-2-yl)-2-oxoethyl)-5-(3-(pent-4-ynoxyloxy)propoxy) phenoxy) propyl-136-oxo-2,5,8,11,14,17,20,23,26,29,33,36,39,42,45,48,51,54,57,60,63,66,69,72,75,78,81,84,87,90,93,96,99,102,105,108,111,114,117,120,123,126,129,132-tetratetracontaoxa-135-azanonatriacontahectan-139-oate in CD ₂ Cl ₂	326
Figure 12.26	¹³ C NMR (126 MHz) spectrum of 3-(3-(1-((4-(4-(bis(2-chloroethyl)amino)phenyl) butanoyl)oxy)-2-(naphthalen-2-yl)-	

	2-oxoethyl)-5-(3-(pent-4-ynoiloxy)propoxy) phenoxy) propyl- 136-oxo- 2,5,8,11,14,17,20,23,26,29,33,36,39,42,45,48,51,54,57, 60,63,66,69,72,75,78,81,84,87,90,93,96,99,102,105,108,111,1 14,117,120,123,1 26,129,132-tetratetracontaoxa-135- azanonatriacontahectan-139-oate in CD ₂ Cl ₂	327
Figure 12.27	¹ H NMR (400 MHz) spectrum of (3,5-dimethoxyphenyl)(2-(4-(dimethylamino) phenyl)-1,3-dithian-2-yl)methyl acetate in CD ₂ Cl ₂	328
Figure 12.28	¹³ C NMR (100 MHz) spectrum of (3,5-dimethoxyphenyl)(2-(4-(dimethylamino) phenyl)-1,3-dithian-2-yl)methyl acetate in CD ₂ Cl ₂	328
Figure 12.29	¹ H NMR (400 MHz) spectrum of 1-(3,5-dimethoxyphenyl)-2-(4-(dimethylamino) phenyl)-2-oxoethyl acetate in CD ₂ Cl ₂	329
Figure 12.30	¹³ C NMR (100 MHz) spectrum of 1-(3,5-dimethoxyphenyl)-2-(4-(dimethylamino) phenyl)-2-oxoethyl acetate in CD ₂ Cl ₂	329
Figure 12.31	¹ H NMR (400 MHz) spectrum of (3,5-dimethoxyphenyl)(2-phenyl-1,3-dithian-2-yl) methyl acetate in CD ₂ Cl ₂	330
Figure 12.32	¹³ C NMR (100 MHz) spectrum of (3,5-dimethoxyphenyl)(2-phenyl-1,3-dithian-2-yl) methyl acetate in CD ₂ Cl ₂	330
Figure 12.33	¹ H NMR (400 MHz) spectrum of (3,5-dimethoxyphenyl)(2-(naphthalen-2-yl)-1,3-dithian-2-yl)methyl acetate in CD ₂ Cl ₂	331
Figure 12.34	¹³ C NMR (100 MHz) spectrum of (3,5-dimethoxyphenyl)(2-(naphthalen-2-yl)-1,3-dithian-2-yl)methyl acetate in CD ₂ Cl ₂	332
Figure 12.35	¹ H NMR (400 MHz) spectrum of 1-(3,5-dimethoxyphenyl)-2-(naphthalen-2-yl)-2-oxoethyl acetate in CD ₂ Cl ₂	332
Figure 12.36	¹³ C NMR (100 MHz) spectrum of 1-(3,5-dimethoxyphenyl)-2-(naphthalen-2-yl)-2-oxoethyl acetate in CD ₂ Cl ₂	332

LIST OF TABLES

Table 4.1	Constituent lanthanide dopants in each layer of all upconverting nanoparticles used in these experiments. ^a	62
Table 6.1	The differences in the intensities for the specific bands for each lanthanide ion transition in the emission spectra of the solutions of 1a-NP and 1b-NP used in Figure 6.1 and 6.2 when the chromophores are converted into their ring-closed forms using 365 nm light.	139
Table 6.2	The differences in the intensities for the bands for each region in the emission spectra of the solution of 1ab-NP used in Figure 6.3 and 6.4 when the chromophores are converted into their specific ring-closed forms using 365 nm and > 630 nm light.	147
Table 6.3	Calculation particle size and mass	160
Table 6.4	Calculation of loading using absorbances in the UV region of the spectra of 3a, 3b, 1a-NP and 1b-NP ^a	160
Table 6.5	Calculation of loading using absorbances in the visible region of the spectra of 3a, 3b, 1a-NP and 1b-NP ^a	161
Table 6.6	Calculation of loading using absorbances in the visible region of the spectra of 3a and 1ab-NP ^a	162
Table 7.1:	Photocages in the 2NB family. Quantum yield (ϕ), maximum absorption (λ_{\max}) and molar absorptivity (ϵ) compiled for the photocage starting material with carboxylate as leaving group. ^[173,182,183]	185
Table 7.2	Photocages related to the coumarin family. Quantum yield (ϕ), maximum absorption (λ_{\max}) and molar absorptivity (ϵ) compiled for the photocage starting material with carboxylate as leaving group. ^[173]	186
Table 7.3	Photocages in the 3'5'-dialkoxybenzoin family. Quantum yield (ϕ), maximum absorption (λ_{\max}) and molar absorptivity (ϵ) compiled for the photocage starting material with carboxylate as leaving group. ^[173]	187
Table 7.4	Photocages related to the p-hydroxyphenacyl family. Quantum yield (ϕ), maximum absorption (λ_{\max}) and molar absorptivity (ϵ) compiled for the photocage starting material with carboxylate as leaving group. ^[173,183,..]	188

Table 7.5	Hydroxy-cinnamoyl photocage. Quantum yield (ϕ), maximum absorption (λ_{\max}) and molar absorptivity (ϵ) for the photocage starting material with alcohol as leaving group. [□]	189
Table 7.6:	Various UV light triggered photocages. Quantum yield (ϕ), maximum absorption (λ_{\max}) and molar absorptivity (ϵ) compiled for the photocage starting material with carboxylate as leaving group.	190

GLOSSARY

>	greater than
<	less than
≥	greater than or equal to
≤	less than or equal to
°C	degree Celsius
Δ	heating
Φ	quantum yield
Φ _ε	photoreaction action cross section (M ⁻¹ cm ⁻¹)
δ	chemical shift
ε	molar absorption/extinction coefficient (M ⁻¹ cm ⁻¹)
λ	wavelength
λ _{max}	wavelength at the absorption maximum in a given region
μl	microlitre
2NB	2-nitrobenzyl photocage (ortho-nitrobenzyl)
2PE	two-photon excitation
AcOH	acetic acid
Anal. Calcd.	analytically calculated
ATP	adenosine triphosphate
bs	broad singlet
calc.	calculated
cm	centimetre
cm ⁻¹	wavenumber
CuAAC	copper-(I)-catalysed azide-alkyne cycloaddition
c.w.	continuous wave
d	doublet

dd	doublet of doublets
DLS	dynamic light scattering
DMSO	dimethylsulfoxide
equiv.	equivalent
ESI	electrospray ionization
DTE	1,2-dithienylethene molecular switch
Et ₂ O	diethyl ether
EtOAc	ethyl acetate
Et ₃ N	triethylamine
FBS	fetal bovine serum
FPT	freeze pump thaw
FRET	fluorescence/Förster resonance energy transfer
FTIR	Fourier transform infrared
g	gram
GM	Goepphert-Mayer (1GM = 10 ⁵⁰ cm ⁴ s/photon)
h	hour
H	proton
hν	photon energy
HOMO	highest occupied molecular orbital
HRMS	high resolution mass spectroscopy
HPLC	high pressure/performance liquid chromatography
<i>in vitro</i>	experiment conducted in cells
<i>in vivo</i>	experiment conducted in organism
IC	internal conversion
ISC	inter system crossing
iPr	isopropyl
IR	infrared
<i>J</i>	coupling constant (Hz)
LRMS	low resolution mass spectrometry
Ln	lanthanide

LUMO	lowest unoccupied molecular orbital
m	multiplet
M	mole/litre
mM	millimole/litre
mg	milligram
MHz	megahertz
min	minutes
ml	millilitre
mmol	millimole
mol-%	mole percentage
M.p.	melting point
mPEG	methyl terminated polyethylene glycol
mW	milliwatt
m/z	mass-to-charge ratio
n-BuLi	n-butyllithium
NIR	near infrared (750 nm – 2500 nm)
nm	nanometer
NMR	nuclear magnetic resonance
NP	nanoparticle
p	pentet
PBS	phosphate buffered saline
PEG	polyethylene glycol
PEG-DMA	polyethylene glycol dimethacrylate
Ph	phenyl
ppm	parts per million
PSS	photostationary state
PTFE	polytetrafluoroethylene
s	singlet
sec	second
T	temperature

t	triplet
TEM	transmission electron microscopy
THF	tetrahydrofuran
Theranostic	the combination of therapy and diagnostics in drug-delivery
TLC	thin layer chromatography
TMS	tetramethylsilane
UCNP	upconverting/upconversion nanoparticle
UV	ultraviolet
UVA	ultraviolet light A (315 – 400 nm)
UV-vis	ultraviolet-visible
vis	visible (400 – 750 nm)
vol-%	volume percentage
W	Watt
wt-%	weight percentage

1: INTRODUCTION TO THE THESIS

1.1 'Remote-control' photochemistry

Light is an appealing source of energy to turn molecular processes 'on' or 'off' since light can be easily tuned and focused to desired energy content (wavelength, power) and volume/area and thus offers the user external spatiotemporal control. However, the major disadvantage of the majority of organic photochemistry is the need for high-energy light, light that has various detrimental properties such as degradation and side-reactions of organic molecules upon extended irradiation and shallow penetration-depth in biological tissues.^[1,2,3]

To circumvent this severe limitation that hampers the practical utility of photochemistry in general, a few different approaches of 'remote-control' photochemistry have been developed:

The most widespread form of 'remote-control' photochemistry using light of lower energy to trigger a reaction is two-photon excitation (2PE) where near infrared (NIR, ~750-1000 nm) light is used to excite the molecule.^[4,5] Since NIR light is of lower energy than UV light, it does not cause undesired photoreactivity to the same degree because most molecules do not directly absorb these NIR wavelengths. However, the majority of all photoactive molecules respond very inefficiently or not at all to the NIR light due to the inherent low energy of the NIR

light and the small NIR absorption cross-section of most photoactive molecules. The scope of molecules that function with this approach of 'remote-control' activation with NIR light is thus severely limited. Moreover, the use of powerful, large and expensive pulsed lasers limits the practical usefulness of this approach of 'remote-control' activation.

A second approach to use long-wavelength visible or NIR light for 'remote-control' is the use of gold-nanoparticles (gold-NP) due to their photothermal effect upon laser excitation.^[6] Although not a method to drive photochemical reactions; in this approach low energy NIR or visible light is converted by the gold-NP into heat of sufficient magnitude to drive organic thermal reactions or cause damage in biological systems.^[6] Such systems are thus limited to secondary reactions gated by heat and cannot be used to drive photochemical reactions. A similar form of photothermal effect is exhibited by magnetic nanoparticles upon radiofrequency (RF) irradiation.^[7]

A fourth approach of 'remote-control' photochemistry that had been utilized prior to the work described in this thesis is NIR-to-visible 'remote-control' photochemistry using upconverting nanoparticles (UCNP). By the NIR-to-visible 'remote-control' upconversion approach, visible light activated photosensitizers could be triggered to undergo photochemical reactions upon excitation with NIR light (980 nm).^[8] However, only a handful of photoactive chromophores discovered so far respond to visible light and this method of 'remote-control' photochemistry was thus severely limited prior to our initial contributions.^[9,10,11]

During the work carried out in this thesis we demonstrated how not only NIR-to-visible upconversion could be used to drive a wider scope of organic photoreactions but also, and more importantly, we demonstrated that NIR-to-UV upconversion could be used to drive organic photochemical reactions, something that had not been previously demonstrated.^[9,10,11] With our discovery of NIR-to-UV 'remote-control' photochemistry we increased the generality of the 'remote-control' upconversion approach since UV light triggers the majority of all photoactive molecules available to this end. The NIR-to-UV upconversion approach thus offers a significant advantage over conventional 2PE triggered photochemistry since the UCNPs emit UV light locally and a larger scope of photoactive organic molecules can thus be used in combination with the UCNPs depending on their UV light absorption profile.

1.2 Photon upconverting nanoparticles

Photon upconversion is a non-linear optical phenomenon in which the energy from multiple lower energy NIR photons is transformed into one photon of higher energy.^[12,13,14,15,16,17] Such anti-Stokes fluorescence can be generated from certain lanthanide and uranide f ions and transition-metal d ions upon NIR laser light irradiation of significantly lower power density than used for conventional 2PE photochemistry.^[12]

1.2.1 Upconversion

There are a number of different mechanisms by which multiphoton upconversion can be generated,^[12,15] although the most efficient form of

upconversion to date is accomplished by co-doping a suitable matrix, often oxides or fluorides of rare earth elements, with one lanthanide ion responsible for absorbing the NIR energy (absorber ion) and subsequently transfer that energy to a co-doped lanthanide ion responsible for subsequent emission (emitter ion), see Figure 1.1.^[12,15] This process is called energy transfer upconversion and is advantageous since it circumvents the need for multiple lasers of different wavelengths, which otherwise would be needed to generate upconversion from one ion responsible for both absorbing and emitting light.^[12] Hence one cheaper and more compact continuous-wave NIR diode laser can be used to generate the photon upconversion in comparison to the large and expensive pulsed lasers used for 2PE photochemistry. In order for the upconversion to be efficient it is paramount that the ions responding to the light are imbedded in a suitable matrix, one that shields the ions from solvent and gas interactions and facilitates energy transfer between ions.^[12,13,14,15,18] The most efficient matrix material to date for bright upconverting (or upconversion) nanoparticles (UCNPs) is hexagonal-phase β -NaYF₄.^[13,14,15,18] The most common absorber ion is the lanthanide ion Yb³⁺ since it can be excited by 980 nm light to an excited state by the $^2F_{7/2} - ^2F_{5/2}$ transition, an excited state from where it can transfer its energy non-radiatively through the matrix to an emitter ion whose energy levels closely match the transferred energy of Yb³⁺.^[12,13,14,15] Upon energy transfer from Yb³⁺, the emitter ion reaches a meta-stable excited state that is long-lived enough to receive additional energy from the Yb³⁺ absorber ion, which is being continuously excited (pumped) by the NIR laser. The excited emitter ion can reach even

higher meta-stable excited states by sequentially absorbing more energy from the Yb^{3+} absorber ion before relaxing to the ground state, emitting one photon of higher energy than that of the exciting NIR light.^[12,13,14,15,17] In order to achieve an efficient upconversion process, it is crucial that the Yb^{3+} absorber ion is co-doped in a higher concentration than the emitter ion, normally ~20-30 % Yb^{3+} absorber ion to ~0.5-2 % emitter ion.^[12,13,14,15,17] There are a number of lanthanide emitter ions that can be used in combination with the Yb^{3+} absorber ion such as Tm^{3+} , Er^{3+} , and Ho^{3+} .^[12] Depending on composition, the upconverted emissions can be tuned to cover a range in the electromagnetic spectrum from the NIR to the UV region by choosing one or a combination of these emitter ions. Since the emission is generated from specific energy levels, the light is emitted in sharp spectral regions of the electromagnetic spectrum and is not broad as is common with regular down-converted (Stokes) fluorescence. The $\text{Yb}^{3+}/\text{Er}^{3+}$ ion pair generate green and red emissions, the $\text{Yb}^{3+}/\text{Tm}^{3+}$ ion pair generates emissions in the UV, blue, red and NIR region and the $\text{Yb}^{3+}/\text{Ho}^{3+}$ ion pair generate red and green emissions upon 980 nm excitation.^[14,15]

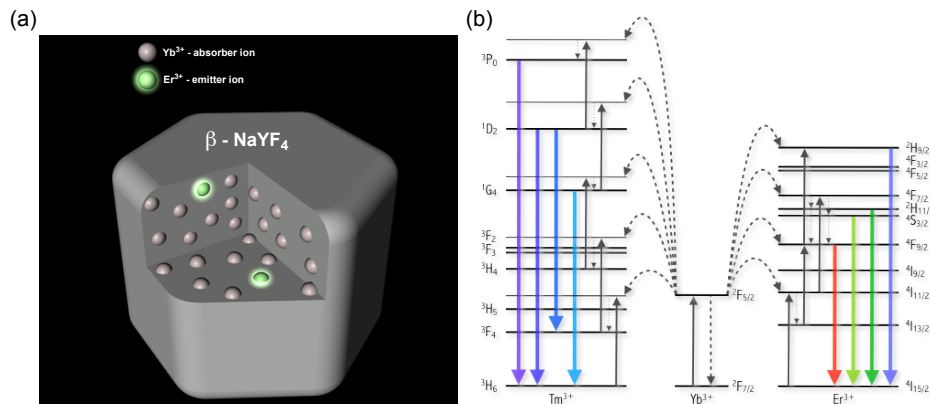


Figure 1.1 (a) Schematic 3D representation of an energy transfer upconversion UCNPs doped with both absorber ions and emitter ions. (b) Non-comprehensive Dieke diagram representation of energy transfer upconversion.

1.2.2 Applications of upconverting nanoparticles

With the dawn of nanotechnology and especially nanomedicine, the interest in upconversion technology was revitalized and synthetic methods for generating efficient and mono-dispersed nanoparticles with tuneable sizes are being developed.^[13,14,15,16] The major driving force for the development of upconversion fluorescent probes was primarily for use in bioimaging technologies since the 980 nm excitation wavelengths falls within the NIR window of biological tissues,^[19,20,21,22] a region in the electromagnetic spectrum (~630-1300 nm) where the absorption of blood, water and pigments, and the scattering of light in tissues is relatively low. The overall best region for light penetration in tissues is approximately 630-900 nm since the light absorption by water is increased at longer wavelengths. In order to minimize water absorption during excitation, recent research has focused on the use of 915 nm instead of 980 nm as the excitation wavelength due to the lower molar absorption coefficient of water at that wavelength, thus leading to less heating and deeper

effective penetration depth of the 915 nm excitation light.^[23] Another fundamental factor for the rapid development of upconversion technology for bioimaging technology is that the UCNPs do not photobleach.^[24] Due to this phenomena the fluorophores can be continuously irradiated for extended periods (days/weeks compared to minutes/hours for organic fluorophores) without loss in performance and the particles can thus be continuously tracked temporally.^[25] Furthermore, due to the low energy of the NIR excitation light, the auto-fluorescence interference from endogenous molecules is diminished leading to greater signal to noise ratio.^[26] Another beneficial factor compared to traditional 2PE fluorescence is that the UCNP can be excited by a non-tightly focused continuous-wave laser of lower power density by means of sequential photon absorption, which should increase the maximum effective penetration depth *in-vivo* compared with 2PE fluorescence (or photorelease) where the tightly focused pulsed laser beam will likely lose its focus due to scattering of tissues.

The Yb³⁺/Er³⁺ ion pair is the most common absorber/emitter ion combination of an upconverting nanoparticle throughout the literature due to the intense green and a less intense red, two-photon upconverted light. Recently however, the Yb³⁺/Tm³⁺ ion pair combination has been selected for deeper tissue imaging *in-vivo* since the very intense 800 nm two-photon upconverted light is bright and not absorbed by blood and tissues to the same extent as green light.^[27] This phenomenon can thus potentially be used to locate particles deeper in tissues *in-vivo* than with any other currently available approach for subsequent NIR-to-UV 'remote-control' photochemistry.

1.3 Upconverting nanoparticles and organic photochemistry

In order to provide proof-of-concept of the 'remote-control' photochemistry we initially chose to assess the ability of the UCNP to trigger organic photoreactions upon NIR light excitation by using organic 1,2-dithienylethene (DTE) photochromic molecular switches as they conveniently change colour upon irradiation with appropriate wavelengths of light. We chose these types of molecules to assess both the NIR-to-visible and the NIR-to-UV 'remote-control' photochemistry due to their many favourable characteristics including high quantum yields, predictable and reversible photoreactions, easy synthesis and tuning of their absorption spectra, and also due to our expertise and wide access to these molecular systems. The bulk of the thesis is devoted to the use of DTE photochromic molecules in combination with the UCNPs and we demonstrate both NIR-to-visible and NIR-to-UV 'remote-control' photochemistry using these systems. As a spin-off on our original 'remote-control' research we also demonstrate fluorescence modulation of the UCNPs using DTE molecular switches decorated on their surfaces for use in imaging technology.

Moreover and potentially more importantly, we further demonstrate the universality of the NIR-to-UV 'remote-control' approach to trigger other organic chromophores and use the UCNP in combination with 3',5'-dialkoxybenzoin photocages in order to release molecules from the surface of the UCNP upon NIR light excitation.

1.3.1 Structure of the thesis

Since the photochromic DTE molecules play a major role in the studies described in this thesis, a chapter devoted to photochromism and the photochemistry and general applications of the DTE molecule is included to give an overview of the photochemistry and serve as background information (*Chapter 2*). A second molecule that play a major role in the studies described in this thesis is the 3',5'-dialkoxybenzoin photocage, a chapter devoted to the photochemistry of this and other photorelease systems is thus included to provide background information to subsequent chapters (*Chapter 7*).

In *Chapter 3*, we demonstrate that by using NIR light and UCNPs of different composition both NIR-to-visible and for the first time NIR-to-UV 'remote-control' photochemistry is possible.^[9] During this initial study we also demonstrate NIR-to-visible 'remote-control' photorelease as a novel approach of releasing molecules using lower energy NIR light.

In *Chapter 4*, we developed and used more advanced UCNPs that can generate either visible or UV light of sufficient energy to drive organic photoreactions depending solely on the power density of the NIR light excitation source.^[11] As in our first study,^[9] we used DTE photochromic dyes to probe the efficiency of the 'remote-control' processes and demonstrated bi-directional photoswitching by only changing the power density of the NIR excitation source.

In *Chapter 5*, we changed our research from 'remote-control' photochemistry toward bioimaging applications.^[28] In this first of two fluorescence modulation studies we used a photochromic DTE dye to modulate

the upconverted fluorescence between two different fluorescent states in aqueous media *in vivo*.

In *Chapter 6*, we developed a more advanced multimodal fluorescence modulation system that can be selectively addressed using light of different wavelengths to selectively generate multiple fluorescent states. We also demonstrated that this more advanced system is capable of conducting ‘remote-control’ photoswitching depending on the NIR excitation power density.^[29]

In *Chapter 8*, we demonstrate the novel concept of NIR-to-UV ‘remote-control’ photorelease using the 3',5'-dialkoxybenzoin photorelease system decorated on the surface of an UCNP.^[10]

Chapter 9 describes the successful development and synthesis of a more advanced and water dispersible photorelease system for potential use in drug-delivery. Unfortunately, the system proved impractical due to the choice of both photorelease system and therapeutic payload. The information presented in this chapter has not been published.

Chapter 10 describes the synthesis and initial investigations into the unique photochemistry of a novel and highly efficient photocage based on the 3',5'-dialkoxybenzoin framework. The information presented in this chapter has not been published.

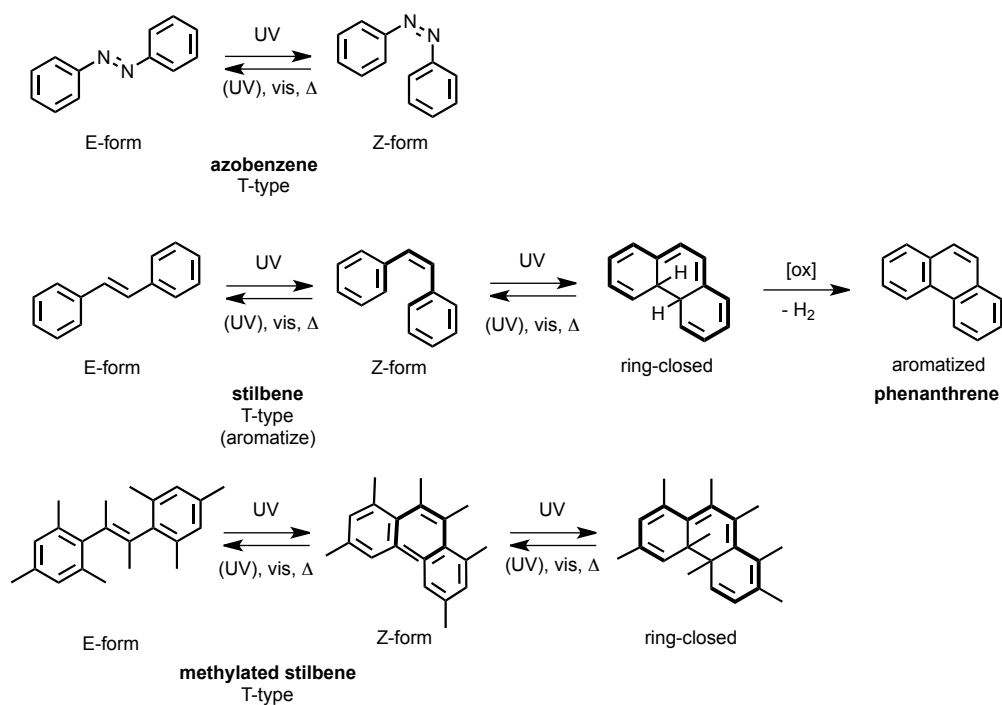
2: PHOTOCROMISM

Photochromism is defined as a light-induced reversible change between two different molecular structures having different absorption spectrum.^[30,31,32] This change in molecular structure can be induced by light in one or both directions and can be unimolecular or bimolecular. Photochromic molecules are largely divided into two groups depending on their inherent thermal stability.^[30,31,32] In the thermal class (T-type), the UV light induced isomer spontaneously reverts back to the thermodynamically stable isomer upon irradiation with visible light and/or thermally in the dark. The photochemical class (P-type) has a greater thermal energy barrier between the two isomers and thus has a reduced ability to spontaneously revert back from the UV light induced isomer in the dark. Even at temperatures as high as a 100°C it can take days before the material reverts back thermally.^[33] The reversed reaction is consequently only induced with visible light.

The majority of photochromic molecular classes studied to date utilize double bond isomerization, pericyclic rearrangements or a combination of the two. Other mechanisms include group transfer, dimerization and ionization.^[30,31,32]

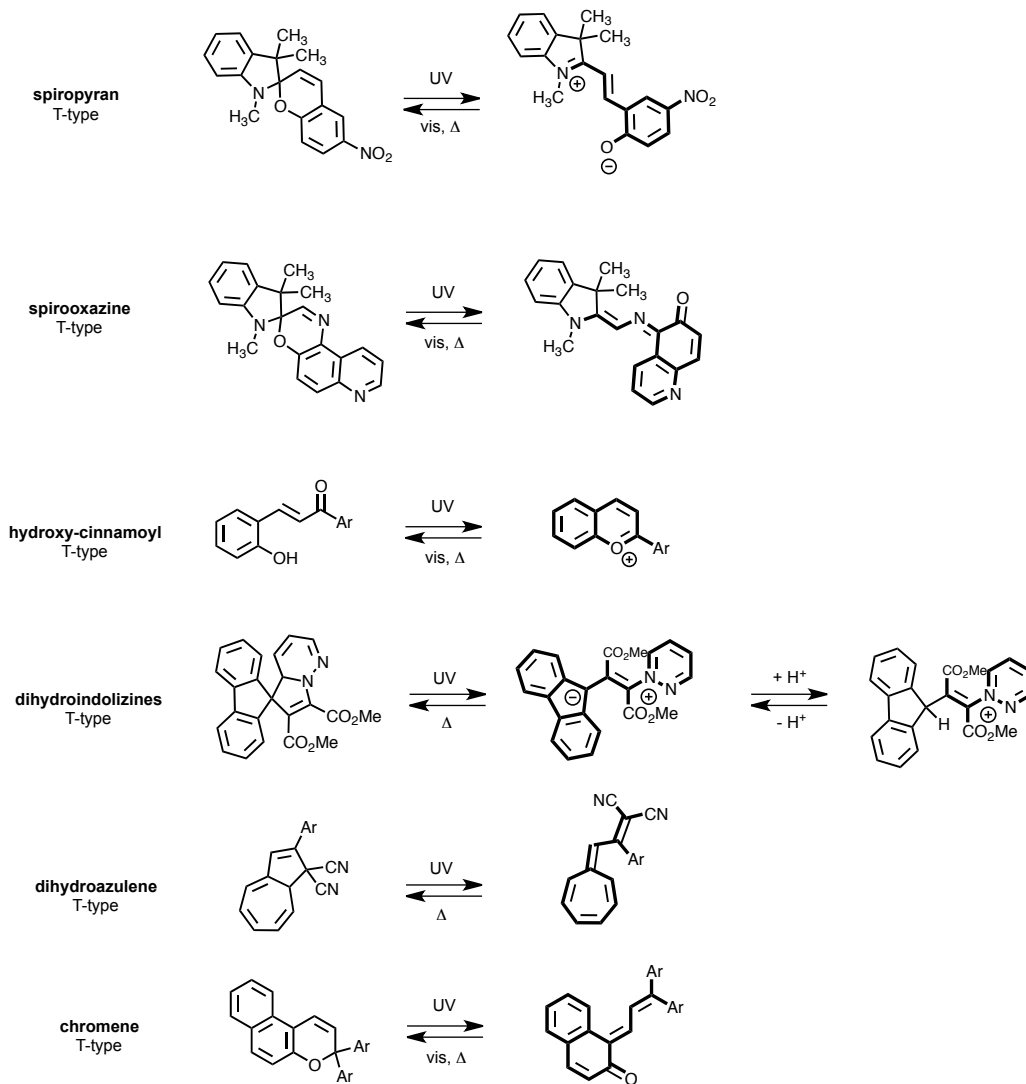
2.1 Thermal (T-type) photochromism

Probably the most well-known and widely used photoswitch is the azobenzene class and the type of photochromism this type of photoswitch displays is double bond isomerization between the thermodynamically stable *trans* (E) isomer and the photoinduced *cis* (Z) isomer, see Scheme 2.1.^[34] The carbon analogue stilbene also displays double bond isomerization upon UV light irradiation.^[35,36] However, due to the 1,3,5-hexatriene configuration in the *cis* (Z) isomer (highlighted in bold in Scheme 2.1), it undergoes a 6- π -electrocyclization reaction to a ring-closed isomer upon further UV light irradiation. This ring-closed isomer can further oxidatively and irreversibly aromatize to phenanthrene.^[36] In order to prevent the aromatization pathway, the ortho-positions are methylated and the process becomes reversible, see Scheme 2.1^[37,38,39]



Scheme 2.1 Azobenzene, stilbene and methylated stilbene T-type photochromism. The bold features of the stilbene molecules highlight both the 1,3,5-hexatriene configurations and the extended conjugation after photoinduced ring-closing reaction.

The photochemically induced double bond isomerization is integral in organic photochemistry and many photoswitches display this type of isomerization in combination with a pericyclic cyclization/decyclization reaction.^[30,31,32] Upon UV light irradiation, these molecules react to form ring-open or ring-closed neutral or ionic coloured isomers, which revert back to the original isomer quantitatively upon visible light irradiation and/or thermally in the dark. In combination with pericyclic reactions, the double bond isomerization configurationally impedes or facilitates the pericyclic reactions by separating or ‘joining’ the reactive centres from/to each other, see Scheme 2.1, 2.2 and 2.3.



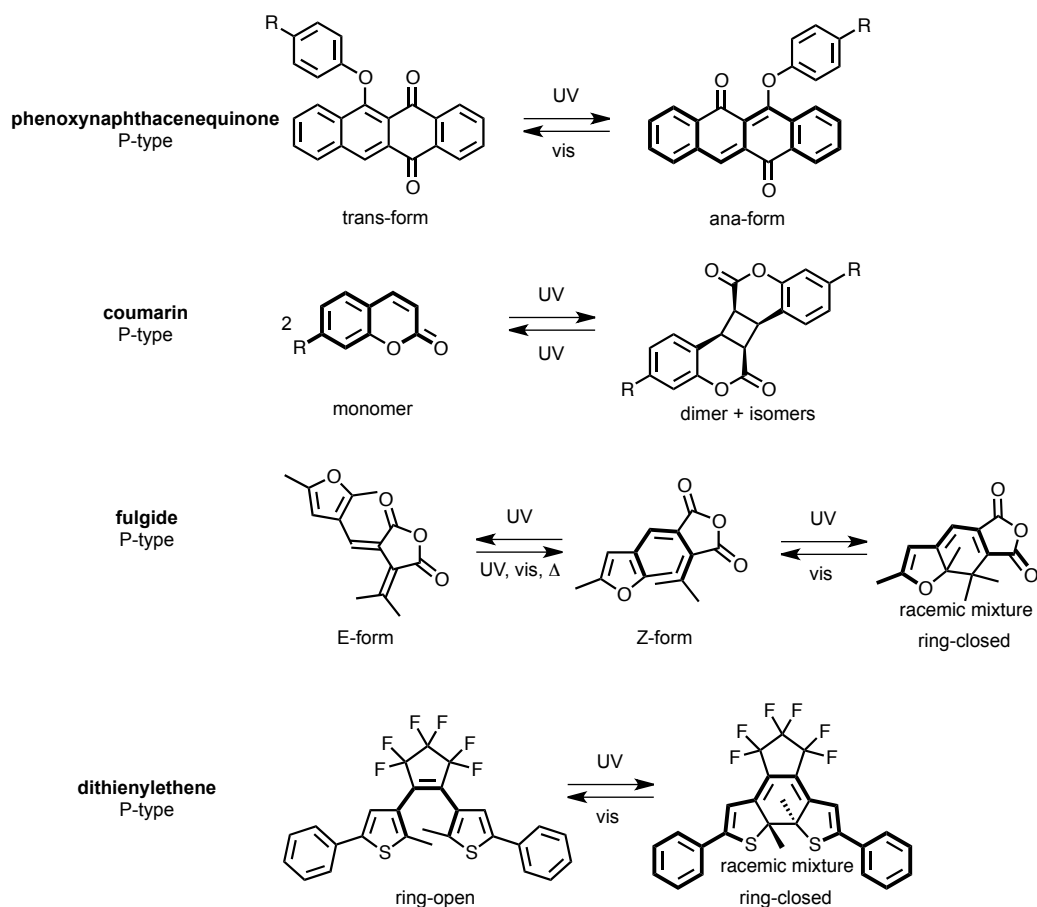
Scheme 2.2 T-type photochromic compounds exhibiting double bond isomerization in combination with pericyclic reactions. The bolded features describe the extended conjugation that is responsible for the colour of the photoinduced isomers due to absorption in the visible range of the electromagnetic spectrum.

2.2 Photochemical (P-type) photochromism

Due to the superior resistance to the thermal back reaction, the photochemical P-type chromophores are useful for applications where it is crucial that the photo-induced isomer do not spontaneously revert back to the original isomer in the dark. Due to the heightened thermal stability of the

photoinduced isomer, novel applications have and can be developed that utilize less energetic visible light, applications that can have major influences in for example medical research.^[30]

In contrast to the T-type photochromic class, the P-type photochromic class has fewer members. The fulgides and the diarylethenes are the primary examples of unimolecular photochromism in the thermally stable P-type photochromic class although other examples exist, see Scheme 2.3. The fulgides and the diarylethene photoswitches are similar to each other since they both possess a central 1,3,5-hexatriene framework and consequently react the same way with light.^[30] Although both molecules form a thermally stable ring-closed photoproduct, the diarylethene class is more versatile due to easier synthesis and thus simpler tailoring of the structure-property relationships.^[30,31,40,41,42,43] For this reason, the diarylethene class and especially the dithienylethene (DTE) subclass have found much more attention in the scientific community than the fulgides and is the choice of photochromic chromophore throughout this thesis.



Scheme 2.3 P-type photochromic molecules. The bolded features indicate both the extended conjugation and the 1,3,5-hexatriene configurations in the cases of the fulgide and dithienylethene molecular switches.

2.3 The dithienylethene P-type photochromic molecular switch

The diarylethenes or more specifically the 1,2-dithienylethenes are the ‘gold-standard’ of thermally stable photochromic materials. This photochromic class of molecules undergo some of the most efficient photoreactions of all photoactive molecules discovered so far and generally display little degradation upon UV light irradiation, depending on design. [40,41,42,43]

2.3.1 Design of the DTE chromophore

The general design of the diarylethene photoswitch entails linking two five-membered S-, O- or N-heteroaromatic rings to a central double bond. In order to prevent a configurational double bond isomerization of the central double bond during UV light irradiation, it is often locked in a ring such as cyclopentene or hexafluorocyclopentene. The best performance in terms of stability is frequently achieved with perfluorinated-dithienylcyclopentene based photoswitches as these photochromic molecules are essentially non-photodegradable and respond rapidly and efficiently to light.^[40,41,42,43]

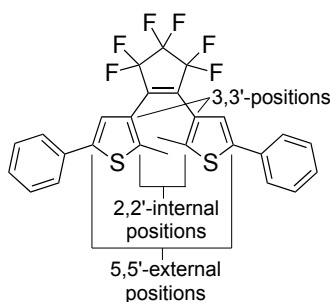


Figure 2.1 Common design of a DTE molecular switch.

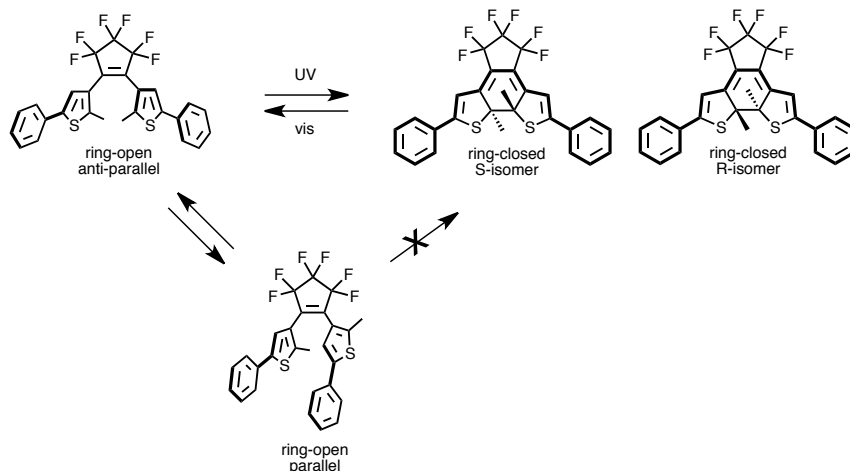
As depicted in Figure 2.1 the two heteroaromatic rings are most often linked to the central double bond at the 3,3'-positions. For the photochemistry to be reversible, substituents at the 2,2'-positions (referred to as the internal positions) other than hydrogen are imperative for desired function, as the ring-closed photoproduct can oxidatively aromatize if the substituents are hydrogen as in the case of stilbene, see Scheme 2.1.^[36] The most common substituents at the internal position is methyl, although aromatic substituents at the internal

position are also viable and tend to raise the efficiency of the visible light induced ring-opening reaction.

At the 5,5'-position (referred to as the external position), an aromatic or carbonyl moiety tend to raise the efficiency of the UV light driven ring-closing reaction and is a way to tune the absorption of the coloured ring-closed photoproduct and design various 'on-off' molecular switches for diverse applications, see section 2.3.5.

2.3.2 The ring-closing reaction and the ring-closed isomer

The as-synthesized DTE photoswitch (see Figure 2.1), which is described as the ring-open isomer, contains a central 6- π -electron 1,3,5-hexatriene π -system that is the core to the photochromism of the DTE class.^[40,41,42,43] Upon UV light irradiation, and when the two thiophene rings are in an antiparallel conformation (C_2 -symmetry), the hexatriene π -system undergoes a conrotatory 6- π -electrocyclization ring-closing reaction due to the orbital symmetry in the excited state in accordance with the Woodward–Hoffmann rules,^[44] see Scheme 2.4 and Figure 2.2. The ring-closed isomer is produced as a racemic mixture of two C_2 -symmetric enantiomers.



Scheme 2.4 The photochromic reaction of a DTE molecular switch producing a racemic mixture of two enantiomers.

The quantum yield of the ring-closing reaction is often high ($\Phi_c = 0.59$)^[33] and the photochemical reaction is fast (10^{12} s^{-1}).^[45] In the photoexcited S_1 wave packet, the electron can either non-radiatively (or fluoresce depending on the molecule) relax back to the ground state starting material or promote the pericyclic rearrangement to the coloured ring-closed isomer. The photoexcited reaction surface of the cyclization reaction from the excited S_1 ring-open state to the ring-closed ground state S_0 has a steep slope along the reaction coordinate toward the formation of ring-closed product and is consequently a downhill process, see Figure 2.2.^[46] An equilibrium, termed the photostationary state (pss), is rapidly established between the formation of ring-closed and ring-open isomer upon irradiation with UV light and can be as high as 5 % ring-open and 95 % ring-closed isomer.^[33] The underlying reason for the establishment of an equilibrium upon UV light irradiation is because both isomers absorb UV light

and can react upon excitation. However, the equilibrium lies toward formation of the ring-closed isomer since the quantum yield of the ring-closing reaction is higher than the ring-opening reaction, see Figure 2.2 and Section 2.3.3.

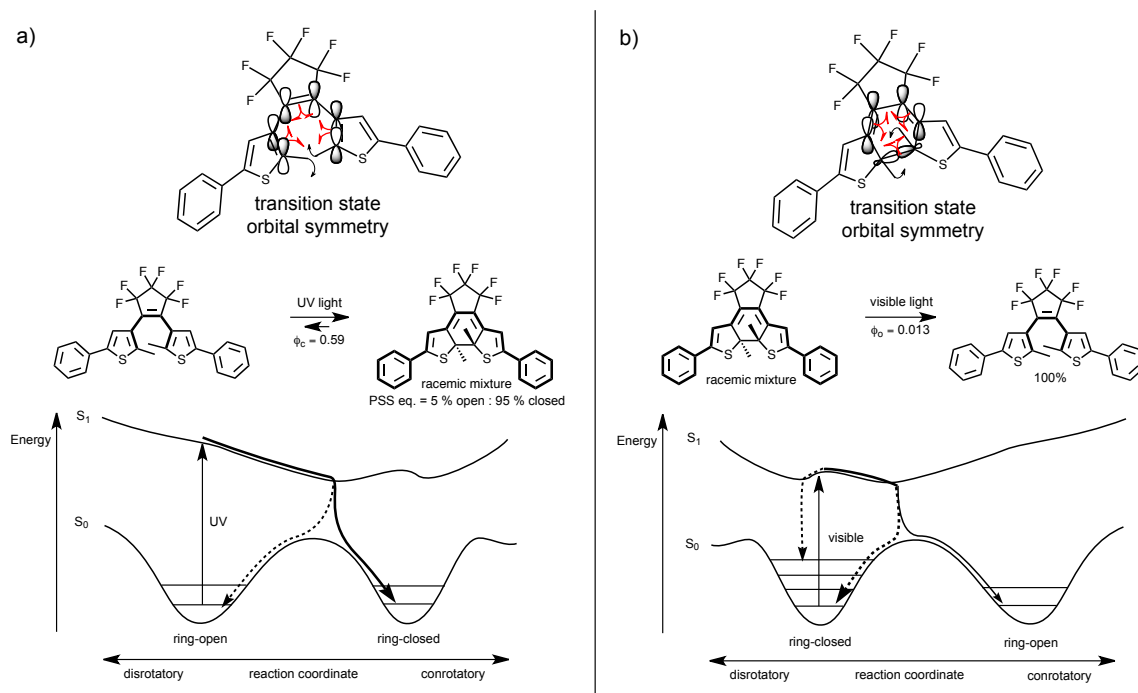


Figure 2.2 Transition state orbital symmetry in the S_1 -excited state according to the Woodward-Hoffman rules and photochemical reaction schemes for the (a) ring-closing and (b) ring-opening reactions and a schematic representation of the potential energy surfaces along the reaction coordinates of the photochromic reactions of the DTE molecular switch.^[46]

After the photoinduced pericyclic rearrangement from the ring-open isomer to the ring-closed isomer, the two external ends of the photoswitch that previously were cross-conjugated are now electronically π -conjugated through the DTE backbone. Due to this extended π -conjugation the molecule absorbs in the visible region of the electromagnetic spectrum and appears coloured to the eye, see Scheme 2.4 and Figure 2.2.

The coloured ring-closed isomer is often extremely stable at room temperature and does not bleach thermally in the dark, even at elevated temperatures it remains stable.^[33] However, if the substituent at the internal position is substituted with bulky alkyl or especially alkoxy groups such as isopropoxy, both the thermal half-life (7 min) of the ring-closed isomer and the quantum yield of the ring-opening reaction ($\Phi_o \approx 6 \times 10^{-4}$) drops markedly,^[47] see Figure 2.3.

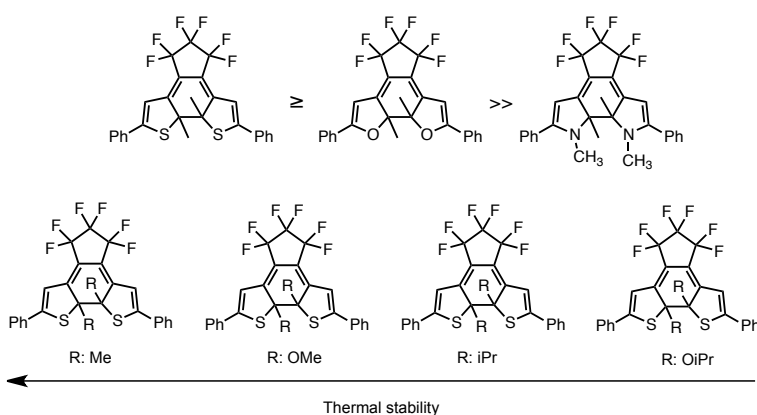


Figure 2.3 Thermal stability of the ring-closed isomer of various diarylethene derivatives.

2.3.3 The ring-opening reaction

Upon visible light irradiation, the ring-closed isomer undergoes a conrotatory 4- π -2- σ -electron cyclo-reversion reaction with a lower quantum yield ($\Phi_o = 0.013$) than the ring-closing reaction.^[33] The quantum yield for the ring-opening reaction is lower since most of the excited electrons relax non-radiatively (or fluoresce depending on the molecule) to the ground state of the ring-closed starting material without promoting the cyclo-reversion reaction to the ring-open isomer, see Figure 2.1.^[46] However, although the quantum yield is low in comparison to the ring-closing reaction, the ring-opening reaction eventually

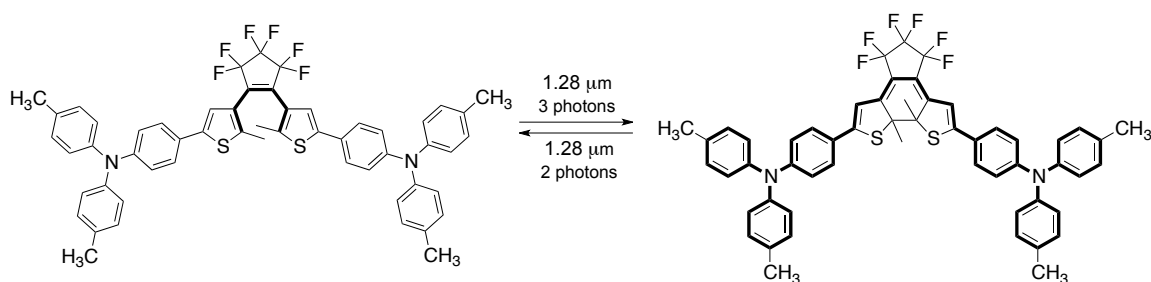
reaches 100 % ring-open isomer (not accounting for any degradation product during UV light irradiation)^[48] since the ring-open isomer does not absorb visible light.

2.3.4 Multiphoton photoswitching

As with many other photoactive molecules, the DTE chromophores can also respond to lower energy near infrared light (NIR) by absorbing multiple photons.^[49] Two- or three-photon excitation is a process in which the chromophore is excited by simultaneously absorbing multiple photons with enough energy to mimic the original one UV or visible light photon.^[4,5] This process is quite inefficient and is determined by the molecules ability to harvest the low energy photons, which is expressed as their multiphoton absorption cross-section expressed in Goepphart-Mayer ($1 \text{ GM} = 10^{50} \text{ cm}^4\text{s}/\text{photon}$).^[4,5] In order for this process to be efficient, the absorption cross-section need to be large and the quantum yield should also be high as to maximize product formation after two or more photons are absorbed. The exciting laser has to be tightly focused and pulsed with an extremely high peak power in order to maximize the concentration of photons in the focal point of the laser beam, which is where the reactions occur. Due to this phenomenon, precise excitation is accomplished in a small volume using multiphoton excitation, which gives the user full 3D control over the excitation process.^[4,5]

DTE photoswitches, along with most other photoresponsive molecules, generally have a low multiphoton absorption cross-section. But they can be tuned to absorb NIR light better by expanding the π -system to large and

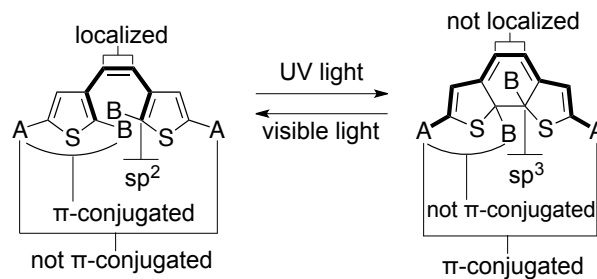
symmetrical pendent groups.^[50] Irie and co-workers recently demonstrated that one such DTE derivative is susceptible to both ring-closing (three-photon) and ring-opening (two-photon) reactions by only changing the power density of the 1.28 μm NIR light laser excitation source,^[49] see Scheme 2.5.



Scheme 2.5 Multiphoton bidirectional photoswitching using NIR light of one wavelength.^[49] The features in bold highlight the 1,3,5-hexatriene configuration of the ring-open isomer and the extended conjugation of the ring-closed isomer. The bold features on the left side of the reaction arrow indicate the 1,3,5-hexatriene configuration whereas on the right side of the reaction arrow it indicates the extended conjugation with absorbance in the visible region of the electromagnetic spectrum.

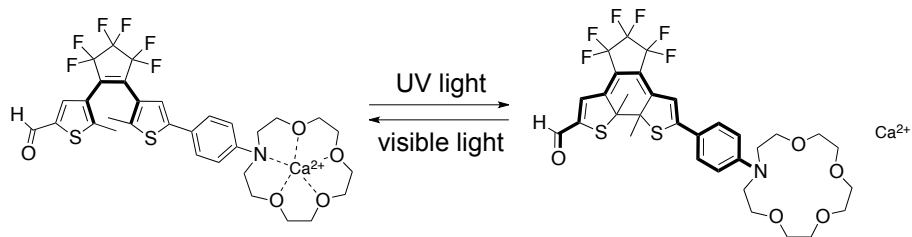
2.3.5 Applications of the DTE class

The DTE framework is versatile and with proper design and ingenuity it can be triggered to perform ‘tasks’ with both UV and visible irradiation, see Scheme 2.6. Especially the ability to use low energy visible light for a triggering event can have great impact in the medical field since light penetrates tissue best at ca. 630-900 nm,^[19,20,21,22] wavelengths the photoswitches can be tuned to absorb.^[49,51,52]

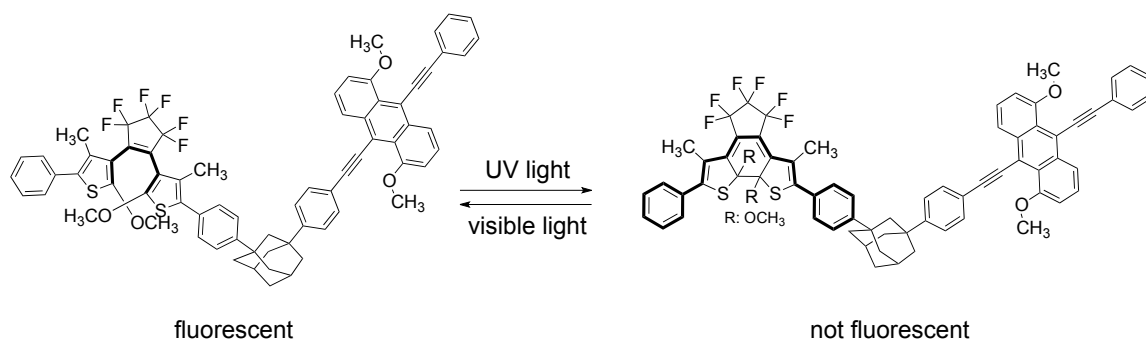


Scheme 2.6 The DTE framework is versatile and with proper design many different applications can be realized. The bolded features describe the 1,3,5-hexatriene configuration and the extended conjugation.

Classically the photoswitches were designed to respond to changes in light absorption or electronic communication upon irradiation as the π -conjugation can be broken or generated upon irradiation with light of appropriate wavelength. In the ring-open colourless form the two heteroaromatic rings are cross-conjugated and the external positions are insulated from each other. After UV light irradiation and subsequent ring-closing reaction, the two external ends of the coloured isomer are electrically π -conjugated and can electronically 'communicate', see Scheme 2.6. Such changes in extended conjugation can be used for a number of applications such as ion complexation^[51] and fluorescence quenching^[53] among many other applications,^[30,42,43] see Scheme 2.7 and 2.8.



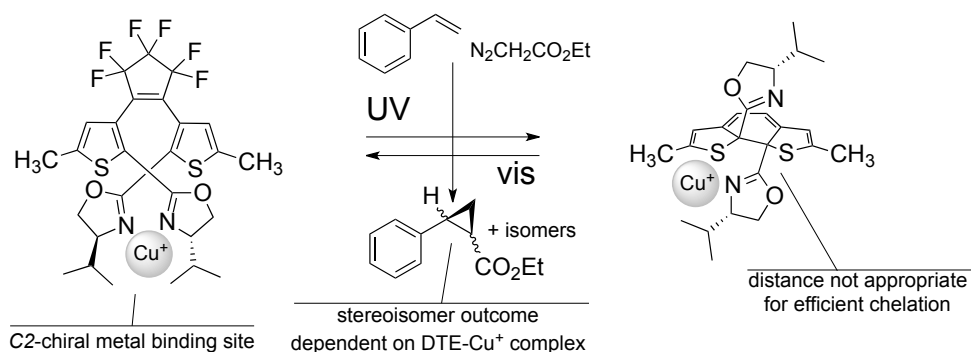
Scheme 2.7 Upon UV light irradiation the electronic density of the aniline nitrogen is decreased and Ca^{2+} is released.^[51] In the ring-closed isomer the aniline nitrogen is conjugated to the aldehyde and a donor acceptor system is generated. The bold features on the left side of the reaction arrow indicate the 1,3,5-hexatriene configuration whereas on the right side of the reaction arrow it indicates the extended conjugation. The ring-closed isomer absorbs red visible light due to the conjugated donor acceptor system.



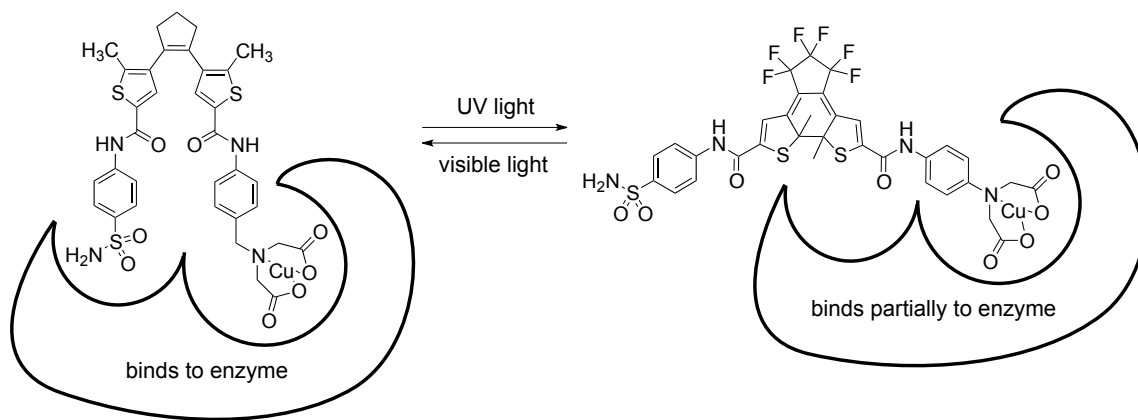
Scheme 2.8 In the ring-open state the molecule exhibits fluorescence. After irradiation with UV light the ring-closed isomer quenches the fluorescence by FRET.^[53] The bold features on the left side of the reaction arrow indicate the 1,3,5-hexatriene configuration whereas on the right side of the reaction arrow it indicates the extended conjugation with absorbance in the visible region of the electromagnetic spectrum.

Many systems have also been designed to undergo changes in their rotational degrees of freedom. In the ring-open form, the two aryl rings can rotate but in the ring-closed isomer the two heteroaromatic rings are configurationally locked in a planar and rigid structure.^[30,40,41,42] Such configurational changes

have many applications including catalysis^[54] and medicine ^[55] among many other applications,^[30,42,43] see Scheme 2.9 and 2.10.



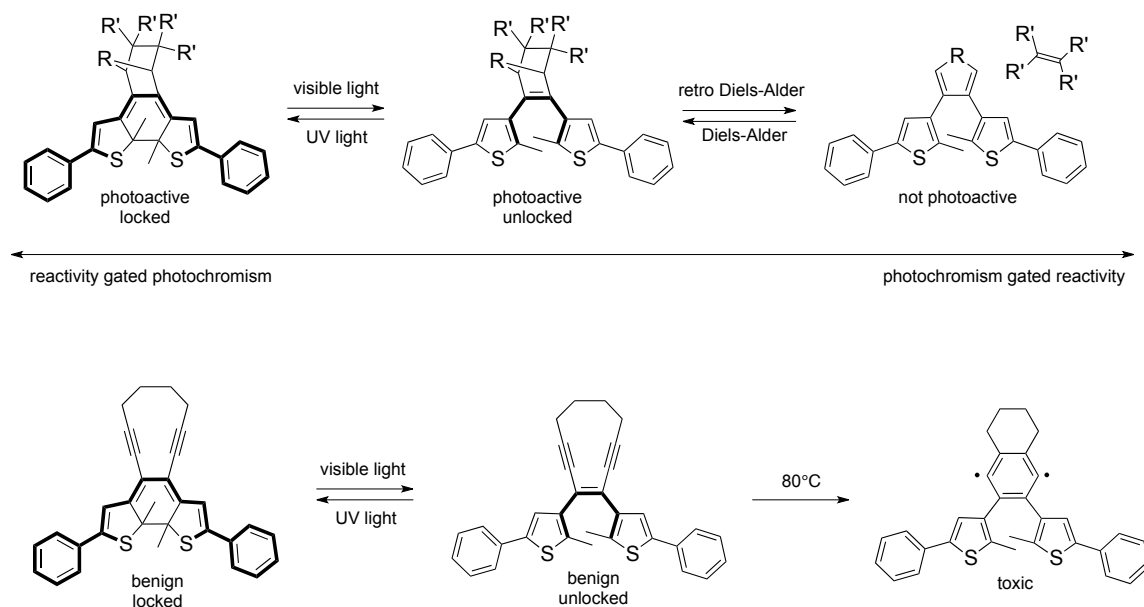
Scheme 2.9 In the ring-open form the chiral DTE molecular switch complex Cu⁺ in a C2-chiral binding site and stereoselectively catalyse a cyclopropanation reaction. After UV light irradiation the distance between the ligands are not appropriate for complexation and the stereochemical outcome of the reaction is altered.^[54]



Scheme 2.10 In the ring-closed form the photoswitch cannot bind properly in the binding site of an enzyme, after irradiation with visible light the ligand fits into the binding site.^[55]

The ability of the DTE photoswitch to rearrange its electron configuration can be used in other ways than electronic communication between the external or external-internal positions and steric change; the central double bond linking

the two heteroaromatic rings is one such example. In the ring-open colourless isomer, the central double bond is located and isolated on the central ring system, but in the ring-closed coloured isomer those electrons are rearranged and in conjugation over the backbone and is thus 'removed' from the central ring with UV light and 'replaced' with visible light, see Scheme 2.6 and 2.11. This phenomenon can be utilized in a number of ways such as reactivity-gated photochromism,^[56,57, 58] photochromism-gated reactivity,^[9,57,59,58] molecule sequestering^[60] and potentially in catalysis,^[60,61,62] see Scheme 2.11.



Scheme 2.11 General examples of reactivity-gated photochromism and photo-gated reactivity for sensing, release technology and activation of toxic species recently developed in the Branda lab.^[9,56,57,58,59] The bolded features describe the extended conjugation and the hexatriene configuration.

2.3.6 Outlook

Since the DTE molecular switch generally has a high photostationary state, not very prone to UV light degradation with proper design, and has a thermally stable ring-closed photoproduct, novel visible light activated applications have been and are being developed.

With proper design, the DTE framework can prove very useful for the molecular- and nano-medical research field as new one-photon red-light (> 630 nm) activated functional switches can be developed which would be a great leap in photo-activated therapeutic activation *in vivo*.

3: REMOTE-CONTROL PHOTOSWITCHING USING NIR LIGHT

3.1 Contributions

The text in this chapter has previously been published as a communication in the Journal of the American Chemical Society and is reproduced herein in its entirety with permission from the journal (C.-J. Carling, J.-C. Boyer, N. R. Branda, *J. Am. Chem. Soc.*, **2009**, *131*, 10838–10839, <http://pubs.acs.org/doi/abs/10.1021/ja904746s>). The project was co-designed by C-J Carling, Dr. J-C Boyer and Prof. Dr. N. R. Branda. All organic synthesis and characterizations of organic molecules were carried out by C-J Carling. Dr. J-C Boyer carried out all nanoparticle synthesis and characterizations thereof. All acrylate films were produced by C-J Carling except for the acrylate rod in Figure 3.8a that was made by Dr. J-C Boyer. C-J Carling and Dr. J-C Boyer jointly measured all ‘remote-control’ photochemistry. The manuscript was co-written by C-J Carling, Dr. J-C Boyer and Prof. Dr. N. R. Branda.

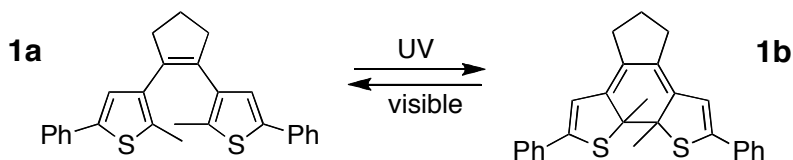
3.2 Abstract

Near-infrared (NIR) light is used to toggle photoswitches back and forth between their two isomers even though the chromophores do not significantly absorb this type of light. The reactions are achieved through a ‘remote-control’ process by using photon upconverting hexagonal NaYF₄ nanocrystals doped with lanthanide ions. These nanoparticles absorb 980 nm light and convert it to

wavelengths that can be used to trigger the photoswitches offering a practical means to achieve 3D-data storage and photolithography.

3.3 Introduction

The use of dithienylethene (DTE) photoswitches to achieve spatial and temporal control of molecular processes and optoelectronic properties has received significant attention in the recent years.^[40,41,42] This attention is well deserved and due to the fact that the photoswitches can be toggled back-and-forth between two structurally and electronically different isomers (Scheme 3.1) having properties that can be fine-tuned by decorating the molecular backbone with functional groups so they can be applied to a wide range of technologies, from optical data storage and processing^[63] to photorelease^[57] and photodynamic therapy.^[59]



Scheme 3.1 Reversible photochromic reaction of dithienylethene photoswitch **1**

One of the major drawbacks of these versatile photoresponsive systems is the need for ultraviolet and visible light to induce the ring-closing and ring-opening reactions, respectively. Both types of light are associated with detrimental effects such as inducing unwanted side reactions and low penetration into biological tissue.^[64] More practical systems are those that undergo multiphoton processes in the near-infrared (NIR) region of the spectrum

where the probability of inducing chemical reactions is reduced and 3D control can be achieved (a key to photodynamic therapy and volumetric data storage applications).^[65] Because photochromic compounds often have low 2-photon-absorbing cross sections,^[65] a better alternative is to induce the DTE reactions in a ‘remote-control’ process by using antennae species that absorb NIR light and transfer the harnessed energy to the photoswitch.

Photon upconverting nanoparticles (UCNPs), in particular hexagonal NaYF₄ nanocrystals doped with lanthanide ions, are ideal for ‘remote-control’ photoswitching.^[66] 1) They efficiently absorb NIR light and convert it to wavelengths that can be used to trigger appropriate DTE photoswitches. 2) The key electronic excitations occur in real energy levels, requiring significantly lower intensities of light than conventional two-photon absorbing dyes. 3) They do not suffer from photobleaching. 4) They can be coated with biocompatible polymers and antibodies to decrease toxicity, prolong circulation time and increase tissue selectivity, rendering them particularly useful in biomedical applications.^[67]

In this paper, we demonstrate how DTE photoswitches undergo their ring-closing and ring-opening reactions using NIR light in the presence of two types of UCNPs that emit UV and visible light. In a preliminary study, we also illustrate the concept of ‘remote-control’ photorelease using the DTE architecture. A recent publication^[68] describes the use of UCNPs and a DTE for optical memory applications. Although effective quenching of the UCNP emission by one of the DTE isomers was achieved, ‘remote-control’ switching was not demonstrated, likely due to the use of the less-efficient upconverting LaF₃ nanoparticles, a

lower laser power and/or the occurrence of an energy-transfer process, which produces a state with different properties from our case.

3.4 Results and Discussion

We chose to use NaYF₄ nanoparticles because they are some of the best UCNPs known to date and depending on their composition they can emit ultraviolet, violet, blue, green, and red light upon absorbing NIR (980 nm) light. The ‘remote-control’ switching of DTE **1** by UCNPs NaYF₄ doped with 0.5 mol % Tm³⁺ and 30 mol % Yb³⁺ (NaYF₄:TmYb), and NaYF₄ doped with 2 mol % Er³⁺ and 20 mol % Yb³⁺ (NaYF₄:ErYb) are the focus of our studies. The ring-open isomer (**1a**) absorbs UV light,^[69] which induces ring-closing to form **1b**. This light can be generated when a dispersion of the UV-emitting NaYF₄:TmYb nanoparticles absorb NIR light. The ring-opening reaction (**1b** → **1a**) is triggered by visible light, which can be produced by a dispersion of the green-emitting NaYF₄:ErYb.

DTE **1a** and both UCNPs are prepared according to literature procedures.^[69] TEM images of the UCNPs demonstrate their nearly monodisperse particle size (Figure 3.1a and 3.1b) of 25.3 ± 1.4 nm and 25.6 ± 1.3 nm for NaYF₄:TmYb and NaYF₄:ErYb, respectively. Powder X-ray diffraction^[10] confirms that the synthesized particles are hexagonal in phase with no significant impurity phases present. The well-defined peaks of the X-ray pattern demonstrate the high crystallinity of the doped NPs, and a crystallite size of approximately 23 nm can be determined for both types of UCNPs from the line broadening of the diffraction peaks, which correlate well to the TEM data.

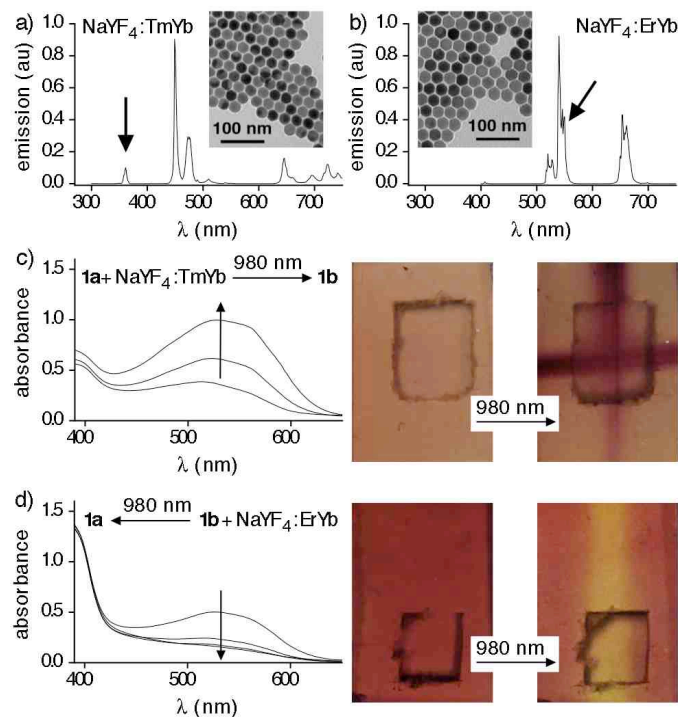


Figure 3.1 Emission spectra of colloidal CHCl_3 solutions of (a) $\text{NaYF}_4:\text{TmYb}$ and (b) $\text{NaYF}_4:\text{ErYb}$ UCNPs when excited with a 980 nm laser diode.^[69] The light used to trigger photoswitch **1** is highlighted. TEM images are shown as insets. Changes in the UV-vis absorption spectra (left) and photographs (right) of acrylate films ($12 \times 8 \times 1$ mm) containing (c) **1a** + $\text{NaYF}_4:\text{TmYb}$, and (d) **1b** + $\text{NaYF}_4:\text{ErYb}$ as they are irradiated with 980 nm light. The stripes observed in the right panel of (c) and (d) correspond to the direction of the beam of the 980 nm laser.^[69] The irradiation in (c) was carried out two times with perpendicular orientations. The small squares in all images are the cut-out holes in the sample holder through where the absorption was measured.

DTE **1a** absorbs UV light (365 nm) and undergoes efficient conversion to its ring-closed counterpart (**1b**) as illustrated by the changes in the UV-vis absorption spectrum^[69] and the visual color change of a CH_3CN solution from colourless to red. Visible light (> 450 nm) triggers the reverse reaction and regenerates both the original spectrum and the color. These wavelengths correspond to those emitted by the UCNPs, which have upconversion emission spectra that correspond to those reported previously.^[66] Of the five emissions

observed for NaYF₄:TmYb ranging from ultraviolet to near-infrared (Figure 3.1a), the highest energy emission is appropriate for photocyclization (**1a** → **1b**). In the case of NaYF₄:ErYb, violet, green and red emissions are observed (Figure 3.1b), with the second one appropriate to induce ring-opening (**1b** → **1a**).^[70,71]

In order to ensure that the UCNPs and DTE remain in close enough proximity to promote re-absorption of the light emitted from the nanocrystals by the organic chromophore, we chose to demonstrate 'remote-control' switching by casting both components in a polymer composite material comprised of cross-linked poly(ethyleneglycol)dimethacrylate and toluene, which provides a flexible environment for the photoreactions of **1**.^[72]

When a pale yellow film containing **1a** and an excess of NaYF₄:TmYb is irradiated with 980 nm diode laser light, the film only changes to a red color along the path of the beam of light (Figure 3.1c), which can be attributed to the photocyclization reaction (**1a** → **1b**). This reaction is supported by the changes in the absorption spectrum, which match those for a sample of **1a** alone.^[69] Similarly, a film containing **1b** and NaYF₄:ErYb undergoes decolorization only along the path of the light (Figure 3.1d). The ring-opening reaction (**1b** → **1a**) is also supported by spectral changes that match those for a sample of **1b** irradiated with visible light.

The fact that the reactions of the DTE chromophore are triggered by absorbing the light generated by the UCNPs is demonstrated by irradiating a film containing **1b** but no NaYF₄:ErYb, which undergoes almost no changes in its color or its UV-vis spectrum (see Figure 3.7 in the experimental section 3.8.7).

We recently demonstrated how visible light could be used to trigger the release of a small molecule from a DTE derivative by inducing the ring-opening reaction of a 'locked' species.^[57] The process is based on the creation of an unstable ring-open compound that spontaneously undergoes a reverse Diels-Alder reaction to generate a fulvene and a dienophile as illustrated by analogous compounds shown in Figure 3.2a. We now demonstrate that we can trigger the release using NIR light and UCNP.

Dithienylfulvene **3** is synthesized using our original methods with some minor modifications.^[69] The ring-closed Diels-Alder product (**2b**) is produced as a mixture of four stereoisomers after treating **3** with an excess of diethyl dicyanofumarate and exposing the unstable intermediate (**2a**) to UV light. When an acrylate film containing **2b** and NaYF₄:ErYb is exposed to 980 nm light in an analogous manner as for **1b**, similar color changes can be observed (Figure 3.2b) showing that 'remote-control' switching also operates in this system. When probed using UV-vis absorption spectroscopy, in addition to the decrease in the absorption band at 550 nm, which signifies ring-opening (**2b** → **2a**), an increase in an absorption band at 400 nm is observed. This increase can be attributed to the appearance of dithienylfulvene **3** through the spontaneous release from **2a**. Irradiation of this film with 365 nm light results in no observable spectral changes supporting the success of the release even in the relatively solid matrix since any remaining ring-open isomer would be converted back to its ring-closed counterpart (**2b**).

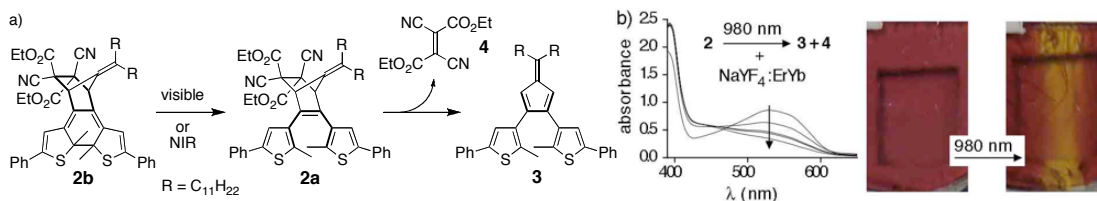


Figure 3.2 (a) Scheme illustrating the ring-opening and release reactions of bicyclic compound **2b** as it is irradiated with visible or NIR light. (b) Changes in the UV-vis absorption spectra (left) and photographs (right) of an acrylate film ($8 \times 7 \times 1$ mm) containing **2b** + NaYF₄:ErYb as it is irradiated with 980-nm light. The stripe observed in the right panel corresponds to the direction of the beam of the 980-nm laser.

3.5 Conclusion

Our demonstration of ‘remote-control’ switching using the versatile DTE architecture and upconverting doped nanocrystals offers new opportunities in photodynamic therapy and 3D data storage. In these studies we have demonstrated that either ring-closing or ring-opening reactions can be triggered by the judicious choice of organic chromophore and UCNP.

3.6 Acknowledgement

This research was supported by the Natural Sciences and Engineering Research Council (NSERC) of Canada, the Canada Research Chairs Program, the University of Victoria and Simon Fraser University.

3.7 Experimental

3.7.1 General methods

3.7.1.1 Materials

All solvents used for synthesis, chromatography and UV–vis absorption spectroscopy measurements were used as received. Solvents for NMR analysis were purchased from Cambridge Isotope Laboratories and used as received. Column chromatography was performed using silica gel 60 (230–400 mesh) from Silicycle Inc. All reagents and starting materials were purchased from Aldrich with the exception of Darocur 4265[®], which was purchased from CIBA and 12-tricosane, which was purchased from TCI America. 1,2-Bis(5'-phenyl-2'-methylthienyl-3'-yl)cyclopentene^[73] (**1a**) and diethyl dicyanofumarate^[74] were prepared as described in the literature. All chemicals utilized in the synthesis of the upconverting nanoparticles and composite samples were purchased from Aldrich and used as received. The NaYF₄: Er³⁺ 2 mol%, Yb³⁺ 20 mol% (NaYF₄:ErYb) and NaYF₄: Tm³⁺ 0.5 mol%, Yb³⁺ 30 mol% (NaYF₄:TmYb) nanoparticles were synthesized as described in the literature^[75] without modifications. The nanoparticles were dispersed in chloroform to give 2 wt-% UCNP stock solutions.

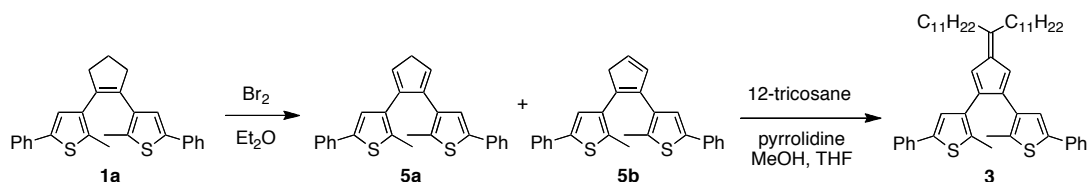
3.7.1.2 Instrumentation

¹H NMR and ¹³C NMR characterizations were performed on a Bruker TCI 600 cryoprobe (proton sensitive, inverse probe) working at 600.33 MHz for ¹H and 150.97 MHz for ¹³C. Chemical shifts (δ) are reported in parts per million

relative to tetramethylsilane using the residual solvent peak as a reference standard. Coupling constants (J) are reported in hertz. UV–vis absorption spectroscopy was performed using a Varian Cary 300 Bio spectrophotometer and an Ocean-Optics USB2000 miniature fiber optic spectrometer. Exact mass measurements were done using a Kratos Concept-H instrument with perfluorokerosene as the standard.

3.7.2 Synthetic procedures

3.7.2.1 Synthesis of dithienylfulvene **3**



A 500 mL round bottom flask equipped with stir bar was flame-dried and cooled under a N_2 purge. The flask was charged with 1,2-bis(5'-phenyl-2'-methylthienyl-3'-yl)cyclopentene **1a** (1.93 g, 4.68 mmol) and anhydrous Et_2O (105 mL). The flask was lowered into a dry-ice/acetone bath at $-78\text{ }^\circ\text{C}$ and Br_2 (0.12 ml, 4.68 mmol) was added drop-wise *via* glass syringe. The yellow dispersion was stirred at $-78\text{ }^\circ\text{C}$ for 25 min before it was removed from the cooling bath and allowed to stir at ambient temperature for 1.5 h, at which time the yellow solution was quenched with water (100 mL) and stirred for 5 min. The layers were separated and the aqueous layer was extracted with EtOAc (2×40 mL). The combined organic layers were washed with NaHCO_3 (40 mL), dried (MgSO_4), vacuum filtered and concentrated on a rotary evaporator at $25\text{ }^\circ\text{C}$ to

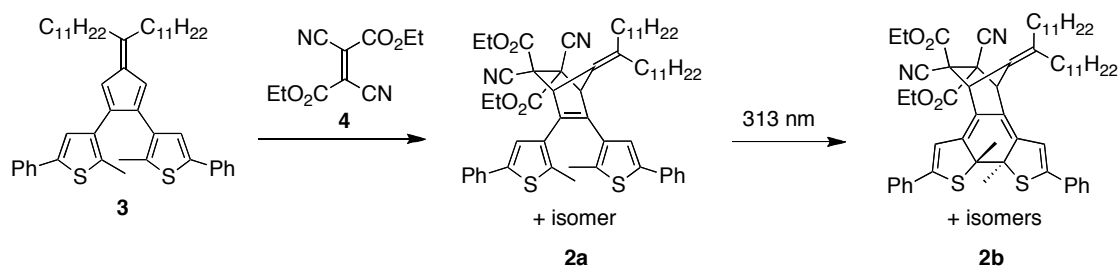
afford a green oil that foams under vacuum. The solid residue was dried *in vacuo* for 10 min in a 100 mL round bottom flask. The solid product of this reaction (**5a** and **5b**) was used without further purification. A stir bar was added to the flask and the system was purged with N₂. A 0.5:3.5 MeOH:THF mixture (33 mL) was added to dissolve the green solid. The solution was treated with a solution of tricosane-12-one (TCI America, 1.58 g, 0.73 mmol) in a 0.5:3.5 MeOH:THF mixture (17 mL). The reaction was then treated with freshly distilled (from sodium) pyrrolidine (1.32 mL, 18.74 mmol) and was allowed to stir at ambient temperature for 17 h, at which time it was quenched with NH₄Cl (30 mL). The reaction mixture was transferred to a separation funnel and diluted with water. The aqueous phase was removed and the organic phase was washed with NH₄Cl (20 mL). The combined aqueous phases were extracted with EtOAc (2 × 75 ml). The combined organic layers were dried (MgSO₄), vacuum filtered and concentrated on a rotary evaporator at 25 °C to afford a brown solid. Purified on a large silica gel column (10% CH₂Cl₂ in hexanes) yielded 570 mg (17%) of compound **3** as a highly viscous yellow/orange oil. Compound **3** was stored in the freezer to prevent decomposition.

¹H NMR (CD₂Cl₂, 600 MHz): δ 7.44 (dd, *J* = 8.3, 1.0 Hz, 4H), 7.30 (dd, *J* = 10.7, 4.8 Hz, 4H), 7.20 (t, *J* = 7.4 Hz, 2H), 6.92 (s, 2H), 6.59 (s, 2H), 2.59–2.62 (m, 4H), 2.32 (s, 6H), 1.63 (td, *J* = 15.4, 7.6 Hz, 4H), 1.28–1.43 (m, 32H), 0.88 (t, *J* = 7.0 Hz, 6H).

^{13}C NMR (CD_2Cl_2 , 151 MHz): δ 159.70, 141.64, 140.05, 139.31, 135.83, 135.51, 135.51, 134.89, 129.11, 127.31, 125.83, 125.65, 120.08, 34.81, 32.30, 30.64, 30.27, 30.06, 30.03, 29.95, 29.86, 29.74, 23.07, 14.63, 14.26.

HRMS (ESI^+) Calculated for $\text{C}_{50}\text{H}_{67}\text{S}_2$ ($[\text{M}+\text{H}^+]$): 731.4684. Found: 731.4665.

3.7.2.2 Synthesis of bicyclic compound 2b



This experiment is composed of two separate experiments that were combined in the end in order to avoid too long irradiation times. Fulvene **3** (#1: 45 mg, 0.06 mmol, #2: 74 mg, 0.10 mmol) was dissolved into a quartz tube in freeze-pump-thawed (FPT) CH_2Cl_2 (3 FPT cycles, #1: 3 mL, #2: 4 mL). Fumarate **4** (#1: 68 mg, 0.31 mmol, #2: 113 mg, 0.51 mmol) was dissolved in FPT CH_2Cl_2 (#1: 12 mL, #2: 24 mL) and added to the quartz tube. The tube was equipped with two stir-bars and purged with argon. The reactions were allowed to reach equilibrium in an ice bath for 10 min before being irradiated with 313 nm light (#1: 75 min, #2: 90 min). The reactions were monitored by TLC. The reactions were combined, concentrated and purified by column chromatography in the dark (9:1 Hexanes:EtOAc) (night vision goggles were employed for visualization) to yield a dark red oil as a complex mixture of 4 stereoisomers (66 mg, 0.07 mmol, 43%).

^1H NMR (CD_2Cl_2 , 600 MHz): δ 7.55–7.52 (m, 4H), 7.42–7.31 (m, 6H), 6.55–6.50 (4s, 2H), 4.41–4.20 (m, 6H), 2.41–2.35 (m, 1H), 2.18–2.12 (m, 3H), 2.06 (s, 3H), 1.96 (s, 3H), 1.46–1.42 (m, 3H), 1.38 (dt, $J = 7.1, 1.8$ Hz, 6H), 1.34 (t, $J = 7.2$ Hz, 2H), 1.25–1.16 (m, 33H), 0.87–0.83 (m, 6H).

^{13}C NMR (CD_2Cl_2 , 151 MHz): δ 164.81, 164.70, 163.40, 162.72, 150.72, 150.64, 150.48, 150.11, 143.57, 142.98, 142.03, 141.97, 134.58, 134.50, 134.43, 134.32, 134.31, 134.29, 134.22, 134.10, 129.64, 129.55, 129.51, 129.05, 129.02, 128.99, 128.94, 128.67, 128.09, 127.27, 126.60, 126.51, 126.48, 126.06, 116.58, 116.37, 116.08, 115.24, 114.69, 114.36, 114.26, 66.98, 65.53, 65.23, 64.78, 64.76, 64.69, 64.59, 57.23, 56.94, 55.96, 52.70, 51.78, 50.90, 49.27, 32.92, 32.78, 32.67, 32.27, 32.24, 30.11, 30.09, 30.05, 29.99, 29.97, 29.94, 29.89, 29.71, 29.67, 29.65, 29.63, 28.87, 28.74, 28.59, 28.46, 26.74, 26.63, 26.53, 23.02, 14.24, 14.23, 14.09, 13.97, 13.94.

HRMS (ESI⁺) Calculated for (M+1) $\text{C}_{60}\text{H}_{77}\text{N}_2\text{O}_4\text{S}_2$ 953.5324. Found: 953.5299.

3.7.3 Preparation of solid-state films

3.7.3.1 General procedure

Viscous solutions containing various components (nanoparticles and photoswitch **1a**, **1b** and **2b**) were prepared by mixing a toluene solution of the appropriate components with PEGDMA (Aldrich, MW 875 g/mol) as the monomer and Darocur 4265[®] as the photoinitiator. The solutions were sandwiched between two microscope slides (75 × 25 × 1 mm) spaced apart by

copper wire and cured by exposing the stacked device to 365 nm light for approximately 20–30 min to produce 1 mm thick, flexible monolithic polymeric composites that could be separated from the stack and used throughout the experiments without any additional support.

3.7.3.2 Background sample

A film to be used as the background sample for spectroscopic analysis was prepared from PEGDMA (30 drops) and Darocur 4265[®] (2 drops). The resulting film was slightly yellow in colour.

3.7.3.3 Control film containing only the photoswitch

Compound **1a** (5.7 mg) was dissolved in toluene (10 drops) by sonication. The solution was treated with PEGDMA (30 drops) and Darocur 4265[®] (1 drop) and the viscous solution was sonicated. The mixture was cured between two microscope slides for 30 min to produce a red polymeric composite material that was cut with scalpel to yield a 8 × 12 × 1 mm film.

3.7.3.4 Films containing 1a and NaYF₄:TmYb

An aliquot (18 drops) of the chloroform stock solution of NaYF₄:TmYb nanoparticles was dried by flowing air over the sample. The solid residue was treated with solid bicyclic compound **1a** (5.5 mg) and toluene (~10 drops), and the mixture was sonicated until a fine dispersion was obtained. The dispersion was treated with PEGDMA (~30 drops) and Darocur 4265[®] (~1 drop) and sonicated until homogenous. The mixture was cured for 20 min to produce a red

polymeric composite material. The film was subsequently subjected to light of wavelengths greater than 434 nm for 40 min to yield a slightly pink composite containing **1a** that was cut with scalpel to yield a 8 × 12 × 1 mm film.

3.7.3.5 Films containing 1b and NaYF₄:ErYb

An aliquot (18 drops) of the chloroform stock solution of NaYF₄:ErYb nanoparticles was dried by flowing air over the sample. The solid residue was treated with solid bicyclic compound **1a** (4.8 mg) and toluene (~10 drops), and the mixture was sonicated until a fine dispersion was obtained. The dispersion was treated with PEGDMA (~30 drops) and Darocur 4265[®] (~2 drops) and sonicated until homogenous. The mixture was cured for 20 min to produce a red polymeric composite material that was cut with scalpel to yield a 8 × 12 × 1 mm film.

3.7.3.6 Films containing 2b and NaYF₄:ErYb

An aliquot (~29 drops) of the chloroform stock solution of NaYF₄:ErYb nanoparticles was dried by flowing air over the sample. The solid residue was treated with solid bicyclic compound **2b** (4.7 mg) and toluene (~27 drops), and the mixture was sonicated until a fine dispersion was obtained. The dispersion was treated with PEGDMA (~37 drops) and Darocur 4265[®] (~4 drops) and sonicated until homogenous. The mixture was cured for 20 min to produce a red polymeric composite material that was cut with scalpel to yield a 8 × 7 × 1 mm film.

3.7.4 Transmission Electron Microscopy (TEM)

TEM imaging of the colloidal nanoparticle samples was performed with a Hitachi H-7000 microscope operating at 75 kV equipped with a charge-coupled device (CCD)-camera. Approximately 0.1 wt-% dispersions of the nanoparticles in hexanes were prepared by dispersing ~1 mg of nanoparticles in 1 g of hexanes. The prepared nanoparticle dispersions were then drop-casted on formvar/carbon films supported on 300 mesh copper grid (3 mm in diameter) and allowed to dry in air at room temperature.

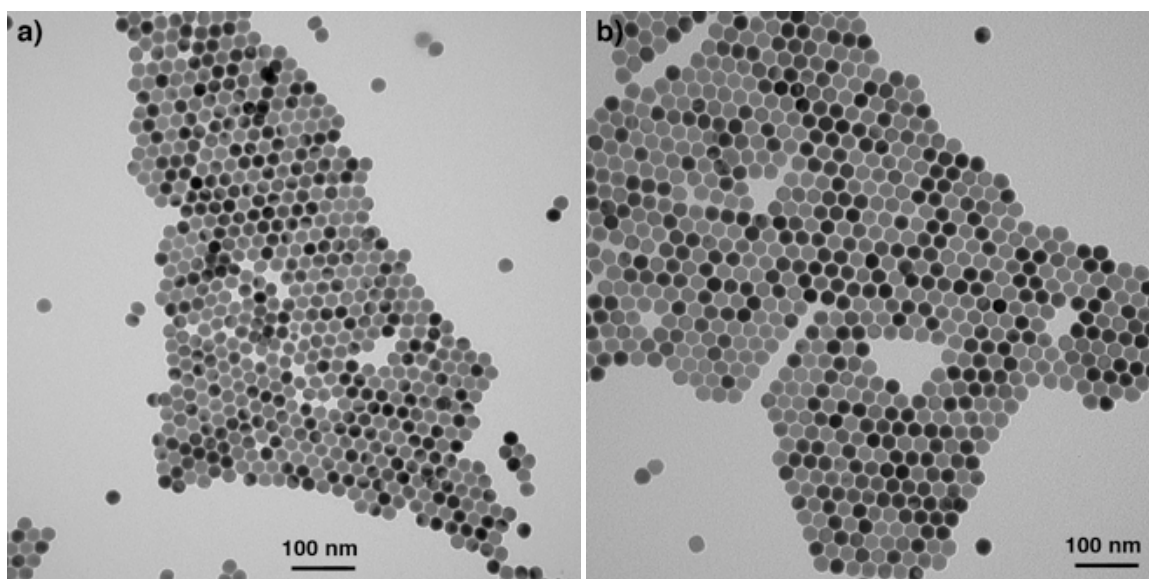


Figure 3.3 Transmission Electron Microscopy (TEM) micrographs of (a) NaYF₄:TmYb and (b) NaYF₄:ErYb nanoparticle samples.

3.7.5 Powder X-ray Diffraction (XRD)

Step-scan powder XRD data were acquired using a Rigaku Miniflex Diffractometer with a Cr radiation source operating at 30 kV and 15 mA with a K β filter. The scattering and receiving slits were 4.2 degrees and 0.3 mm,

respectively. Colloidal dispersions of NaYF₄ nanoparticles in chloroform were concentrated on a rotary evaporator. The resulting concentrated colloidal samples were drop-casted onto a zero-background holder and dried at room temperature. The powder XRD diffractograms were collected from 20–140° (2θ) employing a scanning step size of 0.02° (2θ) and a counting time of 3 s per step.

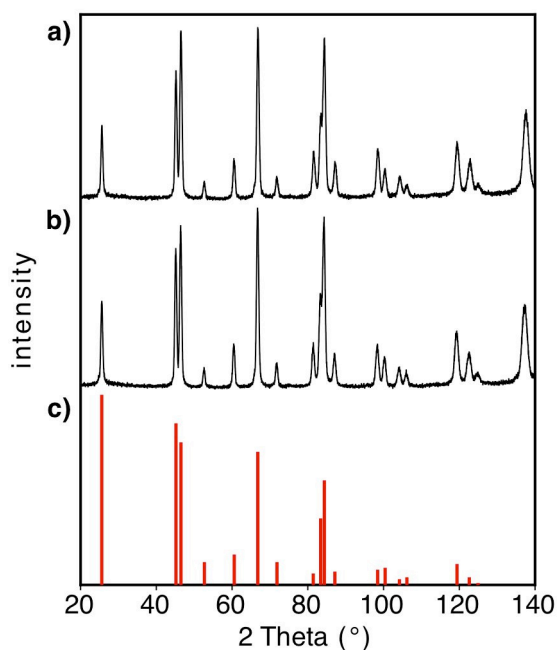


Figure 3.4 Powder X-ray diffraction (XRD) patterns for (a) NaYF₄:TmYb and (b) NaYF₄:ErYb nanoparticle samples and (c) β -NaYF₄ JCPDS standard card #28-1192.

3.7.6 Visible Room Temperature Upconversion Emission Spectroscopy ($\lambda_{exc} = 980 \text{ nm}$)

Upconversion luminescence measurements on the colloidal samples were performed using an Edinburgh Instruments FLS920 fluorimeter. A JDS Uniphase 980 nm laser diode (device type 63-00342) coupled to a 105 μm (core) fibre was employed as the excitation source. The output of the diode laser was collimated

and directed on the samples using a Newport F-91-C1-T Multimode Fiber Coupler. An 850 nm long band-pass filter was placed on the end of the collimator to remove higher energy emissions from the diode laser. Unwanted scattered laser light from the samples was removed using a 900 nm short band-pass filter before the emission monochromator of the fluorimeter. A red-sensitive Peltier-cooled Hamamatsu R955 PMT was used to record the upconversion luminescence spectra. The colloidal nanoparticle samples were held in a square quartz cuvette (path length of 1 cm) for the upconversion measurements.

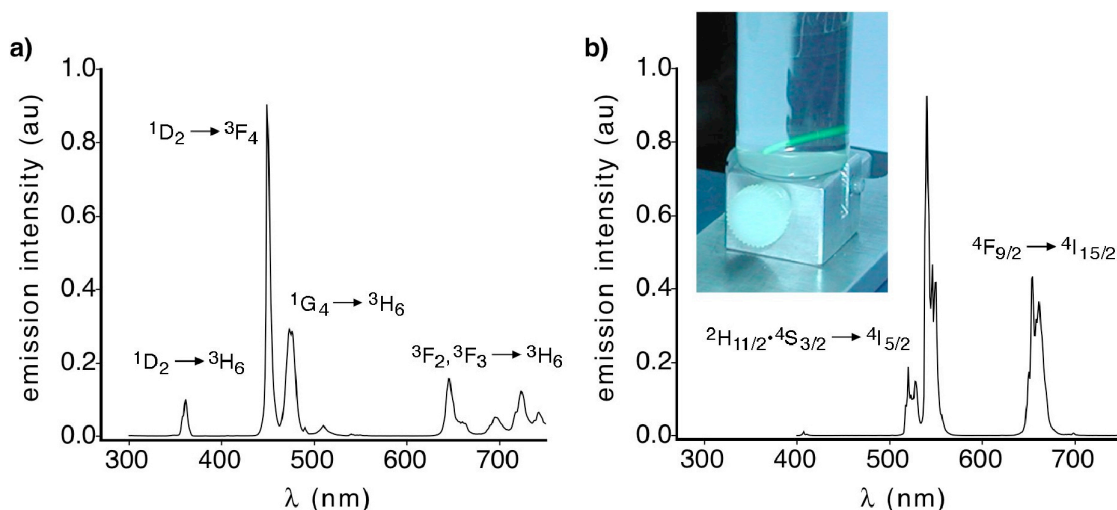


Figure 3.5 Luminescence upconversion emission spectra of 1 wt-% colloidal solutions of (a) NaYF₄:TmYb and (b) NaYF₄:ErYb nanoparticle samples in CHCl₃ excited with a 980 nm laser diode (Power Density = 150 W/cm²). The inset in (b) shows the total upconversion luminescence of a dispersion of NaYF₄:ErYb when stimulated with a 980 nm diode laser.

3.7.7 Photoswitching and Photochemistry

3.7.7.1 Solution-State Photochemistry

All solution ring-closing reactions were carried out using the light source from a lamp used for visualizing TLC plates at 365 nm (Spectroline E-series,

15.9 mW/cm²).

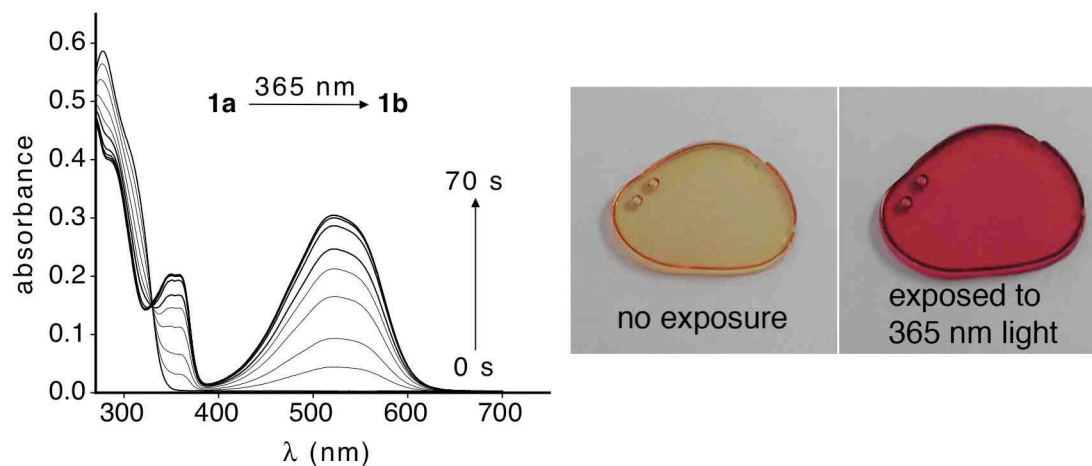


Figure 3.6 Changes in the UV-vis absorption spectra of a CH₃CN solution (2.1×10^{-5} M) of **1a** as it is irradiated with 365 nm light until the photostationary state is reached. The images on the right illustrate how the photoswitch retains its activity when cast in a polyacrylate film.

3.7.7.2 Photoswitching in Gels and the Solid-State

The polymeric composite films were cut with a scalpel to desired length and width. A piece of cardboard (12 × 33 mm) that was pre-cut to fit into the Ocean-Optics spectrophotometer had a hole (5 × 5 mm) cut into it to fit over the recording area of the spectrometer. Each composite film was placed onto the pre-cut cardboard and outlined so that every measurement could be recorded in the same spot to ensure trustworthy data. A spectrum was recorded before the 980 nm CW laser irradiation experiments were started. The films were then irradiated and their spectral changes were recorded over time. The results are shown in Figure 3.1 and 3.2 in the manuscript and in Figure 3.7. Other solid-state versions (bulk gels and solvent-free films) of the composite material were prepared and exhibit similar photochemistry as shown in Figure 3.8.

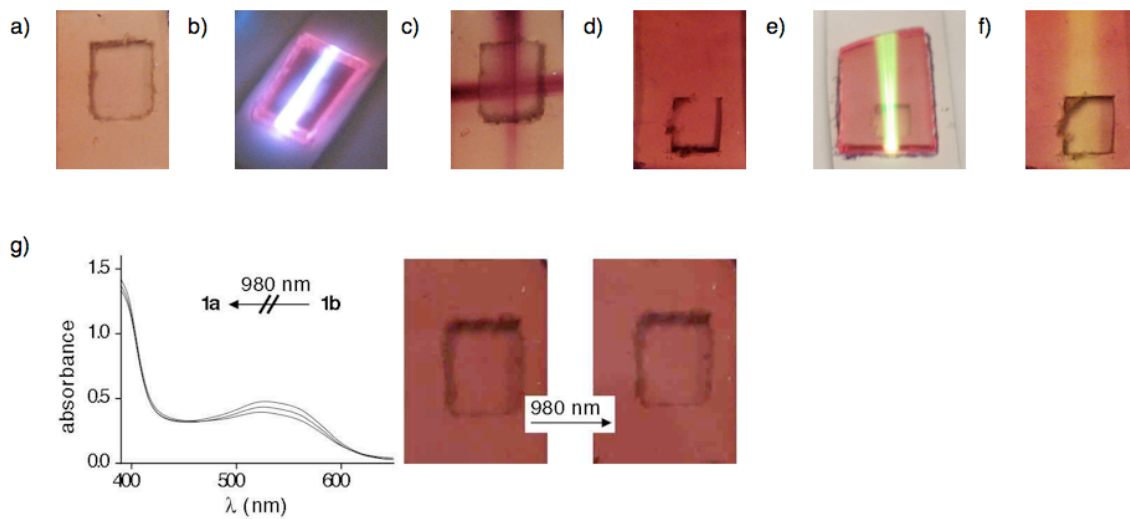


Figure 3.7 Sample of compound **1a** and NaYF₄:TmYb cast in an acrylate film (a) before, (b) during and (c) after exposure to 980 nm light. Sample of compound **1b** and NaYF₄:ErYb cast in an acrylate film (d) before, (e) during and (f) after exposure to 980 nm light. (g) Changes in the UV-vis absorption spectra and images of an acrylate film containing only **1b** before (left) and after (right) being irradiated with 980 nm light.

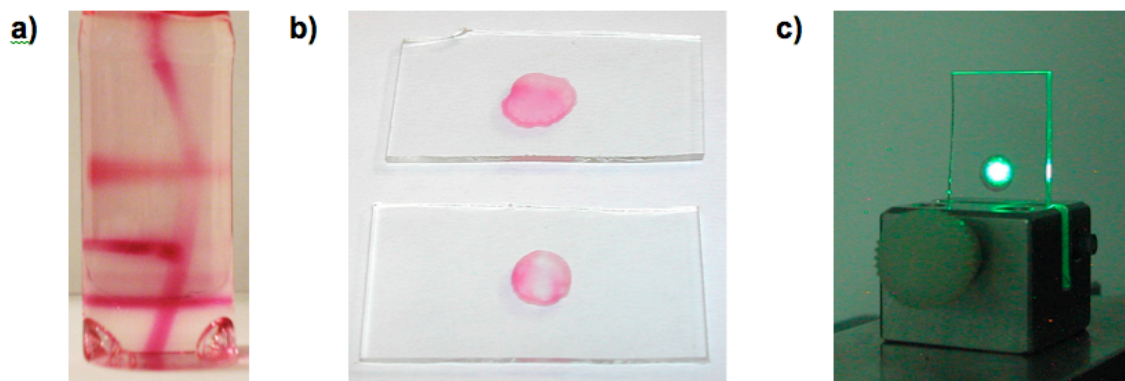


Figure 3.8 (a) Sample of compound **1** and NaYF₄:TmYb cast in a PMMA gel showing coloured lines due to ring-closing induced by 980 nm light. The lines represent the direction of the laser beam. The bulk composite gels were prepared using the colloidal stock nanoparticle dispersion in CHCl₃. The appropriate amount of the stock dispersion was added to a 4 dram screw top vial. Poly(ethylene glycol)-monooleate (typical M_n = 860) (0.15 g) was added to vial and the CHCl₃ was removed under vacuum using a rotary evaporator. Methyl methacrylate (3.85 g) and **1a** (2 mg) were then added to the vial and the resulting dispersion was sonicated for 2 min to obtain a clear dispersion. Azobisisobutyronitrile (AIBN) radical initiator (<1% (w/w)) was subsequently added to the dispersion and sonicated for 30 s. The monomer solution was then transferred to a 1 dram screw top vial with the dimensions 60 mm × 15 mm (length × diameter), which was then sealed. The vial was placed in a 70 °C oil bath for 30 min to initiate the polymerization process and subsequently transferred to a 45–50 °C oven until the polymerization was complete. A transparent NP-**1a**-PMMA composite rod was obtained by breaking the glass vial. (b) A drop-cast sample of **1** in PMMA before (top) and after (bottom) irradiation with 980 nm light. The sample was prepared by dissolving **1** (1.6 mg) and NaYF₄:ErYb (303 mg of a 1.7 wt-% solution in chloroform) in 88 mg of a solution made from PMMA (17.5 mg) and acetone (894 mg). One drop of the solution was spin-cast onto a glass slide (15 × 25 mm; 10 s gradient to 200 rpm, 200 rpm 1 min) using Laurell WS-400A6NPP/LITE spincoater. (c) Experimental set-up showing how the glass plate was exposed to 980 nm light.

4: TWO-WAY PHOTOSWITCHING USING ONE TYPE OF NIR LIGHT, UPCONVERTING NANOPARTICLES AND CHANGING ONLY THE LIGHT INTENSITY

4.1 Contributions

The text in this chapter have previously been published in the Journal of the American Chemical Society as a full paper and is reproduced herein in its entirety with permission from the journal (J.-C. Boyer, C.-J. Carling, B. D. Gates, N. R. Branda, *J. Am. Chem. Soc.*, **2010**, 132, 15766–15772, <http://pubs.acs.org/doi/abs/10.1021/ja107184z>). The project was co-designed by Dr. J-C Boyer, C-J Carling and Prof. Dr. N. R. Branda. All nanoparticle synthesis and characterizations thereof were conducted by Dr. J-C Boyer. SWITCH materials synthesized the molecular photoswitches used in the study. Dr. J-C Boyer measured all data presented in the manuscript. Preliminary data not present in the manuscript using other molecular photoswitches (internal methyl) were co-measured by Dr. J-C Boyer and C-J Carling. The manuscript was co-written by Dr. J-C Boyer and Prof. Dr. N. R. Branda. The experimental section was co-written by Dr. J-C Boyer and Prof. Dr. N. R. Branda.

4.2 Abstract

Only one type of lanthanide-doped upconverting nanoparticle (UCNP) is needed to reversibly toggle photoresponsive organic compounds between their two unique optical, electronic and structural states by merely modulating the

intensity of the 980 nm excitation light. This reversible 'remote-control' photoswitching employs an excitation wavelength not directly absorbed by the organic chromophores and takes advantage of the fact that designer *core-shell-shell* NaYF₄ nanoparticles containing Er³⁺/Yb³⁺ and Tm³⁺/Yb³⁺ ions doped into separate layers change the type of light they emit when the power density of the near infrared light is increased or decreased. At high power densities, the dominant emissions are ultraviolet and are appropriate to drive the ring-closing, forward reactions of dithienylethene (DTE) photoswitches. The visible light generated from the same *core-shell-shell* UCNPs at low power densities triggers the reverse, ring-opening reactions and regenerates the original photoisomers. The 'remote-control' photoswitching using NIR light is as equally effective as the direct switching with UV and visible light, albeit the reaction rates are slower. This technology offers a highly convenient and versatile method to spatially and temporally regulate photochemical reactions using a single light source and changing either its power or focal point.

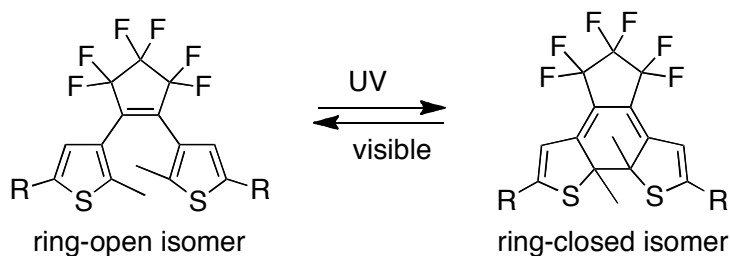
4.3 Introduction

The direct relationship between molecular structure and function has been universally accepted by Materials Scientists, and is part of the foundation being used to develop the next generation of optical, electronic and mechanical materials and devices. Being able to reversibly alter molecular structure and function is equally essential if new dynamic materials are to be practical in applications from information processing to medicine. The logic is simple and based on the argument that if a molecule's structure can be reversibly modified

in a controllable and predictable manner, their properties can be regulated. A convenient way to achieve this control is to incorporate functional molecules that can be toggled back and forth between different isomeric forms in response to external stimuli. These *molecular switches* will provide the 'on-off' control needed to regulate the properties of functional materials, miniaturized components of devices and molecule-based machines.^[76,77] Because light can be easily tuned and focused, it is a particularly appealing stimulus to spatially and temporally trigger changes in the structure of molecules and function of materials containing them in a wide range of environments-of-use, from solution to solid-state.^[78]

Molecular switches based on the photoresponsive dithienylethene (DTE) architecture have attracted special attention for use as the control elements in molecular devices and functional materials due to the short response time, synthetic diversity, and high fatigue-resistance of the ring-closing and ring-opening photoreactions that reversibly interconvert the two isomers (Scheme 4.1 and Figure 4.1).^[43,42,79,80] Two other appealing features, essential for the operation of molecular switches in many molecular devices, are the facts that the two DTE photoisomers (*ring-open* and *ring-closed*) tend not to spontaneously interconvert in the dark, and they possess distinctly different optical and electronic properties. The most visually obvious property that differs is the color of solutions, crystals and films made from DTE derivatives, which is based on the creation of a linearly π -conjugated system during ring-closing.^[81,82] Other differences include how the photoisomers fluoresce or phosphoresce,^[83,84,85,86] how chiral versions of them interact with plane-polarized light,^[87,88,89,90,91] and

how their magnetism^[92,93,94] and conductivity^[95,96,97,98] changes. The choice of which particular property is regulated is dictated by what functional groups are attached to each end of the π -conjugated DTE backbone ('R' groups in Scheme 5.1). It is the tailoring of this structure-property relationship that offers molecular control in a wide range of applications including write-read-erase optical data storage,^[99] information processing,^[100] photorelease,^[57] molecular electronics,^[101] catalysis,^[60,102,103] smart surfaces^[104] and potentially in medicine.^[55,59,105]



Scheme 4.1 The reversible photoreactions interconverting the two DTE isomers.

A shortcoming of the DTE family is no different from one that limits the application of most photoswitches (and organic photochemistry in general) from practical use and is based on the fact that high-energy UV and visible light sources are required to trigger the photoreactions. This need for high-energy light can complicate the use of these versatile molecular systems in many applications where these wavelengths have detrimental effects. One example is their use in biological settings where UV light leads to low tissue penetration as well as mutagenesis of cells. Storing optical information in three-dimensional digital media will also suffer from similar issues and the absorption of light by the

matrix can lead to distortion of the information and shortening of storage lifetime. Unless a method to deliver lower energy light deep into tissue or solid-state materials is developed, photoswitching and organic photochemistry will have restricted appeal.

A possible solution to this problem is to use multiphoton near infrared (NIR) light excitation to trigger the photochemical reactions. Because two-photon excitation (2PE) requires high excitation power densities, molecular systems susceptible to 2PE offer the possibility to spatially address organic materials in all three dimensions. Unfortunately, the low two-photon-absorbing cross-sections typical for DTE photoswitches (and other classes of photoresponsive compounds) is a significant drawback in practical applications where the use of high-intensity lasers is not feasible. This reliance on high power densities is even more of an issue in photoswitching applications since the ring-closing reaction of DTEs requires three photon NIR excitation to generate the necessary UV or blue light, leading to even lower efficiencies. A better alternative is to introduce a photostable, sensitizing system that can absorb NIR light and convert it through a more efficient process into the UV and visible light needed to trigger the photoreactions of the DTE molecular switch in a 'remote-control' process. Lanthanide-doped upconverting nanoparticles (UCNPs)^[106,107,108,109,110,111,112] are ideal sensitizers for this task and are the systems described in this report.

UCNPs convert low energy NIR light into higher energy UV and visible light through several unique mechanisms.^[113] The lower excitation power density requirements of UCNPs versus traditional 2PE fluorophores such as dyes and

quantum dots arises from the fact that the intermediate levels involved in the upconversion mechanisms are real metastable energy levels. The most efficient UCNPs known to date are hexagonal β -phase NaYF_4 nanoparticles doped with either the Er/Yb or Tm/Yb ion couples.^[114] Violet, green and red emissions are generated from the Er/Yb-doped UCNPs, while UV, blue, and NIR emissions have been observed in the case of the Tm/Yb-doped analogues. The high efficiency of the upconversion processes in hexagonal NaYF_4 nanoparticles can be attributed a combination of two factors: (1) the low-energy phonons of the NaYF_4 hexagonal matrix which minimizes non-radiative relaxation of the excited states, and (2) the inter-atom spacing between the dopant ions, which increases the efficacy of the energy transfer processes. The majority of the studies in the literature have focused on the visible emissions from these UCNPs with only a few reporting on the UV upconversion emissions that are capable of being generated from $\text{Tm}^{3+}/\text{Yb}^{3+}$ -doped materials. But, these UV emissions are critical to develop a “universal” method to drive photochemical reactions, especially those necessary in applications where UV radiation cannot be used such as in biological tissues and fluids.^[64,115]

Lanthanide-doped upconverting nanoparticles have many other favourable characteristics that explain the recent interest generated by them including resistance to photodegradation, lack of blinking and the ability to be excited with compact and relatively inexpensive NIR diode lasers.^[116] The bulk of the reported studies on UCNPs are aimed at advancing the synthetic methods for the production of these materials^[106,107,108,109,110,111,112] as well as post-

synthetic surface treatments to enable their use in bioimaging and biomedicine for cell imaging, disease detection and treatment.^[117] Other possible explored uses for UCNPs range from artificial lighting and sensitized solar-cells^[118] to security labeling.^[119] What has not been as well demonstrated is how these nanoparticles can be used to drive important photochemical reactions.

We recently demonstrated how we could trigger DTE photoswitches to undergo both their ring-closing and ring-opening reactions using the same wavelength of NIR light (980 nm) and two different lanthanide-doped UCNPs.^[9] The photoswitches do not absorb this NIR wavelength directly and the photoreactions (including one that has an accompanying thermal release of a small molecule) are induced by the blue light generated from Tm³⁺/Yb³⁺-doped (for ring-closing) and the green light generated from Er³⁺/Yb³⁺-doped (for ring-opening) NaYF₄ nanoparticles. Before our recent report, the few studies that combine dithienylethenes and lanthanide-doped upconverting nanoparticles focused on non-destructive optical memory, where the ring-closed isomer of the DTE photoswitch selectively quenches the luminescence from the UCNP through an energy transfer process, providing a read-out signal in the visible region.^[120,121] However, UV light (for writing) and visible light (for erasing) are still required as these steps are a result of the ring-closing and ring-opening reactions of the photoswitch, respectively. NIR-induced photoswitching in these studies was not observed using 980 nm irradiation due to the low efficiencies of the UCNPs and the low excitation densities used.

What may limit the use of our first-generation multi-photon systems is the fact that only one of the photoreactions can be selected by choosing the appropriate lanthanide dopant (Tm^{3+} or Er^{3+}). We now demonstrate how we can use only one type of layered, hybrid *core-shell-shell* nanoparticle and a single wavelength of NIR light to toggle examples of this important class of photoswitches between their two isomers. We illustrate that the direction of the chromophore's photoreaction can be controlled by increasing (for ring-closing) or decreasing (for ring-opening) the power density of the laser, which controls the color of the light emitted from our designer nanoparticles.

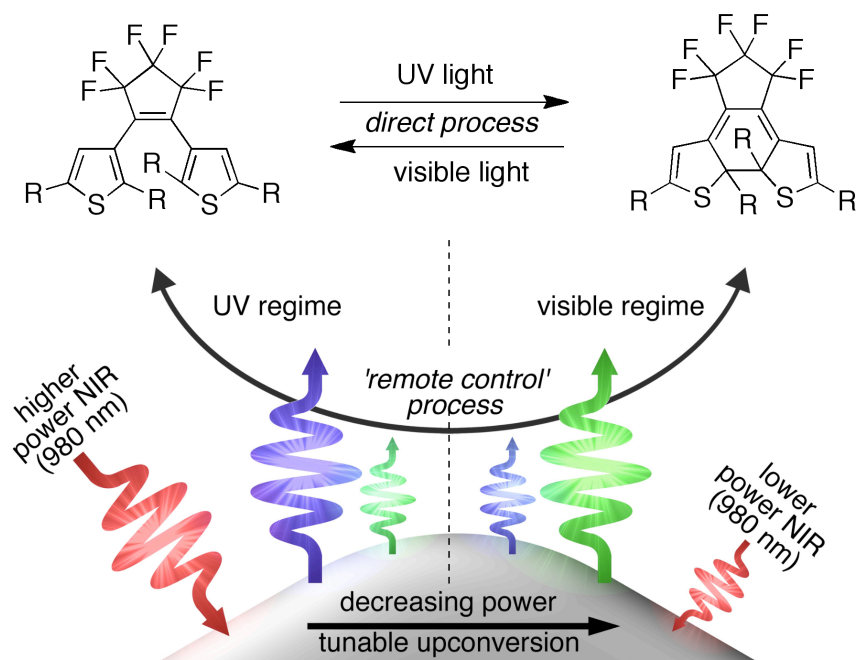


Figure 4.1 The ‘direct’ photoreactions of the DTE derivatives used in this study are triggered by UV light (for ring-closing) and visible light (for ring-opening). These reactions can also be triggered in a ‘remote-control’ process using the UV light generated under high excitation power densities and the visible light generated under low excitation power densities when the *core-shell-shell* UCNPs (**ErTm** and **TmEr**) absorb near-infrared light (980 nm). The sizes of the coloured arrows represent the relative amount of each type of light excited or emitted during the multi-photon process.

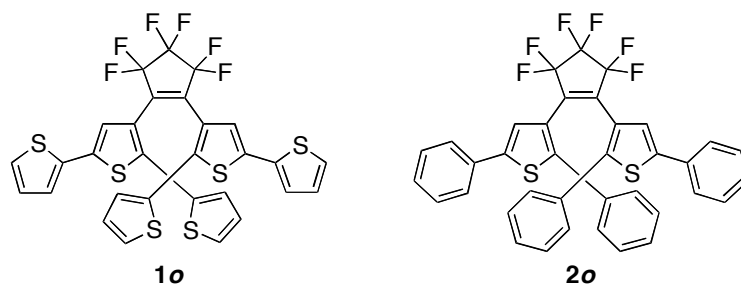
The concept is summarized in Figure 4.1 and is based on the documented fact that the intensities of the upconversion emissions from lanthanide-doped materials are highly dependent on the power density of the excitation source.^[122] The green and red emissions from the Er/Yb-doped UCNPs have a quadratic dependence on the excitation source while the UV and blue emissions in Tm/Yb-doped UCNPs require 4 and 5 photons to induce them. The implication is that at much higher power densities, UV luminescence will be generated from Tm/Yb while green and red emissions can be generated from Er/Yb UCNPs at lower

power densities. The green and red upconversion mechanisms will also saturate and plateau at lower power densities than the UV emissions. The consequence of this phenomenon is that *core-shell-shell* UCNPs synthesized to contain different lanthanide ions in different layers will produce a single nanoparticle system capable of inducing both ring-closing and ring-opening reactions of DTE derivatives. By placing the lanthanides in separate layers, the quenching of the upconversion luminescence by cross-relaxation between the various dopant ions is minimized. This report represents a relatively universal example of how multiphoton processes in nanoparticles can be used to induce important photoreactions of organic chromophores even when they require high-energy, differing wavelengths of light.

4.4 Results and discussion

4.4.1 Choice and Synthesis of DTEs and Nanoparticles

Photoresponsive DTE derivatives **1** and **2** were chosen to demonstrate the concepts described in the introduction to this report and were synthesized using methods previously described by our group.^[80ab] The DTE backbone has been tailored to optimize the efficacy of the 'remote-control' processes in order to avoid the need for a polymer matrix to maintain the close proximity of the photoswitch and UCNPs as was the case in our original report.



All studies described in this manuscript use colloidal solutions of the photoresponsive compounds and the UCNPs. We continued to employ *core-shell* hexagonal NaYF₄ nanoparticles synthesized in high boiling point solvents since these UCNPs have been consistently shown to be the most efficient upconverters known to date. We used a modified method of a literature synthesis procedure to synthesize all the *core-shell* and *core-shell-shell* UCNPs used in these studies.^[75a] Four different lanthanide-doped NaYF₄ nanoparticles were used to demonstrate reversible, power-regulated photoswitching with a single set of UCNPs and determine which lanthanide should be doped in which layer of the *core-shell-shell* nanoparticles. Two of them (referred to as **Er** and **Tm**) have the lanthanides (Er³⁺ and Tm³⁺) doped only in their core, and are surrounded by a shell of NaYF₄ to minimize quenching of the emission due to solvent interactions. The other two (**ErTm** and **TmEr**) have two shells wrapped around a core of lanthanide-doped NaYF₄. The first (**ErTm**) has NaYF₄: 2 mol% Er³⁺, 20 mol% Yb³⁺ as the core material, NaYF₄: 0.5 mol% Tm³⁺, 30 mol% Yb³⁺ as the first shell and NaYF₄ as the outermost shell. The second (**TmEr**) has the two lanthanide-doped layers reversed. In this case, the core is made up of NaYF₄: 0.5 mol% Tm³⁺, 30 mol% Yb³⁺, covered in a shell of NaYF₄: 2 mol% Er³⁺,

20 mol% Yb^{3+} . The outermost shell remains NaYF_4 . The composition of each nanoparticle is listed in Table 4.1.

All UCNPs were prepared using a three-step synthetic method in which lanthanide-doped core nanoparticles were successively coated with a lanthanide-doped first shell followed by an undoped NaYF_4 final shell. This core-shell method has been previously shown to allow for more efficient upconversion from Er^{3+} and Tm^{3+} than doping the two ions into a single UCNP.^[10] For the **ErTm** sample, NaYF_4 : 2 mol% Er^{3+} , 20 mol% Yb^{3+} nanoparticles were utilized as seeds to grow a NaYF_4 : 0.5 mol% Tm^{3+} , 30 mol% Yb^{3+} shell. This was subsequently followed by the growth of an undoped NaYF_4 shell to further increase the efficiency of the upconversion processes as has been effectively established by several research groups.^[10,117] In a similar fashion as for the **TmEr** sample, NaYF_4 : 0.5 mol% Tm^{3+} , 30 mol% Yb^{3+} cores were coated with a NaYF_4 : 2 mol% Er^{3+} , 20 mol% Yb^{3+} followed by an undoped NaYF_4 shell. The architectures of the two types of *core-shell-shell* UCNPs are illustrated in Figure 4.2.

Table 4.1 Constituent lanthanide dopants in each layer of all upconverting nanoparticles used in these experiments.^a

UCNP	core		inner shell	
	mol-% dopant	volume (nm ³)	mol-% dopant	volume (nm ³)
Er	2.0 Er ³⁺ 20 Yb ³⁺	31660	none	–
Tm	0.5 Tm ³⁺ 30 Yb ³⁺	114965	none	–
ErTm	2.0 Er ³⁺ 20 Yb ³⁺	39300	0.5 Tm ³⁺ 30 Yb ³⁺	40605
TmEr	0.5 Tm ³⁺ 30 Yb ³⁺	57800	2.0 Er ³⁺ 20 Yb ³⁺	51040

^a In all cases, the nanoparticle matrix is NaYF₄.

All the synthesized nanoparticles were successfully indexed to hexagonal-phase NaYF₄ (JCPDS standard card 16-0334) according to powder X-ray diffraction (Figure 5.6). Transmission electron microscopy (TEM) images of the UCNPs (Figure 4.2 and 4.7–4.10) show that they are all single crystalline in nature, possess uniform ellipsoid shapes and have nearly monodisperse particle sizes (with average diameters of 35.7 nm and 38.8 nm for the **ErTm** and **TmEr** samples, respectively). As observed in the TEM images of the **ErTm** and **TmEr** UCNPs (Figure 4.2), each successive shell formation resulted in an increase of the average diameter of the nanoparticles indicating successful shell growth. This procedure results in discrete shells with a minimal amount of alloying at the interface between the each of them. The separation of the dopants into two different layers of the nanoparticles is important in order to maximize the efficiency of the upconversion processes as doping all of the lanthanide ions in one layer would lead to nonradiative energy transfers and lower upconversion efficiencies. For each *core-shell-shell* UCNP, the volumes of the core and first

shell containing the lanthanide dopants are similar to each other (Table 4.1). This is important because the ratio of dopants in each nanoparticle must be the same in order to rule out any changes in the multiphoton processes between nanoparticles due to a difference in the amount of lanthanide responsible for the process. The differences in emission and photoswitching that will be discussed later in this manuscript are, therefore, due to where each lanthanide ion is located in the nanoparticle and not its amount.

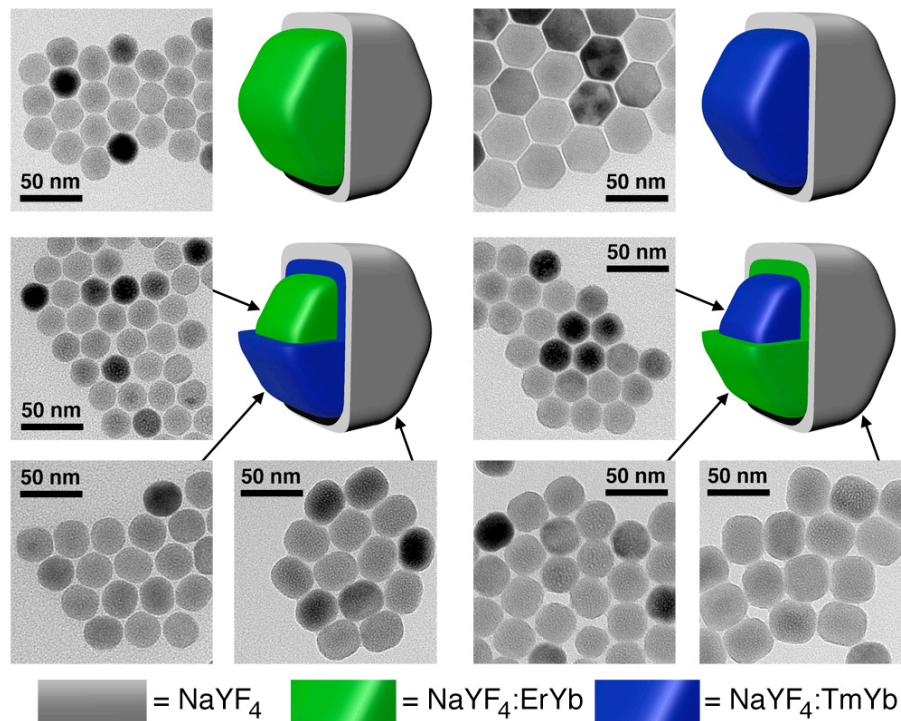


Figure 4.2 TEM images of the *core*, *core-shell*, and *core-shell-shell* nanoparticles for NaYF₄:ErYb–NaYF₄ (**Er**), NaYF₄:TmYb–NaYF₄ (**Tm**), NaYF₄:ErYb–NaYF₄:TmYb–NaYF₄ (**ErTm**) and NaYF₄:TmYb–NaYF₄:ErYb–NaYF₄ (**TmEr**) UCNP illustrating their uniform size and shape.

4.4.2 Optical Properties of UCNPs

The upconversion luminescence spectra ($\lambda_{\text{ex}} = 980 \text{ nm}$) of the **Er** and **Tm** *core-shell* UCNPs dispersed as 1.5 wt-% colloids in THF are shown in Figure 5.2c–d. These spectra were acquired using similar power densities that will eventually be employed to mediate the photoreactions of the photoswitches (500 W/cm² for ring-closing with **Tm** and 15 W/cm² for ring-opening with **Er**). For the **Tm** nanoparticles, upconversion emission peaks at 290, 350, 365, 450 and 475 nm were observed corresponding to the $^3\text{P}_0 \rightarrow ^3\text{H}_6$, $^3\text{P}_0 \rightarrow ^3\text{F}_4$, $^1\text{D}_2 \rightarrow ^3\text{H}_6$, $^1\text{D}_2 \rightarrow ^3\text{F}_4$ and $^1\text{G}_4 \rightarrow ^3\text{H}_6$ transitions. Emissions from 630 to 750 nm were also observed and attributed to the $^1\text{G}_4 \rightarrow ^3\text{F}_4$ and $^3\text{F}_3 \rightarrow ^3\text{H}_6$ transitions. The

particular peaks of interest for ring-closing **1o** and **2o** are those in the UV/blue regions of the spectrum (290, 350–365 nm) as these are the ones that have appropriate spectral overlap with the high-energy absorption bands (300–350 nm) of THF solutions of the ring-open forms of the two photoswitches (Figure 4.2a–b).

For solutions of the **Er** UCNPs, emissions centered at 409, 520, 541 and 653 nm were observed and assigned to the $^4H_{9/2} \rightarrow ^4I_{15/2}$, $^4H_{11/2} \rightarrow ^4I_{15/2}$, $^4S_{3/2} \rightarrow ^4I_{15/2}$ and $^4F_{9/2} \rightarrow ^4I_{15/2}$ transitions, respectively. In this case, it is the green (520–550 nm) and the red (640–670 nm) upconversion emissions that have suitable spectral overlap with the absorption bands corresponding to the ring-closed forms of both photoswitches. These emissions will be utilized to trigger the ring-opening photoreactions of the photoswitches (**1c** \rightarrow **1o** and **2c** \rightarrow **2o**).

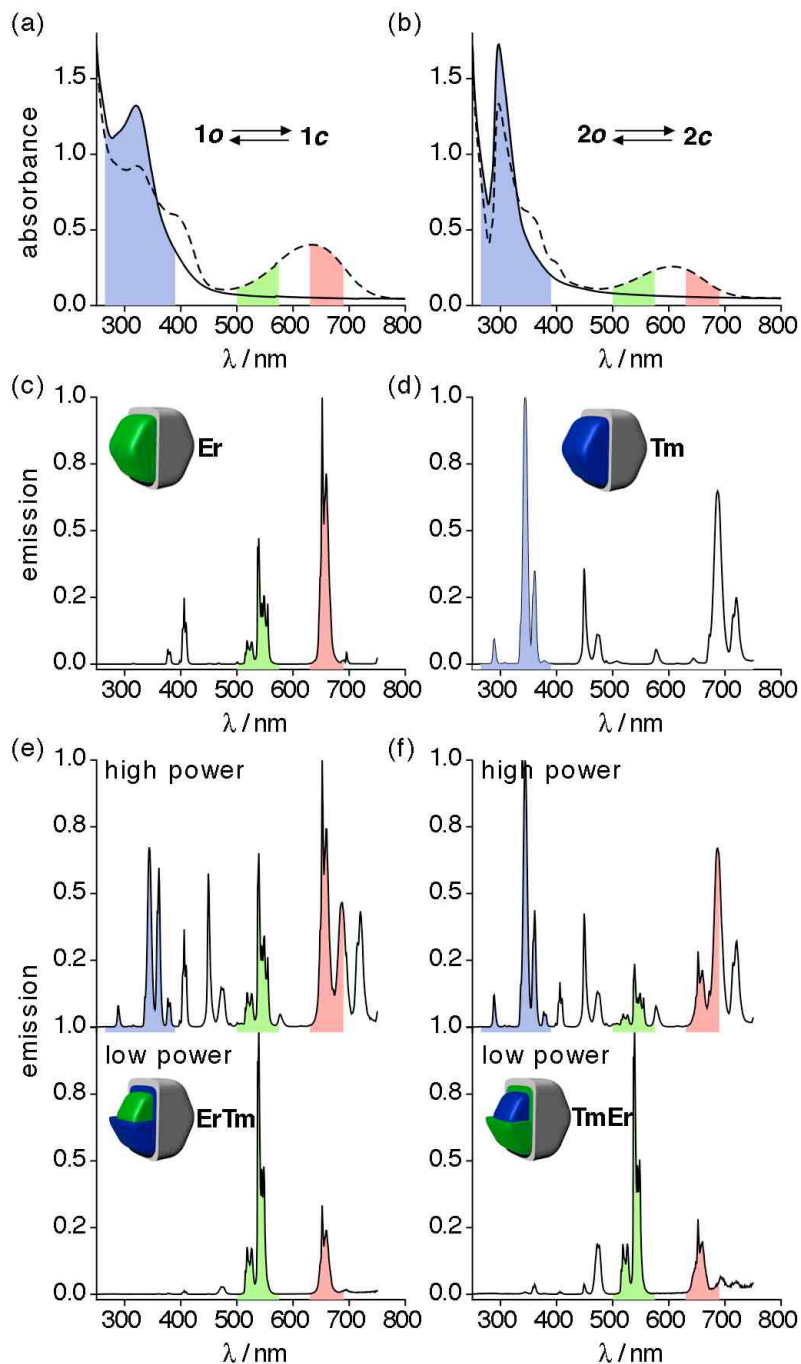


Figure 4.3 UV-vis absorption spectra of THF solutions (1.5×10^{-5} M) of (a) **1o** and (b) **2o** before (solid line) and after irradiation with 365 nm light (dashed line) for 2 min. Emission spectra of THF solutions (1.5 wt-%, $\lambda_{\text{ex}} = 980$ nm) of (c) NaYF₄:ErYb (**Er**) and (d) NaYF₄:TmYb (**Tm**) core-shell UCNPs, and of (e) **ErTm** and (f) **TmEr** core-shell-UCNPs at high power (500 W/cm², top graph) and low power (15 W/cm², bottom graph). The shaded, colored regions in all cases represent each emission region and show the suitable spectral overlap with the appropriate absorption bands for the ring-open and ring-closed isomers of DTEs **1** and **2**.

Figure 4.3e–f show the upconversion luminescence spectra of the **ErTm** and **TmEr** *core-shell-shell* UCNPs at high (500 W/cm^2) and low (15 W/cm^2) power densities, and highlight the changes in the intensities of the emissions. In the high power excitation regime all of the expected Tm^{3+} and Er^{3+} upconversion emissions are present in the spectra for both **ErTm** and **TmEr** UCNPs although there are significant differences in the relative intensities of the emissions. As postulated in the introduction of this paper, the intensities of the emission peaks due to Tm^{3+} are all much larger than those for the Er^{3+} emissions in both nanoparticles. The major difference between the two nanoparticles at high irradiation power is that the dominance of the Tm^{3+} emissions is even greater in the case of the **TmEr** UCNPs demonstrating that placing the Tm^{3+} ions in the core of the nanoparticles maximizes the UV and blue emissions compared to when this lanthanide is doped into the first shell. This is not due to a difference in the amount of Tm^{3+} ions in the core compared to the first shell since the volume of each is virtually the same.

On the other hand, the emissions from Er^{3+} ions dominate in both types of *core-shell-shell* nanoparticle (**ErTm** and **TmEr**) at lower power density (15 W/cm^2), and only trace contributions in the UV and blue regions due to the Tm^{3+} dopant are observable. The results summarized in Figure 4.3 support the hypothesis that by varying only the excitation laser power density and not the wavelength of the excitation beam the emissive properties of the UCNPs and, thus, the direction of DTE photoswitching can be controlled. Both types of *core-shell-shell* nanoparticle are stable under even the high-power irradiation

conditions and no changes in their emission spectra are observed after 1 hour exposure (Figure 4.12).

4.4.3 'Remote-Control' Photoswitching of DTE derivatives

To determine what is the maximum efficiency for the 'remote-control' photoreactions of DTE compounds **1** and **2**, the *core-shell* UCNPs were first examined for their ability to drive the ring-closing reactions (using **Tm**) and the ring-opening reactions (using **Er**). The ability of the UV emissions generated by Tm^{3+} dopant to trigger the photocyclization reactions was assessed by irradiating solutions of **1o** and **2o** (1.5×10^{-5} M) containing **Tm** nanoparticles (1.5 wt-%) with a 980 nm laser (power density of 500 mW/cm^3). The colors of the solutions changed from colorless to a blue or blue/green, which can be attributed to the photocyclization reactions **1o** \rightarrow **1c** and **2o** \rightarrow **2c**, respectively. The success of these reactions are supported by the changes in the absorption spectra of the photoswitches, which match those for **1o** and **2o** when they are irradiated with UV light as shown in the experimental section of this chapter (Section 4.8). Both photoswitches reached similar photostationary states when irradiated with NIR light and the nanoparticle ('remote-control' process) as with a handheld 313 nm mercury lamp ('direct' process; horizontal line in Figure 4.4a) effectively demonstrating that the intensity of the UV upconversion emissions from the **Tm** UCNPs is enough to effectively drive the reaction to completion (or at least as complete as possible).

In a similar fashion, the green and red upconversion emissions from the **Er** UCNPs can equally be employed to drive the ring-opening reactions of the two photoswitches. This is demonstrated by irradiating THF solutions containing **1c** or **2c** (generated with 313 nm light) and **Er** UCNPs with 980 nm laser light (15 W/cm²), which results in the complete decolorizing of the solutions and regeneration of the absorption spectra corresponding to the ring-open isomers (**1o** and **2o**). The ‘remote-control’ ring-opening reactions (**1c** → **1o** and **2c** → **2o**) are supported by spectral changes that match those for samples of **1c** and **2o** when they are irradiated with visible light (wavelengths greater than 450 nm). Once again, both reactions can be driven close to completion using the **Er** UCNPs (Figure 4.4b). The fact that the photoreactions of either DTE photoswitch are driven by absorbing the light generated by the UCNPs is demonstrated by irradiating solutions of each DTE with 980 nm laser light but without any of the nanoparticles, which undergo no visible changes in their colors or UV-vis spectra.

The reversible photoswitching of both dithienylethene photoswitches with a single set of UCNPs was demonstrated using combinations of the **ErTm** and **TmEr** nanoparticles with the two photoswitches (**1** and **2**). The ability of each UCNP to induce the ring-opening and ring-closing photoreactions of the DTEs was examined by comparing how quickly and to what extent the **ErTm** and **TmEr** UCNPs could drive the reactions compared to the **Er** and **Tm** *core-shell* nanoparticles, which were optimized for this task. We call this efficiency “performance”, which is plotted in Figure 4.4c for all DTE/nanoparticle

combinations as a percent. The extent of the ‘remote-control’ photoswitching induced by **Er** and **Tm** were set as 100%.

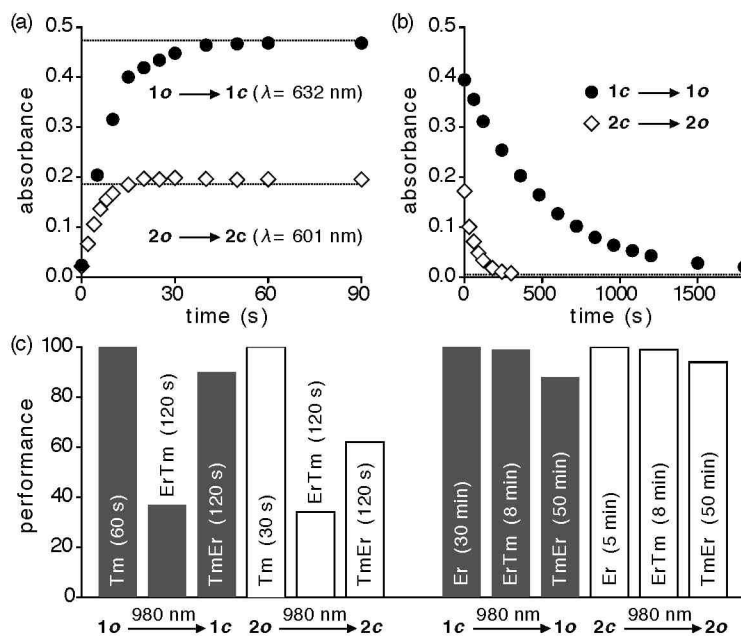


Figure 4.4 Changes in the absorbances ($\lambda_{\text{max}} = 632$ and 601 nm for **1c** and **2c**, respectively) when THF solutions of (a) DTEs **1o** and **2o** containing NaYF₄:TmYb nanoparticles (**Tm**) are irradiated with 980 nm light at high excitation power densities (500 W/cm^2), and (b) DTEs **1c** and **2c** containing NaYF₄:ErYb (**Er**) nanoparticles are irradiated with 980 nm light at low excitation power densities (15 W/cm^2). The horizontal lines show the absorbance values when similar solutions are irradiated with UV light (313 nm) for graph ‘a’ or visible light (> 450 nm) for graph ‘b’ until the photostationary states are obtained. (c) The degree to which the ring-closing and ring-opening reactions are induced with 980 nm light (high power for the former and low power for the latter) using the different types of nanoparticles.

For compound **1**, the best performance was achieved with the **TmEr** UCNPs, which drove the ring-closing photoreaction (**1o** \rightarrow **1c**) to within 90% of the photostationary state obtained with the **Tm** UCNPs, albeit in twice the length of time (120 s). When the **ErTm** nanoparticles are used, the photostationary state is reached after the same irradiation time, however, the amount of ring-closed isomer in this photostationary state is less than half (37%) of what is was

with the **TmEr** nanoparticles. The same is true for compound **2o**, although the photostationary states generated using both types of *core-shell-shell* UCNP are slightly lower than for DTE **1o** (62% when **TmEr** is used and 34% when **ErTm** is used). These observations make sense since the nanoparticles that have the Tm^{3+} ions in the core generate substantially more UV and blue light than when the ion resides in the first shell (compare the spectra in Figure 4.3e–f). The lower photostationary states for **2o** \rightarrow **2c** compared to **1o** \rightarrow **1c** is a reflection of the intrinsic photoswitching behavior of these DTE derivatives, where the former is only 42% when **1o** exposed to direct UV light (313–365 nm), while the latter is 80%.^[80ab]

Because both *core-shell-shell* UCNPs generate similar emissions at low power (Figure 4.3e–f), they should be almost equally effective at driving the ring-opening reactions of the photochromic DTEs. Figure 4.4c shows this to be the case. The **1c** \rightarrow **1o** photoreaction was driving back to within 88% of the level obtained employing the **Er** UCNPs when **TmEr** is used and nearly driven to completion (99%) when **ErTm** is used in a shorter period of time. This allows for a choice in performance between the two sets of *core-shell-shell* UCNPs. Both the **ErTm** and **TmEr** UCNPs were capable of driving the **2o** \rightarrow **2c** photoreaction to within 99% and 94% of the level obtained with the **Er** nanoparticles. Faster kinetics for the ring-opening reaction is again obtained with the **ErTm** sample (8 min) than with the **TmEr** sample (50 minutes) due to the decreased amount of UV emissions at low excitation powers.

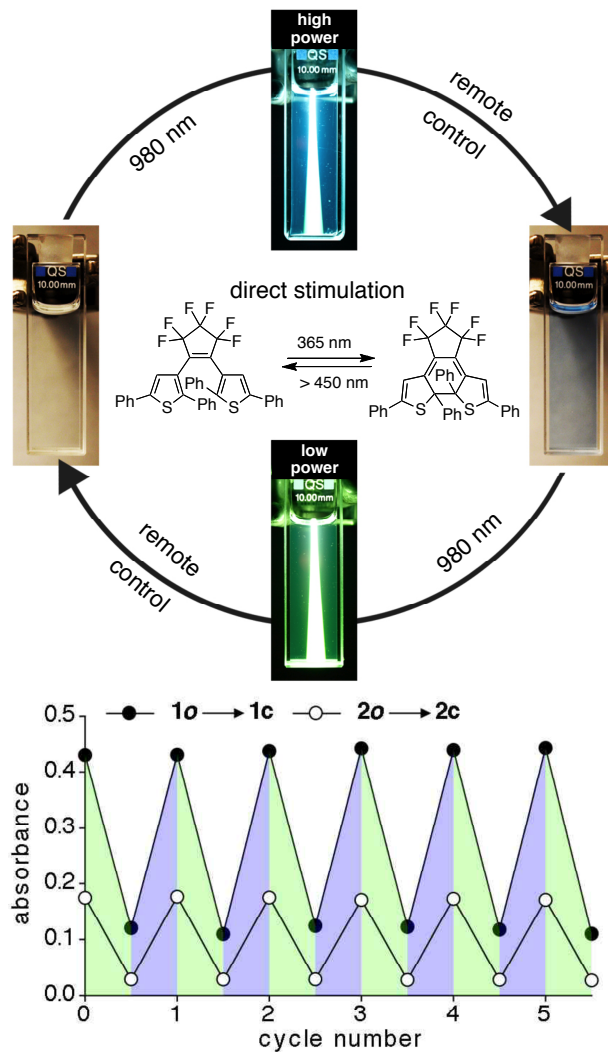


Figure 4.5 Bidirectional photoswitching of a THF solution of DTE **2** dispersed with TmEr *core-shell-shell* nanoparticles by varying only the intensity of the NIR light. The plot shows the absorption intensities corresponding to the ring-closed isomers (632 nm for **1c** and 601 nm for **2c**) as solutions of the photoswitches and the *core-shell-shell* nanoparticles are exposed to alternating intensities of 980 light. The colors correspond to the light emitted by the nanoparticles (green at low power and blue at high power).

Figure 4.5 shows a visual representation of the bidirectional photoswitching for DTE **2** and the TmEr nanoparticles by simply using the power of the 980 nm excitation beam as the control mechanism. The two solutions,

colorless and blue, can be interconverted by irradiating them with 980 nm light and dialing in the power, 'high' to produce the blue and UV light needed to trigger ring-closing (**2o** → **2c**) or 'low' to produce the green light to regenerate the original color due to ring-opening (**2c** → **2o**). Figure 4.5 also shows the absorption intensities at 632 nm for **1** and 601 nm for **2** as solutions of them are cycled between ring-closed and ring-open forms when exposed to varying intensity 980 nm light sources illustrating the reversibility of the system.

4.5 Conclusion

In this report, we have demonstrated how we can employ lanthanide-doped *core-shell-shell* upconverting nanoparticles to reversibly toggle a pair of dithienylethene photoresponsive molecules in a 'remote-control' fashion using a single wavelength of near-infrared light (980 nm) and by adjusting only the excitation power. This was achieved by preferentially doping the Er³⁺ and Tm³⁺ emissive ions into separate layers of the UCNPs resulting in the more efficient upconversion processes required to drive the reversible photoswitching reactions. The key aspect was the nonlinearity of the upconversion mechanisms, which results in the selective generation of UV and blue light under high-power conditions, which triggers ring-closing of the DTEs. Conversely, the reverse, ring-opening reactions can be triggered by simply reducing the power density of the excitation light to point where the visible Er³⁺ upconversion emissions dominate. Through the combination of *core-shell-shell* UCNPs and DTE photoswitches, we have created the first photochromic system that can be modulated simply with the power of the excitation light.

Improvements to the system are still possible. Attaching the photoswitches to the surface of the nanoparticles will increase the amount of energy transfer between the components and decrease the amount of irradiation time required for the photoreactions to occur. In addition, improvements to the upconversion properties of the various UCNPs are still possible and must be examined in greater detail to optimize the amount of each type of emission under various power densities.

4.6 Acknowledgement

This research was supported by the Natural Sciences and Engineering Research Council (NSERC) of Canada, the Michael Smith Foundation for Health Research (MSFHR), the Canada Research Chairs Program, and Simon Fraser University through the Community Trust Endowment Fund. This work made use of 4D LABS shared facilities supported by the Canada Foundation for Innovation (CFI), British Columbia Knowledge Development Fund (BCKDF) and Simon Fraser University.

4.7 Experimental

4.7.1 General methods

4.7.1.1 Materials

Erbium(III) acetate hydrate (99.9%), thulium(III) acetate hydrate (99.9%), ytterbium(III) acetate tetrahydrate (99.9%), yttrium(III) acetate hydrate (99.9%), technical grade oleic acid (90%), technical grade 1-octadecene (90%) and ammonium fluoride (99.99+%) were purchased from Sigma-Aldrich. Hexanes

and tetrahydrofuran (THF) from Caledon Inc. and anhydrous ethyl alcohol from Commercial Alcohols were also used. All chemicals were used as received, without any further purification. All solvents for synthesis of photochromic compounds **1** and **2** were dried and degassed by passing them through steel columns containing activated alumina under nitrogen using an MBraun solvent purification system. Solvents for NMR analysis (Cambridge Isotope Laboratories) were used as received. All synthetic precursors were purchased from Aldrich with the exception of Pd(PPh₃)₄, which was purchased from Strem. Octafluorocyclopentene was obtained from Nippon Zeon Corporation. Column chromatography was performed using silica gel 60 (230-400 mesh) from Silicycle Inc.

4.7.1.2 Instrumentation

¹H NMR characterizations were performed on a Bruker AMX 400 instrument working at 400.103 MHz. ¹³C NMR characterizations were performed on a Bruker AMX 400 instrument working at 100.610 MHz. Chemical shifts (δ) are reported in parts per million relative to tetramethylsilane using the residual solvent peak as a reference standard. Coupling constants (J) are reported in Hertz. FT-IR measurements were performed using a Nexus 670 or a Nicolet Magna-IR 750 instrument. UV-vis absorption spectroscopy was performed using a Varian Cary 300 Bio spectrophotometer. Low-resolution mass spectrometry measurements were performed using a HP5985 with isobutane as the chemical ionization source. All volumes for absorption, photolysis and concentration measurements/studies were measured out using a calibrated autopipette.

4.7.2 Synthetic procedures

4.7.2.1 Synthesis of nanoparticles

The *core-shell* and *core-shell-shell* nanoparticles were synthesized using a modification of a recently reported procedure.^[10,75a]

4.7.2.1.1 Synthesis of β -NaYF₄: 0.5 mol% Tm³⁺, 30 mol% Yb³⁺ core nanoparticles

In a typical synthesis, Y(CH₃CO₂)₃•xH₂O (372 mg, 1.4 mmol), Yb(CH₃CO₂)₃•xH₂O (210 mg, 0.6 mmol) and Tm(CH₃CO₂)₃•xH₂O (3.5 mg, 0.01 mmol) were added to a 100 mL three-neck round-bottom flask containing octadecene (30 mL) and oleic acid (12 mL). The solution was stirred magnetically and heated slowly to 120 °C under vacuum for 30 min to form the lanthanide oleate complexes, and to remove residual water and oxygen. The temperature was then lowered to 50 °C and the reaction flask placed under a gentle flow of nitrogen gas. During this time, a solution of ammonium fluoride (296 mg, 8.0 mmol) and sodium hydroxide (200 mg, 5.0 mmol) dissolved in methanol (20 mL) was prepared *via* sonication. Once the reaction reached 50 °C, the methanol solution was added to the reaction flask and the resulting cloudy mixture was stirred for 30 min at 50 °C. The reaction temperature was then increased to 70 °C and the methanol evaporated from the reaction mixture. Subsequently, the reaction temperature was increased to 300 °C as quickly as possible and maintained at this temperature for 90 min under the nitrogen gas flow. During this time the reaction mixture became progressively clearer until a completely clear, slightly yellowish solution was obtained. The mixture was allowed to cool to room temperature. The nanoparticles were precipitated by the

addition of ethanol and isolated *via* centrifugation at 4500 rpm corresponding to a relative centrifugal field (RCF) of approximately 1000. The resulting pellet was dispersed in a minimal amount of hexanes and precipitated with excess ethanol. The nanoparticles were isolated *via* centrifugation at 4500 rpm and then dispersed in hexanes (10–15 mL) for the subsequent shell growth procedure.

4.7.2.1.2 Synthesis of β -NaYF₄: 0.5 mol% Tm³⁺, 30 mol% Yb³⁺ / β -NaYF₄ core-shell nanoparticles

Y(CH₃CO₂)₃•xH₂O (479 mg, 1.8 mmol) was added to a 100 mL three-neck round-bottom flask containing octadecene (30 mL) and oleic acid (12 mL). The solution was heated slowly to 120 °C under vacuum with magnetic stirring for 30 min. The temperature was lowered to 80 °C, the reaction flask placed under a gentle flow of nitrogen and the dispersion of NaYF₄: 0.5 mol% Tm³⁺, 30 mol% Yb³⁺ core nanoparticles in hexanes was added. The resulting solution was slowly heated to 110 °C and maintained at this temperature until all the hexanes were removed. The reaction mixture was cooled to 50 °C and a solution of ammonium fluoride (259 mg, 7.0 mmol) and sodium hydroxide (175 mg, 4.4 mmol) dissolved in methanol (20 mL) was added. The resulting cloudy mixture was stirred for 30 min at 50 °C at which time the reaction temperature was increased and the methanol evaporated. After the evaporation of the methanol, the reaction temperature was increased to 300 °C as quickly as possible and maintained at this temperature for 90 minutes under the nitrogen gas flow. The mixture was allowed to cool to room temperature and the nanoparticles isolated using the same procedure of precipitate and isolation described for the core nanoparticles.

The isolated NaYF₄:TmYb nanoparticles were dispersed in THF (~15 mL) for subsequent experiments.

4.7.2.1.3 Synthesis of β -NaYF₄: 2 mol% Er³⁺, 20 mol% Yb³⁺ / β -NaYF₄ core-shell nanoparticles

The same procedure outlined above for the synthesis of the β -NaYF₄: 0.5 mol% Tm³⁺, 30 mol% Yb³⁺ / β -NaYF₄ core-shell nanoparticles was employed except that β -NaYF₄: 2 mol% Er³⁺, 20 mol% Yb³⁺ nanoparticles were used as the core.

4.7.2.1.4 Synthesis of β -NaYF₄: 0.5 mol% Tm³⁺, 30 mol% Yb³⁺ / β -NaYF₄: 2 mol% Er³⁺, 20 mol% Yb³⁺ core-shell nanoparticles

Y(CH₃CO₂)₃•xH₂O (372 mg, 1.4 mmol), Yb(CH₃CO₂)₃•xH₂O (123 mg, 0.35 mmol), and Er(CH₃CO₂)₃•xH₂O (12 mg, 0.035 mmol), oleic acid (12 mL) and octadecene (30 mL) were added to a 100 mL 3-neck flask. The solution was heated to 120 °C under vacuum and maintain at this temperature for 30 min. The flask was cooled to 80 °C and a dispersion of NaYF₄: 0.5 mol% Tm³⁺, 30 mol% Yb³⁺ core nanoparticles in 15 mL of hexane was added to the solution. The resulting solution was slowly heated to 110 °C and maintained at this temperature until all the hexanes were removed. The reaction mixture was cooled to 50 °C and a solution of ammonium fluoride (259 mg, 7.0 mmol) and sodium hydroxide (175 mg, 4.8 mmol) dissolved in methanol (20 mL) was added, and then the solution was kept at 50 °C for 30 min. After the methanol was removed, the solution was heated to 300 °C under a flow of nitrogen for 1.5 h and then cooled to room temperature. The nanoparticles were isolated using the

same procedure of precipitate and isolation described for the *core* nanoparticles and redispersed in 15 mL of hexanes for the subsequent shell growth procedure.

4.7.2.1.5 Synthesis of β -NaYF₄: 0.5 mol% Tm³⁺, 30 mol% Yb³⁺ / β -NaYF₄: 2 mol% Er³⁺, 20 mol% Yb³⁺ / β -NaYF₄ *core-shell-shell* nanoparticles

Y(CH₃CO₂)₃•xH₂O (399 mg, 1.5 mmol), oleic acid (12 mL) and octadecene (30 mL) were added to a 100 mL 3-neck flask. The solution was heated to 120 °C under vacuum and maintain at this temperature for 30 min. The flask was cooled to 50 °C and a solution of NH₄F (222 mg, 6.0 mmol) and NaOH (150 mg, 3.8 mmol) dissolved in methanol (20 mL) was added. A dispersion of β -NaYF₄: 0.5 mol% Tm³⁺, 30 mol% Yb³⁺ / β -NaYF₄: 2 mol% Er³⁺, 20 mol% Yb³⁺ *core-shell* nanoparticles in hexane (15 mL) was added to the solution. The flask was cooled to 50 °C and a solution of NH₄F (222 mg, 6.0 mmol) and NaOH (150 mg, 3.8 mmol) dissolved in methanol (20 mL) was added, and then the solution was kept at 50 °C for 30 min. The reaction temperature was then increased and the methanol evaporated. After the methanol was removed, the solution was heated to 300 °C under a flow of nitrogen for 1.5 h and then cooled to room temperature. The *core-shell-shell* nanoparticles were isolated using the same procedure of precipitate and isolation described for the *core* nanoparticles and redispersed in THF (20 mL) for further experiments.

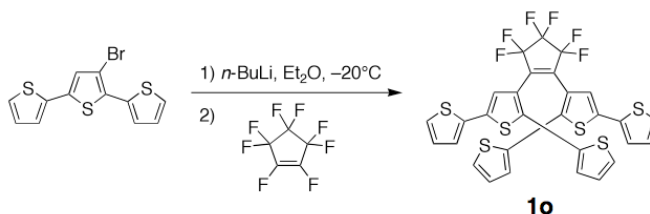
4.7.2.1.6 Synthesis of β -NaYF₄: 2 mol% Er³⁺, 20 mol% Yb³⁺ / β -NaYF₄: 0.5 mol% Tm³⁺, 30 mol% Yb³⁺ / β -NaYF₄ *core-shell-shell* nanoparticles

The same procedure outlined above for the synthesis of the β -NaYF₄: 0.5 mol% Tm³⁺, 30 mol% Yb³⁺ / β -NaYF₄: 2 mol% Er³⁺, 20 mol% Yb³⁺ / β -NaYF₄

NPs was employed except that β -NaYF₄: 2 mol% Er³⁺, 20 mol% Yb³⁺ / β -NaYF₄: 0.5 mol% Tm³⁺, 30 mol% Yb³⁺ nanoparticles were used as the *core-shell*.

4.7.2.2 Synthesis of organic photochromic compound 1o and 2o

4.7.2.2.1 Synthesis of 1,2-bis(2,5-bis(2-thienyl)-3-thienyl)hexafluorocyclopent-1-ene (1o)



A solution of 3'-bromo-2,2';5'2'terthiophene (749 mg, 2.3 mmol) in anhydrous Et₂O (25 mL) cooled to -20 °C was treated with *n*-BuLi (0.91 mL of a 2.5 M solution in hexane) dropwise under an argon atmosphere. After stirring the solution for 30 min, octafluorocyclopentene (0.13 mL, 1.15 mmol) was added dropwise using a cooled gas tight syringe and the solution immediately turned dark red in colour. After stirring for 1 h, the cooling bath was removed and the solution was allowed to warm to room temperature and stirred for 16 h when it was quenched with 5% HCl (10 mL). The aqueous layer was separated and extracted with Et₂O (2 × 10 mL). All organic extracts were combined, washed with H₂O (2 × 10 mL), followed by brine (10 mL), dried (Na₂SO₄) and filtered. The solvent was evaporated under reduced pressure and the crude product was purified using column chromatography through silica gel (hexanes) yielding 175 mg of pure product as a yellow crystalline solid. Yield: 23 %.

M.p. 116-117 °C

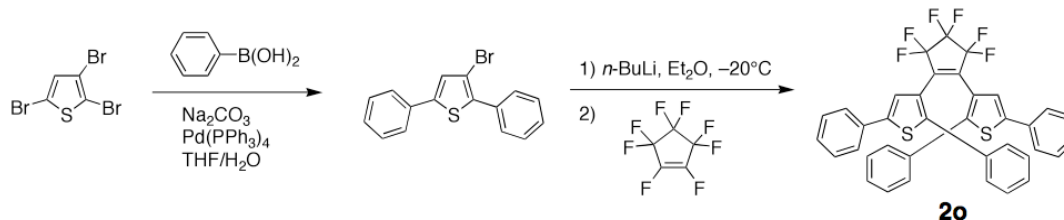
^1H NMR (300 MHz, CD_2Cl_2) δ 7.30 (dd, $J = 5, 1$ Hz, 2H), 7.19 (dd, $J = 5, 1$ Hz, 2H) 7.11 (dd, $J = 4, 1$ Hz, 2H), 7.04 (dd, $J = 5, 4$ Hz, 2H), 6.83 (dd, $J = 5, 3$ Hz, 2H), 6.74 (dd, $J = 3, 1$ Hz, 2H), 6.41 (s, 2H)

^{13}C NMR (125 MHz, CD_2Cl_2) δ 137.9, 136.3, 136.2, 133.0, 128.3, 128.2, 127.9, 127.0, 125.7, 125.0, 124.9, 123.8 (12 of 15 carbons found)

FT-IR (CHCl_3 cast) 3105, 1695, 1685, 1651, 1644, 1616, 1576, 1561, 1538, 1505, 1467, 1415, 1384, 1328, 1274, 1244, 1225, 1191, 1130, 1096, 1046, 1028, 976, 952, 877, 833, 757, 696, 581, 553, 472, 458 cm^{-1}

HRMS (EI) Calcd for M^+ ($\text{C}_{29}\text{H}_{14}\text{F}_6\text{S}_6$): 667.9324. Found: 667.9337.

4.7.2.2.2 Synthesis of 3-bromo-2,5-diphenylthiophene



Phenylboronic acid (756 mg, 6.2 mmol) was added to flask containing deoxygenated THF (10 mL) and a 20 % w/w Na_2CO_3 solution (10 mL) under a nitrogen atmosphere and stirred vigorously. 2,3,5-tribromothiophene (1.022 g, 3.1 mmol) and $\text{Pd(PPh}_3)_4$ (0.107 g, 0.096 mmol) were added and the solution was heated at reflux under a nitrogen atmosphere for 24 h. The heat source was removed, the reaction mixture was allowed to cool to room temperature and extracted with CH_2Cl_2 (3×20 mL). The combined organic extracts were washed

with H₂O (2 × 20 mL) followed by brine (2 × 20 mL), dried (Na₂SO₄) and filtered. The solvent was evaporated under reduced pressure and the crude product was purified using column chromatography through silica gel (hexanes) yielding 553 mg of pure product as a white solid. Yield: 57 %.

M.p. 43-44 °C

¹H NMR (400 MHz, CD₂Cl₂) δ 7.72 - 7.69 (m, 2H), 7.63 - 7.60 (m, 2H), 7.49 - 7.32 (m, 7H), 7.31 (s, 1H)

¹³C NMR (100 MHz; CDCl₃) δ 143.2, 137.3, 133.1, 132.8, 129.0, 128.9, 128.5, 128.3, 128.2, 127.4, 107.9 (11 of 16 carbons found)

FT-IR (CH₂Cl₂ cast) 3062, 3014, 1600, 1484, 1443, 1326, 1076, 1028, 825, 759, 756, 690 cm⁻¹

LRMS (CI) Calcd for M⁺ (C₁₆H₁₁BrS): 314. Found: 317 ([M + H]⁺, [⁸¹Br], 100%), 315 ([M + H]⁺, [⁷⁹Br], 94%)

Anal. Calcd for C₁₆H₁₁BrS: C, 60.96; H, 3.32. Found: C, 61.11; H, 3.56.

4.7.2.2.3 Synthesis of 1,2-bis(2,5-diphenylthien-3-yl)-hexafluorocyclopent-1-ene (2o)

A solution of 3-bromo-2,5-diphenylthiophene (200 mg, 0.63 mmol) in anhydrous Et₂O (10 mL) cooled to -20 °C was treated with *n*-BuLi (0.25 mL of a 2.5 M solution in hexane) dropwise under a nitrogen atmosphere. A white precipitate formed after stirring for 5 min. This reaction mixture was stirred at -20 °C for a total of 15 min followed by addition of octafluorocyclopentene (40 μL,

0.31 mmol) using a cooled gas tight syringe. The precipitate remained therefore anhydrous THF (3 mL) was added to dissolve the precipitate. After stirring for 30 min, the cooling bath was removed and the reaction was allowed to warm to room temperature and stirred for 1 h when it was quenched with 5% HCl (5 mL). The aqueous layer was separated and extracted with Et₂O (2 × 10 mL). All organic extracts were combined, washed with H₂O (2 × 10 mL), followed by brine (10 mL), dried (Na₂SO₄) and filtered. The solvent was evaporated under reduced pressure and the crude product was purified using column chromatography through silica gel (hexanes) yielding 59 mg of pure product as a yellow crystalline solid. Yield: 30 %.

M.p. 223–225 °C

¹H NMR (400 MHz, CD₂Cl₂) δ 7.38 (m, 8H), 7.33 (m, 2H), 7.09 (m, 6H), 7.01 (m, 6H), 6.31 (s, 2H)

¹³C NMR (100 MHz, CDCl₃) δ 144.3, 143.7, 133.3, 132.3, 128.7, 128.7, 128.0, 127.8, 127.8, 125.6, 124.4, 122.8 (12 of 15 carbons found)

FT-IR (CH₂Cl₂ cast) 3069, 3014, 2924, 1600, 1490, 1448, 1324, 1269, 1186, 1124, 1097, 979, 924, 751, 690 cm⁻¹

LRMS (CI) Calcd for *M*⁺ (C₃₇H₂₂F₆S₂): 644. Found: 645 [*M* + H]⁺.

Anal. Calcd for C₃₇H₂₂F₆S₂: C, 68.93; H, 3.44. Found: C, 69.20; H, 3.50.

4.7.2.3 Preparation of photoswitch/nanoparticle solutions

In a typical synthesis, a colloidal dispersion of the nanoparticles (5 mL, 1.5 wt-% in THF) was added to a 20 mL scintillation vial containing **1o** (7.5 × 10⁻⁸

mol) and a stir-bar to give a final concentration of 1.5×10^{-5} M. The dispersion was stirred for 5 min and stored in the dark until needed.

4.7.3 Powder X-ray Diffraction

Powder X-ray diffraction (XRD) data were acquired utilizing a Rigaku R-AXIS RAPID-S diffractometer (Model No. 2163A101). Samples were drop-casted onto thin glass cover slips from THF and then allowed to dry.

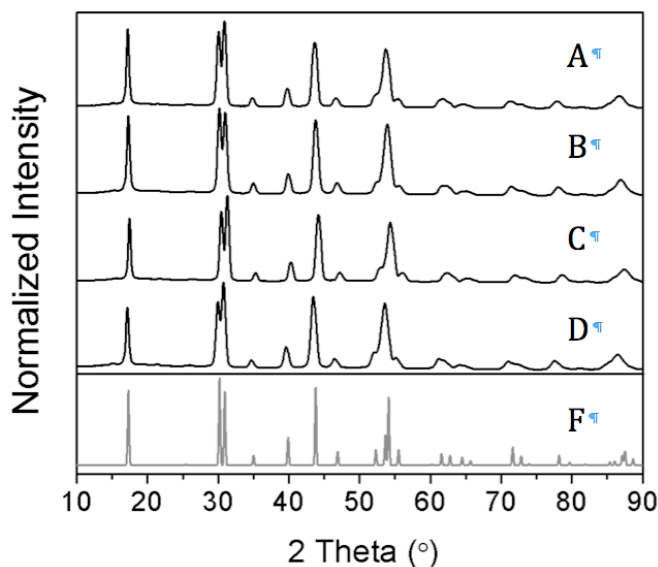


Figure 4.6 Powder X-ray diffraction (XRD) patterns for (a) $\text{NaYF}_4:\text{ErYb}-\text{NaYF}_4$ *core-shell* nanoparticles, (b) $\text{NaYF}_4:\text{TmYb}-\text{NaYF}_4$ *core-shell* nanoparticles, (c) $\text{NaYF}_4:\text{ErYb}-\text{NaYF}_4:\text{TmYb}-\text{NaYF}_4$ *core-shell-shell* nanoparticles, (d) $\text{NaYF}_4:\text{TmYb}-\text{NaYF}_4:\text{ErYb}-\text{NaYF}_4$ *core-shell-shell* nanoparticles and (f) $\beta\text{-NaYF}_4$ JCPDS standard card #28-1192.

4.7.4 Transmission Electron Microscopy

Transmission electron microscopy (TEM) and high-resolution TEM (HR-TEM) images were obtained using a Tecnai 200 keV Field Emission Scanning Transmission Electron Microscope. Dilute colloids of the nanoparticles (0.1 wt%)

dispersed in THF were drop-cast on thin, carbon formvar-coated copper grids for imaging. The nanoparticle shape and crystallinity were evaluated from the collected TEM images, while the particle size was calculated from over 200 TEM particles.

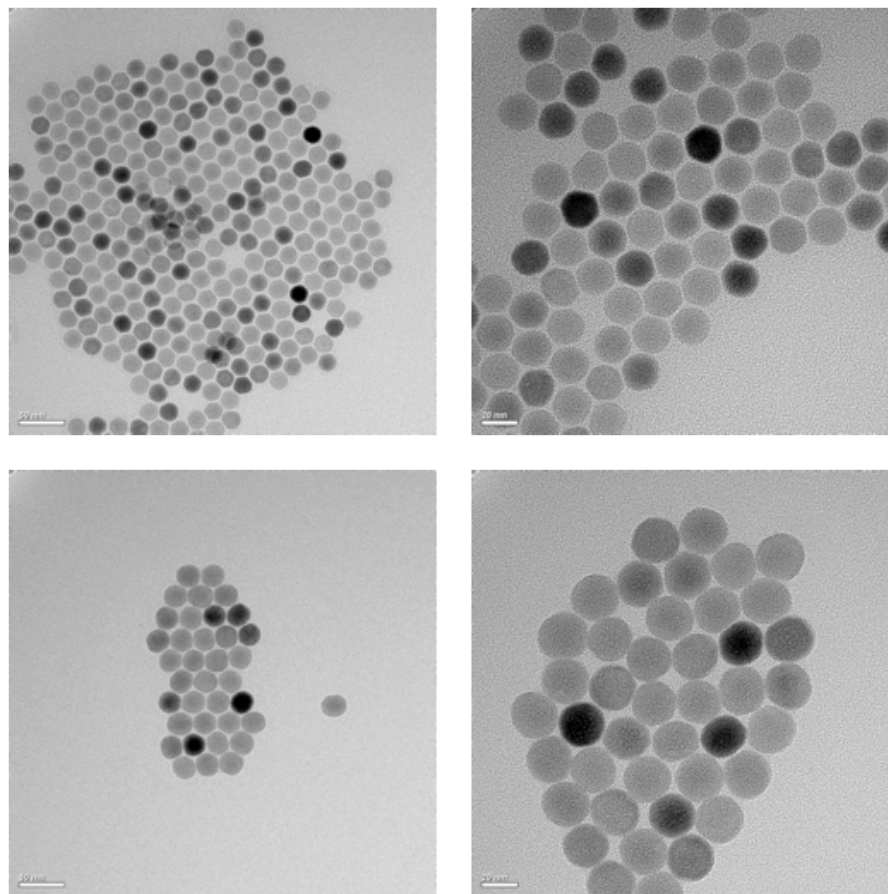


Figure 4.7 Transmission Electron Microscopy (TEM) micrographs of (top) NaYF₄:ErYb nanoparticles and (bottom) NaYF₄:ErYb-NaYF₄ *core-shell* nanoparticles.

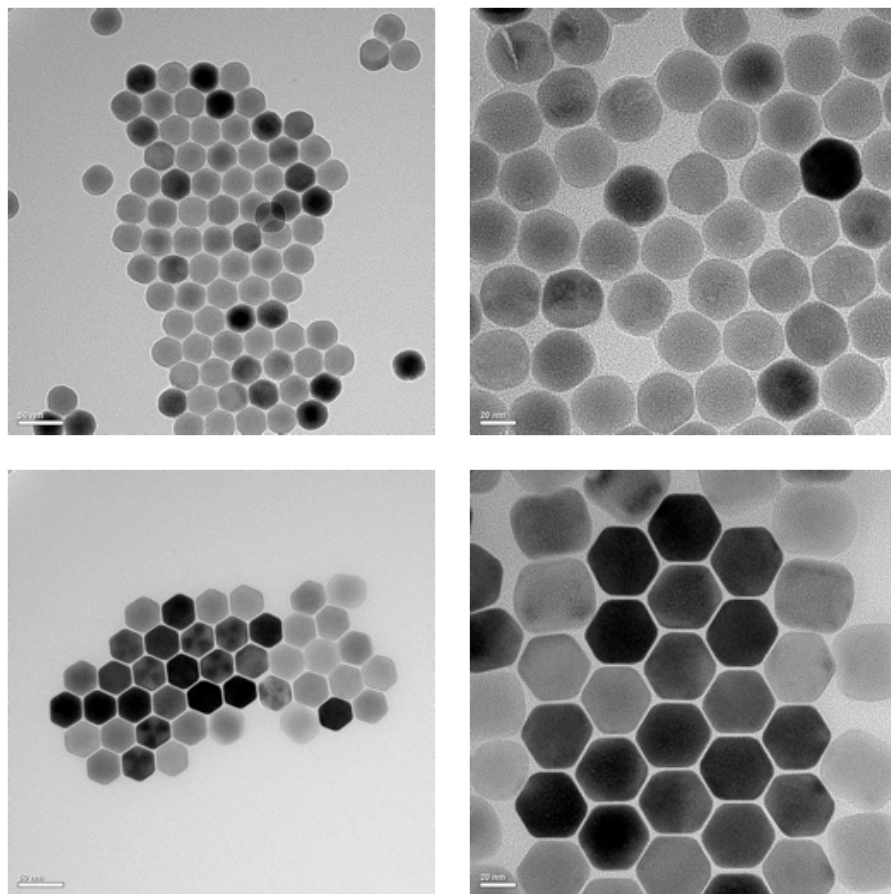


Figure 4.8 Transmission Electron Microscopy (TEM) micrographs of (top) NaYF₄:TmYb nanoparticles and (bottom) NaYF₄:TmYb-NaYF₄ core-shell nanoparticles.

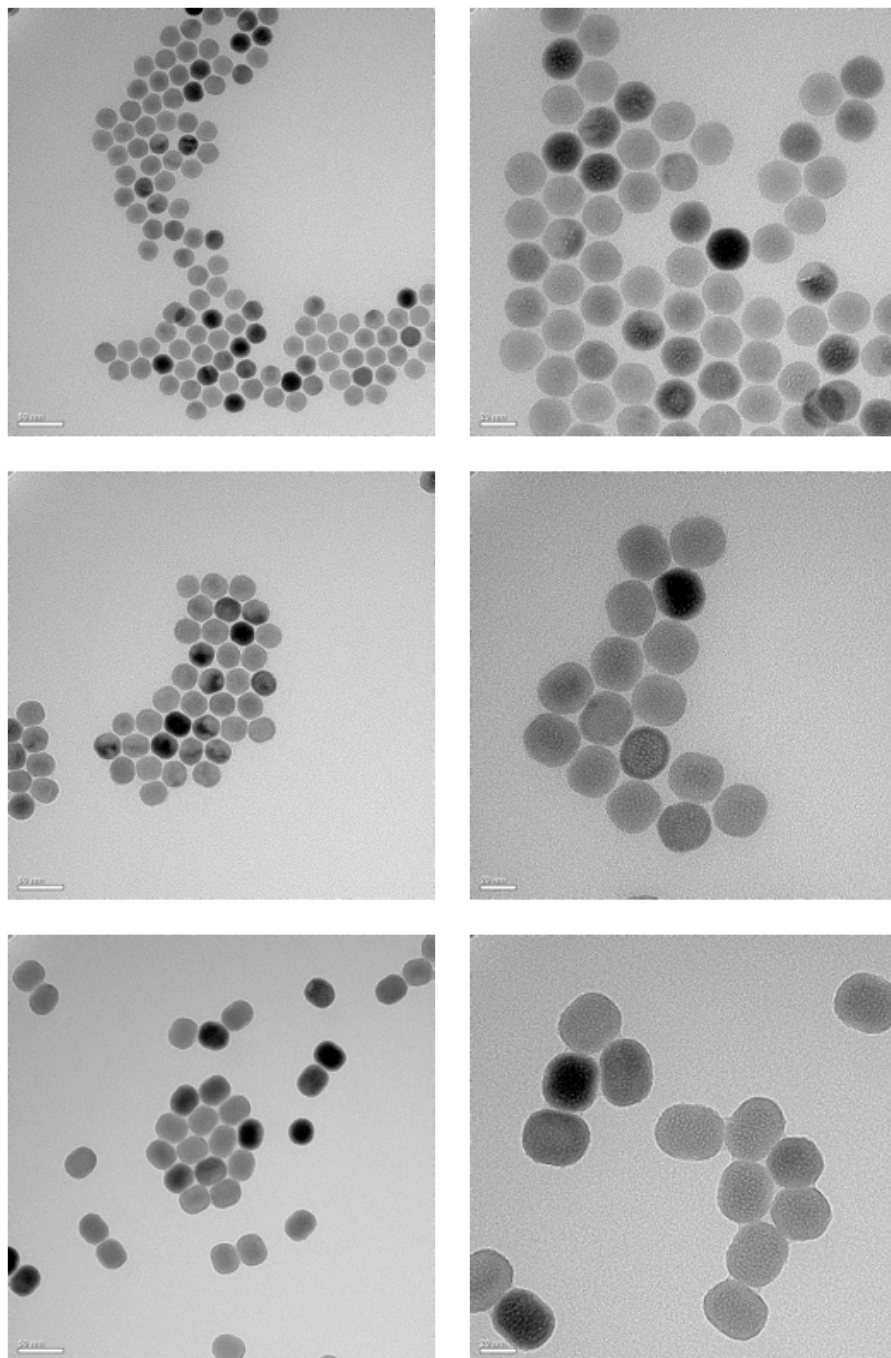


Figure 4.9 Transmission Electron Microscopy (TEM) micrographs of (top) NaYF₄:ErYb nanoparticles, (middle) NaYF₄:ErYb-NaYF₄:TmYb *core-shell* and (bottom) NaYF₄:ErYb-NaYF₄:TmYb-NaYF₄ *core-shell-shell* nanoparticles.

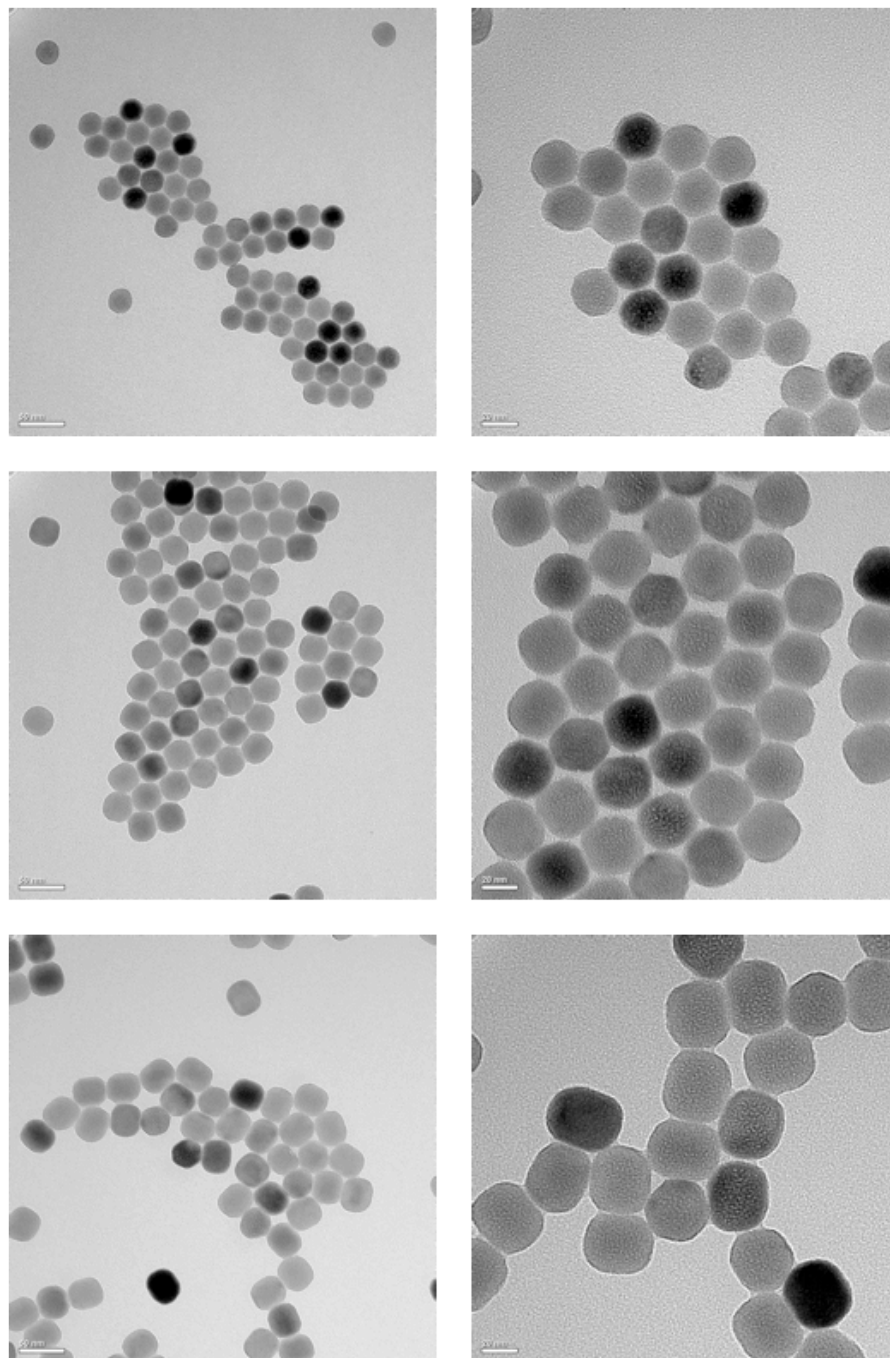


Figure 4.10 Transmission Electron Microscopy (TEM) micrographs of (top) $\text{NaYF}_4:\text{TmYb}$ nanoparticles, (middle) $\text{NaYF}_4:\text{TmYb}-\text{NaYF}_4:\text{ErYb}$ *core-shell* and (bottom) $\text{NaYF}_4:\text{TmYb}-\text{NaYF}_4:\text{ErYb}-\text{NaYF}_4$ *core-shell-shell* nanoparticles.

4.7.5 Spectroscopic measurements

UV–vis absorption spectroscopy was performed using a Varian Cary 300 Bio spectrophotometer. Fluorescence measurements of the nanoparticles were performed on a PTI Quantmaster spectrofluorometer. A JDS Uniphase 980 nm laser diode (device type L4-9897510-100M) coupled to a 105 μm (core) fibre was employed as the excitation source. The output of the diode laser was collimated and directed on the samples using a Newport F-91-C1-T Multimode Fiber Coupler. All high-energy photoreactions of **1** and **2** were carried out using the light source from a lamp used for visualizing TLC plates at 313 nm or 365 nm (Spectroline E-series, 16 mW/cm^2).

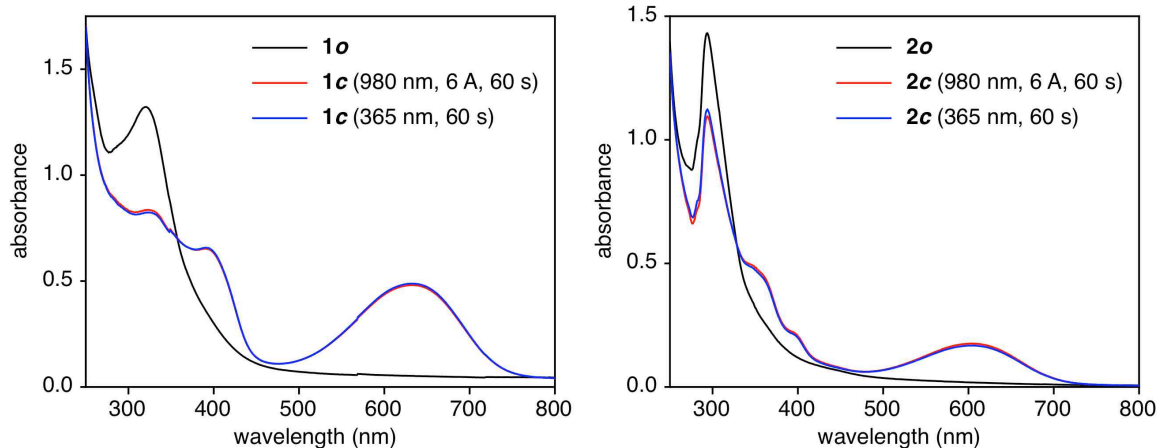


Figure 4.11 UV-vis absorption spectra of THF solutions (1.5×10^{-5} M) of (left) **1o** and (right) **2o** containing 1.5 wt% NaYF₄:TmYb nanoparticles (**Tm**) before (black line) and after irradiation with either 365 nm light (blue line) or 980 nm light at high excitation power densities (500 W/cm^2).

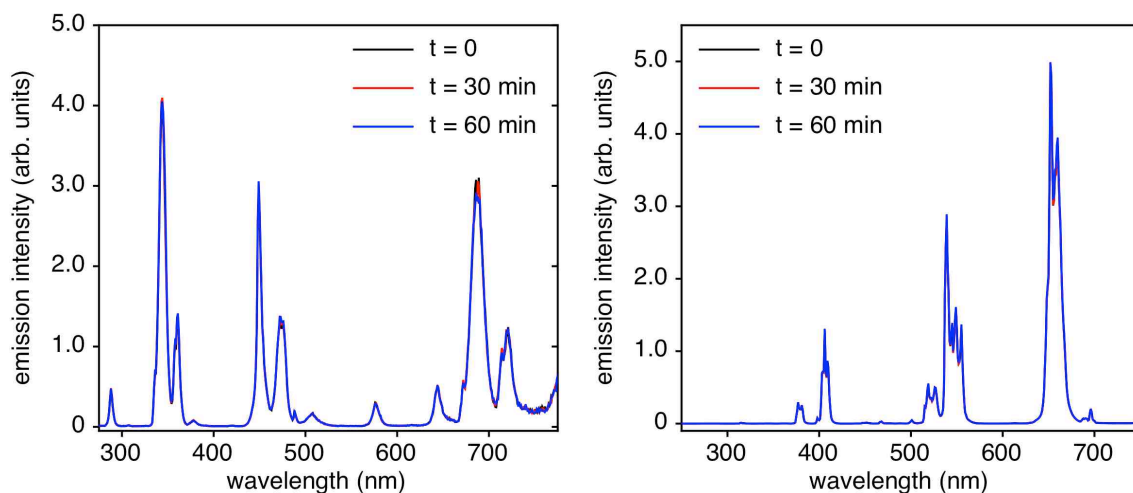


Figure 4.12 Emission spectra of THF solutions of the **TmEr** (left) and **ErTm core-shell-shell** nanoparticles as they are exposed to the higher-power NIR laser light (980 nm , 500 W/cm^2) used in the experiments. The lack of any spectral changes (all three spectra overlap) after 1 h highlights the stability of the nanoparticles.

5: PHOTOMODULATION OF FLUORESCENT UPCONVERTING NANOPARTICLE MARKERS IN LIVE ORGANISMS BY USING MOLECULAR SWITCHES

5.1 Contributions

The text in this chapter have previously been published in Chemistry, a European Journal, as a communication and is reproduced herein in its entirety with permission from the journal (J.-C. Boyer[†], C.-J. Carling[†], S. Y. Chua, D. Wilson, B. Johnsen, D. Baillie, N. R. Branda, *Chem. Eur. J.*, **2012**, *18*, 3122–3126, <http://onlinelibrary.wiley.com/doi/10.1002/chem.201103767/full>, [†]Authors contributed equally to this work). The project was co-designed by Dr. J-C Boyer, C-J Carling and Prof. Dr. N. R. Branda. All organic synthesis and characterizations thereof was conducted by C-J Carling except for molecule **3** that was synthesized by D. Wilson. Hybrid nanoparticles **a-NP** and **1**[NaYF₄:ErYb] was synthesized by Dr. J-C Boyer and characterized by TEM and fluorescence spectroscopy by Dr. J-C Boyer. C-J Carling characterized **1**[NaYF₄:ErYb] by UV-vis spectroscopy and **a-NP** and **1**[NaYF₄:ErYb] by IR spectroscopy. Dr. J-C Boyer measured all lifetimes of **1**[NaYF₄:ErYb]. S. Y. Chua handled all *C. elegans* nematodes. Dr. J-C Boyer, C-J Carling and S. Y. Chua jointly acquired the two-photon microscopy data with the aid of Dr. S. Kamal. The manuscript was co-written by Dr. J-C Boyer and Prof. Dr. N. R. Branda. Experimental section was co-written by Dr. J-C Boyer, C-J Carling, D. Wilson, S. Y. Chua, Prof. Dr. D. Baillie and Prof. Dr. N. R. Branda.

5.2 Abstract

Photoresponsive dithienylethene ligands decorated onto lanthanide doped upconverting nanoparticles are used to modulate the amount of emission from the nanoparticles. The hybrid system can be toggled between 'bright' and 'dark' states using two different types of light in living nematodes.

5.3 Introduction

Although fluorescence microscopy continues to be the method of choice by biomedical researchers to reconstruct images of cells and tissues containing optical labels,^[123] there still exist many limitations. The diffraction of light imposes the major drawback and reduces the spatial resolution achievable by conventional microscopes, which cannot distinguish between molecular or nanoscale probes residing in close proximity to each other. This limitation can be overcome using multiphoton approaches and the help of molecular switches that, by undergoing reversible photoreactions between two isomers having different absorption properties, can turn 'off' and 'on' the fluorescent signal using light sources different from the one used to initiate the emission.^[124] In this way, temporal control of emission offers heightened spatial resolution. Adding the component of time provides better tracking of specific biological species *in vivo* and can potentially distinguish between false positive signals at sub-diffraction scales.^[125]

Several issues must be considered when designing systems for use in this technology and many challenges must be overcome. The type of light used

to induce emission of the probe cannot be the same as those that trigger the forward and reverse isomerization reactions of the photoswitch. (Typically, it must lie outside the UV and visible regions of the spectrum.) This is a particularly difficult issue to avoid when two types of light are needed to drive the photochemistry along its two reaction pathways. The fluorescent probes cannot be prone to photodegradation, which shortens the fluorescence lifetime, as is often the case for organic systems. The probes should also lack undesirable optical and biochemical properties such as the 'blinking' and cytotoxicity observed for inorganic quantum dots.^[126] In this report we highlight how the combination of lanthanide doped NaYF₄ upconverting nanoparticles and photochromic dithienylethene dyes is an excellent choice to overcome these issues.

Upconverting nanoparticles (UCNPs) composed of NaYF₄ doped with Er³⁺ and Yb³⁺ absorb multiple near infrared photons and convert them into light that is emitted as relatively narrow bands in several regions of the visible spectrum.^[127] (NIR light is not capable of triggering the photoreactions of typical photoswitches.) Because they have long-lived excited states when stimulated with NIR light, continuous wave diode lasers can be utilized as excitation sources reducing autofluorescence and background interference. They have already been successfully applied to cell and whole animal imaging, drug-release, photodynamic therapy and 'remote-control' photorelease/photoswitching.^[9,10,11,128] Their non-blinking behaviour and

resistance to luminescence bleaching make them the state-of-the-art in upconverting technology and are the systems of choice for our studies.

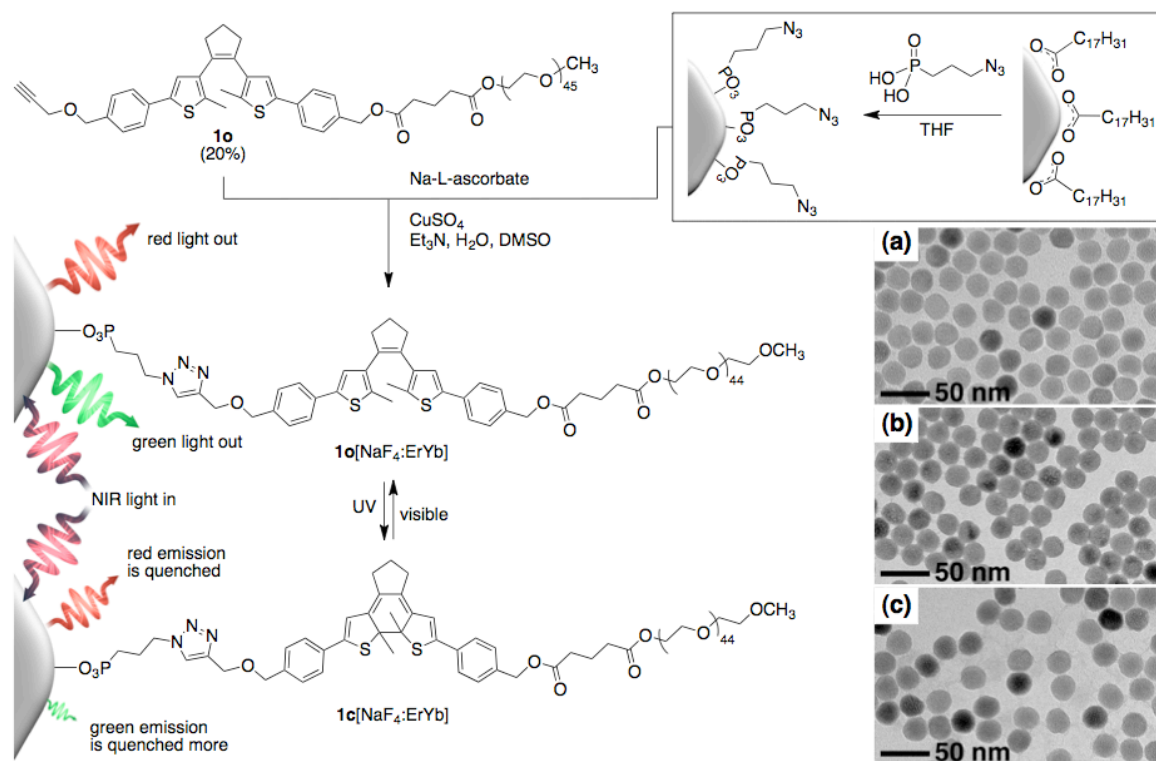


Figure 5.1 Synthesis of the photoresponsive hybrid system (**1o**[$\text{NaF}_4:\text{ErYb}$]) and a conceptual description of selective quenching of the emission from the nanoparticles by ring-closing the photoswitch. The images are TEM micrographs showing (a) the oleate coated nanoparticle starting material, (b) the azide coated nanoparticles and (c) the nanoparticles decorated with the ring-open form of the photoswitch (**1o**[$\text{NaF}_4:\text{ErYb}$]) illustrating their uniform size and shape.

Dithienylethenes (DTEs) are one of the most appealing photoswitching components. They can be efficiently toggled between two optically unique, stable isomers with a high degree of durability using UV and visible light,^[129] which can be tuned by tailoring the molecular backbone. In this manuscript, we

demonstrate how we can photomodulate the fluorescence from UCNPs *in-vitro* and *in-vivo* using DTE-decorated nanoparticle biolabels, the latter of which has not been shown to date. Using the photoresponsive hybrid system shown in Figure 5.1 (**1**[NaYF₄:ErYb]), we can change the fluorescence output from a higher intensity green/red emission to a lower intensity red-dominated fluorescence state. This modulation is feasible because only the ring-closed isomer of the photoresponsive dye (**1c**[NaYF₄:ErYb]) possesses a strong absorption in the appropriate regions of the visible spectrum to overlap with the green emission of UCNPs through energy and/or electron transfer.^[130] The ring-open isomer, on the other hand, does not absorb in the visible region of the spectrum and is incapable of selective quenching.

5.4 Results and discussion

The doped upconverting NaYF₄: 2 mol% Er³⁺, 20 mol% Yb³⁺ nanoparticles (NaYF₄:ErYb) were synthesized using high temperature colloidal methods, which result in UCNPs coated in oleate ligands.^[127] We chose to omit the step where an undoped NaYF₄ protective shell is grown onto the outside surfaces of the nanoparticles to maximize the energy transfer between the two components. While this shell is typically used to increase the UCNP's luminescence, it would also increase the distance between the lanthanide emitters and the DTE photoswitches decorated onto their surfaces, thus decreasing the quenching effect and minimizing any differences in luminescence between the 'on' and 'off' states. Figure 5.1a is a representative transmission electron microscopy (TEM)

image of the oleate coated UCNPs showing their uniform size (~26 nm) and shape.^[131]

The oleate ligands were displaced by azidopropylphosphonate ligands, which were prepared according to published procedures.^[132] The phosphonate group was chosen because of its high affinity for the surface of lanthanide-based nanoparticles, while the azide provides a convenient way to attach the photoswitches through a copper catalyzed cycloaddition (CuAAC) “click” reaction with a DTE bearing an alkyne. The appeal of using “click” chemistry lies in its tolerance to a wide range of functional groups, which will allow for the eventual modular assembly of multifunctional nanoparticles by including additional alkynes in the coupling steps.^[133]

Ligand displacement of the oleates for the azidopropylphosphonates was confirmed using FTIR spectroscopy, which revealed the strong absorbance at $\sim 2100\text{ cm}^{-1}$ attributed to the N=N=N antisymmetric stretch of the azide group, a feature that is completely absent in the case of the original oleate-coated nanoparticles. Strong absorption bands were also observed from 1250 to 990 cm^{-1} corresponding to the P–O and P–O–M stretches of the phosphonate group, respectively.^[131] TEM images of the azide-coated UCNPs show only small observable changes in the size (~25 nm) and shape of the nanoparticles compared to the oleate-coated ones (Figure 5.1b). Dynamic light scattering (DLS) experiments also showed small change in the diameter of UCNPs as the

oleate ligands (~32 nm) are replaced with azidopropylphosphonate ligands (~33 nm).^[131]

The photoresponsive DTE **1o/1c** possesses suitable optical properties for controlling energy transfer from the UCNPs. It also contains the alkyne necessary for the “click” chemistry and an mPEG chain to provide water dispersibility and eventual biocompatibility for future studies. DTE **1o** was prepared in four steps as described in the experimental section (Section 5.7). The final decorated hybrid nanoparticles (**1o**[NaYF₄:ErYb]) were prepared by reacting the two components (**1o** and NaYF₄:ErYb) in the presence of a copper catalyst (Figure 5.1). All reactions were left a minimum of 12 hours before they were diluted with MeOH and centrifuged to isolate the UCNPs. Any unreacted ligands could be easily removed by washing once more with water. The FTIR spectrum of **1o**[NaYF₄:ErYb] shows a reduction in the azide stretch at ~2100 cm⁻¹ when compared to that for the azide-functionalized analogues along with the appearance of a peak at 1554 cm⁻¹ attributed to the 1,2,3-triazole ring system.^[134] The absorption bands attributed to the phosphonate group (1250–990 cm⁻¹) were also still present in the spectrum.

TEM images of the UCNPs after the CuACC reaction showed that they were well-dispersed with no changes in particle morphology (Figure 5.1c). A size analysis of several TEM images generate an average particle size of ~26 nm, which corresponds well to the sizes of the original oleate and azide-coated UCNPs. DLS results showed a more significant increase in particle diameter to

~42 nm after attachment of DTE **1o** to the nanoparticles, which we attribute to the longer length of the photoresponsive molecule compared to the original oleate ligand. As expected, the hydrodynamic diameter of the DTE-functionalized nanoparticles is larger than the diameter measured using TEM, as DLS also takes into account the length of the ligands on the nanoparticle surface.

The decorated **1o**[NaYF₄:ErYb] nanoparticles are highly stable in water and we observed no settling over a period of greater than a month. We also observed them to be stable in 10 mM phosphate buffered saline (pH = 7.2) for several hours before settling occurred, an important property if they are to be used in biological applications. Using the intensity of the bands in the UV-vis absorption spectra corresponding to the ring-open isomer of the free DTE ligand (**1o**) and in the hybrid complex **1o**[NaYF₄:ErYb], and the results from the particle size analysis of the decorated nanoparticles, we estimate an approximate loading of the photoresponsive component on the surface of each individual nanoparticle as ~600 molecules per particle.

Figure 5.2a shows the optical properties of aqueous solutions of the hybrid system (**1o**[NaYF₄:ErYb]) and justifies the choice of nanoparticle and photoresponsive ligand. The organic chromophores on the decorated nanoparticles have similar optical properties and photochromic behaviour as the free ligands (**1o/1c**):^[131] they absorb UV light (365 nm) and undergo an immediate change in their UV-vis absorption spectra. As is typical for the DTE

chromophore, the absorption bands in the high-energy region of the spectrum of both **1o**[NaYF₄:ErYb] (Figure 5.2a and 5.9) and **1o** (Figure 5.9) decrease in intensity and new broad bands in the visible region appear. These are the characteristic changes that occur when the ring-open isomer of the free ligand (**1o**) is converted into its ring-closed counterpart (**1c**). In the present case, the conversion is **1o**[NaYF₄:ErYb] → **1c**[NaYF₄:ErYb] and results in a visual color change of the solutions from colorless to red at the photostationary state, which contains 82% of the ring-closed isomer as measured by ¹H NMR spectroscopy of the free ligand (**1o**). These red solutions can be converted back to their colourless versions by exposing them to visible light of wavelengths greater than 434 nm, which triggers the reverse, ring-opening reaction and regenerates the original spectra.

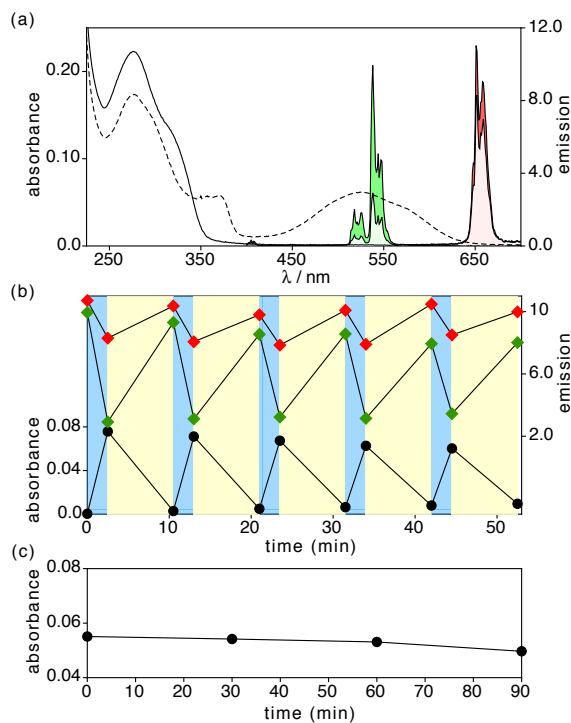


Figure 5.2 (a) UV-vis absorption and emission spectra ($\lambda_{\text{ex}} = 980 \text{ nm}$, 150 W/cm^2) of an aqueous solution ($9.0 \times 10^{-6} \text{ M}$) of **1o**[NaF₄:ErYb] before (solid line/dark shading) and after irradiation with 365 nm light (dashed line/light shading) for 2.5 min (1.3 mW/cm^2). (b) Changes in the absorbance at 530 nm (black circles), and emission intensities at 538 nm (green diamonds) and 652 nm (red diamonds) of a similar solution of **1o**[NaYF₄:ErYb] when it is alternately irradiated with UV and visible light. (c) Changes in the absorbance at 530 nm of a similar solution of **1c**[NaYF₄:ErYb] when it is continuously irradiated with 980 nm light.

The upconversion luminescence of **1o**[NaYF₄:ErYb] under 980 nm laser diode laser excitation (150 W/cm^2) exhibits two main sets of emission peaks in the visible portion of the spectra (Figure 5.2a), from 510–560 (green) and 635–680 nm (red) corresponding to the $[^4\text{H}_{11/2}, ^5\text{S}_{3/2}] \rightarrow ^4\text{I}_{15/2}$ and $^4\text{F}_{9/2} \rightarrow ^4\text{I}_{15/2}$ transitions, respectively. While there is no significant overlap between the absorption bands of **1o**, whether alone^[131] or decorated onto the nanoparticles, the broad, long-wavelength absorption band (450–650 nm) of the ring-closed

isomer (**1c** and **1c**[NaYF₄:ErYb]) completely overlaps with the green emission of the NaYF₄:ErYb UCNP and only slightly with the red emission. This implies that significant luminescence quenching will only be observed after the system is exposed to UV light to convert **1o** into its ring-closed counterpart on the nanoparticles. Figure 5.2a–b show this to be the case.

The green emission (538 nm)^[135] of an aqueous solution of the decorated nanoparticles is 3.5 times less intense (29 % of the original value) when the photoswitch is first converted to its photostationary state.^[136] The red emission (651 nm) is also quenched albeit to a lesser extent (to 75 % of the original value) as can be expected from the lower overlap between the absorption bands of the DTE and the emission bands of the UCNP. The red emission quenching is also explained by the fact that the ⁴F_{9/2} excitation state of the nanoparticles is partially fed via non-radiative decay from the [⁴H_{11/2}, ⁵S_{3/2}] levels.

We are attributing the fluorescence quenching of the nanoparticles decorated with the ring-closed photoisomer (**1c**[NaYF₄:ErYb]) to a combination of fluorescence resonance energy transfer (FRET) and an inner filter effect (the absorption of the visible light emitted from the nanoparticle by the coloured ligands, not necessarily on the same nanoparticle). The dominance of the latter mechanism is reflected in the reduction of the [⁴H_{11/2}, ⁵S_{3/2}] → ⁴I_{15/2} upconversion lifetime of the nanoparticles when the ring-open photoresponsive ligands are converted to their ring-closed counterparts (74 μs for **1o**[NaYF₄:ErYb] and 61 μs for **1c**[NaYF₄:ErYb]), which corresponds to a FRET efficiency of 18 %.^[137]

Exposing the decorated nanoparticles containing the ring-closed photoswitches (**1c**[NaYF₄:ErYb]) to visible light at wavelengths greater than 434 nm (107 mW/cm²) restores the original emission intensities for both the green and red emissions, although as can be seen from the results of subjecting them to several photochemical cycles by alternating between UV and visible light (Figure 5.2b), the quenching efficacy gradually diminishes. Because the absorptions corresponding to the ring-closed isomer of the ligand (black circles in the Figure) also slightly change after each cycle, we believe that the degradation of the photoswitch is the culprit. This claim is supported by the fact that prolonged irradiation of the nanoparticles (**1c**[NaYF₄:ErYb]) with 980 nm light (150 W/cm² for 90 minutes) resulted in negligible ring-opening of the photoresponsive ligand (Figure 5.2c) and no loss in the upconversion efficiency of the nanoparticles. This minor degradation (likely due to photochemical side reactions in the oxygen rich aqueous environment) will not hinder the use of the decorated nanoparticles in biological application where the photoswitch is likely to only be subjected to a few cycles. Future generations of systems may have enhanced performance by employing fluorinated DTE photoswitches since they demonstrate superior stability in oxygen and water environments.

The regulation of fluorescence imaging in live organisms was demonstrated using *Caenorhabditis elegans* N2 hermaphrodites, which were incubated for 3 hours with the decorated nanoparticles **1o**[NaYF₄:ErYb] dispersed in M9 buffer. After immobilizing the nematodes using Levamisole in

M9 buffer, they were isolated by centrifugation, mounted on agarose gel pads and imaged using 2-photon fluorescence microscopy (Figure 5.3).

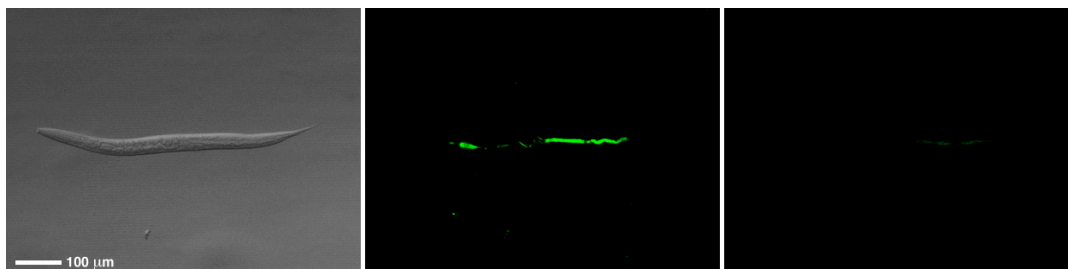


Figure 5.3 Optical (left) and two-photon upconversion fluorescence (middle and right) microscopy images of wild-type N2 *C. elegans* incubated with **1o**[NaYF₄:ErYb] (0.25 mg of a 0.5 mg/mL solution in M9 buffer) showing the changes in fluorescence due to the photoswitching of the DTE component within the bodies of the worms. The middle panel shows the strong initial fluorescence prior to exposure to UV light. The right panel shows the reduced emission that is a result of ring-closing the photoswitch with 365 nm light for 2.5 minutes.

The upconverting fluorescence from **1o**[NaYF₄:ErYb] can be clearly observed in the digestive tract of the nematodes indicating they had ingested the nanoparticles. The ring-closing reaction of the photoresponsive ligands was triggered by irradiating the nematodes with 365 nm light for 180 seconds, which produced a significant reduction in the observable fluorescence (Figure 5.3). The changes in the photoluminescence spectra of the hybrid nanoparticles inside the nematodes before and after UV irradiation corresponds to a 50–60% decrease in emission intensity.^[131] The reduced quenching can be explained by a reduction in the inner filter effect in these more dilute conditions. Importantly, all nematodes showed little evidence for sensitivity (toxicity to the nanoparticles,

damage from the light source) before, during and after the imaging experiments, and were still mobile after irradiation. We also note that the nematodes were still viable and had progeny after incubation.

5.5 Conclusion

We successfully demonstrated the ability to modulate the luminescence from upconverting nanoparticles *in-vitro* and *in-vivo* by taking advantage of the well-understood photochemistry of dithienylethene ‘molecular switches’ decorated onto the nanoparticles’ surfaces using CuACC chemistry. By reversibly converting the photoswitch back and forth between its two isomers using UV and visible light, we are able to toggle the system between ‘on’ (bright fluorescence) and ‘off’ (quenched fluorescence) states. This process can be cycled multiple times before any degradation of the nanoparticles or the photoswitch renders the system impractical. Our system has an advantage over ‘caged’ fluorophores as the luminescence of our designer nanoparticles can be repeatedly cycled through ‘on’ and ‘off’ states. Systems such as the one described in this manuscript not only have the capacity to reversibly control the intensity of the probe emission, through selective absorption, they can also alter the colour of the emitted light from multi-coloured probes further enhancing the imaging capabilities.

5.6 Acknowledgments

This research was supported by the Natural Sciences and Engineering Research Council (NSERC) of Canada, the Canada Research Chairs Program,

and Simon Fraser University through funding from the Community Trust Endowment Fund. This work made use of 4D LABS shared facilities supported by the Canada Foundation for Innovation (CFI), British Columbia Knowledge Development Fund (BCKDF) and Simon Fraser University. J.–C. Boyer thanks the Michael Smith Foundation for Health Research for support. C.–J. Carling thanks Simon Fraser University for a Graduate Fellowship.

5.7 Experimental

5.7.1 General methods

5.7.1.1 Materials

All solvents and reagents used for synthesis, chromatography, photochemistry and UV–vis absorption spectroscopy were purchased from Aldrich and used as received, unless otherwise noted. Erbium(III) acetate hydrate (99.9%), ytterbium(III) acetate tetrahydrate (99.9%), yttrium(III) acetate hydrate (99.9%), oleic acid (technical grade, 90%), 1-octadecene (technical grade, 90%), ammonium fluoride (99.99+%), (+)-sodium L-ascorbate ($\geq 98\%$) and copper(II) sulfate pentahydrate ($\geq 98\%$) were purchased from Sigma-Aldrich. Hexanes, dimethyl sulphoxide (DMSO) and tetrahydrofuran (THF) were purchased from Caledon Inc. Anhydrous ethyl alcohol was purchased from Commercial Alcohols. Triethylamine were purchased from Anachemia. All chemicals were used as received, without any further purification. Solvents for NMR analysis were purchased from Cambridge Isotope Laboratories and used as received. Column chromatography was performed using silica gel 60 (230–400 mesh) from Silicycle Inc. 3-Azidopropylphosphonic acid^[132] and 1,2-bis(5-chloro-2-methylthien-3-yl)cyclopentene (**2**)^[138] were prepared using modifications of literature methods. The upconverting nanoparticles were synthesized using a modification of a recently reported procedure.^[139] All volumes for absorption,

photolysis and concentration studies were measured out using calibrated autopipettes.

5.7.1.2 Instrumentation

^1H NMR and ^{13}C NMR characterizations of all compounds were carried out using a Bruker AVIII 400 BBO Plus (5 mm probe) working at 400.13 MHz for ^1H and 100.60 MHz for ^{13}C . Chemical shifts (δ) are reported in parts per million relative to tetramethylsilane using the residual solvent peak as a reference standard. Coupling constants (J) are reported in hertz.

Melting points were measured using a Gallenkamp melting point apparatus (Registered Design No. 889339) and reported without correction.

Exact mass measurements were done using a Kratos Concept-H instrument with perfluorokerosene as the standard.

Powder X-ray diffraction (XRD) data were acquired utilizing a Rigaku R-AXIS RAPID-S diffractometer (Model No. 2163A101). Samples were drop-casted onto thin glass cover slips from THF and then allowed to dry before analysis.

TEM and high-resolution TEM (HR-TEM) images were obtained using a Tecnai 200 keV Field Emission Scanning Transmission Electron Microscope. Dilute colloids of the NPs (0.1 wt-%) dispersed in THF, ethanol or water were dropcast on thin, carbon formvar-coated copper grids for imaging. In the case of ethanol or water, excess solvent was removed under vacuum. The nanoparticle

shape and crystallinity were evaluated from the collected TEM images, while the particle size was calculated from over 150 particles.

Dynamic Light Scattering (DLS) measurements were carried out using a Malvern Zetasizer Nano-ZS. A nanoparticle concentration of ~ 0.1 mg/mL was employed for the measurements. All DLS measurements were conducted at 25 °C.

UV–vis absorption spectroscopy was performed using a Varian Cary 300 Bio spectrophotometer.

All solution-state photoreactions were carried out using the light source from a lamp used for visualizing TLC plates at 365 nm (Spectroline E-series, 1.3 mW/cm²) and a tungsten light source using a > 434 nm cut-off filter (Elmo Omnigraphic 300AF, 107 mW/cm²).

FTIR spectra were acquired on a Bomem (Hartmann & Braun, MB-Series) spectrometer. The samples were prepared by mixing 1 part of functionalized nanoparticle with 10 parts of KBr, followed by pressing them into translucent discs.

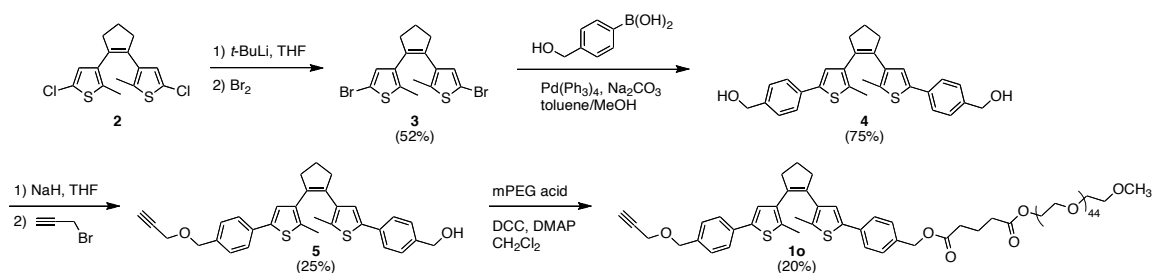
Fluorescence measurements were performed on a PTI Quantamaster spectrofluorometer. A JDS Uniphase 980 nm laser diode (device type L4-9897510-100M) coupled to a 105 μ m (core) fibre was employed as the excitation source. The output of the diode laser was collimated and directed on the

samples using a Newport F-91-C1-T Multimode Fiber Coupler. The visible emissions were collected from the samples at $\pi/2$ from the incident beam in the plane of the spectrometer. All of the colloidal samples were held in a square quartz cuvette (path length of 1 cm). All spectra were corrected for instrument sensitivity.

Lifetime analyses were done by exciting the solution with a 10 Hz Q-Switched Quantel Brilliant, in which the third harmonic of the Nd:YAG laser pumps the optical parametric oscillator (OPO), with an optical range from 410 to 2200 nm. The pulse duration of the laser was 5 ns, and the spot size had a 2 mm diameter. The laser intensity at 980 nm was 2 mJ. Intensities down to 1% of the initial intensities were included in these lifetime analyses. The decay times were calculated from these curves by fitting them with a single exponential model using Origin software (version 7.0) after the in-growth portion of the curve.

Two-Photon Upconversion Imaging ($\lambda_{\text{ex}} = 980 \text{ nm}$) was performed on a Leica confocal / two-photon microscope (model TCS SP5 with DMI 6000 inverted microscope) equipped with a Coherent femtosecond Ti:Sapphire laser (model Chameleon Vision). The NIR laser beam was focused onto the sample using a 10 \times microscope objective with a numerical aperture of 0.75.

5.7.2 Synthesis



5.7.2.1 Synthesis of 1,2-bis(5-bromo-2-methylthien-3-yl)cyclopentene (3)

A solution of 1,2-bis(5-chloro-2-methylthien-3-yl)cyclopentene (**2**) (1.03 g, 3.12 mmol) in anhydrous Et₂O (100 mL) was cooled to -60 °C in a dry ice/acetone bath and then treated with *t*-butyllithium (1.7 M in pentane, 4.1 mL, 6.88 mmol) drop wise over 15 min under an atmosphere of nitrogen. The resulting solution was stirred for an additional 20 min at -60 °C, at which time it was treated with a solution of Br₂ (0.39 mL, 7.59 mmol) in anhydrous Et₂O (10 mL) drop wise using a syringe. After stirring at -60 °C for 30 min, the yellow-orange solution was allowed to warm to room temperature and poured into water (50 mL). The layers were separated and the organic layer was washed with brine (2 × 50 mL), dried over MgSO₄ and filtered. The solvent was removed under reduced pressure to yield a brown oil. Purification by column chromatography using silica gel (hexanes) yielded 0.68 g (52 %) of **3** as a crystalline white solid, which yellowed upon exposure to UV light.

M.p. 85–90 °C.

¹H NMR (400 MHz, CDCl₃) δ 6.74 (s, 2H), 2.75 (t, *J* = 7.5 Hz, 4H), 2.10–2.00 (m, 2H), 1.91 (s, 6H).

¹³C NMR (CDCl₃ 100 MHz) δ 136.2, 136.0, 134.3, 130.4, 107.4, 38.4, 22.8, 14.2.

HRMS m/z : Calculated for $C_{15}H_{14}Br_2S_2$ [M^+], 415.8904, found: 415.8808

5.7.2.2 Synthesis of (4,4'-(4,4'-(cyclopentene-1,2-diyl)bis(5-methylthiophene-4,2-diyl)-bis(4,1-phenylene))dimethanol (4)

A 25 mL round bottom flask equipped with a water-cooled condenser was charged with 1,2-bis(5-bromo-2-methylthien-3-yl)cyclopentene (**3**) (134 mg, 0.32 mmol), 4-methylhydroxyphenyl boronic acid (146 mg, 0.96 mmol), $Na_2CO_3 \cdot H_2O$ (198 mg, 1.6 mmol), toluene (9 mL) and 95 % MeOH (3 mL). After bubbling N_2 through the mixture for 25 min, it was treated with $Pd(PPh_3)_4$. The system was purged with N_2 and the reaction heated to reflux. After 21.5 h, the dark brown reaction mixture was cooled to ambient temperature and poured into a separatory funnel. The reaction flask was rinsed with EtOAc and the combined organic mixture was diluted with saturated aqueous NH_4Cl and H_2O . The layers were separated and the aqueous layer was extracted an additional 2 times with EtOAc. The combined organic extract was dried over anhydrous $MgSO_4$, vacuum filtered and concentrated under reduced pressure to yield a dark oil. Purification by column chromatography using silica gel (1:2 EtOAc:hexanes) yielded 113 mg (75%) of **4** as an oil that converted to a white solid foam under hi-vacuum, which turned red upon exposure to UV light.

M.p. 65–70 °C (decomp.)

1H NMR (CD_2Cl_2 , 400 MHz) δ 7.48 (dd, $J = 8.2, 2.4$ Hz, 4H), 7.31 (dd, $J = 8.2, 2.4$ Hz, 4H), 7.06 (d, $J = 2.4$ Hz, 2H), 4.65 (d, $J = 5.8$ Hz, 4H), 2.85 (t, $J = 7.5$ Hz, 4H), 2.11–2.07 (m, 2H), 2.01 (s, 6H), 1.75 (t, $J = 5.8$ Hz, 2H).

^{13}C NMR (CD_2Cl_2 , 100 MHz) δ 140.63, 139.78, 137.43, 135.36, 135.10, 134.29, 127.95, 125.80, 124.72, 65.30, 38.00, 23.60, 14.72.

HRMS m/z : Calculated for $\text{C}_{29}\text{H}_{29}\text{O}_2\text{S}_2$ [$\text{M}+\text{H}^+$] 473.1603, found: 473.1586.

5.7.2.3 Synthesis of (4-(5-methyl-4-(2-(2-methyl-5-(4-((prop-2-ynoxy)methyl)phenyl)-thiophen-3-yl)cyclopent-1-enyl)thiophen-2-yl)phenyl)methanol (**5**)

A flame-dried round bottom flask equipped with a water-cooled condenser was charged with NaH (95 %, 10 mg, 0.40 mmol) and anhydrous THF (15 mL, via a cannula) under an N_2 atmosphere. The mixture was cooled to 0 °C and treated with bis(alcohol) **4** (90 mg, 0.19 mmol) and propargylbromide (31 mg, 0.21 mmol, 80 w/w %). The reaction mixture was heated to reflux under an N_2 atmosphere. After 18 h, the reaction was cooled to ambient temperature and quenched with saturated aqueous NH_4Cl . The mixture was poured into a separatory funnel and diluted with EtOAc. The phases were separated and the aqueous phase was extracted an additional 2 times with EtOAc. The combined organic extracts were dried over anhydrous MgSO_4 , vacuum filtered and concentrated under reduced pressure to obtain a yellow oil. Purification by column chromatography on silica gel (gradient of 1:2 to 1:1 EtOAc:hexanes) followed by a second purification (1:4 EtOAc:hexanes) yielded 25 mg (25%) of compound **5** as a colourless glass, which turned red upon exposure to UV light.

^1H NMR (CD_2Cl_2 , 400 MHz) δ 7.49 (dd, $J = 8.2, 2.4$ Hz, 4H), 7.31 (dd, $J = 8.2, 2.4$ Hz, 4H), 7.06 (d, $J = 2.4$ Hz, 2H), 4.65 (d, $J = 5.8$ Hz, 2H), 4.56 (s, 2H), 4.17 (d, $J = 2.4$ Hz, 2H), 2.85 (t, $J = 7.5$ Hz, 4H), 2.51 (t, $J = 2.4$ Hz, 1H), 2.11–2.05 (m, 2H), 2.01 (s, 6H), 1.76 (t, $J = 5.8$ Hz, 1H).

^{13}C NMR (CD_2Cl_2 , 100 MHz) δ 140.6, 139.8, 139.7, 137.5, 137.4, 136.9, 135.4, 135.4, 135.2, 135.1, 134.6, 134.3, 129.1, 129.1, 128.0, 125.8, 125.7, 124.8, 124.7, 80.3, 74.9, 71.7, 65.3, 57.6, 39.0, 29.6, 23.6, 14.7.

HRMS m/z : Calculated for $\text{C}_{32}\text{H}_{30}\text{O}_2\text{S}_2$ [$\text{M}+\text{Na}^+$] 533.1579, found: 533.1568.

5.7.2.4 Synthesis of 2-mPEG 4-(5-methyl-4-(2-(2-methyl-5-(4-((prop-2-ynyloxy)-methyl)phenyl)thiophen-3-yl)cyclopent-1-enyl)thiophen-2-yl)benzyl glutarate (**1o**)

A flame-dried round-bottom flask was charged with anhydrous CH_2Cl_2 (7 mL), alcohol **5** (20 mg, 0.039 mmol) and mPEG-glutaric acid (Polymer Source, 123 mg, 0.059 mmol) under an N_2 atmosphere. The mixture was cooled to 0 °C and treated with DMAP (11 mg, 0.09 mmol) and DCC (19 mg, 0.09 mmol). The ice bath was removed and the reaction was stirred for 5.5 h until all starting material was consumed as indicated by silica TLC. The reaction mixture was filtered and the solvent was removed under reduced pressure. The oily residue was taken up in a minimal amount of water, sonicated and filtered through a plug of glass wool in a Pasteur pipette by applying pressure from a pipette bulb. The water was removed under reduced pressure to yield a red waxy solid, which was dissolved in acetone and filtered through a plug of glass wool in a Pasteur pipette. The crude product was purified twice by neutral alumina column chromatography (activity 1, gradient from 100 % CH_3CN to 100:5 $\text{CH}_3\text{CN}:\text{H}_2\text{O}$), followed by several purification steps using size exclusion chromatography (GE healthcare, LH20, THF) to afford 21 mg (20%) of **1o** as an off-white waxy solid, which turned red upon exposure to UV light. Analysis showed that the product

contained some unreacted mPEG. The product was carried over to the next step without any further purification.

M.p. 40–45 °C.

^1H NMR (CD_2Cl_2 , 400 MHz) δ 7.49 (dd, $J = 8.2, 2.4$ Hz, 4H), 7.31 (dd, $J = 8.2, 2.4$ Hz, 4H), 7.06 (d, $J = 2.4$ Hz, 2H), 5.07 (s, 2H), 4.56 (s, 2H), 4.17 (d, $J = 2.4$ Hz, 2H), 3.79–3.76 (m, 2H, mPEG), 3.69–3.63 (m, 10H, mPEG), 3.59 (bs, 237H, mPEG), 3.51–3.49 (m, 2H, mPEG), 3.33 (s, 4H, mPEG), 2.86 (t, $J = 7.4$ Hz, 4H), 2.25 (t, $J = 2.4$ Hz, 1H), 2.46–2.37 (m, 6H, mPEG), 2.14–2.12 (m, 2H), 2.04 (s, 3H), 2.00 (s, 3H), 1.99–1.96 (m, 4H, mPEG), 1.83–1.80 (m, 4H, mPEG).

^{13}C NMR (CD_2Cl_2 , 100 MHz) δ (20 out of 37 peaks found) 129.3, 129.1, 125.8, 125.7, 74.9, 72.5, 71.1, 71.1, 71.0, 71.0, 69.6, 68.3, 64.1, 57.6, 39.0, 33.6, 30.6, 26.2, 20.7, 14.7.

LRMS m/z : Calculated for $\text{C}_{128}\text{H}_{218}\text{O}_{50}\text{S}_2$ [$\text{M}+2\text{NH}_4^+$ ($z = 2$)] 1328.2334, found: 1328.2337. The mass spectrum showed a Gaussian shaped distribution of multiple peaks with 44 g/mol ($\text{CH}_2\text{CH}_2\text{O}$) separation due to the polydispersity of mPEG.

The percentage of each isomer in the photostationary was measured by ^1H NMR spectroscopy in CD_2Cl_2 by irradiating a solution of **1o** with 365 nm light for 35 min (handheld TLC lamp). The progress of the reaction was followed by UV-vis absorption spectroscopy. A small aliquot of the NMR sample was removed at regular intervals and the absorbance of the aliquot was measured before and after irradiation with UV light until no more changes occurred in the spectrum. By comparing the relative integration of the characteristic peaks in the NMR

spectrum of **1c**, the photostationary state was determined to contain 82 % ring-closed isomer, 15 % ring-open isomer and 3 % unidentified side-product.

5.7.2.5 Synthesis of β -NaYF₄: 2 mol% Er⁺, 20 mol% Yb³⁺ nanoparticles (NaYF₄:ErYb)

In a typical synthesis, Y(CH₃CO₂)₃ (1.76 mmol), Yb(CH₃CO₂)₃ (0.40 mmol) and Er(CH₃CO₂)₃ (0.04 mmol) were added to a 100 mL three-neck round-bottom flask containing 30 mL octadecene and 12 mL oleic acid. The solution was stirred magnetically and heated slowly to 120 °C under vacuum for 30 min to form the lanthanide oleate complexes, and to remove residual water and oxygen. The temperature was then lowered to 50 °C and the reaction flask placed under a gentle flow of nitrogen gas. During this time, a solution of ammonium fluoride (0.2964 g, 8 mmol) and sodium hydroxide (0.2 g, 5.0 mmol) dissolved in methanol (20 mL) was prepared *via* sonication. Once the reaction reached 50 °C, the methanol solution was added to the reaction flask and the resulting cloudy mixture was stirred for 30 min at 50 °C. The reaction temperature was then increased to 70 °C and the methanol evaporated from the reaction mixture. Subsequently, the reaction temperature was increased to 300 °C as quickly as possible and maintained at this temperature for 60 min under the nitrogen gas flow. During this time the reaction mixture became progressively clearer until a completely clear, slightly yellowish solution was obtained. The mixture was allowed to cool to room temperature. The nanoparticles were precipitated by the addition of ethanol and isolated *via* centrifugation at 4500 rpm corresponding to a relative centrifugal field (RCF) of approximately 1000. The

resulting pellet was dispersed in a minimal amount of hexanes and precipitated with excess ethanol. The nanoparticles were isolated *via* centrifugation at 4500 rpm and then dispersed in either chloroform or THF for subsequent experiments.

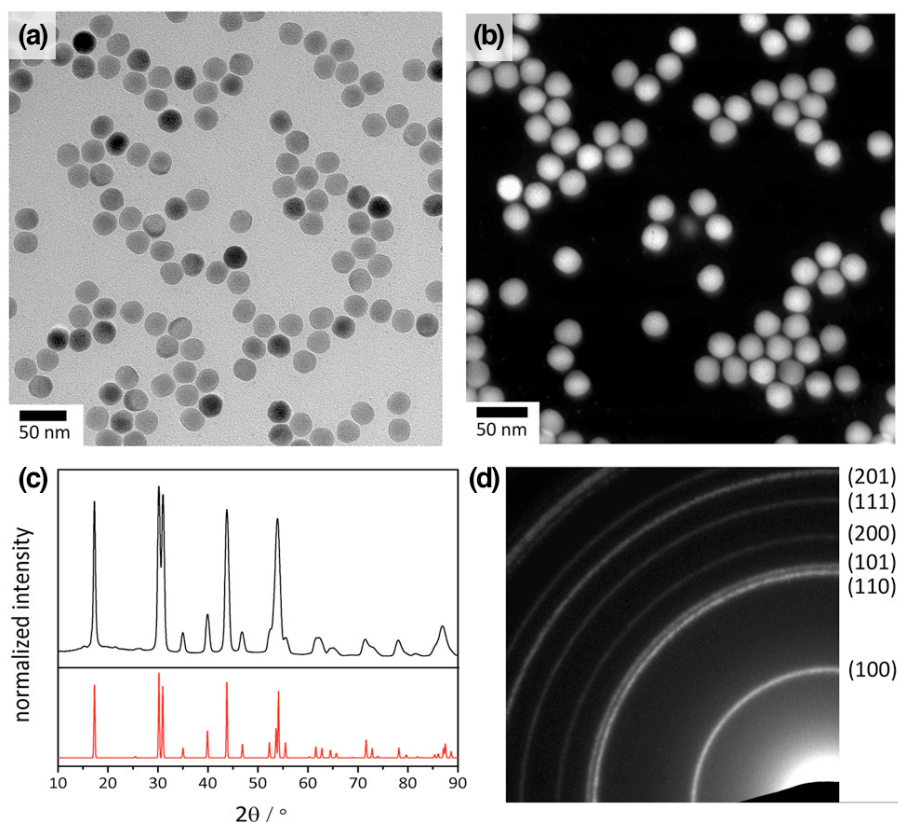


Figure 5.4 (a) Transmission Electron Microscopy (TEM) micrograph of oleate-coated NaYF₄:ErYb nanoparticles. (b) High-angle annular dark-field (HAADF) image of NaYF₄:ErYb nanoparticles (c) Powder X-ray diffraction (XRD) patterns for (top) NaYF₄:ErYb nanoparticles and (bottom) β-NaYF₄ JCPDS standard card #28-1192. (d) Selected area electron diffraction (SAED) pattern of the NaYF₄:ErYb nanoparticles.

5.7.2.6 Ligand Exchange on NaYF₄:ErYb UCNPs with Phosphonate Azide Ligands

Approximately 150 mg of precipitated nanoparticles were added to a 20 mL scintillation vial along with CHCl₃ (8 mL) and absolute EtOH (2 mL). In a separate vial, the azidopropylphosphonate ligand (600 mg) was dissolved in a mixture of CHCl₃ (2 mL) and absolute EtOH (2 mL). The azidopropylphosphonate ligand solution was then added to the nanoparticle solution via Pasteur pipette with vigorous magnetic stirring. The resultant

mixture was stirred overnight at room temperature, at which point it was transferred to a centrifuge tube and hexanes were added until the mixture became cloudy. The reaction mixture was then centrifuged at 5000 rpm for 10 min and the supernatant was discarded. The precipitated NaYF₄:ErYb nanoparticles were then redispersed in DMSO (3 mL) for further experiments. FTIR (cm⁻¹): 2115 (vs), 1742 (s), 1468 (m), 1252 (s), 1148 (s), 1074 (s), 991 (s).

5.7.2.7 Procedure for copper(I) catalyzed azide-alkyne cycloaddition of **1o onto the UCNPs (**1o**[NaYF₄:ErYb])**

In a 1-dram vial, the azide-coated nanoparticles dispersed in DMSO (0.5 mL of the stock solution) was combined with DTE **1o** (5 mg) and sonicated for 5 min to dissolve the alkyne ligand. This mixture was treated with 10 μL of a 20 mM CuSO₄·5H₂O (3.1 mg, 0.008 mmol) solution, 20 μL of a 100 mM sodium ascorbate solution, 10 μL of triethylamine and 40 μL of distilled water. The reaction mixture stirred in air at 35°C in a temperature controlled oil bath for 24 h. After this time, the reaction solution was cooled to room temperature and added to a 1.5 mL centrifuge tube containing MeOH (~1 mL). The mixture was centrifuged at 13500 rpm for 30 min to isolate the nanoparticles. The supernatant was discarded and the pellet was redispersed in distilled water (1.5 mL) with sonication. The mixture was centrifuged at 13500 rpm for 30 min. The collected **1o**[NaYF₄:ErYb] nanoparticles were dispersed in distilled water (5 mL) for further experiments.

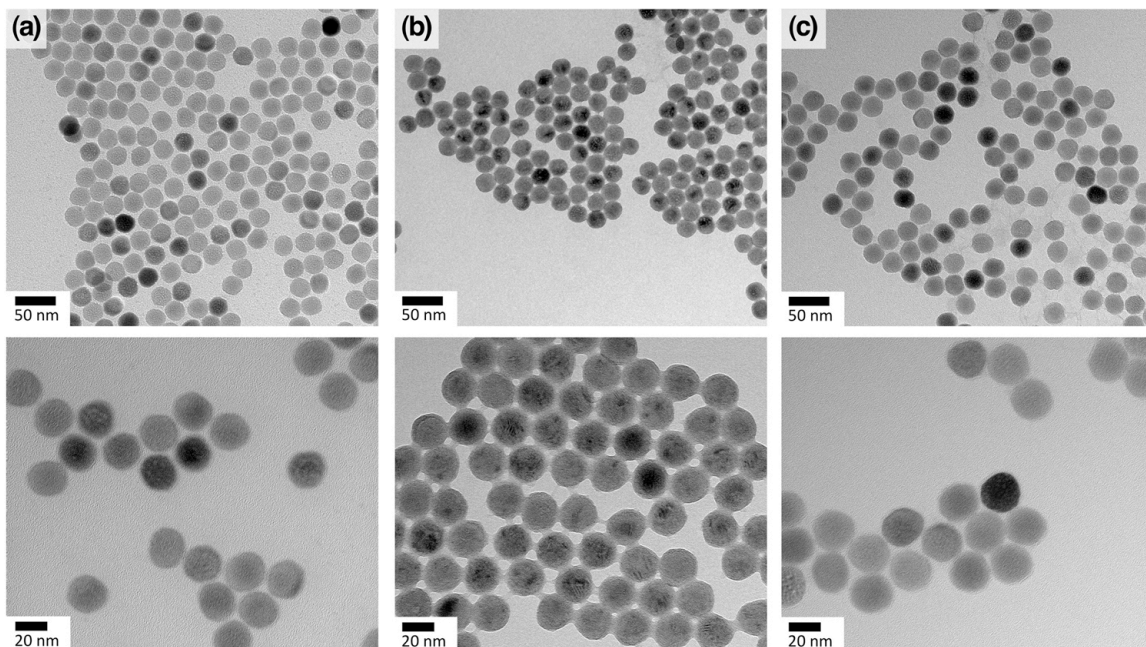


Figure 5.5 Transmission Electron Microscopy (TEM) micrographs of (a) oleate-coated $\text{NaYF}_4:\text{ErYb}$ nanoparticles, (b) azide-coated $\text{NaYF}_4:\text{ErYb}$ nanoparticles and (c) "clicked" $\text{NaYF}_4:\text{ErYb}$ nanoparticles.

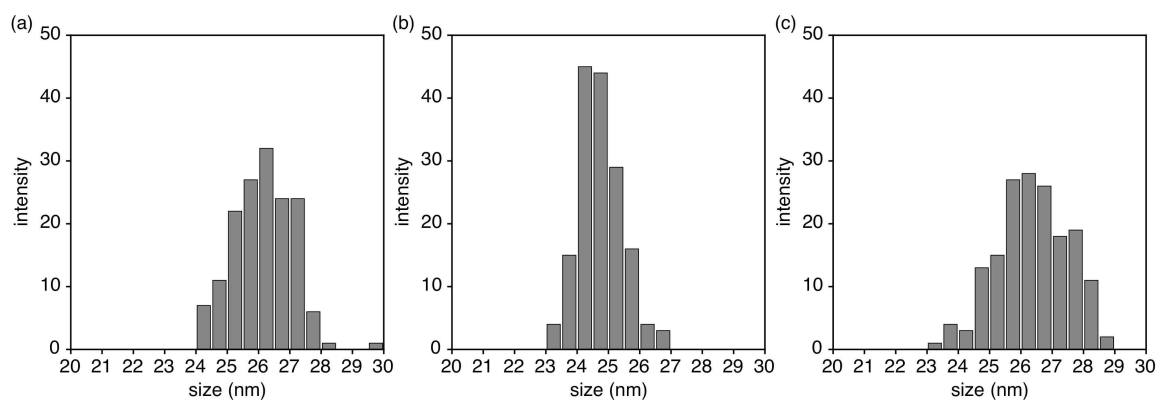


Figure 5.6 Size histograms (diameter) from TEM micrographs for (a) oleate-coated $\text{NaYF}_4:\text{ErYb}$ nanoparticles, (b) azide-coated $\text{NaYF}_4:\text{ErYb}$ nanoparticles and (c) "clicked" $\text{NaYF}_4:\text{ErYb}$ nanoparticles.

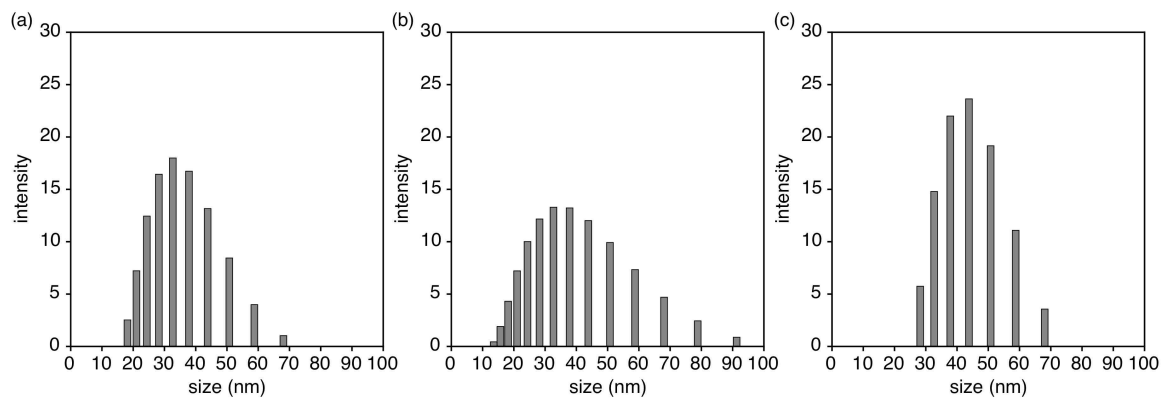


Figure 5.7 Size histograms (diameter) from DLS results for (a) oleate-coated $\text{NaYF}_4:\text{ErYb}$ nanoparticles, (b) azide-coated $\text{NaYF}_4:\text{ErYb}$ nanoparticles and (c) "clicked" $\text{NaYF}_4:\text{ErYb}$ nanoparticles.

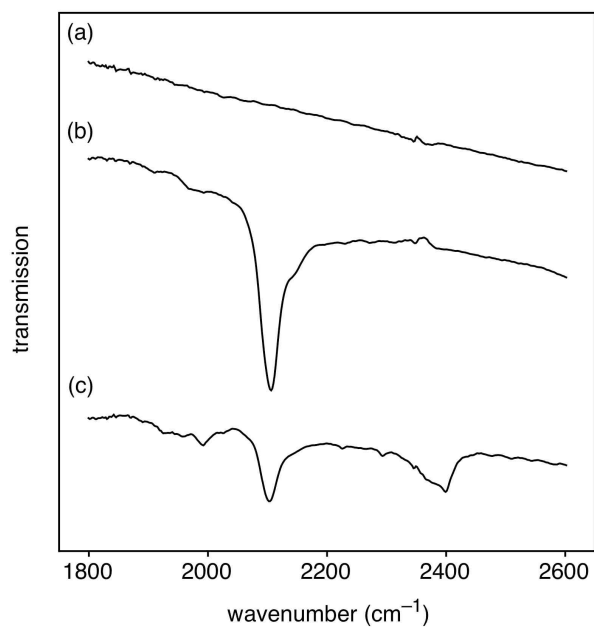


Figure 5.8 Selected region of the FTIR spectra for (a) oleate-coated $\text{NaYF}_4:\text{ErYb}$ nanoparticles, (b) azide-coated $\text{NaYF}_4:\text{ErYb}$ nanoparticles and (c) "clicked" $\text{NaYF}_4:\text{ErYb}$ nanoparticles.

5.7.2.8 Preparation of Photoswitch – Nanoparticle Solutions for Absorption Measurements

A colloidal dispersion of decorated nanoparticles stock solution (0.2 mL, 0.5 wt-% in water) was added to 2 mL of distilled water. The dispersion was stirred for 5 minutes and stored in the dark until needed.

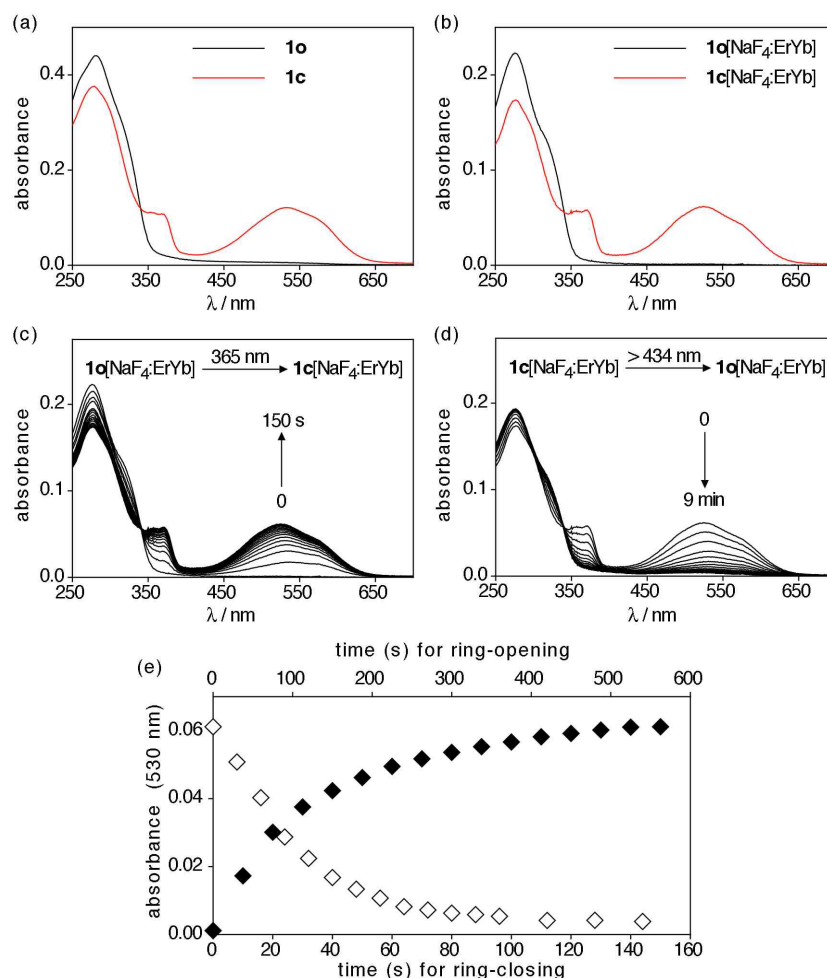


Figure 5.9 UV-vis absorption spectra for aqueous solutions of (a) ligand **1** and (b) the decorated nanoparticles (**1**[NaYF₄:ErYb]) in their original ring-open (black lines) and photostationary (red lines). The photostationary states were generated by irradiating the solutions with 365 nm light until no more changes were observed. The changes in the spectra when the complexes are exposed to (c) UV (365 nm) and (d) visible light. (e) Summary of the changes in absorbance over time.

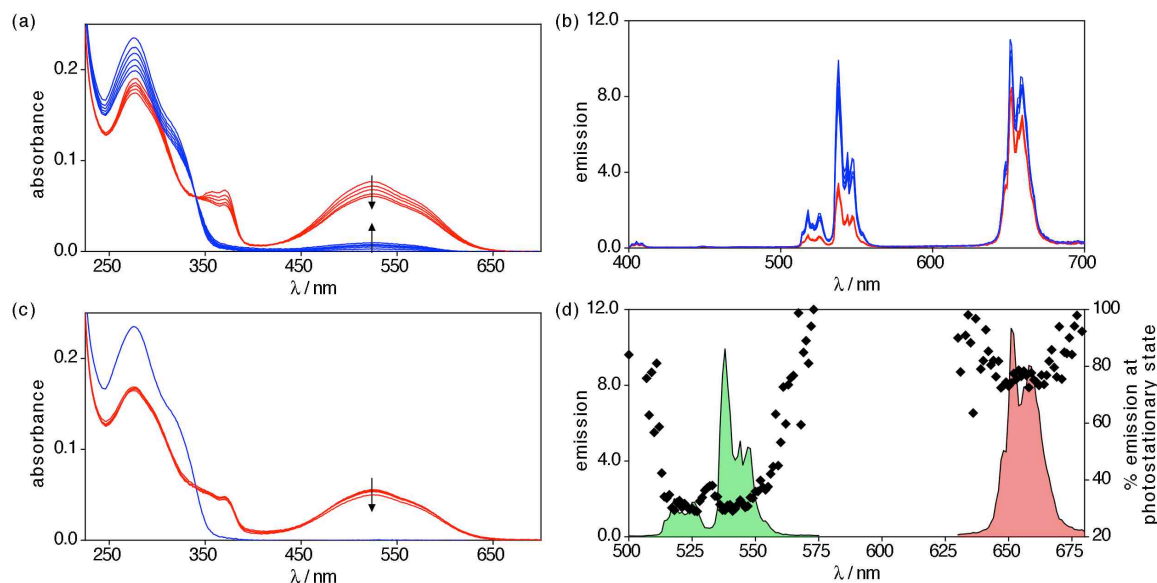


Figure 5.10 (a) UV-vis absorption cycling data for aqueous solutions of the decorated nanoparticles ($1[\text{NaYF}_4:\text{ErYb}]$). (b) Emission spectra ($\lambda_{\text{ex}} = 980 \text{ nm}$, 150 W/cm^2) for cycling experiments of an aqueous solution of $1[\text{NaF}_4:\text{ErYb}]$. (c) UV-vis absorption spectra for an aqueous solution of the decorated nanoparticles ($1[\text{NaYF}_4:\text{ErYb}]$) before and after 90 minutes of continuously irradiated with 980 nm light (150 W/cm^2). (d) Percent quenching versus wavelength for an aqueous solutions of the decorated $1\text{c}[\text{NaYF}_4:\text{ErYb}]$ nanoparticles (black diamonds) superimposed on the green and red emissions.

5.7.3 Biological Experiments

The worm handling methods described by Brenner were used.^[140] *Caenorhabditis elegans* N2 hermaphrodites were incubated on OP50-seeded plates at $20 \text{ }^\circ\text{C}$. After 4 days, the nematodes were lightly washed off the plates with M9 buffer and aliquoted into separate $200 \text{ }\mu\text{L}$ microtubes containing 0.25 mg of hybrid nanoparticles ($1\text{c}[\text{NaYF}_4:\text{ErYb}]$) in $0.5\times\text{M9}$ buffer. After a 3 h incubation period, nematodes were immobilized using 2.5 mM Levamisole, mounted on 2% agarose gel pads and imaged using the two-photon upconversion imaging microscope.

Samples with reduced background fluorescence due to presence of the nanoparticles were prepared by washing the nematodes in 100 μ L of 2.5 mM Levamisole in M9 buffer and then centrifuged at 1200 rpm for 5 min. This wash was repeated twice before the nematodes were immobilized and imaged.

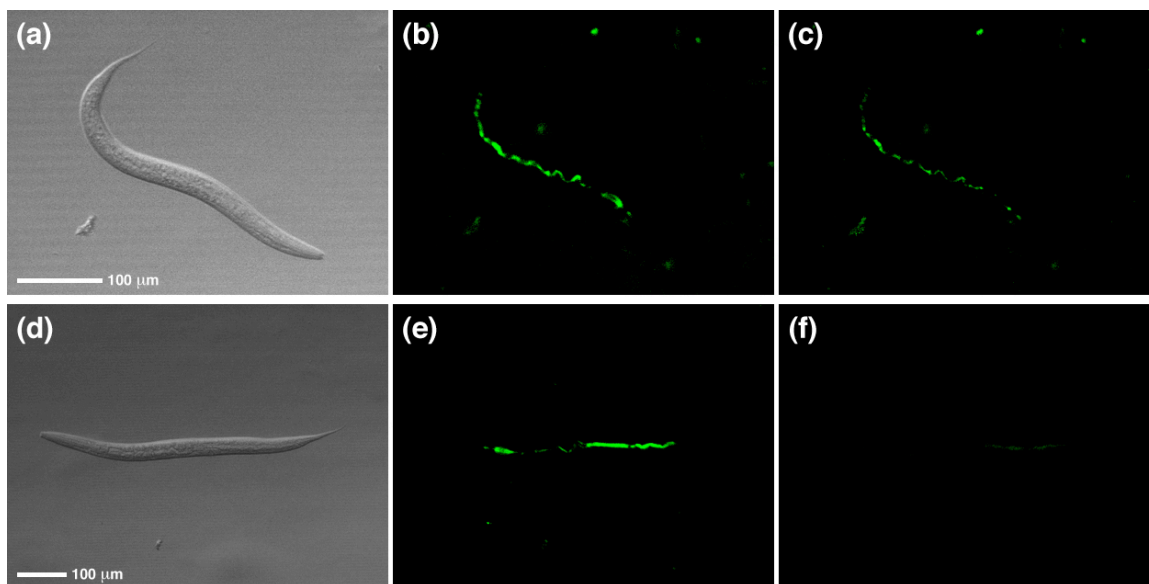


Figure 5.11 Optical (left) and two-photon upconversion fluorescence (middle and right) microscopy images of wild-type N2 *C. elegans* incubated with **1o**[NaYF₄:ErYb] showing the changes in fluorescence due to the photoswitching of the DTE component within the bodies of the worms. The middle panels show the strong initial fluorescence prior to exposure to UV light. The right panels show the reduced emission that is a result of ring-closing the photoswitch with 365 nm light for 2.5 minutes. The difference between the two samples is the omission (top) or inclusion (bottom) of a washing/centrifugation step in the preparation and accounts for the small changes in background fluorescence.

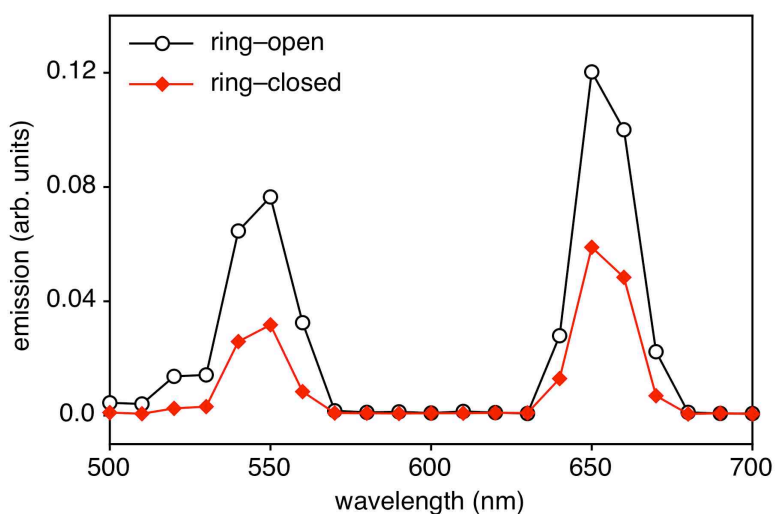


Figure 5.12 The upconverting fluorescence ($\lambda_{\text{ex}} = 980 \text{ nm}$) from the hybrid **1o**[NaYF₄:ErYb] and **1c**[NaYF₄:ErYb] from inside the digestive tract of the nematodes obtained with the 2-photon microscope.

6: MULTIMODAL FLUORESCENCE MODULATION USING MOLECULAR PHOTOSWITCHES AND UPCONVERTING NANOPARTICLES

6.1 Contributions

The text in this chapter have previously been published in Organic and Biomolecular Chemistry as a full paper and is reproduced herein in its entirety with permission from the journal (C.-J. Carling, J.-C. Boyer, N. R. Branda, *Org. Biomolec. Chem*, **2012**, DOI: 10.1039/C2OB25368B, <http://pubs.rsc.org/en/content/articlelanding/2012/OB/C2OB25368B>). The project was designed by C-J Carling. All organic synthesis and characterizations of organic molecules were conducted by C-J Carling. Dr. J-C Boyer synthesized Nanoparticle **o-NP** and hybrid nanoparticle **a-NP**. Hybrid nanoparticles **1a-NP**, **1b-NP** and **1ab-NP** were synthesized by C-J Carling. IR, UV-vis and emission spectroscopy data was acquired by C-J Carling. Dr. J-C Boyer acquired TEM images of all nanoparticles. Photographs were taken by C-J Carling. Prof. Dr. N. R. Branda conducted peak-fitting calculations. The manuscript was co-written by C-J Carling and Prof. Dr. N. R. Branda. Experimental section was co-written by C-J Carling, Dr. J-C Boyer and Prof. Dr. N. R. Branda.

6.2 Abstract

The intensity and colour of the light emitted from upconverting nanoparticles is controlled by the state of photoresponsive dithienylethene

ligands decorated onto the surface of the nanoparticles. By selectively activating one or both ligands in a mixed, 3-component system, a multimodal read-out of the emitted light is achieved.

6.3 Introduction

Nanoscale fluorescent probes decorated with photoresponsive organic ligands offer heightened control in optical materials applications by reversibly turning the emission signal 'on' or 'off', or by modulating the visual output from one colour to another.^[28,130,141,142,143,144,145,146,147,148,149,150,151,152] Both optical properties are based on the photoresponsive ligands undergoing controlled and predictable reactions between two isomers having different optoelectronic characteristics.^[153] Hybrid systems that have these properties have the potential to advance technologies such as non-destructive ultra-dense optical memory^[148,149] and bio-imaging.^[28,143,144,151,152] The latter application is a particularly appealing use for these optical probes as it offers advantages over conventional systems when false-positive signals need to be better identified. Temporal tracking of the nanoparticles is also possible when the end-user can control the optical signal 'on command'.^[154]

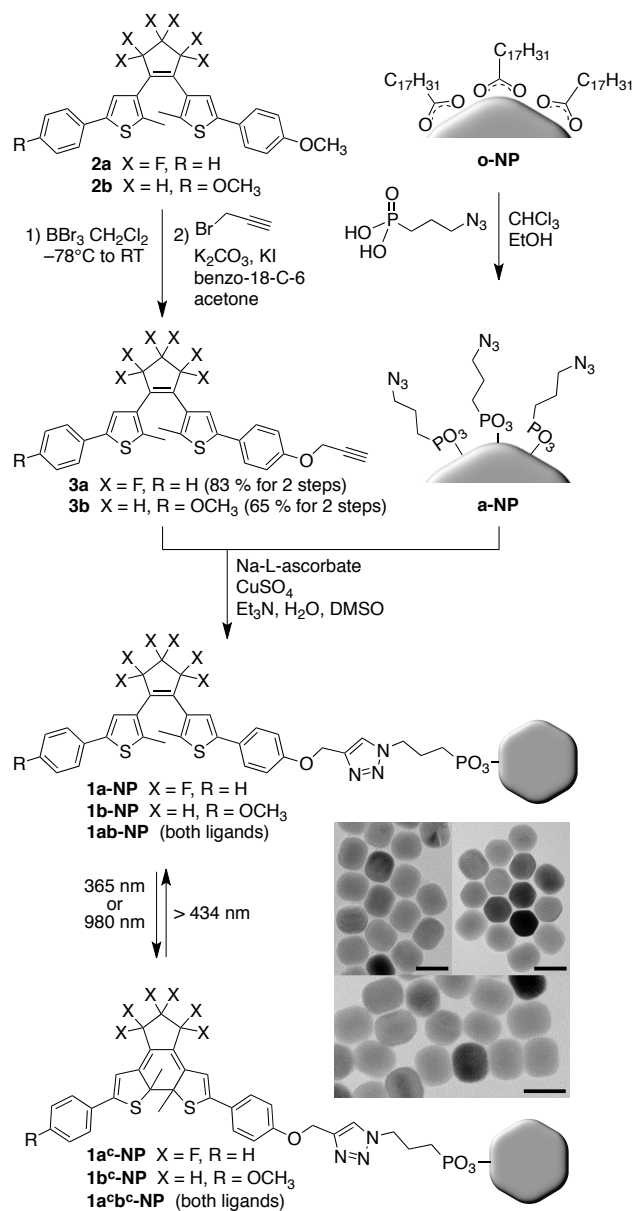
Both organic and organic-inorganic hybrid nanoparticles have been developed for modulating fluorescence but limitations in the current technology still exist. One of the major limitations is the need for high-energy light as the fluorescence excitation source, which causes auto-fluorescence of bio-molecules and non-selective photoswitching of the organic ligands since the ligands absorb

in the same spectral regions as the source. Non-selective photoswitching could potentially lead to distortions of the fluorescent signal during prolonged excitation due to unwanted organic photoreactions and subsequent degradation of the signal quality. Because many photoresponsive systems such as spiropyrans and spirooxazines were designed to undergo spontaneous reactions (T-type photochromic compounds), their use in temporal imaging studies is less appealing than compounds that exhibit bistability over a wide range of temperatures. The last limitation relevant to discuss in the context of this manuscript is the fact that fluorescent probes based on organic compounds are prone to photo-degradation, which limits the time they can be used in imaging applications. Although quantum dots have been demonstrated as a viable solution to this problem, their blinking behaviour and toxicity (unless specially coated) limits their use as well.^[126]

These limitations can be avoided by developing hybrid systems based on lanthanide-doped upconverting nanoparticles (UCNP) decorated with 'thermally stable' P-type dithienylethene photochromic ligands, which can modulate the multi-photon NIR-to-visible emission. The nanoparticles can convert 980 nm light into several other types of light that are emitted in the UV, visible and NIR regions of the spectrum.^[155] They are also non-toxic and do not exhibit blinking.^[156,157,158] Photoresponsive dithienylethene derivatives are one of the most versatile class of photochromic compounds.^[40] They undergo predictable ring-closing and ring-opening reactions when stimulated with UV and visible light, respectively, often with a high degree of fatigue resistance (see the bottom

of Scheme 6.1 for an example of this reaction). The combination of these inorganic and organic systems is well suited to address the limitations described above.

We recently reported an example of ‘on command’ fluorescence modulation *in vivo* using a dithienylethene-UCNP hybrid system.^[28] In this manuscript, we describe our more advanced systems where a heightened level of control over the emission intensity and wavelength, and colour output is achieved by decorating the nanoparticles with pure or mixed dithienylethene ligands. We chose to use one of our recently developed *core-shell-shell* upconverting, multi-colour nanoparticles^[11] in combination with two different dithienylethene chromophores to photo-modulate the NIR-to-visible fluorescence of the UCNP (**1a-NP**, **1b-NP** and **1ab-NP**, Scheme 6.1). By taking advantage of the multi-colour nature of the upconverted fluorescence and the fact that the two dithienylethenes can be selectively activated using specific wavelengths of light, we demonstrate selective quenching of the emission and multimodal modulation. We also show that we can trigger the ring-closing of the photoswitches in a ‘remote-control’ manner by increasing the power density of the NIR excitation source and using the multi-photon NIR-to-UV emission from the nanoparticles.



Scheme 6.1 Synthesis of photoresponsive ligands **3a** and **3b**, the azide-functionalized *core-shell-shell* UCNP **a-NP**, and the hybrid one- and two-component systems using UV, visible and NIR light are also shown. The insets show the TEM images of the nanoparticles in their different decorated forms (**1a-NP**, top left; **1b-NP**, top right; **1ab-NP**, bottom). The scale bars in all 3 images represent 40 nm.

6.4 Results and discussion

6.4.1 Synthesis of dithienylethene ligands and decorated nanoparticles

The hybrid 2- and 3-component chromophore-UCNP systems were prepared as shown in Scheme 6.1. The photoresponsive ligands, **3a**^[159] and **3b**, bearing the alkyne group necessary for the copper(I)-catalyzed azide-alkyne cycloaddition (CuAAC) 'click' reaction were synthesized in two steps from the known dithienylethenes **2a**^[160] and **2b**^[161] and characterized by ¹H and ¹³C NMR spectroscopy, mass spectrometry and UV-vis absorption spectroscopy. The azide coated *core-shell-shell* upconverting nanoparticles, **a-NP** were prepared through a ligand-exchange reaction^[28] by stirring the previously reported oleate coated **o-NP**^[11] with azidopropylphosphonate^[132] in CHCl₃ and ethanol. The composition of these UCNPs is β -NaYF₄:0.5 % Tm³⁺:30 % Yb³⁺ in the *core*, β -NaYF₄:2.0 % Er³⁺:20 % Yb³⁺ in the inner *shell* and β -NaYF₄ in the outer *shell*. These azide-decorated nanoparticles were characterized by IR spectroscopy, which showed a band in the spectrum at 2110 cm⁻¹ corresponding to the azide N=N=N stretch (Figure 6.6).^[162] The photoresponsive organic chromophores were attached to the surface of the nanoparticles using CuAAC 'click' chemistry.^[133] Treating **a-NP** with pure **3a**, pure **3b** or a mixture of both acetylenes with a copper catalyst and an ascorbate reductant afforded the two 2-component systems **1a-NP** and **1b-NP**, and the 3-component system **1ab-NP**, respectively. All three hybrid systems were characterized by IR spectroscopy, transmission electron microscopy (TEM) (inset to Scheme 6.1), and UV-vis absorption and fluorescence spectroscopy. The success of the 'click' reaction

was verified by the almost complete disappearance of the azide N=N=N stretch at 2110 cm^{-1} in the IR spectrum (Figure 6.6).

6.4.2 Absorption spectroscopy and selective quenching of emission

Inconveniently, the two 2-component hybrid systems, **1a-NP** and **1b-NP**, could not be dispersed in the same solvent for characterization. Although the ligands (**3a** and **3b**) were freely soluble in CH_3CN , the solvent in which most of the photochromic studies were carried out (Figure 6.7),^[162] neither **1a-NP** nor **1b-NP** could be dispersed in CH_3CN . Other organic solvents worked well, and **1a-NP** and **1b-NP** formed clear colloidal suspensions in THF and in CH_2Cl_2 , respectively. The mixed 3-component system (**1ab-NP**) formed a faintly hazy colloidal dispersion in THF. These solvents were used for all studies described in this paper.^[163]

The UV-vis absorption spectra of the 2-component systems (**1a-NP** and **1b-NP**) are shown in Figure 6.1 along with the emission spectra of the UCNPs in the various states based on the photoresponsive ligands and the power of the 980 nm excitation light. These spectra illustrate our design principle and our rationale for choosing the specific nanoparticles and photoresponsive ligands. When the dithienylethenes are in their ring-open forms (**1a-NP** and **1b-NP**), they absorb only in the UV region of the spectrum ($< 400\text{ nm}$). These absorption bands decrease when the solutions are irradiated with UV light (365 nm) as is typical for dithienylethene derivatives (Figure 6.1a–b, and 6.9).^[162] This decrease is accompanied by the appearance of broad bands in the visible region of the

spectrum as the ring-open isomers are converted into their ring-closed counterparts (**1a-NP** → **1a^c-NP** and **1b-NP** → **1b^c-NP**). These changes account for the change in colour of the solutions from colourless to blue in the case of **1a-NP** and red in the case of **1b-NP**. Although the amount of ring-closed isomers in the photostationary states cannot be conveniently measured on the decorated nanoparticles, we can only make the assumption that they are similar to those for similar solutions of the ligands, which were measured by ¹H NMR spectroscopy to be 72 % and 56 % for **3a^c** and **3b^c**, respectively. When the coloured solutions of **3a^c** and **3b^c** are irradiated with visible light at wavelengths greater than 434 nm, the colours of the solutions return to their original states and the ring-open isomers are regenerated.^[164]

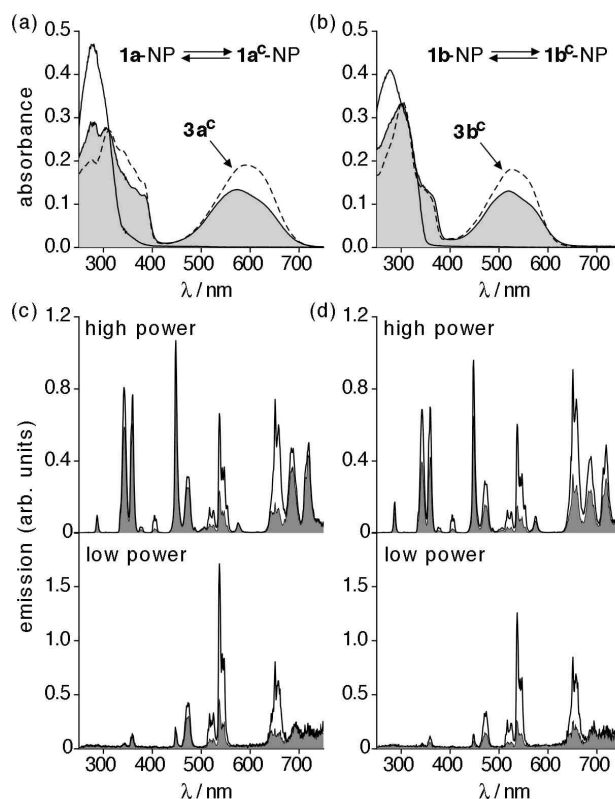


Figure 6.1 UV-vis absorption spectra of solutions (10^{-5} M) of two-component systems (a) **1a-NP** (THF) and (b) **1b-NP** (CH_2Cl_2) before (solid lines) and after irradiation with 365 nm (16 mW/cm^2) light (shaded areas) for 120 s. The spectra for the ligands (**3a** and **3b**) are shown for comparison (dashed lines). The molar concentration refers to the estimated amount of photoswitch in each sample,^[165] while the amount of decorated nanoparticle in each solution is 0.05 wt-% for **1a-NP** and 0.03 wt-% for **1b-NP**. Emission spectra of the same solutions ($\lambda_{\text{ex}} = 980 \text{ nm}$) of (c) **1a-NP** and (d) **1b-NP** at high 980 nm excitation power (38 W/cm^2 , top graphs) and low 980 nm excitation power (2 W/cm^2 , bottom graphs) showing how the intensity of specific bands in the original emission spectrum (white areas) are reduced when the photoswitches are converted into their ring-closed forms (shaded areas) based on the overlap with the absorption bands of **1a^c-NP** and **1b^c-NP**.

A closer inspection reveals that the absorption spectra for the ring-closed isomers decorated on the nanoparticles are not identical to those for the free ligands (Figure 6.1a–b, 6.7 and 6.9). In both cases, the absorption bands appear to have more pronounced features. Peak fitting the bands (Figure 6.10) shows

that none of them are Gaussian in shape. Instead, they are comprised of at least 3 overlapping bands corresponding to an equivalent number of electronic transitions. The difference between the electronic properties of the ring-closed isomers when free or anchored to the nanoparticles must be due to the non-equivalent shifting of each of these overlapping bands a phenomenon we also noticed was present in our previously reported system.^[28] The exact reason for these spectral changes is not clear at this stage, although it likely results from the electronic coupling between the nanoparticle and the ring-closed chromophores in their ground states.

The number of molecules of each photoresponsive ligand was calculated by estimating the concentration of organic ligands based on their UV-vis spectra and measuring the dimensions of the nanoparticles using their TEM images. This calculation resulted in an estimated loading of approximately 5000–7000 molecules per nanoparticle for both **1a-NP** and **1b-NP**.^[162] In the case of the mixed, 3-component system (**1ab-NP**), which will be discussed later in this paper, the ratio of the chromophores **1a** and **1b** was calculated to be approximately 5:4 (Figure 6.11),^[162] which corresponds to an approximate loading of approximately 10000 molecules of **1a** and **1b** per nanoparticle.

We chose these two photoresponsive compounds because they have similar absorption spectra in their ring-open forms but differ significantly in their ring-closed counterparts. These features make them ideal for decorating them onto multi-wavelength emitting UCNPs to offer a heightened level of control over

the emissive properties of the nanoparticles compared to our previous version.¹⁴ Our *core-shell-shell* UCNPs^[11] have six major emissions in the UV-vis regions of the spectrum when excited at high 980 nm power density as shown in Figure 6.1c–d. These emissions are due the different states of the lanthanide dopants: Tm³⁺ (UV, blue, red and NIR) and Er³⁺ (green and red) as previously reported.^[11] The longer wavelength emission bands (670–750 nm) visible in the wavelength-sensitivity corrected spectra upon high power density 980 nm excitation are not true emissions but are the second order diffraction of the UV Tm³⁺ emissions off the grating of the emission monochromator and should be ignored.^[166] We^[11] and others^[167,168] have mistakenly acknowledged these red emissions as real.

Figure 6.1c–d illustrate our ability to modulate the emissions from the UCNPs depending on the state of the photoresponsive ligands and the power density of the excitation light. When the ligands are in their colourless, ring-open states in **1a-NP** and **1b-NP**, the multi-photon emission from the nanoparticles is ‘bright’ when excited with high power 980 nm light (38 W/cm²) and slightly less bright when the power is lowered (2 W/cm²). Because there are three major visible emissions present (blue, green and red) under high excitation power, the fluorescence is perceived as white light. When the power is lowered, the colour appears green. When the photostationary states are produced by exposing the systems to 365 nm light, the emissions from **1a^c-NP** and **1b^c-NP** are quenched under both high and low 980 nm excitation power (Figure 6.1c–d). We ascribe this fluorescence quenching effect to a combination of resonance energy transfer and an inner filter effect from nearby nanoparticles.

Although both ligands quench the nanoparticle's emission in their ring-closed forms, they do so to different degrees and are wavelength dependent (Figure 6.1 and Table 6.1). Both **3a^c** and **3b^c** have absorbance bands in the 350–400 nm region of the spectrum, which overlap with the UV emissions from the nanoparticles. Therefore, they both reduce the intensity of these emissions. In the case of compound **3a^c**, which is blue in colour due to its absorbing between 430–720 nm with absorption maxima centered at 592 nm, the green and red emissions are also reduced. When this occurs, the colour of the emitted light from **1a^c-NP** appears blue as shown in Figure 6.12 and 6.13.^[162] The ring-closed chromophore in **1b^c-NP** also quenches the green emission. However, because absorption bands of **1b^c-NP** are blue shifted (420–640 nm with absorption maxima centered at 521 nm) with respect to those of **1a^c-NP**, the extent of quenching is not the same. In this case, there is less quenching of the longer wavelength emissions and more of the shorter wavelength ones. Although the absorption bands of **1b^c-NP** do not overlap with the red emission, it is still quenched in **1b^c-NP** due to the fact that the excited state responsible for the green emission ($^2H_{11/2}$, $^4S_{3/2}$) in Er^{3+} is partially populating the lower energy state ($^4F_{9/2}$) from which the red light is emitted through a nonradiative decay process. Due to the low absorption for both chromophores in the 400–450 nm region of the spectrum, neither effectively quenches the blue emissions to a large extent.

An interesting observation is the quenching of the highest energy UV emission bands, which is less in **1a^c-NP** than in **1b^c-NP** even though the relative

overlap of the two systems are similar. We suspect that the quenching of the blue emissive states also quenches the UV states by preventing excited Tm^{3+} ions from reaching higher excited states.

When the power density of the 980 nm excitation source is reduced from 38 W/cm^2 to 2 W/cm^2 , the UV and visible emissions from the *core-shell-shell* UCNP change as we have previously demonstrated.^[11] The underlying reason for this behaviour is the fact that the very strong two-photon upconverted 800 nm emission from Tm^{3+} dominates at lower power densities and the UV and visible emissions from Tm^{3+} almost cease. As a result, at low 980 nm power density, the primary visible light emitter is Er^{3+} . Figure 6.1c–d show how these emissions are similarly modulated by the state of the photoswitches decorated on to their surfaces. The quenching behaviour of the ring-closed forms **1a^c-NP** and **1b^c-NP** at low power density excitation is similar to those observed at high power density. It is primarily the emission from Er^{3+} that is quenched by the photoswitches (Figure 6.1 and Table 6.1).

Table 6.1 The differences in the intensities for the specific bands for each lanthanide ion transition in the emission spectra of the solutions of **1a-NP** and **1b-NP** used in Figure 6.1 and 6.2 when the chromophores are converted into their ring-closed forms using 365 nm light.

emitting ion	transition	number of photons	λ_{em} (nm) ($\lambda_{ex} = 980$ nm)	% of original emission ^a			
				high-intensity NIR light ^b		low-intensity NIR light ^b	
				1a^c-NP	1b^c-NP	1a^c-NP	1b^c-NP
Tm ³⁺	³ P ₀ → ³ H ₆	5	276–292	0	69	–	–
Tm ³⁺	³ P ₀ → ³ F ₄	5	323–351	73	57	96	82
Tm ³⁺	¹ D ₂ → ³ H ₆	4	352–368	80	60	80	59
Er ³⁺	² H _{9/2} → ⁴ I _{15/2}	4	392–411	26	26	–	–
Tm ³⁺	¹ D ₂ → ³ F ₄	4	430–457	93	66	85	67
Tm ³⁺	¹ G ₄ → ³ H ₆	3	458–486	82	54	71	47
Er ³⁺	² H _{11/2} , ⁴ S _{3/2} → ⁴ I _{15/2}	2	501–562	37	27	29	26
Er ³⁺ Tm ³⁺	⁴ F _{9/2} → ⁴ I _{15/2} ¹ G ₄ → ³ I ₄	2 3	626–670	30	39	35	39
total			276–670	53	50	66	53

^a Values are based on the areas under the curves for each spectral region. The bands from 671–750 nm were not included in the analysis because these emissions are due to the second order diffraction of the upconverted UV light off the grating of the emission monochromator. ^b High-intensity light = 38 W/cm². Low-intensity light = 2 W/cm². The nomenclature, **1a^c-NP** and **1b^c-NP** refer to the photostationary states containing an estimated 72% and 56% of the ring-closed isomers, respectively.

As is the case for the ring-closed forms of the ligands (**3a^c** and **3b^c**), irradiating solutions of the equivalent ring-closed systems **1a^c-NP** and **1b^c-NP** with visible light of wavelengths greater than 434 nm triggers the reverse photoreaction and quantitatively regenerates the ring-open isomers. It also restores the original bright emissive states of the nanoparticles. Both systems

could be cycled between a bright and quenched emissive states several times by alternating the type of light (Figure 6.2c–f), although significant degradation of the signal was observed in the case of **1b-NP**. The absorption corresponding to this less robust photoswitch is also reduced upon cycling (Figure 6.2a–b) showing that the reduced performance is due to degradation of the ligand.

6.4.3 Selective photochromism and quenching in the mixed system

The fact that the two ring-closed isomers absorb in different regions of the visible spectrum implies that they can be selectively activated. This concept is demonstrated using the mixed, 3-component system **1ab-NP**. Figure 6.3 shows how the photoresponsive chromophores can be independently addressed.^[169] As expected, the absorption spectra of both the ring-open and ring-closed states of the mixed system are equivalent to the sum of the two systems. When both ring-open isomers are present (**1ab-NP**), there are no bands in the visible region of the spectrum. Exposure to UV light (365 nm) activates both chromophores, generates the mixed photostationary state and produces broad absorbances in the visible region (Figure 6.3a). Although there appears to be a slight difference in the growth of the absorbances corresponding to each isomer (570 nm for the equivalent of **1a-NP** and 520 nm for the equivalent of **1b-NP**) as shown in the inset to Figure 6.3a, this may be due to slight differences in the amount of light absorbed by each chromophore.

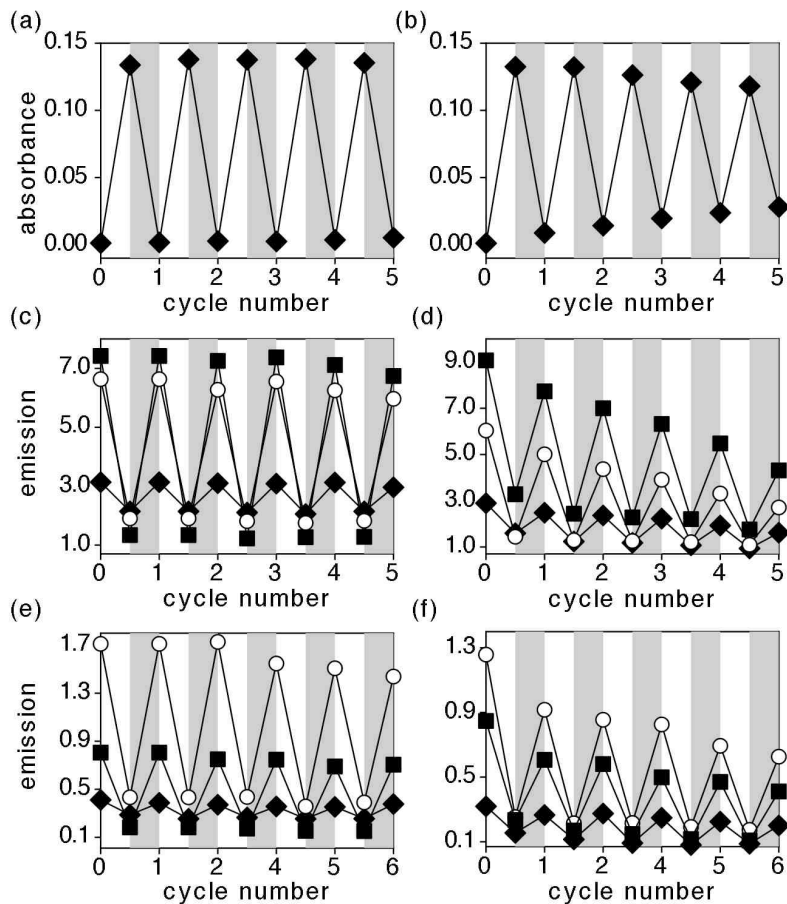


Figure 6.2 Changes in the absorbances at (a) 570 nm when the same solution of **1a-NP** used in Figure 6.1(a,c) and (b) 520 nm when the same solution of **1b-NP** used in Figure 6.1(b,d) are irradiated alternately with 365 nm light (16 mW/cm^2) for 120 s for **1a-NP** and 130 s for **1b-NP** (white areas), and $> 434 \text{ nm}$ (377 mW/cm^2) light for 60 s for **1a-NP** and 120 s for **1b-NP** (shaded areas). (c–f) Changes in the emission intensities at 471 nm (\blacklozenge), 537 nm (\blacksquare) and 651 nm (\circ) when the same solutions are irradiated under identical conditions at (c,d) high 980 nm excitation power and (e,f) low 980 nm excitation power.^[170]

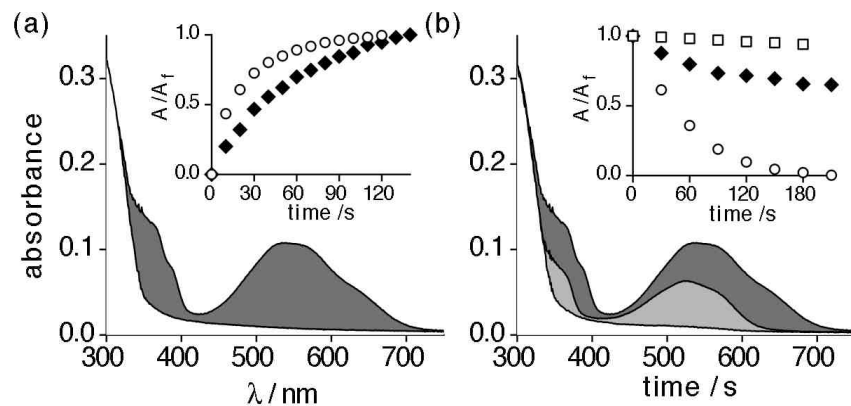
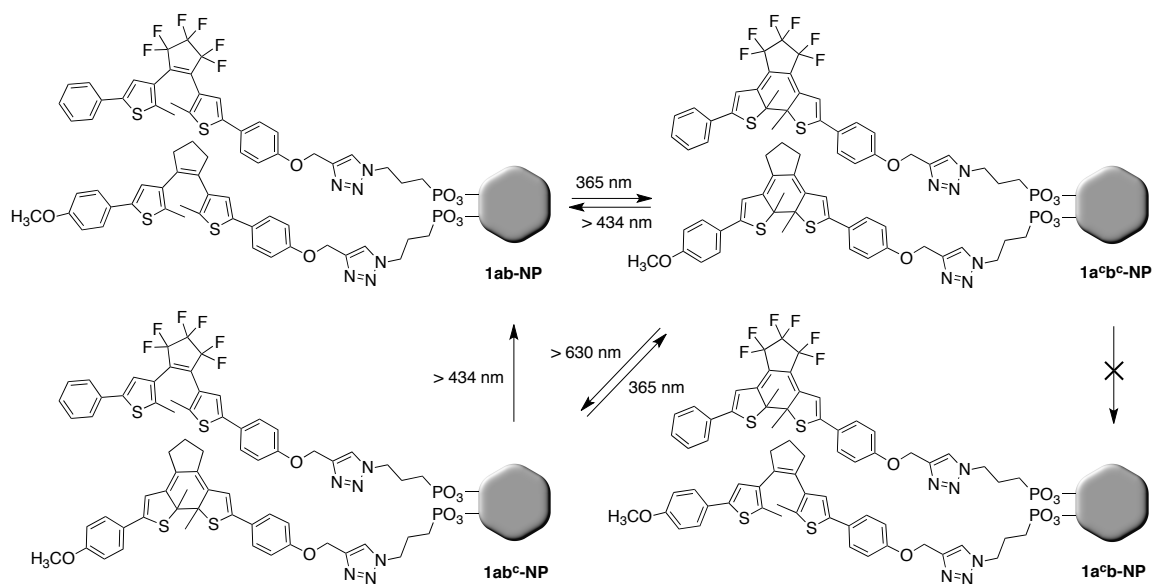


Figure 6.3 (a) The UV-vis absorption spectrum of a THF solution of the two-component hybrid system **1ab-NP** before (white) and after (dark shaded) irradiation with 365 nm light (16 mW/cm^2). The total concentration of chromophore is 10^{-5} M (in a 5:4 **1a**:**1b** ratio), while the amount of decorated nanoparticle is 0.03 wt-%. The inset shows the time-dependent growth of the absorptions at 570 nm (○) and 520 nm (◆) corresponding to the two ring-closed isomers in **1a^cb^c-NP**. (b) The UV-vis absorption spectrum of the same photostationary state before (dark shaded), after irradiation with $> 630 \text{ nm}$ light (120 mW/cm^2) (light shaded) and after irradiation with $> 434 \text{ nm}$ light (377 mW/cm^2) (white). The inset shows the time-dependent changes of the absorptions at 570 nm (○) and 520 nm (◆) during the $> 630 \text{ nm}$ irradiation, and at 520 nm (□) for a CH_3CN solution of ligand **3b** ($1.0 \times 10^{-5} \text{ M}$) when it is irradiated with $> 630 \text{ nm}$ light.

Because the ring-closed form of the chromophore in **1a^c-NP** absorbs longer wavelength of light to trigger the ring-opening reaction than the chromophore in **1b^c-NP**, it can be selectively activated using light at wavelengths greater than 630 nm as shown in Figure 6.3b. Irradiation at these wavelengths results in the decrease in the longer wavelength absorptions while retaining the shorter wavelength ones. This state corresponds to one where only the blue-shifted chromophore is in its ring-closed state (**1ab^c-NP**). The inset to Figure 6.3b shows that the wavelengths corresponding to each isomer are reduced in intensity to a different extent during the $> 630 \text{ nm}$ exposure. While the absorption

band corresponding to the red-shifted chromophore (570 nm) is completely reduced, those corresponding to the blue-shifted isomer and the corresponding ligand (**3b^c**) are not. Irradiation of this state with light at wavelengths longer than 434 nm activates the blue-shifted chromophore and regenerates the original system.

The four different states of the mixed, 3-component system are illustrated in Scheme 6.2. While the all ring-closed state (**1a^ob^c-NP**) and the state where the red-shifted chromophore is ring-opened (**1ab^c-NP**) can be accessed, the latter can only be formed through the former owing to the fact that both dithienylethenes absorb in the same region of the UV spectrum in their ring-open forms, and therefore, cannot be independently activated. The state where the blue-shifted chromophore is ring-open and the red-shifted is ring-closed (**1a^ob-NP**) is not accessible because the ring-closed isomer of the red-shifted form also absorbs in the region between 450 and 500 nm.



Scheme 6.2 Using 365 nm light, the three-component hybrid system (**1ab-NP**) can be converted into its coloured (violet) state where both photoswitches are in their ring-closed forms (**1a^cb^c-NP**). Long-wavelength visible light (> 630 nm) selectively ring-opens the blue chromophore and generates the mixed system **1a^cb^c-NP**. Both photoswitches in **1a^cb^c-NP** or **1ab^c-NP** can be ring-opened back to **1ab-NP** using shorter-wavelength visible light (> 434 nm). The **1a^cb^c-NP** cannot be accessed.

By selectively activating the photoresponsive ligands in the mixed, 3-component system, their emission can also be regulated in a multi-modal fashion (Figure 6.4, 6.18 and 6.19, and Table 6.2). When both of the photoswitches are in their ring-open forms (**1ab-NP**), the observed multi-photon fluorescence is bright as is expected given the sum of the UV-Vis absorption spectra does not have bands in the visible region of the spectrum. When the photostationary state containing the ring-closed forms of both ligands (**1a^cb^c-NP**) is generated using 365 nm light, the broad absorption bands in the visible region of the spectrum result in the quenching of the emission from the UCNPs. The effect is synergistic

since the sum of the absorption spectra of the two ligands absorbs across a wider region of the spectrum. There are two fates for this doubly ring-closed isomer depending on the light used to activate ring-opening as discussed above. Each has a different effect on the emission from the nanoparticles. As can be seen from Figure 6.4c, 6.18 and 6.19, and Table 6.2, not all emissions are equally sensitive to selective modulation and those arising from Er^{3+} appear to be the most effected.

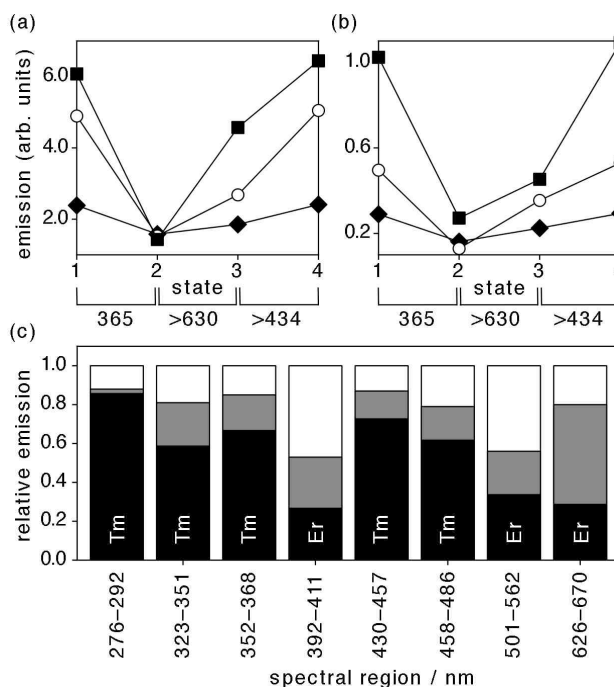


Figure 6.4 Changes in the emission intensities at 471 nm (◆), 537 nm (■) and 651 nm (○) when the same solution of **1ab-NP** used in Figure 6.3 is exposed to 365 nm, > 630 nm and > 434 nm light at (a) high 980 nm excitation power and (b) low 980 nm excitation power. (c) Relative areas under the peaks in the emission spectra of the same solution before, (white) and after irradiation with 365 nm light (black) and > 630 nm light (grey). High 980 nm excitation power was used in (c). In each case, the emitting ion is labelled.

Table 6.2 The differences in the intensities for the bands for each region in the emission spectra of the solution of **1ab-NP** used in Figure 6.3 and 6.4 when the chromophores are converted into their specific ring-closed forms using 365 nm and > 630 nm light.

λ_{em} (nm) ($\lambda_{ex} = 980$ nm)	relative emission ^a		
	1ab-NP	1a^cb^c-NP^b	1ab^c-NP^b
276–292	1	0.86	0.88
323–351	1	0.59	0.81
352–368	1	0.67	0.85
392–411	1	0.27	0.53
430–457	1	0.73	0.87
458–486	1	0.62	0.79
501–562	1	0.34	0.56
626–670	1	0.29	0.80

^a Values are based on the areas under the curves for each spectral region. High-intensity light (38 W/cm²) excitation light was used. ^b These states refer to the photostationary states when the systems are irradiated with UV and visible light. They do not imply pure ring-closed isomers. The nomenclature, **1a^c-NP** and **1b^c-NP** refer to the photostationary states containing an estimated 72% and 56% of the ring-closed isomers, respectively.

6.4.4 ‘Remote-control’ ring-closing

We have previously demonstrated that the light emitted from the UCNPs when excited with 980 nm light can be used to trigger the photochemical reactions of dithienylethenes^[9,11] and ‘caged’ compounds.^[10,171] They have subsequently been used by others for photoswitching^[167] and photorelease.^[168] This ‘remote-control’ NIR-to-UV ring-closing is possible for the cases reported here although the power density of the 980 nm excitation source must be significantly increased in dilute conditions (Figure 6.5 and 6.20). When solutions of either nanoparticle (**1a-NP** or **1b-NP**) is exposed to 980 nm light for prolonged periods of time, the solutions gradually changed to the coloured forms corresponding to the ring-closed states (blue for **1a^c-NP** and red for **1b^c-NP**). Due to presence of both UV and visible light in the multiphoton emissions, the

photostationary states generated using 980 nm light will contain a lower amount of ring-closed isomers than the photostationary states generated using 365 nm light where no interfering visible emission is present.

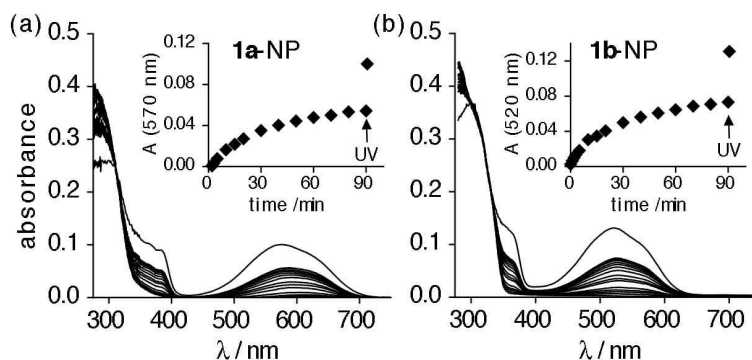


Figure 6.5 Changes in the UV-vis absorption spectra when (a) a THF solution of **1a-NP** (10^{-5} M, 0.05 wt-%) and (b) a CH_2Cl_2 solution of **1b-NP** (10^{-5} M, 0.03 wt-%) are irradiated with 980 nm light (143 W/cm^2). The insets show the growth of the absorbances at 570 nm for **1a-NP** \rightarrow **1a^c-NP** and 520 nm for **1b-NP** \rightarrow **1b^c-NP** corresponding to the ring-closed isomers. The arrows in each inset plot indicate when the excitation light was changed from 980 nm to 365 nm.

6.5 Conclusions

We have shown here that depending on the choice of photoresponsive ligand anchored onto the surface of upconverting nanoparticles, multimodal regulation of the emission signal can be achieved. The 2-component systems (**1a-NP** and **1b-NP**) can be selectively toggled between a colourless, bright NIR-to-visible fluorescent state and a coloured, quenched state using light of different wavelengths than the fluorescence excitation light source. The modulated quenching of the two 2-component hybrid systems **1a^c-NP** and **1b^c-NP** was similar as they both primarily quench the green and red emissions of Er^{3+} over the blue emission of Tm^{3+} . Multimodal regulation of the 3-component hybrid

system (**1ab-NP**) offers the ability to selectively alternate between three different fluorescent states due to the selective control over the $1a^c \rightarrow 1a$ ring-opening reaction of **1a^cb^c-NP** using visible light of wavelengths greater than 630 nm. Although multiple fluorescent states were achievable using our photoswitches, they both primarily quench the emission from Er^{3+} . More distinct blue/white to green/white fluorescence modulation is achievable by selectively quenching the blue emissions of Tm^{3+} instead of the green and red emissions of Er^{3+} with a yellow-coloured ring-closed photoswitch.^[172] These fluorescent hybrid systems have the capacity to be useful in various applications such as bio-imaging, non-destructive data storage and security.

6.6 Acknowledgements

This research was supported by the Natural Sciences and Engineering Research Council (NSERC) of Canada, the Canada Research Chairs Program, and Simon Fraser University through funding from the Community Trust Endowment Fund. This work made use of 4D LABS shared facilities supported by the Canada Foundation for Innovation (CFI), British Columbia Knowledge Development Fund (BCKDF) and Simon Fraser University. J.-C. Boyer thanks the Michael Smith Foundation for Health Research for support. C.-J. Carling thanks Simon Fraser University for a Graduate Fellowship and a President's Research Stipend.

6.7 Experimental

6.7.1 General methods

6.7.1.1 Materials

All reagents and solvents used for synthesis, chromatography, photochemistry and UV–vis spectroscopy measurements were purchased from Aldrich and used as received, unless otherwise noted. Anhydrous ethanol (EtOH) was purchased from Commercial Alcohols. Triethylamine was purchased from Anachemia. Anhydrous CH₂Cl₂ was purchased from Aldrich and passed through activated alumina using a solvent purification system before use. CD₂Cl₂ was purchased from Cambridge Isotope Laboratories and used as received. Column chromatography was performed using silica gel 60 (230–400 mesh) from Silicycle Inc. The oleate coated UCNPs (**o-NP**),^[11] 3-azidopropylphosphonic acid,^[132] and photoresponsive dithienethylenes **2a**,^[160] **2b**^[161] and **3a**^[159] were synthesized according to published procedures with slight modifications.

6.7.1.2 Instrumentation

¹H NMR and ¹³C NMR characterizations were carried out using a Bruker AVANCE III (5 mm TXI inverse probe) working at 500.19 MHz for ¹H- and at 125.77 MHz for ¹³C NMR. Chemical shifts (δ) are reported in parts per million relative to tetramethylsilane using the residual solvent peak as a reference standard. Coupling constants (*J*) are reported in hertz. Melting points were measured using a Gallenkamp melting point apparatus (Registered Design No. 889339) and reported without correction. Exact mass measurements were done

using a Kratos Concept-H instrument with perfluorokerosene as the standard. Photographs were taken with an Olympus E-410 digital single lens reflex camera fixed on a tripod and recorded with shutter speed: 1/80 and aperture: F5.6 for photos with ambient light on, and shutter speed: 1/2 and aperture: F5.6 for photos with the ambient light off. Laser and light power was measured on a Gentec TPM-300. The power density of the laser beam was calculated by dividing the recorded power by the laser beam area (focused beam (high power): filled circle, d: 0.6 mm, A: 0.028 cm², defocused beam (low power): hollow ellipse, a: 0.65 mm, b: 3 mm, A: 0.612 cm²).

Transmission electron microscopy (TEM) and high-resolution TEM (HR-TEM) images were obtained using a Tecnai 200 keV Field Emission Scanning Transmission Electron Microscope. Dilute colloids of the NPs (0.1 wt-%) dispersed in THF (**1a-NP**, **1ab-NP**) or Toluene (**1b-NP**) were drop-casted on thin, carbon formvar-coated copper grids for imaging. The NP shape and crystallinity were evaluated from the collected TEM images, while the particle size was calculated from over 150 particles.

6.7.1.3 Spectroscopic studies

IR spectra were acquired on a Bomem (Hartmann & Braun, MB-Series) spectrometer. IR samples were prepared by mixing 1 part of dried, functionalized nanoparticles with 10 parts of KBr after which they were pressed into translucent discs. A Varian Cary 300 Bio spectrophotometer was used to acquire all UV-vis spectra. The nanoparticle samples were prepared by mixing 0.05 mL stock

solution of **1a-NP**, **1b-NP** or **1ab-NP** with 3 mL of solvent in a square quartz fluorescence cuvette (1 × 1 × 4.5 cm). All volumes were measured out using 1 mL disposable syringes and 22 gauge needles. Emission spectra for solutions of **1a-NP**, **1b-NP** and **1ab-NP** were measured on a PTI Quantamaster spectrofluorometer. A JDS Uniphase 980 nm continues-wave laser diode (device type L4-9897510-100M) coupled to a 105 μm (core) fiber was employed as the excitation source. The output of the diode laser was collimated and directed through the sample perpendicular to the read-out plane of the fluorospectrometer using a Newport F-91-C1-T Multimode Fiber Coupler. All of the colloidal samples were held in a square quartz fluorescence cuvette (1 × 1 × 4.5 cm). All spectra were corrected for the instrument sensitivity. The fluorescence was recorded with a slit size of 1.5 nm, step size: 1 nm and integration: 0.1 nm. The power density of the 980 nm laser beam was adjusted from high to low by turning the focus dial on the laser mount. The laser beam defocus from a filled circle to a hollow ellipse by turning the dial 34 1/6 turns (focused beam: $r = 0.3$ mm, $A = 0.028$ cm² and 38 W/cm²; defocused beam: $a = 0.65$ mm, $b = 3$ mm, $A = 0.612$ cm² and 2 W/cm²).

6.7.1.4 Photochemistry

Ring-closing reactions for all dithienylethenes (**3a**, **3b**, **1a-NP**, **1b-NP** and **1ab-NP**) were carried out using the light source from a lamp used for visualizing TLC plates at 365 nm (Spectroline E-series, 15.9 mW/cm²). Ring-opening reactions were carried out using a slide projector with a > 434 nm longpass filter (377 mW/cm²) and a > 630 nm longpass filter (120 mW/cm²). The samples were

irradiated approximately 1–2 cm from the light source under scarce light conditions to eliminate interference from ambient light during the procedures. NIR to UV remote control ring-closing of **1a-NP**, **1b-NP** and **1ab-NP** were performed using a JDS Uniphase 980 nm laser diode (device type L4-9897510-100M) coupled to a 105 μm (core) fibre. The laser beam was collimated and directed horizontally through the sample using a Newport F-91-C1-T Multimode Fiber Coupler. The samples were magnetically stirred in fluorescence cuvettes (1 \times 1 \times 4.5 cm).

6.7.1.5 Emission quenching experiments

The percent emission quenching was calculated with Microsoft Excel software by calculating the area under each line segment of the emission graph by the formula: $0.5 \times (\text{wavelength } 2 - \text{wavelength } 1) \times (\text{emission } 2 + \text{emission } 1)$ followed by adding up all of the values for that specific wavelength or emission segment.

6.7.2 Synthesis

6.7.2.1 Synthesis of 4-(4-(2-(5-(4-methoxyphenyl)-2-methylthiophen-3-yl)cyclopent-1-en-1-yl)-5-methylthiophen-2-yl)phenol

A flame-dried round-bottom flask cooled under an N_2 atmosphere was charged with **2b** (100 mg, 0.21 mmol). Anhydrous CH_2Cl_2 (30 mL) was added via a cannula and the system was cooled in a dry-ice/acetone bath. The solution was treated with BBr_3 (0.34 mL, 3.60 mmol) drop-wise and was subsequently allowed to reach ambient temperature. The reaction was followed closely by TLC

(1:1 EtOAc:hexanes, Rf: 0.7, pink upon 365 nm exposure) and after 30 min when most starting material was consumed, the solution was cooled to 0 °C and quenched with approximately 15 mL ice (exothermic). The reaction mixture was poured into a separatory funnel and diluted with saturated aqueous NH₄Cl and CH₂Cl₂. The phases were separated and the aqueous phase was extracted 3 times with CH₂Cl₂. The combined organic extracts were dried over anhydrous MgSO₄, vacuum-filtered and concentrated under reduced pressure. The product was purified by column chromatography (1:4 EtOAc:hexanes) and obtained as a colourless solid which turned pink upon exposure to UV light (75 mg, 76 %). The compound rapidly decomposes at ambient temperature, store at –20 °C.

M.p. 48–50 °C.

¹H NMR (500 MHz, CD₂Cl₂) δ 7.42 (d, *J* = 8.7 Hz, 2H), 7.37 (d, *J* = 8.6 Hz, 2H), 6.94 (s, 1H), 6.93 (s, 1H), 6.87 (d, *J* = 8.7 Hz, 2H), 6.80 (d, *J* = 8.6 Hz, 2H), 5.13 (s, 1H), 3.79 (s, 3H), 2.82 (t, *J* = 7.5 Hz, 4H), 2.05 (p, *J* = 7.5 Hz, 2H), 1.97 (s, 6H).

¹³C NMR (126 MHz, CD₂Cl₂) δ 159.4, 155.5, 139.8, 139.7, 137.2, 135.1, 135.1, 133.9, 127.9, 127.8, 127.1, 126.9, 123.5, 116.0, 114.6, 55.8, 38.9, 23.5, 14.6.

HRMS: Calculated for C₂₈H₂₆O₂S₂: (M+H)⁺ 459.1374. Found: (M+H)⁺ 459.1443.

6.7.2.2 Synthesis of 5-(4-methoxyphenyl)-2-methyl-3-(2-(2-methyl-5-(4-(prop-2-yn-1-yloxy)phenyl)thiophen-3-yl)cyclopent-1-en-1-yl)thiophene (3b)

A round-bottom flask was charged with 4-(4-(2-(5-(4-methoxyphenyl)-2-methylthiophen-3-yl)cyclopent-1-en-1-yl)-5-methylthiophen-2-yl)phenol (63.9 mg, 0.14 mmol), K₂CO₃ (76.8 mg, 0.56 mmol), benzo-18-crown-6 (2.2 mg, 0.007

mmol), KI (1.2 mg, 0.007 mmol) and reagent grade acetone (10 mL). Propargylbromide (80 wt-% in toluene, 31 mg, 0.21 mmol) was added and the system was equipped with a condenser and heated to reflux. After 18.5 h when the reaction was complete as indicated by TLC (1:3 EtOAc:hexanes, Rf: 0.52, pink upon 365 nm exposure), the reaction was cooled to ambient temperature, poured into a separatory funnel and diluted with EtOAc and saturated aqueous NH₄Cl. The phases were separated and the aqueous phase was extracted 3 times with EtOAc. The combined organic extracts were dried over anhydrous MgSO₄, vacuum-filtered and concentrated under reduced pressure. The product was purified by column chromatography (1:7 EtOAc:hexanes) and obtained as a colourless slightly sticky solid which turned pink upon exposure to UV light (59 mg, 86 %). The compound was stored at -20 °C.

M.p. 35–38 °C.

¹H NMR (500 MHz, CD₂Cl₂) δ 7.43 (t, *J* = 8.8 Hz, 4H), 6.95 (dd, *J* = 8.8, 2.4 Hz, 4H), 6.88 (s, 1H), 6.86 (s, 1H), 6.93 (d, *J* = 8.8 Hz, 2H), 6.86 (d, *J* = 8.8 Hz, 1H), 4.70 (d, *J* = 2.4 Hz, 2H), 3.80 (s, 3H), 2.84 (t, *J* = 7.5 Hz, 4H), 2.58 (t, *J* = 2.4 Hz, 1H), 2.08 (p, *J* = 7.5 Hz, 2H), 2.00 (s, 3H), 2.00 (s, 3H).

¹³C NMR (126 MHz, CD₂Cl₂) δ 159.4, 157.2, 139.8, 139.5, 137.3, 137.2, 135.2, 135.1, 134.2, 133.9, 128.7, 127.7, 126.9, 123.8, 123.5, 115.6, 114.6, 79.0, 75.9, 56.3, 55.8, 38.9, 23.5, 14.6, 14.6.

HRMS: Calculated for C₃₁H₂₈O₂S₂: (M+H)⁺ 497.1531. Found: (M+H)⁺ 497.1614.

6.7.2.3 Synthesis of 3-(3,3,4,4,5,5-hexafluoro-2-(2-methyl-5-(4-(prop-2-yn-1-yloxy)phenyl)-thiophen-3-yl)cyclopent-1-en-1-yl)-2-methyl-5-phenylthiophene (3a)

Although the molecule has been reported earlier, this synthesis differs slightly and is therefore reported again here. A mixture of the phenol starting material²⁵ (644 mg, 1.2 mmol), K₂CO₃ (663 mg, 4.8 mmol), KI (10 mg, 0.06 mmol), benzo-18-crown-6 (19 mg, 0.06 mmol) and propargylbromide (208 mg, 1.4 mmol) and acetone (30 mL) was brought to reflux. After 20 h at reflux, the mixture was cooled to ambient temperature and quenched with saturated aqueous NH₄Cl, poured into a separatory funnel and diluted with EtOAc and treated with water. The phases were separated and the aqueous phase was extracted 3 times with EtOAc. The combined organic extracts were dried over MgSO₄, vacuum filtered and concentrated under reduced pressure. The product was purified by silica gel column chromatography (9.8 hexanes:0.2 EtOAc) to yield a white solid (570 mg, 83 %) which turned blue upon exposure to UV light. The compound was stored at -20 °C.

¹H NMR (500 MHz, CDCl₃) δ 7.54–7.51 (m, 2H), 7.48–7.45 (m, 2H), 7.39–7.35 (m, 2H), 7.30–7.28 (m, 1H), 7.26 (s, 1H), 7.16 (s, 1H), 7.00–6.96 (m, 2H), 4.70 (d, *J* = 2.4 Hz, 2H), 2.52 (d, *J* = 2.4 Hz, 1H), 1.94 (s, 3H), 1.93 (s, 3H).

6.7.2.4 Synthesis of a-NP

Approximately 150 mg of **o-NP** was dispersed in 8 mL of CHCl₃ and 2 mL of absolute EtOH and added to a 20 mL scintillation vial. In a separate vial, 3-azidopropylphosphonic acid² (500 mg) was dissolved in a mixture of CHCl₃ (2 mL) and absolute EtOH (2 mL). The 3-azidopropylphosphonic acid solution was

then added to the nanoparticle dispersion via a Pasteur pipette. The resultant mixture was stirred overnight at room temperature. The reaction solution was transferred to a centrifuge tube and hexanes were added until the mixture became cloudy. The reaction mixture was then centrifuged at 5000 rpm for 10 min and the supernatant was discarded. The precipitated nanoparticles were then redispersed in 5 mL of DMSO (3.8 wt-%) for further experiments. FTIR (cm^{-1}): 2935, 2879, 2110 (strong, N_3), 1660, 1252, 1140, 1070, 920.

6.7.2.5 Synthesis of of 2-component systems **1a-NP** and **1b-NP**

A solution of compound **3a** (3.47 mL of a stock solution of 6.0 mg, 0.01 mmol, 3.0×10^{-3} M in CH_3CN) or **3b** (3.83 mL of a stock solution of 5.2 mg, 0.01 mmol, 2.7×10^{-3} M in CH_3CN) was added to a 20 mL scintillation vial and the solvent was removed under reduced pressure. A dispersion of the azide nanoparticles **a-NP** (0.5 mL, 3.8 wt-% in DMSO) was added to the vial and the mixture sonicated. The resulting clear dispersion was transferred to a 3 mL vial equipped with a stir-bar. Freshly prepared $\text{CuSO}_4 \times 5\text{H}_2\text{O}$ (24 μL , 1.04×10^{-4} mmol, 4.41×10^{-3} M in H_2O), sodium *L*-ascorbate (18 μL , 1.04×10^{-3} mmol, 5.75×10^{-2} M in H_2O), H_2O (8 μL) and Et_3N (10 μL) were added via calibrated auto-pipette and the reaction vessel was sealed and stirred at 35 °C for 24 h. The reaction mixture was transferred to a 1.5 mL eppendorf tube and diluted with absolute EtOH (1 mL). After centrifugation (13500 rpm, 30 min) the supernatant was discarded and the pellet redispersed in THF (1 mL) or CH_2Cl_2 (1 mL) for **3a** and **3b**, respectively, and centrifuged (13500 rpm, 20 min). The supernatant was

discarded and the pellet was redispersed in suitable solvent (2 mL), the clear colloidal dispersions (**1a-NP**: 3 wt-% in THF, **1b-NP**: 2 wt-% in CH₂Cl₂) were used for subsequent experiments without any further purification. Loading: **1a-NP**: 5000–7000 molecules per nanoparticle, **1b-NP**: 6000–8000 molecules per particle (Table S1–S3). FTIR (cm⁻¹): **1a-NP**: 2964, 2928, 2855, 2360, 2110 (weak, N₃), 1655, 1515 (s), 1274, 1101, 1056, 988, 822. **1b-NP**: 2956, 2928, 2839, 2364, 2110 (weak, N₃), 1656, 1511, 1252, 1100, 1070, 1035, 824.

6.7.2.6 Synthesis of mixed 3-component system **1ab-NP**

A mixture of compounds **3a** (1.73 mL of a stock solution of 3.0 mg, 0.005 mmol, 3.01×10^{-3} M in CH₃CN) and **3b** (1.92 mL of a stock solution of 2.6 mg, 0.005 mmol, 2.72×10^{-3} M in CH₃CN) was added to a 20 mL scintillation vial and the solvent was removed under reduced pressure. A dispersion of the azide nanoparticles **a-NP** (0.5 mL, 3.8 wt-% in DMSO) was added, the mixture sonicated and the resulting clear dispersion was transferred to a 3 mL vial equipped with a stir-bar. Freshly prepared CuSO₄ × 5H₂O (11 μL, 1.0×10^{-4} mmol, 9.4×10^{-3} M in H₂O), sodium *L*-ascorbate (28 μL, 1.0×10^{-3} mmol, 3.79×10^{-2} M in H₂O), H₂O (11 μL) and Et₃N (10 μl) were added via auto-pipette and the reaction vessel was sealed and stirred at 35 °C for 24 h. The reaction mixture was transferred to a 1.5 mL eppendorf tube and diluted with absolute EtOH (1 mL). After centrifugation (13500 rpm, 30 min) the supernatant was discarded and the pellet redispersed in THF (1 mL) and centrifuged (13500 rpm, 20 min). The supernatant was discarded and the pellet was redispersed in THF

(2 mL). The slightly hazy colloidal dispersion (2 wt-%) was used for subsequent experiments without any further purification. FTIR (cm^{-1}): **1ab-NP** 2959, 2997, 2940, 2362, 2110 (weak, N_3), 1654, 1515, 1251, 1114, 1056, 989, 824.

6.7.3 Calculation of loading

Table 6.3 Calculation particle size and mass

particle size (o-NP) hexagonal prism
$h = 38.8 \text{ nm} = 38.8 \times 10^{-7} \text{ cm}$
$l, r = 33.6 \text{ nm} = 33.6 \times 10^{-7} \text{ cm}$
volume = $((3\sqrt{3})/2) \times r^2 \times h = 1.14 \times 10^{-16} \text{ cm}^3$
density ^[242] $\text{NaYF}_4 = 4.2 \text{ g/cm}^3$
mass of each UCNP = $4.79 \times 10^{-16} \text{ g}$

Table 6.4 Calculation of loading using absorbances in the UV region of the spectra of **3a**, **3b**, **1a-NP** and **1b-NP**^a

$A^{3a}_{\text{THF}} (282-300 \text{ nm}) = 0.47255$	$A^{3b}_{\text{CH}_2\text{Cl}_2} (282-289 \text{ nm}) = 0.39173$
$\epsilon^{3a}_{\text{THF}} (282-300 \text{ nm}) = 45005 \text{ M}^{-1}\text{cm}^{-1}$	$\epsilon^{3a}_{\text{CH}_2\text{Cl}_2} (282-289 \text{ nm}) = 37308 \text{ M}^{-1}\text{cm}^{-1}$
$A^{1a\text{-NP}}_{\text{THF}} (274-287 \text{ nm}) = 0.46107$	$A^{1b\text{-NP}}_{\text{CH}_2\text{Cl}_2} (275-282 \text{ nm}) = 0.40818$
$C^{1a\text{-NP}} = A^{1a\text{-NP}} / (\epsilon^{3a} \times l) = 1.02 \times 10^{-5} \text{ M}$	$C^{1a\text{-NP}} = A^{1b\text{-NP}} / (\epsilon^{3b} \times l) = 1.09 \times 10^{-5} \text{ M}$
$MW^{1a} = 739.9 \text{ g mol}^{-1}$	$MW^{1b} = 661.8 \text{ g mol}^{-1}$
$V = 3.05 \text{ mL}, n^{1a} = 3.23 \times 10^{-8} \text{ mol}, \text{mass}^{1a} = 2.39 \times 10^{-5} \text{ g} = 1.95 \times 10^{16} \text{ molecules}$	$V = 3.05 \text{ mL}, n^{1b} = 3.32 \times 10^{-8} \text{ mol}, \text{mass}^{1b} = 2.20 \times 10^{-5} \text{ g} = 2.04 \times 10^{16} \text{ molecules}$
$\text{mass NP} = \text{mass}^{1a\text{-NP}} - \text{mass}^{1a} = 0.00131 - 2.39 \times 10^{-5} \text{ g} = 1.29 \times 10^{-3} \text{ g}$	$\text{mass NP} = \text{mass}^{1b\text{-NP}} - \text{mass}^{1b} = 0.00121 - 2.20 \times 10^{-5} \text{ g} = 1.19 \times 10^{-3} \text{ g}$
number of NP in sample = 2.69×10^{12} particles	number of NP in sample = 2.48×10^{12} particles
loading wt-% = 1.85 wt-%	loading wt-% = 1.85 wt-%
loading molecules per particle = 7249	loading molecules per particle = 8225

^a These calculations do not take into account any scatter.

Table 6.5 Calculation of loading using absorbances in the visible region of the spectra of **3a**, **3b**, **1a-NP** and **1b-NP**^a

$A_{\text{THF (584-607 nm)}}^{3ac} = 0.1892$	$A_{\text{DCM (524-539 nm)}}^{3bc} = 0.1788$
$\epsilon_{\text{THF (584-607 nm)}}^{3ac} = 25379 \text{ M}^{-1}\text{cm}^{-1}$	$\epsilon_{\text{DCM (524-539 nm)}}^{3bc} = 30408 \text{ M}^{-1}\text{cm}^{-1}$
$A_{\text{THF (567-589 nm)}}^{1ac\text{-NP}} = 0.1321$	$A_{\text{DCM (513-531 nm)}}^{1bc\text{-NP}} = 0.1311$
$C^{1ac\text{-NP}} = A^{1ac\text{-NP}} / (\epsilon^{3ac} \times l) = 5.21 \times 10^{-6} \text{ M}$	$C^{1bc\text{-NP}} = A^{1bc\text{-NP}} / (\epsilon^{3bc} \times l) = 4.31 \times 10^{-6} \text{ M}$
$C^{1a\text{-NP}} = (C^{1ac\text{-NP}} \times 0.29) / 0.71 = 2.13 \times 10^{-6} \text{ M}$	$C^{1b\text{-NP}} = (C^{1bc\text{-NP}} \times 0.44) / 0.56 = 3.39 \times 10^{-6} \text{ M}$
M	M
$C^{1a\text{-NP}} = C^{1ac\text{-NP}} + C^{1ao\text{-NP}} = 7.33 \times 10^{-6} \text{ M}$	$C^{1b\text{-NP}} = C^{1bc\text{-NP}} + C^{1bo\text{-NP}} = 7.70 \times 10^{-6} \text{ M}$
$MW^{1a} = 739.9 \text{ g mol}^{-1}$	$MW^{1b} = 661.8 \text{ g mol}^{-1}$
$V = 3.05 \text{ mL}$, $n^{1a} = 2.23 \times 10^{-8} \text{ mol}$, $\text{mass}^{1a} = 1.65 \times 10^{-5} \text{ g}$ $= 1.34 \times 10^{16} \text{ molecules}$	$V = 3.05 \text{ mL}$, $n^{1b} = 2.35 \times 10^{-8} \text{ mol}$, $\text{mass}^{1b} = 1.55 \times 10^{-5} \text{ g}$ $= 1.42 \times 10^{16} \text{ molecules}$
$\text{mass NP} = \text{mass}^{1a\text{-NP}} - \text{mass}^{1a} = 0.00131 - 1.65 \times 10^{-5} \text{ g} = 1.29 \times 10^{-3} \text{ g}$	$\text{mass NP} = \text{mass}^{1b\text{-NP}} - \text{mass}^{1b} = 0.00121 - 1.55 \times 10^{-5} \text{ g} = 1.19 \times 10^{-3} \text{ g}$
number of NP in sample = 2.69×10^{12} particles	number of NP in sample = 2.48×10^{12} particles
loading wt-% = 1.28 wt-%	loading wt-% = 1.30 wt-%
loading molecules per particle = 4992	loading molecules per particle = 5726

^a These calculations assume the photostationary state for the photoswitches are the same in the free ligands (**3a** and **3b**) and the nanoparticles (**1a-NP** and **1b-NP**).

Table 6.6 Calculation of loading using absorbances in the visible region of the spectra of **3a** and **1ab-NP**^a

$A_{\text{THF (650-660 nm)}}^{3ac} = 0.09821$
$\epsilon_{\text{THF (650-660 nm)}}^{3ac} = 9553.6 \text{ M}^{-1} \text{ cm}^{-1}$
$A_{\text{THF (650-660 nm)}}^{1acbc-NP} = 0.03899$
$C^{1acbc-NP} (\mathbf{a}^c \text{ component}) = A^{1ac-NP} / (\epsilon^{3ac} \times l) = 4.17 \times 10^{-6} \text{ M}$
$C^{1ab-NP} (\mathbf{a}^o \text{ component}) = (C^{1acbc-NP} \times 0.29) / 0.71 = 1.70 \times 10^{-6} \text{ M}$
$C^{1ab-NP} (\mathbf{a} \text{ component}) = C^{1acb-NP} + C^{1aob-NP} = 5.87 \times 10^{-6} \text{ M}$
$C^{1ab-NP} (\mathbf{b} \text{ component}) = (4 \times C^{1ab-NP} (\mathbf{a} \text{ component})) / 5 = 4.70 \times 10^{-6} \text{ M}$
Total concentration 1ab-NP = $C^{1ab-NP} (\mathbf{a} \text{ component}) + C^{1ab-NP} (\mathbf{b} \text{ component}) = 1.05 \times 10^{-5} \text{ M}$
$V = 3.05 \text{ mL}, n^{1a} = 1.79 \times 10^{-8} \text{ mol}, \text{mass}^{1a} = 1.32 \times 10^{-5} \text{ g}$ $= 1.08 \times 10^{16} \text{ molecules}$
$V = 3.05 \text{ mL}, n^{1b} = 1.43 \times 10^{-8} \text{ mol}, \text{mass}^{1b} = 9.49 \times 10^{-6} \text{ g}$ $= 8.63 \times 10^{15} \text{ molecules}$
$\text{mass NP} = \text{mass}^{1ab-NP} - (\text{mass}^{1a} + \text{mass}^{1b}) = 0.00089 \text{ g} - 2.27 \times 10^{-5} \text{ g} = 0.87 \times 10^{-3} \text{ g}$
number of NP in sample = $0.87 \times 10^{-3} \text{ g} / 4.79 \times 10^{-16} \text{ g} = 1.81 \times 10^{12} \text{ particles}$
Loading wt-% = 2.6 wt-%
Loading molecules per particle = $(1.08 \times 10^{16} + 8.63 \times 10^{15}) / 1.81 \times 10^{12} = 10734 \text{ molecules/NP}$

^a These calculations assume the photostationary state for the photoswitches are the same in the free ligands (**3a**) and the nanoparticles (**1ab-NP**), and that the absorption of the **1b** component does not interfere with the absorption of the **1a** component at the region sampled.

6.7.4 Spectroscopy and photographs

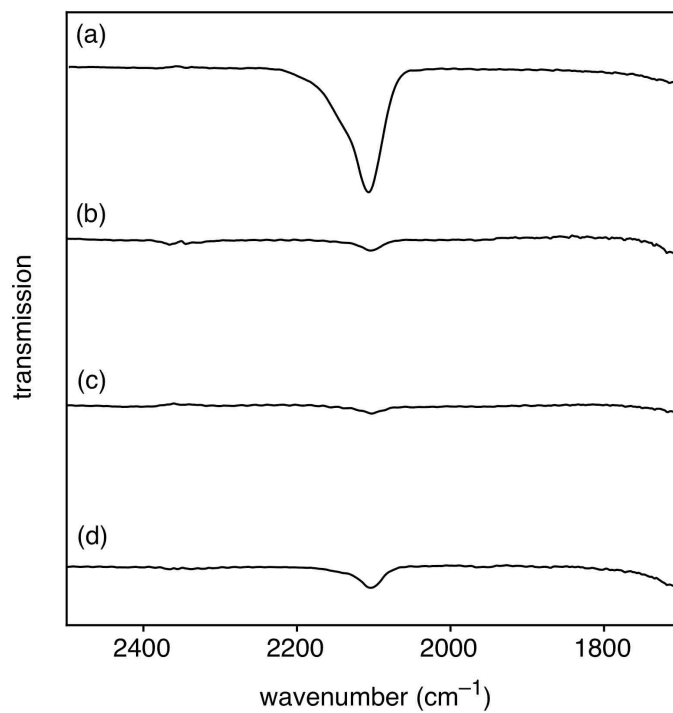


Figure 6.6 Selected region of the FTIR spectra for (a) azide-coated *core-shell-shell* NaYF₄:TmYb:ErYb nanoparticles (**a-NP**), (b) the 2-component nanoparticles **1a-NP**, (c) the 2-component nanoparticles **1b-NP**, and (d) the mixed 3-component nanoparticles **1ab-NP**.

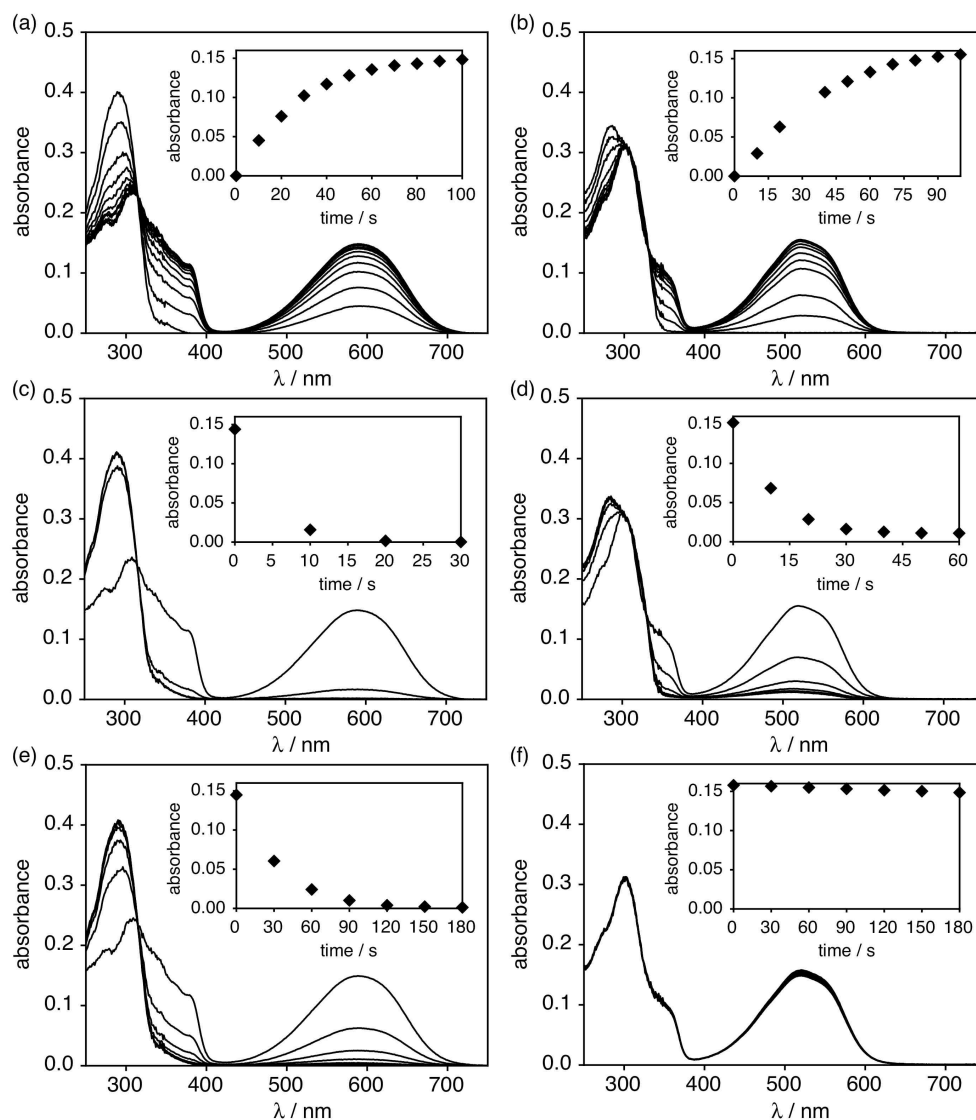


Figure 6.7 Changes in the UV-vis absorption spectra when CH_3CN solutions (1×10^{-5} M) of (a) **3a** and (b) **3b** are irradiated with 365 nm light (16 mW/cm^2). The insets show the growth of the bands at 590 nm for **3a** \rightarrow **3a^c** and 520 nm for **3b** \rightarrow **3b^c** corresponding to the ring-closed isomers, which are present in 72% for **3a** and 56% for **3b** in the photostationary states according to ^1H NMR spectroscopy (in CD_2Cl_2). Changes in the UV-vis absorption spectra when the same solutions of the photostationary states of (c) **3a^c** and (d) **3b^c** are irradiated with > 434 nm light (377 mW/cm^2). The insets show the reduction of the bands at 590 nm for **3a^c** \rightarrow **3a** and 520 nm for **3b^c** \rightarrow **3b**. Changes in the UV-vis absorption spectra when the same solutions of the photostationary states of (e) **3a^c** and (f) **3b^c** are irradiated with > 630 nm light (120 mW/cm^2). The insets show the reduction of the bands at 590 nm for **3a^c** \rightarrow **3a** and 520 nm for **3b^c** \rightarrow **3b**.

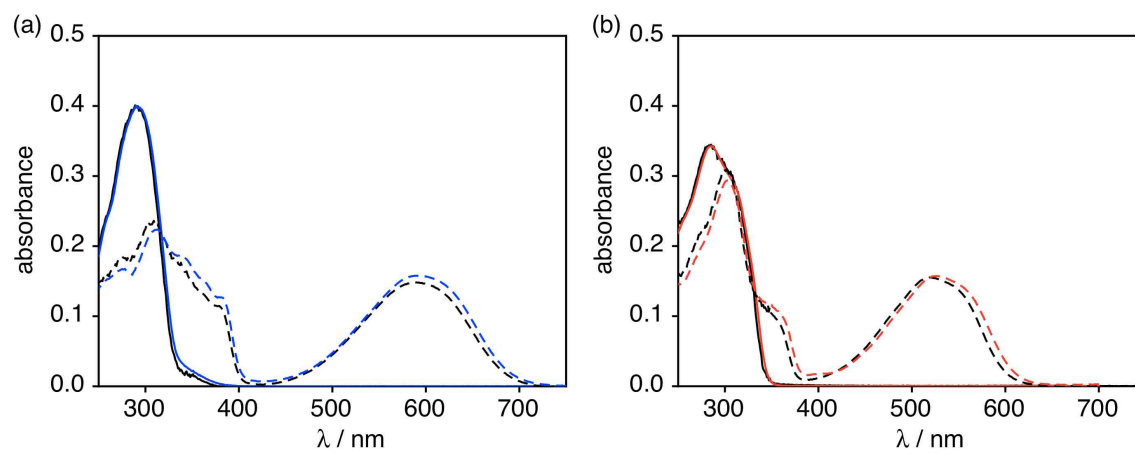


Figure 6.8 UV-vis absorption spectra of solutions (10^{-5} M) of the ligands (a) **3a** in CH_3CN (black) and THF (blue) and (b) **3b** in CH_3CN (black) and CH_2Cl_2 (red) before (solid lines) and after irradiation with 365 nm (16 mW/cm^2) light (dashed lines). The spectra were normalized for any small errors in concentration.

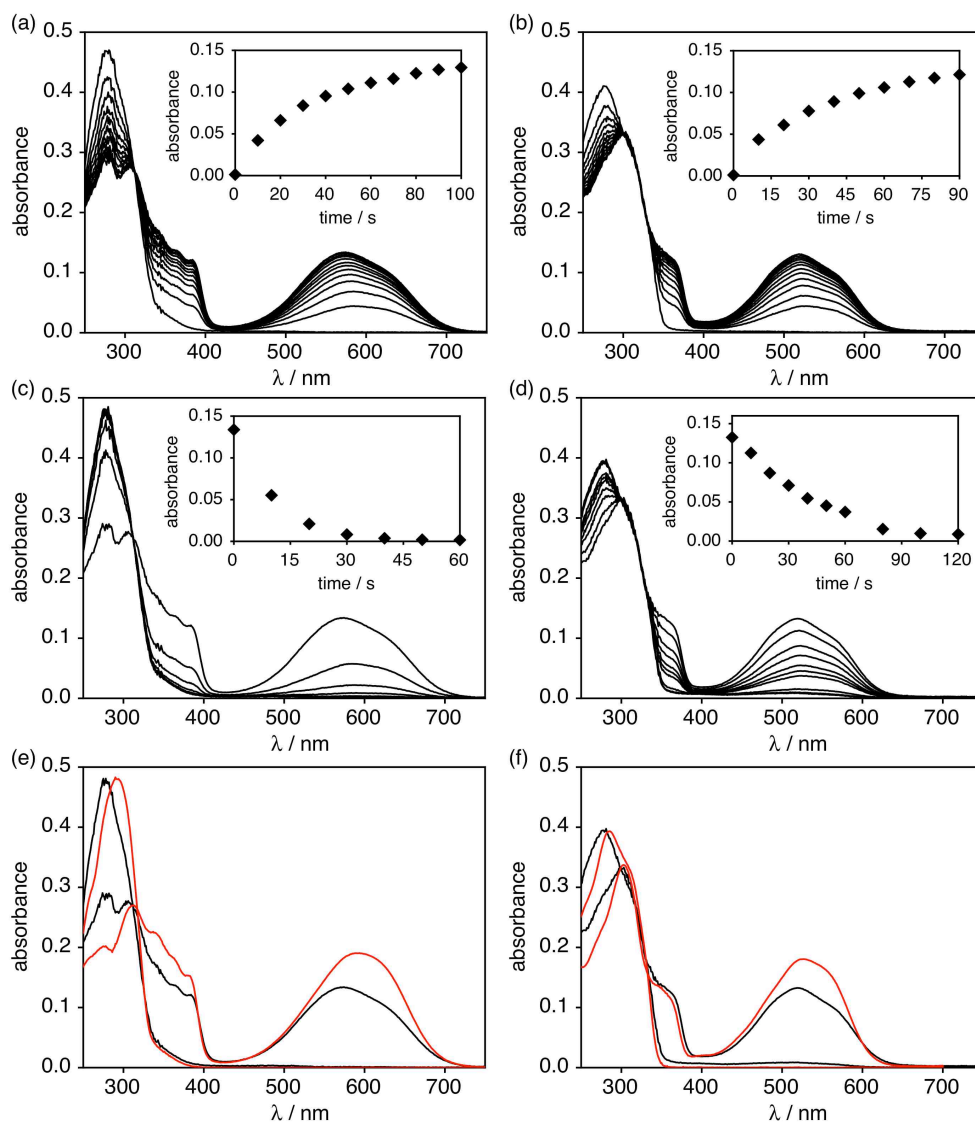


Figure 6.9 Changes in the UV-vis absorption spectra when (a) a THF solution (1×10^{-5} M, 0.05 wt-%) of **1a-NP** and (b) a CH_2Cl_2 solution (1×10^{-5} M, 0.03 wt-%) of **1b-NP** are irradiated with 365 nm light (16 mW/cm^2). The molar concentration refers to the amount of photoswitch in each sample, while the wt-% refers to the amount of decorated nanoparticle in each solution. The insets show the growth of the bands at 570 nm for **1a-NP** \rightarrow **1a^c-NP** and 520 nm for **1b-NP** \rightarrow **1b^c-NP** corresponding to the ring-closed isomers. Changes in the UV-vis absorption spectra when the same solutions of the photostationary states of (c) **1a^c-NP** and (d) **1b^c-NP** are irradiated with > 434 nm light (377 mW/cm^2). The insets show the reduction of the bands at 570 nm for **1a^c-NP** \rightarrow **1a-NP** and 520 nm for **1b^c-NP** \rightarrow **1b-NP**. The spectra for **1a-NP** and **1b-NP** (black lines) are compared to the ligands **3a** and **3b** (red lines) in (e) and (f), respectively in the same solvents (THF for **1a-NP** and **3a** and CH_2Cl_2 for **1b-NP** and **3b**).

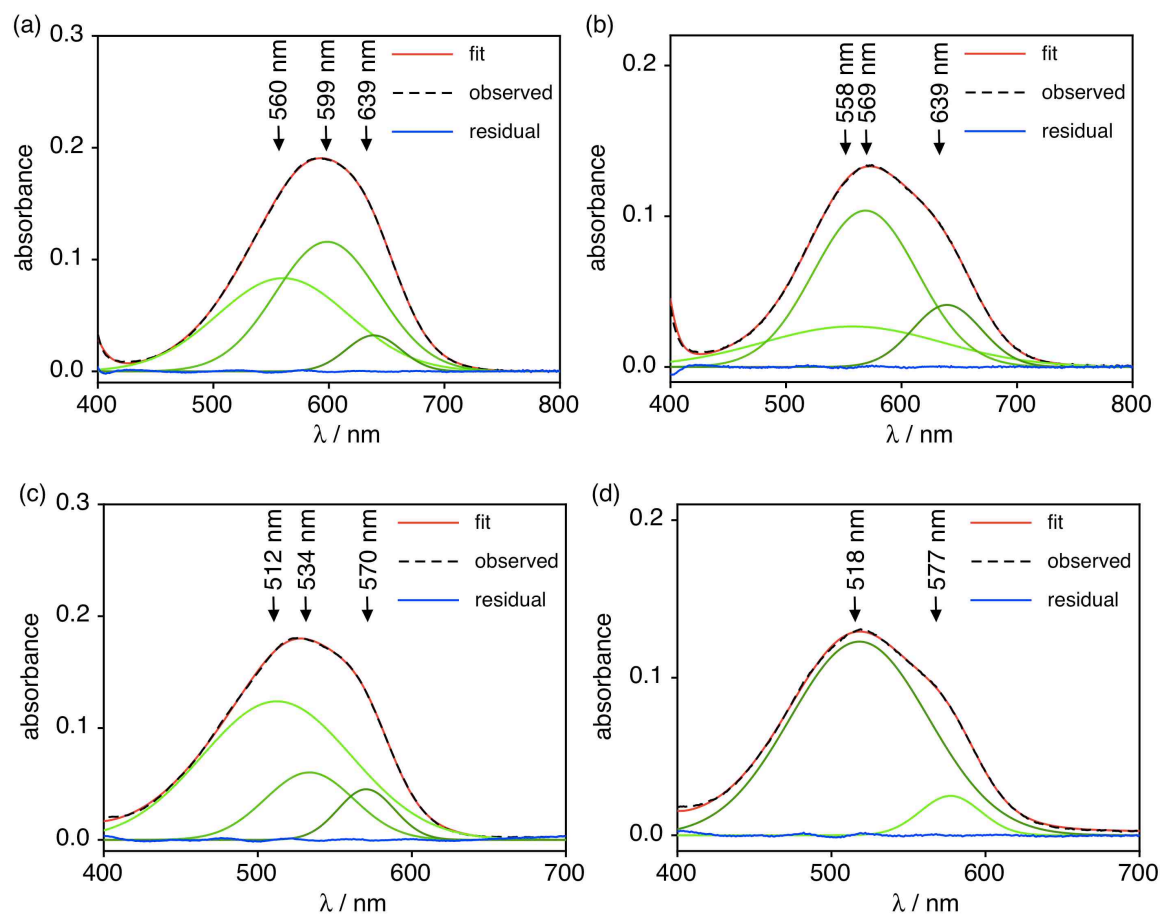


Figure 6.10 Observed (black dashed line), individual calculated bands (green lines), sum of the fit (red line) and the residual (blue line) for the UV-vis absorption spectra of (a) ligand **3a**, (b) hybrid system **1a-NP**, (c) ligand **3b** and (d) hybrid system **1b-NP**. The calculated bands in the UV region of the spectrum were removed from the figures for clarity. The peak fitting was performed using MagicPlot software from MagicPlot Systems.

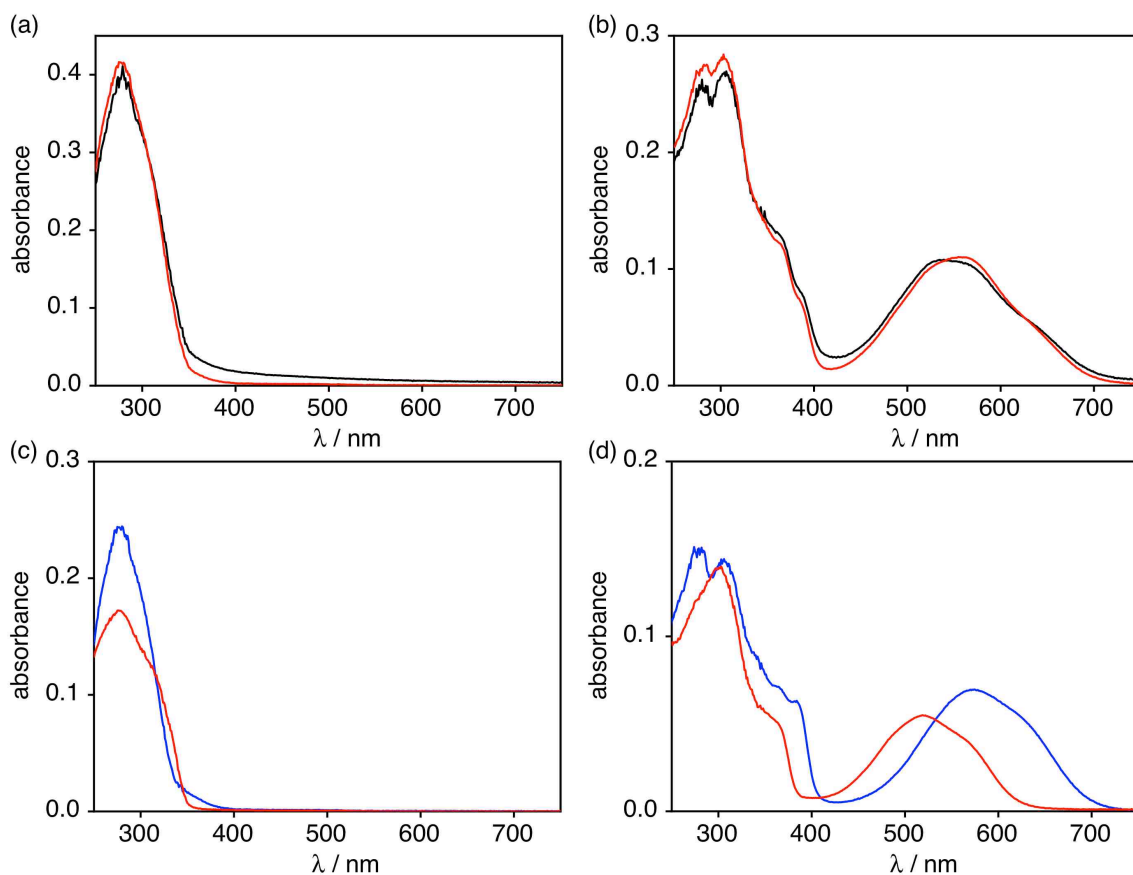


Figure 6.11 (a) The observed UV-vis absorption spectra of a THF solution of the two-component hybrid system **1ab-NP** (black trace) and the calculated spectrum obtained by combining the spectra of the one-component systems **1a-NP** and **1b-NP** in a 5:4 ratio (red trace). The concentration of chromophore is approximately 5.9×10^{-6} M for **1a** and 4.7×10^{-6} M for **1b**, while the amount of decorated nanoparticle is 0.03 wt-%. (b) The observed UV-vis absorption spectra of the same THF solutions of the photostationary state for **1a^cb^c-NP** (black trace) and the calculated spectrum obtained by combining the spectra of the one-component systems **1a-NP** and **1b-NP** in a 5:4 ratio (red trace). (c) The UV-vis absorption spectra of **1a-NP** and **1b-NP** in a 5:4 ratio. (d) The UV-vis absorption spectra of **1a^c-NP** and **1b^c-NP** at their photostationary states in a 5:4 ratio.

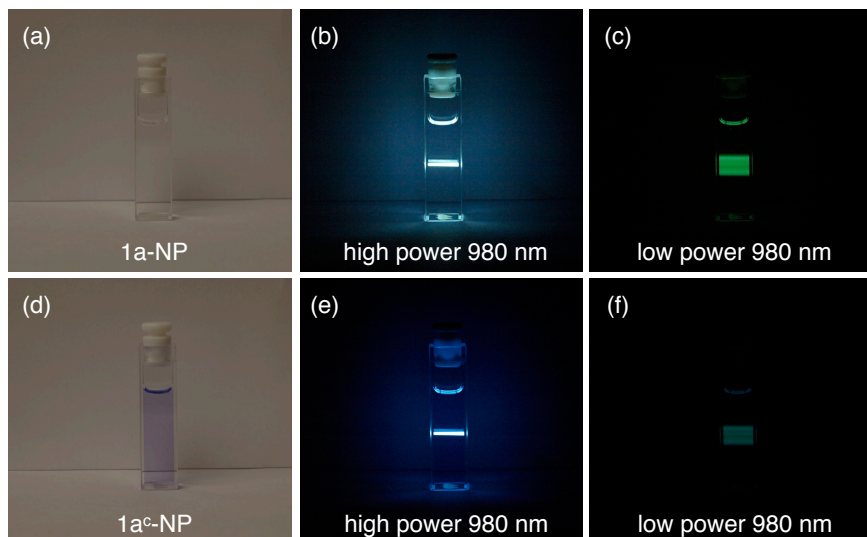


Figure 6.12 Images of (a) the colour of a THF solution (1×10^{-5} M, 0.05 wt-%) of **1a-NP**, (b) the emission when this solution is irradiated with high 980 nm excitation power (38 W/cm^2), (c) the emission when this solution is irradiated with low 980 nm excitation power (2 W/cm^2), (d) the colour after irradiating the solution with 365 nm light (16 mW/cm^2) until the photostationary state is reached, (e) the emission when this solution is irradiated with high 980 nm excitation power (38 W/cm^2), and (f) the emission when this solution is irradiated with low 980 nm excitation power (2 W/cm^2).

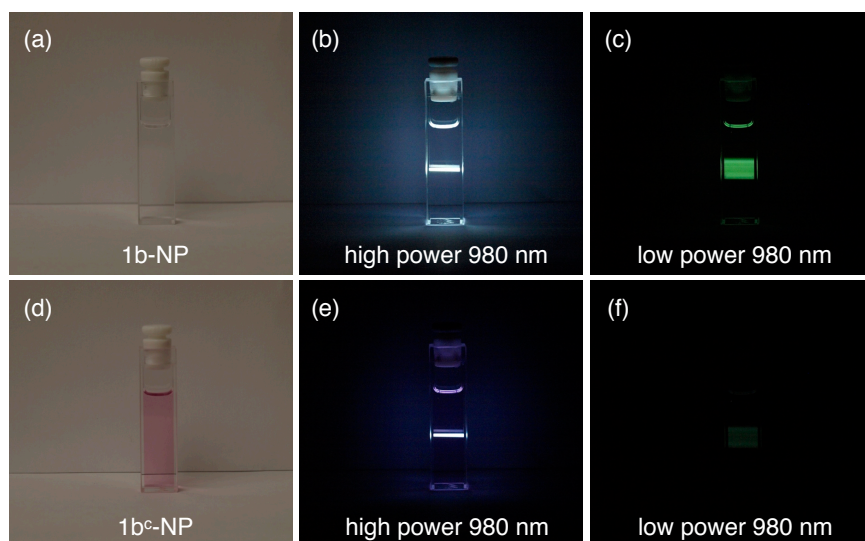


Figure 6.13 Images of (a) the colour of a CH₂Cl₂ solution (1×10^{-5} M, 0.03 wt-%) of **1b-NP**, (b) the emission when this solution is irradiated with high 980 nm excitation power (38 W/cm^2), (c) the emission when this solution is irradiated with low 980 nm excitation power (2 W/cm^2), (d) the colour after irradiating the solution with 365 nm light (16 mW/cm^2) until the photostationary state is reached, (e) the emission when this solution is irradiated with high 980 nm excitation power (38 W/cm^2), and (f) the emission when this solution is irradiated with low 980 nm excitation power (2 W/cm^2).

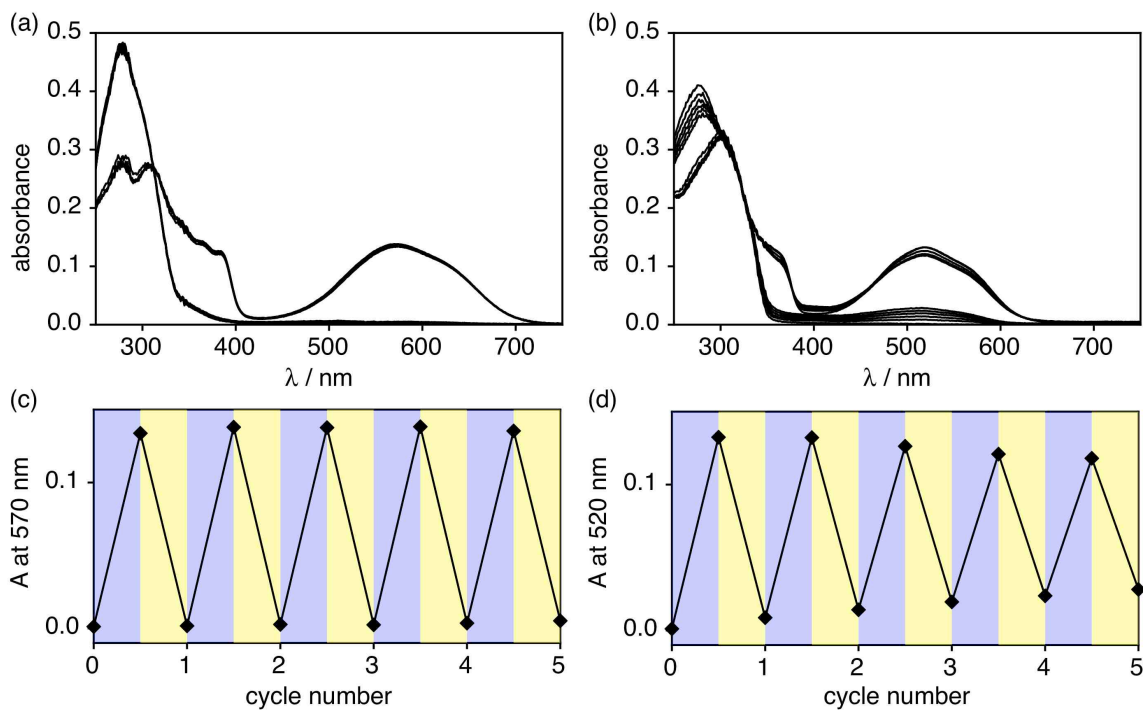


Figure 6.14 Changes in the UV-vis absorption spectra when (a) the same solution of **1a-NP** used in Figure 6.7(a) and (b) the same solution of **1b-NP** used in Figure 6.7(b) are irradiated alternately with 365 nm light (16 mW/cm^2) for 120 s for 1a-NP and 130 s for 1b-NP, and $> 434 \text{ nm}$ (377 mW/cm^2) light for 60 s for **1a-NP** and 120 s for **1b-NP**. Changes in the absorbances (c) at 570 nm and (d) at 520 nm when the same solutions are irradiated alternately with 365 nm (blue shaded areas) and $> 434 \text{ nm}$ light (yellow shaded areas).

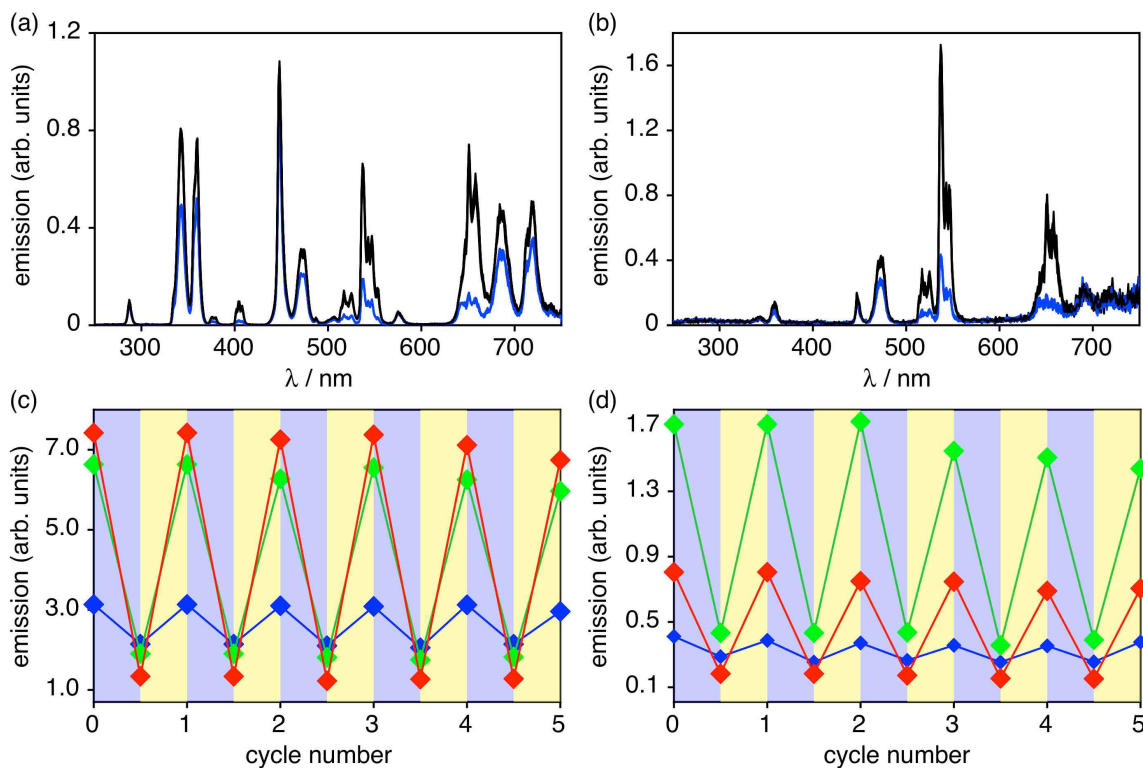


Figure 6.15 Changes in the emission spectra when the same solution of **1a-NP** used in Figure 6.7(a) is irradiated alternately with 365 nm light (16 mW/cm^2) for 120 s and $> 434 \text{ nm}$ (377 mW/cm^2) light for 60 s (a) at high 980 nm excitation power (38 W/cm^2) and (b) at low 980 nm excitation power (2 W/cm^2). Changes in the emission intensities at 471 nm (\blacklozenge), 537 nm (\blacklozenge) and 651 nm (\blacklozenge) when the same solution is irradiated alternately with 365 nm (blue shaded areas) and $> 434 \text{ nm}$ light (yellow shaded areas) at (c) high 980 nm excitation power and (d) low 980 nm excitation power.

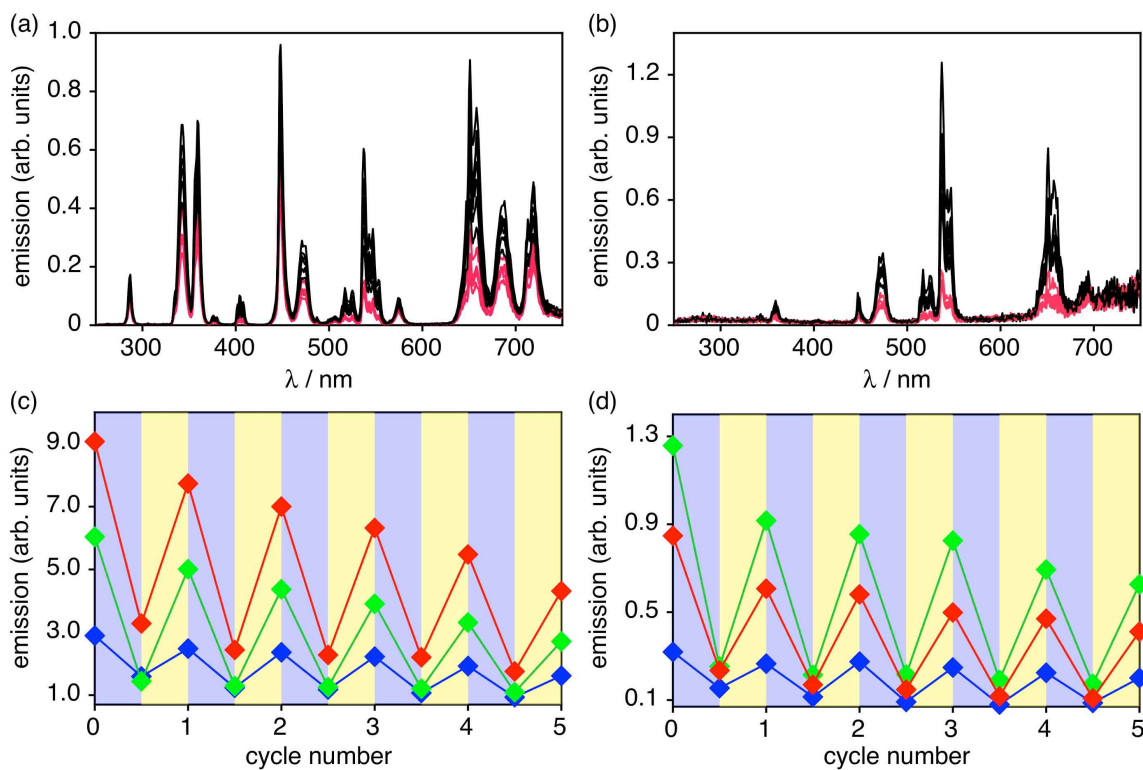


Figure 6.16 Changes in the emission spectra when the same solution of **1b-NP** used in Figure 6.7(b) is irradiated alternately with 365 nm light (16 mW/cm^2) for 130 s and > 434 nm (377 mW/cm^2) light for 120 s (a) at high 980 nm excitation power (38 W/cm^2) and (b) at low 980 nm excitation power (2 W/cm^2). Changes in the emission intensities at 471 nm (\blacklozenge), 537 nm (\blacklozenge) and 651 nm (\blacklozenge) when the same solution is irradiated alternately with 365 nm (blue shaded areas) and > 434 nm light (yellow shaded areas) at (c) high 980 nm excitation power and (d) low 980 nm excitation power.

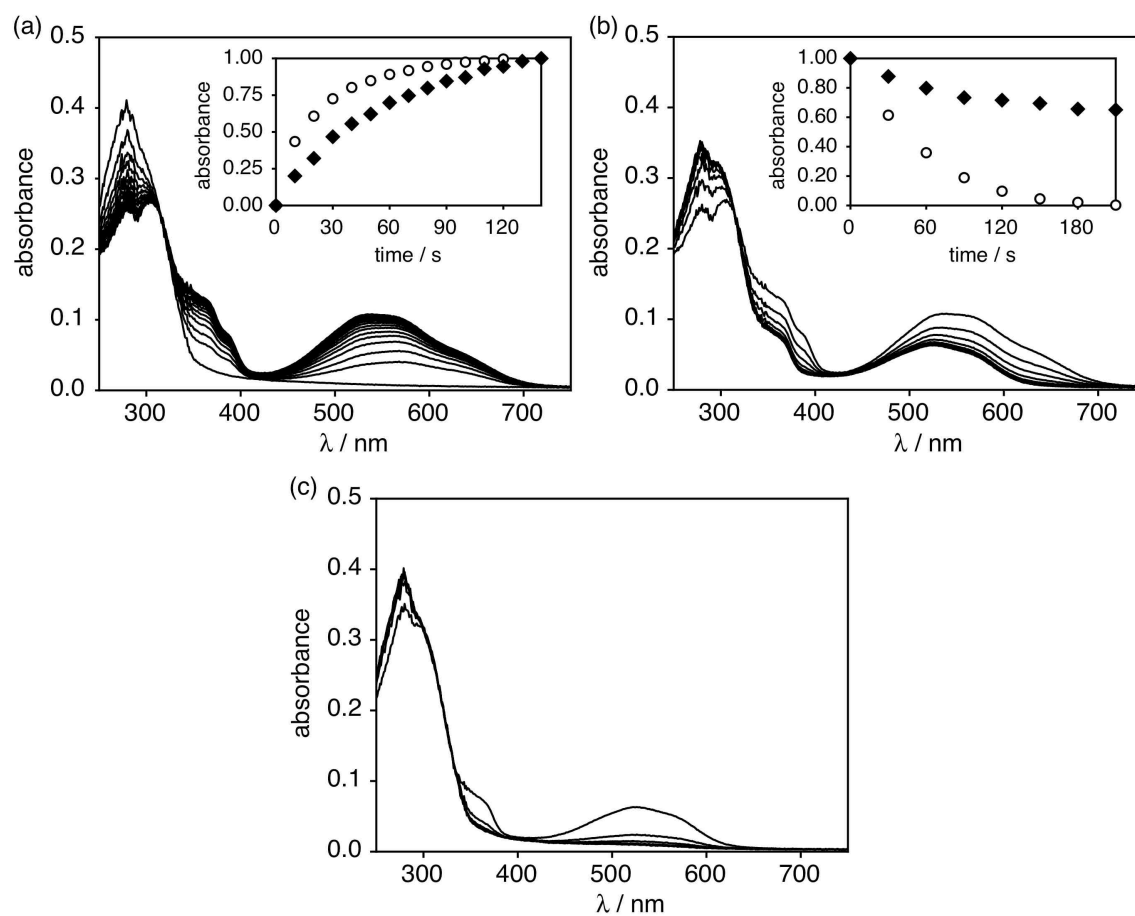


Figure 6.17 (a) Changes in the UV-vis absorption spectrum of a THF solution of the two-component hybrid system **1ab-NP** as it is irradiated with 365 nm light (16 mW/cm^2). The concentration of chromophore is approximately $5.9 \times 10^{-6} \text{ M}$ for **1a** and $4.7 \times 10^{-6} \text{ M}$ for **1b**, while the amount of decorated nanoparticle is 0.03 wt-%. The inset shows the growth of the absorptions at 570 nm (○) and 520 nm (◆) corresponding to the two ring-closed isomers in **1a^cb^c-NP**. (b) Changes in the spectrum of the same photostationary state as it is irradiated with $> 630 \text{ nm}$ light (120 mW/cm^2). The inset shows the changes in the absorptions at 570 nm (○) and 520 nm (◆) corresponding to the two ring-closed isomers in **1a^cb^c-NP**. (c) Changes in the spectrum of the photostationary state in Figure 6.10(b) as it is irradiated with $> 434 \text{ nm}$ light (377 mW/cm^2).

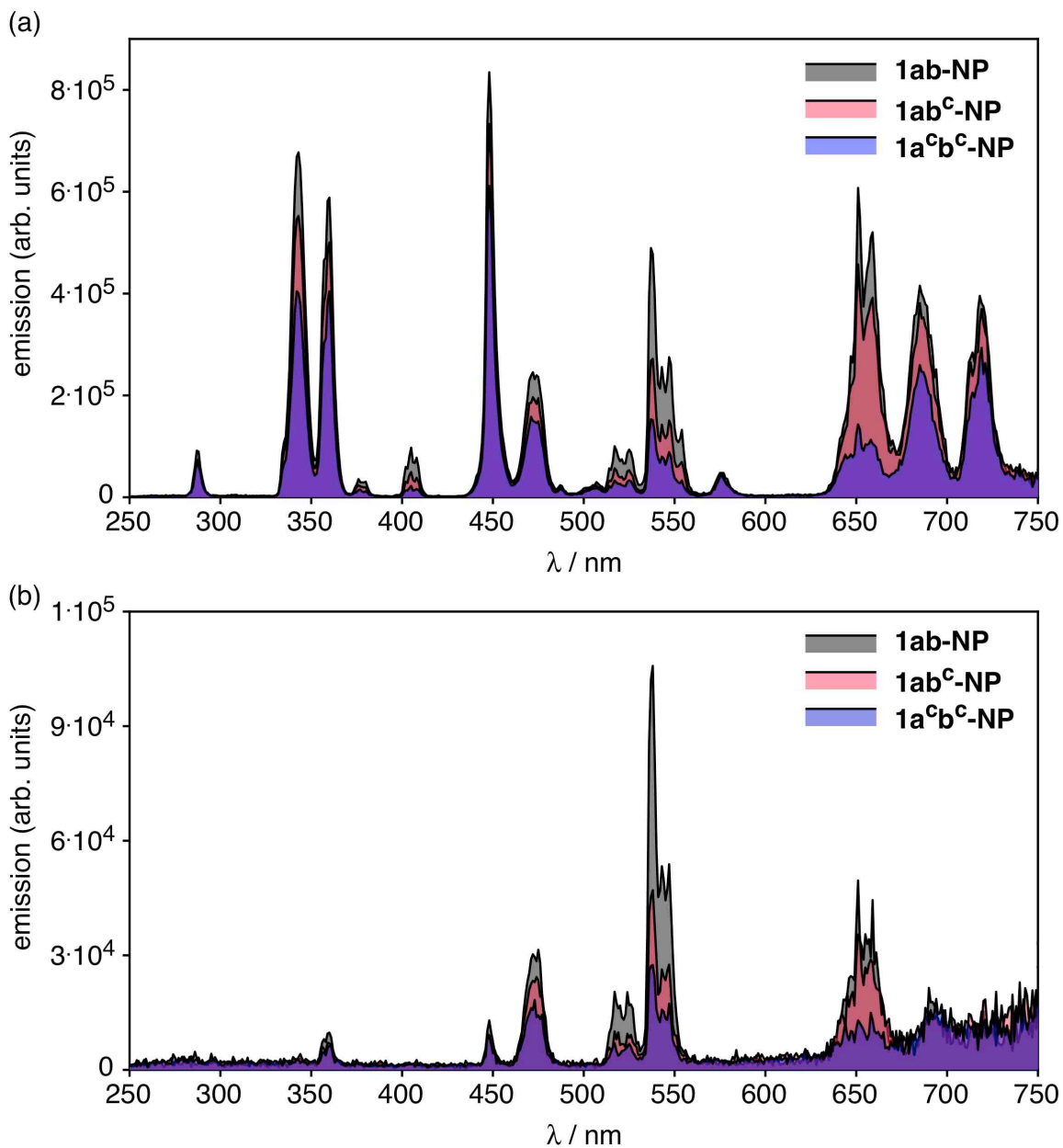


Figure 6.18 The emission spectra a THF solution of the two-component hybrid system **1ab-NP** before (grey) and after irradiation with 365 nm light (16 mW/cm²) (violet) and > 630 nm light (120 mW/cm²) (red). The concentration of chromophore is approximately 5.9×10^{-6} M for **1a** and 4.7×10^{-6} M for **1b**, while the amount of decorated nanoparticle is 0.03 wt-% at (a) high 980 nm excitation power (38 W/cm²) and (b) low 980 nm excitation power (2 W/cm²).

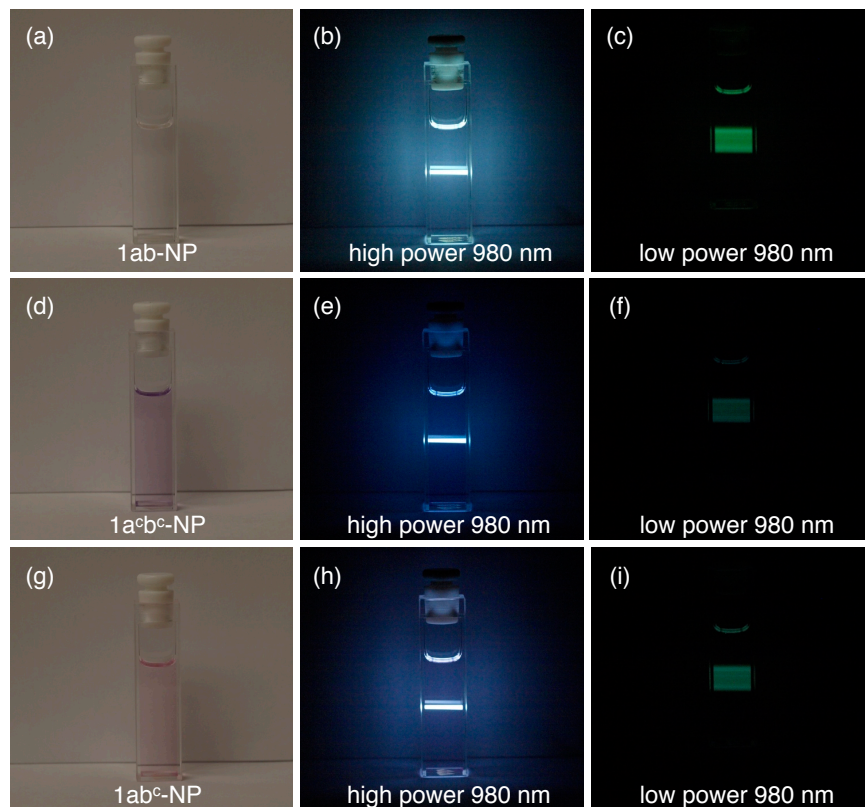


Figure 6.19 Images of (a) the colour of a THF solution of **1ab-NP**, (b) the emission when this solution is irradiated with high 980 nm excitation power (38 W/cm^2), (c) the emission when this solution is irradiated with low 980 nm excitation power (2 W/cm^2), (d) the colour after irradiating the solution with 365 nm light (16 mW/cm^2) until the photostationary state is reached, (e) the emission when this solution is irradiated with high 980 nm excitation power (38 W/cm^2), (f) the emission when this solution is irradiated with low 980 nm excitation power (2 W/cm^2), (g) the colour after irradiating the solution with $> 630 \text{ nm}$ light (120 mW/cm^2) until no changes were observed in the spectrum, (h) the emission when this solution is irradiated with high 980 nm excitation power (38 W/cm^2), and (i) the emission when this solution is irradiated with low 980 nm excitation power (2 W/cm^2).

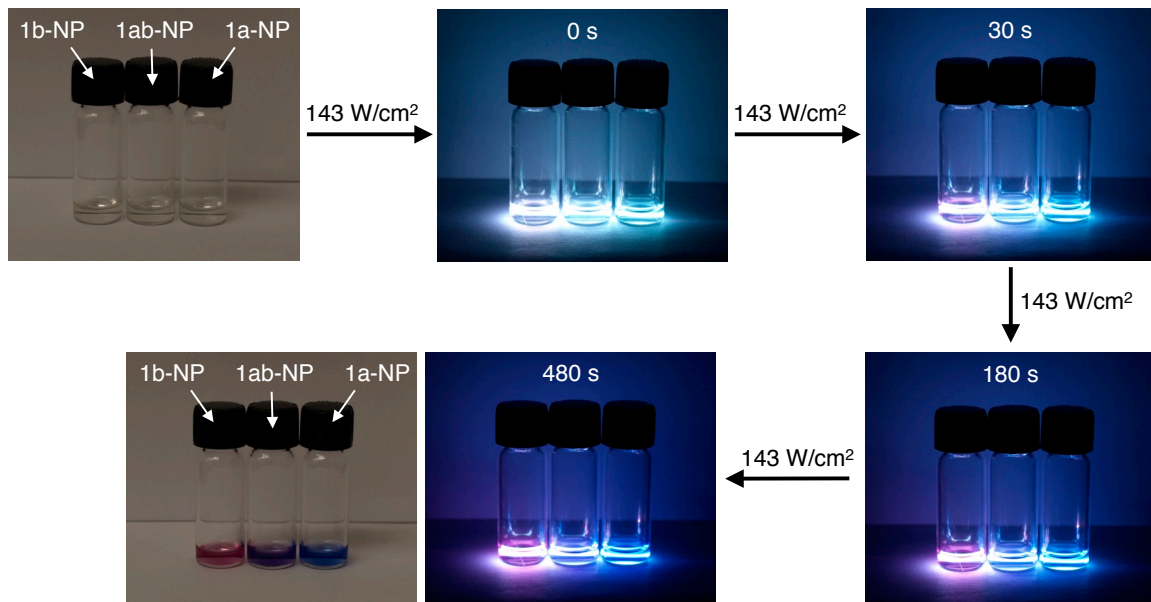


Figure 6.20 Images of a THF solution of **1a-NP**, a CH₂Cl₂ solution of **1b-NP**, and a THF solution of **1ab-NP** as they are irradiated with very high 980 nm excitation power (143 W/cm²), showing the 'remote-control' photoswitching.

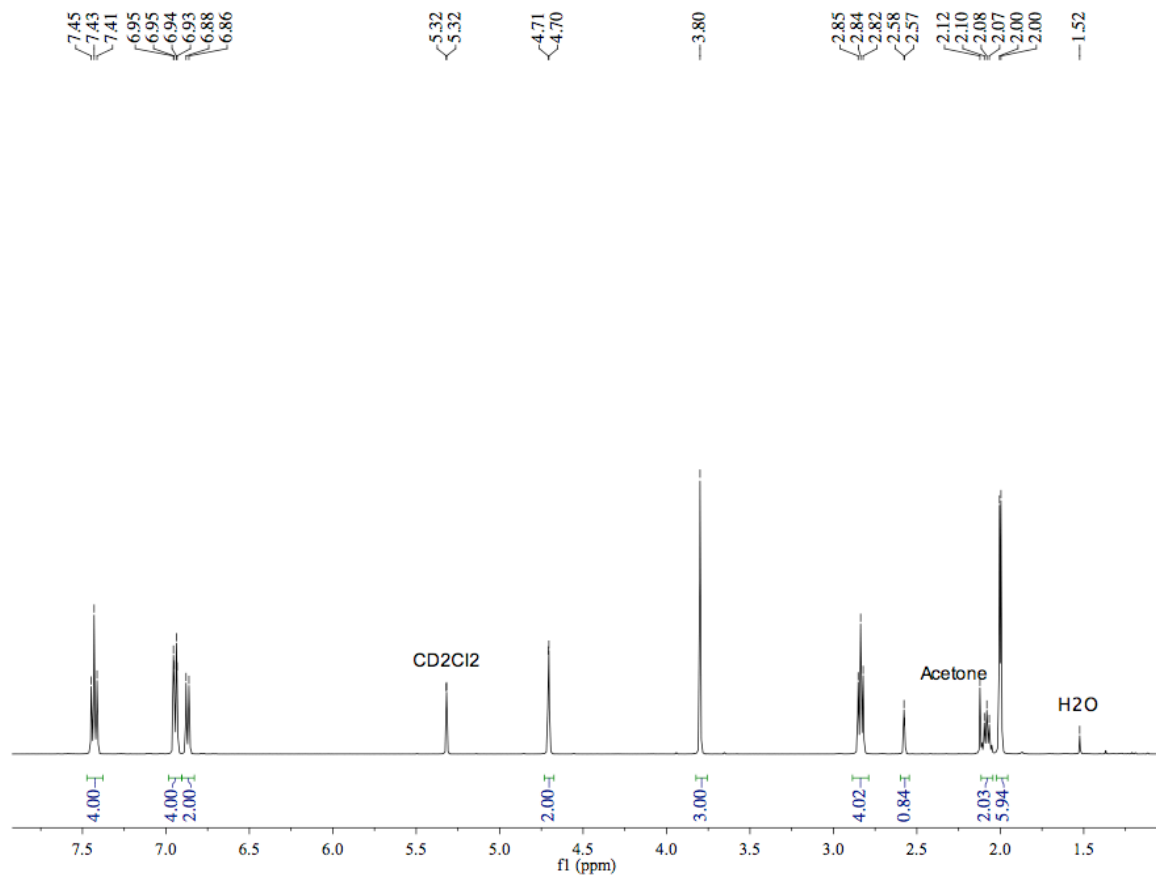


Figure 6.21 ^1H NMR spectrum for a CD_2Cl_2 solution of ligand **3b**. The residual solvent peaks are highlighted.

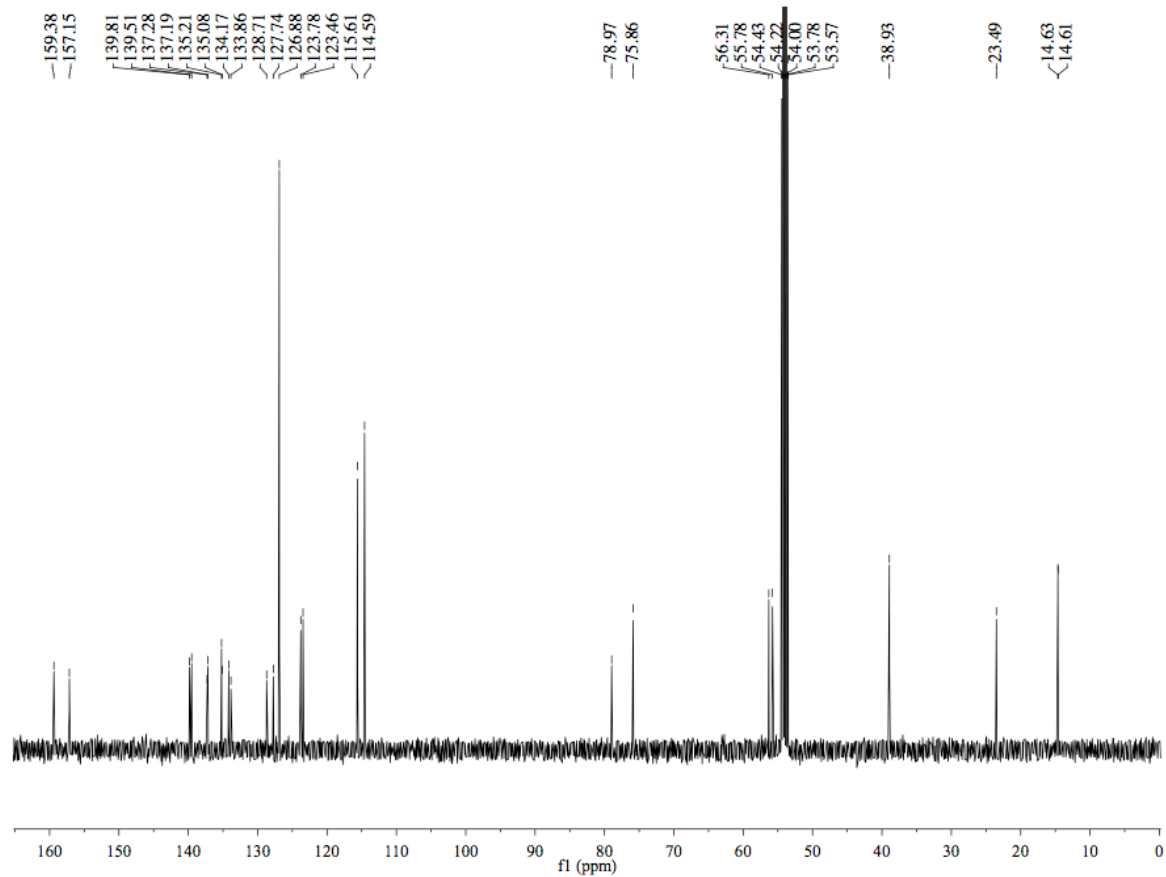


Figure 6.22 ^{13}C NMR spectrum for a CD_2Cl_2 solution of ligand **3b**.

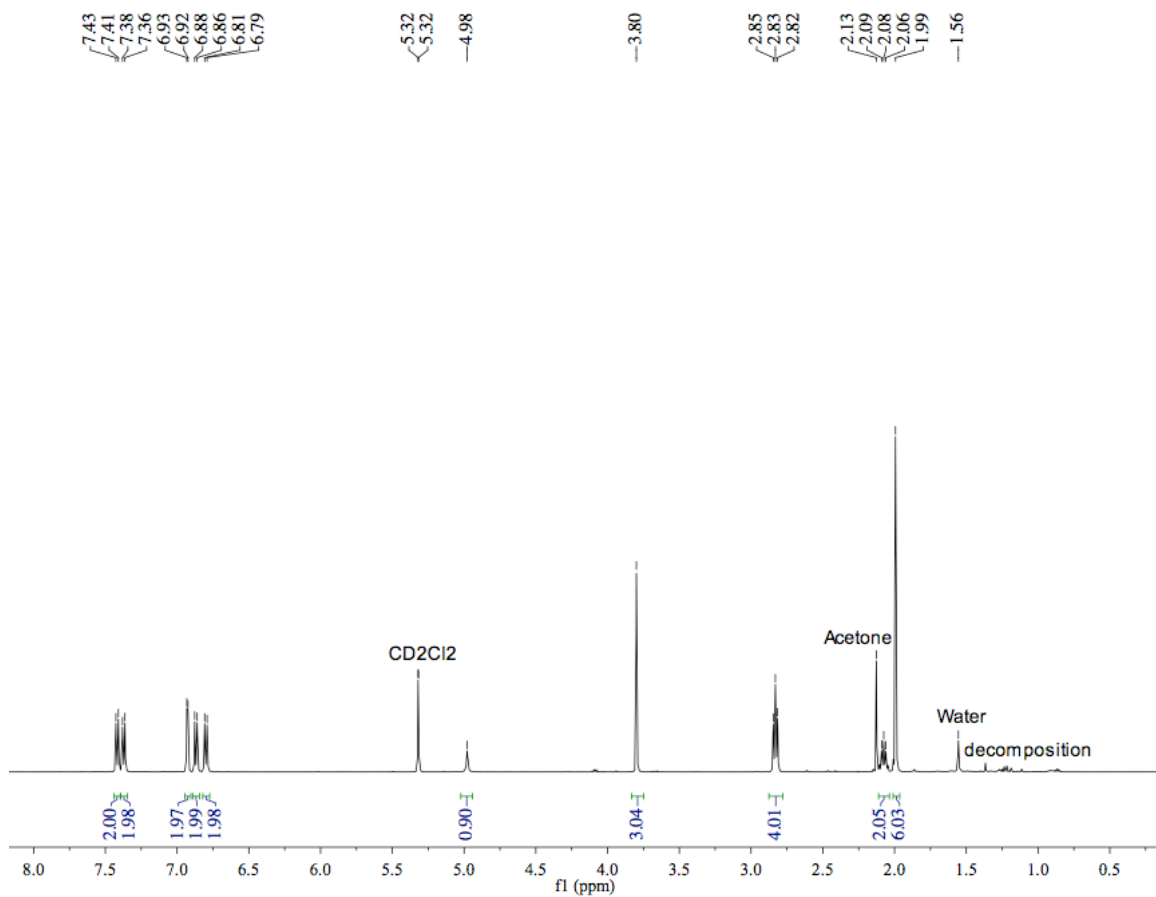


Figure 6.23 ¹H NMR spectrum for a CD₂Cl₂ solution of 4-(4-(2-(5-(4-methoxyphenyl)-2-methylthiophen-3-yl)cyclopent-1-en-1-yl)-5-methylthiophen-2-yl)phenol. The compound decomposes rapidly at ambient temperature.

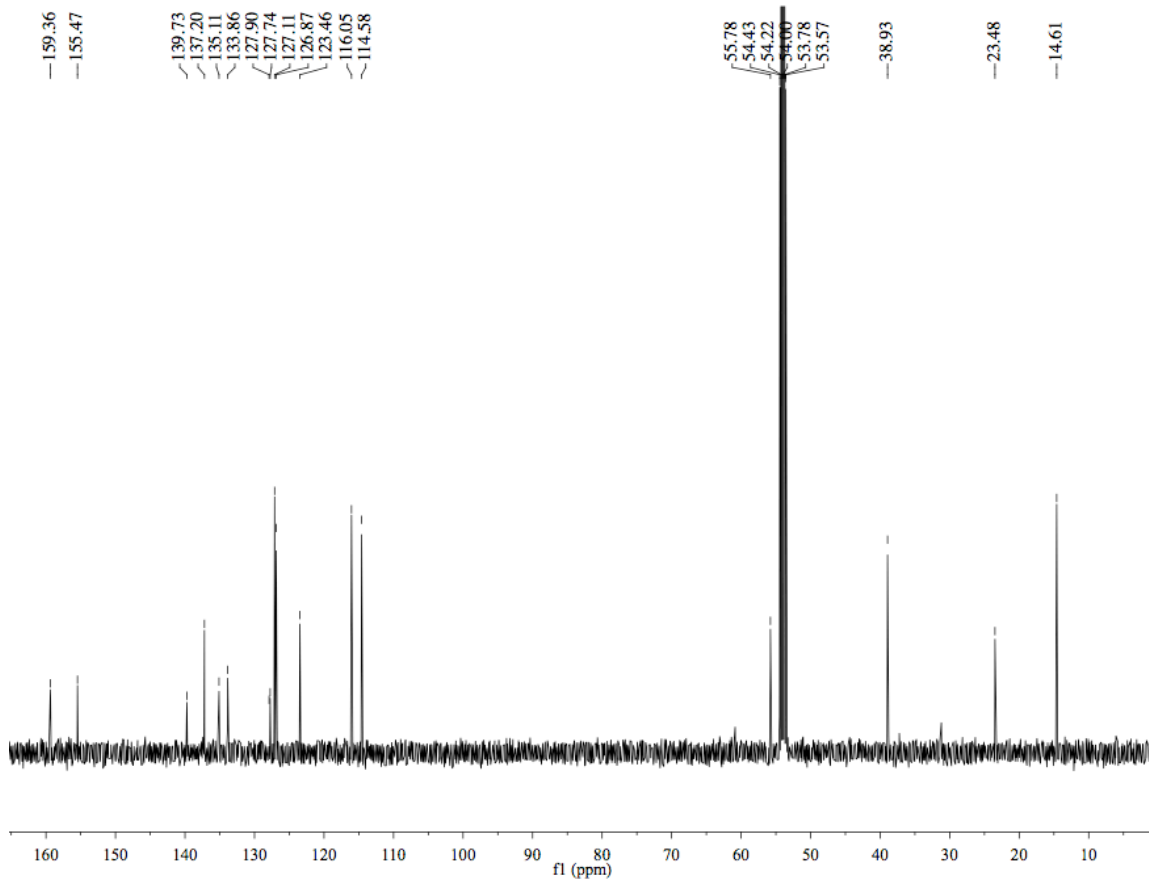


Figure 6.24 ^{13}C NMR spectrum for a CD_2Cl_2 solution of 4-(4-(2-(5-(4-methoxyphenyl)-2-methylthiophen-3-yl)cyclopent-1-en-1-yl)-5-methylthiophen-2-yl)phenol.

7: LIGHT-TRIGGERED RELEASE

Photoremovable protecting groups commonly known as photocages have found widespread applications in synthesis, biotechnology and cell biology.^[5,173,174,175]

With the advent of nano-medicine, the development of new light-triggered nanosized-carriers from which therapeutics can be released on-demand has received much attention from the scientific community.^[176,177,178] The major driving force behind this research is to develop less toxic therapies for severe health conditions like cancer. The therapies can also be beneficial in treating health conditions such as rheumatism (among other ailments) since the light can be directed to the area(s) of interest in a spatiotemporal fashion.

Many different photocages have been developed together with various attachment systems that have been demonstrated to release a wide variety of functional groups including phosphates, sulfonic acid, aldehydes, ketones, carboxylic acids, alcohols, amines, thiols, halogen anions, protons, and even ions such as Ca^{2+} .^[173]

In order to be considered a useful photocage in a biological environment, the following criteria must be met:

1. For *in vitro* studies it is imperative that the photocage absorb UVA (315-400 nm) light (or visible light) in order to cause minimal photo-damage to DNA

and other endogenous molecules during photolysis. How well the photocage responds to the light is determined by the combination of the quantum yield (the probability of forming products after a photon is absorbed) and the molar absorption coefficient at that wavelength (the probability to absorb a photon).

For *in vivo* applications however, it is imperative that the photocage responds well to far-visible light or NIR light because in this region (~630-900 nm), tissues absorb and light scatters much less than at UVA wavelengths and the light can thus penetrate deeper without causing damage.^[19,20,21,22] The current technique of choice is two-photon excitation (2PE) photolysis with pulsed NIR laser light. The excitation and subsequent reaction occurs in the focal point where the density of photons is highest. Since the excitation occurs in a small volume, 3D spatial resolution is possible.^[4,5] However, it should be noted that due to light scattering of tissues the laser will, most likely, be defocused and the 2PE photolysis efficiency would thus be severely reduced at deeper locations within the tissue.

2. The photocage and its photoproduct should be water soluble and easy to both synthesize and derivatize.

3. The photocage should be cleanly photolysed in high yield and both the photocage and the photoproduct of the photocage should be stable and benign to biological systems if used to study cellular events. If used to treat a disease however, the toxicity requirement is more relaxed as the potential cytotoxicity of the photoproduct can be used as a drug by itself.

4. The photocage should be stable without light activation both *in vitro* and *in vivo*.

7.1 Common UV light triggered photocages

7.1.1 The 2-nitrobenzyl photocage

The most well-known and utilized photocage is the 2-nitrobenzyl (2NB) photocage class.^[173] Upon irradiation with UVA light, this class of photo-triggered molecules undergoes clean photochemistry. Its synthesis and photochemistry are well documented and it is readily available commercially – both compelling reasons why the 2NB photocage is so famous and widely used. However, the photochemical by-product of the 2NB photolysis is a nitroso-carbonyl compound, which has electrophilic reactivity towards primarily cysteine and is thus mildly toxic.^[179,180,181]

The 2NB class also responds to NIR laser light irradiation, but the 2PE cross-section of the first generation of 2NB derivatives is not large enough for practical use and the reaction generally requires high-power NIR pulsed laser light, which causes tissue damage in the focal point.^[173] However, improved derivatives of this important class of photocages has recently appeared in the literature^[182,183] and derivatives in the propyl series with unprecedented 2PE action cross section (δ_u (800 nm): 11 GM) has been developed, see Table 7.1 entry 3.

Table 7.1: Photocages in the 2NB family. Quantum yield (ϕ), maximum absorption (λ_{\max}) and molar absorptivity (ϵ) compiled for the photocage starting material with carboxylate as leaving group.^[173,182,183]

<p>4,5-Dimethoxy-2-nitrobenzyl</p>	$\phi_{365\text{nm}}:$ 0.02	$\lambda_{\max}:$ 330 nm	$\epsilon_{330\text{nm}}:$ 5000 M ⁻¹ cm ⁻¹
<p>2-nitrophenylethyl</p>	$\phi_{365\text{nm}}:$ 0.3	$\lambda_{\max}:$ 260 nm	$\epsilon_{355\text{nm}}:$ 400 M ⁻¹ cm ⁻¹
<p>2-(4'-(dialkylamino)-4-nitro-[1,1'-biphenyl]-3-yl)propan-1-ol</p>	$\phi_{397\text{nm}}:$ 0.15	$\lambda_{\max}:$ 397 nm	$\epsilon_{397\text{nm}}:$ 7500 M ⁻¹ cm ⁻¹
	$\phi_{380\text{nm}}:$ 0.63	$\lambda_{\max}:$ 259 nm	$\epsilon_{350\text{nm}}:$ 1289 M ⁻¹ cm ⁻¹
<p>1-acyl-7-nitroindoline</p>	$\phi_{347\text{nm}}:$ 0.085	$\lambda_{\max}:$ 246 nm	$\epsilon_{246\text{nm}}:$ 17500 M ⁻¹ cm ⁻¹

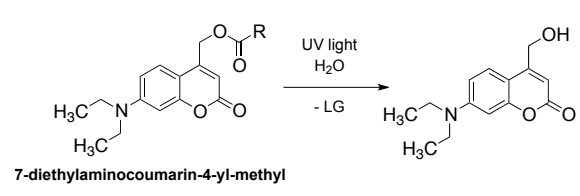
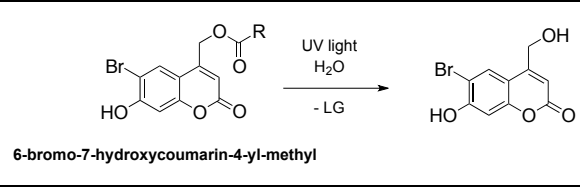
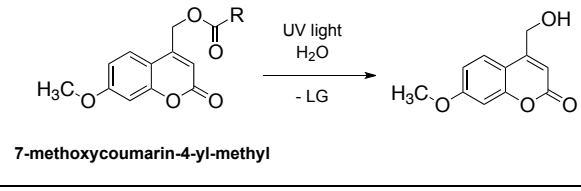
7.1.2 The coumarin photocage

In the 1980's the coumarin photocage was introduced as an alternative to the 2NB photocage family since it has red-shifted and tuneable absorption with large molar absorption coefficients, moderate 2PE cross-sections and 'release and report' fluorescence (the photoproduct fluoresce), and both the photocage and its photoproduct are biologically benign.^[173,175,184] However, the coumarin photocage class have a low quantum yield for the release of carboxylate groups (ϕ_u : 0.04-0.004), but since they absorb in the far UV near visible region with large

molar absorption coefficients they are a fairly good substitute to the 2NB photocage, see Table 7.2.

Among the coumarins the 6-Bromo-7-hydroxycoumarin-4-yl-methyl photocage (see Table 7.2, entry 2) has the highest 2PE action cross-section (δ_u (740 nm): 1.99 GM)^[185] and has recently been used to degrade a polymeric nanoparticle with biologically benign power levels of NIR irradiation (750 nm).^[186]

Table 7.2 Photocages related to the coumarin family. Quantum yield (ϕ), maximum absorption (λ_{max}) and molar absorptivity (ϵ) compiled for the photocage starting material with carboxylate as leaving group.^[173]

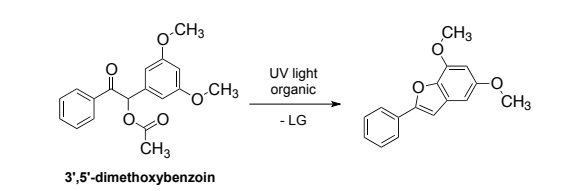
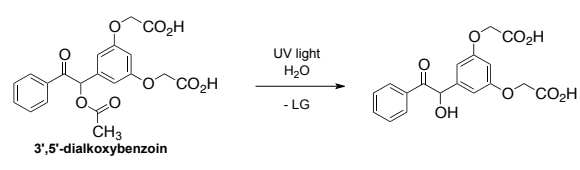
 <p>7-diethylaminocoumarin-4-yl-methyl</p>	ϕ_{365nm} : 0.0058	λ_{max} : 396 nm	ϵ_{396nm} : 17300 M ⁻¹ cm ⁻¹
 <p>6-bromo-7-hydroxycoumarin-4-yl-methyl</p>	ϕ_{365nm} : 0.037	λ_{max} : 370 nm	ϵ_{370nm} : 15000 M ⁻¹ cm ⁻¹
 <p>7-methoxycoumarin-4-yl-methyl</p>	ϕ_{365nm} : 0.0043	λ_{max} : 324 nm	ϵ_{324nm} : 13500 M ⁻¹ cm ⁻¹

7.1.3 The 3',5'-dialkoxybenzoin photocage

The 3',5'-dialkoxybenzoin class of photocages has the highest quantum yield (ϕ_{366} : 0.64)^[187] and most rapid release rate (1-2x10⁹ s⁻¹)^[188,189] of all photocages to date, accompanied by an excellent chemical yield (> 95 %)^[10,187] and clean photolysis, see Table 7.3. Another advantage is that both the photocage and its photoproducts (whose distribution is solvent-dependent) are

biologically benign. Although efficient photochemically, the 3',5'-dialkoxybenzoin photocage has blue-shifted absorbance with a small molar absorption coefficient at UVA wavelengths and its photoproduct (in organic solvent) has a much greater absorbance leading to a self-filtering effect. Furthermore the photocage is insoluble in water without special chemical groups attached to it, which limits its usefulness. See Section 7.5 for further details about the 3',5'-dialkoxybenzoin photocage.

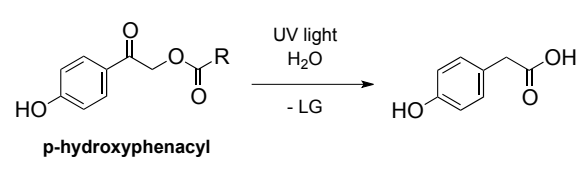
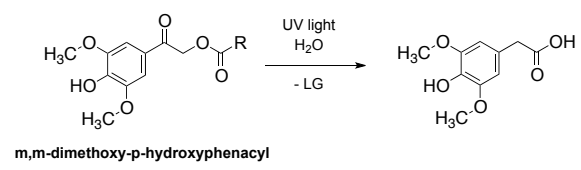
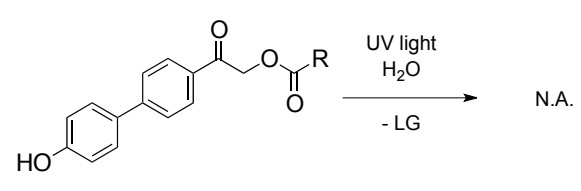
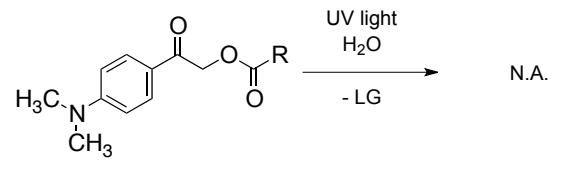
Table 7.3 Photocages in the 3',5'-dialkoxybenzoin family. Quantum yield (ϕ), maximum absorption (λ_{\max}) and molar absorptivity (ϵ) compiled for the photocage starting material with carboxylate as leaving group.^[173]

 <p>3',5'-dimethoxybenzoin</p>	ϕ_{366} : 0.64	λ_{\max} : 246 nm	$\epsilon_{350\text{nm}}$: 291 M ⁻¹ cm ⁻¹
 <p>3',5'-dialkoxybenzoin</p>	$\phi_{366\text{nm}}$: N.A.	λ_{\max} : 246 nm	$\epsilon_{350\text{nm}}$: N.A.

7.1.4 The p-hydroxyphenacyl photocage

The p-hydroxyphenacyl photocage is an efficient photocage with many favourable characteristics including a high photochemical yield, an acceptable quantum yield concomitant with relatively large molar absorption coefficients at UVA wavelengths, see Table 7.4. The rearrangement which leads to the photoproduct has blue-shifted absorbance compared to the photocage starting material and, advantageously, does not compete for light absorption.^[173,184]

Table 7.4 Photocages related to the p-hydroxyphenacyl family. Quantum yield (ϕ), maximum absorption (λ_{\max}) and molar absorptivity (ϵ) compiled for the photocage starting material with carboxylate as leaving group.^[173,183,190,191]

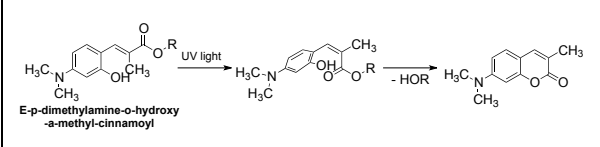
 <p>p-hydroxyphenacyl</p>	$\phi_{307\text{nm}}:$ 0.1	$\lambda_{\max}:$ 279 nm	$\epsilon_{307\text{nm}}:$ 7930 M ⁻¹ cm ⁻¹
 <p>m,m-dimethoxy-p-hydroxyphenacyl</p>	$\phi_{325\text{nm}}:$ 0.035	$\lambda_{\max}:$ 370 nm	$\epsilon_{304\text{nm}}:$ 11730 M ⁻¹ cm ⁻¹
 <p>N.A.</p>	$\phi_{313\text{nm}}:$ 0.21	$\lambda_{\max}:$ 313 nm	$\epsilon_{313\text{nm}}:$ 14800 M ⁻¹ cm ⁻¹
 <p>N.A.</p>	$\phi_{347\text{nm}}:$ N.A.	$\lambda_{\max}:$ 347 nm	$\epsilon_{347\text{nm}}:$ 26000 M ⁻¹ cm ⁻¹

7.1.5 The hydroxy-cinnamoyl photocage

The hydroxy-cinnamoyl photocage is an efficient photorelease system which has both a large molar absorption coefficient and an acceptable quantum yield at UVA wavelengths, see Table 7.5.^[192,193] This photocage is closely related to the photochromic ketone-version (see Scheme 2.2, entry 3) in that a reversible UV light-induced double bond isomerization activates it to cyclize by proximity effect of the carbonyl carbon to the phenolic oxygen. In contrast to the ketone-isomer, the cyclization is irreversible for the ester-isomer, which releases an alcohol upon cyclization to yield a fluorescent coumarin derivative. Since the hydroxy-cinnamoyl photocage is limited to releasing only alcohols and is rather

thermally unstable,^[193] it hampers its practical use even though it is one of the most efficient photocages to date.

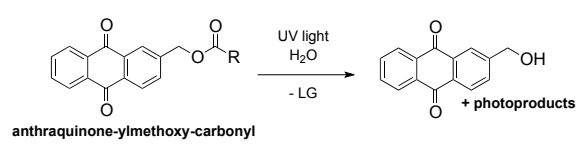
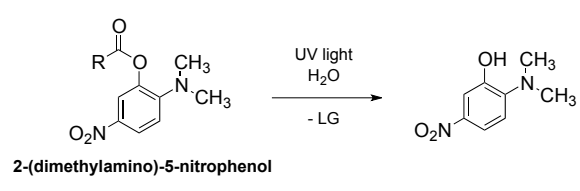
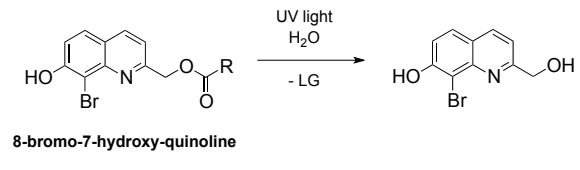
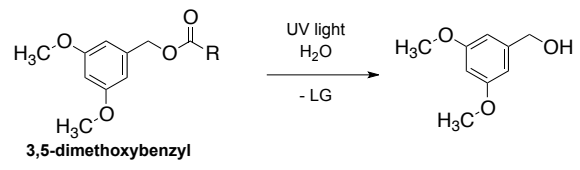
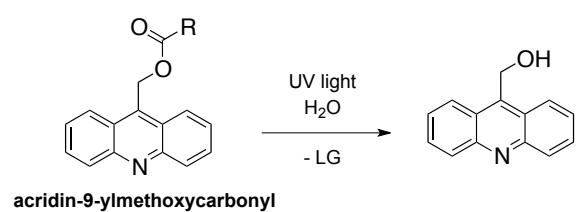
Table 7.5 Hydroxy-cinnamoyl photocage. Quantum yield (ϕ), maximum absorption (λ_{\max}) and molar absorptivity (ϵ) for the photocage starting material with alcohol as leaving group.^[193]

 <p>E-p-dimethylamino-o-hydroxy-a-methyl-cinnamoyl</p>	ϕ_{E-Z} : 0.1	λ_{\max} : 362 nm	$\epsilon_{366\text{nm}}$: 31000 M ⁻¹ cm ⁻¹
---	-----------------------	------------------------------	---

7.1.6 Other UV light triggered photocages

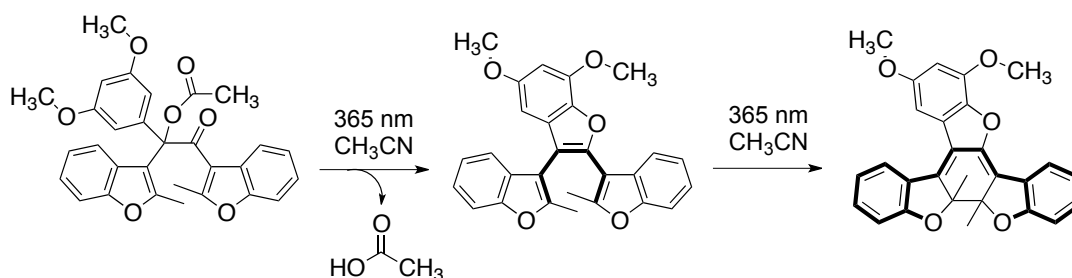
Apart from the photocages discussed above, there are many other UV light triggered photocages described in the literature, see Table 7.6 for various examples.

Table 7.6: Various UV light triggered photocages. Quantum yield (ϕ), maximum absorption (λ_{\max}) and molar absorptivity (ϵ) compiled for the photocage starting material with carboxylate as leaving group.

 <p>anthraquinone-ylmethoxy-carbonyl</p>	$\phi_{350\text{nm}}:$ 0.1	$\lambda_{\max}:$ 327 nm	$\epsilon_{350\text{nm}}:$ 1500 M ⁻¹ cm ⁻¹
 <p>2-(dimethylamino)-5-nitrophenol</p>	$\phi_{335\text{nm}}:$ 0.03	$\lambda_{\max}:$ 400 nm	$\epsilon_{400\text{nm}}:$ 9077 M ⁻¹ cm ⁻¹
 <p>8-bromo-7-hydroxy-quinoline</p>	$\phi_{365}:$ 0.29	$\lambda_{\max}:$ 369 nm	$\epsilon_{369\text{nm}}:$ 2600 M ⁻¹ cm ⁻¹
 <p>3,5-dimethoxybenzyl</p>	$\phi:$ N.A.	$\lambda_{\max}:$ 280 nm	$\epsilon_{280\text{nm}}:$ 1400 M ⁻¹ cm ⁻¹
 <p>acridin-9-ylmethoxycarbonyl</p>	$\phi_{360\text{nm}}:$ 0.021	$\lambda_{\max}:$ 360 nm	$\epsilon_{360\text{nm}}:$ 9050 M ⁻¹ cm ⁻¹

A recently developed hybrid-photocage by Wu and Branda relevant to this thesis is a hybrid system based on the 3',5'-dimethoxybenzoin photocage and a pre-diarylethene photochromic dye.^[194] This photocage is capable of releasing a carboxylic acid upon UVA irradiation and the release event (in organic solvent) subsequently activates the diarylethene moiety, which undergoes a ring-closing reaction with the same UVA light used for the release (reactivity-gated photochromism). This ring-closing event turns solutions containing the

photoproduct red-coloured, and conveniently reports that the release event was successful, see Scheme 7.1.

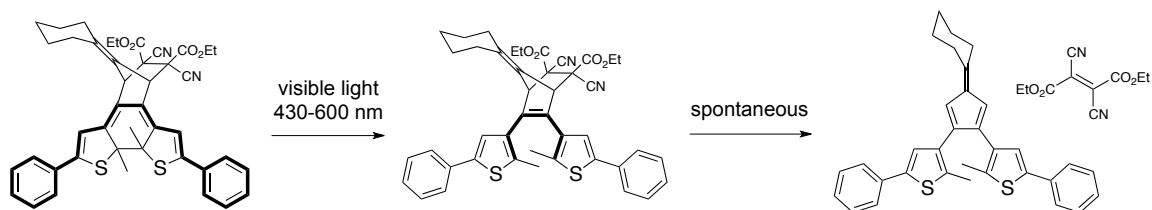


Scheme 7.1 The 3',5'-dimethoxybenzoin-diarylethene hybrid photocage developed by Wu and Branda *et. al.* changes colour upon extended UV light irradiation in organic solvent which conveniently reports successful release.^[194] The bold features highlight the 1,3,5-hexatriene configuration formed after the first photoreaction and the extended conjugation induced after the second photoreaction. The formation of the coloured isomer is an example of reactivity-gated photochromism.

7.2 Visible light triggered photocages

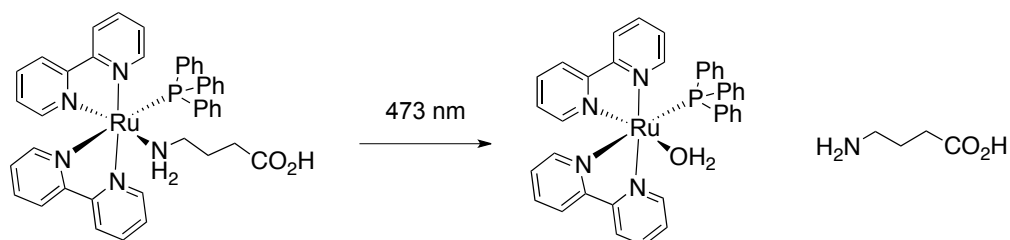
Apart from UV light activated photocages, there also exist a limited number of visible light-triggered and 'stimuli-hybrid' triggered photocages.

A recently developed example of a one-photon visible light triggered photorelease system is based on a DTE dye and the retro Diels-Alder reaction.^[10,57,58] This type of molecule is able to quantitatively release an electron deficient alkene upon visible light irradiation (430-600 nm). Despite being an elegant example of visible light triggered photorelease using low intensity visible light,^[57] electron deficient alkenes of the type required for the Diels-Alder reactivity are reactive, most likely toxic, and append to the released 'active' molecule, which minimizes the scope of its application to practical problems, see Scheme 7.2.



Scheme 7.2 The DTE based photocage originally developed by Lemieux, Gauthier and Branda is capable of releasing an electron deficient dienophile upon visible light irradiation.^[57] The bold features indicate the extended conjugation with absorbance in the visible range of the electromagnetic spectrum and the 1,3,5-hexatriene configuration after ring-opening reaction with visible light. The ring-open isomer spontaneously undergoes a retro Diels-Alder reaction. The release of the dienophile is an example of photochromism-gated reactivity.

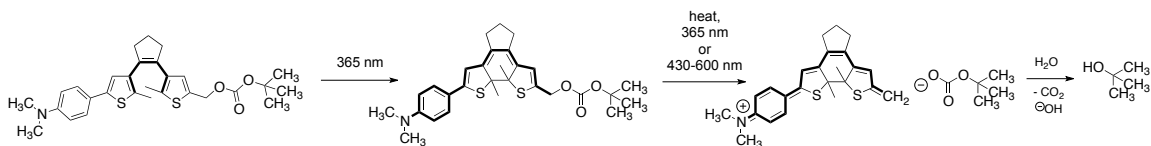
Other visible light triggered photocages are based on Ruthenium complexes, which upon visible light irradiation can release amines and nitric oxide, see Scheme 7.3.^[195,196]



Scheme 7.3 Ruthenium based photocages can be triggered to release an amine upon irradiation with visible light.^[195]

C-J Carling, C. C. Warford and N. R. Branda recently developed a new ‘stimuli-hybrid’ photorelease system.^[197] This novel photocage is based on a ‘self-immolative’^[198] DTE derivate, which is efficiently triggered to an ‘armed’ state upon UVA light irradiation, from which it undergoes the release process with either heat, UV or visible light, see Scheme 7.4. This photocage has been

demonstrated to release tert-butanol attached to the photocage by way of the carbonate. However, the ionic photoproduct has not been fully characterized to date and the complete results of this study have not yet been published. Nevertheless, this photorelease system is unique in that it can be activated with multiple stimuli. Since it can be (partly) triggered by visible light, this new photocage can potentially open new avenues for phototriggered therapeutic release *in vivo*. The absorption of the ring-closed isomer of DTEs can be tuned in the visible region, which makes it attractive for use in living tissue. The photocage could thus potentially be ‘armed’ with UVA light prior to administration, then ‘triggered’ on site *in vivo* either with slow, heat-induced release or one-photon visible light-triggered release. However, the structure of the photoproduct must be identified and the toxicity evaluated prior to any such endeavours, as the photoproduct reacts with nucleophiles (including water) to an uncharacterized product(s).



Scheme 7.4 The ‘stimuli-hybrid’ photocage developed by Carling, Warford and Branda is ‘armed’ with UV light to a coloured intermediate that can be further triggered to release an alcohol with either heat in the dark or upon irradiation with either UV or visible light. The tentative photoproduct on the right side of the scheme has not been fully characterized to date.^[197]

7.3 The 3',5'-dialkoxybenzoin photocage

As partly described in Section 1.4.1.3, the 3',5'-dialkoxybenzoin photocage has both the highest quantum yield of photolysis ($\phi_{366\text{nm}}$: 0.64)^[187] and the most rapid release rate of carboxylate functionality ($1\text{-}2 \times 10^9 \text{ s}^{-1}$) of all known photocages.^[173,188,189] The chemical yield of the clean photoreaction is excellent (> 95 %)^[10,187] and the photoproducts from photolysis in organic solvent or photosolvolysis in water are stable and biologically benign. Despite these excellent features, it does have some unfavourable features that make it less suitable as a photocage in biological settings. Foremost, it is not completely water-soluble unless specific ligands are attached, and the molar absorption coefficient at UVA wavelengths is very small ($\epsilon_{350\text{nm}}$: $291 \text{ M}^{-1}\text{cm}^{-1}$). Furthermore, it is chiral and will produce diastereomers upon coupling with chiral appendices. Moreover, the benzofuran photoproduct (which is the major photoproduct in organic solvents) absorbs light much more intensely than the starting material at UVA wavelengths, which leads to a detrimental self-filtering effect of the incident light, but also a useful 'release and report' fluorescence signal to the user since the photoproduct is fluorescent.

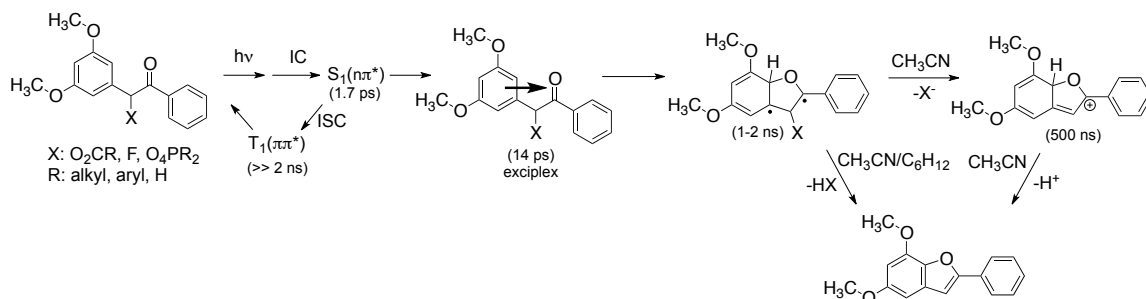
Due to the lack of interest from the scientific community at large in comparison to other photorelease systems, the 3',5'-dialkoxybenzoin photocage family has not been explored to its full potential. For example, the absorption of the photocage has not been adequately red-shifted to absorb UVA light with a large molar absorption coefficient while retaining its characteristic efficiency.^[199,200] Moreover, its two-photon excitation cross-section has not been

characterized or tuned (most likely due to a low intrinsic 2PE cross-section), and examples of fully water soluble derivatives are scarce.^[201]

7.3.1 Photolysis mechanism of 3',5'-dialkoxybenzoin in organic solvent

The mechanism of the photodeprotection reaction of the 3',5'-dimethoxybenzoin photocage has long been debated and many alternative mechanisms have been proposed throughout the years.^[187,188,189,200,201,202,203,204,205] It has been found that the photoproduct distribution of the photoreaction is strongly dependent on solvent.^[188,189,201] In both polar organic solvents such as CH₃CN and in nonpolar organic solvents such as cyclohexane the product outcome of the photoreaction is similar and 5,7-dimethoxy-2-phenylbenzofuran is the major observed photoproduct apart from the released substrate.^[188,189] However, the branching ratio of the photogenerated transient intermediates leading up to the formation of benzofuran is different in these two solvents.^[188,189] By using Femtosecond transient absorption spectroscopy^[188,189] and nanosecond time-resolved resonance Raman spectroscopy^[189] the transient intermediates leading up to product formation have recently been probed. Electronic interaction between the two benzoyl and dimethoxybenzyl sub-chromophores is responsible for initiating a rapid and stepwise cyclization-deprotection pathway in the S₁ excited state in organic solvent.^[188,189,205] After the benzoyl moiety is excited to the S₁(nπ*) state by UV light, a charge transfer exciplex^[188,189,203,205] is rapidly established between the electron-rich dimethoxybenzyl moiety and the benzoyl moiety in the excited state which subsequently leads to cyclization and the formation of a

biradical species.^[188,189,201] Depending on organic solvent polarity this biradical species has two fates.^[188,189] The primary reaction pathway that occurs in both CH₃CN and in cyclohexane is the concerted elimination of HX and formation of the benzofuran, see Scheme 7.5.^[188,189] In CH₃CN, however, a second reaction pathway exists which eliminates X⁻ and produces a cyclic cation with a large molar extinction coefficient that is relatively long lived but apparently not^[188,189] the primary photoproduct of the reaction as has been previously postulated.^[200,203,204] Moreover, when the CH₃CN solvent is doped with small quantities of water the transient species assigned to the cyclic cation is not observed.^[188,203]

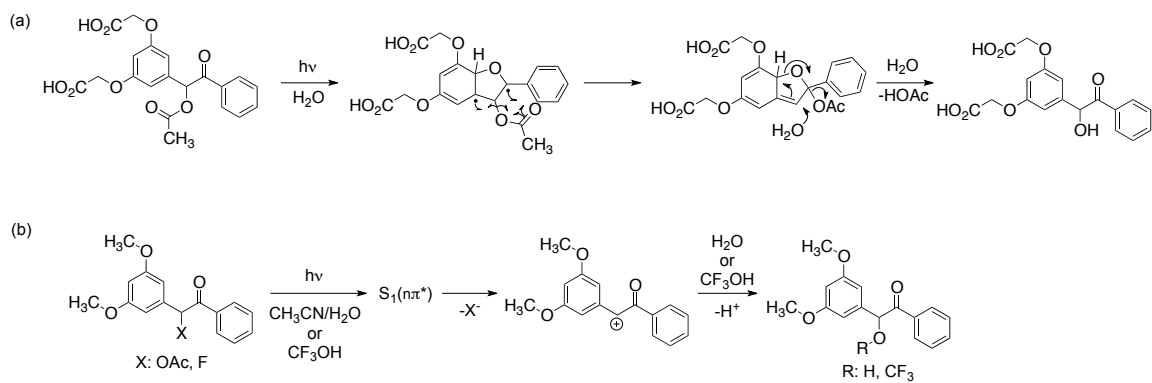


Scheme 7.5 Mechanism of 3',5'-dimethoxybenzoin photolysis in organic solvent according to recent literature.^[188,189,205] IC: internal conversion, ISC: inter system crossing.

7.3.2 Photosolvolysis mechanism of 3',5'-dialkoxybenzoin in water

Due to the water insoluble nature of the 3',5'-dimethoxybenzoin photocage, no in-depth mechanistic studies have been conducted on the photocage in pure water.^[188,201,203] The major photoproduct of the 3',5'-dialkoxybenzoin^[188,201] and benzoin^[206] photocages upon UV light irradiation in water is the solvent captured

benzoin, and not the benzofuran photoproduct as is encountered in organic solvent. It is thus apparent that in water the reaction mechanism of the 3'5'-dialkoxybenzoin photocage is somewhat different than in organic solvent and that the benzylic carbon is accessible to the nucleophilic attack by water at some point during the photolysis pathway. Two different mechanisms have been proposed for the photosolvolysis mechanism in water to explain this phenomenon.^[188,189,201,204,206] The first mechanism proposed by Rock and Chan,^[201] who were the first to observe the benzoin photoproduct formation in water, is based on the formation of a cyclized biradical intermediate followed by acetoxy migration to an intermediate that can either be trapped by water to form benzoin or react to the benzofuran, see Scheme 7.6a. The second major proposed mechanism is based on heterolytic cleavage to a benzylic cation that can subsequently be trapped by water, see Scheme 7.6b.^[188,204,189,206] Although conclusive evidence does not exist to support either pathway, recent research papers suggests the second mechanism is favoured due to the high dissociation and solvation capacity of water.^[188,189]



Scheme 7.6 (a) Photosolvolytic mechanism of 3',5'-dialkoxybenzoin in water according to Rock and Chan.^[201] (b) Photosolvolytic mechanism of 3',5'-dimethoxybenzoin in aqueous CH₃CN (60 % water v/v) or in CF₃OH according to Wirz *et. al.*^[188] and supported by others.^[189,204,206]

8: 'REMOTE-CONTROL' PHOTO-RELEASE OF 'CAGED' COMPOUNDS USING NEAR INFRARED LIGHT AND UPCONVERTING NANOPARTICLES

8.1 Contributions

The text in this chapter has previously been published as a communication in *Angewandte Chemie International Edition* (and was featured as a 'hot paper' by the journal) and is reproduced herein in its entirety with permission from the journal (C.-J. Carling, F. Nourmohammadian, J.-C. Boyer, N. R. Branda, *Angew. Chem. Int. Ed.*, **2010**, 49, 3782-3785, <http://onlinelibrary.wiley.com/doi/10.1002/anie.201000611/abstract>). The project was co-designed by C-J Carling, Dr. J-C Boyer and Prof. Dr. N. R. Branda. 80 % of the synthesis of **1** was performed by Prof. Dr. F. Nourmohammadian and the rest by C-J Carling by following literature procedures. The synthesis of the *core-shell* oleate coated nanoparticle and characterizations of all nanoparticles (TEM, XRD) were performed by Dr. J-C Boyer. The functionalization of the UCNP with **1** was performed by Dr. J-C Boyer and C-J Carling. All one-photon and 'remote-control' photochemistry were measured by C-J Carling. The ¹H NMR photolysis study of **1** was performed by C-J Carling. Calculation of loading was performed by C-J Carling. Fluorescence spectroscopy of **1a**[NaYF₄:TmYb] was performed by Dr. J-C Boyer. The manuscript was co-written by C-J Carling, Dr. J-C Boyer and Prof. Dr. N. R. Branda. The experimental section was co-written by C-J Carling, Dr. J-C Boyer and Prof. Dr. N. R. Branda.

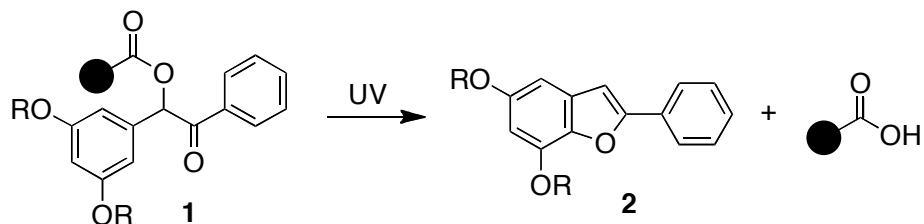
8.2 Abstract

Lanthanide doped upconverting nanoparticles are used to convert near infrared light into ultraviolet light to drive the photoinduced release of a 'caged' species decorated onto the nanoparticles' surface. This approach overcomes the problem that low energy light is necessary for penetrating deeper into tissue without damage but cannot be used to directly trigger important organic photochemical reactions.

8.3 Introduction

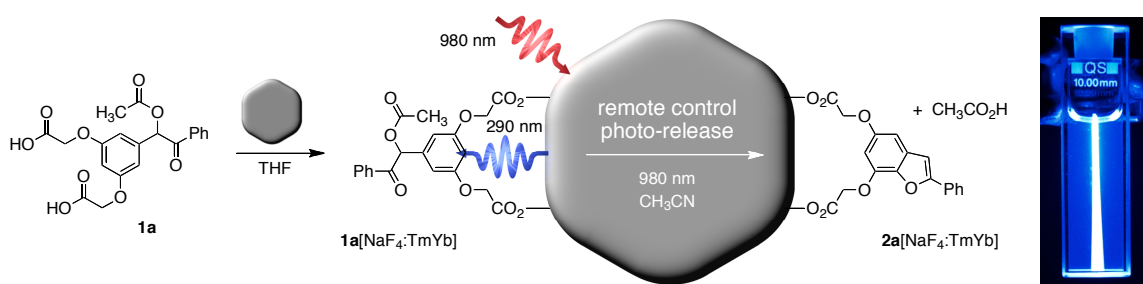
Releasing molecules from 'caged' forms using light as the trigger offers the potential to deliver innocuous agents to cells, tissues and organisms, where they can be unmasked to their active states.^[173] Because light can be readily tuned and focused, it can be spatially and temporally controlled to provide 'on-command' drug delivery, unmasking of biochemical agents for enzyme and protein activation, and other biochemical and physiological studies. Several classes of small-molecule systems have been developed for use in these applications but all suffer from a serious drawback – they demand high-energy ultra-violet or visible light as the trigger. Until methods using less detrimental, lower-energy light that penetrates deeper into tissue without causing unwanted side reactions are developed, this technology will not find the widespread acceptance it deserves.^[173,207]

Multi-photon excitation with near-infrared (NIR) light has been presented as a practical solution to the issues associated with using UV or visible light, given it is less damaging and reaches deeper into tissue.^[208,209] What is preventing the general use of the multi-photon excitation technique is that many 'cages' do not have large enough multi-photon cross-sections to be susceptible to NIR light, or that their susceptibility is linked to wavelengths of light that lie outside of the tuning-range of pulsed lasers.^[210,211] One illustrative example is the 3',5'-dialkoxybenzoin cage **1** (Scheme 8.1), which along with 2-nitrobenzyl, coumarin-4-yl-methyl, *p*-hydroxyphenacyl and 7-nitroindoline derivatives, is one of the most commonly employed classes of 'photo-cages'.^[173] This versatile compound exhibits many appealing features. Its photochemistry is relatively universal, and esters, carbonates, carbamates and phosphates can all be employed for photorelease.^[199,201,202,212,213,214,215] The high quantum yield (> 0.6) and fast rate (10^{10} – 10^{12} s⁻¹) of photolysis allows efficient release (typically greater than 95 %) using short laser pulses.^[173,215] The photorelease also generally lacks side reactions, and a single 5,7-dialkoxy-2-phenylbenzo[*b*]furan (**2**) species (other than the released acid, alcohol, amine or phosphate) in organic solvents is generated.^[173,216]



Scheme 8.1 Photolysis and release of 'caged' compounds from the generalized 3',5'-dialkoxybenzoin structure **1** using UV light to produce 2-phenylbenzo[*b*]furan **2** and a carboxylic acid. Alcohols, amines, and phosphates can also be released using this technology.

The 'cage' compound's need for unsuitable UV light can be overcome by coupling the 3',5'-dialkoxybenzoin to near-infrared (NIR) absorbing species that act as antennae, harvest the light and convert it into the necessary UV light through a multiphoton process. Monodispersed, core-shell, upconverting nanoparticles (UCNPs) composed of NaYF₄ nanocrystals doped with lanthanides such as Tm³⁺ and Yb³⁺ (NaYF₄:TmYb) are excellent candidates for this task.^[9,217,218,219] These UCNPs convert continuous-wave 980 nm laser light into a range of different wavelengths of light throughout the UV, visible and NIR regions, many of which can be harnessed to drive the photoreactions of compounds anchored to their surfaces.^[9,217,218,219,220,221,222] This 'remote-control' photorelease is illustrated in Scheme 8.2 and is the focus of the studies described herein. Although we demonstrate the success of this strategy using a model compound that releases a carboxylic acid, this technology is expected to be very general and be able to perform equally well to release other caged compounds.



Scheme 8.2 Decoration of upconverting nanoparticles with 3',5'-di(carboxymethoxy)benzoic acid 'cage' **1a** produces the 'remote-control' releasing system (**1a**[NaF₄:TmYb]), which can be triggered by indirect irradiation with NIR light to generate **2a**[NaF₄:TmYb] and release a carboxylic acid. The photograph shows the blue light emitted when a solution of the UCNPs is irradiated with 980 nm light.

The appeal of UCNPs over multi-photon absorbing molecules can be justified on many levels. First and foremost, the Tm³⁺ and Yb³⁺ energy levels involved in the photophysics of the NaYF₄:TmYb nanoparticles are real and the multiple absorptions are sequential as opposed to the simultaneous absorptions needed for typical two-photon excitation.^[223] This reduces the power density of the excitation source to about 10⁴–10⁷ orders of magnitude lower than what is required for multi-photon photolysis, and allows for the employment of more economical, continuous wave diode laser instead of a pulsed laser.^[223] In biological applications, the use of a nanoparticle as a delivery vehicle offers additional benefits compared to molecular photorelease. (1) UCNPs can be coated with biocompatible polymers rendering them water soluble to lengthen blood circulation time and attenuate uptake by the reticuloendothelial system,^[224,225] (2) their surfaces can be loaded with multiple, different therapeutic agents to offer synergistic effects,^[226,227] and with antibodies or other ligands to provide targeting and selectivity,^[222] (3) because water solubility and

biocompatibility are both provided by the decorated UCNPs, the 'cage' itself can be lipophilic overcoming one of the most significant problems associated with the benzoin class of compounds,^[201] and (4) the luminescent nature of the UCNPs make them ideal for providing information about where and when the release event has taken place ('release-and-report').^[228,229] UCNP based on lanthanide-doped NaYF₄ nanoparticles have already been shown to be biocompatible and non-toxic,^[230] and have been used for *in vitro* photodynamic therapy,^[224,225,226] *in vitro* and *in vivo* fluorescence bio-imaging,^[231,232,233] and other biological applications.^[234,235,75a]

8.4 Results and discussion

The core-shell, lanthanide-doped NaYF₄:TmYb nanoparticles (core = NaYF₄:0.5 mol% Tm³⁺:30 mol% Yb³⁺; shell = NaYF₄) were synthesized by following the protocol of Zhang and co-workers^[9,75] with some minor modifications.^[236] TEM images of the UCNPs demonstrate their nearly monodisperse particle size of height 44.7 ± 1.8 nm and diameter 41.4 ± 1.4 nm.^[236] Powder X-ray diffraction^[236] confirms that the nanoparticles are highly crystalline and are hexagonal in phase with no significant impurity phases present. The synthesis results in nanoparticles coated in oleate, which we anticipated could be displaced by a compound bearing two carboxylic acid groups. The previously described 3',5'-bis(carboxymethoxy)benzoin acetate **1a** (Scheme 4.2) suits this requirement well and was synthesized according to the literature procedures.^[201]

Figure 4.1a illustrates how the absorption spectrum of 3',5'-bis(carboxymethoxy)benzoin acetate **1a** partially overlaps ($\lambda = 282$ nm) with the emission spectrum of the NaYF₄:TmYb nanoparticles ($\lambda = 290$ nm), and illustrates the rationale behind our choice of UCNPs and 'photo-cage'. When a CD₃CN solution of benzoin **1a** (8.87×10^{-3} M) is exposed to UV light (313 nm), it is converted within 100 min^[237] into its 5,7-bis(carboxymethoxy)-2-phenylbenzo[*b*]furan (**2a**) counterpart and acetic acid in high yield (> 95 %) as measured by ¹H NMR spectroscopy.^[238] As expected, no hydrolyzed benzoin derivative was observed. The ¹D₂ → ³H₆ transition of the NaYF₄:TmYb nanoparticles also provides the UV light indirectly when irradiated with 980 nm light and should be effective to trigger the un-caging process in a 'remote-control' process.

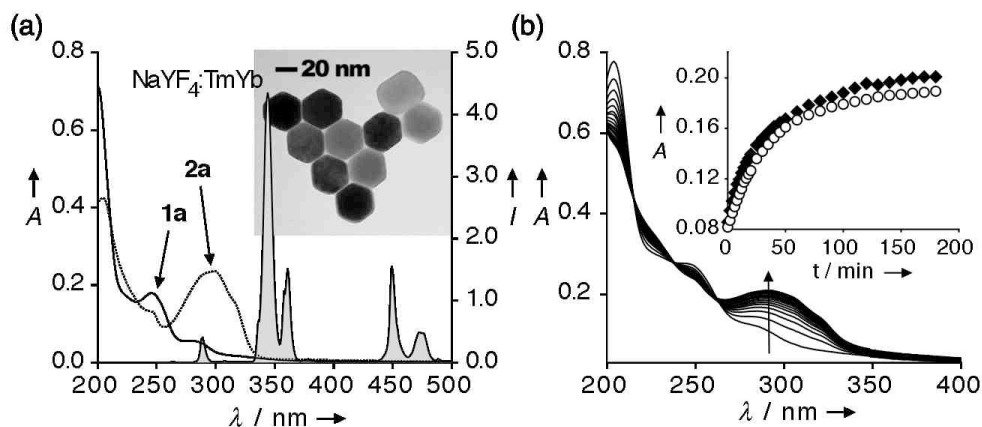


Figure 8.1 (a) UV-vis absorption spectra of a CH₃CN solution (8.54×10^{-6} M) of 3',5'-di(carboxymethoxy)benzoin **1a** before (solid line) and after irradiation with 365 nm light (dashed line) for 35 min, and the emission spectrum of a THF solution (1 wt-%, $\lambda_{\text{ex}} = 980$ nm) of the NaYF₄:TmYb core-shell UCNPs (shaded). The inset shows the TEM photograph of **1a**[NaYF₄:TmYb] illustrating their uniform size and hexagonal prism shape. (b) Changes in the UV-vis absorption spectra of a CH₃CN solution of **1a**[NaYF₄:TmYb] when it is irradiated with 980 nm light (power = 4.4 W, power density = 550 W/cm²).^[236,239] The inset shows the changes in the absorbance at 300 nm when samples of the same solution are irradiated with 290 nm (circles) and 980 nm light (diamonds).

The NaYF₄:TmYb nanoparticles were loaded with 3',5'-bis(carboxymethoxy)benzoin acetate **1a** by simply stirring a colloidal dispersion of the two components overnight in THF.^[236] After a number of centrifuging–resuspending purification cycles, the decorated nanoparticles (**1a**[NaYF₄:TmYb]) were dispersed in CH₃CN to provide a stock solution that is stable at room temperature for more than 4 weeks if stored in the dark (see inset to Figure 8.1a for a TEM image of the decorated UCNPs). Sample solutions for subsequent photolysis experiments were prepared by further dilution with CH₃CN. The loading of 3',5'-di(carboxymethoxy)benzoin **1a** onto the NaYF₄:TmYb nanoparticles was estimated by calculating the number of particles in an aliquot amount of the CH₃CN stock solution and the amount of chromophore **1a**

removed from the UCNP surfaces when a similar aliquot was treated with excess methylphosphonic acid to induce ligand exchange, and analyzed by UV-vis absorption spectroscopy. 3',5'-Di(carboxymethoxy)benzoin **1a** was loaded onto the NaYF₄:TmYb nanoparticles with an average amount of approximately 2 wt-% corresponding to approximately 6800 molecules of 'cage' per nanoparticle.^[236]

Exposing a CH₃CN solution of free benzoin 'cage' **1a** to 980 nm continuous wave laser light (power = 4.37 W, power density = 556 W/cm²) resulted in no observable changes in the UV-vis absorption spectrum even after 1 hour of irradiation^[236] demonstrating that the photo-cage is, as expected, not susceptible to direct multi-photon release in the absence of the UCNP. On the other hand, the 'remote-control' strategy employing **1a**[NaYF₄:TmYb] is very effective as shown by the changes in the spectrum of a CH₃CN dispersion of the decorated nanoparticles when it is exposed to NIR light. As illustrated in Figure 8.1b, NIR light (980 nm) triggers a decrease in the absorptions in the UV region (λ_{max} = 203 nm and 248 nm) and a concomitant increase in longer wavelength absorptions (λ_{max} = 283–292 nm) corresponding to 5,7-bis(carboxymethoxy)-2-phenylbenzo[*b*]furan attached to the nanoparticles (**2a**[NaYF₄:TmYb]), which have spectral profile that are the same as those recorded when a dispersion of the **1a**[NaYF₄:TmYb] nanoparticles are exposed to UV light (290 nm) to trigger the direct photorelease.^[236,240] It can be assumed that the photorelease is due to the 290 nm light generated by the multiphoton process. The changes in the

absorptions at 300 nm corresponding to benzofuran **2a**[NaYF₄:TmYb] induced using 980 nm ('remote-control' excitation) are almost identical to those produced using direct excitation (290 nm) suggesting that the two photolysis reactions are the same (inset to Figure 1b).^[241] These experiments also imply that both direct and indirect irradiation drive the photolysis reaction yield to the same extent.

8.5 Conclusion

The NIR-activated organic-nanoparticle hybrid system described in this report has the potential to increase selectivity in photodynamic therapy and biochemical studies. The harnessing of low-energy NIR light and converting it into high-energy UV light overcomes the drawback that typical organic reactions cannot be triggered by the former even though this type of light is necessary for biological applications. Our next generation of 'cage-decorated' UCNP will take advantage of the fact that the NaYF₄:TmYb nanoparticles have their most intense emission bands at 333–355 nm when excited by 980 nm light (Figure 8.1a). Designing 3',5'-dialkoxybenzoin derivatives having red-shifted absorptions will better match the chromophore's absorbances with the nanoparticles' emission, and enhance the efficiency of the 'remote-control' photo-release. If properly designed the improved system should also have red-shifted bands only in its benzoin form eliminating any self-filtering effects the benzofuran photoproduct has due to its absorbing 290 nm more effectively. The results of these studies will be reported in due course.

8.6 Acknowledgement

This research was supported by the Natural Sciences and Engineering Research Council (NSERC) of Canada, the Canada Research Chairs Program, and Simon Fraser University through funding from the Community Trust Endowment Fund. J.–C. Boyer thanks the Michael Smith Foundation for Health Research for support. We are grateful to Prof. Melanie O'Neill for use of a spectrophotometer and to Dr. Andrew Lewis for help with the ^1H NMR spectroscopy studies.

8.7 Experimental

8.7.1 General methods

8.7.1.1 Materials

All solvents and reagents used for synthesis, chromatography, UV–vis spectroscopy measurements and photolysis studies were purchased from Aldrich and used as received, unless otherwise noted. Solvents for NMR analysis were purchased from Cambridge Isotope Laboratories and used as received. Column chromatography was performed using silica gel 60 (230–400 mesh) from Silicycle Inc. The NaYF_4 Tm^{3+} 0.5%, Yb^{3+} 30% / NaYF_4 core/shell nanoparticles were synthesized using a modification of a recently reported procedure.^[9,75] Molecule **1a** was synthesized as described in the literature.^[201] All volumes for absorption, photolysis and concentration measurements/studies were measured out using an autopipette.

8.7.1.2 Instrumentation

^1H NMR and ^{13}C NMR characterizations of all synthetic precursors to **1a** were performed on a Bruker TCI 600 cryoprobe (proton sensitive, inverse probe) working at 600.33 MHz for ^1H and 150.97 MHz for ^{13}C and was found to match the reported data. The ^1H NMR photolysis studies were performed on CD_3CN solutions using a Bruker BioSpin 500 with 32 scans per measurement. UV–vis absorption spectroscopy was performed using a Varian Cary 300 Bio spectrophotometer and a Varian Cary 100 Bio spectrophotometer. X-ray Diffraction (XRD) was measured utilizing a Rigaku R-AXIS RAPID-S diffractometer (Model No. 2163A101). TEM images were recorded on a FEI Tecnai 200 keV Field Emission Scanning Transmission Electron Microscope. Fluorescence measurements of the $\beta\text{-NaYF}_4: 0.5\% \text{Tm}^{3+}, 30\% \text{Yb}^{3+}$ / $\beta\text{-NaYF}_4$ Core/Shell Nanocrystals and direct light photolysis experiments of **1a**[$\text{NaYF}_4:\text{TmYb}$] were performed on a PTI Quantamaster spectrofluorometer. Indirect light photolysis of the **1a**[$\text{NaYF}_4:\text{TmYb}$] were performed a JDS Uniphase 980 nm laser diode (device type L4-9897510-100M) coupled to a 105 μm (core) fibre as the excitation source. The output of the diode laser was collimated and directed on the samples using a Newport F-91-C1-T Multimode Fiber Coupler. All solution-state photoreactions of **1a** were carried out using the light source from a lamp used for visualizing TLC plates at 313 nm or 365 nm (Spectroline E-series, 2.1 mW/cm^2 , 1.4 mW/cm^2).

8.7.2 Synthetic procedures

8.7.2.1 Synthesis of β -NaYF₄: 0.5% Tm³⁺, 30% Yb³⁺ core nanoparticles

In a typical synthesis, Y(CH₃CO₂)₃ hydrate (99.9 %, 0.4560 g, 1.39 mmol), Yb(CH₃CO₂)₃ hydrate (99.9 %, 0.2533 g, 0.60 mmol) and Tm(CH₃CO₂)₃ hydrate (99.9 %, 0.0042 g, 0.01 mmol) were added to a 100 mL three-neck round-bottom flask containing octadecene (30 mL) and oleic acid (12 mL). The solution was stirred magnetically and heated slowly to 115 °C under vacuum for 30 min to form the lanthanide oleate complexes, and to remove residual water and oxygen. The temperature was then lowered to 50 °C and the reaction flask placed under a gentle flow of nitrogen gas. During this time, a solution of ammonium fluoride (0.2964 g, 8 mmol) and sodium hydroxide (0.2 g, 5.0 mmol) dissolved in methanol (20 mL) was prepared *via* sonication. Once the reaction reached 50 °C, the methanol solution was added to the reaction flask and the resulting cloudy mixture was stirred for 30 min at 50 °C. The reaction temperature was then increased to 70 °C and the methanol evaporated from the reaction mixture. Subsequently, the reaction temperature was increased to 300 °C as quickly as possible and maintained at this temperature for 60 min under the nitrogen gas flow. During this time the reaction mixture became progressively clearer until a completely clear, slightly yellowish solution was obtained. The mixture was allowed to cool to room temperature. The nanoparticles were precipitated by the addition of ethanol and isolated *via* centrifugation at 4500 rpm corresponding to a relative centrifugal field (RCF) of approximately 1000. The resulting pellet was dispersed in a minimal amount of hexanes and precipitated with excess ethanol.

The nanoparticles were again isolated *via* centrifugation at 4500 rpm and then dispersed in hexanes (10–15 mL) for the subsequent shell growth procedure.

8.7.2.2 Synthesis of β -NaYF₄: 0.5% Tm³⁺, 30% Yb³⁺/ β -NaYF₄ core/shell nanocrystals (NaYF₄:TmYb)

Y(CH₃CO₂)₃ hydrate (99.9 %, 0.5741 g, 1.75 mmol) of was added to a 100 mL three-neck round-bottom flask containing octadecene (30 mL) and oleic acid (12 mL). The solution was heated slowly to 115 °C under vacuum with magnetic stirring for 30 min to form Y(oleate)₃ and to remove residual water and oxygen. The temperature was lowered to 80 °C, the reaction flask placed under a gentle flow of nitrogen and treated with the hexanes solution of core NaYF₄: 0.5% Tm³⁺, 30% Yb³⁺ nanoparticles (10–15 mL). The resulting solution was maintained at 80 °C until all the hexanes were removed. The reaction mixture was cooled to 50 °C and treated with a solution of ammonium fluoride (0.2593 g, 7 mmol) and sodium hydroxide (0.1400 g, 3.5 mmol) dissolved in methanol (20 mL). The resulting cloudy mixture was stirred for 30 min at 50 °C at which time the reaction temperature was increased and the methanol evaporated. After the evaporation of the methanol, the reaction temperature was increased to 300 °C as quickly as possible and maintained at this temperature for 60 min under the nitrogen gas flow. The mixture was allowed to cool to room temperature and the nanoparticles isolated using the same procedure of precipitate and isolation described for the core nanoparticles. The isolated NaYF₄:TmYb nanoparticles were then dispersed in THF (~15 mL) for subsequent experiments.

8.7.2.3 Synthesis of **1a**[NaYF₄:TmYb]

A colloidal dispersion of NaYF₄:TmYb nanocrystals (1 g, 4.5 wt-% in THF) was added to a vial containing **1a** (1.6 mg) and a stir-bar. The dispersion was diluted with THF (3 mL) and stirred over night wrapped in foil. The clear suspension was transferred to 4 Eppendorf tubes and EtOH was added to the 1.5 mL mark. The vials were agitated and centrifuged (13500 g, 25 min). The supernatant was removed and the translucent pellet was re-suspended in CH₃CN by sonication. The sample was centrifuged (13500 g, 25 min) and the supernatant removed. The translucent pellet was re-suspended in CH₃CN and used for subsequent experiments.

8.7.3 Powder X-ray Diffraction

The nanoparticles samples were characterized by X-ray Diffraction (XRD) utilizing a Rigaku R-AXIS RAPID-S diffractometer (Model No. 2163A101). Samples were drop-cast onto thin glass cover slips from THF and then allowed to dry.

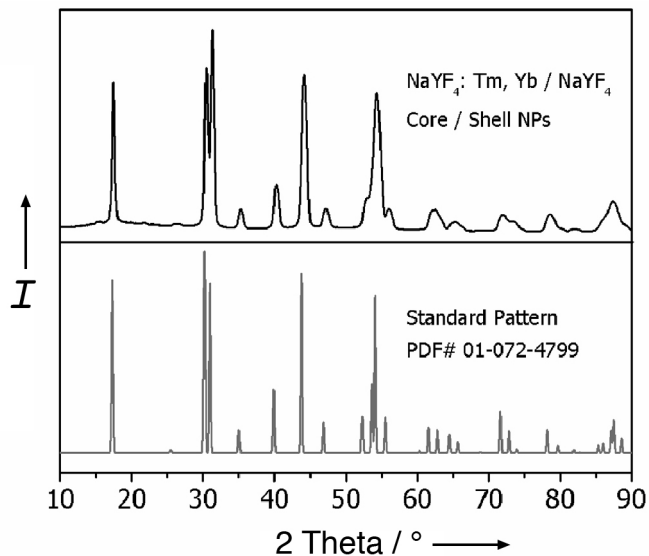


Figure 8.2 Powder X-ray diffraction (XRD) patterns for NaYF₄:TmYb nanoparticles (top) and β-NaYF₄ standard pattern (bottom). The intensities (*I*) were normalized in both cases.

8.7.4 Transmission Electron Microscopy (TEM)

A FEI Tecnai 200 keV Field Emission Scanning Transmission Electron Microscope was used to collect transmission electron microscopy (TEM) and high-resolution TEM (HR-TEM) images. Dilute colloids of the nanoparticles (0.1 wt%) dispersed in THF were dropcasted on thin, carbon formvar-coated copper grids for imaging. The NP shape and crystallinity were evaluated from the collected TEM images, while the particle size was calculated from over 200 TEM particles.

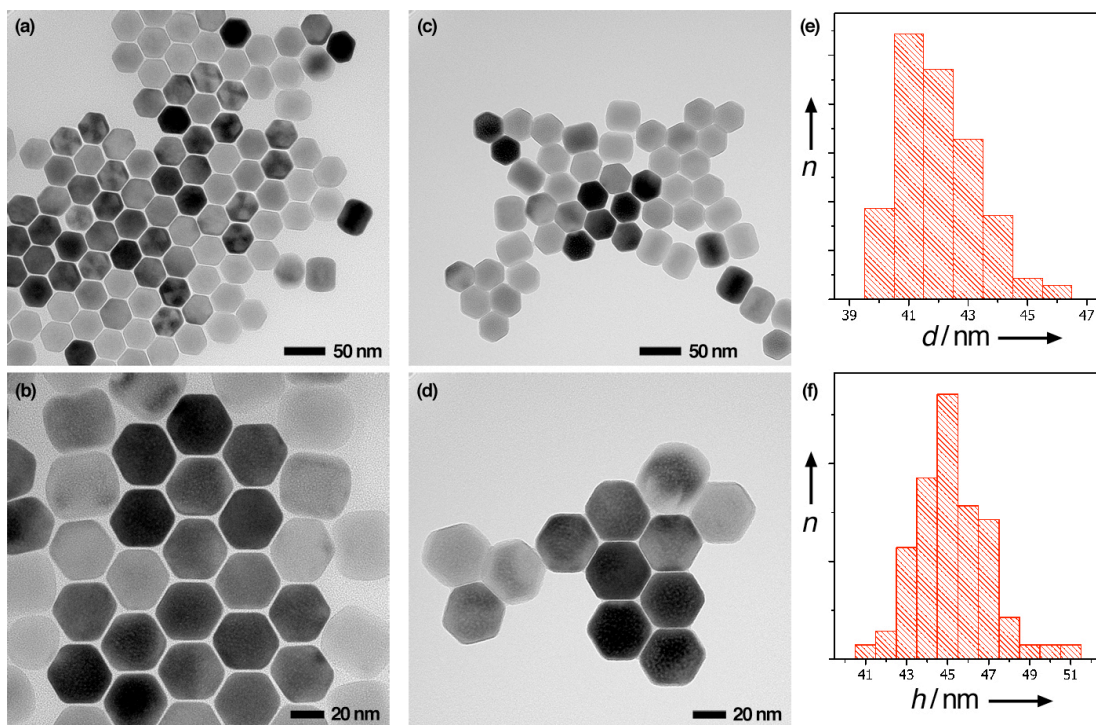
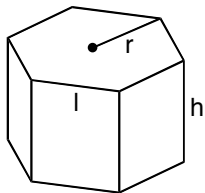


Figure 8.3 Transmission Electron Microscopy (TEM) micrographs of (a,b) NaYF₄:TmYb nanoparticles and (c,d) decorated **1a**[NaYF₄:ErYb] nanoparticles, and (e,f) size histograms for NaYF₄:TmYb showing the number of nanoparticles (n) for diameter (d) and height (h).

8.7.5 Estimating the loading of ‘cage’ **1a** onto NaYF₄:TmYb nanoparticles

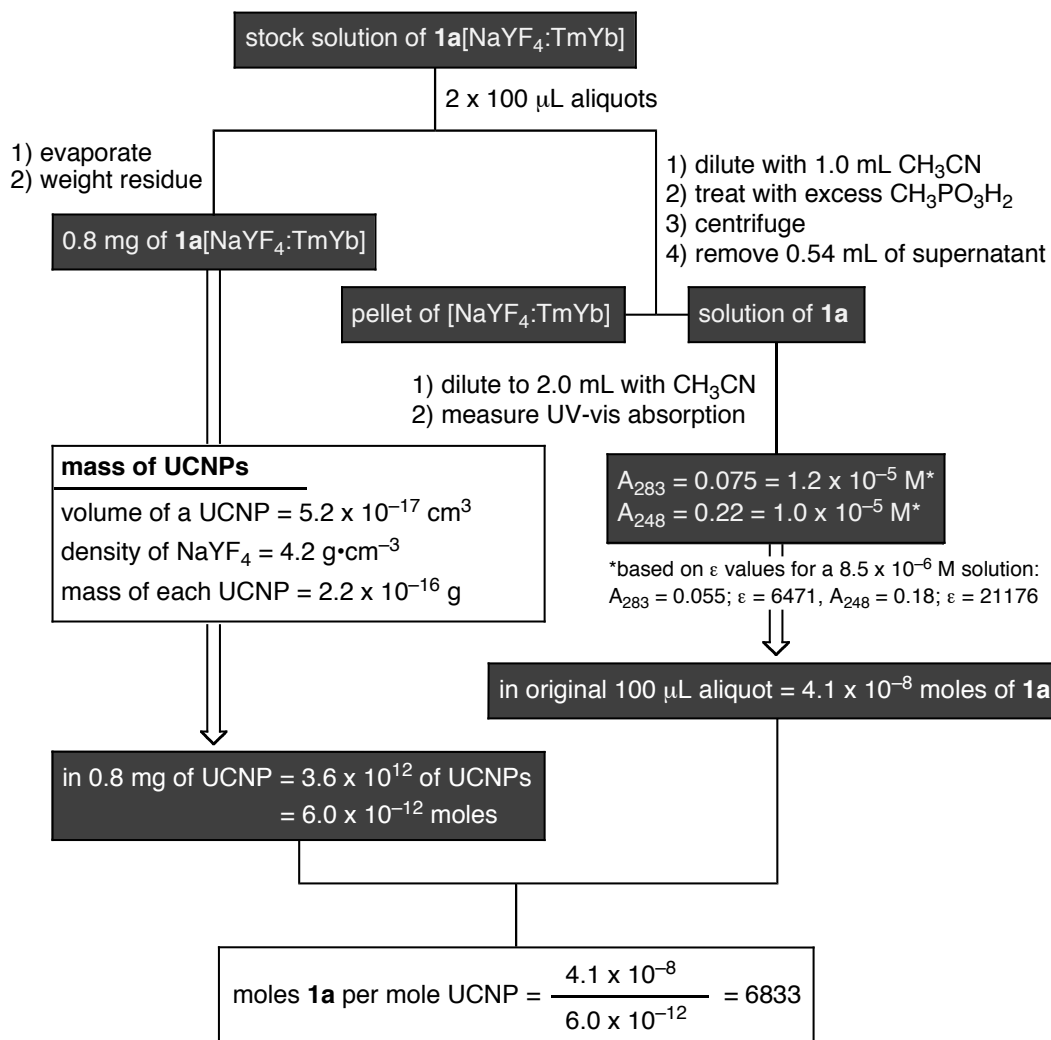
The amount of organic chromophore loaded onto the UCNPs was estimated by comparing the number of moles of the nanoparticles in an aliquot amount of the stock solution to the number of moles of **1a** removed from the UCNPs when excess methylphosphonic acid is added to induce ligand exchange. The mass of the UCNPs was calculated from the size and the density of crystalline NaYF₄ reported in the literature^[242] as outlined below. The amount of **1a** released into the solution was measured using UV-vis absorption spectroscopy.



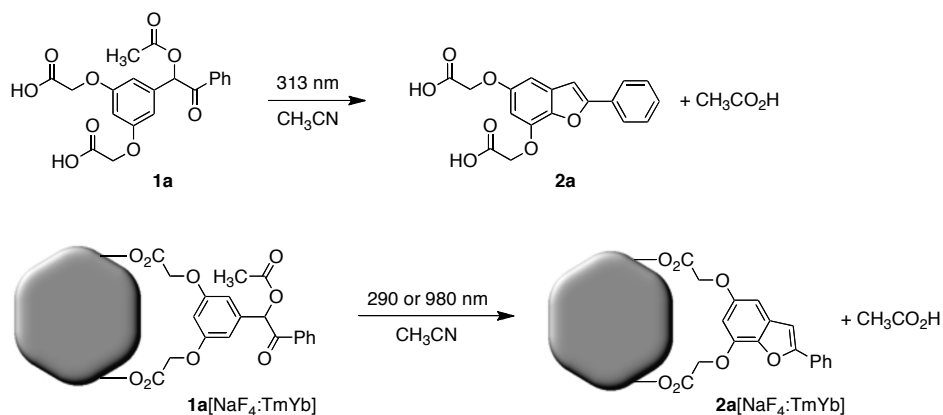
$$l, r = 21 \text{ nm}$$

$$h = 45 \text{ nm}$$

$$\text{volume} = \frac{3\sqrt{3}}{2} r^2 h$$



8.7.6 Photolysis experiments



8.7.6.1 Monitoring the photolysis by ^1H NMR spectroscopy

'Cage' **1a** (2.5 mg, 6.2 μmol) was dissolved in CD_3CN (0.7 mL) to afford a 8.87×10^{-3} M solution. This solution was irradiated with 313 nm light and the changes in its ^1H NMR spectrum were recorded (100 min) until all the starting material was consumed (Figure 8.4).

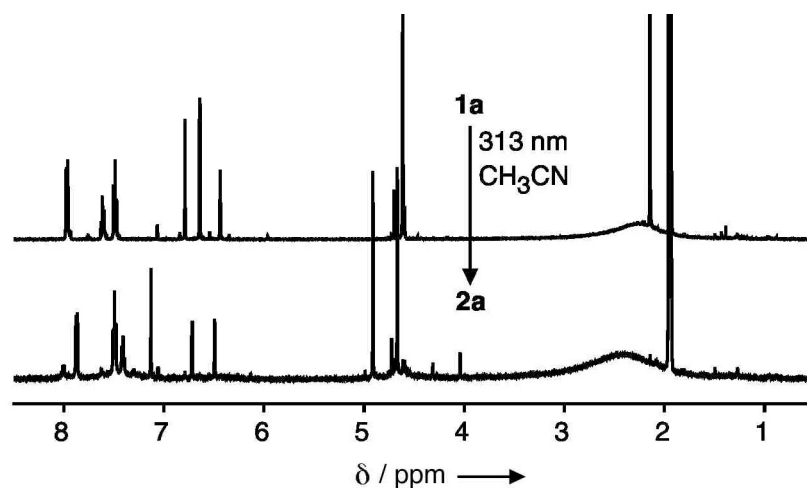


Figure 8.4 ^1H NMR spectra of a CD_3CN solution of **1a** before (top) and after (bottom) it was exposed to 313 nm light for 100 min.

8.7.6.2 Monitoring the photolysis by UV-vis absorption spectroscopy

Two identical samples of decorated UCNPs were prepared by diluting an aliquot amount (0.05 mL) of the stock solution of **1a**[$\text{NaYF}_4\text{:TmYb}$] with CH_3CN (2 mL). Each sample was irradiated with the appropriate light source to induce direct photolysis (290 nm, 3 nm slit width, Figure 8.5c) and ‘remote-control’ photolysis (980 nm, power = 4.37 W, power density = 556 W/cm^2 , Figure 8.5d) until no further spectral changes were observed.

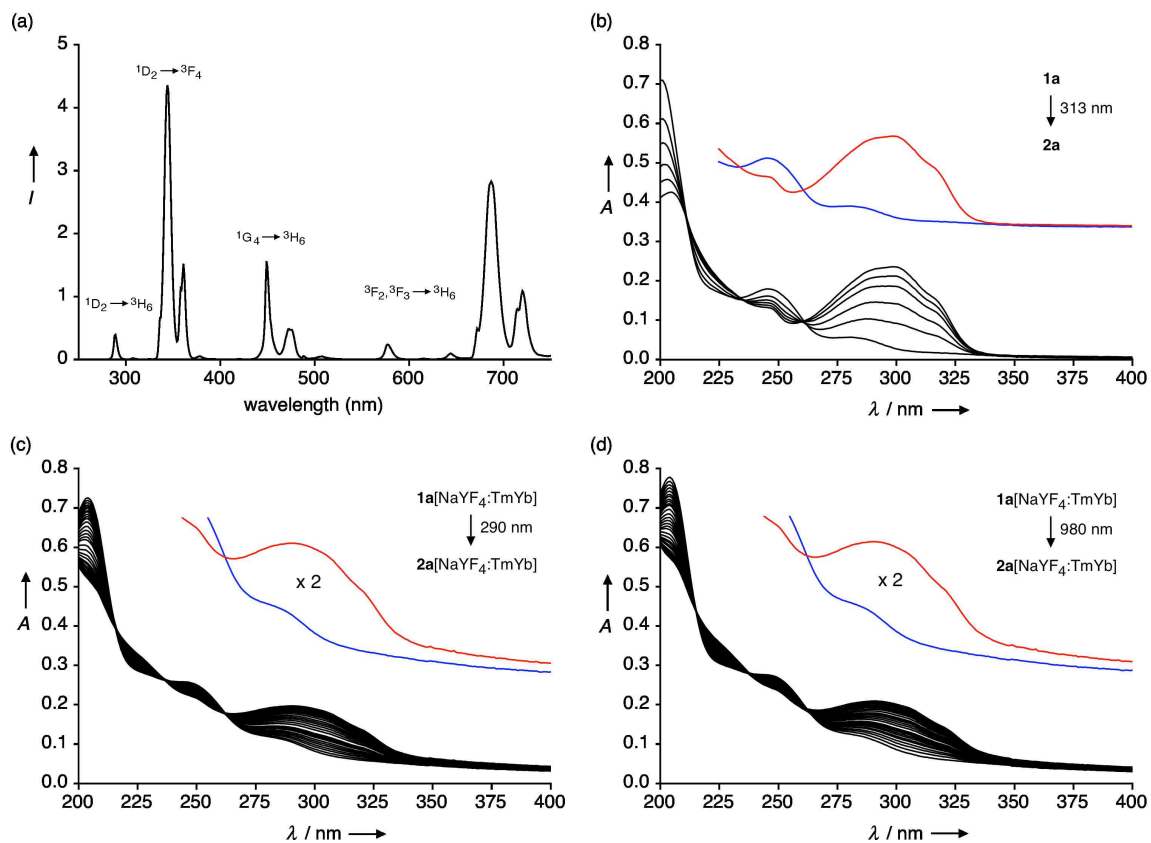


Figure 8.5 (a) Luminescence upconversion emission spectra of a 1 wt-% colloidal solution of $\text{NaYF}_4:\text{TmYb}$ core-shell nanoparticles in THF excited with a 980 nm laser diode (Power Density = 150 W/cm^2). Changes in the UV-vis absorption spectra of CH_3CN solutions of (b) **1a** as it is irradiated with 312-nm light, (c) **1a** $[\text{NaYF}_4:\text{TmYb}]$ as it is irradiated with 290-nm light, and (d) **1a** $[\text{NaYF}_4:\text{TmYb}]$ as it is irradiated with 980-nm light until no further spectral changes are observed. The data in (c) and (d) were used to generate Figure 8.1c. The insets in (b), (c) and (d) show the initial (blue) and final (red) traces corresponding to **1a** and **1a** $[\text{NaYF}_4:\text{TmYb}]$, and **2a** and **2a** $[\text{NaYF}_4:\text{TmYb}]$, respectively.

9: DEVELOPMENT OF A MULTIFUNCTIONAL THERANOSTIC DRUG-DELIVERY SYSTEM

9.1 Contributions

The data presented in this chapter has not been published. The project was co-designed by C-J Carling, Dr. J-C Boyer and Prof. Dr. N. R. Branda. All synthesis and data collection was carried out by C-J Carling except for the synthesis of **o-NP**, **a-NP** and TEM images of all nanoparticles, which was done by Dr. J-C Boyer. The chapter is written by C-J Carling. The experimental section 9.8 is co-written by C-J Carling and Dr. J-C Boyer.

9.2 Introduction

After introducing the concept of NIR-to-UV 'remote-control' photorelease as a novel means of releasing molecules from the surface of upconverting nanoparticles (UCNP) using NIR light in 2010,^[10] we sought to further develop the technology into a multifunctional and practical theranostic NIR light-triggered drug delivery system.^[168,243,244,245,246,247,248,249] The excellent qualities of the 5 % Thulium and 30 % Ytterbium co-doped core-shell hexagonal(β)-phase NaYF₄ UCNP makes it an attractive candidate for this purpose as it offers a high level of multi-functionality with proper design.^[243,168] Due to its luminescent character, especially the strong quantum efficiency of the 980-to-800 nm upconversion process, the particles can be detected *in vivo* at deeper locations than with conventional UV-to-vis or vis-to-vis down-conversion fluorescence.^[168,243,250] We

have demonstrated NIR-to-UV 'remote-control' photoswitching and photorelease,^[9,10,11,29] and since the time of the initial publications other reports using UCNPs to drive organic photoreactions have appeared including photoswitching^[251,252] and as recently demonstrated, NIR-to-UV 'remote-control' photorelease *in vitro* and *in vivo*.^[168,243] UCNPs can also be functionalized with either radioactive^[253,254] or paramagnetic elements^[255,256] for positron emission topography (PET) or magnetic resonance imaging (MRI) detection respectively; these spectroscopic properties can substantially aid in the location of the nanoparticles *in vivo* for subsequent NIR-to-UV 'remote-control' drug-release. Due to these reasons the UCNPs show great potential as a remotely triggered, fluorescent and trackable multifunctional theranostic drug delivery vehicle.^[249]

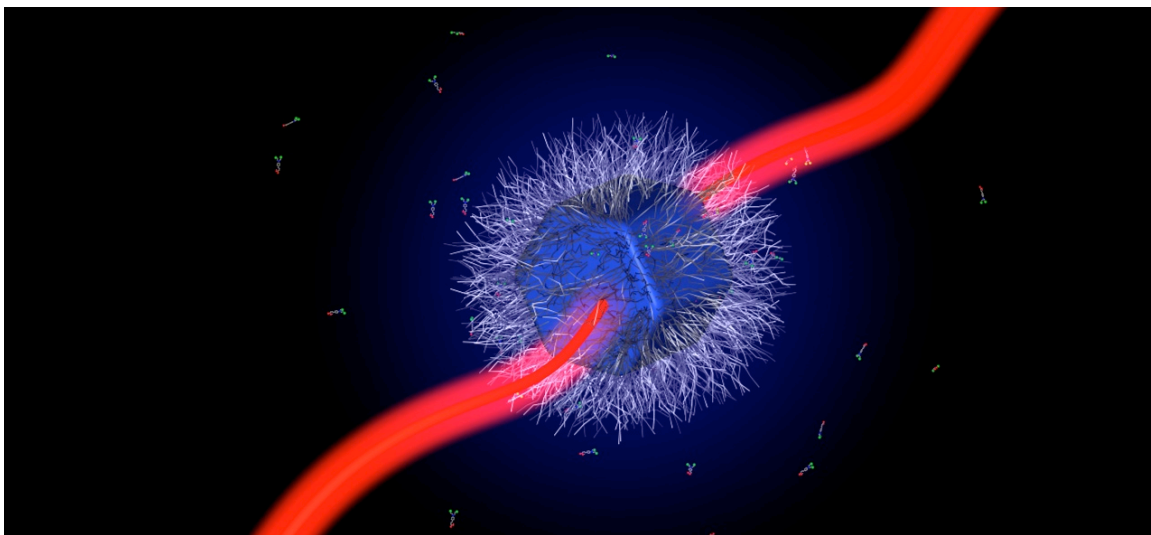


Figure 9.1 Schematic representation of NIR-to-UV 'remote-control' photorelease from a fluorescent UCNP coated with PEG.

It was envisioned that for the drug-release system to be optimal, the system should obey the following criteria: 1) The organic-nanoparticle hybrid system must be highly water-dispersible and be sufficiently stable in aqueous media containing inorganic phosphate and organic phosphates such as adenosine triphosphate (ATP) to prevent pre-stimuli release of ligands and subsequent aggregation of nanoparticles.^[257,258,259] 2) The therapeutic cargo should be relatively easily and irreversibly loaded onto the nanoparticles in high efficiency. 3) The therapeutic cargo should be shielded from the outside environment prior to irradiation with NIR light to minimize non-specific toxicity or interactions. 4) The therapeutic cargo should stay intact, but be able to diffuse from the UCNP to the surrounding environment after NIR-to-UV phototriggered release. 5) The power-density of the 980 nm excitation source must be of biologically benign intensity to prevent thermal tissue damage.

This chapter describes the successful development of a drug delivery vehicle that satisfies criteria 1-3 of the 5 postulated above.

9.3 Development of ligand attachment systems and water-dispersible upconverting nanoparticles – a historical perspective about the development process

9.3.1 Introduction

It is well known in the literature that polyethylene glycol (PEG) is a biocompatible polymer that can both induce water-dispersibility of nanoparticles and lengthen the circulation time *in vivo*. This occurs by protecting the nanoparticles from rapid uptake by the reticulo-endothelial system (RES) by

shielding the nanoparticle-surface from adhesion of opsonin proteins present in blood.^[245,260] We consequently reasoned that a PEGylated nanoparticle surface, if properly designed, would both provide water dispersibility of the UCNP as well as shield toxic cargo from interacting with the external environment. Hence, to provide water dispersibility of the UCNP we aimed to synthesize a ligand containing a PEG moiety that could be attached to the UCNP surface.

9.3.2 PEGylated bis-carboxylate anchor

Our first approach to functionalize the surface of the UCNP using a bis-carboxylate anchor was successful in organic solvent.^[10] A methyl terminated (mPEG) bis-carboxylate PEG ligand **1** was synthesized and attached to the UCNP surface **1-NP** by ligand exchange, see Figure 9.2 (experimental data not shown), and the resulting UCNPs were water-dispersible. However, in aqueous 0.01 M phosphate buffered saline (PBS) the mPEGylated bis-carboxylate ligand **1** was rapidly displaced by inorganic phosphate, which have a stronger affinity to the surface.^[258,259] This caused aggregation of the nanoparticles within minutes and finally precipitation of the nanoparticles, see Figure 9.2.

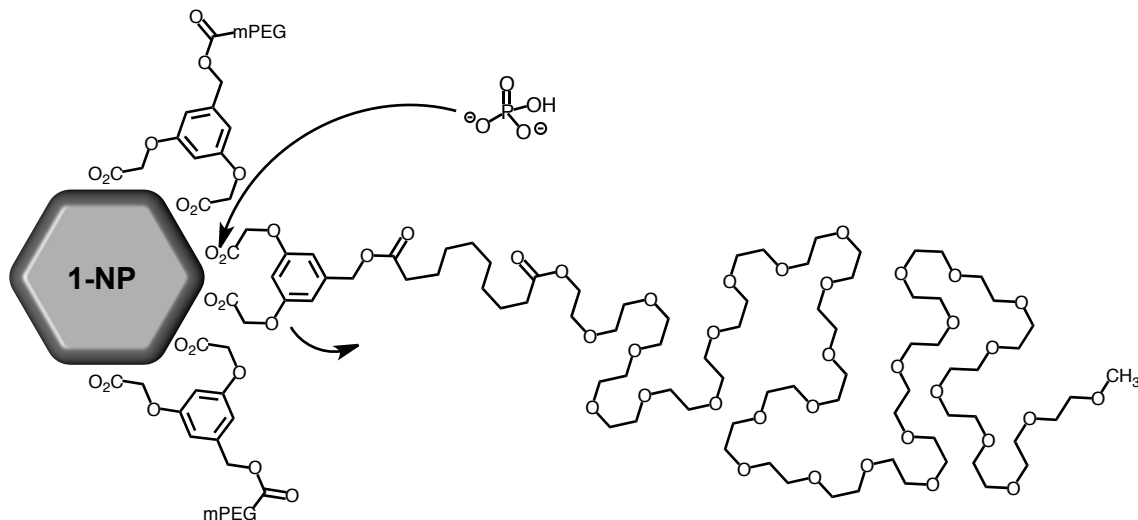


Figure 9.2 The bis-carboxylate PEGylated ligand attached to the UCNP **1-NP** is displaced by inorganic phosphate in 0.01 M PBS buffer, which rapidly led to aggregation and precipitation of the nanoparticles.

9.3.3 Phosphate/phosphonate anchor

The precipitation described above implied that the phosphate anion has a stronger binding affinity to the rare earth UCNP surface than do carboxylates;^[258,259] this led us to target the synthesis of a phosphate-functionalized photochromic molecule (ROPO₃H₂) **2**. The synthesis of **2** was attempted in the early stages of the surface-functionalization development stage, see Figure 9.3. Several attempted syntheses did yield phosphate-functionalized photochromic molecules, albeit in low yield and impure form (experimental data not shown). Due to both a lack of selectivity of the attempted reactions and the highly polar nature of product and side-products, the purification proved challenging and no products devoid of impurities could be isolated. Though pure products were not produced, when semi-purified phosphate-functionalized ligands were mixed with oleate-coated UCNPs, the nanoparticles were indeed

coated with photochromic molecules that indicated that the phosphate-functionalized ligands had affinity for the UCNP surface (experimental data not shown).

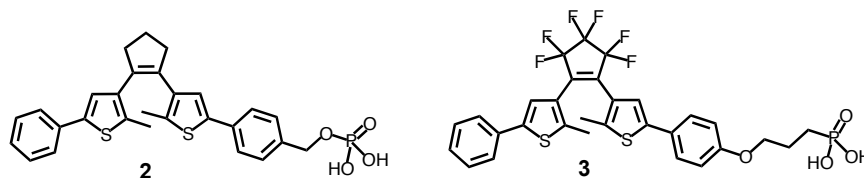


Figure 9.3 Synthesized phosphate (**2**) and phosphonate (**3**) functionalized photochromic molecules. The highly polar molecules were extremely hard to purify and neither molecule were isolated devoid of impurities.

Since phosphonates (RPO_3H_2) have a carbon-phosphorous bond, they are easier to selectively manipulate synthetically than phosphate-derivatives (ROPO_3H_2), though still reasonably difficult to purify in both the protected form ($\text{RPO}_3\text{R}'_2$) and more difficult to purify in its de-protected form (RPO_3H_2). A successful attempt was made to functionalize a photochromic molecule with a phosphonate functionality **3**, see Figure 9.3 (experimental data not shown). However, the final product **3** proved very difficult to purify with either silica or C_{18} -silica gel column chromatography as it was not observed to elute off the baseline.

9.3.4 Surface functionalization through ‘click’ chemistry

In order to circumvent working with highly polar and thus challenging compounds during multi-step syntheses of complex molecules, we consequently decided to use the previously described 3-azidopropylphosphonic acid^[132] ligand as a high affinity anchor to the UCNP surface. The azide-phosphonate anchor

serves as a connection point for subsequent derivatization by using copper(I)-catalyzed azide-alkyne cycloaddition (CuAAC) 'click' chemistry.^[133,261,262,263,264] By this general method of surface-functionalization we have been able to attach a number of alkyne functionalized molecules to the azide coated UCNP-surface in one high yielding and irreversible step as was described in Chapter 5 and 6.^[28,29]

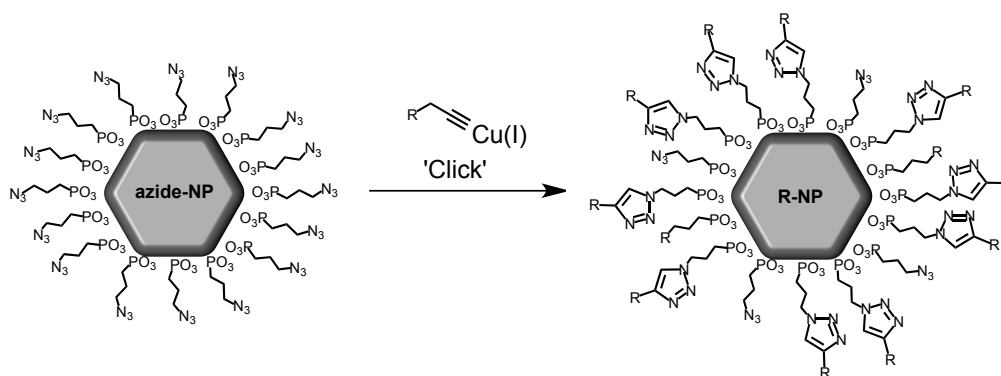


Figure 9.4 General functionalization strategy using CuAAC 'click' chemistry.

9.4 Development of a functional drug-release system part 1

9.4.1 Choice of anti-cancer drug

Having solved the surface-functionalization problem,^[28,29] a suitable anticancer drug-candidate needed to be selected for the drug-release system we attempted to develop. Many compounds were considered during this process including Paclitaxel, Doxorubicin, Fluorouracil and Chlorambucil among many other anticancer and biologically active compounds, see Figure 9.5.

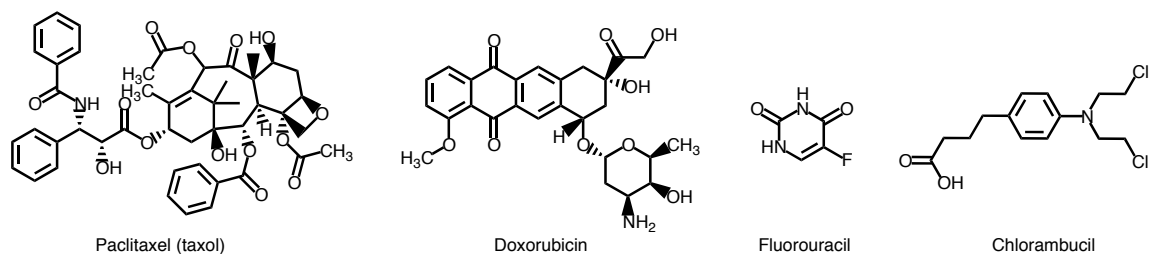


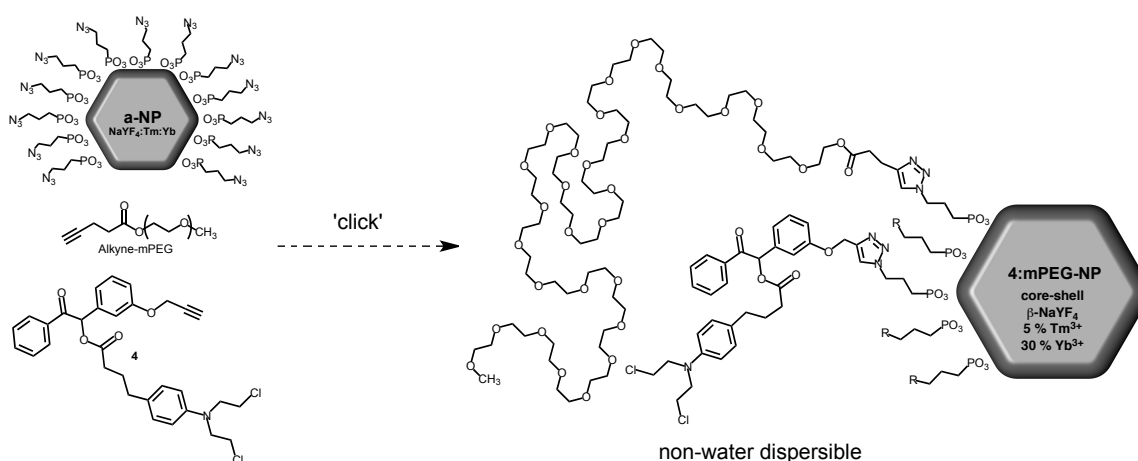
Figure 9.5 Common anticancer drugs

Chlorambucil was eventually selected as the model anticancer compound as it has many attractive features: Chlorambucil is an anticancer drug of the N-mustard class and acts as an alkylating agent of DNA.^[265] Apart from the toxic N-bis-2-chloroethyl moieties, it displays only one other functionalizable group, which may serve as a selective attachment point to photocage through an ester bond, which we previously used with the benzoin photocage.^[10] Since Chlorambucil is commercially available in gram quantities, is achiral, relatively inexpensive, and lacks additional functional groups (maximizing chemical selectivity during synthesis), and has previously been used for photorelease,^[266,267] it was chosen as the model-drug.

9.4.2 First-generation drug-delivery system

To circumvent the challenging synthesis of an mPEGylated photorelease system in the early stages of the project we attempted to co-functionalize the UCNP surface with an alkyne-Chlorambucil-benzoin photocage **4** and commercially available alkyne-mPEG in one step (experimental data not shown). The CuAAC 'click' co-functionalization reaction was attempted with different ratios of photocage **4** to mPEG (1:5, 1:10) but the resulting UCNPs **4:mPEG-NP**

were not dispersible in water after the reaction, see Scheme 9.1 (experimental data not shown). These negative results could possibly depend on a number of physical factors such as formation of hydrophobic nano-domains on the surface of the nanoparticle, which cause aggregation of the nanoparticles in water. Another possibility is that the reaction was run for too long at elevated temperature, which could have resulted in ester hydrolysis of the alkyne-mPEG ligand, something we started suspecting at a later stage of development while trying to mono-functionalize the surface with various PEG ligands and during the synthesis of **5-NP** (experimental data not shown).



Scheme 9.1 The co-functionalization of **a-NP** with **4** and alkyne-mPEG failed to provide water dispersible hybrid nanoparticles.

9.4.3 Tuning of the absorption-emission overlap

During our initial NIR-to-UV 'remote-control' photorelease study using the 3',5'-dialkoxybenzoin photocage^[10] (*Chapter 8*) we became aware that the overlap between the largest UV emission from the UCNP and the absorption of the photocage was exceptionally poor, a phenomenon which led to slow bulk-

photolysis rate using high power density continuous-wave 980 nm light (550 W/cm²), light that readily damages human tissue in a few seconds. We were aware^[268] that both the coumarin and the 2-nitrobenzyl photocage classes had better absorption overlap with the largest UV emission of the UCNP compared to the dialkoxybenzoin class but we decided against using these photocages since the coumarin class suffer from low quantum yields and thus uncaging action cross section^[269] and the nitroso-photoproduct of the 2NB photocage has been shown to interact with various proteins and thus be mildly toxic.^[270,271,272] However, recent research has demonstrated that the photoproducts from various 2NB derivatives have a very low toxic effect on living cells.^[273,274] In fact, the UV light needed for photolysis appears to be more damaging to living systems than the nitroso-photoproduct.^[168] Moreover, it has been recently demonstrated that the 2NB photocage does respond to NIR-to-UV 'remote-control' photorelease.^[168,171,243]

Deciding not to use either the coumarin or the 2NB photorelease systems, we continued to use the 3',5'-dialkoxybenzoin photocage throughout this work, but attempted to achieve a better overlap between the largest UV emission from the UCNP at 330-360 nm, by synthesizing the naphthalene derivative^[199,200] of the 3',5'-dialkoxybenzoin photocage. This derivative has a larger molar extinction coefficient at 350 nm ($\epsilon_{350\text{nm}}: 1957 \text{ M}^{-1}\text{cm}^{-1}$) compared to the phenyl version ($\epsilon_{350\text{nm}}: 291 \text{ M}^{-1}\text{cm}^{-1}$). We envisioned that by better absorption/emission overlap, the NIR-to-UV 'remote-control' photolysis reaction could be conducted using a lower NIR power density than in our original photorelease study.^[10]

9.5 Development of a functional drug-release system part 2

9.5.1 Introduction

As the initial co-functionalization strategy failed, a more complex ligand **5** functionalized with PEG was designed, successfully synthesized and attached to the nanoparticle surface, see figure 9.6 and 9.7, scheme 9.2 and experimental section 9.8 for details.

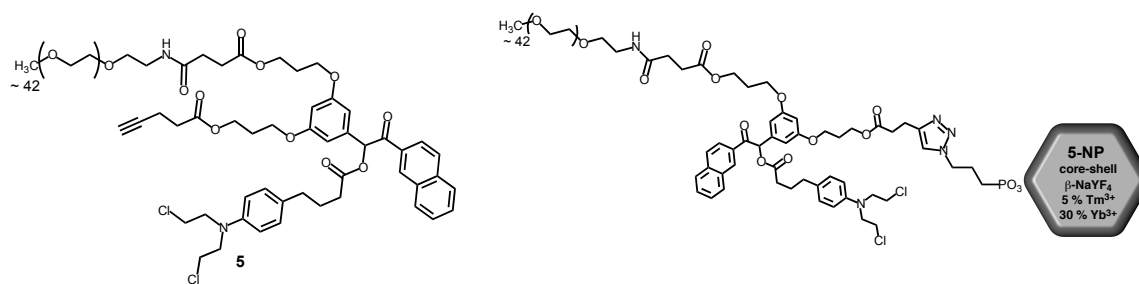


Figure 9.6 Structures of the synthesized organic ligand **5** and organic-nanoparticle hybrid system **5-NP**.

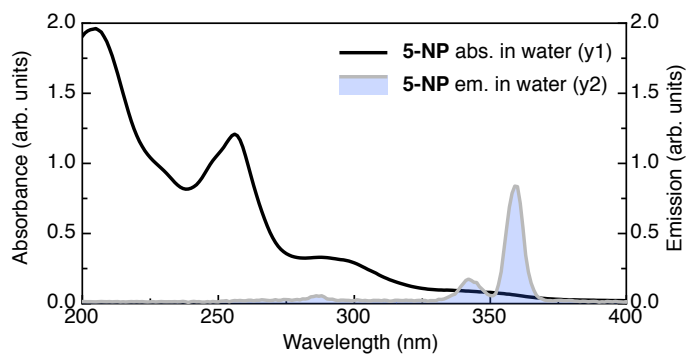
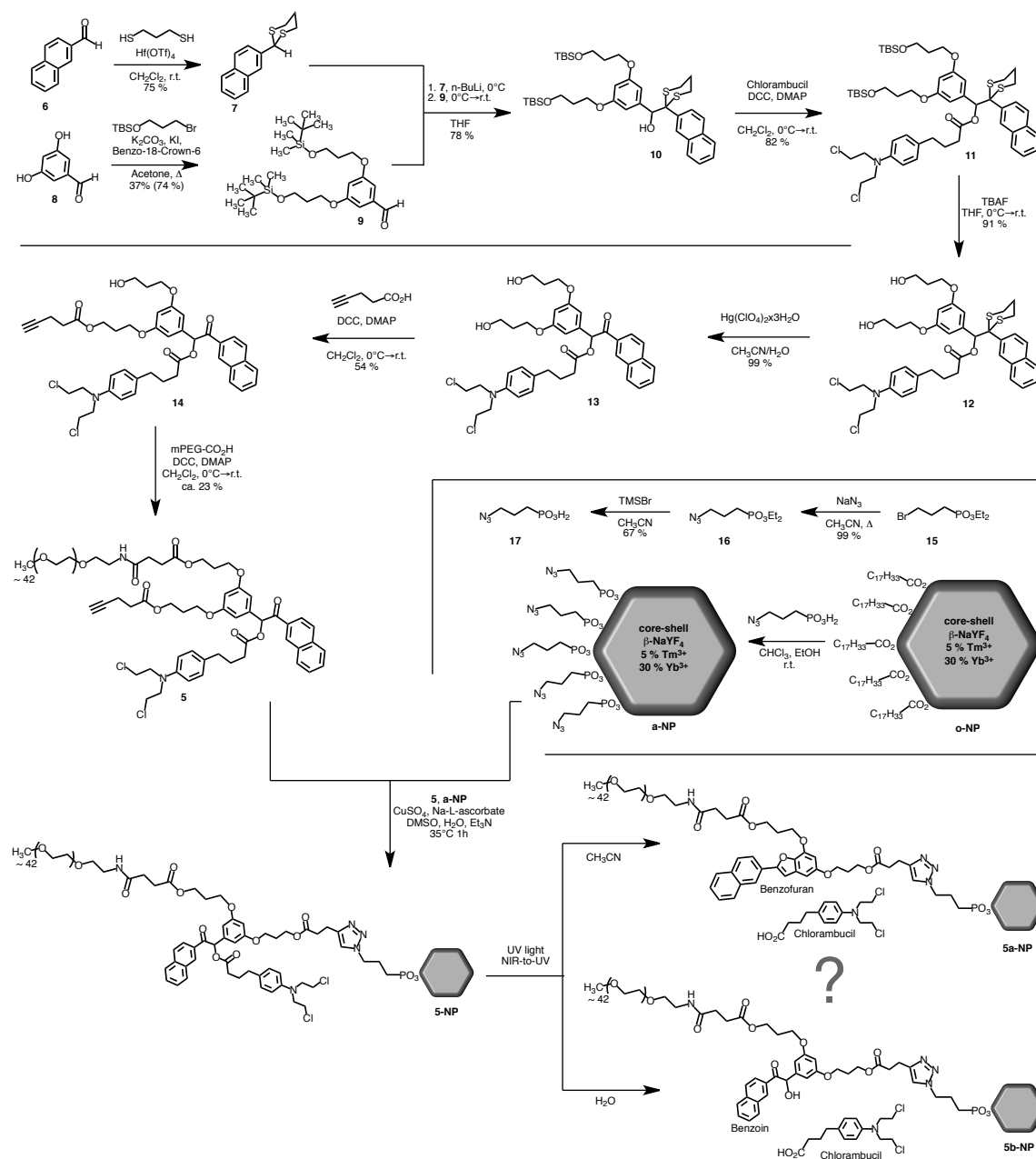


Figure 9.7 Absorbance and emission spectra of **5-NP** in water. *Left y-axis:* Absorbance spectrum of **5-NP** in water (0.05 ml stock-solution in 2 ml H_2O). *Right y-axis:* Emission spectra of the same sample upon 980 nm excitation (1.45 W/cm^2 , 0.41 W).

9.5.2 Results and discussion

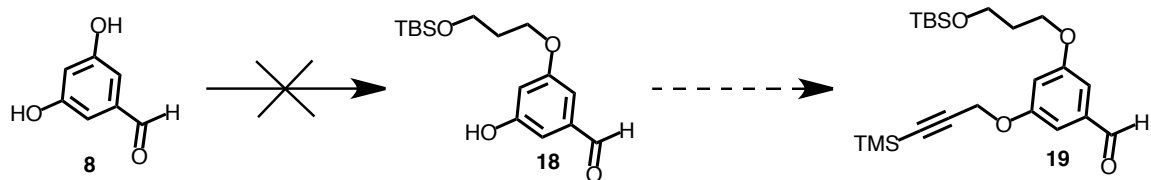
9.5.3 Synthesis of the second generation drug delivery system 5-NP



Scheme 9.2 Total synthesis of the organic ligand **5** and the organic-nanoparticle hybrid system **5-NP**. The question mark after photolysis/photosolvolyis represents unknown information, as Chlorambucil was not detected and the photoproducts were not fully characterized.

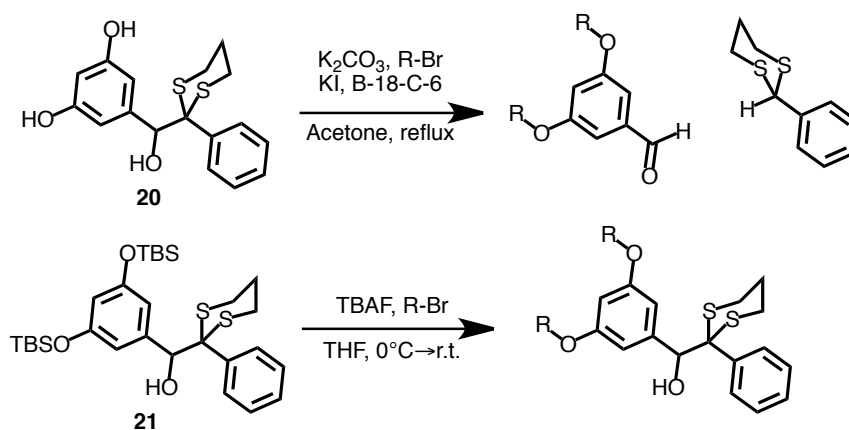
The synthesis of ligand **5** was carried out by first converting 2-naphthaldehyde **6** into the corresponding 1,3-propyldithiane derivate **7**^[275] in the presence of a catalytic amount of Hf(OTf)₄ in CH₂Cl₂ in 75 % yield.^[276]

The bis-alkylated aldehyde **9** was synthesized from the corresponding 3,5-dihydroxybenzaldehyde **8** by alkylating it with (3-bromopropoxy)(*tert*-butyl)dimethylsilane in acetone in the presence of K₂CO₃ and catalytic amounts of KI and benzo-18-crown-6 in 37 % yield. However, the original synthetic target in this reaction was the mono-alkylated isomer **18** as the original target of the synthesis was the asymmetric alkynylated ligand **19**, see Scheme 9.3. Although the reaction was carried out with 1 equivalent alkyl-bromide to 1 equivalent 3,5-dihydroxybenzaldehyde **8**, only the bis-alkylated isomer **9** and the non-alkylated starting material **8** was recovered from the reaction mixture and only trace quantities of the mono-alkylated isomer **18** was isolated as it appeared that the mono-alkylated isomer **18** is more reactive than the 3,5-dihydroxybenzaldehyde starting material **8**. Due to this reason, the bis-alkylated isomer **9** was carried forward throughout the synthesis.



Scheme 9.3 The mono-alkylated isomer **18** could only be isolated in trace quantities

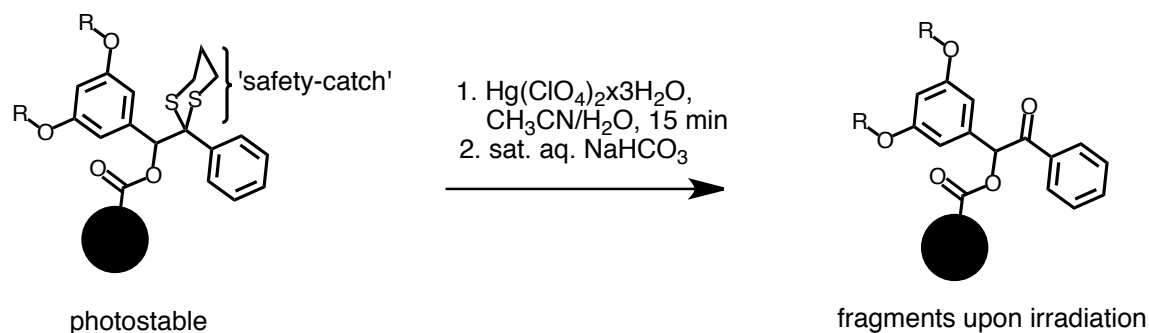
Moreover, the propyl-spacer between the hydroxy groups in molecule **9** was chosen to circumvent subsequent use of electron withdrawing ester bonds directly attached to the benzyl-moiety of the benzoin photocage; they were also installed early in the synthesis since **20** was found to fragment under basic alkylating conditions, see Scheme 9.4 (experimental data not shown). However, alkylation without fragmentation is possible by generating the reactive phenolic-anion *in-situ* by deprotection of a tertbutyldimethylsilyl (TBS)-protected precursor **21** with tetrabutylammonium fluoride (TBAF) in the presence of an alkylbromide in THF^[201] (Scheme 9.4).



Scheme 9.4 Molecule **20** was found to fragment under basic alkylating conditions. In contrast, the OTBS protected isomer **21** can be alkylated without fragmentation by deprotecting the OTBS-protected phenol *in-situ* with TBAF in the presence of an alkylbromide.^[201]

Lithiation of naphthyl-1,3-propyldithiane **7** in anhydrous THF and reacting it with 3,5-dialkoxy-benzaldehyde **9** yielded the dithiane-protected benzoin **10** in 78 % yield. This Corey-Seebach umpolung reaction^[277] is highly advantageous over other benzoin producing reactions^[199,200,202] as it produces the asymmetric

dithiane-protected benzoin in high yields and with correct stereochemistry.^[201,214,278] A further advantage is that the 1,3-dithiane protecting group also acts as a 'safety-catch'^[201,214,279] until facile deprotection which prevents premature photorelease that could occur in standard laboratory lighting. Such photoprotection is beneficial in a practical sense as it limits the time spent working under dark conditions (Scheme 9.5).



Scheme 9.5 Until deprotection, the dithiane-protected precursor is photostable. After facile deprotection the photocage responds to UV light irradiation and fragments

Chlorambucil was coupled to the dithiane-protected benzoin **10** by the mild Steglich esterification reaction^[280] using dicyclohexylcarbodiimide (DCC) and catalysed by 4-dimethylaminopyridine (DMAP) in anhydrous CH₂Cl₂ to yield **11** in 82 % yield.

The OTBS protecting groups of **11** were removed in the presence of TBAF in THF to yield the bis-alcohol **12** in 91 % yield.

The dithiane-protecting group of **12** was removed in the presence of Hg(ClO₄)₂·3H₂O in a CH₃CN/water mixture to yield the light-sensitive 3,5-dialkoxy benzoin photocage **13** in 99 % yield. The dithiane-protecting group was

removed at an earlier stage than necessary in the synthesis because the reactions have had a tendency to become highly acidic and have caused many secondary reactions and low yields of product recovery in the past by following literature procedures.^[201] However, the problems associated with this reaction can largely be mitigated by first dissolving/dispersing $\text{Hg}(\text{ClO}_4)_2 \cdot 3\text{H}_2\text{O}$ in a mixture of CH_3CN and water before adding the dithiane substrate as a CH_3CN solution and quenching the reaction properly with saturated aqueous NaHCO_3 before work-up. Another problem with this reaction is the formation of a by-product that is quite difficult to eliminate by column chromatography when using a polar eluent system. However, the by-product is poorly soluble in CH_2Cl_2 and the majority can be filtered off before column chromatography.

Diol **13** was reacted with 4-pentynecarboxylic acid in the presence of DCC and DMAP in CH_2Cl_2 . By closely following the reaction progression by thin-layer chromatography (TLC) and quenching the reaction at an appropriate time, the unstable mono-alkyne derivative **14** was isolated in 54 % yield.

Alcohol **14** was converted to the mPEG ester in the presence of DCC, DMAP and mPEG- CO_2H in CH_2Cl_2 to yield the slightly impure mPEGylated-ligand **5** isolated after multiple purification methods in approximately 23 % yield, with the main by-product represented by unreacted mPEG- CO_2H .

The 3-azidopropylphosphonic acid ligand^[132] **17** was prepared in two steps from diethyl-3-bromopropylphosphonate **15** by following literature procedures.^[132]

The azide-functionalized *core-shell* β -NaYF₄:0.5%Tm:30%Yb **a-NP** was prepared by stirring the previously reported^[10] oleate coated precursor **o-NP** with the 3-azidopropylphosphonic acid ligand **17**^[132] in CHCl₃ and EtOH.^[28,29]

5-NP was obtained as highly water dispersible UCNPs by reacting the alkyne-functionalized 3',5'-dialkoxybenzoin mPEG ligand **5** with a colloidal dispersion of **a-NP** in the presence of freshly prepared aqueous CuSO₄•5H₂O and Na-(L)-Ascorbate in triethylamine (Et₃N), water, and dimethylsulfoxide (DMSO) at 35°C for one hour. The reaction was only stirred at 35°C for one hour to minimize any ester-hydrolysis from taking place as non-water dispersible particles were obtained after reacting the mixture at 35°C overnight (experimental data not shown). The hybrid nanoparticles **5-NP** were purified and isolated by multiple centrifugation/re-dispersion cycles and stored at -20°C in CH₃CN covered in aluminium foil to prevent any undesired ester-hydrolysis from taking place in water or premature photorelease from ambient UV light. Samples for subsequent studies were prepared by taking a small aliquot of the stock solution followed by dilution by water or CH₃CN (see the experimental section 9.8 for further details).

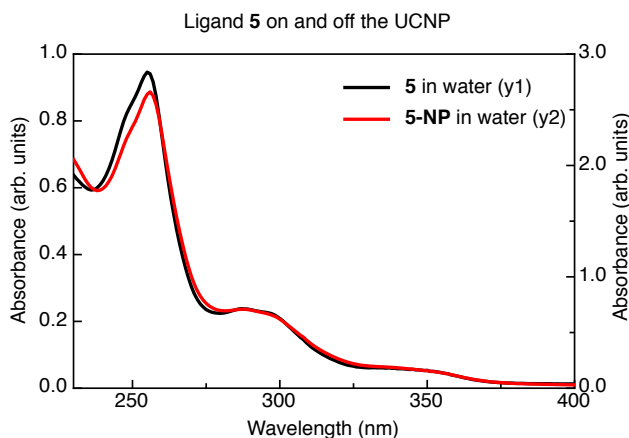


Figure 9.8 Absorbance spectra of the ligand **5** (black trace, left y-axis) and **5-NP** (red trace, right y-axis) in water.

9.5.4 Characterization of organic-nanoparticle hybrid system

The nanoparticles **a-NP** and **5-NP** were examined with IR spectroscopy and the azide stretch is substantially decreased in **5-NP** compared to **a-NP** indicating successful derivatization, which is further confirmed by UV-vis spectroscopy and illustrated by the high water dispersibility of the nanoparticles **5-NP**, see figure 9.8. The azide stretch IR signal is not completely absent however, indicating that unreacted azide functionalities are still present on the surface (experimental data not shown).

By examining transmission electron microscopy (TEM) images of the functionalized nanoparticles **5-NP**, they remained mono-disperse and non-aggregated after the 'click' reaction with an average width of 27 nm and length of 36 nm collected from 140 particles, see Figure 9.9b. By dynamic light scattering (DLS) measurements of **5-NP** in water, the mean hydrodynamic diameter was measured to 62 nm as this spectroscopic technique account for the organic ligands extending from the surface, see Figure 9.9a. In Figure 9.9a, the

hydrodynamic size distribution of **5-NP** in water before and after irradiation with UV light during 20 minutes is slightly altered. If not an artifact, it appears that larger particles have formed with a concomitant decrease in smaller particles during the irradiation period, see Figure 9.9a. The reasons for this artifact/phenomenon in the spectra is unclear at this stage but could potentially be an effect caused by nanoparticle aggregation induced during UV light irradiation (potentially due to loss of polymers – see Section 9.5.9.2 and Figure 9.19), or due to spontaneous aggregation due to instability of the nanoparticles in the aqueous environment, which can be verified by a temporal DLS study.

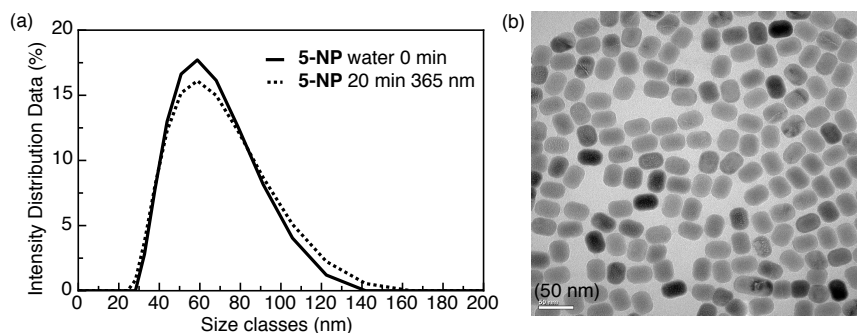


Figure 9.9 (a) DLS spectra of **5-NP** in water before (solid line) and after irradiation with 365 nm light (dashed line). (b) TEM images of **5-NP**, the scale bar is 50 nm.

9.5.5 Stability of the hybrid organic-nanoparticles (**5-NP**) in physiological medium

The stability of the hybrid nanoparticles **5-NP** in semi-physiological conditions was examined by dispersing the nanoparticles in 100 % fetal bovine serum (FBS). The nanoparticle dispersion in FBS was stirred in a capped vial at 37°C in an oil-bath and the vial was continuously examined for aggregation/precipitation by shining the 980 nm laser through the sample. No

aggregation was observed by the naked eye after 4 days of stirring at 37°C. The light beam going through the sample looks clear in this experiment; aggregation of the UCNPs causes small clusters clearly visible in the beam and finally full precipitation of the nanoparticles. This result suggests the nanoparticles would remain stable at physiological conditions in the bloodstream for an extended time (experimental data not shown). As this technique of evaluating the stability of the nanoparticles is subjective and does not take into account any potential protein adhesion, DLS would be a more appropriate technique to further examine the stability/aggregation/adhesion behaviour of the nanoparticles in a more objective manner as the size-dimensions of the nanoparticles can be probed over time. However, no temporal DLS study was performed on **5-NP**.^[281]

Since the concentration of organic and inorganic phosphates is elevated in the interior of cells compared to the bloodstream,^[282,283] the stability of **5-NP** was investigated at elevated concentrations of ATP and inorganic phosphate. The nanoparticles were dispersed in ca. 50% FBS containing 10 mM (0.17 mg/ml) ATP and 10 mM (0.66 mg/ml) inorganic phosphate as these levels correspond to the intracellular concentrations of rat heart cells (experimental data not shown).^[282] Though displacement of the ligands at heightened concentrations of phosphate compared to serum would potentially be harnessed as a beneficial effect, enabling automated release in the cytoplasm, no aggregation was observed by the naked eye after 3 days at 37°C suggesting the nanoparticles would remain stable also in the cytoplasm. Only by increasing the levels of ATP to greater concentrations (ca. 4 mg/ml) than naturally occurring

levels, was any aggregation observed. However, the rate of aggregation was slow and not observed until several hours (> 3 h) at room temperature further indicating the stability of the particles toward phosphate ions in solution (experimental data not shown). For any future *in vivo* study it should be noted that the ability of the UCNP to adsorb phosphate could potentially be linked to toxicity in organs such as the liver and should be further investigated.

9.5.6 Emission of the PEGylated nanoparticles in water and acetonitrile

As water absorbs 980 nm light to a larger degree than organic solvent does,^[23] the emissions from **5-NP** in water and CH₃CN was compared by measuring the emission at approximately the same concentration using the same power-density of the 980 nm excitation source, see Figure 9.10. It was found that the total emission output in water was decreased by approximately 54 % and the largest UV emissions at 330-360 nm was decreased by 83 % compared to the emission in CH₃CN. These results are most likely due to the larger NIR light absorption by water compared to CH₃CN and potentially also due to secondary quenching interactions between the water and the nanoparticle, as have been previously reported.^[284,285]

Based on these results it is expected that NIR-to-UV 'remote-control' photoreactions (excited at 980 nm) carried out in water should be less efficient and more prone to heat generation compared to reactions performed in organic solvents.

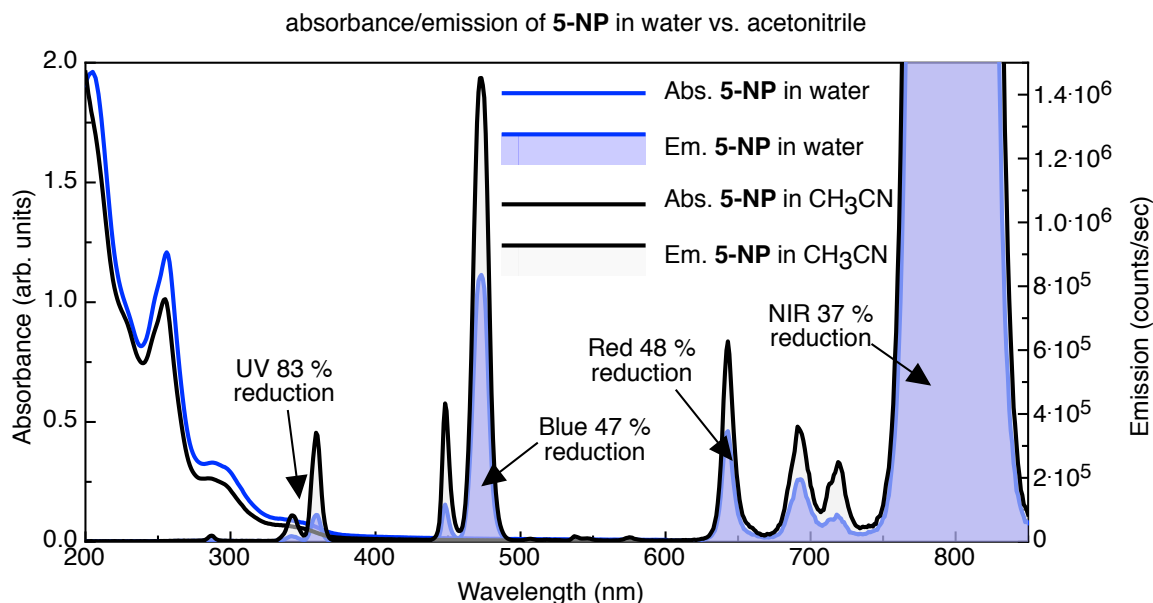


Figure 9.10 *Left y-axis:* Absorbance of **5-NP** in H_2O (blue trace) and CH_3CN (black trace) indicating similar concentration (0.05 ml **5-NP** in 2 ml solvent). *Right y-axis:* Emission from the same samples in H_2O (blue shaded) and CH_3CN (grey shaded) upon 980 nm excitation (1.45 W/cm^2 , 0.41 W). The emission quenching values are calculated based on the areas under the curves. The emission bands from 671–750 nm were not included in the analysis because these emissions are due to the second order diffraction of the upconverted UV light off the grating of the emission monochromator

9.5.7 One photon photoreactivity of **5** and **5-NP**

Depending on the solvent, the mechanism of photolysis of the 3',5'-dialkoxybenzoin photocage is different as was described in section 7.2.2. It has been reported that in aqueous solvent the dialkoxybenzoin photocage undergoes a photosolvolytic reaction mechanism yielding benzoin, instead of the photolysis reaction mechanism observed in organic solvent yielding benzofuran.^[201] Upon UV light irradiation of **5** and **5-NP** in water we observed a similar behaviour in the UV-vis absorption spectra as reported by Rock and Chan,^[201] see Figure 9.11b,d. However, no further study was performed to identify the proposed benzoin photoproduct in water due to lack of pure material. Such study can be

performed by using NMR spectroscopy which would also give additional insightful information about the release event.^[286]

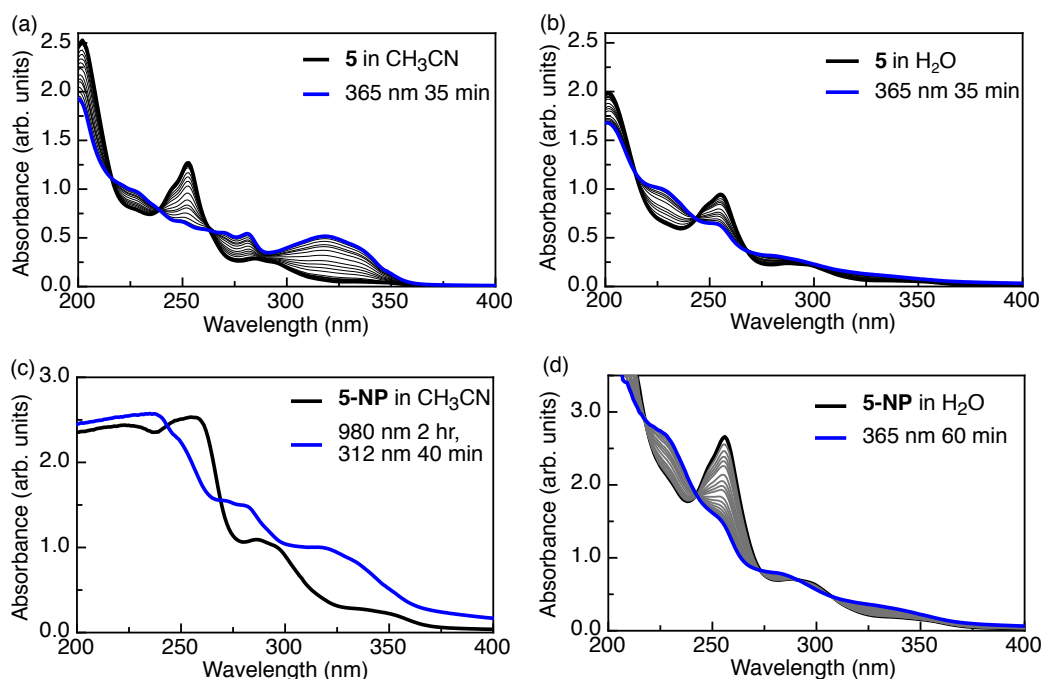


Figure 9.11 Changes in absorbance of **5** (2×10^{-5} M) during irradiation with 365 nm light (1.4 mW/cm^2 , 3.9 mW) in (a) CH₃CN and (b) water. (c) Absorbance of **5-NP** in CH₃CN (0.05 ml stock dispersion in 0.2 ml CH₃CN) before and after irradiation with 980 nm along the horizontal axis (1 hour 1.45 W/cm^2 and 1 hour 4.27 W/cm^2) and 312 nm light (40 minutes, 2.1 mW/cm^2). (d) Changes in absorbance of **5-NP** in water (0.1 ml stock dispersion in 2 ml H₂O) during irradiation with 365 nm light (1.4 mWcm^{-2} , 3.9 mW).

9.5.8 Multiphoton NIR-to-UV ‘remote-control’ photoreactivity of 5-NP

9.5.8.1 Choice of NIR power-density

In our previous studies,^[9,10,29] the power-density of the 980 nm excitation source has been above what can be considered practically useful in biological applications as NIR light at the intensities originally employed will cause tissue-damage. To be practical, the 980 nm (or 915 nm^[23]) excitation source must be of ‘biologically benign’ power-levels to minimize any tissue damage caused by the

NIR light. The power-density of the continuous-wave 980 nm laser beam was thus subjectively chosen based on its effect on my finger tip. In the focal point of the 980 nm continuous-wave laser beam at around 1.45 W/cm^2 (0.41 W) the pain caused by the laser beam was bearable until approximately 10 s at which point the heat generated from the absorption of the NIR light by water became too intense. By having small intervals (ca. 2 s) between light irradiation periods (ca. 5-10 s) made the pain generated from the irradiation procedure bearable for a much greater time period. This method of choosing power density is subjective as it is based on the pain threshold of one person. For future biological studies, the NIR power density threshold should be further studied and based on its effect on cells and tissues.

9.5.8.2 Choice of concentration for NIR-to-UV 'remote-control' experiments

In previous experiments we have noticed that NIR-to-UV 'remote-control' bulk-reactions appear to proceed more efficiently when the samples are in higher-concentration compared to more dilute UV-vis conditions.^[29,287] This phenomenon is most likely due to a heightened inner-filter effect and that every particle spends more time in the excitation beam compared to more dilute samples. However, at such 'high' concentrations the reaction can become problematic to monitor by UV-vis spectroscopy due to greater absorbance potentially outside the linear region of the spectrometer. To circumvent using very high concentrations yet still have a relatively efficient bulk-reaction that can be monitored by UV-vis spectroscopy, the NIR-to-UV 'remote-control' photolysis/photosolvolytic experiments were conducted in smaller volumes (400

μl) than previous studies^[10,11,29] (3 ml) to maximize the time particles spend in the excitation beam. The experiments were consequently conducted in a micro-cuvette (maximum sample volume: 710 μl , sample compartment: 5 x 5 x 45 mm).

However, in a clinical setting the particles would be even more confined as the diffusion rate in tissues/cells are arguably much lower than in solution due to cell/tissue-barriers. The NIR-to-UV 'remote-control' reaction would thus (most likely) be more efficient than in solution as the nanoparticles cannot diffuse away from the excitation beam to the same extent as they can in solution and both the inner-filter effect and the time the particle stay in the beam would (most likely) increase.

9.5.8.3 NIR-to-UV 'remote-control' photosolvolysis of 5-NP in water

During irradiation of **5-NP** in water along the vertical axis of the cuvette with 980 nm (1.45 W/cm^2 , 0.41 W) continuous-wave laser light, minimal changes in the UV spectra were observed after 60 minutes of irradiation indicating a very inefficient process at 'biologically benign' power-densities, see Figure 9.12a,b. Increasing the power-density (4.27 W/cm^2 , 1.21 W) caused rapid heating of the water sample. However, when the cuvette was placed in a water bath to dissipate the heat generated during the irradiation procedure, relatively small but clearly visible changes in the UV-vis spectra was rapidly evident during higher power density 980 nm light irradiation (4.27 W/cm^2 , 1.21 W) along the vertical axis of the cuvette (Figure 9.12c,d).

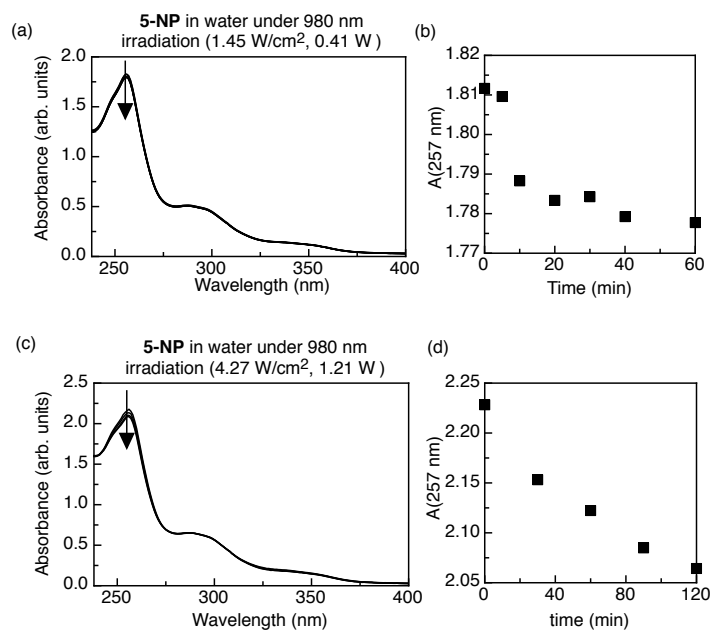


Figure 9.12 UV-vis absorbance changes of **5-NP** (0.05 ml **5-NP** in 0.4 ml water) during NIR-to-UV 'remote-control' photosolvolytic in a micro cuvette. (a) Changes in absorbance during irradiation with 980 nm light (1.45 W/cm², 0.41 W) along the vertical axis. (b) Changes in absorbance of the same sample during time plotted at 257 nm. (c) Changes in absorbance of a second sample cooled in a water bath during irradiation with 980 nm light (4.27 W/cm², 1.21 W) along the vertical axis. (d) Changes in absorbance of the same sample during time plotted at 257 nm.

9.5.8.4 NIR-to-UV 'remote-control' photosolvolytic of **5-NP** in CH₃CN

During irradiation of **5-NP** in CH₃CN along the horizontal axis of the cuvette with 'biologically benign' power density of 980 nm (1.45 W/cm², 0.41 W) continuous wave laser light, minimal changes in the UV spectra was observed after 60 minutes of irradiation indicating a very inefficient process also in organic solvent, see Figure 9.13a,b. By increasing the power-density of the 980 nm excitation source (4.27 W/cm², 1.21 W), relatively small but clearly visible changes in the UV-vis spectra was evident after 60 minutes of irradiation along the horizontal axis of the cuvette (Figure 9.13c,d).

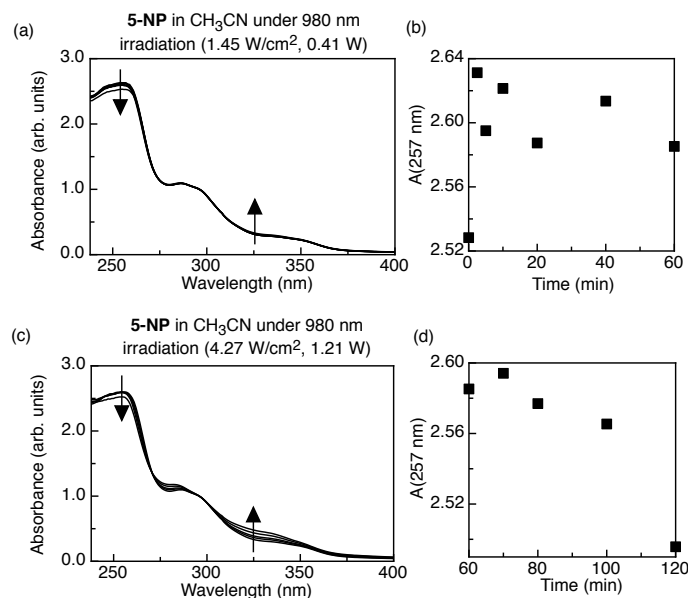


Figure 9.13 UV-vis absorbance changes of **5-NP** (0.05 ml **5-NP** in 0.2 ml CH₃CN) during NIR-to-UV ‘remote-control’ photosolvolysis in a micro cuvette. (a) Changes in absorbance during irradiation with 980 nm light (1.45 W/cm², 0.41 W) along the horizontal axis. (b) Changes in absorbance of the same sample during time plotted at 257 nm. (c) Changes in absorbance of the same sample during irradiation with 980 nm light (4.27 W/cm², 1.21 W) along the vertical axis. (d) Changes in absorbance of the same sample during time plotted at 257 nm.

9.5.8.5 NIR-to-UV ‘remote-control’ photoswitching of **22-NP** in THF

The partly unfavourable results in Section 9.5.8.3 and 9.5.8.4 stand in stark contrast to a comparison using the DTE switch functionalized UCNP **22-NP**, see Figure 9.14a. The previously reported DTE photoswitch^[29,159,288] **22** (compound **1a** in Chapter 6) was attached to **a-NP** by CuAAC ‘click’ chemistry (see experimental section 9.8 for details). It was found that **22-NP** in THF undergoes the NIR-to-UV ‘remote-control’ photoreaction to a much greater extent than **5-NP** in CH₃CN during 60 minutes of ‘biologically benign’ 980 nm light irradiation (1.45 W/cm², 0.41 W) along the horizontal axis of the cuvette (Figure 9.14b,c). This improved efficiency in acetonitrile is likely due to a better

photoswitching action cross section at around 350 nm where the nanoparticles emits most UV light and demonstrates that NIR-to-UV 'remote-control' photoreactions can indeed proceed relatively efficiently at low excitation power-densities by choosing correct photoactive substrate based on its photoreaction action cross section.

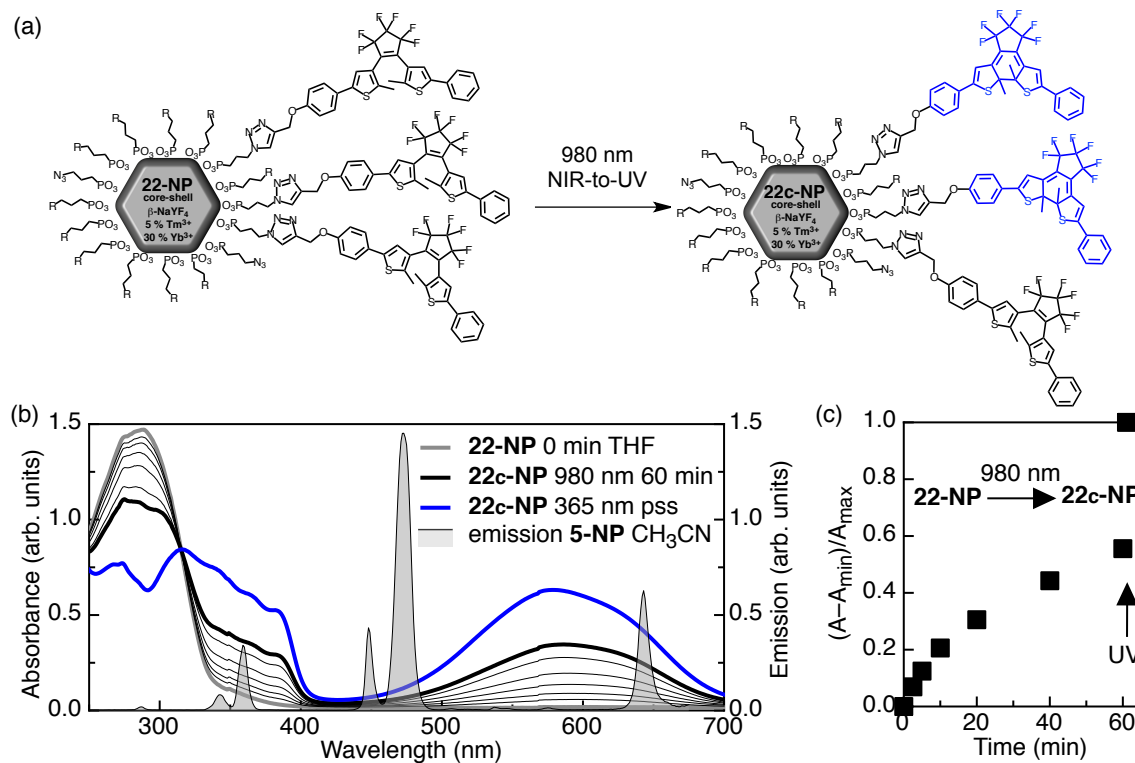


Figure 9.14 (a) Schematic representation of the synthesized DTE functionalized nanoparticle **22-NP** before and after photoswitching. (b) *Left y-axis*: Changes in the UV-vis absorbance spectra during the 'remote-control' photochemical reaction **22-NP**→**22c-NP** upon 'biologically benign' power levels of 980 nm irradiation (0-60 min, 1.45 W/cm², 0.41 W) in THF (0.025 ml stock dispersion of **22-NP** in 0.2 ml THF). The blue trace is the absorbance of **22c-NP** at the photostationary state after irradiation with 365 nm light (60 s, 1.4 mW/cm², 3.9 mW). *Right y-axis*: Emission spectra of **5-NP** in CH₃CN upon 980 nm excitation (1.45 W/cm², 0.41 W), emissions past 670 nm are not included in the spectra. (c) Normalized changes in absorbance during time, plotted at 608 nm. The arrow indicates the time the excitation source was changed from 980 nm to broadband 365 nm light (1.4 mW/cm², 3.9 mW).

9.5.9 Phototriggered release from 5-NP, detection of Chlorambucil

In order for the nano-photorelease system **5-NP** to be useful as designed, Chlorambucil must stay intact and be able to diffuse from the surface after photoinduced release. To prove that Chlorambucil is able to diffuse from the mPEGylated UCNP surface after photorelease, it is imperative to detect Chlorambucil after photosolvolysis in water.

9.5.9.1 Detection of Chlorambucil by UV-vis spectroscopy – direct UV irradiation experiment

As HPLC did not prove to be a great technique of Chlorambucil detection due to technical difficulties, UV-vis spectroscopy was chosen as a means to detect the presence of Chlorambucil after UV light and NIR-to-UV irradiation based on Chlorambucil's distinctive UV absorption profile, see Figure 9.16 and 9.17.

Several samples of **5-NP** were irradiated with either broadband 312, 365 or monochromatic 350 nm UV light in water to induce the release. The presence of Chlorambucil was examined by UV-vis spectroscopy in both the spin-filtrate after centrifugation through a 10 KDa spin-filter and in the supernatant after centrifugation. The spin-filtering technique is superior over the latter technique as it removes the nanoparticles more efficiently.

In Figure 9.15 the result of a typical spin-filtering experiment are presented using 365 nm light as the excitation source: An aliquot of **5-NP** stock-solution (0.05 ml, CH₃CN) was diluted with water (0.4 ml) in a spin-filter. After three centrifugation washes with water (0.4 ml), the UV-vis absorption profiles of both the last wash spin-filtrate and the diluted **5-NP** sample (0.4 ml water) from

the spin-filter was examined by UV-vis spectroscopy. The **5-NP** sample was irradiated for 10 minutes with broadband 365 nm light (1.4 mW/cm^2 , 3.9 mW), the absorbance was measured and the sample was centrifuged in a spin-filter and the spin-filtrate was examined. The spin-filtrate did indeed contain a heightened UV absorption trace compared to the wash prior to irradiation, which indicates successful release of molecules from the surface of the nanoparticles, see Figure 9.15.

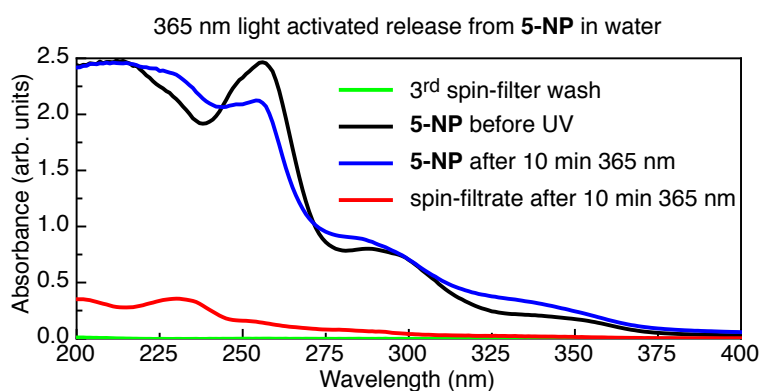


Figure 9.15 The figure describes a photorelease experiment examined by UV-vis spectroscopy. An aliquot of acetonitrile stock dispersion of **5-NP** (0.05 ml) was diluted with water (0.4 ml) in a 10 kDa spin-filter and washed with water (3 x 0.4 ml) by three centrifugation/re-dispersion cycles. The green trace is the filtrate from the third wash. The black trace is the sample in the filter after three washes, re-diluted with water (0.4 ml). The blue trace is after irradiation with broadband 365 nm light (1.4 mW/cm^2 , 3.9 mW) for 10 minutes. The red trace is the spin-filtrate after irradiation.

However, none of the UV absorption spectra from any broadband 365 nm irradiation experiments match the UV absorbance profile of Chlorambucil, not even when **5-NP** is irradiated with monochromatic light centered at 350 nm (9 nm slit-width, 167 mW/cm^2 , experimental data not shown) where Chlorambucil absorbs with a minimal molar absorption coefficient. In Figure 9.16 the UV absorbance profile of the spin-filtrate after 10 min of broadband 365 nm light

irradiation (red trace), is overlaid with the absorbance trace of Chlorambucil (black trace) to demonstrate the dissimilarities.

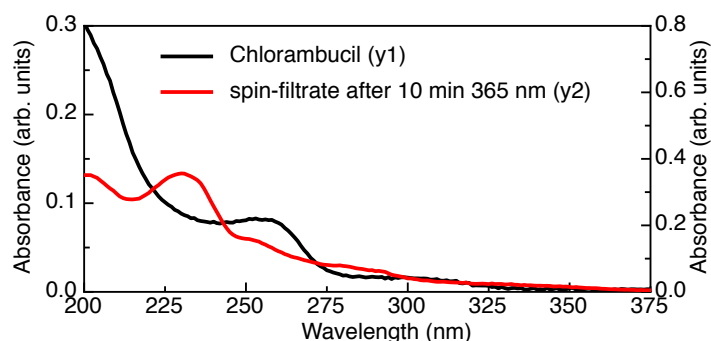
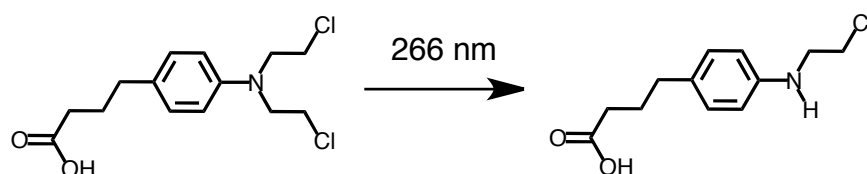


Figure 9.16 UV-vis absorption spectra of Chlorambucil (1×10^{-5} M in water, black trace, *left y-axis*) and the spin-filtrate of **5-NP** from figure 9.15 after 10 min broadband 365 nm light irradiation (red trace, *right y-axis*) (1.4 mW/cm^2 , 3.9 mW).

It was previously reported that Chlorambucil underwent a de-alkylation reaction upon 266 nm light irradiation, see Scheme 9.6.^[267] In contrast to this, it was found that Chlorambucil stayed intact upon 420 nm light irradiation.^[266]



Scheme 9.6 Chlorambucil has previously been found to decompose under 266 nm light irradiation.^[267]

To investigate the photostability of Chlorambucil under UVA irradiation, a sample was irradiated with broadband 365 nm light (1.4 mW/cm^2 , 3.9 mW) and changes were rapidly observed in its UV-vis spectrum, see Figure 9.17. A sharp decrease of the peak centered at 257 nm was observed over the first few

minutes of irradiation and after 20 minutes of irradiation the changes in the spectrum were very small, see figure 9.17. This behaviour suggests rapid photo-degradation/reactivity to a relatively photostable photoproduct under UVA light irradiation, in accordance with the findings of Härtner, Kim and Hampp under 266 nm light irradiation.^[267]

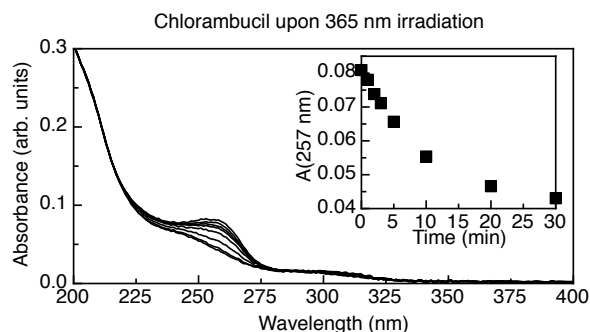


Figure 9.17 Changes in absorption of Chlorambucil (1×10^{-5} M in H_2O) upon broadband 365 nm light irradiation (1.4 mW/cm^2 , 3.9 mW). The inset display the changes in absorption plotted at 257 nm.

However, none of the UV-vis absorbance spectra acquired from the spin-filtrates/supernatants of **5-NP** after irradiation with broadband 365 nm light match the UV-vis absorbance spectrum of Chlorambucil after 365 nm light irradiation in water as can be seen in figure 9.18.

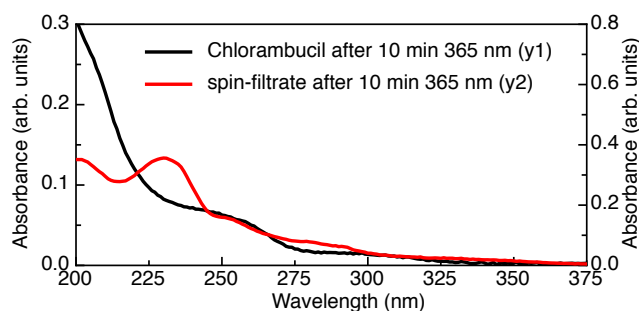


Figure 9.18 UV-vis absorbance spectra of Chlorambucil after 10 minutes of 365 nm light irradiation (1.4 mW/cm^2 , 3.9 mW) (black trace, *left y-axis*) and the spin-filtrate of **5-NP** after 10 minutes of 365 nm light irradiation (1.4 mW/cm^2 , 3.9 mW) from Figure 9.15 (red trace, *right y-axis*).

It thus appears that the photoproduct(s) released from **5-NP** upon broadband 365 nm light irradiation are different from the photoproduct obtained by irradiating pure Chlorambucil under the same conditions. To further investigate the nature of the released product, the spin-filtrate after 10 min irradiation with broadband 365 nm light from Figure 9.15 was examined by low resolution mass spectrometry (LRMS) and major peaks at $m/z = 173.1$, $m/z = 235.0$ and $m/z = 268.2$ were observed in the spectra, neither which correspond to Chlorambucil (exact mass: 303.0793 g/mol) or its proposed de-alkylated photoproduct^[267] (exact mass: 241.0870 g/mol), see Figure 9.19. However, a very small intensity peak at $m/z = 304.1$ was observed in the low-resolution mass spectrum that could potentially correspond to Chlorambucil $[M+H]^+$. Moreover, peaks ranging from $m/z = 400 - 800$ are present in the mass spectrum suggesting that polymers are potentially^[289] released from the surface during direct 365 nm light irradiation as such peaks appear typical for polydispersed polymeric materials, see Figure 9.19. The release of polymers

from the surface during irradiation with 365 nm light could potentially explain why a size-expansion is observed in the DLS experiment after irradiation with 365 nm light due to potential aggregations of 'bare' surfaces, see Figure 9.9.

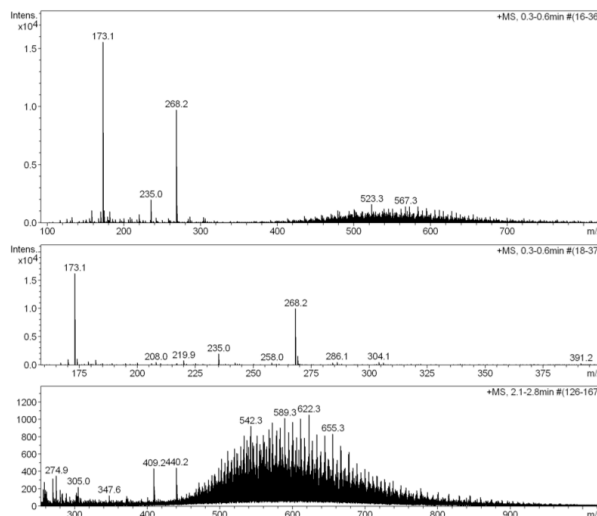


Figure 9.19 LRMS raw data of the spin-filtrate from figure 9.15 after 10 min broadband 365 nm light irradiation (1.4 mW/cm², 3.9 mW). Chlorambucil exact mass: 303.0793 g/mol. Proposed de-alkylated photoproduct^[267] exact mass: 241.0870 g/mol.

9.5.9.2 Detection of Chlorambucil by UV-vis spectroscopy - NIR-to-UV 'remote-control' experiment

Since Chlorambucil was found to decompose during direct UV light irradiation, an experiment to detect Chlorambucil or its proposed de-alkylated photoproduct (see Scheme 9.6) after NIR-to-UV 'remote-control' photosolvolytic was carried out. As in section 9.5.9.1, the sample was first washed in a spin-filter to remove any impurities. The re-dispersed sample (in nano-pure water) was irradiated with 980 nm light (4.27 W/cm², 1.21 W) while cooled in a water bath at ambient temperature. The reaction progression of the sample was followed by

UV-vis spectroscopy and after 2 hours the sample was spin-filtered. A very small change in the UV-vis absorption spectra before and after irradiation was detected, see Figure 9.21.

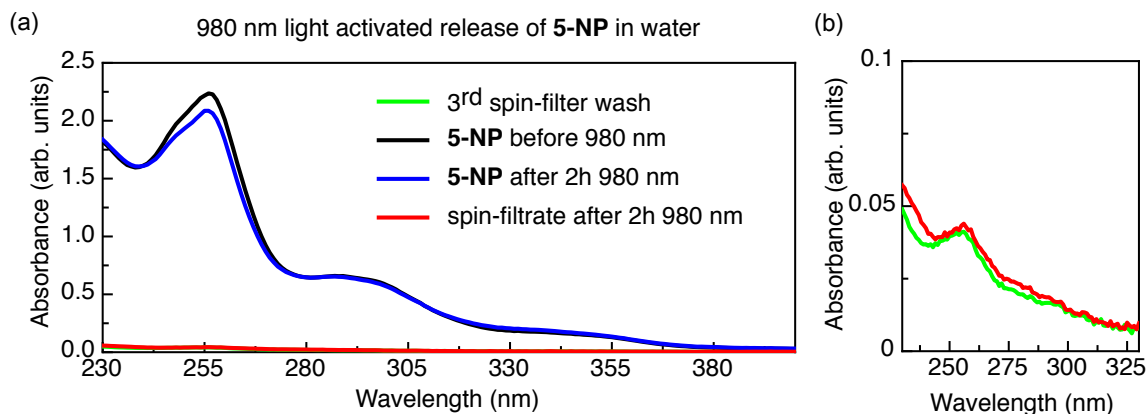


Figure 9.20 (a) The figure describes a photorelease experiment examined by UV-vis spectroscopy. An aliquot of acetonitrile stock dispersion of **5-NP** (0.05 ml) was diluted with water (0.4 ml) in a 10 kDa spin-filter and washed with water (3 x 0.4 ml) by three centrifugation/re-dispersion cycles. The green trace is the spin-filtrate from the third wash. The black trace is the sample in the filter after three washes, re-diluted with water (0.4 ml). The blue trace is after irradiation with 980 nm light (4.27 W/cm^2 , 1.21 W) for 120 minutes. The red trace is the spin-filtrate after irradiation. (b) Magnification of the UV-vis absorbances of the spin-filter wash (green trace) and the spin-filtrate after 980 nm irradiation (red trace).

The spin-filtered sample from Figure 9.20 was further examined by LRMS but no peaks corresponding to either Chlorambucil or its proposed de-alkylated photoproduct were detected in the spectra, see Figure 9.21. Moreover, no peaks attributed to polymers as in the direct UV light photosolvolytic experiment were observed in the LRMS spectra as was encountered in the sample irradiated with 365 nm light, see Figure 9.15, 9.19 and 9.21.

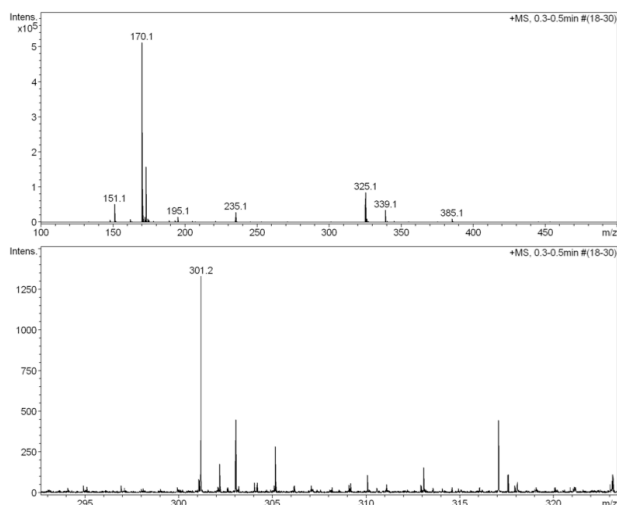


Figure 9.21 LRMS raw data of the spin-filtrate from Figure 9.21 after 2 hours irradiation with 980 nm light irradiation. Chlorambucil exact mass: 303.0793 g/mol. Proposed de-alkylated photoproduct^[267] exact mass: 241.0870 g/mol.

9.6 Conclusion

At the present stage of development, out of the 5 constituted criteria presented in the introduction of this chapter; criteria 1 through 3 have been successfully solved. It has been demonstrated that PEGylated molecules can be easily loaded onto azide-functionalized UCNPs without silica coating using CuAAC ‘click’ chemistry and produce highly water-dispersible and stable nanoparticles in FBS and in the presence of ATP at elevated temperature.

A further accomplishment was the completion of a multi-step synthesis of a fully water-soluble mPEGylated 3',5'-dialkoxybenzoin photocage functionalized with a hydrophobic biologically active ligand, something that has scarcely been demonstrated previously using photocages in the 3',5'-alkoxybenzoin family.^[201]

However, due to the choice of both photorelease system and therapeutic cargo, the current system **5-NP** is impractical and criteria 4 and 5 were not solved.

The NIR-to-UV 'remote-control' photolysis/photosolvolysis reaction proceeded exceptionally sluggish at 'biologically benign' 980 nm power levels (1.45 W/cm², 0.41 W) in both organic and aqueous solvent at the conditions examined, although the reactions did proceed while irradiated with higher 'non-biologically benign' 980 nm light power-densities (4.27 W/cm², 1.21 W).

Furthermore, the detection of Chlorambucil was not successful and Chlorambucil was found to decompose upon broadband 365 nm light irradiation. Even though a heightened absorption trace was observed after broadband 365 nm light photosolvolysis in water using UV-vis spectroscopy as a detection method, the acquired UV absorption trace after irradiation of **5-NP** did not match that of Chlorambucil before or after direct UV light irradiation. Moreover, a similar negative result was obtained after NIR-to-UV 'remote-control' irradiation and Chlorambucil could not be detected after photosolvolysis using this method of release either. The spin-filtered solutions from the nanoparticle after direct and indirect irradiation was examined by low-resolution mass spectrometry, but only unassignable peaks were observed.

Since the NIR-to-UV 'remote-control' photorelease reaction did not proceed efficiently enough upon 'biologically benign' 980 nm light power-density irradiation at the conditions tested, and because Chlorambucil could not be

detected after either direct (UV) or indirect (NIR) irradiation, the current version of the photorelease system is impractical.

However, some of the design concepts and technological advances developed throughout this thesis are anticipated to be useful and can potentially be adopted for future, better and more advanced versions of NIR-to-UV 'remote-control' photorelease systems.

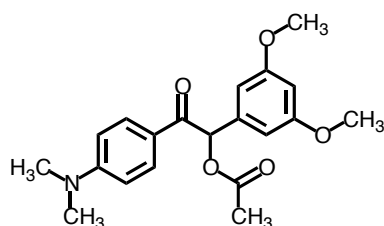
9.7 Future directions

9.7.1 Release system

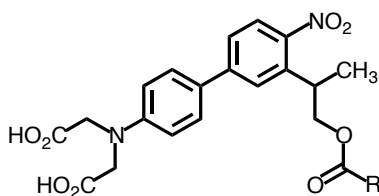
In order to solve the problem of poor absorption overlap of the photorelease system with the largest upconverted UV emission from the UCNP to make the system practically useful many different options can be considered:

1) A more efficient UVA light-absorbing dialkoxybenzoin photocage can be developed that has a greater absorption overlap with the strongest NIR-to-UV emission of the nanoparticle compared to the previously used 3',5'-dialkoxybenzoin photocages. The following chapter (*Chapter 10*) describes the successful synthesis and preliminary characteristics of such a photocage release system. The new donor-acceptor 4-dimethylamino-3',5'-dialkoxybenzoin photocage has substantially more absorption ($\epsilon_{347\text{nm}}: 25966 \text{ M}^{-1}\text{cm}^{-1}$) than both the phenyl- and naphthyl-benzoin systems previously described and is likely the most efficient photorelease system for UVA light triggered release to date.^[290,291] Furthermore, it is demonstrated that the NIR-to-UV 'remote-control' photorelease reaction of this novel photocage proceeds relatively efficiently at biologically benign NIR power-densities in CH_2Cl_2 , which potentially solves criteria 5

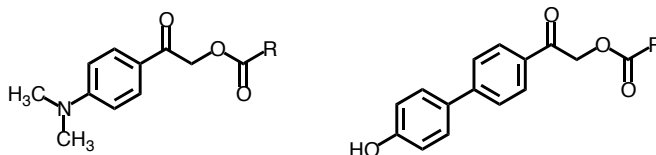
presented in the introduction of this chapter. However, although exhibiting successful release, not all the photoproducts or the mechanism of this unexpected and unique photoreaction have been fully identified at this stage, see chapter 10.



2) Another option is to revert to the already proven successful 2-Nitrobenzyl photocage system.^[168,171,243] A recently-developed donor-acceptor biphenyl derivative in the propyl series^[182,183] appears to be a promising candidate for this purpose. It has a somewhat acceptable one-photon uncaging action cross section at UVA wavelengths ($\epsilon_{397\text{nm}}$: $7500 \text{ M}^{-1}\text{cm}^{-1}$, $\Phi_{400 \text{ nm}}$: 0.15, $\Phi\epsilon$: $1125 \text{ M}^{-1}\text{cm}^{-1}$)^[182] and has a large two-photon excitation (2PE) uncaging cross section (11 GM) upon 800 nm pulsed laser irradiation.^[182] A relatively efficient photorelease system would thus likely be obtained by combining the NIR-to-UV upconversion from the nanoparticles with the 800 nm 2PE to activate release of the photocage using two different laser sources.

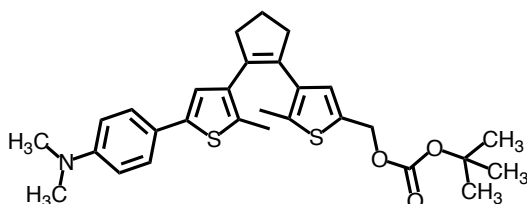


3) Other promising photocages in combination with NIR-to-UV ‘remote-control’ photolysis are either the 4-dimethylaminophenacyl photocage^[190,191] ($\epsilon_{347\text{nm}}$: $\sim 26000 \text{ M}^{-1}\text{cm}^{-1}$,^[292] Φ : N.A., $\Phi\epsilon$: N.A) or the 4'-hydroxybiphenylacyl photocage^[183] ($\epsilon_{313\text{nm}}$: $14800 \text{ M}^{-1}\text{cm}^{-1}$, Φ : 0.21, $\Phi\epsilon$: $3100 \text{ M}^{-1}\text{cm}^{-1}$). Apart from good absorption overlap with the UCNP UV emission, the photoproduct of the 4-hydroxyphenacyl photocage class has a blue-shifted absorbance compared to the starting material. It is thus expected that the NIR-to-UV ‘remote-control’ photolysis should proceed efficiently as the photoproduct does not compete for UV light absorbance to a large degree. However, the photoproducts of the 4-dimethylaminophenacyl^[190,191] and 4'-hydroxybiphenylacyl^[183] derivatives have not been characterized sufficiently and it is therefore uncertain if they react the same way as the parent 4-hydroxyphenacyl photocage.



4) Another option is to use our recently developed multimodal photo-triggered self-immolative photorelease system that is based on the DTE framework.^[197] Since DTE based molecules evidently respond efficiently to NIR-to-UV activation using biologically benign laser power-densities the photocage would likely respond efficiently to NIR-to-UV ‘remote-control’ activation, see Figure 9.14 and 6.20. However, since the photocage is ‘armed’ with UV light and subsequently triggered to undergo release with heat, UV or visible light the release process of this photocage system is not optimum for solely NIR-to-UV ‘remote-control’ photorelease and should be used in conjunction with visible light

irradiation. However, the unidentified ionic photoproduct of this novel photorelease reaction is potentially cytotoxic as it reacts with various nucleophiles (including water) to an unidentified product(s) and must be further investigated.^[197]

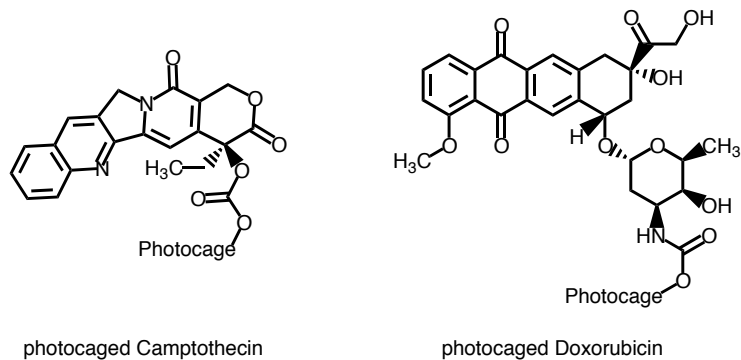


9.7.2 Therapeutic drug

When choosing the therapeutic drug to be released, it is important to choose robust molecules that will not photodegrade during NIR-to-UV irradiation (or direct UV light).

One drug candidate to be considered for this purpose is the anticancer drug Doxorubicin as this fluorescent molecule has previously and successfully been used for photorelease with UV light.^[293,294,295] However, even though this molecule is commercially available, it is rather expensive, chiral and possesses numerous reactive functional groups that could potentially interfere during extensive synthetic work, unless protected or attached in the last step.

Another anticancer drug to be considered is Camptothecin as it is commercially available (cheaper than Doxorubicin), has a relatively simple structure, can be connected to a photocage through a carbonate bond and has been successfully released with UV light previously.^[295,296] However, this fluorescent molecule absorbs UV light with a maxima centered at 360 nm and will thus compete with the photocage for NIR-to-UV absorption.^[297]



9.7.3 Ligands for selective targeting and remote detection

By using the 'click' chemistry approach, the surface of the UCNP can (theoretically) be co-functionalized in one step with multiple functionality such as targeting ligands, remotely detectable probes and photocaged therapeutics. Such a multifunctional phototriggered theranostic^[249] drug-delivery system can be selectively retained at a tissue target by active action of the targeting ligands and passive action by the enhanced permeability and retention (EPR) effect. Probes attached to the UCNP can be used to detect the location of the nanoparticles remotely and non-invasively using existing technology such as positron emission topography (PET) or magnetic resonance imaging (MRI). The UCNP can be further detected remotely by the NIR-to-NIR/vis upconversion fluorescence and subsequently triggered to release bioactive molecules on-demand by NIR-to-UV 'remote-control' photochemistry.

Co-functionalizing the UCNP surface with bi-functional PEG polymers^[298] and mPEGylated photocaged therapeutics may provide water dispersibility of the nanoparticle when simultaneously co-functionalized with a low concentration of

non-PEGylated hydrophobic probes. A schematic illustration of such a system is described in Figure 9.23.

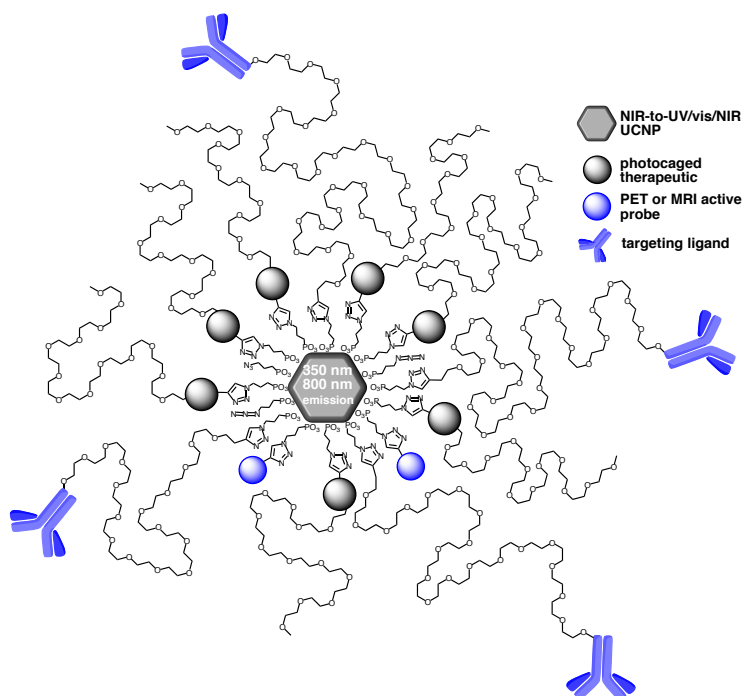


Figure 9.22 Schematic illustration of a multifunctional UCNP for advanced theranostic drug delivery using CuAAC chemistry as a means to decorate the nanoparticle with multiple ligands.

9.8 Experimental

9.8.1 General methods

All reagents and solvents used for synthesis, chromatography, photochemistry and UV–vis spectroscopy measurements were purchased from Aldrich and used as received, unless otherwise noted. 3,5-dihydroxybenzaldehyde was purchased from Matrix Scientific. Anhydrous ethanol (EtOH) was purchased from Commercial Alcohols. Triethylamine was purchased from Anachemia. Anhydrous CH_2Cl_2 was purchased from Aldrich and

passed through activated alumina using a solvent purification system before use. CD_2Cl_2 was purchased from Cambridge Isotope Laboratories and used as received. mPEG-CO₂H was purchased from Rapp Polymere. Column chromatography was performed using silica gel 60 (230–400 mesh) from Silicycle Inc. The oleate coated 5 % Thulium and 30 % Ytterbium co-doped core-shell hexagonal(β)-phase NaYF₄ UCNP (**o-NP**)^[10] and 3-azidopropylphosphonic acid^[132] were synthesized according to published procedures. Melting points were measured using a Gallenkamp melting point apparatus (Registered Design No. 889339) and reported without correction.

9.8.1.1 Spectroscopic studies

¹H NMR and ¹³C NMR characterizations were carried out using a Bruker AVANCE III (5 mm TXI inverse probe) working at 500.19 MHz for ¹H NMR and at 125.77 MHz for ¹³C NMR and a Bruker AVIII 400 BBO Plus (5 mm probe) working at 400.13 MHz for ¹H NMR and 100.60 MHz for ¹³C NMR. Chemical shifts (δ) are reported in parts per million relative to tetramethylsilane using the residual solvent peak as a reference standard. Coupling constants (J) are reported in hertz. Transmission electron microscopy (TEM) images were obtained using a Tecnai 200 keV Field Emission Scanning Transmission Electron Microscope. Dilute colloid of **5-NP** (0.1 wt-%) dispersed in CH₃CN were drop-casted on thin, carbon formvar-coated copper grids for imaging. The NP shape and crystallinity were evaluated from the collected TEM images, while the particle size was calculated from 140 particles using Adobe acrobat reader software. Dynamic Light Scattering (DLS) measurements were carried out using

a Malvern Zetasizer Nano-ZS. A nanoparticle concentration of 0.05 ml **5-NP** stock-solution in 3 ml nanopure H₂O filtered through a 0.2 µm PTFE syringe-filter was employed for the measurements. All DLS measurements were conducted at 25 °C. IR spectra were acquired on a Bomem (Hartmann & Braun, MB-Series) spectrometer. IR samples were prepared by mixing approximately 1 part of dried, functionalized nanoparticles with 10 parts of KBr after which they were pressed into translucent discs (experimental data not shown). A Varian Cary 300 Bio spectrophotometer was used to acquire all UV-vis spectra. All volumes were measured out using 1 mL disposable syringes and 22 gauge needles. Emission spectra of colloidal solutions of **5-NP** were measured on a PTI Quantmaster spectrofluorometer. A JDS Uniphase 980 nm continues-wave laser diode (device type L4-9897510-100M) coupled to a 105 µm (core) fiber was employed as the excitation source. The output of the diode laser was collimated and directed through the sample perpendicular to the read-out plane of the fluorospectrometer using a Newport F-91-C1-T Multimode Fiber Coupler. All emission spectra were corrected for the instrument sensitivity. The fluorescence was recorded with a slit size of 4 nm, step size: 1 nm and integration: 0.5 s. Laser and light power was measured on a Gentec TPM-300. The power density of the laser beam was calculated by dividing the recorded power by the laser beam area. Exact mass measurements were measured using a Kratos Concept-H instrument with perfluorokerosene as the standard.

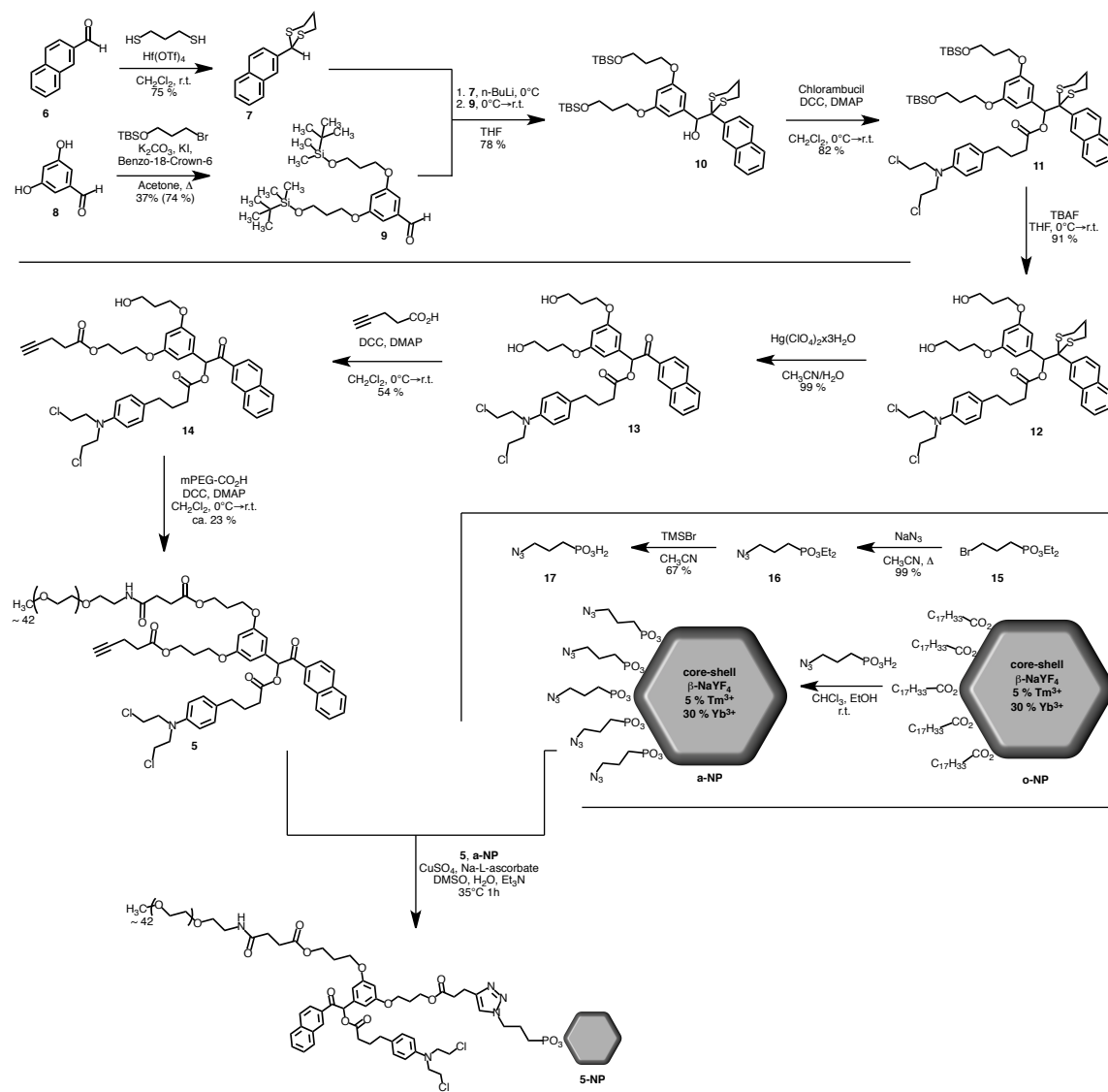
9.8.1.2 Photochemistry

Direct UV light irradiations of **5-NP** and **5** were carried out using the light source from a lamp used for visualizing TLC plates at 365 nm (1.4 mW/cm², 3.9 mW) or 312 nm (2.1 mW/cm², 5.9 mW). Monochromatic light centred at 350 nm (slit size: 9 nm, 167 mW/cm²) using the light source from the spectrofluorometer was also used (experimental data not shown). NIR light excitation of **5-NP** was executed using a JDS Uniphase 980 nm laser diode (device type L4-9897510-100M) coupled to a 105 µm (core) fibre. The laser beam was collimated, focused and directed horizontally or vertically through the samples using a Newport F-91-C1-T Multimode Fiber Coupler. NIR-to-UV 'remote-control' photolysis/photosolvolyis were performed in a micro cuvette (total volume: 0.71 ml, sample compartment: 5 × 5 × 40 mm). All photochemistry was performed under scarce light conditions to eliminate any potential interference from ambient light during the irradiation procedures.

9.8.1.3 Emission quenching experiments

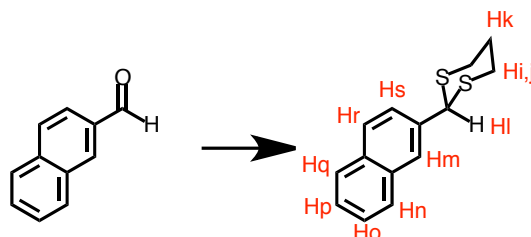
The amount of emission quenching in H₂O compared to CH₃CN of **5-NP** was calculated using Microsoft Excel software by calculating the area under each line segment of the emission graph by the formula: $0.5 \times (\text{wavelength } 2 - \text{wavelength } 1) \times (\text{emission } 2 + \text{emission } 1)$ followed by adding up all of the values (=Sum) for that specific wavelength or emission segment.

9.8.2 Synthesis of organic molecules and organic-nanoparticle hybrid systems



Scheme 9.7 Total synthesis of hybrid nanoparticle 5-NP

9.8.2.1 Synthesis of 7



2-(naphthalen-2-yl)-1,3-dithiane^[275]

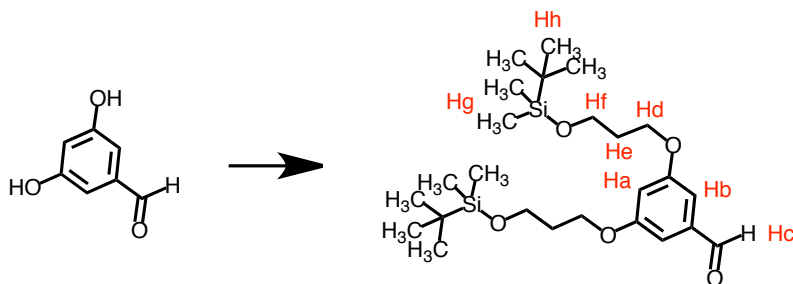
2-Naphthaldehyde (4.5 g, 28.83 mmol) was dissolved in CH₂Cl₂ (50 ml), 1,3-propanedithiol (2.9 ml, 28.83 mmol) followed by Hf(Otf)₄ (111.7 mg, 0.144 mmol) was added. The colourless solution was stirred over night, at which point the hazy solution was filtered through a Celite pad and rinsed several times with CH₂Cl₂. The solvent was evaporated to yield a white solid that was recrystallized from hexanes and acetone. The title compound **7** was afforded as off-white needles (5.33 g, 21.64 mmol, 75 % + uncrystallized product 1.31 g)

M.p. 105-107°C

¹H NMR (CDCl₃, 400 MHz) δ: 7.95 (bs, 1H, **Hm**), 7.84-7.78 (m, 3H, **Hn**, **Hr**, **Hq**), 7.59-7.56 (m, 1H, **Hs**), 7.48-7.44 (m, 2H, **Hp**, **Ho**), 5.32 (s, 1H, **Hl**), 3.12-3.05 (m, 2H, **Hi**), 2.95-2.90 (m, 2H, **Hj**), 2.21-2.16 (m, 1H, **Hk**), 2.15-1.94 (m, 1H, **Hk**)

¹³C NMR (CDCl₃, 100 MHz) δ: 136.66, 133.49, 133.43, 128.67, 128.24, 127.83, 127.01, 126.48, 126.45, 125.86, 51.74, 32.30, 25.35

9.8.2.2 Synthesis of 9



3,5-bis(3-((*tert*-butyldimethylsilyl)oxy)propoxy)benzaldehyde

Note: It was intended to make the monofunctional molecule **18** (see Scheme 9.3) but that molecule was only isolated in trace quantities – therefore the bis-alkylated isomer **9** was carried forward in the synthesis.

A flame dried round bottom flask, stir bar and condenser was cooled to ambient temperature under N₂ purge. 3,5-Dihydroxybenzaldehyde **8** (Matrix Scientific) (2.07 g, 14.98 mmol), K₂CO₃ (anhydrous, 6.21 mg, 44.93 mmol), KI (124.30 mg, 0.75 mmol) and Benzo-18-crown-6 (234 mg, 0.75 mmol) was added and the system was purged with N₂. The solids were dissolved in CH₃CN (anhydrous, 20 ml, Aldrich) and (3-Bromopropoxy)-*tert*-butyldimethylsilane (3.47 ml, 14.98 mmol) was added. The reaction mixture was heated to reflux and stirred for 7 hours after which it was cooled to ambient temperature and transferred to a separatory funnel. The crude reaction mixture was diluted with sat. aq. NH₄Cl, H₂O and EtOAc. The resulting emulsion was vacuum filtered, the layers separated and the aqueous layer was extracted 3 times with EtOAc. The combined organic extracts were dried over anhydrous MgSO₄, vacuum filtered and concentrated under reduced pressure to a dark red oil. The crude oil was purified by silica gel column chromatography (gradient 0.75:9.25→1:1 EtOAc:Hexanes). The title compound **9** was obtained as an orange oil which was

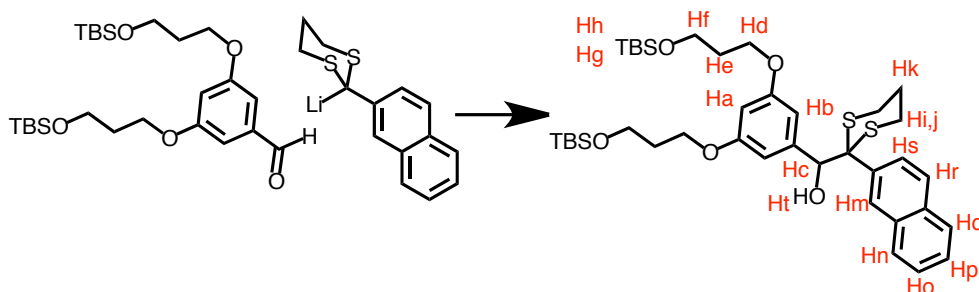
repurified by silica gel chromatography (0.2:9.8 EtOAc:Hexanes) to yield a light yellow oil. (2.7 g, 5.59 mmol, 37 % (74 % when calculated using 3-bromopropoxy)-tert-butyldimethylsilane as the limiting reagent))

^1H NMR (CD_2Cl_2 , 400 MHz) δ : 9.88 (s, 1H, **Hc**) 6.99 (d, $J = 2.28$ Hz, 2H, **Hb**), 6.72 (t, $J = 2.28$ Hz, 1H, **Ha**), 4.41 (t, $J = 6.16$ Hz, 4H, **Hd**), 3.80 (t, $J = 5.96$ Hz, 4H, **Hf**), 1.96 (p, $J = 6.08$ Hz, 4H, **He**), 0.88 (s, 18H, **Hh**), 0.044 (s, 12H, **Hg**)

^{13}C NMR (CD_2Cl_2 , 100 MHz) δ : 192.39, 161.36, 139.09, 108.30, 108.04, 65.56, 59.84, 32.86, 32.16, 26.27, 5.14

HRMS (ESI $^+$) Anal. Calc. for $\text{C}_{25}\text{H}_{47}\text{O}_5\text{Si}_2$ (M+H) $^+$ 483.2962 Found: (M+H) $^+$ 483.2958

9.8.2.3 Synthesis of 10



(3,5-bis(3-((*tert*-butyldimethylsilyl)oxy)propoxy)phenyl)(2-(naphthalen-2-yl)-1,3-dithian-2-yl)methanol

A flame dried followed by oven dried round bottom flask and stir bar was cooled to ambient temperature under N_2 purge. The flask was charged with **7** (970.8 mg, 3.94 mmol) and further purged with N_2 . Freshly distilled THF (ca. 20 ml) was cannulated into the reaction flask. The solution was cooled to 0°C in an

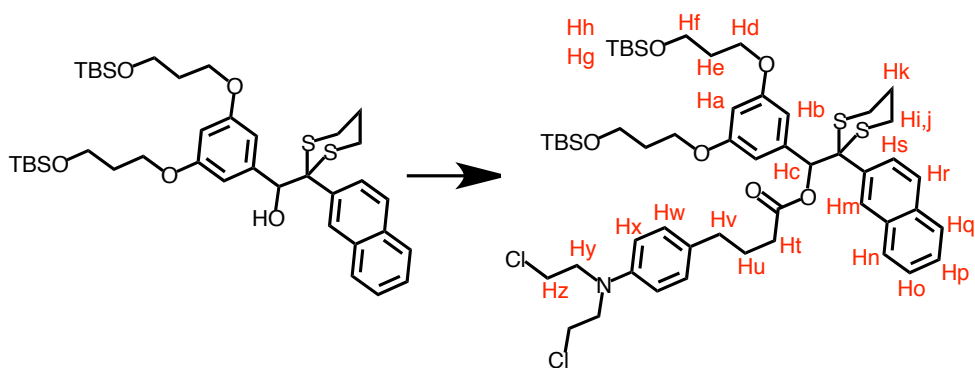
ice/water bath. n-BuLi (1.58 ml, 3.94 mmol, 2.5 M in THF) was slowly added drop wise. The resulting dark brown solution was stirred at 0°C for 30 minutes before **9** (2 g, 4.14 mmol) was quickly added by opening the septa followed by N₂ purge. The resulting light yellow solution was removed from the ice-bath and stirred for 40 minutes before the reaction was quenched with sat. aq. NH₄Cl. The crude mixture was diluted with H₂O and EtOAc and transferred to a separatory funnel. The layers were separated and the aqueous layer was extracted 3 times with EtOAc. The combined organic extracts were dried over MgSO₄, vacuum filtered and concentrated under reduced pressure to yield a yellow oil (which bubbles/foams heavily under hi-vacuum). The title compound **10** was purified by silica gel column chromatography (gradient: 0.5:9.5→1:9→2:8 EtOAc:Hexanes) and obtained as a light yellow sticky oil (2.23 g, 78 %). (Great care should be taken when working under vacuum with this compound as it foams/bubbles heavily and is very sticky)

¹H NMR (CD₂Cl₂, 400 MHz) δ: 8.19 (d, *J* = 1.32 Hz, 1H, **Hq**), 7.90-7.87 (m, 1H, **Hn**), 7.83-7.78 (m, 3H, **Hr**, **Ho**, **Hp**), 7.52-7.43 (m, 2H, **Hs**, **Hm**), 6.25 (t, *J* = 2.20 Hz, 1H, **Ha**), 5.97 (d, *J* = 2.20 Hz, 2H, **Hb**), 4.96 (d, *J* = 3.92 Hz, 1H, **Hc**), 3.62-3.56 (m, 8H, **Hf**, **Hd**), 2.93 (d, *J* = 3.92 Hz, 1H, **Ht**), 2.75-2.63 (m, 4H, **Hi**, **Hj**), 1.91-1.89 (m, 2H, **Hk**), 1.71 (p, *J* = 6.20 Hz, 4H, **He**), 0.88 (s, 18H, **Hh**), 0.044 (s, 12H, **Hg**)

¹³C NMR (CD₂Cl₂, 100 MHz) δ: 159.48, 140.02, 136.03, 133.71, 133.14, 131.16, 128.93, 128.48, 128.07, 127.71, 127.03, 126.60, 107.28, 102.14, 81.56, 66.91, 64.94, 60.02, 32.85, 28.02, 27.90, 26.26, 25.43, 18.73, 5.09

HRMS (ESI⁺) Anal. Calc. for C₃₉H₆₁O₅Si₂S₂ (M+H)⁺ 722.3499 Found: (M+H)⁺ 729.3487

9.8.2.4 Synthesis of 11



(3,5-bis(3-((*tert*-butyldimethylsilyl)oxy)propoxy)phenyl)(2-(naphthalen-2-yl)-1,3-dithian-2-yl)methyl 4-(4-(bis(2-chloroethyl)amino) phenyl)butanoate

A flame dried and oven dried round bottom flask and stir bar was cooled under N₂ purge. The flask was charged with **10** (1.186 g, 1.63 mmol) and purged with N₂, anhydrous CH₂Cl₂ (15 ml) was cannulated over. The solution was cooled to 0°C in an ice/water bath. DMAP (218.6 mg, 1.79 mmol) and DCC (369.1 mg, 1.79 mmol) were added by opening the septa, after the addition the system was purged with N₂. After addition the flask was removed from the cold bath and stirred at ambient temperature for 20 hours. The resulting dispersion was vacuum filtered and washed with CH₂Cl₂ several times. The filtrate was diluted with water, layers separated and the aqueous phase was extracted 3 times with CH₂Cl₂. The combined organic extracts were dried over anhydrous MgSO₄, vacuum filtered and concentrated under reduced pressure to a yellow

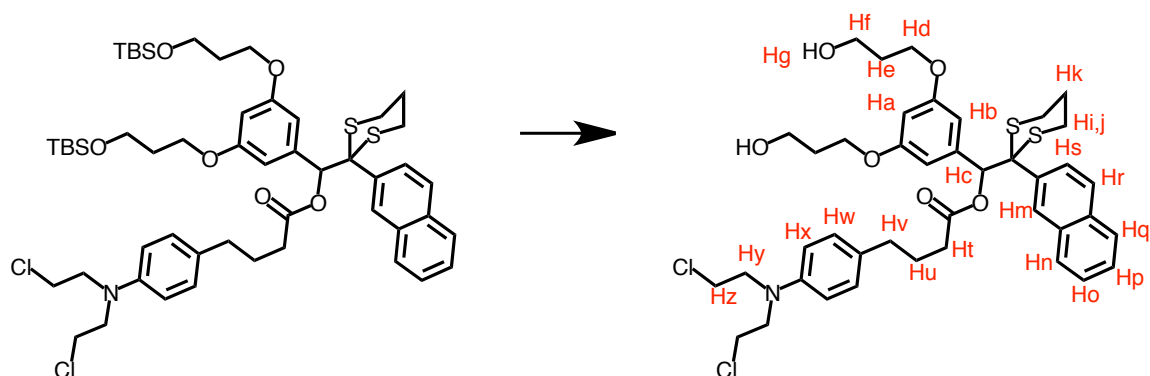
oil. (Care should be taken as the compound foams very much both under both low and hi vacuum.) The title compound **11** was purified by silica gel chromatography (1:9 EtOAc: Hexanes) and obtained as a light yellow, highly viscous and sticky oil (which foams heavily under vacuum) (1.36 g, 82 %, stored at -20°C)

^1H NMR (CD_2Cl_2 , 400 MHz) δ : 8.22 (s, 1H, **Hq**), 7.98-7.95 (m, 1H, **Hn**), 7.86-7.77 (m, 3H, **Hr**, **Ho**, **Hp**), 7.53-7.45 (m, 2H, **Hs**, **Hm**), 7.02 (d, $J = 8.64$ Hz, 2H, **Hw**), 6.62 (d, $J = 8.64$ Hz, 2H, **Hx**), 6.29 (t, $J = 2.20$ Hz, 1H, **Ha**), 6.10 (s, 1H, **Hc**), 6.00 (d, $J = 2.20$ Hz, 2H, **Hb**), 3.72-3.60 (m, 16H, **Hd**, **Hf**, **Hy**, **Hz**), 2.72-2.63 (m, 4H, **Hi**, **Hj**), 2.49 (t, $J = 6.92$ Hz, 2H, **Hv**), 2.38-2.29 (m, 2H, **Ht**), 1.87-1.83 (m, 4H, **Hk**, **Hu**), 1.71 (p, $J = 6.20$ Hz, 4H, **He**), 0.88 (s, 18H, **Hh**), 0.03 (s, 12H, **Hg**)

^{13}C -NMR (CD_2Cl_2 , 100 MHz) δ : 159.48, 140.22, 136.03, 133.71, 133.14, 131.16, 128.93, 128.49, 128.08, 127.71, 127.03, 126.60, 107.28, 102.14, 81.56, 66.91, 64.94, 60.02, 32.85, 28.03, 27.79, 26.27, 25.43, 18.73, -5.09

HRMS (ESI^+) Anal. Calc. for $\text{C}_{53}\text{H}_{78}\text{Cl}_2\text{NO}_6\text{S}_2\text{Si}_2$ ($\text{M}+\text{H}$) $^+$ 1014.4186 Found: ($\text{M}+\text{H}$) $^+$ 1014.4181

9.8.2.5 Synthesis of 12



(3,5-bis(3-hydroxypropoxy)phenyl)(2-(naphthalen-2-yl)-1,3-dithian-2-yl)methyl 4-(4-(bis(2-chloroethyl)amino)phenyl)butanoate

In a round bottom flask, **11** (938.7 mg, 0.92 mmol) was dissolved in THF (15 ml) and cooled to 0°C in an ice/water bath. TBAF (4.6 ml, 4.6 mmol, 1 M in THF) was added slowly via syringe. After addition, the ice bath was removed and the reaction was stirred for 90 minutes and subsequently quenched with sat. aq. NH₄Cl. The mixture was diluted with EtOAc and transferred to a separatory funnel. The phases were separated and the aqueous phase was extracted 3 times with EtOAc. The combined organic extracts were dried over anhydrous MgSO₄, vacuum filtered and concentrated under reduced pressure to a yellow oil. The title compound **12** was purified by silica gel chromatography (gradient: 2:1 → 3:1 EtOAc:Hexanes) and obtained as a very light yellow oil that fluffs to a white solid under hi-vacuum (661.4 mg, 0.84 mmol, 91 %).

M.p. 55-59°C

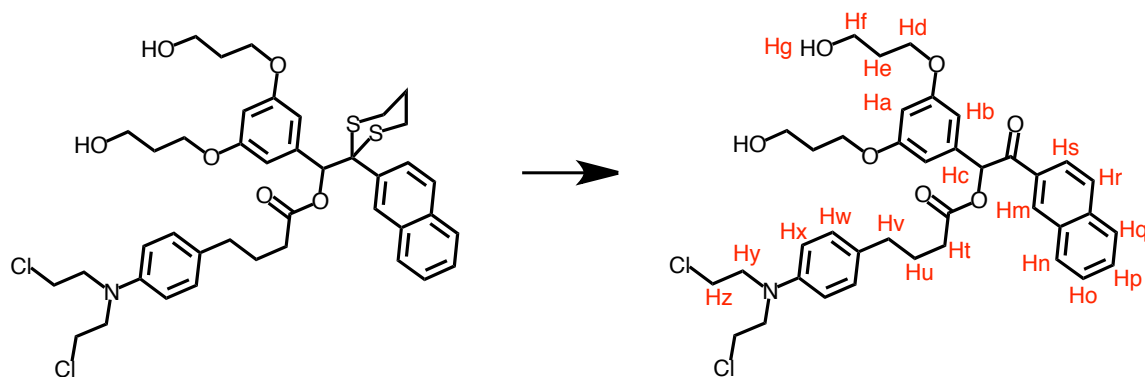
¹H NMR (CD₂Cl₂, 500 MHz) δ: 8.21 (s, 1H, **Hq**), 8.01-7.98 (m, 1H, **Hq**), 7.87-7.78 (m, 3H, **Hr**, **Ho**, **Hp**), 7.54-7.47 (m, 2H, **Hs**, **Hm**), 7.00 (d, *J* = 8.65 Hz, 2H, **Hw**), 6.60 (d, *J* = 8.65 Hz, 2H, **Hx**), 6.30 (t, *J* = 2.15 Hz, 1H, **Ha**), 6.10 (s, 1H, **Hc**), 5.98 (d, *J* = 2.15 Hz, 2H, **Hb**), 3.71-3.59 (m, 16H, **Hd**, **Hf**, **Hy**, **Hz**), 2.76-2.61 (m, 4H, **Hi**, **Hj**), 2.49-2.46 (m, 2H, **Hv**), 2.37-2.32 (m, 2H, **Ht**), 1.87-1.84 (m, 4H, **Hk**, **Hu**), 1.77 (p, *J* = 6.05 Hz, 4H, **He**), 1.47 (bs, 2H, **Hg**)

¹³C NMR (CD₂Cl₂, 126 MHz) δ: 172.28, 159.41, 137.91, 135.31, 133.63, 133.20, 131.73, 131.19, 130.14, 128.99, 128.95, 127.94, 127.74, 127.10, 126.59,

112.74, 107.84, 102.46, 80.89, 66.05, 60.51, 54.06, 41.33, 34.39, 34.27, 32.52,
27.97, 27.88, 27.32, 25.29

HRMS (ESI⁺) Anal. Calc. for C₄₁H₅₀Cl₂NO₆S₂ (M+H)⁺ 786.2457 Found: (M+H)⁺
786.2463

9.8.2.6 Synthesis of 13



1-(3,5-bis(3-hydroxypropoxy)phenyl)-2-(naphthalen-2-yl)-2-oxoethyl-4-(4-(bis(2-chloroethyl)amino)phenyl)butanoate

In a round bottom flask, Hg(ClO₄)₂·x3H₂O (279 mg, 0.615 mol) was added to a mixture of CH₃CN (30 ml) and H₂O (8 ml). The resulting dark yellow non-transparent mixture was wrapped in foil. **12** (242 mg, 0.308 mmol) dissolved in CH₃CN (3 ml) was added, the color rapidly changes from dark yellow to transparent and light bright yellow. After 11 minutes the reaction was quenched with sat. aq. NaHCO₃, further diluted with H₂O and EtOAc. *Under red light illumination*: The phases were separated and the aqueous phase was extracted 3 times with EtOAc. The combined organic extracts were dried over anhydrous MgSO₄, vacuum filtered and concentrated under reduced pressure to a light yellow oil. The crude mixture was taken up in CH₂Cl₂ and filtered through a 0.2

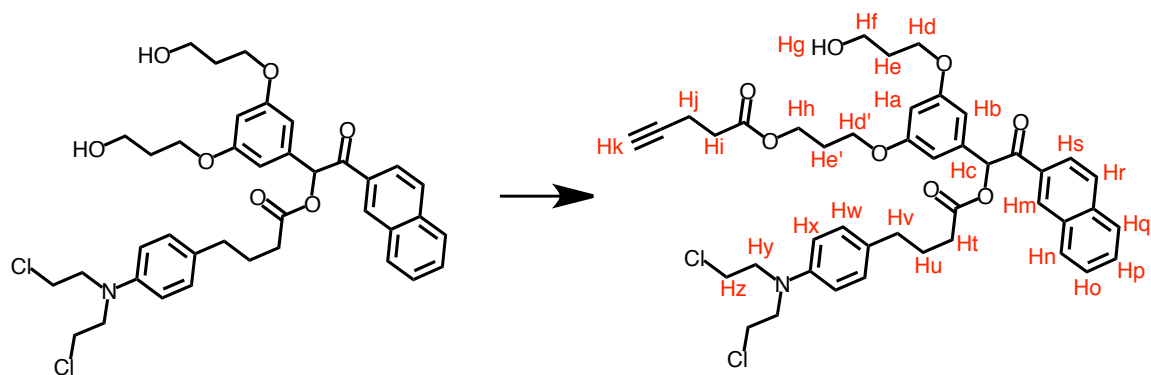
μm PTFE syringe-filter and concentrated under reduced pressure, the procedure was performed one more time. The title compound **13** was further purified by silica gel chromatography (2:1 EtOAc:Hexanes) and obtained as a colourless and photochemically unstable oil which was stored at -20°C wrapped in foil. (212 mg, 99 %)

^1H NMR (CD_2Cl_2 , 500 MHz) δ : 8.51 (s, 1H, **Hm**), 7.96-7.95 (m, 2H, **Hn**, **Hq**), 7.89-7.86 (m, 2H, **Hs**, **Hr**), 7.62-7.54 (m, 2H, **Hp**, **Ho**), 7.06 (d, $J = 8.55$ Hz, 2H, **Hw**), 6.88 (s, 1H, **Hc**), 6.64-6.62 (m, 4H, **Hx**, **Hb**), 6.43 (t, $J = 2.05$ Hz, 1H, **Ha**), 4.04 (t, $J = 6.05$ Hz, 4H, **Hd**), 3.76 (m, 4H, **Hf**), 3.71-3.68 (m, 4H, **Hy**), 3.65-3.62 (m, 4H, **Hz**), 2.58 (t, $J = 7.60$ Hz, 2H, **Hv**), 2.53-2.41 (m, 2H, **Ht**), 1.97-1.92 (m, 6H, **Hu**, **He**), 1.59 (bs, 2H, **Hg**)

^{13}C NMR (CD_2Cl_2 , 126 MHz) δ : (25 out of 26 peaks found) 194.09, 173.43, 161.09, 145.01, 136.39, 136.23, 132.89, 132.55, 130.20, 129.13, 128.28, 127.51, 124.63, 112.70, 107.78, 102.26, 78.00, 66.22, 60.37, 41.31, 34.31, 33.79, 32.56, 31.16, 27.42

HRMS (ESI⁺) Anal. Calc. for $\text{C}_{38}\text{H}_{44}\text{Cl}_2\text{NO}_7$ (M+H)⁺ 696.2495 Found: (M+H)⁺ 696.2497

9.8.2.7 Synthesis of 14



3-(3-(1-((4-(4-(bis(2-chloroethyl)amino)phenyl)butanoyl)oxy)-2-(naphthalen-2-yl)-2-oxoethyl)-5-(3-hydroxypropoxy)phenoxy)propyl pent-4-ynoate

A flame dried and oven dried round bottom flask cooled under N₂ purge was charged with **13** (393 mg, 0.56 mmol) and 4-pentynoic acid (55 mg, 0.56 mmol). Anhydrous CH₂Cl₂ (ca. 100 ml) was cannulated over, the flask was wrapped in foil and cooled to 0°C in an ice/water bath. DMAP (136.8 mg, 1.12 mmol) and DCC (231 mg, 1.12 mmol) were rapidly added by removing the septa followed by N₂ purge. After addition the flask was removed from the cold bath and the mixture was allowed to reach ambient temperature. The reaction was followed closely by TLC and the reaction was quenched with sat. aq. NH₄Cl after 1 hour and 15 min. *Under illumination with red light:* The mixture was quenched with sat. aq. NH₄Cl and transferred to a separatory funnel. The phases were separated and the aqueous phase was extracted three times with CH₂Cl₂. The combined organic extracts were dried over anhydrous MgSO₄, vacuum filtered and concentrated under reduced pressure. The residue was taken up in a minimal amount of acetone and filtered through a 0.2 μm PTFE syringe-filter, air was pressed through the filter by the syringe to ensure all solvent came out. The

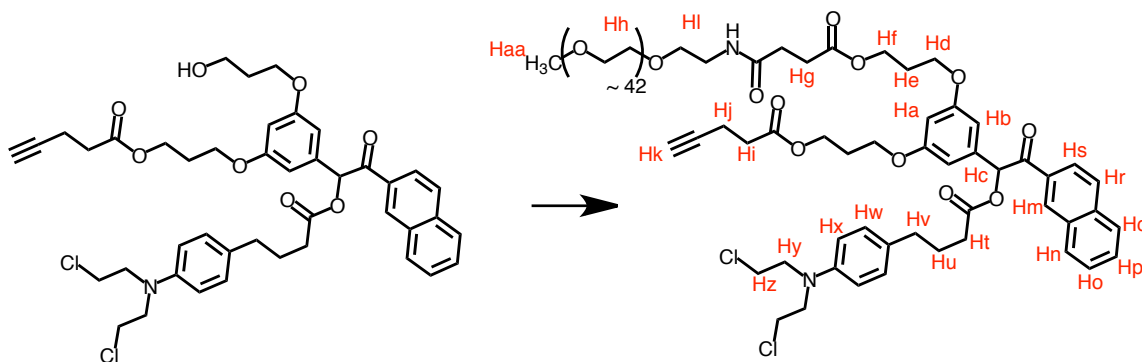
solvent was evaporated and an oil was acquired. The crude mixture was purified by gradient column chromatography to separate the product from the starting material and the bis-functionalized material (1:1 EtOAc:Hexanes eluted bis and mono functionalized material, 3:1 EtOAc:Hexanes eluted the starting material). The product was concentrated to an oil containing white solids, it was taken up in acetone and filtered twice through a 0.2 μm PTFE syringe-filter. The title compound **14** was further purified by column chromatography (1:1.5 EtOAc:Hexanes) and obtained as a light yellow oil (233 mg, 0.30 mmol, 54 %, the compound is thermally and photochemically unstable – store at -20°C wrapped in foil)

^1H NMR (CD_2Cl_2 , 500 MHz) δ : 8.53 (s, 1H, **Hm**), 7.99-7.95 (m, 2H, **Hn**, **Hq**), 7.90, 7.86 (m, 2H, **Hs**, **Hr**), 7.58-7.55 (m, 2H, **Hp**, **Ho**), 7.06 (d, $J = 8.6$ Hz, 2H, **Hw**), 6.90 (s, 1H, **Hc**), 6.67-6.62 (m, 4H, **Hx**, **Hb**), 6.43 (t, $J = 2.15$ Hz, 1H, **Ha**), 4.24 (t, $J = 6.27$ Hz, 2H, **Hh**), 4.04 (t, $J = 6.07$ Hz, 2H, **Hd'**), 3.99 (t, $J = 6.12$ Hz, 2H, **Hd**), 3.76 (t, $J = 5.87$ Hz, 2H, **Hf**), 3.71-3.69 (m, 4H, **Hy**), 3.66-3.62 (m, 4H, **Hz**), 2.61-2.58 (m, 2H, **Hv**), 2.55-2.42 (m, 6H, **Hj**, **Hi**, **Ht**), 2.07 (p, $J = 6.20$ Hz, 2H, **Hu**), 2.04 (t, $J = \text{Hz}$, 2H, **Hk**), 2.01-1.95 (m, 4H, **He**, **He'**), 1.74 (bs, 1H, **Hg**)

^{13}C NMR (CD_2Cl_2 , 126 MHz) δ : 194.13, 173.43, 172.08, 161.12, 161.03, 145.04, 136.44, 136.25, 132.92, 132.59, 131.08, 130.18, 129.14, 128.29, 127.53, 124.64, 112.78, 107.83, 107.79, 102.35, 83.18, 78.01, 69.30, 66.24, 65.18, 61.87, 60.35, 54.06, 41.33, 34.34, 33.83, 33.81, 32.59, 29.64, 29.06, 27.42, 14.82.

HRMS (ESI⁺) Anal. Calc. for C₄₃H₄₈Cl₂NO₈ (M+H)⁺ 776.2757 Found: (M+H)⁺ 776.2762

9.8.2.8 Synthesis of 5



3-(3-(1-((4-(4-(bis(2-chloroethyl)amino)phenyl)butanoyl)oxy)-2-(naphthalen-2-yl)-2-oxoethyl)-5-(3-(pent-4-ynoyloxy)propoxy)phenoxy)propyl-136-oxo-2,5,8,11,14,17,20,23,26,29,33,36,39,42,45,48,51,54,57,60,63,66,69,72,75,78,81,84,87,90,93,96,99,102,105,108,111,114,117,120,123,126,129,132-tetratetracontaoxa-135-azanonatriacontahectan-139-oate

A flame dried and oven dried round bottom flask and stir bar was cooled under N₂ purge. The flask was charged with **14** (26 mg, 0.0335 mmol), the system N₂ purged and anhydrous CH₂Cl₂ (2.5 ml) was cannulated over. mPEG-CO₂H (MW_{average}: 2000 g/mol, 67.5 mg, 0.0335 mmol, Rapp Polymere) and DMAP (12.3 mg, 0.100 mmol) was rapidly added by opening the septa followed by N₂ purge. The flask was wrapped in foil and the mixture was cooled to 0°C in an ice/water bath. DCC (20.7 mg, 0.100 mmol) was added by the same procedure after which the flask was removed from the cold bath and the reaction mixture was allowed to reach ambient temperature. *Under red light illumination:*

After 5 hours when most starting material was exhausted the reaction mixture was taken up in a plastic 1 ml syringe without a needle and filtered through a 0.2 μm PTFE syringe-filter, rinsed once with CH_2Cl_2 . Air was pushed through the filter by the syringe to get all the solvent out of the filter. The solvent was evaporated under reduced pressure to yield a waxy solid. The crude material was taken up in deionized water (1 ml) by sonication and the resulting slurry was filtered through a 0.2 μm PTFE syringe-filter to yield a clear solution. The solution was transferred to a 50 ml round-bottom flask wrapped in foil and frozen in liquid nitrogen after which hi-vacuum was applied. After 1 hour the cooling bath was switched to dry-ice/*i*-PrOH and left overnight. The white solid (which still had traces of water) was taken up in acetone, transferred to a scintillation vial (4 dram), concentrated under reduced pressure and dried under hi-vacuum overnight wrapped in foil. The solid was further purified twice by Sephadex LH20 (GE healthcare) size-exclusion chromatography with THF as eluent. The product **5** co-eluted rapidly with DMAP and the resulting colourless solid was further purified twice by C_{18} -silica gel chromatography (9:1 MeOH:H₂O), **5** eluted quite rapidly and the MeOH was evaporated under reduced pressure and the remaining H₂O was evaporated by lyophilization as described above. The title compound **5** was obtained as a colourless solid contaminated with mainly leftover mPEG-CO₂H and other unidentified minor impurities (ca. 75 mol-% **5** to 25 mol-% mPEG-CO₂H, based on the integration of the terminal singlet OCH₃ signal from the mPEG). The photochemically unstable compound **5** was stored wrapped in foil at -20°C (31.5 mg, ca. 0.0085 mmol, ca. 23 %)

Note: Purification using Sephadex GH25 size-exclusion chromatography in water followed by lyophilization is anticipated to be more efficient than using Sephadex LH20 size-exclusion chromatography in THF where the mPEGylated product and leftover mPEG-CO₂H (and other minor impurities including DMAP) co-elute in the first few fractions.

M.p. 39-41°C

¹H NMR (CD₂Cl₂, 400 MHz) δ: 8.51 (s, 1H, **Hm**), 7.97-7.95 (m, 2H, **Hn**, **Hq**), 7.94-7.84 (m, 2H, **Hs**, **Hr**), 7.63-7.54 (m, 2H, **Hp**, **Ho**), 7.06 (d, *J* = 8.68 Hz, 2H, **Hw**), 6.88 (s, 1H, **Hc**), 6.64-6.60 (m, 4H, **Hx**, **Hb**), 6.41 (t, *J* = 2.24 Hz, 1H, **Ha**), 4.24-4.18 (m, 4H, **Hd**, **Hd'**), 4.00-3.97 (m, 4H, **Hf**, **Hf'**), 3.80-3.75 (m, 2H, **PEG**), 3.71-3.67 (m, 6H, **PEG**), 3.65-3.63 (m, 6H, **Hy**, **Hz** 4H), 3.62-3.57 (m, 238H, **PEG**), 3.52-3.50 (m, 5H, **PEG**), 3.43-3.35 (m, 4H, **PEG**), 3.33 (s, 4H, **OCH₃** **PEG**), 2.60-2.56 (m, 5H, **Hv** 2H), 2.50-2.44 (m, 9H, **Hj**, **Hi**, **Ht**, **Hg** 10H), 2.11-2.03 (m, 5H, **Ht** 2H), 2.00 (t, *J* = 2.65 Hz, 1H, **Hk**), 1.95-1.92 (m, 5H, **He** 4H), 1.41-1.26 (m, 6H, **impurities**)

¹³C NMR (CD₂Cl₂, 100 MHz) δ: 194.44, 173.39, 173.29, 172.05, 171.76, 160.99, 145.01, 136.36, 136.21, 132.89, 132.53, 131.10, 130.17, 129.38, 129.12, 128.27, 127.51, 124.61, 112.72, 107.89, 102.33, 83.16, 77.98, 72.44, 71.10, 71.08, 71.08, 71.07, 71.04, 71.01, 71.00, 70.96, 70.92, 70.78, 70.32, 65.22, 65.17, 61.85, 61.72, 59.16, 53.95, 41.32, 39.83, 34.50, 34.32, 33.80, 33.77, 31.24, 31.11, 29.87, 29.07, 29.03, 28.70, 27.39, 26.42, 26.20, 25.97, 14.80

LRMS Anal. Calc. for $C_{133}H_{224}O_{53}N_2Cl_2$ (M) 2767.43, due to the polydispersity of the material no precise peak could be located due the Gaussian shape of the mass spectra, see Figure 9.23.

UV-vis spectroscopy: See Figure 9.8, 9.11ab

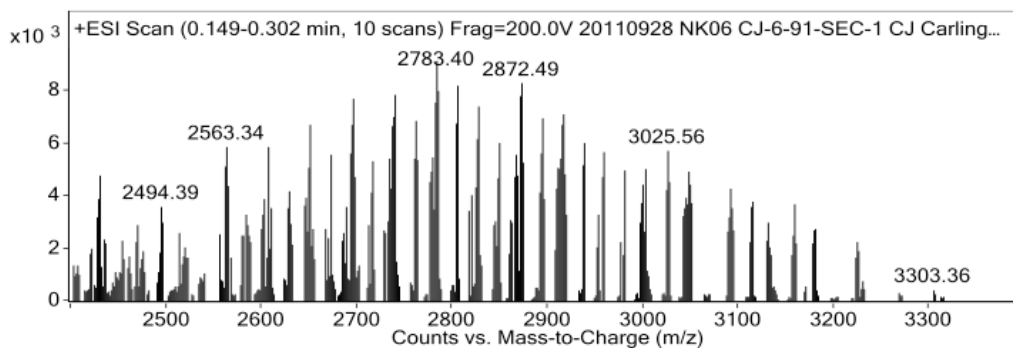


Figure 9.23 LRMS spectra of **5**, due to the polydispersity of the sample no precise peak could be picked out.

9.8.2.9 Synthesis of a-NP

Approximately 50 mg of precipitated nanoparticles **o-NP**^[10] were added to a 20 mL scintillation vial along with $CHCl_3$ (9 mL) and absolute EtOH (3 mL). In a separate vial, the azidopropylphosphonate ligand^[132] (50 mg) was dissolved in a mixture of $CHCl_3$ (1 mL) and absolute EtOH (1 mL). The azidopropylphosphonate ligand solution was then added to the nanoparticle solution via Pasteur pipette with vigorous magnetic stirring. The resultant mixture was stirred overnight at room temperature, at which point it was transferred to a 50 ml centrifuge tube. The majority of the Chloroform was evaporated under reduced pressure using a rotary evaporator. Excess hexanes were added until the mixture became cloudy and the nanoparticles flocculated. The reaction mixture was then centrifuged at 5000 rpm for 10 min and the

supernatant was discarded. The precipitated azide:NaYF₄:TmYb **a-NP** nanoparticles were then redispersed in DMSO (5 mL) for further experiments.

FTIR (cm⁻¹): 3052, 2919, 2398, 2292 (azide), 1991, 1654, 1479, 1434, 1181, 1121, 1094, 742, 693, 518

9.8.2.10 Synthesis of 5-NP

5 (30 mg, ca. 0.008 mmol) was dissolved in acetone (0.5 ml) and transferred to a scintillation vial (1 dram). The solvent was evaporated and **a-NP** (0.5 ml, DMSO) was added to the vial. Freshly prepared CuSO₄·5H₂O (0.0008 mmol, 11.3 μl, 0.071 M in H₂O) and Na-L-Ascorbate (0.008 mmol, 16.4 μl, 0.49 M in H₂O) was added. Et₃N (10 μl), water (22.3 μl) and a stir bar were added. The vial was capped, wrapped in foil and heated in an oil bath at 35°C for 1 hour.

Under red light illumination: The reaction mixture was subsequently divided up in two eppendorf centrifugation tubes and each diluted to 1 ml with distilled water. The samples were centrifuged at 14000 rpm for 25 minutes. The supernatants were discarded and the slightly yellow pellets were redispersed in water (1 ml in each eppendorf tube) by sonication. The samples were centrifuged at 14000 rpm for 25 minutes. The supernatants were discarded and the pellets were redispersed in CH₃CN (1 ml in each eppendorf tube) by sonication. The samples were combined in a glass vial (1 dram) and stored at -20°C wrapped in foil.

FTIR (cm^{-1}): 3052, 2919, 2398, 2292 (azide, weak), 1990, 1654, 1479, 1434, 1181, 1121, 1094, 742, 518

UV-vis spectroscopy: See Figure 9.7,9.8, 9.10, 9.11, 9.12, 9.13, 9.15, 9.20

Fluorescence spectroscopy: See Figure 9.7, 9.10

9.8.2.11 Synthesis of **22-NP**

DTE switch **22** (molecule **1a** in Chapter 6)^[29,159] (3.5 mg, 0.0062 mmol, 2.075 ml, 0.003 M in EtOAc) was added to a scintillation vial (4 dram) and the solvent was evaporated under reduced pressure. **a-NP** (0.3 ml, DMSO) was added to dissolve **22**, the mixture was subsequently transferred to a smaller vial (1 dram) equipped with a stir bar. Freshly prepared $\text{CuSO}_4 \cdot 5\text{H}_2\text{O}$ (6.2×10^{-5} mmol, 7.7 μl , 8.01×10^{-3} M in H_2O) and Na-L-Ascorbate (6.2×10^{-4} mmol, 17.3 μl , 3.58×10^{-2} M in H_2O) was added followed by distilled H_2O (5 μl) and Et_3N (6 μl). The vial was capped and stirred in an oil bath at 35°C for 2 hours. The reaction mixture was poured into an eppendorf centrifuge tube, diluted with THF to 1 ml and centrifuged at 14000 rpm for 25 minutes. The supernatant was discarded and the blue pellet was redispersed in THF (1 ml) by sonication. The mixture was transferred to a new eppendorf tube and centrifuged at 14000 rpm for 25 minutes. The supernatant was discarded and the sample was redispersed in THF (1 ml), transferred to a glass vial (1 dram) and stored at -20°C .

FTIR (cm^{-1}): Data not measured.

UV-vis spectroscopy: See figure 9.14

Fluorescence spectroscopy: Data not measured

9.8.3 Photochemistry of **5**, **5-NP** and **22-NP**

9.8.3.1 Preparation of **5-NP** samples for fluorescence spectroscopy

The nanoparticle colloidal samples used for fluorescence spectroscopy were prepared by mixing 0.15 mL stock solution of **5-NP** with 3 mL of solvent (water or CH₃CN) in a square quartz fluorescence cuvette (1 × 1 × 4.5 cm), see Figure 9.10.

9.8.3.2 Preparation of samples **5** and **5-NP** for one-photon photochemistry

The **5-NP** nanoparticle colloidal samples used were prepared by mixing 0.15 mL stock solution with 3 mL of solvent (water or CH₃CN) in a quartz cuvette (1 × 1 × 4.5 cm). The **5** samples (2×10^{-5} M in water or CH₃CN) were prepared in a quartz cuvette (1 × 1 × 4.5 cm). All the samples in Figure 9.11 were irradiated with 365 nm light (1.4 mW/cm², 3.9 mW) except for the **5-NP** sample in CH₃CN (Fig. 9.11c) which was first irradiated with 980 nm light before it was irradiated with 312 nm light (2.1 mW/cm², 5.9 mW).

9.8.3.3 NIR-to-UV 'remote-control' photochemistry of **5-NP** and **22-NP**

The nanoparticle colloidal samples used were prepared by mixing 0.05 mL stock solution of **5-NP** or **22-NP** with 0.4 mL of solvent (water, CH₃CN or THF) in a quartz micro cuvette (0.05 × 0.05 × 4 cm).

The two **5-NP** samples in water in Figure 9.12 were irradiated with 980 nm light from the top along the vertical axis. Experiment 1 (Figure 9.12a,b), power density: 1.45 W/cm², 0.41 W. Experiment 2 (Figure 9.12c,d), power density: 4.27 W/cm², 1.21 W. The sample in Experiment 2 was cooled in a water

bath at ambient temperature to minimize heat generation during the irradiation procedure.

The **5-NP** sample in CH₃CN in Figure 9.13 was irradiated with 980 nm light along the horizontal axis. Experiment 1 (Figure 9.13a,b), power density: 1.45 W/cm², 0.41 W. Experiment 2 (Figure 9.13c,d), power density: 4.27 W/cm², 1.21 W.

The **22-NP** sample in THF in Figure 9.14 was irradiated with 980 nm light along the horizontal axis (power density: 1.45 W/cm², 0.41 W.) during 1 hour after which it was irradiated with 365 nm light (1.4 mW/cm², 3.9 mW).

10: THE PRELIMINARY PHOTOCHEMISTRY OF A NOVEL DONOR-ACCEPTOR 4-DIMETHYLAMINO-3',5'-DIMETHOXYBENZOIN PHOTOCAGE

10.1 Contributions

The data presented in this chapter has not been published. The project was designed by C-J Carling. All synthesis, characterization and data collection was carried out by C-J Carling except for the synthesis of **4**^[299] which was synthesized by C. Warford. Dr. J-C Boyer and M. Barker synthesized the oleate coated UCNP (**o-NP**)^[10] used for the NIR-to-UV 'remote-control' photochemistry. The chapter is written by C-J Carling. The experimental section 10.5 is co-written by C-J Carling and C. Warford.

10.2 Introduction

New or improved existing photocages are in high demand due to their many applications in synthetic and biological settings.^[173,175] Especially desirable are efficient photocages that respond rapidly and efficiently to the applied light to minimize the extent of UVA light irradiation procedure as the high-energy UV light has detrimental effects.

Since the 3',5'-dialkoxybenzoin photocages has the highest quantum yield of all currently available photocages but a particularly poor UVA absorption, we sought to improve upon this important photocage and make it more useful to us and the scientific community at large. It was envisioned that by

bathochromatically shifting (red-shifting) the absorbance and increasing the molar extinction coefficient of the S_0 - $S_1(n\pi^*)$ transition of the photocage, the probability to absorb a UVA photon would increase and as a result the bulk photolysis reaction rate would increase.

To realize this idea the novel donor-acceptor 4-dimethylamino-3',5'-dimethoxybenzoin photocage **1** was synthesized; it exhibits both red-shifted absorbance and an unprecedented UVA molar absorption coefficient in the benzoin series. However, photocage **1** undergoes photolysis with a unique mechanism that has not been fully elucidated so far.

10.3 Results and Discussion

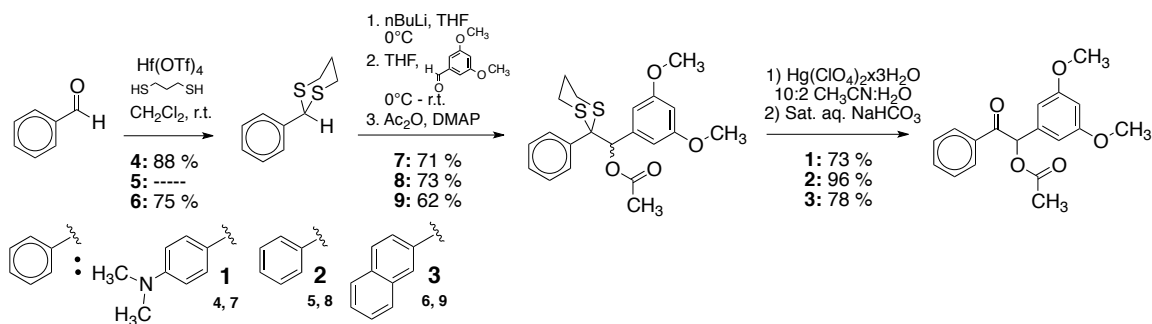
The chromophore of the 3',5'-dimethoxybenzoin photocage can be separated into two parts: the benzoyl and 3,5-dimethoxybenzyl moieties. The benzoyl moiety is responsible for absorbing a UV photon and reaching the S_1 excited state and the electron-rich 3,5-dimethoxybenzyl moiety is responsible for reacting with the carbonyl oxygen in the S_1 excited state, which subsequently leads to release, see Scheme 7.5.^[189,205] In order to increase the probability of the chromophore to absorb a UVA photon, we consequently chose to alter the benzoyl moiety.

It is well known that donor-acceptor systems red-shift absorption while increasing the molar absorption coefficient.^[300,301] Consequently, we envisioned that a 4-dimethylaminobenzoyl system would both increase the molar absorption coefficient and sufficiently red-shift the absorption of the photocage to respond

more efficiently to UVA light and also have a better overlap with the UV emission from NIR-to-UV fluorescent UCNPs.

10.3.1 Synthesis

In order to selectively install the benzoyl moiety into the unsymmetrical benzoin we first converted the corresponding aromatic-aldehyde into the corresponding 1,3-propyldithiane,^[276] which allows us to use it as a nucleophile to react with 3,5-dimethoxybenzaldehyde by the Corey-Seebach^[277] umpolung reaction.^[201,214] In addition to reaction selectivity, the 1,3-propyldithiane protecting group also acts as a 'safety-catch' to prevent premature photorelease which eliminates the need to work under dark conditions until its deprotection.^[202,214] The 1,3-propyldithiane protecting group is efficiently and rapidly removed^[201] by $\text{Hg}(\text{ClO}_4)_2 \cdot 3\text{H}_2\text{O}$ in $\text{CH}_3\text{CN}/\text{H}_2\text{O}$ to generate the active aryl-3',5'-dimethoxybenzoin chromophores **1**, **2** and **3**. The photocages **2**^[215,302] and **3** were synthesized for comparison, see Scheme 10.1 and experimental section 10.5 for details.



Scheme 10.1 Synthesis of photocages **1**, **2** and **3**.

10.3.2 Comparison of photocages **1**, **2** and **3**

The new donor-acceptor photocage **1** has both red-shifted absorbance extending out to 375 nm (λ_{max} : 347 nm) and a significantly larger molar absorption coefficient ($\epsilon_{347\text{nm}}$: 25966 M⁻¹cm⁻¹) than either the phenyl **2** or naphthyl **3** isomers (Figure 10.2). In fact, the molar absorption coefficient at this wavelength is among the largest of all known photocages, see Section 7.1.1.^[173,175,190,191,192]

Apart from the improvement in UVA light absorption, photocage **1** has distinctly different photochemical characteristics compared to **2** and **3** under equal conditions:

The bulk photolysis rate of **1** is significantly more rapid upon irradiation with UVA light compared to **2** and **3**, see Figure 10.1. Moreover, the UV-vis absorbance characteristic of **1** during photolysis is considerably different compared to **2** and **3**: Instead of an absorbance build-up due to the formation of benzofuran which acts as an inner-filter (as is encountered for photocage **2** and **3** during photolysis), the absorbance of **1** decreases during photolysis in organic solvent. By the UV-vis absorbance data collected it is clear that photocage **1**

rapidly react to an unstable photoproduct(s) that further reacts upon prolonged irradiation, even in the absence of oxygen, see Figure 10.1 and 10.2.

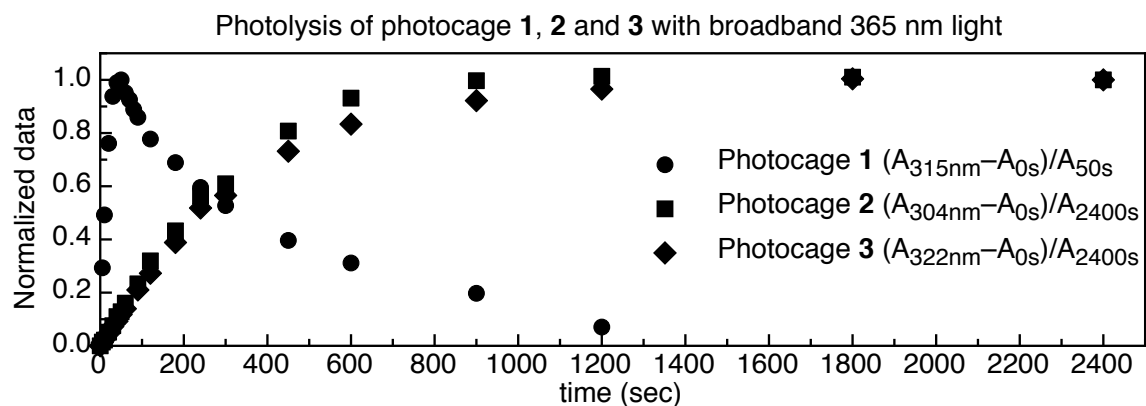


Figure 10.1 Normalized kinetic data of 1, 2 and 3 in CH_2Cl_2 (1×10^{-5} M) under 365 nm light (2.9 mW/cm^2 , 8.1 mW) irradiation. Photocage 1 was irradiated in oxygen free CH_2Cl_2 . The data is plotted from the data presented in Figure 10.2.

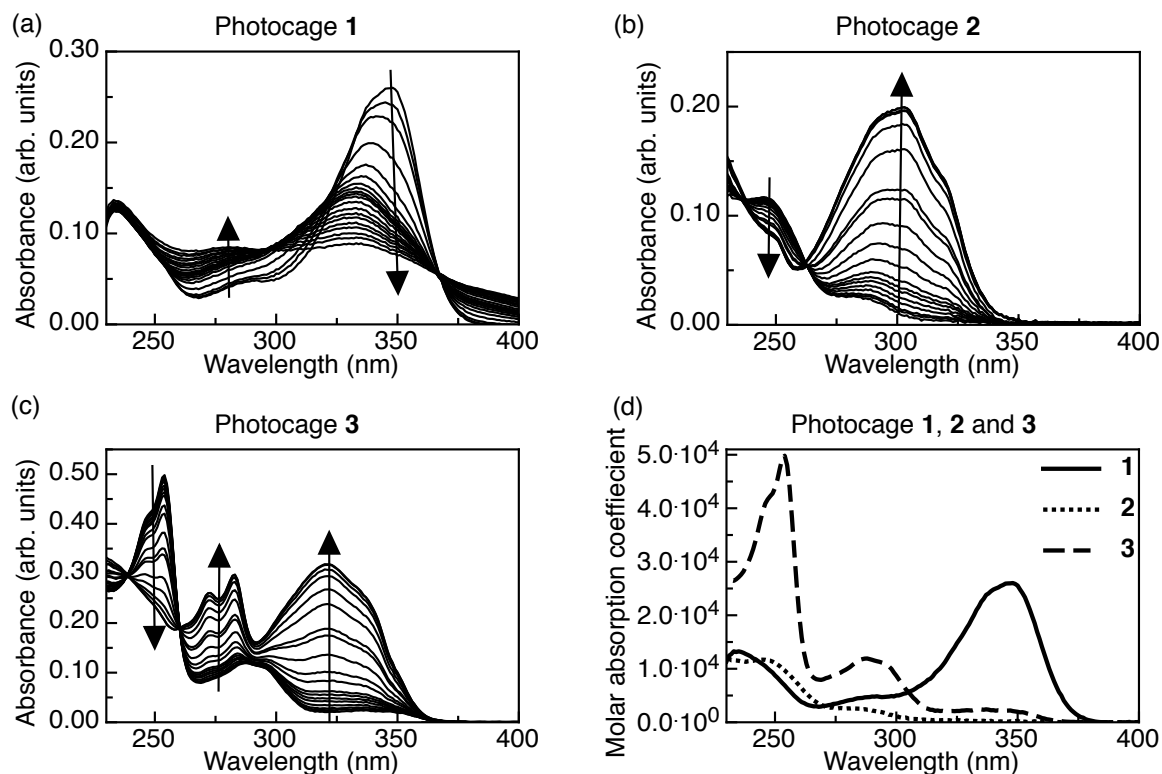
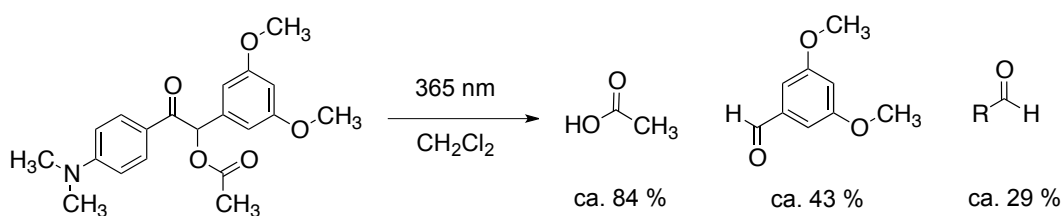


Figure 10.2 UV-vis absorption spectra of 1×10^{-5} M CH_2Cl_2 solutions of photocage **1**, **2** and **3** during photolysis with broadband 365 nm light (2.9 mW/cm^2 , 8.1 mW). (a) **1** in oxygen-free CH_2Cl_2 , (b) **2** in CH_2Cl_2 and (c) **3** in CH_2Cl_2 . (d) Molar absorption coefficient (ϵ) plot comparison of photocages **1**, **2** and **3**.

When a 1 mg sample of photocage **1** in 0.55 ml CD_2Cl_2 (5.1×10^{-3} M) was probed by ^1H NMR spectroscopy during 365 nm light irradiation (2.9 mW/cm^2 , 8.1 mW) full photolysis was accomplished after 20 minutes of irradiation, which is significantly faster than for a derivative of photocage **2** irradiated with 313 nm light, see Figure 8.4.^[10] It was elucidated from the ^1H NMR spectra using the residual solvent peak from EtOAc as internal standard^[303] that Acetic acid was formed in approximately 84 % yield after full photolysis. 3,5-dimethoxybenzaldehyde is the other main photoproduct formed in approximately 43 % yield during the photolysis as elucidated from the ^1H NMR spectrum and

further confirmed by mass spectrometry (experimental data not shown). In the ^1H NMR spectrum one other unidentified aldehyde peak (formed in approximately 29 % yield) is present but all other peaks/signals corresponding to the 4-dimethylaminobenzoyl moiety of **1** was not detected, see Figure 10.3 and 10.4. These peculiar results indicates that the main photoproduct(s) formed during the photolysis is not detectable by standard ^1H NMR spectroscopic techniques which could be due to a number of reasons such as proton exchange with solvent or aggregation. Another reason could be due to formation of unpaired electrons, however a sample was examined by EPR spectroscopy but no signal corresponding to a radical or carbene was detected in the spectrum (experimental data not shown).

Moreover, the signal corresponding to the residual water in the sample rapidly broadens during the photolysis to the point it is hardly visible at the endpoint of the photolysis. The reasons for these behaviours have not been elucidated at the present stage.



Scheme 10.2 During the photolysis of photocage **1**, acetic acid and 3,5-dimethoxybenzaldehyde was detected as main products in the ^1H NMR spectra along with an unidentified aldehyde peak and other unidentified peaks at 3.5-2.75 ppm.

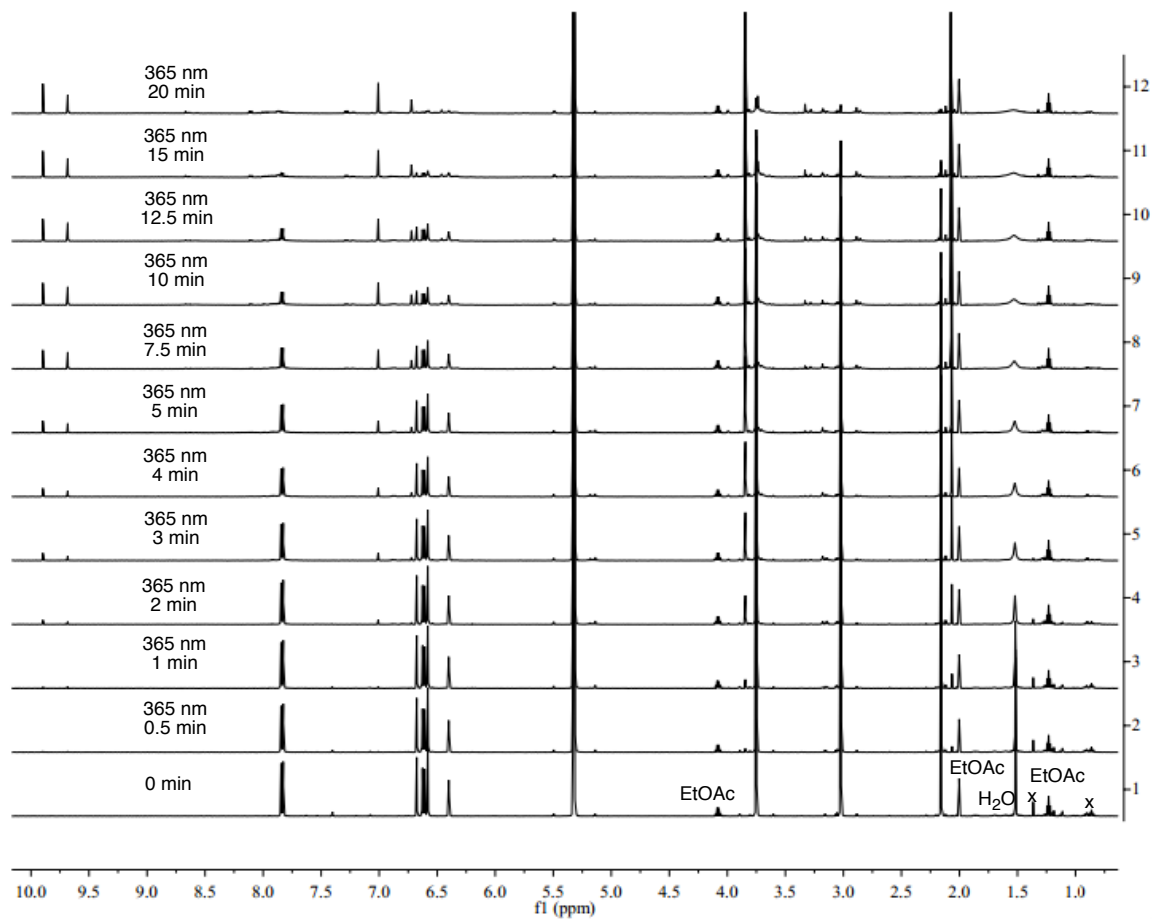


Figure 10.3 Changes in ¹H NMR spectra of photocage **1** (1 mg in 0.55 ml CD₂Cl₂, 5.1×10⁻³ M) during irradiation with 365 nm light (1.4 mW/cm², 3.9 mW).

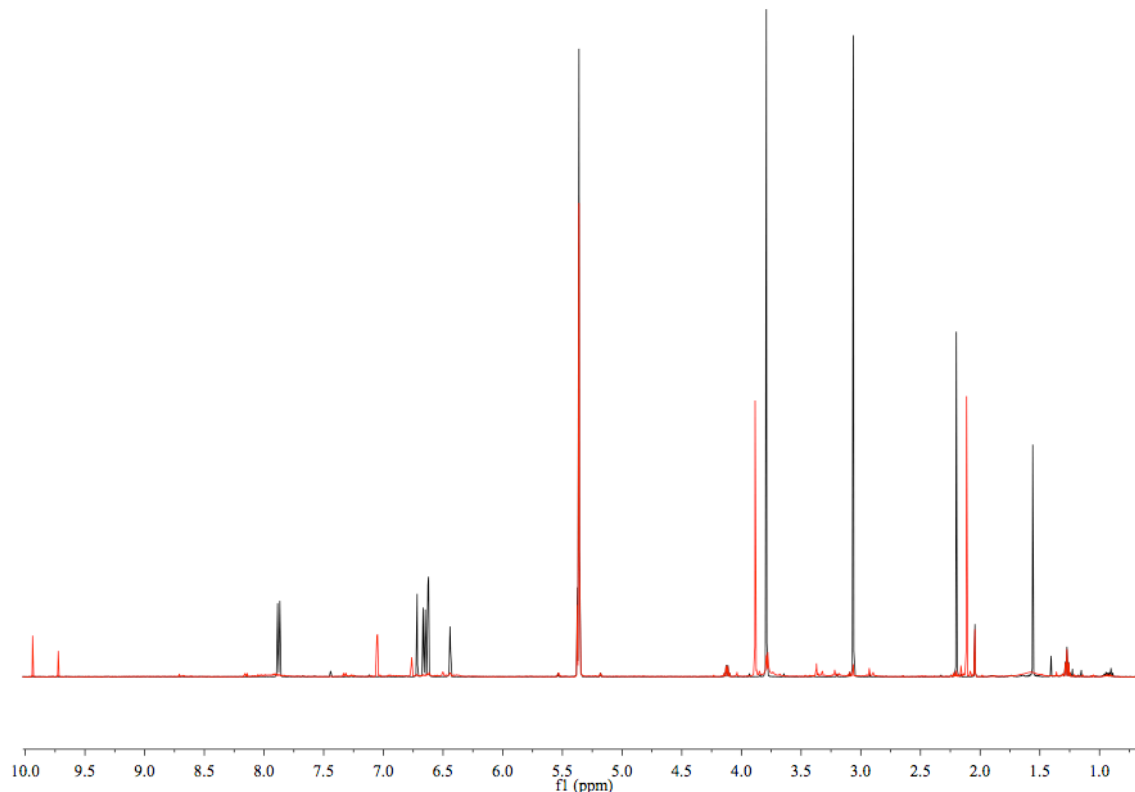


Figure 10.4 ^1H NMR spectrum of photocage **1** (1 mg in 0.55 ml CD_2Cl_2) before (black trace) and after 20 min of 365 nm light irradiation ($1.4 \text{ mW}/\text{cm}^2$, 3.9 mW) (red trace).

10.3.3 NIR-to-UV ‘remote-control’ photolysis of photocage **1**

The primary motivation for developing photocage **1** was to use it in combination with UV light emitting UCNP. Since the absorption of photocage **1** overlaps perfectly with the upconverted UVA emission from the UCNP we anticipated that somewhat efficient NIR-to-UV ‘remote-control’ photolysis could be achieved with 980 nm light irradiation of ‘biologically benign’ power-density. To assess the feasibility of NIR-to-UV photorelease in organic solvent (CH_2Cl_2), photocage **1** was mixed with **o-NP** at two concentrations of UCNP. When a 1×10^{-5} M solution of **1** was mixed with 0.07 wt-% and 0.46 wt-% UCNP **o-NP** and irradiated with 980 nm light ($1.45 \text{ W}/\text{cm}^2$, 0.41 W), both solutions underwent

partial NIR-to-UV photolysis during 60 minutes of irradiation, albeit the dispersion with larger concentration UCNP proceeded to a larger extent as was expected, see Figure 10.5.

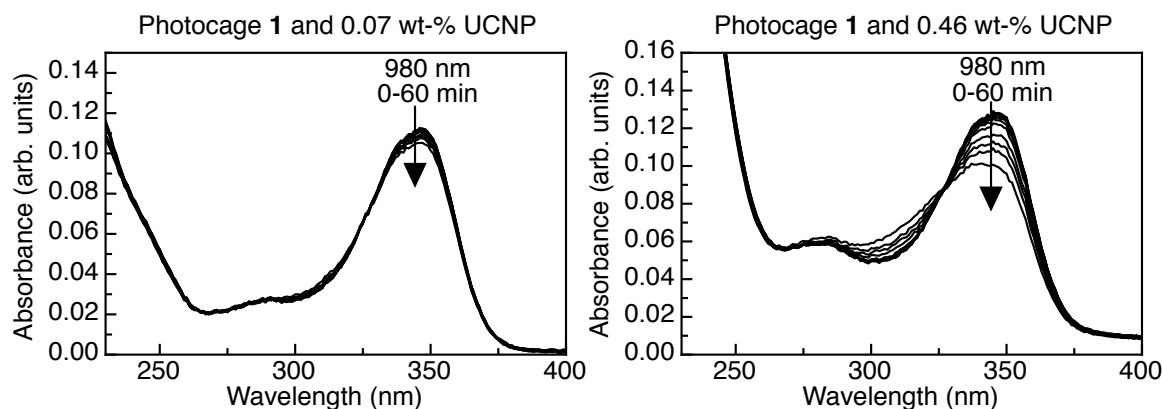


Figure 10.5 Changes in absorption spectra of photocage **1** (1×10^{-5} M in CH_2Cl_2) mixed with **o-NP** in (a) 0.07 wt-% and (b) 0.46 wt-% during irradiation with 980 nm light (1.45 W/cm^2 , 0.41 W).

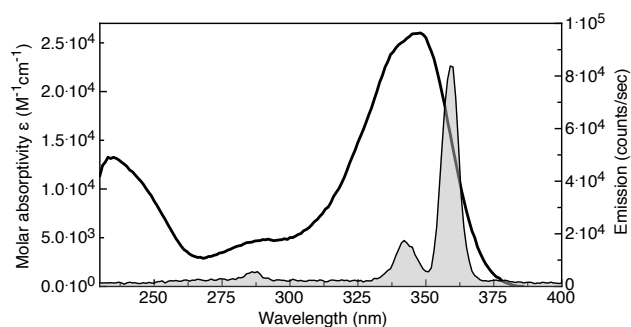


Figure 10.6 Absorption overlap of photocage **1** in CH_2Cl_2 with the emission of **5-NP** (Chapter 9) in water.

10.4 Conclusion

The novel donor-acceptor 4-dimethylamino-3',5'-dimethoxybenzoin photocage **1** was designed and synthesized and its preliminary photochemistry was examined. Photocage **1** displays both a red-shifted absorbance and a

significantly larger molar absorption coefficient than the photocage isomers **2**^[215,302] and **3**, see Figure 10.2d. Furthermore, the bulk photolysis rate of photocage **1** is significantly more rapid than **2** and **3** and 1 mg is completely photolysed after 20 minutes with a standard handheld UV lamp at 365 nm with an 84 % yield of acetic acid, see Figure 10.1, 10.3 and 10.4. However, despite successful release of acetic acid (as verified by ¹H NMR spectroscopy, see Figure 10.3 and 10.4) the photocage underwent photorelease by a unique mechanism and neither the distribution of photoproducts nor the mechanism of photolysis have been confirmed; the photochemistry of photocage **1** thus remains to be properly elucidated.

Furthermore, the photocage **1** was found to undergo relatively efficient NIR-to-UV 'remote-control' photolysis with 'biologically benign' 980 nm light power density (1.45 W/cm², 0.41 W) when mixed in solution with core-shell Yb³⁺/Tm³⁺ UCNPs (**o-NP**) as probed by UV-vis spectroscopy, see Figure 10.5. When **1** was mixed with **o-NP** at 0.45 wt-% the 'remote-control' reaction was close to complete after 1 hour of irradiation. The reaction is anticipated to be even more efficient if a derivative of **1** is attached to the surface of the UCNP.

10.5 Experimental

10.5.1 General methods

All reagents and solvents used for synthesis, chromatography, photochemistry and UV-vis spectroscopy measurements were purchased from Aldrich and used as received, unless otherwise noted. Anhydrous THF was purchased from Aldrich and passed through activated alumina using a solvent

purification system before use. CD_2Cl_2 was purchased from Cambridge Isotope Laboratories and used as received. Column chromatography was performed using silica gel 60 (230–400 mesh) from Silicycle Inc. The oleate coated 5 % Thulium and 30 % Ytterbium co-doped core-shell hexagonal(β)-phase NaYF_4 UCNPs (**o-NP**) were synthesized according to published procedures.^[10] Melting points were measured using a Gallenkamp melting point apparatus (Registered Design No. 889339) and reported without correction.

10.5.1.1 Spectroscopic studies

^1H NMR and ^{13}C NMR characterizations were carried out using a Bruker AVIII 400 BBO Plus (5 mm probe) working at 400.13 MHz for ^1H NMR and 100.60 MHz for ^{13}C NMR. Chemical shifts (δ) are reported in parts per million relative to tetramethylsilane using the residual solvent peak as a reference standard. Coupling constants (J) are reported in hertz. A Varian Cary 300 Bio spectrophotometer was used to acquire all UV-vis spectra. Stock-solutions of photocages **1**, **2** and **3** were prepared in volumetric flasks. All volumes for subsequent UV-vis studies were measured out using 1 mL disposable syringes and 22 gauge needles except for the oxygen-free solution of **1** that was measured out using auto pipette. Laser and light power was measured on a Gentec TPM-300. The power density of the laser beam was calculated by dividing the recorded power by the laser beam area. Exact mass measurements were measured using a Kratos Concept-H instrument with perfluorokerosene as the standard.

10.5.1.2 Photochemistry

Direct UV light irradiations of **1**, **2** and **3** were carried out using the light source from a lamp used for visualizing TLC plates at 365 nm (1.4 mWcm^{-2} , 3.9 mW). NIR (980 nm) light excitation of **o-NP** was executed using a JDS Uniphase 980 nm laser diode (device type L4-9897510-100M) coupled to a 105 μm (core) fibre. The laser beam was collimated, focused and directed horizontally through the samples using a Newport F-91-C1-T Multimode Fiber Coupler. NIR-to-UV 'remote-control' photolysis was performed in a micro cuvette (sample compartment: $5 \times 5 \times 40 \text{ mm}$). The **1/o-NP** samples in CH_2Cl_2 were irradiated with 980 nm light (1.45 W/cm^2 , 0.41 W) along the horizontal axis. All photochemistry and work with photoactive compounds was performed under scarce light conditions to eliminate any potential interference from ambient light.

10.5.2 Synthesis

10.5.2.1 Synthesis of **4**

4-(1,3-dithian-2-yl)-*N,N*-dimethylaniline^[299]

White solid 4-dimethylaminobenzaldehyde (6.21 g, 41 mmol) and clear colourless liquid 1,3-propanedithiol (4.18 mL, 4.50 g, 41 mmol) were added to dichloromethane (100 mL) at room temperature to form a clear colourless solution. Addition of white solid Hafnium (IV) triflate (102 mg, 0.131 mmol, 3 mol %) resulted in a prompt colour change to bright orange-yellow. The solution was stirred overnight at room temperature for 14h, and then refluxed for 90 minutes. After cooling to room temperature the orange solution was filtered through a

Celite pad, rinsed with dichloromethane and the filtrate concentrated to an orange-tinted solid, which was recrystallized from ethyl acetate to the title compound **4** (8.6 g, 39.5 mmol, 88% yield) as a white solid which turns yellow over time in air at room temperature,

M.p. 108-110 °C.

¹H NMR (CDCl₃, 400 MHz) δ: 7.33-7.29 (m, 2H), 6.67-6.63 (m, 2H), 5.01 (s, 1H), 3.06-2.99 (m, 2H), 2.92 (s, 6H), 2.89-2.84 (m, 2H), 2.16-2.09 (m, 1H), 1.94-1.82 (m, 1H)

¹³C NMR (CDCl₃, 100 MHz) δ: 150.52, 128.70, 126.67, 112.58, 51.16, 40.69, 32.54, 25.39

HRMS (ESI⁺) Anal. Calc. for C₁₂H₁₈NS₂ (M+H)⁺ 240.0881 Found: (M+H)⁺ 240.0880

10.5.2.2 Synthesis of **7**

(3,5-dimethoxyphenyl)(2-(4-(dimethylamino)phenyl)-1,3-dithian-2-yl)methyl acetate

A flame dried and oven dried round bottom flask and stir bar was cooled under N₂ purge and charged with **4** (170 mg, 0.71 mmol). Anhydrous THF (ca. 70 ml) was cannulated into the flask and the solution was cooled to 0°C in an ice/water bath. n-BuLi (0.35 ml, 0.78 mmol, 2.2 M in Hexanes) was added drop wise via plastic syringe. The resulting yellow solution was stirred for 10 minutes before 3,5-dimethoxybenzaldehyde (129.6 mg, 0.78 mmol) was added. After addition the cold bath was removed and the reaction stirred for an additional 40

minutes before acetic anhydride (Ac₂O) (0.13 ml, 1.42 mmol) and DMAP (43.4 mg, 0.355 mmol) were added. The reaction was stirred for an additional 20 hours at which point it was diluted with H₂O and EtOAc. The layers were separated and the aqueous layer was extracted 3 times with EtOAc. The combined organic extracts were dried over anhydrous MgSO₄, vacuum filtered and concentrated to a yellow solid. The crude material was purified by silica gel column chromatography (1:5 EtOAc:Hexanes) to yield **7** as very light yellow oil which foams to a white solid under hi vacuum (225.7 mg, 0.504 mmol, 71 %)

M.p. 55-58°C

¹H NMR (CDCl₃, 400 MHz) δ: 7.57-7.53 (m, 2H), 6.66-6.62 (m, 2H), 6.30 (t, *J* = 2.32 Hz, 1H), 6.04 (d, *J* = 2.32 Hz, 2H), 6.03 (s, 1H), 3.58 (s, 6H), 2.94 (s, 6H), 2.69-2.64 (m, 4H), 2.11 (s, 3H), 1.89-1.84 (m, 2H)

¹³C NMR (CDCl₃, 100 MHz) δ: 169.78, 159.59, 149.97, 137.55, 132.12, 124.23, 111.89, 106.83, 101.24, 80.90, 63.59, 55.36, 40.68, 27.53, 27.39, 25.13, 21.25

HRMS (ESI⁺) Anal. Calc. for C₂₃H₃₀NO₄S₂ (M+H)⁺ 448.1616 Found: (M+H)⁺ 448.1624

10.5.2.3 Synthesis of **1**

1-(3,5-dimethoxyphenyl)-2-(4-(dimethylamino)phenyl)-2-oxoethyl acetate

Hg(ClO₄)₃·3H₂O (97.5 mg, 0.215 mmol) was added to a mixture of CH₃CN (8 ml) and H₂O (2 ml) in a round bottom flask wrapped in foil to yield a bright yellow non-transparent solution. Compound **7** (38.5 mg, 0.086 mmol, in 2 ml CH₃CN) was added and the colour of the reaction mixture rapidly changed to

orange and more slowly to yellow. After 20 minutes the reaction was quenched with sat. aq. NaHCO₃ and diluted with EtOAc. *Under red light illumination:* The layers were separated and the aqueous layer was extracted 3 times with EtOAc. The combined organic extracts were dried over anhydrous MgSO₄, vacuum filtered and concentrated to a yellow oil. The crude mixture was purified by silica gel chromatography (1:3 EtOAc:Hexanes) to yield **1** as a colourless solid (22.4 mg, 0.063 mmol, 73 %). The compound was stored at -20°C wrapped in foil.

M.p. 40-43°C

¹H NMR (CD₂Cl₂, 400 MHz) δ: 7.85-7.81 (m, 2H), 6.68 (s, 1H), 6.63-6.60 (m, 2H), 6.58 (d, *J* = 2.28 Hz, 2H), 6.40 (t, *J* = 2.28 Hz, 1H), 3.75 (s, 6H), 3.02 (s, 6H), 2.16 (s, 3H)

¹³C NMR (CDCl₃, 100 MHz) δ: (13 out of 14 found) 190.96, 170.61, 161.71, 154.14, 137.43, 131.33, 11.18, 107.03, 101.10, 77.67, 55.96, 40.32, 21.22

HRMS (ESI⁺) Anal. Calc. for C₂₀H₂₄NO₅ (M+H)⁺ 358.1654 Found: (M+H)⁺ 358.1657

10.5.2.4 Synthesis of **8**

(3,5-dimethoxyphenyl)(2-phenyl-1,3-dithian-2-yl)methyl acetate

A flame dried round bottom flask cooled under N₂ purge was charged with 2-phenyl-1,3-dithiane **5** (327 mg, 1.67 mmol, Aldrich). Anhydrous THF (15 ml) was cannulated over and the system was cooled to -78°C in dry ice/acetone bath. N-BuLi (0.67 ml, 1.67 mmol, 2.5 M in Hexanes) was added drop wise via plastic syringe. After addition the cold bath was changed to an ice/water bath and the yellow solution was stirred for an additional 40 minutes before 3,5-

dimethoxybenzaldehyde (305.8 mg, 1.84 mmol) was added. The resulting light yellow solution was removed from the cold bath and stirred for 15 minutes before acetic anhydride (0.17 ml, 1.84 mmol) and DMAP (224.8 mg, 1.84 mmol) was added. The resulting colourless solution was stirred for an additional 18 hours at which point the reaction was poured into water and diluted with EtOAc. The layers were separated and the aqueous phase was extracted 3 times with EtOAc. The combined organic extracts were dried over MgSO₄, vacuum filtered and concentrated under reduced pressure to light yellow oil. The title compound **8** was purified twice by silica gel column chromatography (1:8 EtOAc:Hexanes) to a colourless oil which fluffs to a white solid under hi-vacuum (493.7 mg, 1.22 mmol, 73 %).

M.p. 89-93°C

¹H NMR (CDCl₃, 400 MHz) δ: 7.77-7.74 (m, 2H), 7.33-7.26 (m, 3H), 6.30 (t, *J* = 2.28 Hz, 1H), 6.08 (s, 1H), 6.00 (d, *J* = 2.28 Hz), 3.56 (s, 6H), 2.72-2.61 (m, 4H), 2.10 (s, 3H), 1.90-1.87 (m, 2H)

¹³C NMR (CDCl₃, 100 MHz) δ: 169.61, 159.68, 137.36, 137.16, 131.22, 128.20, 127.77, 106.77, 101.19, 80.51, 63.53, 55.35, 27.56, 27.43, 24.88, 21.16

HRMS (ESI⁺) Anal. Calc. for C₂₁H₂₄NaO₄S₂ (M+Na)⁺ 427.1000 Found: (M+Na)⁺ 427.1008

10.5.2.5 Synthesis of **2**

1-(3,5-dimethoxyphenyl)-2-oxo-2-phenylethyl acetate^[187, 302]

Hg(ClO₄)₃·3H₂O (151.6 mg, 0.334 mmol) was added to a mixture of CH₃CN (8 ml) and H₂O (2 ml) in a round bottom flask wrapped in foil to yield a bright yellow non-transparent solution. Compound **8** (54.1 mg, 0.134 mmol, in 2 ml CH₃CN) was added and the colour of the reaction mixture rapidly changed to clear light yellow. After 13 minutes the reaction was quenched with sat. aq. NaHCO₃ and diluted with EtOAc. *Under red light illumination*: The layers were separated and the aqueous layer was extracted 3 times with EtOAc. The combined organic extracts were dried over anhydrous MgSO₄, vacuum filtered and concentrated to a light yellow oil. The crude mixture was purified by silica gel chromatography (1:6 EtOAc:Hexanes) to yield the title compound **2** as a colourless oil which becomes a white solid under hi-vacuum (32.8 mg, 0.129 mmol, 96 %). The compound was stored at –20°C wrapped in foil.

M.p. 93-95°C

¹H NMR (CD₂Cl₂, 400 MHz) δ: 7.92-7.90 (m, 2H), 7.52-7.48 (m, 1H), 7.41-7.36 (m, 2H), 6.73 (s, 6H), 6.57 (d, *J* = 2.24 Hz, 2H), 6.40 (t, *J* = 2.24 Hz, 1H), 3.74 (s, 6H), 2.19 (s, 3H)

¹³C NMR (CD₂Cl₂, 100 MHz) δ: 193.75, 170.63, 161.44, 135.75, 134.81, 133.71, 129.00, 128.85, 106.91, 101.43, 77.88, 55.66, 21.02

10.5.2.6 Synthesis of **6**

2-(naphthalen-2-yl)-1,3-dithiane^[275]

2-naphthaldehyde (4.5 g, 28.83 mmol) was dissolved in CH₂Cl₂ (50 ml), 1,3-propanedithiol (2.9 ml, 28.83 mmol) followed by Hf(Otf)₄ (111.7 mg, 0.144 mmol) was added. The colourless solution was stirred over night, at which point

the hazy solution was filtered through a celite pad and rinsed several times with CH₂Cl₂. The solvent was evaporated to yield a white solid that was recrystallized from hexanes and acetone. The title compound **6** was afforded as off-white needles (5.33 g, 21.64 mmol, 75 % + uncrystallized product 1.31 g)

M.p. 105-107°C

¹H NMR (CDCl₃, 400 MHz) δ: 7.95 (s, 1H), 7.84-7.78 (m, 3H), 7.59-7.56 (m, 1H), 7.48-7.44 (m, 2H), 5.32 (s, 1H), 3.12-3.05 (m, 2H), 2.95-2.90 (m, 2H), 2.21-2.16 (m, 1H), 2.15-1.94 (m, 1H)

¹³C NMR (CDCl₃, 100 MHz) δ: 136.66, 133.49, 133.43, 128.67, 128.24, 127.83, 127.01, 126.48, 126.45, 125.86, 51.74, 32.30, 25.35

10.5.2.7 Synthesis of **9**

(3,5-dimethoxyphenyl)(2-(naphthalen-2-yl)-1,3-dithian-2-yl)methyl acetate

2-(naphthalen-2-yl)-1,3-dithiane **6** (300 mg, 1.22 mmol) was added to a flame dried round bottom flask under N₂ and the system was purged. Anhydrous THF (15 ml) was cannulated over and the system was cooled to 0°C in a ice/water bath. n-BuLi (2.5 M, 0.49 ml, 1.22 mmol) was added drop wise and the resulting dark brown solution was stirred for 25 min before the septa was removed and 3,5-dimethoxybenzaldehyde (222.5 mg, 1.34 mmol) was quickly added and the system purged with N₂. The light yellow solution was allowed to reach room temperature during 25 min before acetic anhydride (0.13 ml, 1.34 mmol) and DMAP (163.6 mg, 1.34 mmol) was added. The colourless solution was stirred over night, poured into water, diluted with Et₂O and extracted twice more. The combined organic extracts were dried over MgSO₄ and concentrated

under reduced pressure to yield a yellow oil which was purified on a short silica gel column (1:6 EtOAc:Hexanes). The title compound **9** was obtained as a white solid (344.3 mg, 0.76 mmol, 62 %)

M.p. 68-71°C

¹H NMR (CDCl₃, 400 MHz) δ: 8.18 (d, *J* = 1.64 Hz, 1H), 7.95 (dd, *J* = 2.02, 8.70 Hz, 1H), 7.83-7.76 (m, 3H), 7.50-7.43 (m, 2H), 6.27 (t, *J* = 2.28 Hz, 1H), 6.15 (s, 1H), 5.97 (d, *J* = 2.28 Hz, 2H), 3.38 (s, 6H), 2.75-2.61 (m, 4H), 2.11 (s, 3H), 1.94-1.84 (m, 2H)

¹³C NMR (CDCl₃, 100 MHz) δ: 169.62, 159.69, 137.09, 134.75, 133.24, 132.76, 131.36, 128.65, 128.45, 127.69, 127.42, 126.77, 126.28, 106.72, 101.43, 80.69, 63.77, 55.17, 27.63, 27.52, 24.87, 21.17

HRMS (ESI⁺) Anal. Calc. for C₂₅H₂₆NaO₄S₂ (M+Na)⁺ 477.1163 Found: (M+Na)⁺ 477.1165

10.5.2.8 Synthesis of **3**

1-(3,5-dimethoxyphenyl)-2-(naphthalen-2-yl)-2-oxoethyl acetate

Hg(ClO₄)₃·3H₂O (139.7 mg, 0.308 mmol) was added to a mixture of CH₃CN (8 ml) and H₂O (2 ml) in a round bottom flask wrapped in foil to yield a bright yellow non-transparent solution. Compound **9** (56.0 mg, 0.123 mmol, in 2 ml CH₃CN) was added and the colour of the reaction mixture rapidly changed to clear light yellow. After 11 minutes the reaction was quenched with sat. aq. NaHCO₃ and diluted with EtOAc. *Under red light illumination*: The layers were separated and the aqueous layer was extracted 3 times with EtOAc. The combined organic extracts were dried over anhydrous MgSO₄, vacuum filtered

and concentrated to a light yellow oil. The crude mixture was purified by silica gel chromatography (1:5 EtOAc:Hexanes) to yield **3** as a colourless oil which fluffs to a white sticky solid under hi-vacuum (35.1 mg, 0.096 mmol, 78 %) The compound was stored at -20°C wrapped in foil.

M.p. 50-52°C

¹H NMR (CD₂Cl₂, 400 MHz) δ: 8.48 (s, 1H), 7.97 (dd, *J* = 1.72, 8.64 Hz, 1H), 7.89 (d, *J* = 8.08 Hz, 1H), 7.83-7.80 (m, 2H), 7.58-7.50 (m, 2H), 6.91 (s, 1H), 6.63 (d, *J* = 2.24 Hz, 2H), 6.38 (t, *J* = 2.24 Hz, 1H), 3.73 (s, 6H), 2.15 (s, 3H)

¹³C NMR (CD₂Cl₂, 100 MHz) δ: 193.72, 170.70, 161.45, 135.91, 132.53, 132.15, 130.90, 129.92, 128.98, 128.77, 127.96, 127.06, 124.42, 106.92, 101.40, 100.19, 77.88, 55.65, 21.06

HRMS (ESI⁺) Anal. Calc. for C₂₂H₂₀NaO₅ (M+Na)⁺ 387.1212 Found: (M+Na)⁺ 387.1203

10.5.2.9 Preparation of oxygen-free solution of **1**

CH₂Cl₂ (50 ml) was degassed by 3 freeze-pump-thaw (FPT) cycles: A round bottom flask containing CH₂Cl₂ was frozen in liquid nitrogen after which the flask was evacuated under hi-vacuum. The vacuum valve was turned off and the CH₂Cl₂ was thawed in a water bath. The FPT procedure was repeated 2 more times. After the 3rd cycle, N₂ gas was introduced into the flask and the flask was brought into a glovebox. A volumetric flask (25 ml) was charged with **1** (2.5 mg, 0.00699 mmol) and brought into the glovebox and filled up to the line with FPT CH₂Cl₂. The photocage **1** UV-vis sample (1x10⁻⁵ M) was prepared in the glovebox by mixing the stock solution (0.066 ml, 2.80x10⁻⁴ M) with O₂-free

CH₂Cl₂ (2.93 ml) in a screw-cap cuvette (1 x 1 x 4.5 cm) using auto pipettes. The sample was used immediately after preparation.

10.5.2.10 Preparation of 1/o-NP

As **o-NP** is poorly dispersible in CH₂Cl₂ an **o-NP** stock solution was prepared by first mixing **o-NP** (0.5 ml, dispersed in CHCl₃) with CH₂Cl₂ (1 ml). The sample was concentrated to about 0.4 ml by blowing a stream of air over the sample taking care not to splash or dry it out fully. CH₂Cl₂ (1 ml) was added and the concentration procedure was repeated. The concentrated sample was diluted with CH₂Cl₂ (ca. 1.6 ml – total volume ca. 2 ml). The 0.07 wt-% **1/o-NP** sample was prepared by mixing **1** (3 ml, 1x10⁻⁵ M in CH₂Cl₂) with the **o-NP** stock solution (0.1 ml) to yield a clear colloidal dispersion. The 0.46 wt-% **1/o-NP** sample was prepared by mixing **1** (0.11 ml, 2.80x10⁻⁴ M in CH₂Cl₂) with CH₂Cl₂ (2.60 ml) and **o-NP** stock solution (0.29 ml) to yield a slightly hazy colloidal dispersion (1x10⁻⁵ M). The **1/o-NP** samples were used immediately after preparation.

11: CONCLUSIONS AND OUTLOOK

The uses of molecular photoswitches and molecular photorelease systems have found widespread applications in various technologies ranging from medicine, biochemistry and synthesis to photolithography, data storage, molecular electronics and security. However, a major disadvantage of most current photoresponsive molecular systems is the need for high-energy light, in particular UV light.

In this thesis we initially demonstrated that by using photon upconverting nanoparticles we could use low-energy near-infrared light to drive important organic photoreactions. The dependence of UV light for desired function of most current photoactive molecules is a major problem and it was partially solved by our approach since we used the UV light dependence to our advantage. The UCNPs upconvert lower energy NIR light into higher energy UV and visible light that can be used to drive organic photoreactions. With this approach of NIR-to-UV 'remote-control' photochemistry using UCNPs and NIR light to drive organic photoreactions, a larger scope of photoactive molecules can be triggered to undergo their respective reactions using NIR light compared to traditional two-photon excitation 'remote-control' photochemistry.

In *Chapter 3*^[9] we introduced the concepts of NIR-to-UV and NIR-to-visible 'remote-control' photoswitching and NIR-to-visible 'remote-control' photorelease. It was demonstrated that NaYF₄ UCNPs co-doped with either

Tm³⁺ and Yb³⁺ or Er³⁺ and Yb³⁺ could be used to convert NIR light into UV and visible light sufficient in energy and intensity to drive the ring-closing and ring-opening photoreactions of DTE molecular switches. The concepts of both 'remote-control' photoswitching and photorelease were demonstrated in PEG-DMA composites.

In *Chapter 4*^[11] we demonstrated bi-directional photoswitching of DTE molecular switches in solution using a single NIR wavelength (980 nm) of light by only changing the excitation power density. The NIR-to-UV and NIR-to-visible 'remote-control' bi-directional photoswitching was accomplished by using NaYF₄ *core-shell-shell* UCNPS co-doped with Tm³⁺, Er³⁺ and Yb³⁺. The key aspect to the bi-directional photoswitching was the non-linearity of the upconversion process. At high power density excitation UV light produced from Tm³⁺ is dominant whereas at lower excitation power density green light emitted from Er³⁺ dominate.

In *Chapter 5*^[28] we demonstrated reversible fluorescence modulation of an UCNP by DTE molecular switches anchored on its surfaces *in vivo*. The Er³⁺ and Yb³⁺ co-doped NaYF₄ UCNPs were functionalized with PEGylated DTE molecular switches by 'click' chemistry, which rendered the UCNPs water dispersible without the need for silica coating. The NIR-to-visible fluorescence from the UCNP was quenched after irradiation with UV light and restored to the original bright state after irradiation with visible light due to the reversible photochemistry of the DTE molecular switch.

In *Chapter 6*^[29] we demonstrated reversible multimodal fluorescence modulation of a multicolour *core-shell-shell* UCNP by two different DTE molecular switches decorated on the surface of the UCNP by 'click' chemistry. The fluorescence of the 3-component UCNP could be selectively alternated between three different fluorescent states by irradiation with UV and visible light. The key aspect to the multimodal control over the fluorescence was the selective control over the ring-opening reaction of one of the two molecular switches decorated on the surface of the UCNP.

In *Chapter 8*^[10] we introduced the concept of NIR-to-UV 'remote-control' photorelease in solution. The surface of a *core-shell* NaYF₄ UCNP co-doped with Tm³⁺ and Yb³⁺ was functionalized with a 3',5'-dialkoxybenzoin photocage by electrostatic interaction. It was demonstrated that the UV light generated from the UCNP upon high-power density NIR light excitation could drive the photorelease reaction.

In *Chapter 9* a drug-delivery vehicle was developed. A PEGylated 3',5'-dialkoxybenzoin photocage functionalized with a therapeutic moiety was synthesized and anchored to the surface of a *core-shell* NaYF₄ UCNP co-doped with Tm³⁺ and Yb³⁺ by 'click' chemistry. The resulting hybrid UCNPs was fully water dispersible and stable in 100 % fetal bovine serum. However, due to the choice of photorelease system the NIR-to-UV 'remote-control' photorelease reaction did not proceed efficiently enough upon irradiation with 'biologically benign' NIR light power density in water. Furthermore the detection of the therapeutic payload could not be detected after either UV light or NIR-to-UV

irradiation. Due to these reasons the drug-delivery vehicle was impractical as designed.

In *Chapter 10* the absorption of the 3',5'-dialkoxybenzoin photocage was tuned to better overlap with the NIR-to-UV emission from the NaYF₄ UCNP co-doped with Tm³⁺ and Yb³⁺. The absorption of the donor-acceptor 4-dimethylamino-3',5'-dimethoxybenzoin photocage was both red-shifted and the molar absorption coefficient was significantly increased compared to previously known derivatives. It was further demonstrated that the NIR-to-UV 'remote-control' photorelease reaction did proceed upon irradiation with 'biologically benign' NIR light power density. However, due to the electronic nature of the 4-dimethylamino-3',5'-dimethoxybenzoin photocage it reacted by a unique photolysis pathway and its photochemistry has not been fully elucidated to this end.

In summary the technology developed in this thesis have the potential to offer new opportunities in drug-delivery, bioimaging, optical data storage, photolithography and security. In fact, independent researchers have already shown that the NIR-to-UV 'remote-control' photochemistry concept developed in this thesis is functional and many different applications using this strategy of 'remote-control' photochemistry have been successfully demonstrated.^[171,167,168,243,252]

Although much progress has been made using the technology presented in this thesis, limitations still exists that need to be addressed. The most pressing issue of the NIR-to-UV 'remote-control' technology is concerned with the

efficiency of the hybrid systems. In order for the NIR-to-UV 'remote-control' photochemistry to be practically useful the organic chromophore has to respond more efficiently using low-power density excitation NIR light that will not cause damage by itself, especially in biological applications. It is therefore imperative that the action cross-section of the organic chromophore be adequately tuned to respond efficiently to the upconverted UV light. Although such efforts were demonstrated in *Chapter 10*, more work is needed to further demonstrate the practical feasibility of future systems.

12: APPENDICES

12.1 NMR spectra of new compounds from *Chapter 3*

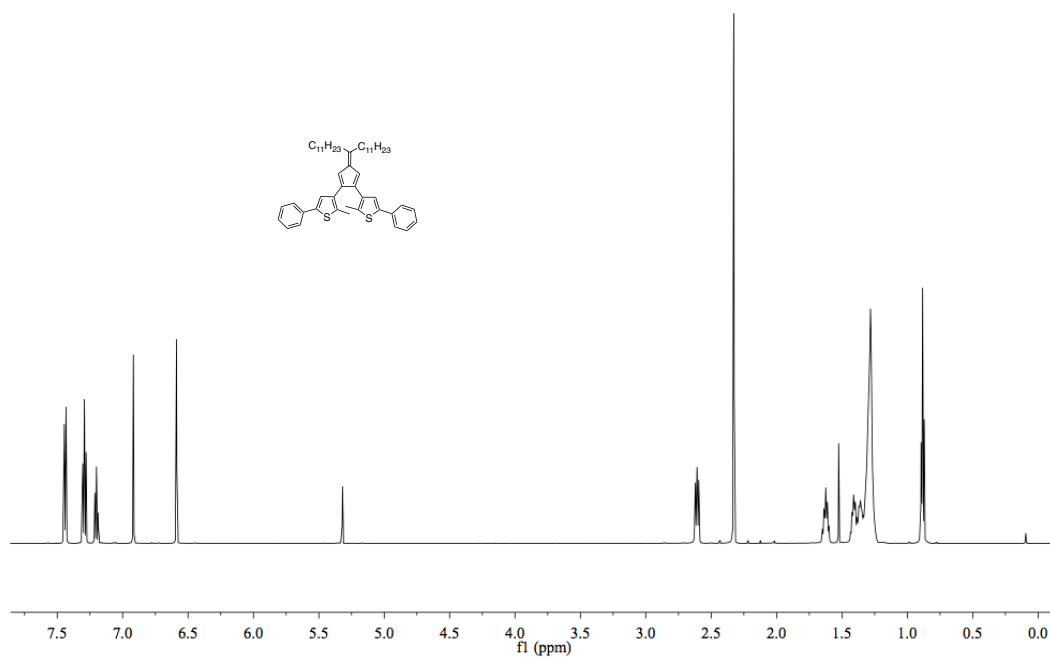


Figure 12.1 ^1H NMR (600 MHz) spectrum of 3,3'-(4-(tricosan-12-ylidene)cyclopenta-2,5-diene-1,2-diyl)bis(2-methyl-5-phenylthiophene) in CD_2Cl_2 .

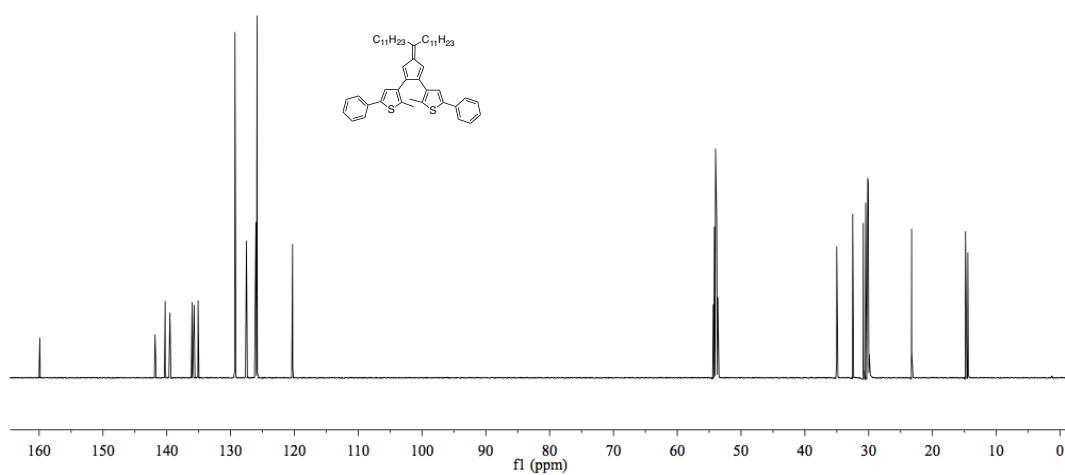


Figure 12.2 ^{13}C NMR (151 MHz) spectrum of 3,3'-(4-(tricosan-12-ylidene)cyclopenta-2,5-diene-1,2-diyl)bis(2-methyl-5-phenylthiophene) in CD_2Cl_2 .

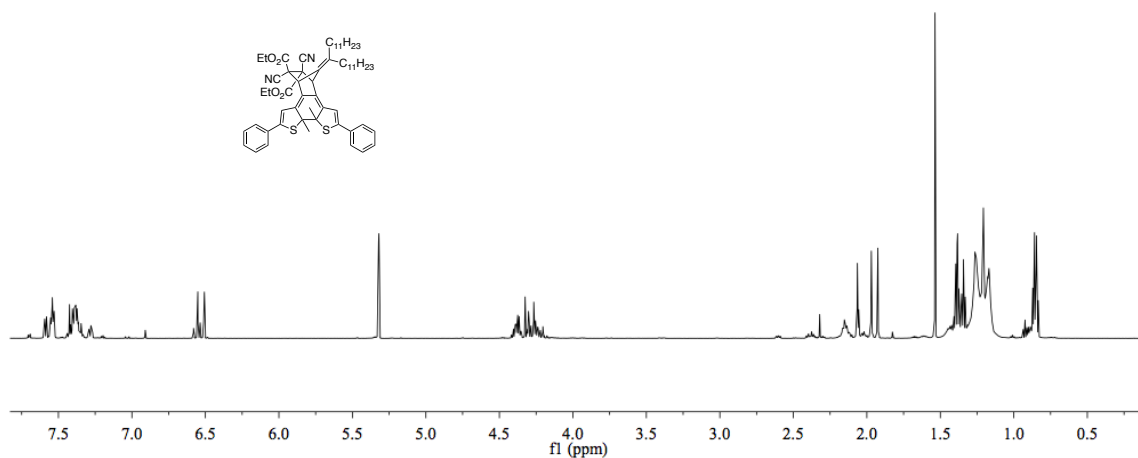


Figure 12.3 ^1H NMR (600 MHz) spectrum of (4 stereoisomers)-diethyl 5,6-dicyano-10a,10b-dimethyl-2,9-diphenyl-11-(tricosan-12-ylidene)-4,5,6,7,10a,10b-hexahydro-4,7-methanonaphtho[2,1-*b*:3,4-*b'*]dithiophene-5,6-dicarboxylate in CD_2Cl_2 .

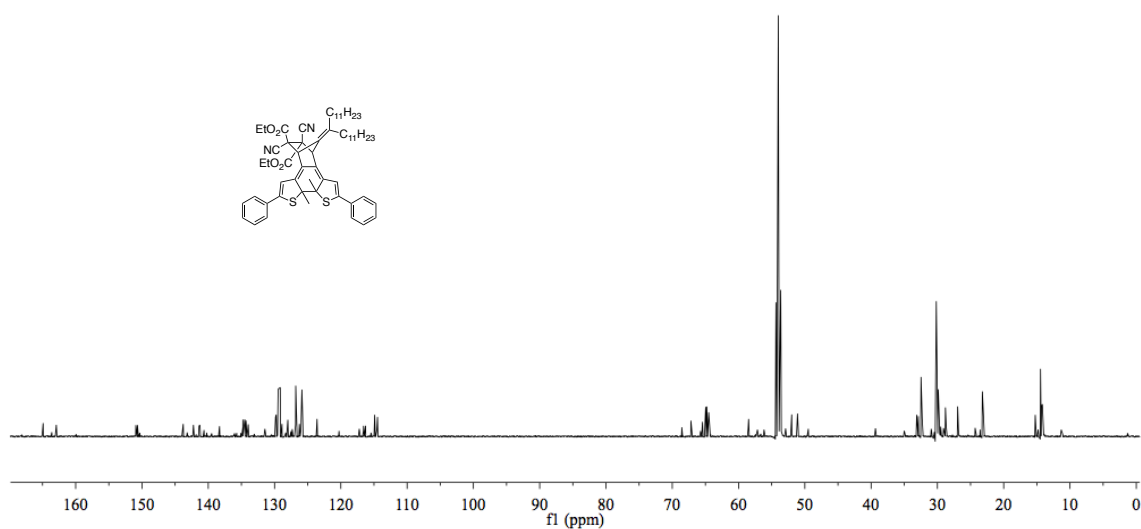


Figure 12.4 ^{13}C NMR (151 MHz) spectrum of (4 stereoisomers)-diethyl 5,6-dicyano-10a,10b-dimethyl-2,9-diphenyl-11-(tricosan-12-ylidene)-4,5,6,7,10a,10b-hexahydro-4,7-methanonaphtho[2,1-*b*:3,4-*b'*]dithiophene-5,6-dicarboxylate in CD_2Cl_2 .

12.2 NMR spectra of new compounds from *Chapter 5*

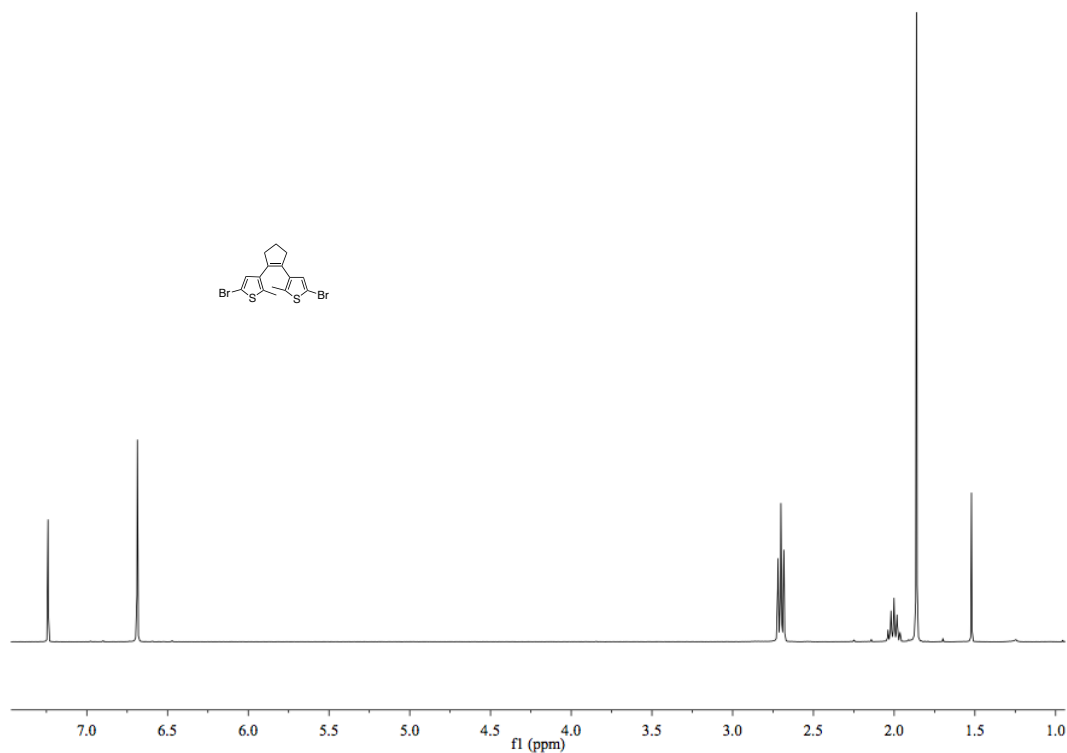


Figure 12.5 ¹H NMR (400 MHz) spectrum of 1,2-bis(5-bromo-2-methylthiophen-3-yl)cyclopent-1-ene in CD₂Cl₂.

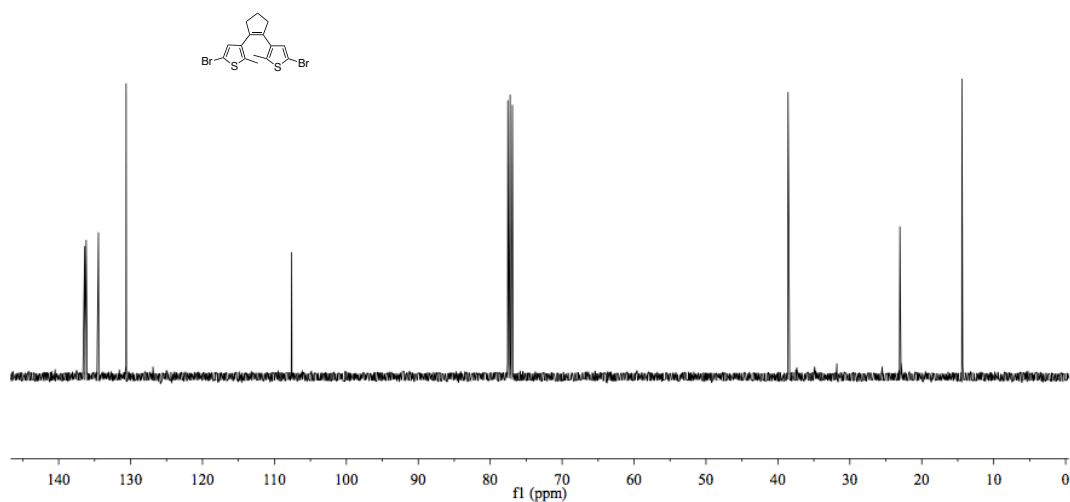


Figure 12.6 ¹³C NMR (100 MHz) spectrum of 1,2-bis(5-bromo-2-methylthiophen-3-yl)cyclopent-1-ene in CD₂Cl₂.

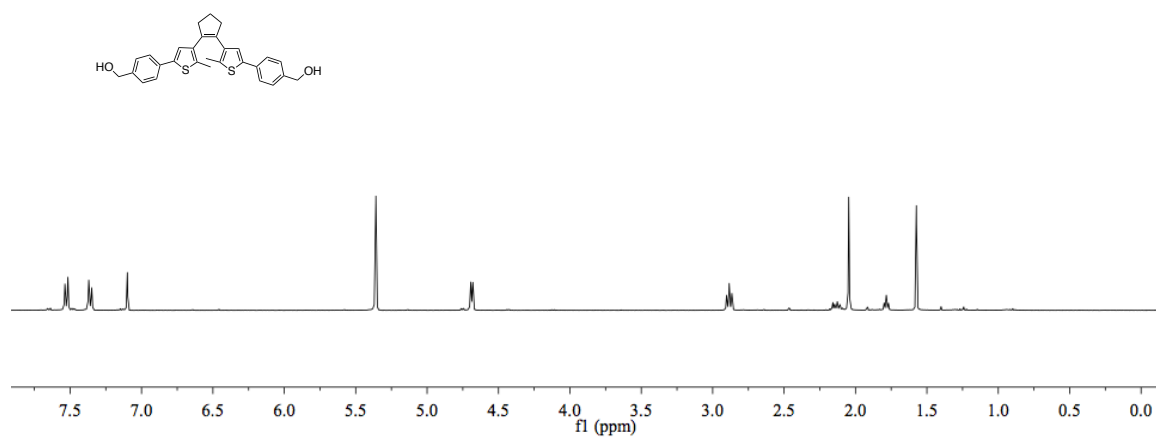


Figure 12.7 ^1H NMR (400 MHz) spectrum of (4,4'-(4,4'-(cyclopentene-1,2-diyl)bis(5-methylthiophene-4,2-diyl)-bis(4,1-phenylene))dimethanol in CD_2Cl_2 .

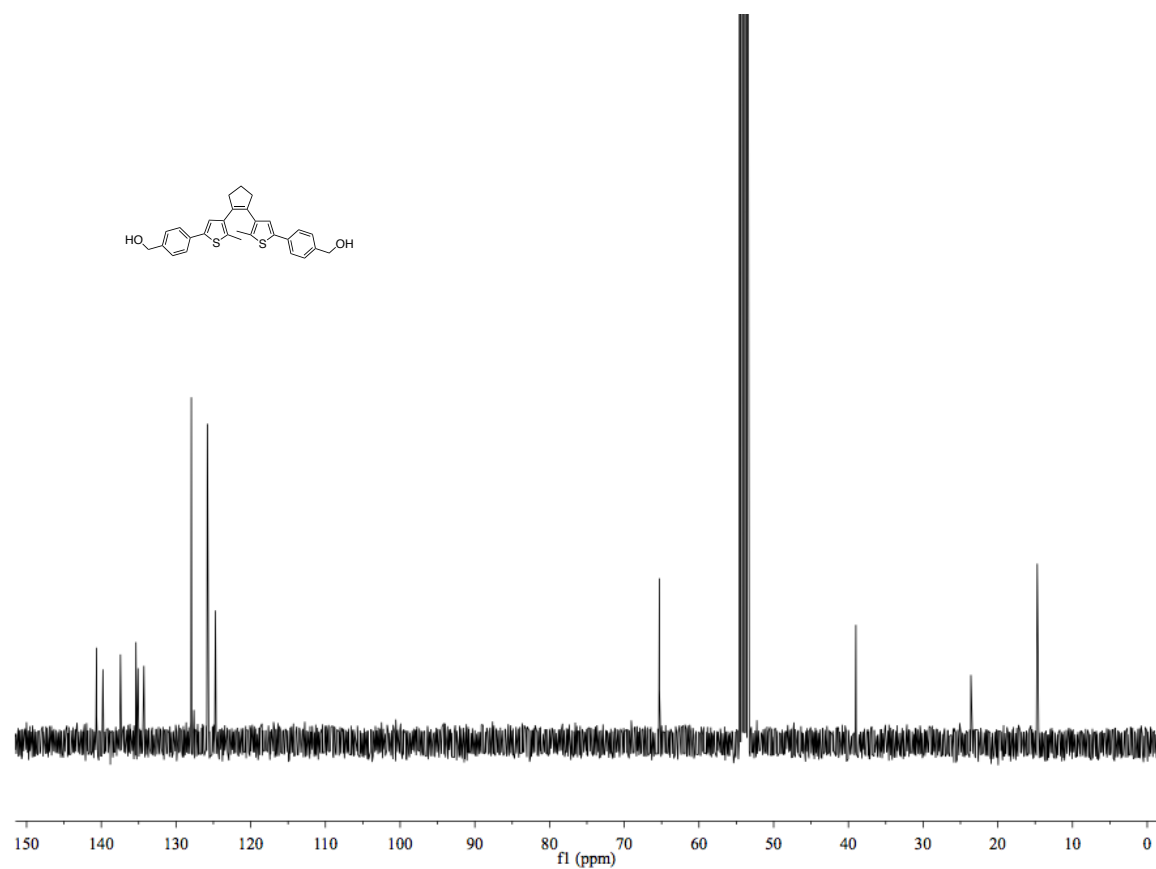


Figure 12.8 ^{13}C NMR (100 MHz) spectrum of (4,4'-(4,4'-(cyclopentene-1,2-diyl)bis(5-methylthiophene-4,2-diyl)-bis(4,1-phenylene))dimethanol in CD_2Cl_2 .

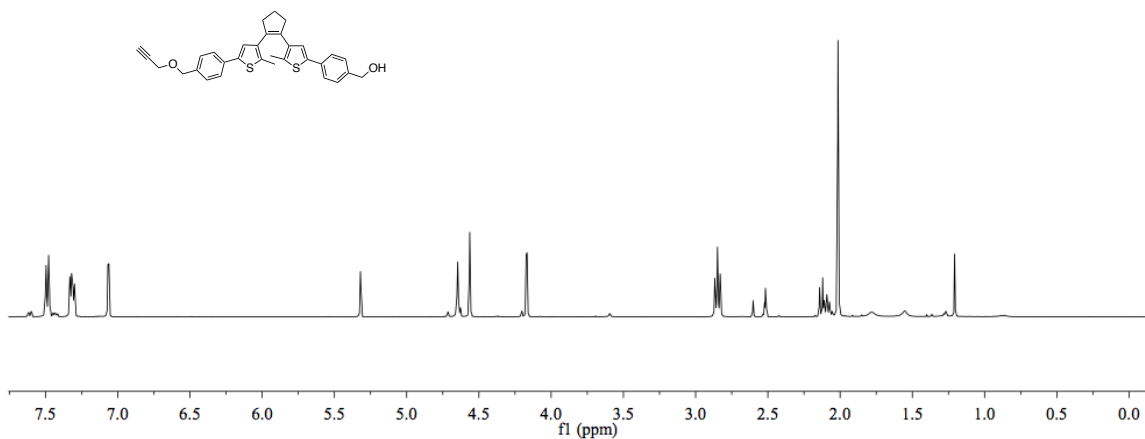


Figure 12.9 ^1H NMR (400 MHz) spectrum of (4-(5-methyl-4-(2-(2-methyl-5-(4-((prop-2-nyloxy)methyl) phenyl)-thiophen-3-yl)cyclopent-1-enyl)thiophen-2-yl)phenyl)methanol in CD_2Cl_2 .

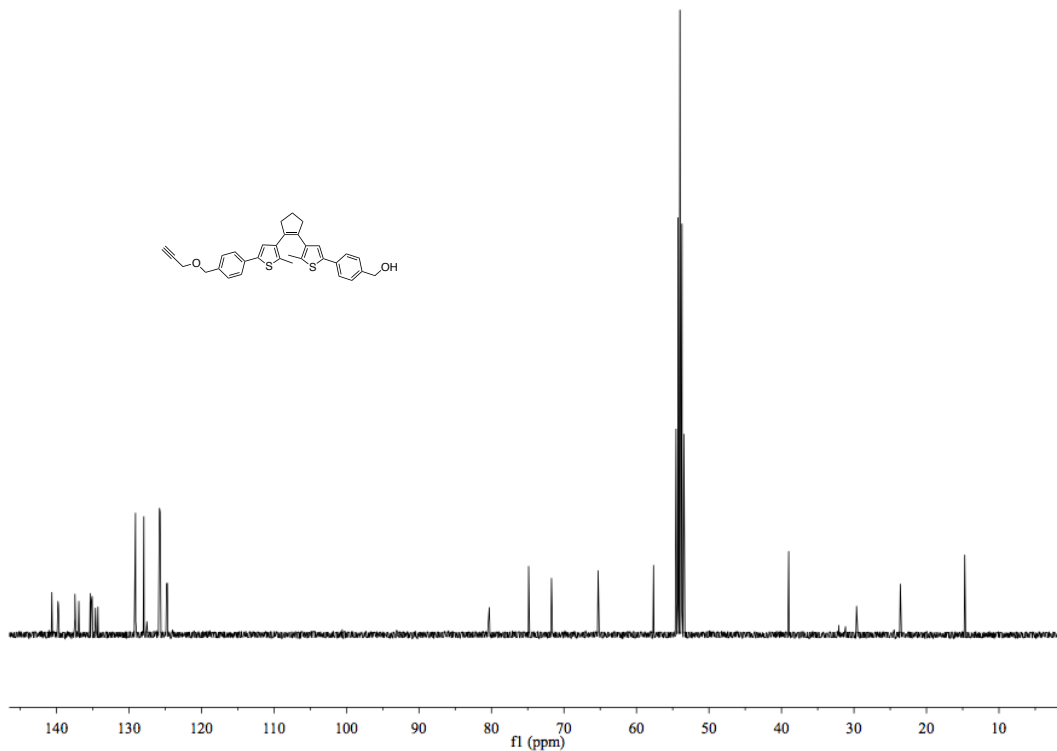


Figure 12.10 ^{13}C NMR (100 MHz) spectrum of (4-(5-methyl-4-(2-(2-methyl-5-(4-((prop-2-nyloxy)methyl) phenyl)-thiophen-3-yl)cyclopent-1-enyl)thiophen-2-yl)phenyl)methanol in CD_2Cl_2 .

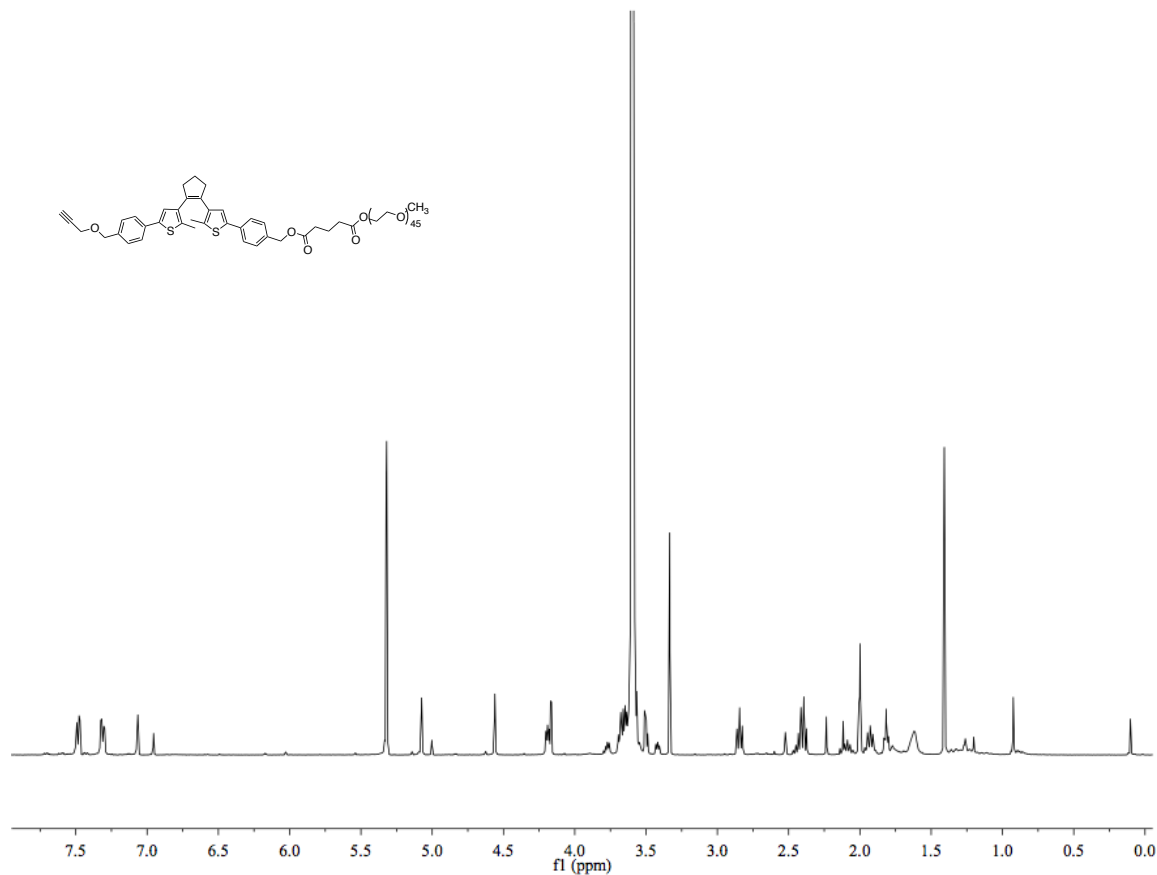


Figure 12.11 ^1H NMR (400 MHz) spectrum of 2-mPEG 4-(5-methyl-4-(2-(2-methyl-5-(4-((prop-2-ynyloxy)-methyl)phenyl)thiophen-3-yl)cyclopent-1-enyl)thiophen-2-yl)benzyl glutarate in CD_2Cl_2 .

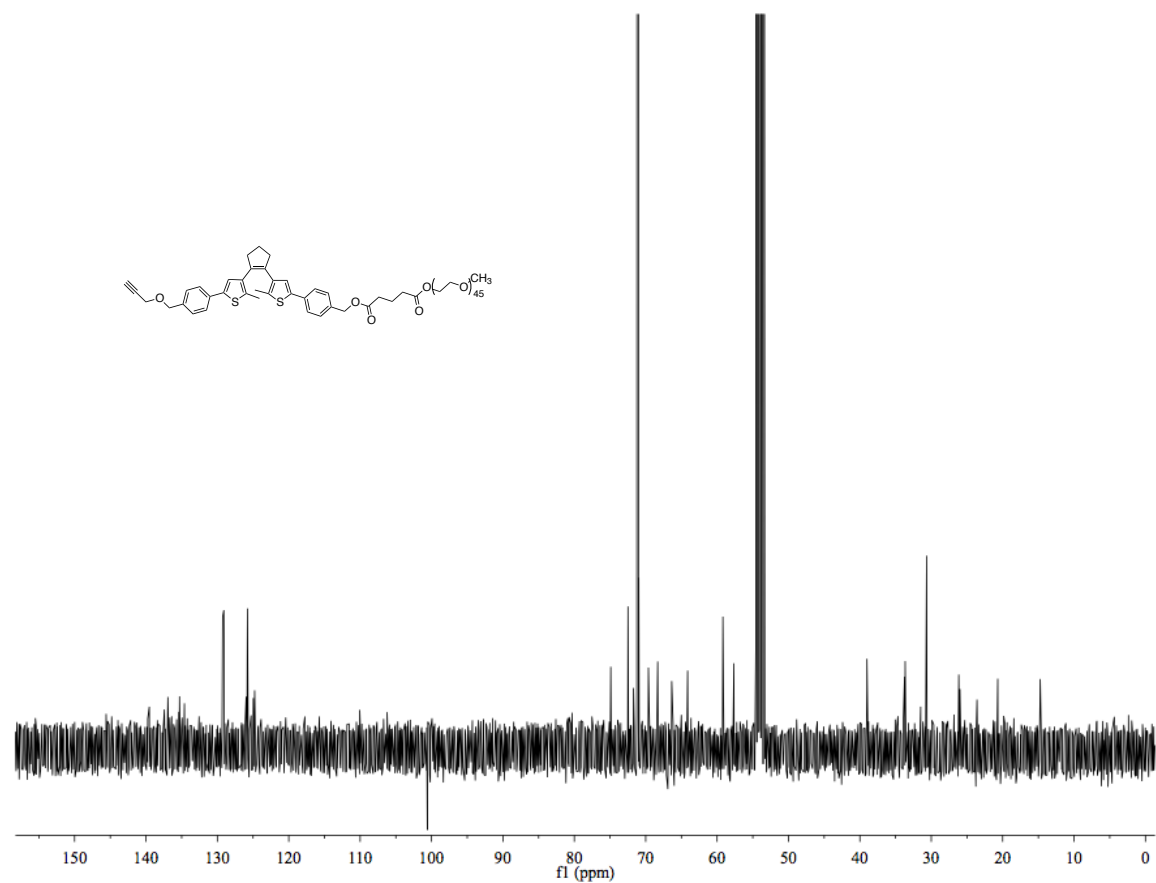


Figure 12.12 ¹³C NMR (100 MHz) spectrum of 2-mPEG 4-(5-methyl-4-(2-(2-methyl-5-(4-((prop-2-ynoxy)-methyl)phenyl)thiophen-3-yl)cyclopent-1-enyl)thiophen-2-yl)benzyl glutarate in CD₂Cl₂.

12.3 NMR spectra of new compounds from Chapter 9

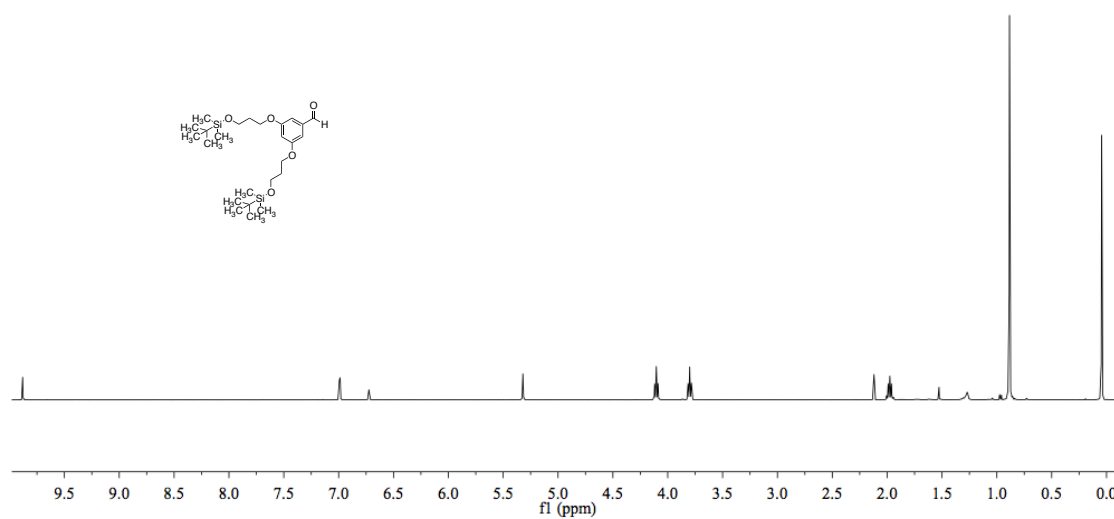


Figure 12.13 ^1H NMR (400 MHz) spectrum of 3,5-bis(3-((*tert*-butyldimethylsilyl)oxy)propoxy)benzaldehyde in CD_2Cl_2 .

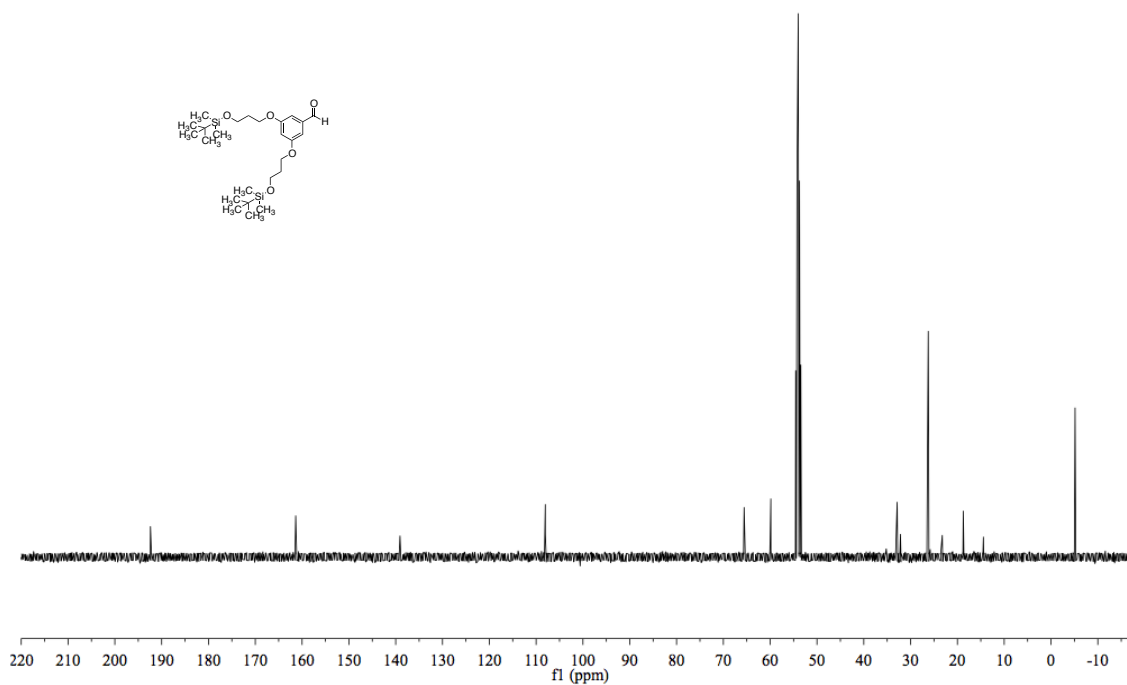


Figure 12.14 ^{13}C NMR (100 MHz) spectrum of 3,5-bis(3-((*tert*-butyldimethylsilyl)oxy)propoxy)benzaldehyde in CD_2Cl_2 .

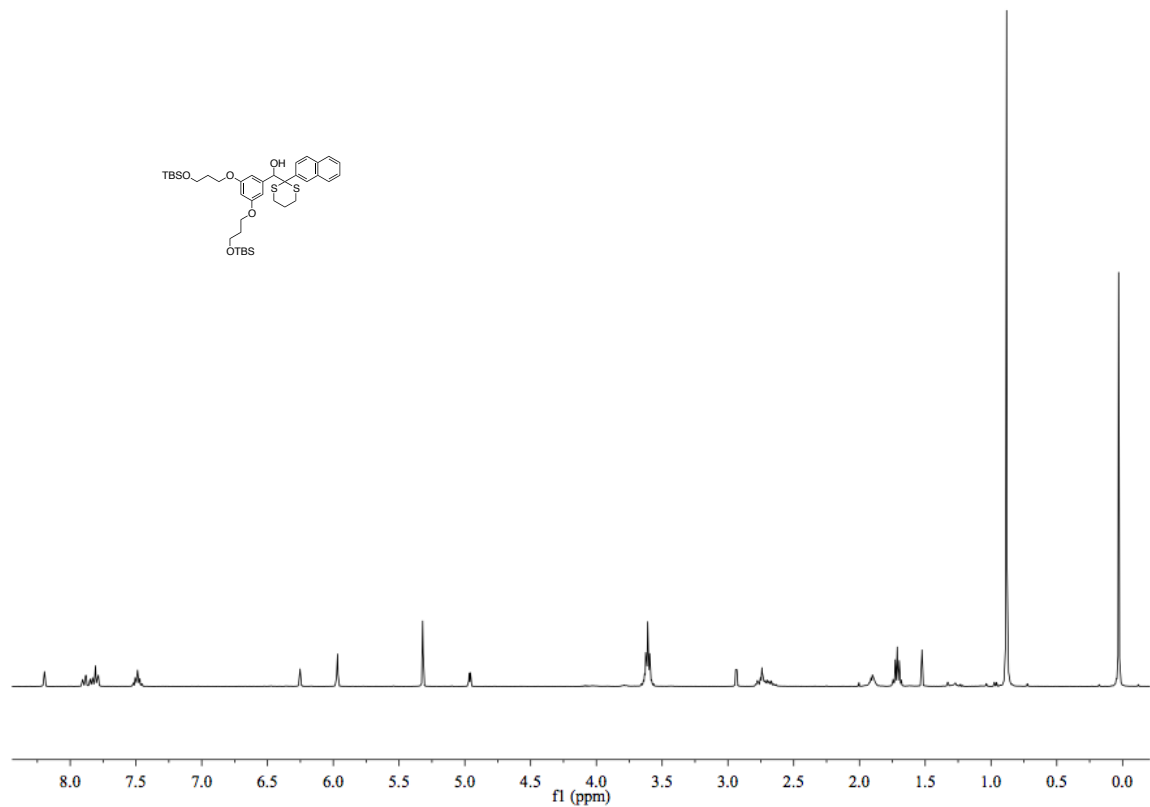


Figure 12.15 ^1H NMR (400 MHz) spectrum of (3,5-bis(3-((*tert*-butyldimethylsilyloxy)propoxy)phenyl)(2-(naphthalen-2-yl)-1,3-dithian-2-yl)methanol in CD_2Cl_2 .

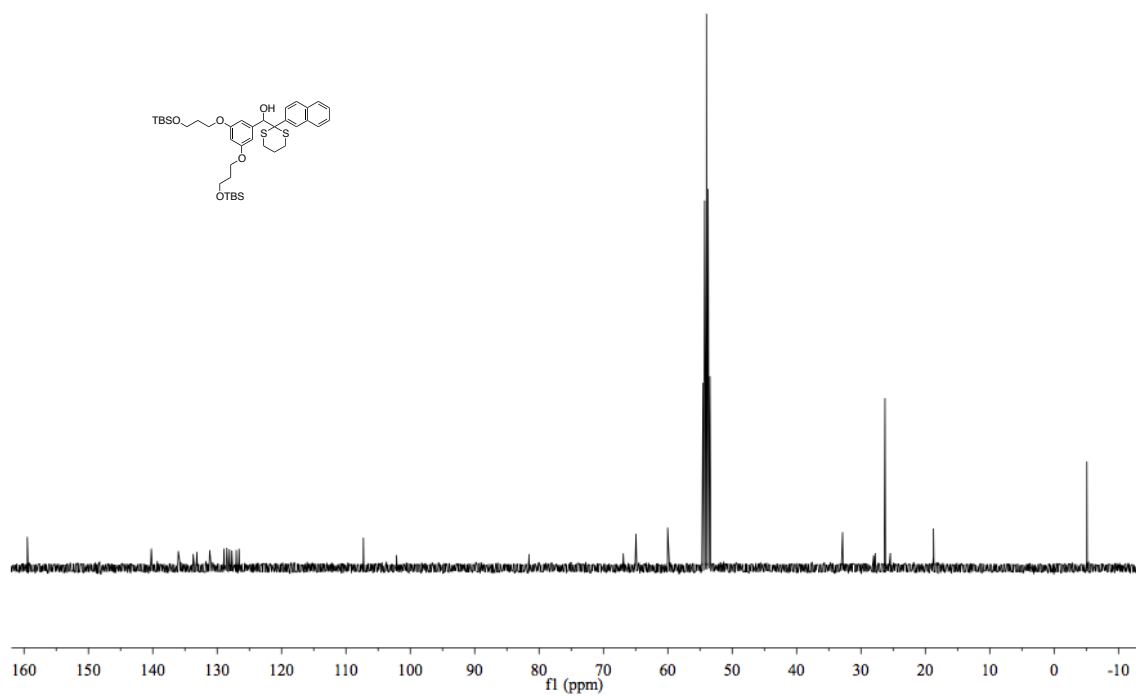


Figure 12.16 ^{13}C NMR (100 MHz) spectrum of (3,5-bis(3-((*tert*-butyldimethylsilyloxy)propoxy)phenyl)(2-(naphthalen-2-yl)-1,3-dithian-2-yl)methanol in CD_2Cl_2 .

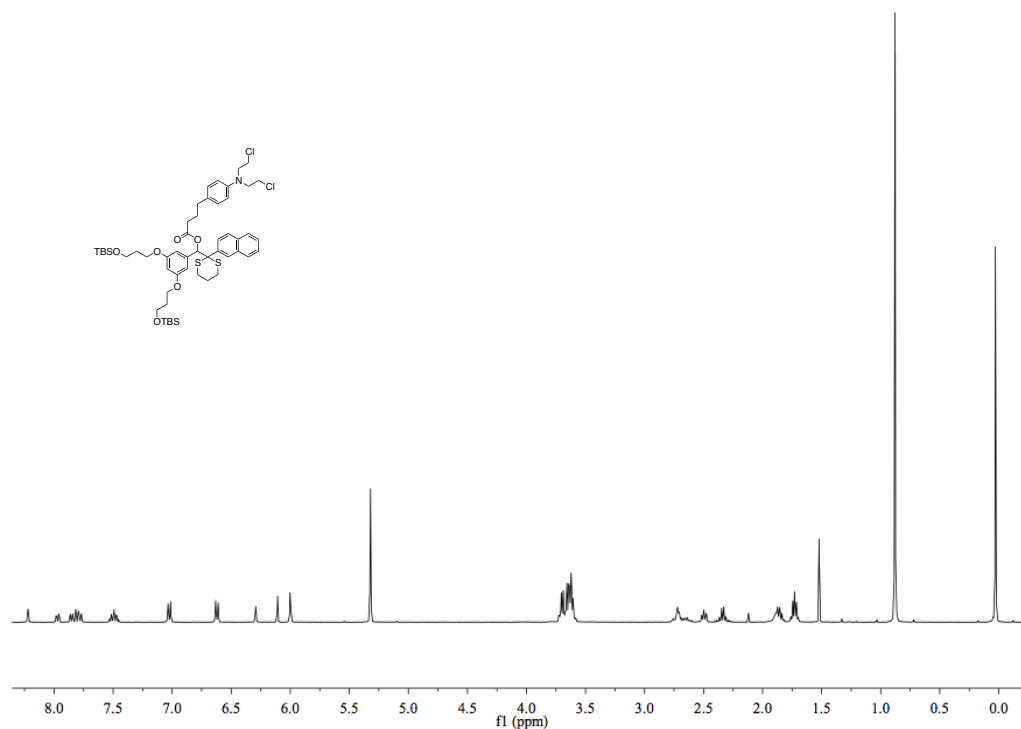


Figure 12.17 ^1H NMR (400 MHz) spectrum of (3,5-bis(3-((*tert*-butyldimethylsilyl)oxy)propoxy)phenyl)(2-(naphthalen-2-yl)-1,3-dithian-2-yl)methyl-4-(4-(bis(2-chloroethyl)amino)phenyl)butanoate in CD_2Cl_2 .

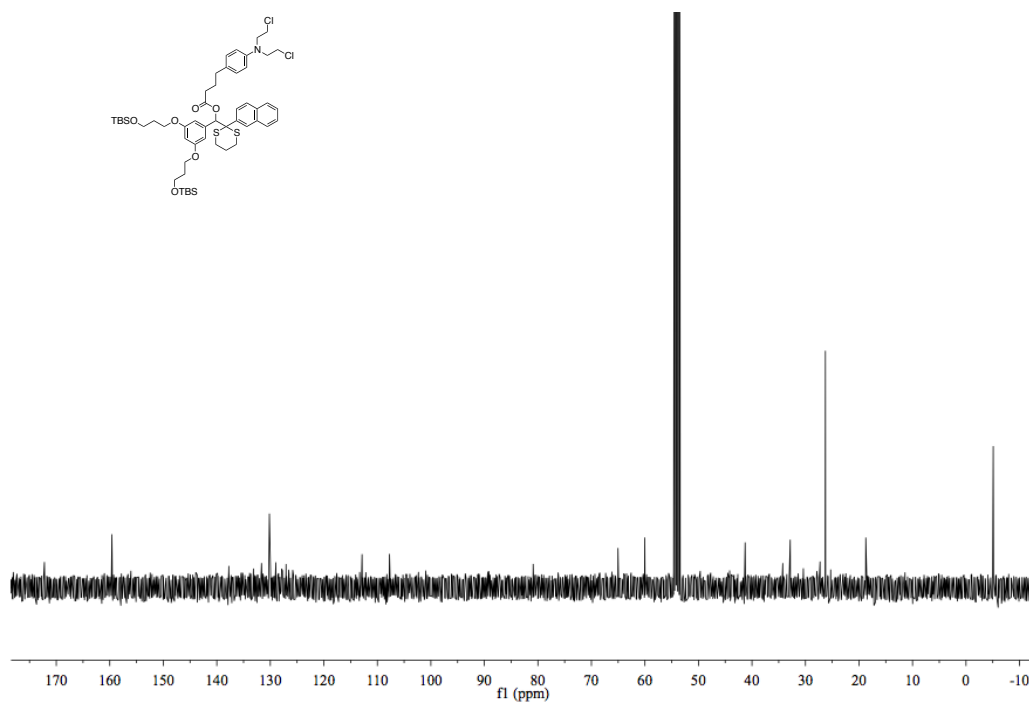


Figure 12.18 ^{13}C NMR (100 MHz) spectrum of (3,5-bis(3-((*tert*-butyldimethylsilyl)oxy)propoxy)phenyl)(2-(naphthalen-2-yl)-1,3-dithian-2-yl)methyl-4-(4-(bis(2-chloroethyl)amino)phenyl)butanoate in CD_2Cl_2 .

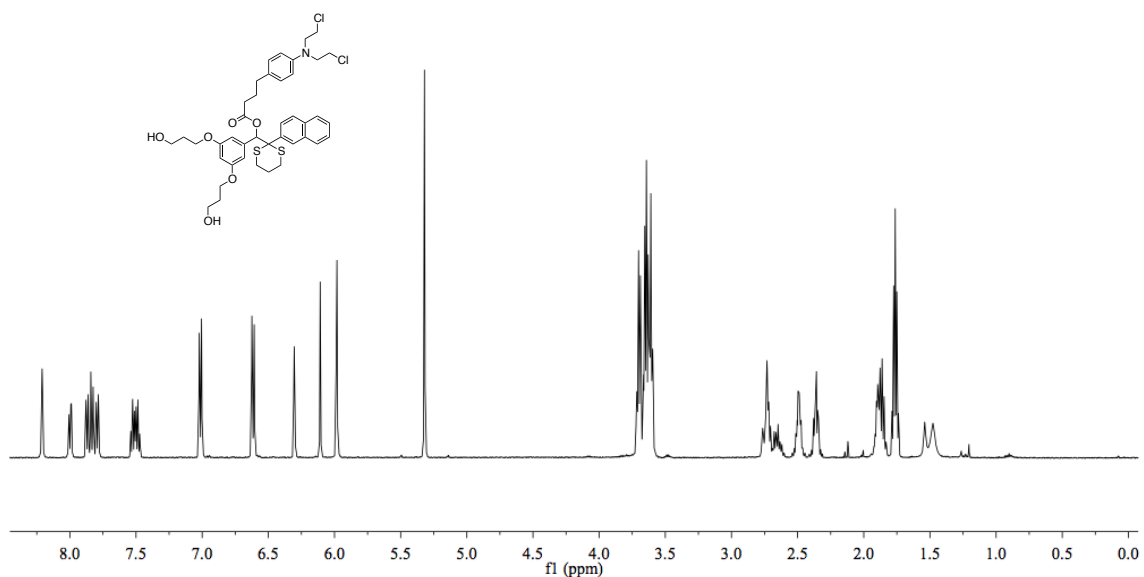


Figure 12.19 ^1H NMR (500 MHz) spectrum of (3,5-bis(3-hydroxypropoxy)phenyl)(2-(naphthalen-2-yl)-1,3-dithian-2-yl)methyl 4-(4-(bis(2-chloroethyl)amino)phenyl)butanoate in CD_2Cl_2 .

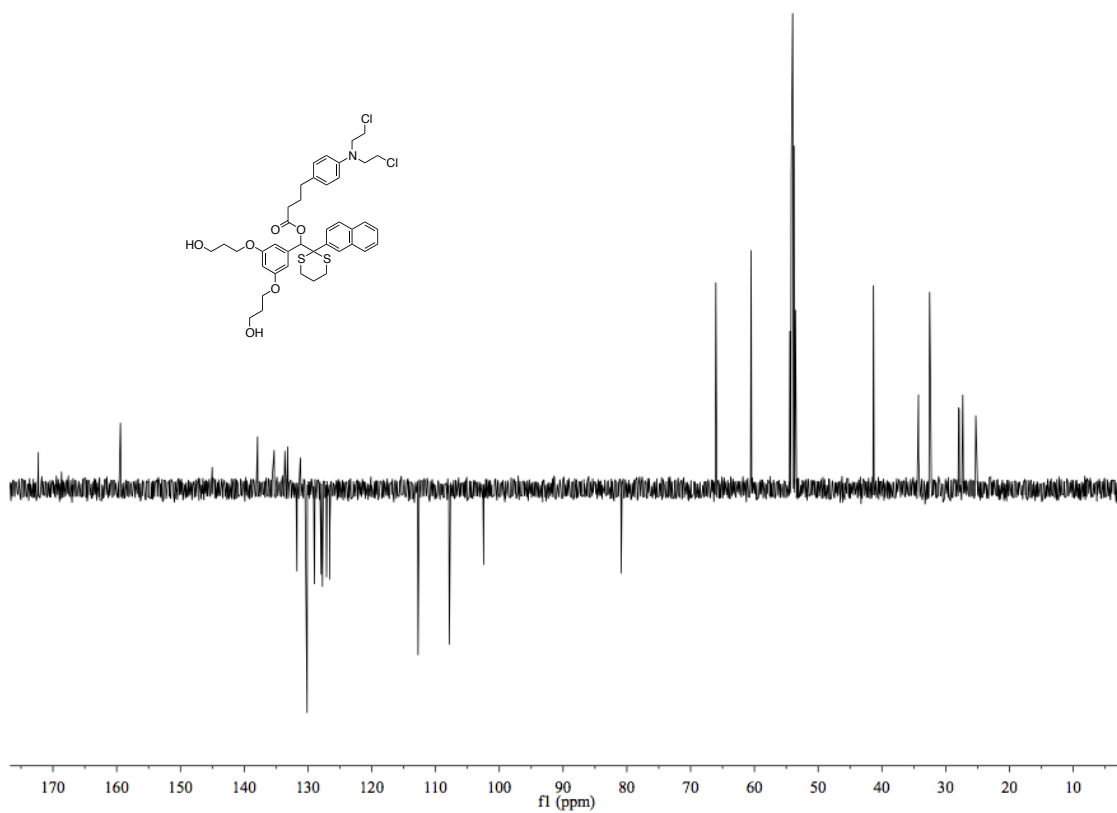


Figure 12.20 ^{13}C NMR (126 MHz) spectrum of (3,5-bis(3-((*tert*-butyldimethylsilyloxy)propoxy)phenyl)(2-(naphthalen-2-yl)-1,3-dithian-2-yl)methyl 4-(4-(bis(2-chloroethyl)amino)phenyl)butanoate in CD_2Cl_2 .

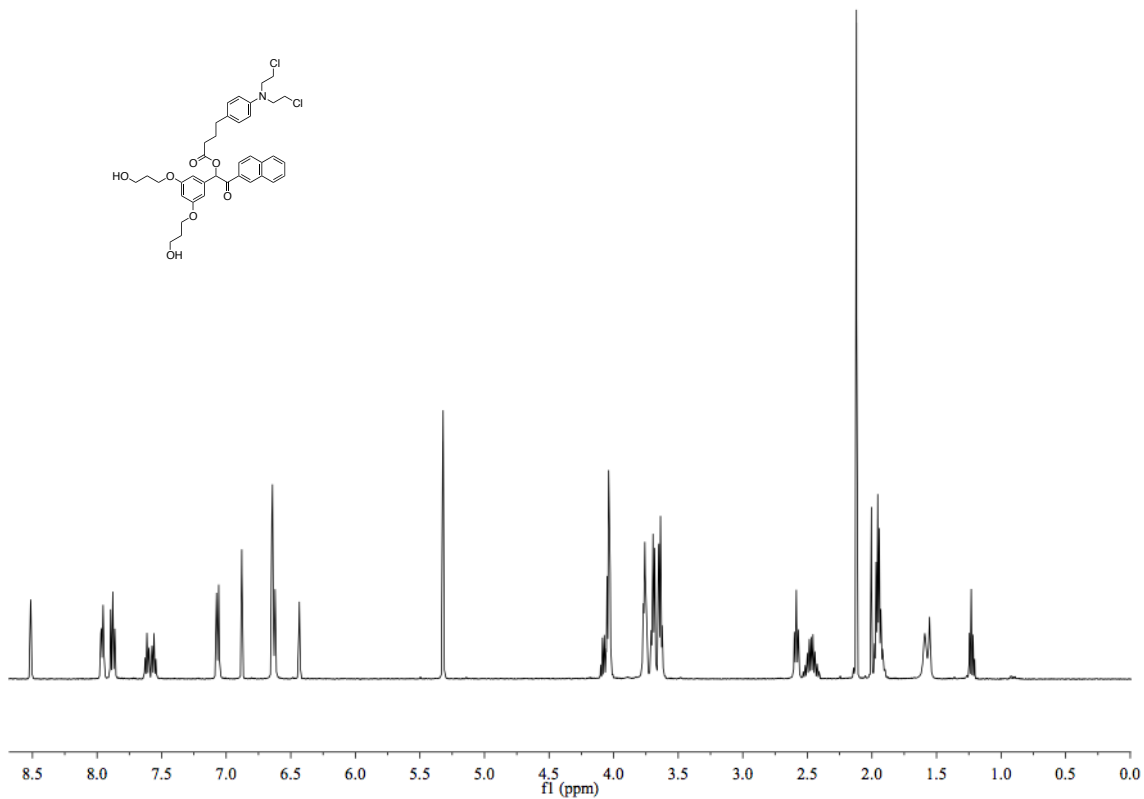


Figure 12.21 ¹H NMR (500 MHz) spectrum of 1-(3,5-bis(3-hydroxypropoxy)phenyl)-2-(naphthalen-2-yl)-2-oxoethyl-4-(4-(bis(2-chloroethyl)amino)phenyl)butanoate in CD₂Cl₂.

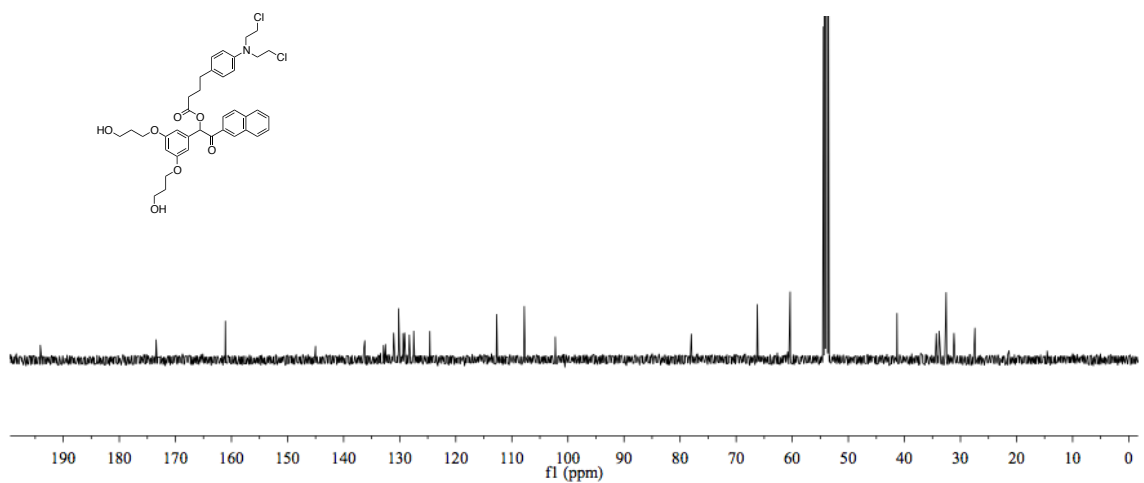


Figure 12.22 ¹³C NMR (126 MHz) spectrum of 1-(3,5-bis(3-hydroxypropoxy)phenyl)-2-(naphthalen-2-yl)-2-oxoethyl-4-(4-(bis(2-chloroethyl)amino)phenyl)butanoate in CD₂Cl₂.

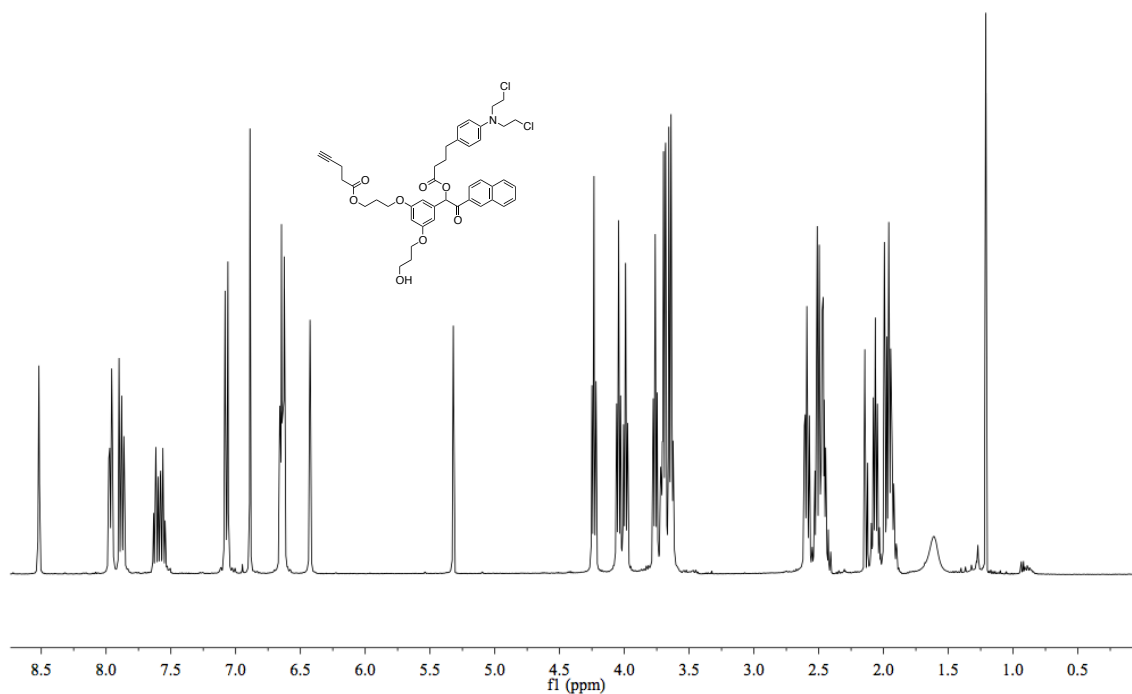


Figure 12.23 ¹H NMR (500 MHz) spectrum of 3-(3-(1-((4-(4-(bis(2-chloroethyl)amino)phenyl)butanoyl)oxy)-2-(naphthalen-2-yl)-2-oxoethyl)-5-(3-hydroxypropoxy)phenoxy)propyl pent-4-ynoate in CD₂Cl₂.

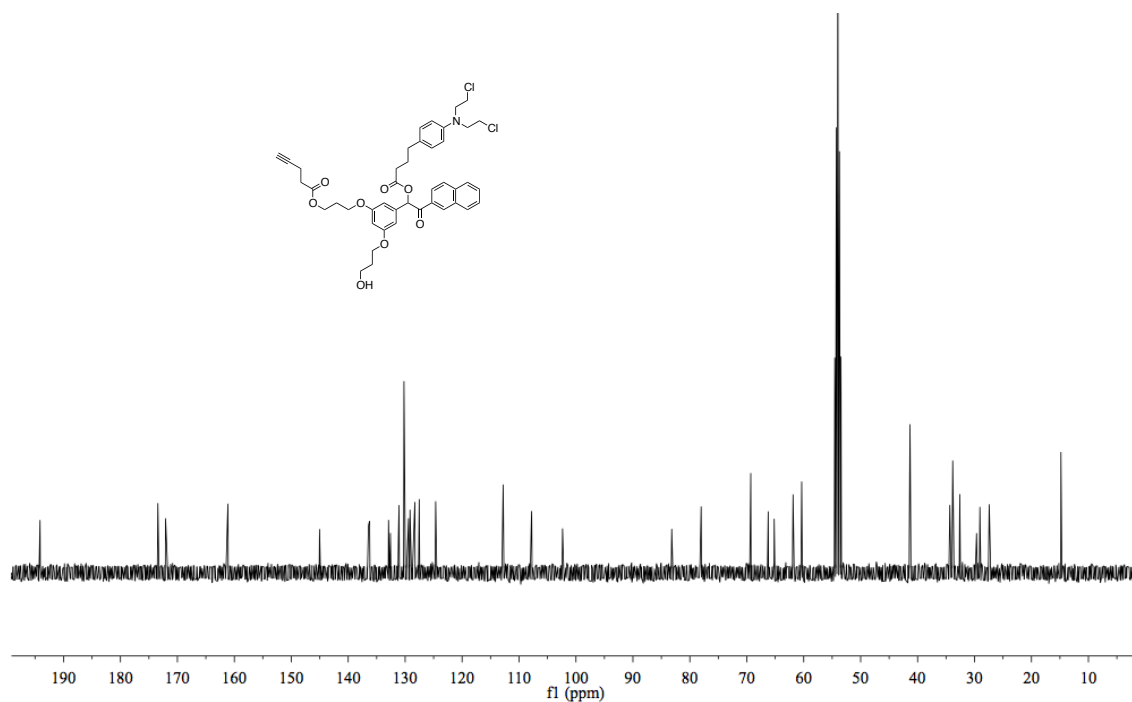


Figure 12.24 ¹³C NMR (126 MHz) spectrum of 3-(3-(1-((4-(4-(bis(2-chloroethyl)amino)phenyl)butanoyl)oxy)-2-(naphthalen-2-yl)-2-oxoethyl)-5-(3-hydroxypropoxy)phenoxy)propyl pent-4-ynoate in CD₂Cl₂.

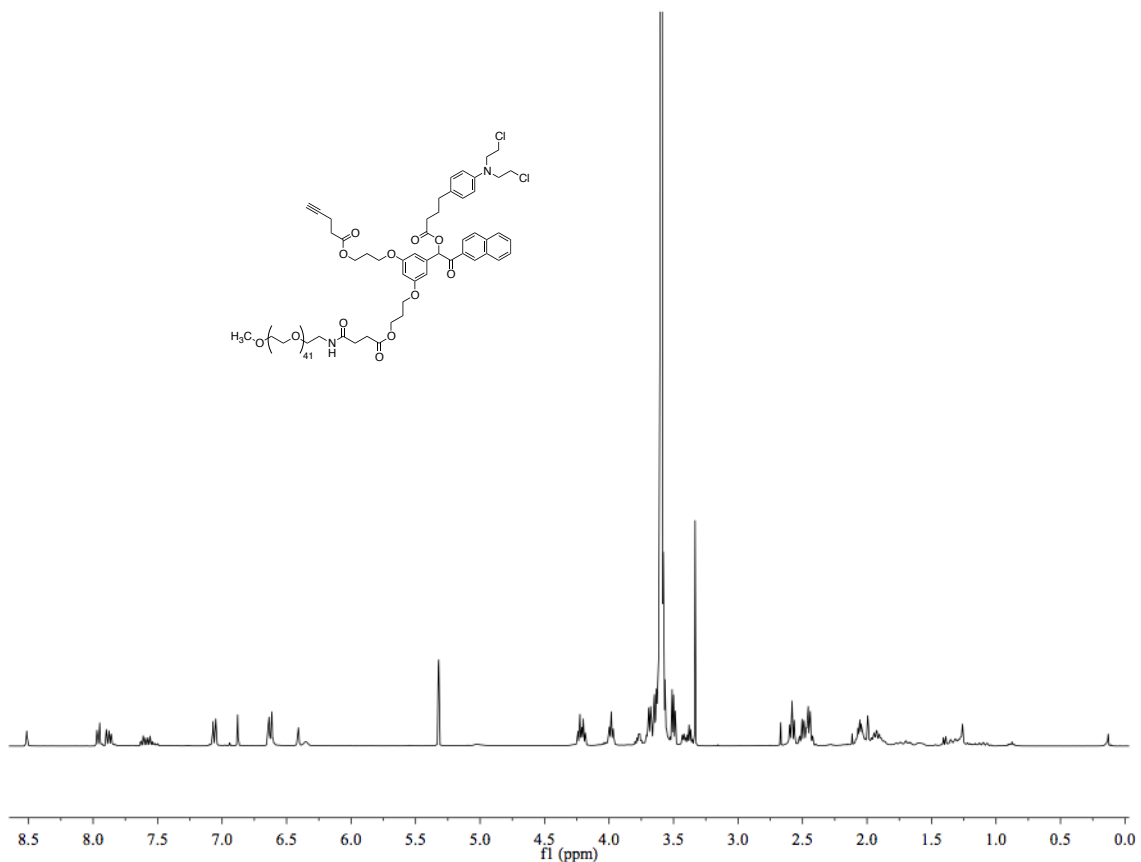


Figure 12.25 ¹H NMR (500 MHz) spectrum of 3-(3-(1-((4-(4-(bis(2-chloroethyl)amino)phenyl)butanoyl)oxy)-2-(naphthalen-2-yl)-2-oxoethyl)-5-(3-(pent-4-ynoyloxy)propoxy)phenoxy)propyl-136-oxo-2,5,8,11,14,17,20,23,26,29,33,36,39,42,45,48,51,54,57,60,63,66,69,72,75,78,81,84,87,90,93,96,99,102,105,108,111,114,117,120,123,126,129,132-tetratetracontaoxa-135-azanonatriacontahectan-139-oate in CD₂Cl₂.

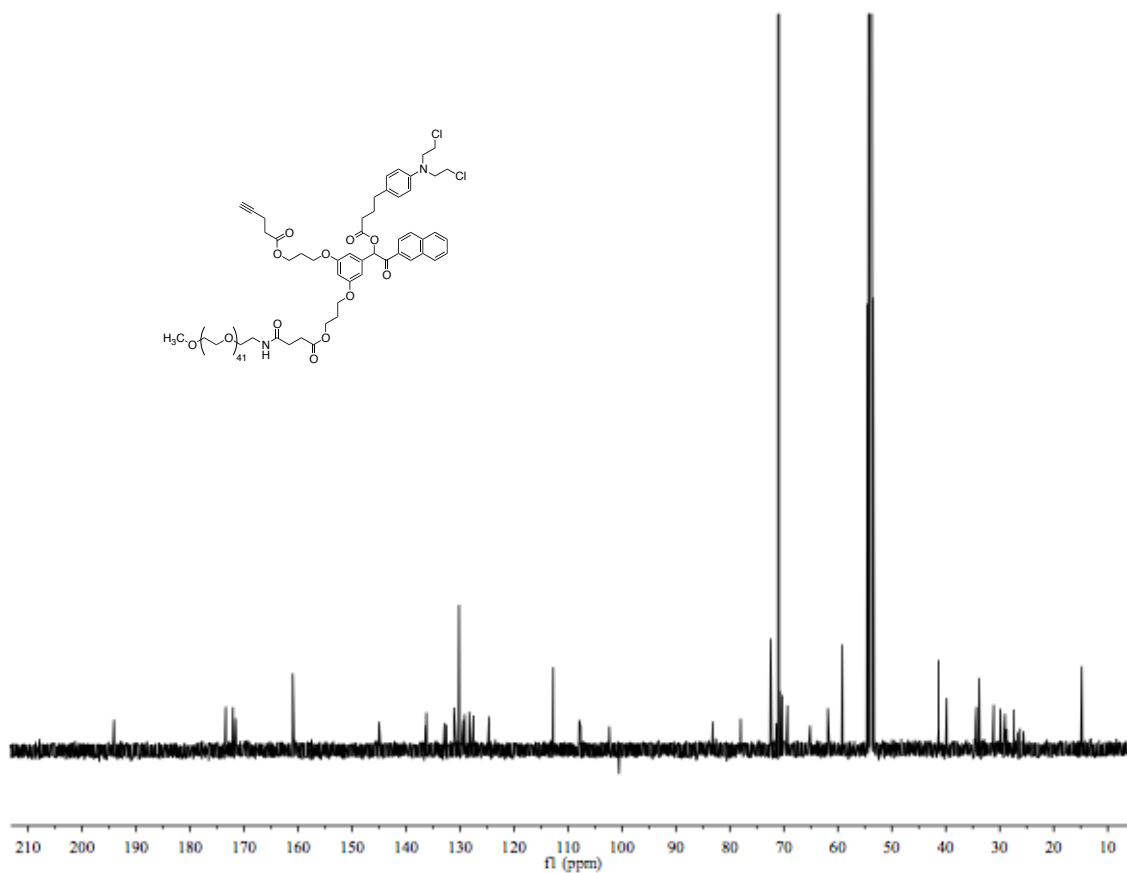


Figure 12.26 ^{13}C NMR (126 MHz) spectrum of 3-(3-(1-((4-(4-(bis(2-chloroethyl)amino)phenyl)butanoyl)oxy)-2-(naphthalen-2-yl)-2-oxoethyl)-5-(3-(pent-4-ynoyloxy)propoxy)phenoxy)propyl-136-oxo-2,5,8,11,14,17,20,23,26,29,33,36,39,42,45,48,51,54,57,60,63,66,69,72,75,78,81,84,87,90,93,96,99,102,105,108,111,114,117,120,123,126,129,132-tetratetracontaoxa-135-azanonatriacontahectan-139-oate in CD_2Cl_2 .

12.4 NMR spectra of new compounds from *Chapter 10*

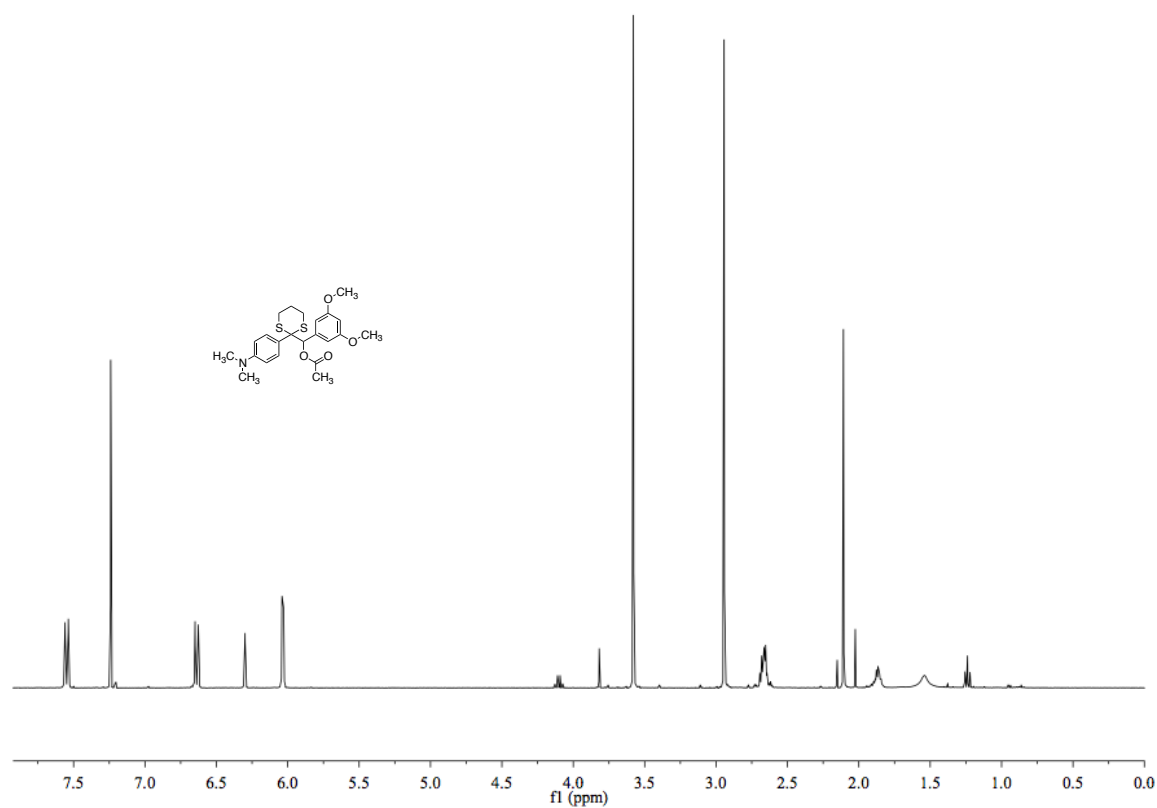


Figure 12.27 ¹H NMR (400 MHz) spectrum of (3,5-dimethoxyphenyl)(2-(4-(dimethylamino)phenyl)-1,3-dithian-2-yl)methyl acetate in CD₂Cl₂.

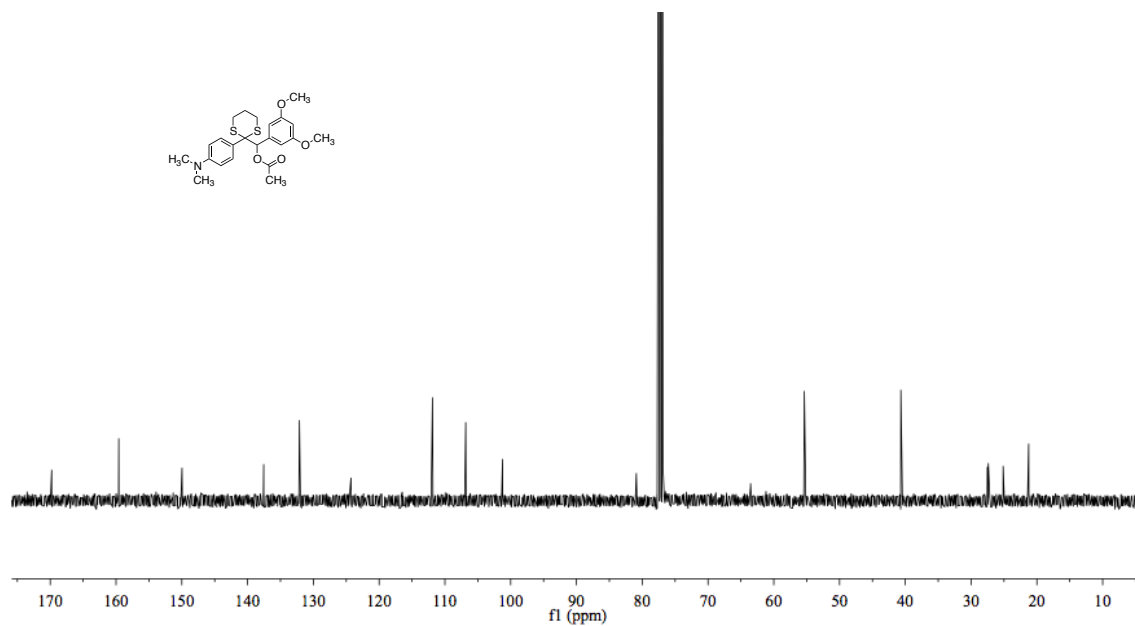


Figure 12.28 ¹³C NMR (100 MHz) spectrum of (3,5-dimethoxyphenyl)(2-(4-(dimethylamino)phenyl)-1,3-dithian-2-yl)methyl acetate in CD₂Cl₂.

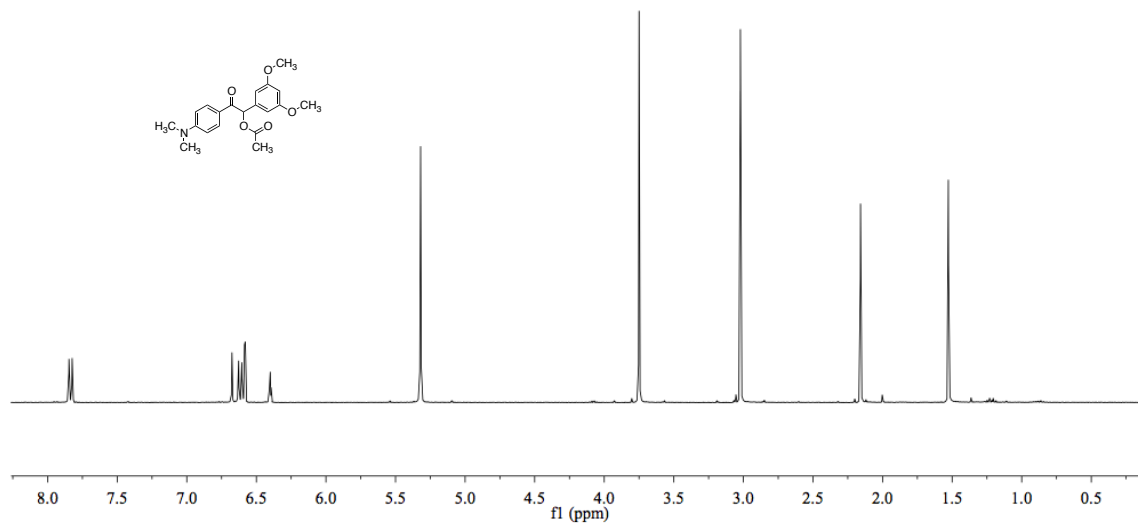


Figure 12.29 ^1H NMR (400 MHz) spectrum of 1-(3,5-dimethoxyphenyl)-2-(4-(dimethylamino)phenyl)-2-oxoethyl acetate in CD_2Cl_2 .

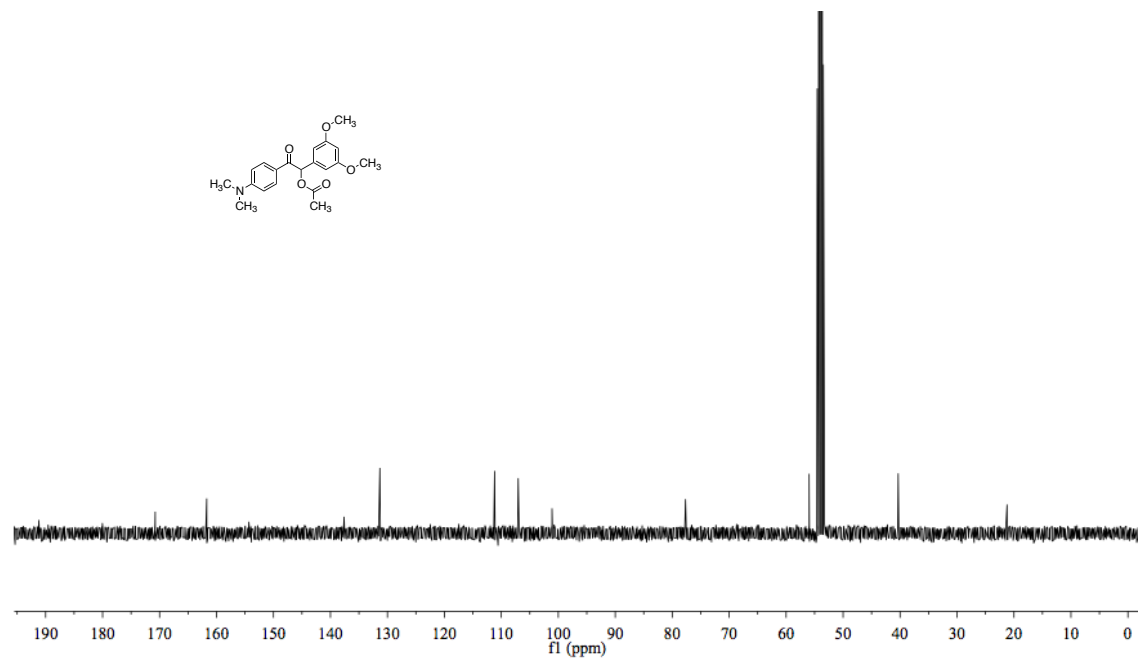


Figure 12.30 ^{13}C NMR (100 MHz) spectrum of 1-(3,5-dimethoxyphenyl)-2-(4-(dimethylamino)phenyl)-2-oxoethyl acetate in CD_2Cl_2 .

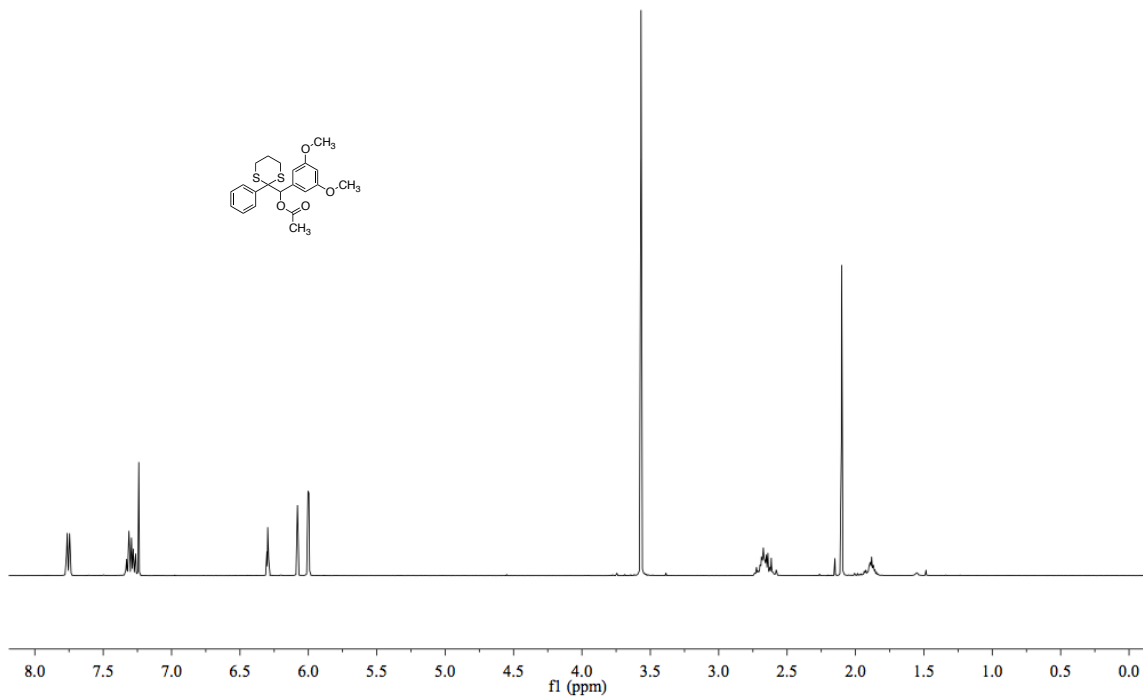


Figure 12.31 ¹H NMR (400 MHz) spectrum of (3,5-dimethoxyphenyl)(2-phenyl-1,3-dithian-2-yl) methyl acetate in CD₂Cl₂.

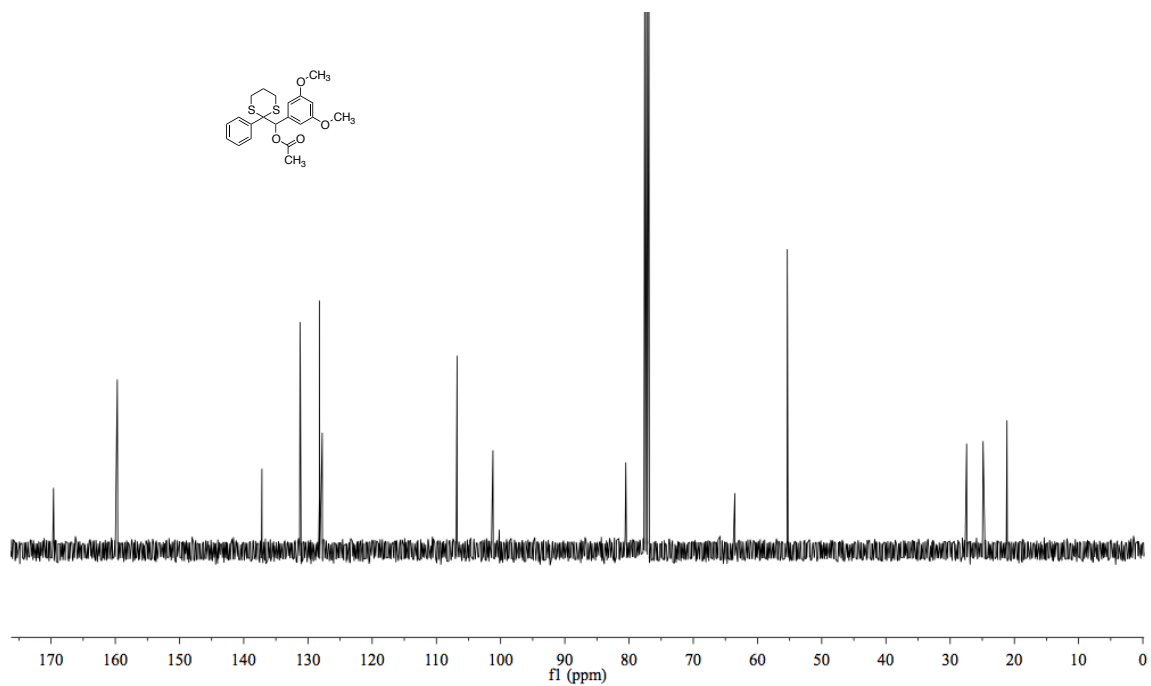


Figure 12.32 ¹³C NMR (100 MHz) spectrum of (3,5-dimethoxyphenyl)(2-phenyl-1,3-dithian-2-yl) methyl acetate in CD₂Cl₂.

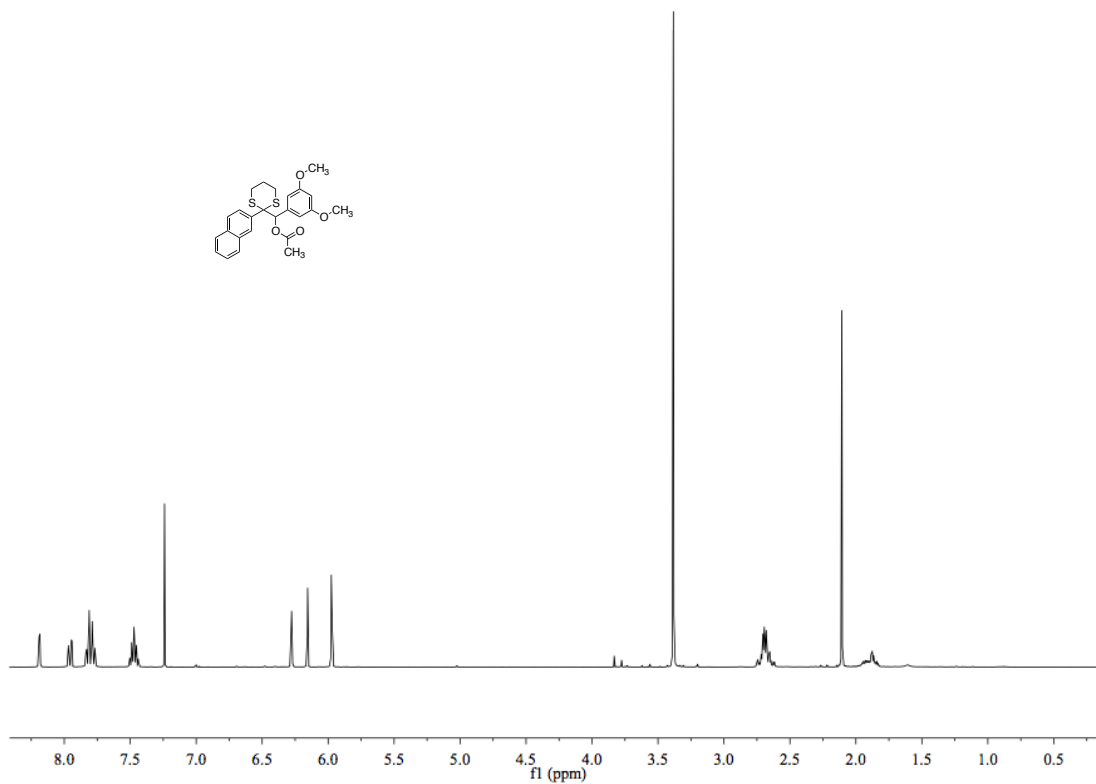


Figure 12.33 ¹H NMR (400 MHz) spectrum of (3,5-dimethoxyphenyl)(2-(naphthalen-2-yl)-1,3-dithian-2-yl)methyl acetate in CD₂Cl₂.

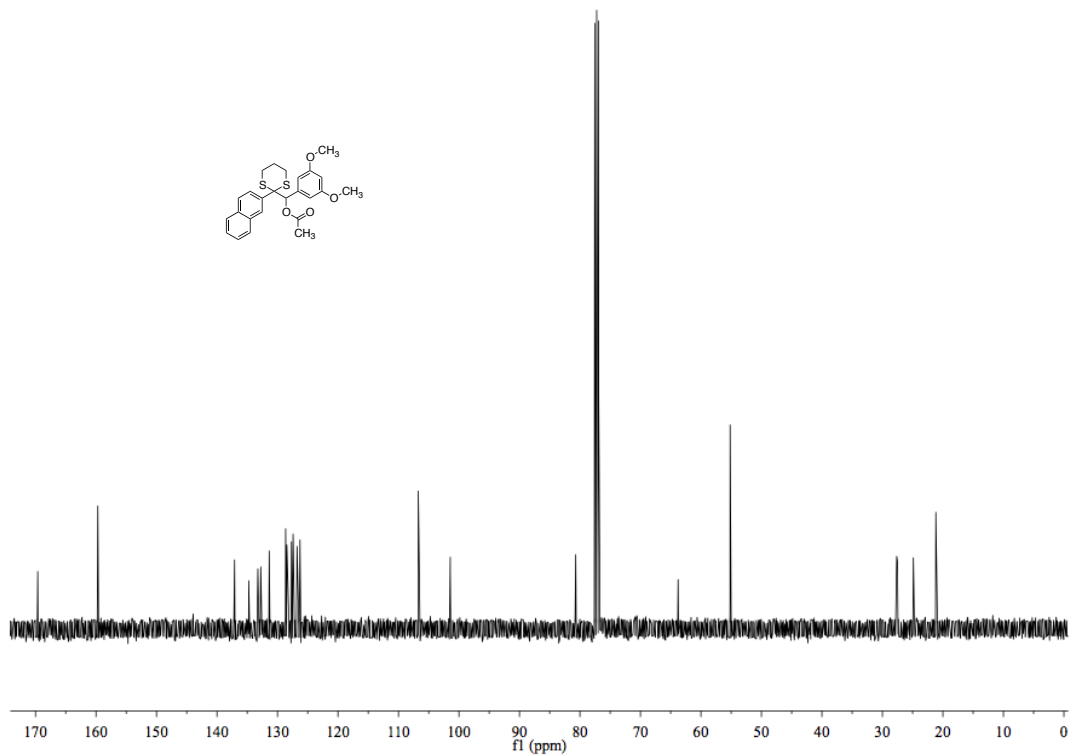


Figure 12.34 ^{13}C NMR (100 MHz) spectrum of (3,5-dimethoxyphenyl)(2-(naphthalen-2-yl)-1,3-dithian-2-yl)methyl acetate in CD_2Cl_2 .

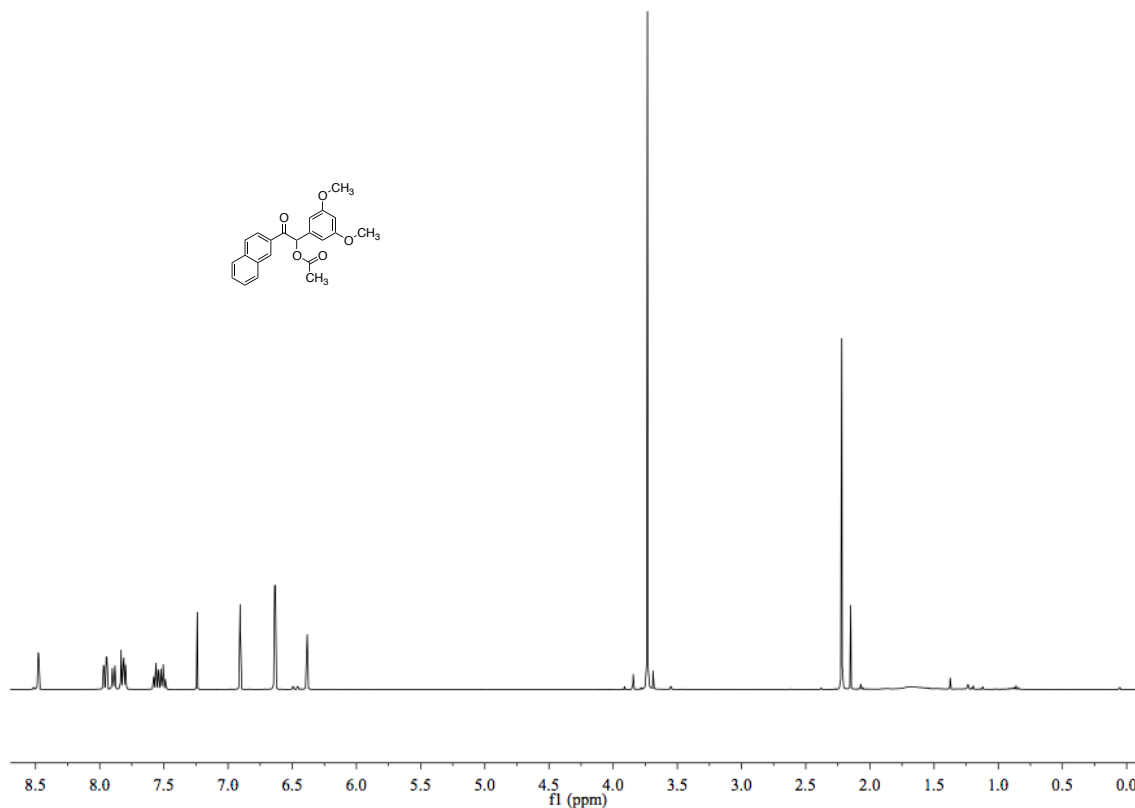


Figure 12.35 ^1H NMR (400 MHz) spectrum of 1-(3,5-dimethoxyphenyl)-2-(naphthalen-2-yl)-2-oxoethyl acetate in CD_2Cl_2 .

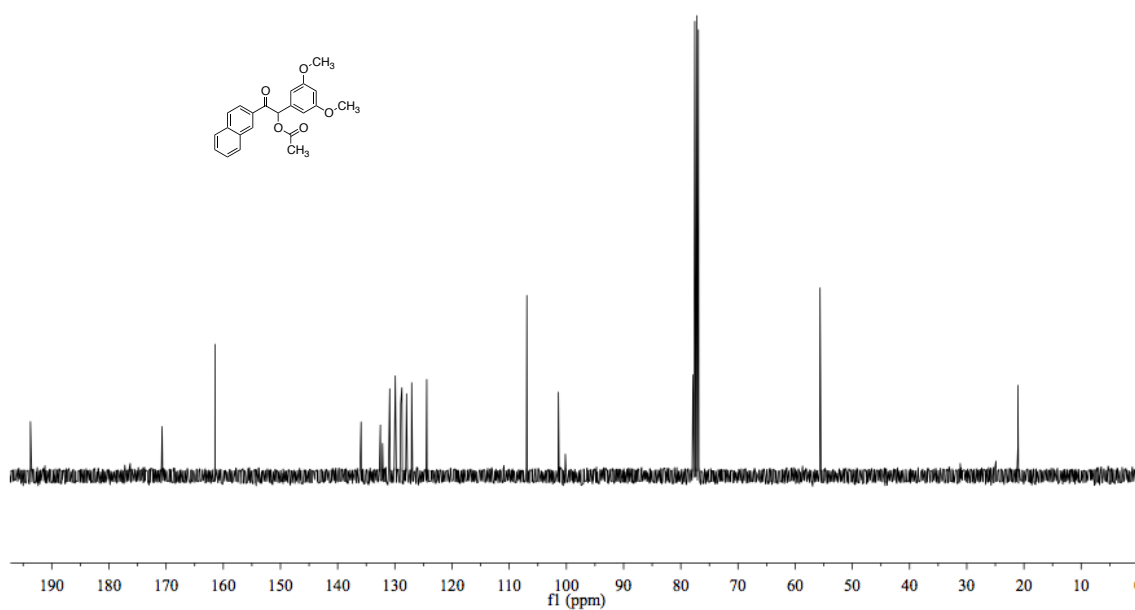


Figure 12.36 ^{13}C NMR (100 MHz) spectrum of 1-(3,5-dimethoxyphenyl)-2-(naphthalen-2-yl)-2-oxoethyl acetate in CD_2Cl_2 .

12.5 Curriculum vitae

Education

2007-2012 – Ph.D., Simon Fraser University, Burnaby, British Columbia, Canada

(Prof. N. R. Branda)

2005-2006 – M.Sc. project, Queen's University, Kingston, Ontario, Canada

(Prof. R. P. Lemieux, Prof. K. Wärnmark)

2001-2007 – M.Sc., Lund University, Lund, Sweden

Fellowships and Stipends

- Simon Fraser University President's Research Stipend
- Simon Fraser University Graduate Fellowship
- Sixten Gemzéus Stiftelse Stipend

Publications

1. C.-J. Carling, J.-C. Boyer and N. R. Branda, *Org. Biomolec. Chem.*, **2012**, *10*, 6159-6168. "Multimodal Fluorescence Modulation Using Molecular Photoswitches and Upconverting Nanoparticles"
2. J.-C Boyer[†], C.-J. Carling[†], S. Y. Chua, D. Wilson, B. Johnsen, D. Baillie and N. R. Branda, *Chem. Eur. J.*, **2012**, *18*, 3122–3126. "Photomodulation of Fluorescent Upconverting Nanoparticle Markers in Live Organisms by Using Molecular Switches" ([†]Authors contributed equally)

3. S.-J. Lim, C.-J. Carling, C. C. Warford, D. Hsiao, B. D. Gates, N. R. Branda, *Dyes and Pigments*, **2011**, 89, 230-235. “*Multifunctional Photo- and Thermo-Responsive Copolymer Nanoparticles*”
4. C. S. Arribas, O. F. Wendt, A. P. Sundin, C.-J. Carling, R. Wang, R. P. Lemieux, K. Wärnmark, *Chem. Commun.* **2010**, 46, 4381-4383. “*Formation of an Heterochiral Supramolecular Cage by Diastereomer Self-Discrimination: Fluorescence Enhancement and C₆₀ Sensing*”
5. J.-C. Boyer, C.-J. Carling, B. D. Gates, N. R. Branda, *J. Am. Chem. Soc.*, **2010**, 132, 15766-15772. “*Two-Way Photoswitching Using One Type of Near-Infrared Light, Upconverting Nanoparticles, and Changing Only the Light Intensity*”
6. C.-J. Carling, F. Nourmohammadian, J.-C. Boyer, N. R. Branda, *Angew. Chemie. Int. Ed.*, **2010**, 49, 3782-3785. “*Remote-Control Photorelease of Caged Compounds Using Near-Infrared Light and Upconverting Nanoparticles*” (This manuscript was designated as a “Hot Paper” by the journal and appeared April 23, 2010 in the Faculty of 1000 Biology, an award-winning online service that highlights and evaluates the most interesting papers published in the biological sciences, based on the recommendations of over 2000 of the world's top researchers.)
7. M. N. Roberts, C.-J. Carling, J. K. Nagle, N. R. Branda, M. O. Wolf, *J. Am. Chem. Soc.*, **2009**, 131, 16644-16645. “*Successful Bifunctional Photoswitching and Electronic Communication of Two Platinum(II) Acetylide Bridged Dithienylethenes*”

8. C.-J. Carling, J.-C. Boyer, N. R. Branda, *J. Am. Chem. Soc.*, **2009**, *131*, 10838-10839. “Remote-Control Photoswitching Using NIR Light”

Oral Presentations

1. 2012 – “NIR-to-UV Photorelease from the Surface of Upconverting Nanoparticles in water: Development of a Theranostic Drug-Delivery Vehicle” (MRS conference, San Francisco)
2. 2011 – “Remote control photochemistry and fluorescence modulation using NIR-to-UV and NIR-to-visible upconverting nanoparticles, dithienylethene photochromic dyes and dialkoxybenzoin photocages” (UCSD, Prof. Almutairi, San Diego)
3. 2011 – “Remote control photochemistry and fluorescence modulation using NIR-to-UV and NIR-to-visible upconverting nanoparticles, dithienylethene photochromic dyes and dialkoxybenzoin photocages” (The Scripps Research Institute, Prof. Rebek Jr., San Diego)
4. 2011 – “Remotely controlled photochemistry using low energy light and upconverting nanoparticles” (SFU oral competition, Burnaby)
5. 2010 – “Remote-control photorelease of caged compounds using NIR light and upconverting nanoparticles” (University of Toronto, Prof. McGuigan, Toronto)
6. 2010 – “Remote-control photorelease of caged compounds using NIR light and upconverting nanoparticles” (CSC conference, Toronto)

7. 2010 – “Remote-control photorelease of caged compounds using NIR light and upconverting nanoparticles” (SFU oral competition, Burnaby)
8. 2009 – “Controlling reactivity with light – a bright way to treat cancer” (SFU oral competition, Burnaby)

Poster Presentations

1. 2011 – “Photomodulation of upconverting nanoparticles using dithienylethene photochromic dyes” (SFU poster competition, Burnaby - first price)
2. 2010 – “Controlling photochemistry remotely using low energy near-infrared light and upconverting nanoparticles” (UBC, PCAMM conference, Vancouver)
3. 2010 – “Controlling photolabile chemistry remotely with low energy near-infrared light” (SFU poster competition, Burnaby)
4. 2009 – “The bright touch – controlling reactivity with low energy light” (SFU poster competition, Burnaby)

Coursework at SFU

1. Synthetic Organic Chemistry (A+, Prof. Wilson)
2. Magnetic Resonance (B+, Prof. Walsby)

Extracurricular Academic Activities

1. 2011 – Halloween chemistry show assistant (SFU, Prof. Wilson)
2. 2011 – Station assistant at “chemistry-quest” during the international year

of chemistry (SFU)

3. 2011 – Halloween chemistry show assistant (SFU, Prof. Wilson)

REFERENCES AND NOTES

- ¹ W. Bäuml, J. Regensburger, A. Knak, A. Felgenträger, T. Maisch, *Photochem. Photobiol. Sci.*, **2012**, *11*, 107–117.
- ² M. Tedetti, R. Sempéré, *Photochem. Photobiol.*, **2006**, *82*, 389-397.
- ³ G. J. Clydesdale, G. W. Dandie, H. K. Muller, *Immunol. Cell Biol.*, **2001**, *79*, 547-568.
- ⁴ P. T. C. So, C. Y. Dong, B. R. Masters, K. M. Berland, *Annu. Rev. Biomed. Eng.*, **2000**, *2*, 399–429.
- ⁵ G. C. R. Ellis-Davis, *Nat. Methods*, **2007**, *4*, 619–628.
- ⁶ X. Huang, M. A. El-Sayed, *J. Adv. Res.*, **2010**, *1*, 13-28.
- ⁷ Y. Xu, A. Karmakar, W. E. Heberlein, T. Mustafa, A. R. Biris, A. S. Biris, *Adv. Healthcare Mater.*, **2012**, Doi: 10.1002/adhm.201200079
- ⁸ J. Shan, S. J. Budijono, G. Hu, N. Yao, Y. Kang, Y. Ju, R. K. Prud'homme, *Adv. Funct. Mater.*, **2011**, *21*, 2488-2495.
- ⁹ C.-J. Carling, J.-C. Boyer, N. R. Branda, *J. Am. Chem. Soc.* **2009**, *131*, 10838–10839–10839.
- ¹⁰ C.-J. Carling, F. Nourmohammadian, J.-C. Boyer, N. R. Branda, *Angew. Chem. Int. Ed.* **2010**, *49*, 3782–3785
- ¹¹ J.-C. Boyer, C.-J. Carling, B. D. Gates, N. R. Branda, *J. Am. Chem. Soc.*, **2010**, *132*, 15766–15772.
- ¹² F. Auzel, *Chem. Rev.*, **2004**, *104*, 139-173.
- ¹³ M. Haase, H. Schäfer, *Angew. Chem. Int. Ed.*, **2011**, *50*, 5808-5829.
- ¹⁴ H. S Mader, P. Kele, S. M Saleh, O. S Wolfbeis, *Curr. Opin. Chem. Biol.*, **2010**, *14*, 582-596.
- ¹⁵ M. Wang, G. Abbineni, A. Clevenger, C. Mao, S. Xu, *Nanomedicine*, **2011**, *6*, 710-729.
- ¹⁶ F. Wang, D. Banerjee, Y. Liu, X. Chen, X. Liu, *Analyst*, **2010**, *135*, 1839-1854.
- ¹⁷ L. C. Ong, M. K. Gnanasammandhan, S. Nagarajan, Y. Zhang, *Luminescence*, **2010**, *25*, 290–293.
- ¹⁸ S. Heer, K. Kömpe, H.-U. Güdel, M. Haase, *Adv. Mater.*, **2004**, *16*, 2102-2105.
- ¹⁹ B. Chance, M. Cope, E. Gratton, N. Ramanujam, B. Tromberg, *Rev. Sci. Instrum.*, 1998, *69*, 3457- 3481.
- ²⁰ S. Stolik, J. A. Delgado, A. Pérez, L. Anasagasti, *J. Photochem. Photobiol. B.* **2000**, *57*, 90-93.
- ²¹ R. G. Aswathy, Y. Yoshida, T. Maekawa, and D. S. Kumar, *Anal. Bioanal. Chem.*, **2010**, *397*, 1417-1435.
- ²² R. Weissleder, *Nat. Biotechnol.* 2001, *19*, 316-317.
- ²³ Q. Zhan, J. Qian, H. Liang, G. Somesfalean, D. Wang, S. He, Z. Zhang and S. Andersson-Engels, *ACS Nano*, **2011**, *5*, 3744-3757.

- ²⁴ S. Wu, G. Han, D. J. Milliron, S. Aloni, V. Altoe, D. V. Talapin, B. E. Cohen, P. J. Schuck, *Proc. Natl. Acad. Sci. USA*, **2009**, *106*, 10917-10921
- ²⁵ S. H. Nam, Y. M. Bae, Y. I. Park, J. H. Kim, H. M. Kim, J. S. Choi, K. T. Lee, T. Hyeon and Y. D. Suh, *Angew. Chem. Int. Ed.*, **2011**, *50*, 6093–6097.
- ²⁶ M. K. G. Jayakumara, N. M. Idrisa, and Y. Zhang, *Proc. Natl. Acad. Sci. USA*, **2012**, doi: 10.1073/pnas.1114551109
- ²⁷ J. Pichaandi, J.-C. Boyer, K. R. Delaney, and F. C. J. M. van Veggel, *J. Phys. Chem. C*, **2011**, *115*, 19054-19064.
- ²⁸ J.-C Boyer, C.-J. Carling, S. Y. Chua, D. Wilson, B. Johnsen, D. Baillie and N. R. Branda, *Chem. Eur. J.* **2012**, *18*, 3122–3126.
- ²⁹ C.-J. Carling, J.-C. Boyer and N. R. Branda, *Org. biomolec. Chem.*, **2012**, *10*, 6159-6168.
- ³⁰ (a) *Molecular Switches*; B. L. Feringa, Ed.; Wiley-VCH: Weinheim, Germany, **2001**. (b) *Molecular Switches, Second Edition*; B. L. Feringa, Ed.; Wiley-VCH: Weinheim, Germany, **2011**.
- ³¹ *Photochromic and Thermochromic Compounds*; J. C. Crano, R. J. Guglielmetti, Eds.; Plenum: New York, **1999**; Vol.1
- ³² H. Bouas-Laurent and H. Dürr, *Pure Appl. Chem.*, **2001**, *73*, 639–665.
- ³³ M. Irie, T. Lifka, S. Kobatake, N. Kato, *J. Am. Chem. Soc.*, **2000**, *122*, 4871-4876.
- ³⁴ I. K. Lednev, T.-Q. Ye, R. E. Hester, J. N. Moore, *J. Phys. Chem.*, **1996**, *100*, 13338-13341.
- ³⁵ L. Babes, A. A. Heikal, A. H. Zewail, *J. Phys. Chem.*, **1992**, *96*, 4127-4130
- ³⁶ K. B. Jørgensen, *Molecules*, **2010**, *15*, 4334-4358.
- ³⁷ M. Takeshita, M. Ogawa, K. Miyata, T. Yamato, *J. Phys. Org. Chem.*, **2003**, *16*, 148–151.
- ³⁸ S. Nakamura, M. Irie, *J. Org. Chem.* **1988**, *53*, 6138-6139.
- ³⁹ C. E. Ramey, V. Boekelheide *J. Am. Chem. Soc.*, **1970**, *92*, 3681-3584.
- ⁴⁰ M. Irie, In *Molecular Switches*; B. L. Feringa, Ed.; Wiley-VCH: Weinheim, Germany, 2001; p 37.
- ⁴¹ M. Irie, In *Photochromic and Thermochromic Compounds*; J. C. Crano, R. J. Guglielmetti, Eds.; Plenum: New York, 1999; Vol.1, p 207.
- ⁴² (a) H. Tian, S. J. Yang, *Chem. Soc. Rev.* **2004**, *33*, 85. (b) H. Tian, S. Wang, *Chem. Commun.* **2007**, 781.
- ⁴³ M. Irie, *Chem. Rev.*, **2000**, *100*, 1685-1716.
- ⁴⁴ R. B. Woodward and R. Hoffmann, *J. Am. Chem. Soc.*, **1965**, *87*, 395-397.
- ⁴⁵ H. Miyasaka, T. Nobuto, A. Itaya, N. Tamai, M. Irie, *Chem. Phys. Lett.*, **1997**, *269*, 281-285.
- ⁴⁶ N. Tamai and H. Miyasaka, *Chem. Rev.*, **2000**, *100*, 1875–1890.
- ⁴⁷ K. Morimitsu, K. Shibata, S. Kobatake, and M. Irie, *J. Org. Chem.*, **2002**, *67*, 4574-4578.
- ⁴⁸ K. Higashiguchi, K. Matsuda, S. Kobatake, T. Yamada, T. Kawai, M. Irie, *Bull. Chem. Soc. Jpn.*, **2000**, *73*, 2389-2394.

- ⁴⁹ K. Mori, Y. Ishibashi, H. Matsuda, S. Ito, Y. Nagasawa, H. Nakagawa, K. Uchida, S. Yokojima, S. Nakamura, M. Irie, and H. Miyasaka, *J. Am. Chem. Soc.*, **2011**, *133*, 2621–2625
- ⁵⁰ M. Albota, D. Beljonne, J.-L. Bredas, J. E. Ehrlich, J.-Y. Fu, A. A. Heikal, S. E. Hess, T. Kogej, M. D. Levin, S. R. Marder, D. McCord-Maughon, J. W. Perry, H. Röckel, M. Rumi, G. Subramaniam, W. W. Webb, X.-L. Wu, C. Xu, *SCIENCE*, **1998**, *281*, 1653-1656
- ⁵¹ J.-P. Malval, I. Gosse, J.-P. Morand, and R. Lapouyade, *J. Am. Chem. Soc.*, **2002**, *124*, 904-905.
- ⁵² V. Aubert, V. Guerschais, E. Ishow, K. Hoang-Thi, I. Ledoux, K. Nakatani, and H. Le Bozec, *Angew. Chem. Int. Ed.*, **2008**, *47*, 577-580
- ⁵³ M. Irie, T. Fukaminato, T. Sasaki, N. Tamai, T. Kawai, *Nature*, **2002**, *420*, 759-760.
- ⁵⁴ D. Sud, T. B. Norsten, N. R. Branda, *Angew. Chem. Int. Ed.*, **2005**, *44*, 2019-2021.
- ⁵⁵ D. Vomasta, C. Högner, N. R. Branda, B. König, *Angew. Chem. Int. Ed.*, **2008**, *47*, 7644-7647.
- ⁵⁶ V. Lemieux and N. R. Branda, *Org. Lett.*, **2005**, *7*, 2969–2972.
- ⁵⁷ V. Lemieux, S. Gauthier, N. R. Branda, *Angew. Chem. Int. Ed.*, **2006**, *45*, 6820.
- ⁵⁸ Z. Erno, A. M. Asadirad, V. Lemieux and N. R. Branda, *Org. Biomol. Chem.*, **2012**, *10*, 2787–2792.
- ⁵⁹ D. Sud, T. J. Wigglesworth, N. R. Branda, *Angew. Chem. Int. Ed.*, **2007**, *46*, 8017.
- ⁶⁰ V. Lemieux, M. D. Spantulescu, K. K. Baldrige, N. R. Branda, *Angew. Chem. Int. Ed.* **2008**, *120*, 5112–5115.
- ⁶¹ V. W.-W. Yam, J. K.-W. Lee, C.-C. Ko, and N. Zhu, *J. Am. Chem. Soc.*, **2009**, *131*, 912–913
- ⁶² G. Duan, W.-T. Wong and V. W.-W. Yam, *New J. Chem.*, **2011**, *35*, 2267–2278.
- ⁶³ M. Irie, *Chem. Rev.* **2000**, *100*, 1685.
- ⁶⁴ (a) M. Goeldner, R. Givens, *Dynamic Studies in Biology: Phototriggers, Photoswitches and Caged Biomolecules*; Wiley-VCH: Weinheim, Germany, **2005**. (b) S. Stolika, J. A. Delgado, A. Pérez, L. Anasagasti, *J. Photochem. Photobiol. B.* **2000**, *57*, 90.
- ⁶⁵ I. A. Mikhailov, K. D. Belfield, A. E. Masunov, *J. Phys. Chem. A.* **2009**, *113*, 7080.
- ⁶⁶ (a) J. Shan, J. Chen, J. Meng, J. Collins, W. Soboyejo, J. S. Friedberg, Y. J. Ju, *Appl. Phys.* **2008**, *104*, 094308/1. (b) M. Nyk, R. Kumar, T. Y. Ohulchanskyy, E. J. Bergey, P. N. Prasad, *Nano Lett.* **2008**, *8*, 3834. (c) H.-S. Qian, Y. Zhang, *Langmuir* **2008**, *24*, 12123. (d) S. Heer, K. Kompe, H. U. Güdel, M. Haase, *Adv. Mater.* **2004**, *16*, 2102.
- ⁶⁷ (a) M. Kumar, Y. Guo, P. Zhang, *Biosens. Bioelectron.* **2009**, *24*, 1522. (b) M. Yu, F. Li, Z. Chen, H. Hu, C. Zhan, H. Yang, C. Huang, *Anal. Chem.* **2009**, *81*,

930. (c) B. Ungun, R. K. Prud'homme, S. J. Budijono, J. Shan, S. F. Lim, Y. Ju, R. Austin, *Opt. Express* **2009**, *17*, 80.

⁶⁸ Z. Zhou, H. Hu, H. Yang, T. Yi, K. Huang, M. Yu, F. Li, C. Huang, *Chem. Commun.* **2008**, 4786.

⁶⁹ See experimental section 3.8 for details.

⁷⁰ The transitions responsible for the luminescence are given in Figure 3.5.

⁷¹ The inset of Figure 3.5b in the experimental section 3.8.6 shows a digital photograph of the total upconversion luminescence of a dispersion of NaYF₄:ErYb when stimulated with a 980 nm diode laser.

⁷² See Figure 3.6 in the experimental section 3.8.7. Other solid-state versions (bulk gels and solvent-free films) of the composite material were prepared and exhibit similar photochemistry as shown in Figure 3.8.

⁷³ J. J. D. de Jong, L. N. Lucas, R. Hania, A. Pugzlys, B. L. Feringa, K. Duppen, J. H. van Esch, *Eur. J. Org. Chem.* **2003**, 1887.

⁷⁴ C. J. Ireland, K. Jones, J. S. Pizey, S. Johnson, *Synth. Commun.*, **1976**, *6*, 185.

⁷⁵ (a) H.-S. Qian, Y. Zhang, *Langmuir* **2008**, *24*, 12123–12125. (b) Z. Li, Y. Zhang, *Nanotechnology* **2008**, *19*, 345606/1.

⁷⁶ B. L. Feringa (Ed.), *Molecular Switches*, Wiley-VCH, Weinheim, 2001.

⁷⁷ V. Balzani, A. Credi, M. Venturi, *Molecular Devices and Machines – A Journey into the Nano World*, Wiley-VCH, Weinheim, 2003.

⁷⁸ J. C. Crano, R. J. Gugliemetti (Eds.), *Organic Photochromic and Thermochromic Compounds*, Plenum Press, New York 1999.

⁷⁹ L. Ubaghs, D. Sud, N. R. Branda In *Thiophene-Based Materials for Electronics and Photonics*; Perepichka, I. D., Perepichka D., Eds.; Wiley-VCH, Germany; 2009, Vol. 2, pp 783–812.

⁸⁰ The interconversion between the two structural isomers has also been demonstrated using electricity. See: (a) A. Peters, N. R. Branda, *J. Am. Chem. Soc.* **2003**, *125*, 3404–3405. (b) A. Peters, N. R. Branda, *Chem. Commun.* **2003**, 8, 954–955. (c) B. Gorodetsky, H. Samachetty, R. L. Donkers, M. S. Workentin, N. R. Branda, *Angew. Chem. Int. Ed.* **2004**, *43*, 2812–2815. (d) B. Gorodetsky, N. R. Branda, *Adv. Funct. Mater.* **2007**, *17*, 786–796. (e) Y. Moriyama K. Matsuda, N. Tanifuji, S. Irie, M. Irie, *Org. Lett.* **2005**, *7*, 3315–3318. (f) W. R. Browne, J. J. D. de Jong, T. Kudernac, M. Walko, L. N. Lucas, K. Uchida, J. H. van Esch, B. L. Feringa, *Chem. Eur. J.* **2005**, *11*, 6414–6429. (g) W. R. Browne, J. J. D. de Jong, T. Kudernac, M. Walko, L. N. Lucas, K. Uchida, J. H. van Esch, B. L. Feringa, *Chem. Eur. J.* **2005**, *11*, 6430–6441.

⁸¹ M. Irie, K. Sakemura, M. Okinaka, K. Uchida, *J. Org. Chem.* **1995**, *60*, 8305–8309.

⁸² Y. Nakayama, K. Hayashi, M. Irie, *Bull. Chem. Soc. Jpn.* **1991**, *64*, 789–795.

⁸³ T. Nakagawa, Y. Hasegawa, T. Kawai, *J. Phys. Chem. A* **2008**, *112*, 5096–5103.

⁸⁴ A. Fernandez-Acebes, J.-M. Lehn, *Chem. Eur. J.* **1999**, *5*, 3285–292.

⁸⁵ E. Murguly, T. Norsten, N. R. Branda, *Angew. Chem. Intl. Ed.* **2001**, *40*, 1752–1755.

- ⁸⁶ H. Zhao, U. Al-Atar, T. Pace, C. Bohne, N. R. Branda, *J. Photochem. Photobiol.* **2008**, *200*, 74–82.
- ⁸⁷ T. Yamaguchi, K. Uchida, M. Irie, *J. Am. Chem. Soc.* **1997**, *119*, 6066–6071.
- ⁸⁸ T. Kodani, K. Matsuda, T. Yamada, S. Kobatake M. Irie, *J. Am. Chem. Soc.* **2000**, *122*, 9631–9637.
- ⁸⁹ S. Yamamoto, K. Matsuda, M. Irie, *Org. Lett.* **2003**, *5*, 1769–1772.
- ⁹⁰ K. Matsuda, S. Yamamoto M. Irie, *Tetrahedron Lett.* **2001**, *42*, 7291–7293.
- ⁹¹ T. Yamaguchi, K. Nomiyama, M. Isayama, M. Irie, *Adv. Mater.* **2004**, *16*, 643–645.
- ⁹² K. Matsuda, M. Irie, *Polyhedron* **2005**, *24*, 2477–2483.
- ⁹³ N. Tanifuji, M. Irie, K. Matsuda, *J. Am. Chem. Soc.* **2005**, *127*, 13344–13353.
- ⁹⁴ L. Sun, H. Tian, *Tetrahedron Lett.* **2006**, *47*, 9227–9231.
- ⁹⁵ D. Dulic, S. J. van der Molen, T. Kudernac, H. T. Jonkman, J. J. D. de Jong, T. N. Bowden, J. van Esch, B. L. Feringa, B. J. van Wees, *Phys. Rev. Lett.* **2003**, *91*, 207402.
- ⁹⁶ K. Matsuda, H. Yamaguchi, T. Sakano, M. Ikeda, N. Tanifuji, M. Irie, *J. Phys. Chem. C*, **2008**, *112*, 17005–17010.
- ⁹⁷ A. J. Kronemeijer, H. B. Akkerman, T. Kudernac, B. J. van Wees, B. L. Feringa, P. W. M. Blom, B. de Boer, *Adv. Mater.* **2008**, *20*, 1467–1473.
- ⁹⁸ A. C. Whalley, M. L. Steigerwald, X. Guo, C. Nuckolls, *J. Am. Chem. Soc.* **2007**, *129*, 12590–12591.
- ⁹⁹ A. J. Myles, N. R. Branda, *Adv. Funct. Mater.* **2002**, *12*, 167–173.
- ¹⁰⁰ J. Andreasson, S. D. Straight, T. A. Moore, A. L. Moore, D. Gust, *J. Am. Chem. Soc.* **2008**, *130*, 11122–11128.
- ¹⁰¹ P. Belser, L. De Cola, F. Hartl, V. Adamo, B. Bozic, Y. Chriqui, V. M. Iyer, R. T. F. Jukes, J. Kuhni, M. Querol, S. Roma, N. Salluce, *Adv. Funct. Mater.* **2006**, *16*, 195–208.
- ¹⁰² H. D. Samachetty, V. Lemieux, N. R. Branda, *Tetrahedron* **2008**, *64*, 8392–8300.
- ¹⁰³ H. D. Samachetty, N. R. Branda, *Pure Appl. Chem.* **2006**, *78*, 2351–2359.
- ¹⁰⁴ W. R. Browne, T. Kudernac, N. Katsonis, J. Areephong, B. L. Feringa, *J. Phys. Chem. C* **2008**, *112*, 1183–1190.
- ¹⁰⁵ U. Al-Atar, R. Fernandes, B. Johnsen, D. Baillie, N. R. Branda, *J. Am. Chem. Soc.* **2009**, *131*, 15966–15967.
- ¹⁰⁶ S. Heer, K. Kompe, H. U. Güdel, M. Haase, *Adv. Mater.* **2004**, *16*, 2102–2105.
- ¹⁰⁷ H. X. Mai, Y. W. Zhang, R. Si, Z. G. Yan, L. D. Sun, L. P. You, C. H. Yan, *J. Am. Chem. Soc.* **2006**, *128*, 6426–6436.
- ¹⁰⁸ J.-C. Boyer, F. Vetrone, L. A. Cuccia, J. A. Capobianco, *J. Am. Chem. Soc.* **2006**, *128*, 7444–7445.
- ¹⁰⁹ J.-C. Boyer, L. A. Cuccia, J. A. Capobianco, *Nano. Lett.* **2007**, *7*, 847–852.
- ¹¹⁰ H. X. Mai, Y. W. Zhang, L. D. Sun, C. H. Yan, *J. Phys. Chem. C* **2007**, *111*, 13730–13739.
- ¹¹¹ Z. Q. Li, Y. Zhang, *Nanotechnology* **2008**, *19*, 345606.
- ¹¹² Z. Q. Li, Y. Zhang, S. Jiang, *Adv. Mater.* **2008**, *20*, 4765–4769.

- ¹¹³ R. Scheps, *Prog. Quantum Electron.* **1996**, *20*, 271–358.
- ¹¹⁴ K. W. Krämer, D. Biner, G. Frei, H. U. Güdel, M. P. Hehlen, S. R. Lüthi, *Chem. Mater.* **2004**, *16*, 1244–1251.
- ¹¹⁵ S. R. Adams, R. Y. Tsien, *Annu. Rev. Physiol.* **1993**, *55*, 755–784.
- ¹¹⁶ S. W. Wu, G. Han, D. J. Milliron, S. Aloni, V. Altoe, D. V. Talapin, B. E. Cohen, P. J. Schuck, *PNAS*, **2009**, *106*, 10917–10921.
- ¹¹⁷ J.-C. Boyer, M. P. Manseau, J. I. Murray, F. C. J. M. van Veggel, *Langmuir* **2010**, *26*, 1157–1164.
- ¹¹⁸ A. Shalav, B. S. Richards, T. Trupke, K. W. Kramer, H. U. Gudel, *Appl. Phys. Lett.* **2005**, *86*, 013505.
- ¹¹⁹ W. J. Kim, M. Nyk, P. N. Prasad, *Nanotechnology* **2009**, *20*, 185301.
- ¹²⁰ Z. Zhou, H. Yang, Y. Tao, K. Huang, M. Yu, F. Li, C. Huang, *Chem. Comm.* **2008**, *39*, 4786–4788.
- ¹²¹ C. Zhang, H. P. Zhou, L.-Y Liao, W. Feng, W. Sun, Z.-X Li, C.-H Xu, C.-J Fang, L.-D. Sun, Y. W. Zhang, C.-H. Yan, *Adv. Mater.* **2009**, *22*, 633–637.
- ¹²² J.-C. Boyer, N. J. J. Johnson, F. C. J. M. van Veggel, *Chem. Mater.* **2009**, *21*, 2010–2012.
- ¹²³ (a) J. R. Lakowicz, *Principles of Fluorescence Spectroscopy*, Springer, New York, 2006; (b) D. B. Murphy, *Fundamentals of Light Microscopy and Electronic Imaging*, Wiley-Liss, New York, 2001.
- ¹²⁴ a) I. Yildiz, E. Deniz and F. M. Raymo, *Chem. Soc. Rev.* **2009**, *38*, 1859–1867; b) J. Cusido, E. Deniz, F. M. Raymo, *Eur. J. Org. Chem.* **2009**, 2031–2045; c) Y. Yan, M. E. Marriott, C. Petchprayoon, G. Marriott, *Biochem. J.* **2011**, *433*, 411–422; d) C. Petchprayoon, Y. Yan, S. Mao, G. Marriott, *Bioorg. Med. Chem.* **2011**, *19*, 1030–1040.
- ¹²⁵ (a) L. Cheng, K. Yang, M. Shao, S.-T. Lee, Z. Liu, *J. Phys. Chem. C* **2011**, *115*, 2686–2692; (b) L. Zhu, W. Wu, M.-Q. Zhu, J. J. Han, J. K. Hurst, A. D. Q. Li, *J. Am. Chem. Soc.* **2007**, *129*, 3524–3526; (c) M.-Q. Zhu, L. Zhu, J. J. Han, W. Wu, J. K. Hurst, A. D. Q. Li, *J. Am. Chem. Soc.* **2006**, *128*, 4303–4309; (d) I. Yildiz, S. Impellizzeri, E. Deniz, B. McCaughan, J. F. Callan, F. M. Raymo, *J. Am. Chem. Soc.* **2011**, *133*, 871–879.
- ¹²⁶ Coating nanoparticles with a biocompatible material reduces the toxicity but does not eliminate ‘blinking’. (a) M. Bruchez, Jr., M. Moronne, P. Gin, S. Weiss, A. P. Alivisatos, *Science* **1998**, *281*, 2013–2016. (b) W. C. W. Chan, S. Nie, *Science* **1998**, *281*, 2016–2018. (c) X. Michalet, F. F. Pinaud, L. A. Bentolila, J. M. Tsay, J. J. Li, G. Sundaresan, A. M. Wu, S. S. Gambhir, S. Weiss, *Science* **2005**, *307*, 538–544.
- ¹²⁷ (a) Z. Q. Li, Y. Zhang, S. Jiang, *Adv. Mater.* **2008**, *20*, 4765–4769; (b) F. Wang, Y. Han, C. S. Lim, Y. Lu, J. Wang, J. Xu, H. Chen, C. Zhang, M. Hong, X. Liu, *Nature* **2010**, *463*, 1061–1065; (c) X. Yea, J. E. Collins, Y. Kang, J. Chen, D. T. N. Chen, A. G. Yodh, C. B. Murray, *Proc. Natl. Acad. Sci. USA* **2010**, *107*, 22430–22435.
- ¹²⁸ (a) D. K. Chatterjee, Y. Zhang, *Nanomedicine* **2008**, *3*, 73–82; (b) H. S. Mader, P. S. Kele, S. M. Saleh, O. S. Wolfbeis, *Curr. Opin. Chem. Biol.* **2010**,

14, 582–596; (c) F. Wang, D. Banerjee, Y. Liu, X. Chen, X. Liu, *Analyst* **2010**, *135*, 1839–1854.

¹²⁹ (a) B. L. Feringa, *Molecular Switches*, WILEY-VCH, Weinheim, 2010; (b) H. Tian, S. Yang, *Chem. Soc. Rev.* **2004**, *33*, 85–97; (c) L. Ubaghs, D. Sud, N. R. Branda, in *Thiophene-Based Materials for Electronics and Photonics*, Vol. 2 (Eds: I. D. Perepichka, D. Perepichka) WILEY-VCH, Weinheim, 2009, pp 783–812.

¹³⁰ For examples of photoswitches that have been engineered to reversibly regulate emission from neighbouring inorganic and organic probes, see: (a) F. M. Raymo, M. Tomasulo, *Chem. Soc. Rev.* **2005**, *34*, 327–336; (b) Y.L. Feng, Y.L. Yan, S. Wang, W.H. Zhu, S.X. Qian, H. Tian, *J. Mater. Chem.* **2006**, *16*, 3685–3692; (c) H. Zhao, U. Al-Atar, T. C.S. Pace, C. Bohne, N. R. Branda, *J. Photochem. Photobiol. A–Chem.* **2008**, *200*, 74–82; (d) Z. Erno, I. Yildiz, B. Gorodetsky, F. M. Raymo, N. R. Branda, *Photochem. Photobiol. Sci.* **2010**, *9*, 249–253.

¹³¹ See Experimental Section 5.8 for details.

¹³² A. K. Tucker-Schwartz, R. L. Garrell, *Chem. Eur. J.* **2010**, *16*, 12718–12726.

¹³³ H. S. Mader, M. Link, D. E. Achatz, K. Uhlmann, X. Li, O. S. Wolfbeis, *Chem. Eur. J.* **2010**, *16*, 5416–5424.

¹³⁴ FTIR spectroscopy shows that not all the azide groups have reacted (Figure 5.8).

¹³⁵ The relative amounts of emission were measured at a single wavelength for each emission (green and red). The areas under the peak were not compared as the relative amount of quenching at each wavelength stays constant throughout the emission bands (see Figure 5.10 in the Experimental Section 5.8 for details).

¹³⁶ This amount of quenching corresponds to the maximum possible assuming a 83% photostationary state. If the open-isomer could be completely converted to its ring-closed counterpart, the emission would be quenched to only 16% of its original intensity.

¹³⁷ We attribute the low FRET efficiency to the relatively small number of molecular switches on the surface of the nanoparticles. The lifetimes for the red emission were not measured.

¹³⁸ L. N. Lucas, J. van Esch, R. M. Kellogg, B. L. Feringa, *Chem. Commun.* **1998**, 2313–2314

¹³⁹ Z. Li, Y. Zhang, *Nanotechnology* **2008**, *19*, 345606–345611.

¹⁴⁰ S. Brenner, *Genetics* **1974**, *77*, 71–94.

¹⁴¹ I. Yildiz, E. Deniz and F. M. Raymo, *Chem. Soc. Rev.*, **2009**, *38*, 1859–1867.

¹⁴² J. Cusido, E. Deniz and F. M. Raymo, *Eur. J. Org. Chem.*, **2009**, 2031–2045.

¹⁴³ M.-Q. Zhu, L. Zhu, J. J. Han, W. Wu, J. K. Hurst and A. D. Q. Li, *J. Am. Chem. Soc.*, **2006**, *128*, 4303–4309.

¹⁴⁴ L. Zhu, W. Wu, M.-Q. Zhu, J. J. Han, J. K. Hurst, A. D. Q. Li, *J. Am. Chem. Soc.*, **2007**, *129*, 3524–3526.

¹⁴⁵ J. Fölling, S. Polyakova, V. Belov, A. van Blaaderen, M. L. Bossi and S. W. Hell, *Small* **2008**, *4*, 134–142.

- ¹⁴⁶ Z. Hu, Q. Zhang, M. Xue, Q. Sheng and Y.-G. Liu, *Opt. Mater.* **2008**, *30*, 851–856.
- ¹⁴⁷ M. Tomasulo, E. Deniz, R. J. Alvarado and F. M. Raymo, *J. Phys. Chem. C.* **2008**, *112*, 8038–8045.
- ¹⁴⁸ Z. Zhou, H. Hu, H. Yang, T. Yi, K. Huang, M. Yu, F. Li, and C. Huan, *Chem. Commun.*, **2008**, 4786–4788.
- ¹⁴⁹ C. Zhang, H.-P. Zhou, L.-Y. Liao, W. Feng, W. Sun, Z.-X. Li, C.-H. Xu, C.-J. Fang, L.-D. Sun, Y.-W. Zhang, C.-H. Yan, *Adv. Mater.*, **2010**, *22*, 633–637.
- ¹⁵⁰ J. Chen, P. Zhang, G. Fang, P. Yi, X. Yu, X. Li, F. Zeng and S. Wu, *J. Phys. Chem. B*, **2011**, *115*, 3354–3362.
- ¹⁵¹ I. Yildiz, S. Impellizzeri, E. Deniz, B. McCaughan, J. F. Callan and F. M. Raymo, *J. Am. Chem. Soc.*, **2011**, *133*, 871–879.
- ¹⁵² L. Cheng, K. Yang, M. Shao, S.-T. Lee, Z. Liu, *J. Phys. Chem. C*, **2011**, *115*, 2686–2692.
- ¹⁵³ *Organic Photochromic and Thermochromic Compounds*, ed. J. C. Crano and R. J. Gugliemetti, Plenum, New York, **1999**.
- ¹⁵⁴ S. H. Nam, Y. M. Bae, Y. I. Park, J. H. Kim, H. M. Kim, J. S. Choi, K. T. Lee, T. Hyeon and Y. D. Suh, *Angew. Chem. Int. Ed.*, **2011**, *50*, 6093–6097.
- ¹⁵⁵ S. Wu, G. Han, D. J. Milliron, S. Aloni, V. Altoe, D. V. Talapin, B. E. Cohen and P. J. Schuck, *PNAS*, **2009**, *106*, 10917–10921.
- ¹⁵⁶ L. Cheng, K. Yang, M. Shao, X. Lu and Z. Liu, *Nanomedicine*, **2011**, *6*, 1327–1340.
- ¹⁵⁷ D. K. Chatterjee, Y. Zhang, *Nanomedicine* **2008**, *3*, 73–82.
- ¹⁵⁸ H. S. Mader, P. Kele, S. M. Saleh, O. S. Wolfbeis, *Curr. Opin. Chem. Biol.* **2010**, *14*, 582–596.
- ¹⁵⁹ J. Finden, T. Kunz, N. R. Branda and M. O. Wolf, *Adv. Mater.* **2008**, *20*, 1998–2002.
- ¹⁶⁰ A. J. Myles, T. J. Wigglesworth and N. R. Branda, *Adv. Mater.* **2003**, *15*, 745–748.
- ¹⁶¹ J. J. D. de Jong, L. N. Lucas, R. Hania, A. Pugzlys, R. M. Kellogg, B. L. Feringa, K. Duppen and J. H. van Esch, *Eur. J. Org. Chem.* **2003**, 1887–1893.
- ¹⁶² See Experimental Section 6.8 for details.
- ¹⁶³ Although most of the photochromic studies on the free ligands were carried out using CH₃CN solutions, we did not observe any changes in the spectra when they were measured in THF (for **1a-NP**) and CH₂Cl₂ (for **1b-NP**). See Figure 6.8 in the Experimental Section 6.8 for details.
- ¹⁶⁴ Photoswitch **3b^c** and **1b^c-NP** degrades during UV light irradiation and the original spectra is not fully regenerated upon > 434 nm irradiation, see Figure 6.14 for details.
- ¹⁶⁵ The concentrations of the photoswitches were estimated by comparing the absorbances for solutions of the hybrid systems (**1a-NP** and **1b-NP**) to the free ligands in the same solvent. This assumes that the photostationary states are the same. See the Experimental Section 6.8 for details.
- ¹⁶⁶ When a > 434 nm filter is placed between the cuvette and the detector, the 670–750 nm emissions are not present in the spectra indicating that these

emission are due to the second order diffraction off the emission monochromator grating of the UV emissions from Tm³⁺.

¹⁶⁷ W. Wu, L. Yao, T. Yang, R. Yin, F. Li and Y. Yu, *J. Am. Chem. Soc.* **2011**, *133*, 15810–15813.

¹⁶⁸ Y. Yang, Q. Shao, R. Deng, C. Wang, X. Teng, K. Cheng, Z. Cheng, L. Huang, Z. Liu, X. Liu and B. Xing, *Angew. Chem. Int. Ed.* **2012**, *51*, 3125–3129.

¹⁶⁹ For additional information, see Figure 7.16 in the Experimental Section 7.8.

¹⁷⁰ All the spectra for these studies can be found in the Experimental Section 7.8 Figure 7.21–7.24.

¹⁷¹ B. Yan, J.-C. Boyer, N. R. Branda and Y. Zhao, *J. Am. Chem. Soc.* **2011**, *133*, 19714–19717.

¹⁷² C.-J. Carling, J.-C. Boyer and N. R. Branda, *unpublished results*.

¹⁷³ M. Goeldner, R. Givens, *Dynamic Studies in Biology: Phototriggers, Photoswitches and Caged Biomolecules*; Wiley-VCH: Weinheim, Germany, **2005**.

¹⁷⁴ G. Mayer, A. Heckel, *Angew. Chem. Int. Ed.*, **2006**, *45*, 4900–4921.

¹⁷⁵ A. P. Pelliccioli and J. Wirz, *Photochem. Photobiol. Sci.*, **2002**, *1*, 441–458

¹⁷⁶ P. Rai, S. Mallidi, X. Zheng, R. Rahmzadeh, Y. Mir, S. Elrington, A. Khurshid, T. Hasan, *Adv. Drug Deliv. Rev.*, **2010**, *62*, 1094–1124.

¹⁷⁷ N. Fomina, J. Sankaranarayanan, A. Almutairi, *Adv. Drug Deliv. Rev.*, **2012**, doi:10.1016/j.addr.2012.02.006.

¹⁷⁸ Y. Zhao, *Macromolecules*, **2012**, *45*, 3647–3657.

¹⁷⁹ L.-J. Chen and L. T. Burka, *Tetrahedron Lett.*, **1998**, *39*, 5351–5354.

¹⁸⁰ A. Barth, J. E. T. Corrie, M. J. Gradwell, Y. Maeda, W. Mäntele, T. Meier and D. R. Trentham, *J. Am. Chem. Soc.* **1997**, *119*, 4149–4159.

¹⁸¹ L. Zhang, R. Buchet, and G. Azzar, *Biophys. J.*, **2004**, *86*, 3873–3881.

¹⁸² L. Donato, A. Mouro, C. M. Davenport, C. Herbivo, D. Warther, J. Léonard, F. Bolze, J.-F. Nicoud, R. H. Kramer, M. Goeldner, and A. Specht, *Angew. Chem. Int. Ed.*, **2012**, *51*, 1840–1843.

¹⁸³ A. Specht, F. Bolze, L. Donato, C. Herbivo, S. Charon, D. Warther, S. Gug, J.-F. Nicoud and M. Goeldner, *Photochem. Photobiol. Sci.*, **2012**, *11*, 578–586.

¹⁸⁴ R. S. Givens, M. Rubina, J. Wirz, *Photochem. Photobiol. Sci.*, **2012**, *11*, 472–488.

¹⁸⁵ T. Furuta, S. S. H. Wang, J. L. Dantzker, T. M. Dore, W. J. Bybee, E. M. Callaway, W. Denk, R. Y. Tsien, *Proc. Natl. Acad. Sci. USA*, **1999**, *96*, 1193–1200.

¹⁸⁶ N. Fomina, C. L. McFearin, M. Sermsakdi, J. M. Morachis, A. Almutairi, *Macromolecules*, **2011**, *44*, 8590–8597.

¹⁸⁷ J. C. Sheehan, R. M. Wilson, A. W. Oxford, *J. Am. Chem. Soc.*, **1971**, *93*, 7222–7228.

¹⁸⁸ H. Boudebous, B. Kosmrlj, B. Sket, J. Wirz, *J. Phys. Chem. A*, **2007**, *111*, 2811–2813.

¹⁸⁹ C. Ma, W. M. Kwok, H.-Y. An, X. Guan, M. Y. Fu, P. H. Toy, D. L. Phillips, *Chem. Eur. J.*, **2010**, *16*, 5102–5118.

- ¹⁹⁰ S. Ueda, M. Fujita, H. Tamamura, N. Fujii, and A. Otaka, *ChemBioChem*, **2005**, *6*, 1983-1986.
- ¹⁹¹ A. Taniguchi, M. Skwarczynski, Y. Sohma, T. Okada, K. Ikeda, H. Prakash, H. Mukai, Y. Hayashi, T. Kimura, S. Hirota, K. Matsuzaki and Y. Kiso, *ChemBioChem*, **2008**, *9*, 3055-3065.
- ¹⁹² P. M. Koenigs, B. C. Faust and N. A. Porter *J. Am. Chem. Soc.*, **1993**, *115*, 9371-9379.
- ¹⁹³ N. Gagey, P. Neveu, C. Benbrahim, B. Goetz, I. Aujard, J.-B. Baudin, and L. Jullien, *J. Am. Chem. Soc.*, **2007**, *129*, 9986-9998.
- ¹⁹⁴ T. Wu, H. Tang, C. Bohne, N. R. Branda, *Angew. Chem. Int. Ed.*, **2012**, *51*, 2741-2744.
- ¹⁹⁵ E. M. R. Verde, L. Zayat, R. Etchenique, R. Yuste, *Front. Neural. Circuits.*, **2008**, *2*, 1-8
- ¹⁹⁶ N. L. Fry and P. K. Mascharak, *Acc. Chem. Res.*, **2011**, *44*, 289-298.
- ¹⁹⁷ C.-J. Carling, C. C. Warford, N. R. Branda, *unpublished results*. The photocage was first synthesized and its unprecedented photochemistry elucidated by C.-J. Carling. Results of this peculiar and novel photoreaction will be described in full in C. Chad Warford's *Ph.D. Thesis* if publication is not achievable due to the uncharacterizable nature of the ionic photoproduct.
- ¹⁹⁸ C. A. Blencowe, A. T. Russell, F. Greco, W. Hayes, and D. W. Thornthwaite, *Polym. Chem.*, **2011**, *2*, 773-790.
- ¹⁹⁹ J. F. Cameron, C. G. Willson, J. M. J. Fréchet, *J. Chem. Soc., Perkin Trans. 1*, **1997**, 2429-2442.
- ²⁰⁰ J. F. Cameron, C. G. Willson, J. M. J. Fréchet, *J. Am. Chem. Soc.*, **1996**, *118*, 12925-12937.
- ²⁰¹ R. S. Rock, S. I. Chan, *J. Am. Chem. Soc.*, **1998**, *120*, 10766-10767.
- ²⁰² J. C. Sheehan, R. M. Wilson, *J. Am. Chem. Soc.*, **1964**, *86*, 5277-5281.
- ²⁰³ Y. Shi, J. E. T. Corrie, P. Wan, *J. Org. Chem.*, **1997**, *62*, 8278-8279.
- ²⁰⁴ M. C. Pirrung, T. Ye, Z. Zhuo, J. D. Simon, *Photochem. Photobiol.*, **2006**, *82*, 1258-1264.
- ²⁰⁵ X. Chen, C. Ma, D. L. Phillips, W.-H. Fang, *Org. Lett.*, **2010**, *12*, 5108-5111.
- ²⁰⁶ C. Ma, Y. Du, W. M. Kwok, D. L. Phillips, *Chem. Eur. J.*, **2007**, *13*, 2290-2305.
- ²⁰⁷ S. R. Adams, R. Y. Tsien, *Annu. Rev. Physiol.* **1993**, *55*, 755-784.
- ²⁰⁸ T. Furuta, S. S.-H. Wang, J. L. Dantzker, T. M. Dore, W. J. Bybee, E. M. Callaway, W. Denk, R. Y. Tsien, *Proc. Natl. Acad. Sci. USA*, **1999**, *96*, 1193-1200.
- ²⁰⁹ K. Szacitowski, W. Macyk, A. Drzewiecka-Matuszek, M. Brindell, G. Stochel, *Chem. Rev.* **2005**, *105*, 2647-2694.
- ²¹⁰ W. Denk, *Proc. Natl. Acad. Sci. USA* **1994**, *91*, 6629.
- ²¹¹ M. Goeldner, R. Givens, *Dynamic Studies in Biology*, Wiley-VCH Verlag GmbH & Co. KGaA, Weinheim, **2005**, pp. 437 and 441.
- ²¹² C. S. Rajesh, R. S. Givens, J. Wirz, *J. Am. Chem. Soc.* **2000**, *122*, 611-618.
- ²¹³ A. Routledge, C. Abell, S. Balasubramanian, *Tetrahedron Lett.* **1997**, *38*, 1227-1230.

-
- ²¹⁴ R. S. Rock, S. I. Chan, *J. Org. Chem.* **1996**, *61*, 1526–1529.
- ²¹⁵ J. C. Sheehan, R. M. Wilson, A. W. Oxford, *J. Am. Chem. Soc.* **1971**, *93*, 7222–7228.
- ²¹⁶ In aqueous environments, the hydrolyzed 3',5'-dialkoxybenzoin analogue of **1** is also produced.^[201]
- ²¹⁷ Y. Y. Zhang, L. W. Yang, C. F. Xu, J. X. Zhong, C. Q. Sun, *Appl. Phys. B* **2010**, *98*, 243–247.
- ²¹⁸ V. Mahalingam, F. Vetrone, R. Naccache, A. Speghini, J. A. Capobianco, *Adv. Mater.* **2009**, *21*, 4025–4028.
- ²¹⁹ G. Wang, W. Qin, L. Wang, G. Wei, P. Zhu, R. Kim, *Opt. Express* **2008**, *16*, 11907–11914.
- ²²⁰ B. Ungun, R. K. Prud'homme, S. J. Budijono, J. Shan, S. F. Lim, Y. Ju, R. Austin, *Opt. Express*, **2009**, *17*, 80–86.
- ²²¹ D. K. Chatterjee, Z. Yong, *Nanomedicine* **2008**, *3*, 73–82.
- ²²² P. Zhang, W. Steelant, M. Kumar, M. Scholfield, *J. Am. Chem. Soc.* **2007**, *129*, 4526–4527.
- ²²³ S. Heer, K. Kömpe, H.-U. Gudel, M. Haase, *Adv. Mater.* **2004**, *16*, 2102–2105.
- ²²⁴ V. P. Torchilin, V. S. Trubetsky, *Adv. Drug Delivery Rev.* **1995**, *16*, 141–155.
- ²²⁵ D. Bechet, P. Couleaud, C. Frochot, M.-L. Viriot, F. Guillemin, M. Barberi-Heyob, *Trends Biotechnol.* **2008**, *26*, 612–621.
- ²²⁶ X. R. Songa, Z. Caib, Y. Zheng, G. Hea, F. Y. Cuia, Dao Qiong Gong, S. X. Houc, S. J. Xiong, X. J. Lei, Y. QuanWei, *Eur. J. Pharm. Sci.* **2009**, *37*, 300–305.
- ²²⁷ C. E. Soma, C. Dubernet, D. Bentolila, S. Benita, P. Couvreur, *Biomaterials* **2000**, *21*, 1–7.
- ²²⁸ J. R. R. Majjigapu, A. N. Kurchan, R. Kottani, T. P. Gustafson, A. G. Kutateladze, *J. Am. Chem. Soc.* **2005**, *127*, 12458–12459.
- ²²⁹ R. Weinstain, A. Segal, R. Soult-Fainaro, D. Shabot, *Chem. Commun.* **2010**, *46*, 553–555.
- ²³⁰ J. Shan, J. Chen, J. meng, J. Collins, W. Soboyejo, J. S. Friedberg, Y. Ju, *J. Appl. Phys.* **2008**, *104*, 094308–1–7.
- ²³¹ R. Kumar, M. Nyk, T. Y. Ohulchanskyy, C. A. Flask, P. N. Prasad, *Adv. Funct. Mater.* **2009**, *19*, 853–859.
- ²³² H. Kobayashi, N. Kosaka, M. Ogawa, N. Y. Morgan, P. D. Smith, C. B. Murray, X. Ye, J. Collins, G. A. Kumar, H. Bell, P. L. Choyke, *J. Mater. Chem.* **2009**, *19*, 6481–6484.
- ²³³ S. Wu, G. Han, D. J. Milliron, S. Aloni, V. Altoe, D. V. Talapin, B. E. Cohen, P. J. Schuck, *Proc. Natl. Acad. Sci. U.S.A.* **2009**, *106*, 10917–10921.
- ²³⁴ K. Kuningas, T. Rantanen, U. Karhunen, T. Lövgren, T. Soukka, *Anal. Chem.* **2005**, *77*, 2826–2834.
- ²³⁵ F. v. d. Rijke, H. Zijlmans, S. Li, T. Vail, A. K. Raap, S. Niedbala, H. J. Tanke, *Nature Biotechnol.* **2001**, *19*, 273–276.
- ²³⁶ See the Experimental Section 8.8 for details.
- ²³⁷ The relatively long reaction time is not a reflection of the efficiency of the photochemistry, but to the fact that the ¹H NMR measurements require high

concentrations (10^{-3} M) of the chromophore. At more realistic concentrations for practical applications (10^{-5} M), the release takes 5 times less time.

²³⁸ All solution-state photoreactions of 'cage' **1a** were carried out using the light source from a lamp used for visualizing TLC plates at 313 nm (Spectroline ENF-260C, 1.3 mW/cm²).

²³⁹ Given the absorption intensity is similar to that for the free 'cage' **1a**, the amount of decorated UCNPs is estimated to be 10^{-5} M. This assumes the photochemistry of the free and anchored benzoin remains the same.

²⁴⁰ Monochromatic light centred at 290 nm was generated using a fluorescence spectrometer (PTI Quantmaster) with a 3 nm slit width.

²⁴¹ It is critical to stir the two identical CH₃CN solutions of **1a**[NaYF₄:TmYb] during the irradiation to ensure that representative UV-vis spectra are measured due to the small spot size of the light sources. Spectral changes were recorded over time until no further changes were observed at which time it was judged that the photo-release was complete.

²⁴² F. Hund, *Zeitschrift für anorganische Chemie* **1949**, 261, 106.

²⁴³ M. K. G. Jayakumara, N. M. Idrisa, and Y. Zhang, *Proc. Natl. Acad. Sci. USA*, **2012**, doi: 10.1073/pnas.1114551109.

²⁴⁴ C. Wang, L. Cheng, and Z. Liu, *Biomaterials*, **2011**, 32, 1110–1120.

²⁴⁵ J. A. Barreto, W. O'Malley, M. Kubeil, B. Graham, H. Stephan, and L. Spiccia, *Adv. Mater.* **2011**, 23, H18–H40.

²⁴⁶ X. Xue, F. Wang, and X. Liu, *J. Mater. Chem.*, **2011**, 21, 13107–13127.

²⁴⁷ S. Bhaskar, F. Tian, T. Stoeger, W. Kreyling, J. M. de la Fuente, V. Grazú, P. Borm, G. Estrada, V. Ntziachristos, and D. Razansky, *Particle and Fibre Toxicology*, **2010**, 7:3.

²⁴⁸ S. Jiang, M. K. Gnanasammandhan, and Y. Zhang, *J. R. Soc. Interface*, **2010**, 7, 3–18.

²⁴⁹ P. Rai, S. Mallidi, X. Zheng, R. Rahmzadeh, Y. Mir, S. Elrington, A. Khurshid, T. Hasan, *Adv. Drug Deliv. Rev.*, **2010**, 62, 1094–1124.

²⁵⁰ J. Pichaandi, J.-C. Boyer, K. R. Delaney, and F. C. J. M. van Veggel, *J. Phys. Chem. C*, **2011**, 115, 19054–19064.

²⁵¹ W. Wu, L. Yao, T. Yang, R. Yin, F. Li and Y. Yu, *J. Am. Chem. Soc.* **2011**, 133, 15810–15813.

²⁵² B. F. Zhang, M. Frigoli, F. Angiuli, F. Vetrone, J. A. Capobianco, *Chem. Commun.*, **2012**, DOI: 10.1039/c2cc33052k

²⁵³ Q. Liu, M. Chen, Y. Sun, G. Chen, T. Yang, Y. Gao, X. Zhang, and F. Li, *Biomaterials*, **2011**, 32, 8243–8253.

²⁵⁴ Y. Sun, M. Yu, S. Liang, Y. Zhang, C. Li, T. Mou, W. Yang, X. Zhang, B. Li, C. Huang, and F. Li, *Biomaterials*, **2011**, 32, 2999–3007.

²⁵⁵ Z. Zhao, Y. Han, C. Lin, D. Hu, F. Wang, X. Chen, Z. Chen, and N. Zheng, *Chem. Asian J.*, **2012**, on-line, doi: 10.1002/asia.201100879.

²⁵⁶ F. Chen, W. Bu, S. Zhang, X. Liu, J. Liu, H. Xing, Q. Xiao, L. Zhou, W. Peng, L. Wang, and J. Shi, *Adv. Funct. Mater.*, **2011**, 21, 4285–4294.

²⁵⁷ Phosphate and phosphonates has a high affinity to the nanoparticle surface.

- ²⁵⁸ C. T. Horovitz, *Biochemistry of Scandium and Yttrium, Part 1: Physical and Chemical Fundamentals*, Kluwer Academic/Plenum Publishers, New York, **1999**, p. 235-308
- ²⁵⁹ P. M. Smith, *Metall. Mater. Trans. B*, **2007**, *38B*, 763-768.
- ²⁶⁰ A. S. Karakoti, S. Das, S. Thevuthasan, and S. Seal, *Angew. Chem. Int. Ed.*, **2011**, *50*, 1980-1994.
- ²⁶¹ J. E. Hein and V. V. Fokin, *Chem. Soc. Rev.*, **2010**, *39*, 1302-1315.
- ²⁶² M. G. Finn and V. V. Fokin, *Chem. Soc. Rev.*, **2010**, *39*, 1231-1232.
- ²⁶³ H. C. Kolb, M. G. Finn and K. B. Sharpless, *Angew. Chem., Int. Ed.*, **2001**, *40*, 2004-2021.
- ²⁶⁴ V. V. Rostovtsev, L. G. Green, V. V. Fokin, K. B. Sharpless, *Angew. Chem. Int. Ed.*, **2002**, *41*, 2596-2599.
- ²⁶⁵ (a) A. S. Prakash, W. A. Denny, T. A. Gourdie, K. K. Valu, P. D. Woodgate, and L. P. G. Wakelin, *Biochemistry*, **1990**, *29*, 9799-9807. (b) J. L. Holley, A. Mather, R. T. Wheelhouse, P. M. Cullis, J. A. Hartley, J. P. Bingham, and G. M. Cohen, *CANCER RESEARCH*, **1992**, *52*, 4190-4195.
- ²⁶⁶ Q. Lin, Q. Huang, C. Li, C. Bao, Z. Liu, F. Li, and L. Zhu, *J. Am. Chem. Soc.*, **2010**, *132*, 10645-10647.
- ²⁶⁷ S. Härtner, H.-C. Kim, N. Hampp, *J. Polym. Sci. Part A: Polym. Chem.*, **2007**, *45*, 2443-2452.
- ²⁶⁸ *Dynamic Studies in Biology. Phototriggers, Photoswitches and Caged Biomolecules*. Edited by M. Goeldner, R. Givens, WILEY-VCH Verlag GmbH & Co. KGaA, Weinheim, **2005**, ISBN: 3-527-30783-4, pp. 31, 83 and references therein
- ²⁶⁹ *Dynamic Studies in Biology. Phototriggers, Photoswitches and Caged Biomolecules*. Edited by M. Goeldner, R. Givens, WILEY-VCH Verlag GmbH & Co. KGaA, Weinheim, **2005**, ISBN: 3-527-30783-4, pp. 32, 38, 42 and references therein
- ²⁷⁰ L.-J. Chen and L. T. Burka, *Tetrahedron Lett.*, **1998**, *39*, 5351-5354.
- ²⁷¹ A. Barth, J. E. T. Corrie, M. J. Gradwell, Y. Maeda, W. Mäntele, T. Meier and D. R. Trentham, *J. Am. Chem. Soc.* **1997**, *119*, 4149-4159.
- ²⁷² L. Zhang, R. Buchet, and G. Azzar, *Biophys. J.*, **2004**, *86*, 3873-3881.
- ²⁷³ A. M. Kloxin, A. M. Kasko, C. N. Salinas, K. S. Anseth, *SCIENCE*, **2009**, *324*, 59-63.
- ²⁷⁴ A. Almutairi *et. al.*, *unpublished results*.
- ²⁷⁵ (a) C. Wiles, P. Watts, S. J. Haswell, *Tetrahedron Lett.*, **2007**, *48*, 7362-7365. (b) S. K. De, *Tetrahedron Lett.*, **2004**, *45*, 2339-2341. (c) S. K. De, *Tetrahedron Lett.*, **2004**, *45*, 1035-1036. (d) A. T. Khan, E. Mondal, P. R. Sahu, S. Islam, *Tetrahedron Lett.*, **2003**, *44*, 919-922
- ²⁷⁶ Y.-C. Wu, J. Zhu, *J. Org. Chem.* **2008**, *73*, 9522-9524.
- ²⁷⁷ D. Seebach and E. J. Corey, *J. Org. Chem.*, **1975**, *40*, 231-237.
- ²⁷⁸ The reaction produces the dithiane-protected benzoin as a racemate of two enantiomers.
- ²⁷⁹ H. B. Lee and S. Balasubramanian, *J. Org. Chem.*, **1999**, *64*, 3454-3460.
- ²⁸⁰ B. Neises and W. Steglich, *Angew. Chem. Int. Ed.*, **1978**, *17*, 522-524.

- ²⁸¹ Such a DLS study should be performed under strictly sterile conditions to prevent formation of bacteria and/or other microbes from developing in the nutrient-rich serum, as they will cause artifacts in the DLS spectra.
- ²⁸² E. A. Newsholme and P. J. Randle, *Biochem. J.*, **1964**, *93*, 641-651.
- ²⁸³ D. Ferrari, P. Chiozzi, S. Falzoni, M. D. Susino, L. Melchiorri, O. R. Baricordi, and F. Di Virgilio, *J. Immunol.*, **1997**, *3*, 1451-1458.
- ²⁸⁴ J.-C. Boyer, M. P. Manseau, J. I. Murray, F. C. J. M. van Veggel, *Langmuir*, **2010**, *26*, 1157-1164.
- ²⁸⁵ F. Wang, J. Wang, X. Liu, *Angew. Chem. Int. Ed.*, **2010**, *49*, 7456-7460.
- ²⁸⁶ The ¹H NMR spectra of the mPEGylated ligand **5** is quite complex and the fate of Chlorambucil can potentially be difficult to elucidate.
- ²⁸⁷ C.-J. Carling, *unpublished results*.
- ²⁸⁸ See molecule **1a** in Chapter 6.
- ²⁸⁹ The water used in the experiment was distilled water from the laboratory tap and could potentially be the source of the peaks ranging from 400-800 m/z.
- ²⁹⁰ C.-J. Carling, C. C. Warford, J.-C. Boyer and N. R. Branda, *unpublished results*.
- ²⁹¹ The quantum yield of the photocage has not been measured to date and this statement remains to be verified.
- ²⁹² Data not available from the papers,^[190,191] but based on the findings from chapter 10 it should display similar molar absorption coefficient as the novel donor-acceptor benzoin photocage **1** in chapter 10.
- ²⁹³ M. M. Dcona, D. Mitra, R. W. Goehe, D. A. Gewirtz, D. A. Lebman, and M. C. T. Hartman, *Chem. Commun.*, **2012**, *48*, 4755-4757.
- ²⁹⁴ S. Ki Choi, T. Thomas, M.-H. Li, A. Kotlyar, A. Desai, and J. R. Baker, Jr, *Chem. Commun.*, **2010**, *46*, 2632.
- ²⁹⁵ J. A. Johnson, Y. Y. Lu, A. O. Burts, Y. Xia, A. C. Durrell, D. A. Tirrell, and R. H. Grubbs, *Macromolecules*, **2010**, *43*, 10326-10335.
- ²⁹⁶ J. A. Johnson, *Ph.D. Thesis*. Construction of stimuli-responsive polymers and polymer networks using controlled, living polymerizations and highly efficient organic reactions, p. 123-130.
- ²⁹⁷ N. Sanna, G. Chillemi, L. Gontrani, A. Grandi, G. Mancini, S. Castelli, G. Zagotto, C. Zazza, V. Barone, A. Desideri, *J. Phys. Chem. B*, **2009**, *113*, 5369-5375.
- ²⁹⁸ Reactive end groups such as amine, carboxylic acid, maleimide or succinimidyl succinate can be used to further derivatize the PEG with biologically active targeting ligands.
- ²⁹⁹ (a) H. Veisi, R. Ghorbani-Vaghei, D. Ramin, A. Somayeh, *J. Heterocycl. Chem.*, **2011**, *48*, 699-705. (b) C.-T. Chen, Y.-D. Lin, C.-Y. Liu, *Tetrahedron*, **2009**, *65*, 10470-10476. (c) Y. Ouyang, D. Dong, Y. Liang, Y. Chai, Q. Liu, *Synth. Commun.*, **2007**, *37*, 993-1000. (d) D. Dong, Y. Ouyang, H. Yu, Q. Liu, J. Liu, M. Wang, J. Zhu, *J. Org. Chem.*, **2005**, *70*, 4535-4537. (e) S. Naik, R. Gopinath, M. Goswami, B. K. Patel, *Org. Biomolec. Chem.*, **2004**, *2*, 1670-1677.
- ³⁰⁰ G. L. Gibson, T. M. McCormick, D. S. Seferos, *J. Am. Chem. Soc.*, **2012**, *134*, 539-547.

³⁰¹ U. A. Hrozhyk, S. V. Serak, N. V. Tabiryan, L. Hoke, D. M. Steeves, B. Kimball, G. Kedziora, *Mol. Cryst. Liq. Cryst.*, **2008**, 489, 257/[583]-272/[598].

³⁰² (a) J.-L. Debieux, A. Cosandey, C. Helgen, C. G. Bochet, *Eur. J. Org. Chem.*, **2007**, 13, 2073-2077. (b) M. C. Pirrung, T. Ye, Z. Zhou, J. D. Simon, *Photochem. Photobiol.*, **2006**, 82, 1258-1264. (c) M. C. Pirrung, S. W. Shuey, *J. Org. Chem.*, **1994**, 59, 3890-3897.

³⁰³ Since the concentration of EtOAc is not known these results are preliminary and a new proper ¹H NMR release study should be performed to properly identify the yield of the photolysis.